UNCLASSIFIED

AD NUMBER
AD384855

CLASSIFICATION CHANGES

TO:	UNCLASSIFIED
FROM:	CONFIDENTIAL

LIMITATION CHANGES

TO:

Approved for public release; distribution is unlimited.

FROM:

Distribution authorized to U.S. Gov't. agencies and their contractors; Critical Technology; SEP 1967. Other requests shall be referred to Air Force Rocket Propulsion Laboratory, Attn: Research and Technology Division, AFRPL(RPPR-STINFO), Edwards AFB, CA 93523. This document contains export-controlled technical data.

AUTHORITY

AFRPL ltr dtd 15 Mar 1971; AFRPL ltr dtd 5 Feb 1986

THIS PAGE IS UNCLASSIFIED

AD **384 855**

AFRPL-T R-67-246-Vol I

AD 384855

U

(Unclassified Title)

FINAL REPORT, ADVANCED AERODYNAMIC SPIKE CONFIGURATIONS

Volume I
Analytical and Cold Flow Studies

Rocketdyne Advanced Projects, Large Engines

Rocketdyne
A Division of North American Aviation, Inc.

TECHNICAL REPORT AFRPL-TR-67-246-Vol I

September 1967

Group 4
Downgraded at 3- Year Intervals
Declassified After 12 Years

C

In addition to security requirements which must be met, this document is subject to special export controls and each transmittal to foreign governments or foreign nationals may be made only with prior approval of AFRPL(RPPR-STINFO), Edwards, California 93523.

Air Force Rocket Propulsion Laboratory
Research and Technology Division
Edwards, California 93523
Air Force Systems Command
United States Air Force

When U.S. Government drawings, specifi-
cations, or other data are used for any
purpose other than a definitely related
Government procurement operation, the
Government thereby incurs no responsi-
bility nor any obligation whatsoever,
and the fact that the Government may
have formulated, furnished, or in any
way supplied the said drawings, speci-
fications, or other data, is not to be
regarded by implication or otherwise,
or in any manner licensing the holder
or any other person or corporation, or
conveying any rights or permission to
manufacture, use, or sell any patented
invention that may in any way be re-
lated thereto.

DISCLAIMER NOTICE
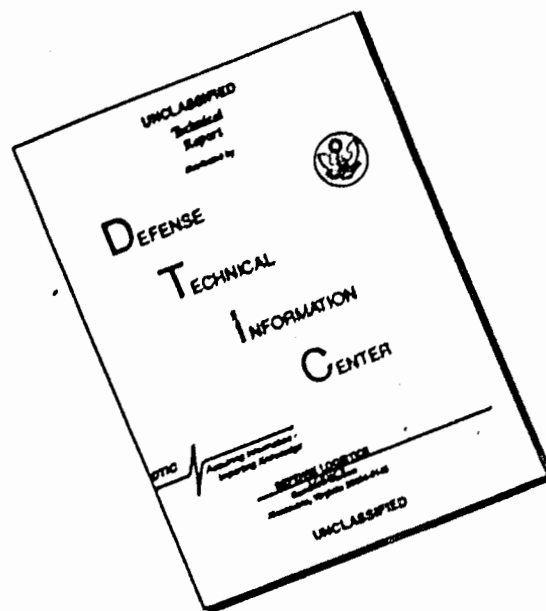
THIS DOCUMENT IS BEST
QUALITY AVAILABLE. THE COPY
FURNISHED TO DTIC CONTAINED
A SIGNIFICANT NUMBER OF
PAGES WHICH DO NOT
REPRODUCE LEGIBLY.

AFRPL-TR-67-246-Vol I

(Unclassified Title)

FINAL REPORT, ADVANCED
AERODYNAMIC SPIKE CONFIGURATIONS

VOLUME I
ANALYTICAL AND COLD FLOW STUDIES

Rocketdyne Advanced Projects, Large Engines

```
Group 4
Downgraded at 3-Year Intervals
Declassified After 12 Years
```

In addition to security requirements which must be met, this document is
subject to special export controls and each transmittal to foreign govern-
ments or foreign nationals may be made only with prior approval of
AFRPL (RPPR-STINFO), Edwards, California 93523.

FOREWORD

(U) This report was prepared in compliance with Contract AF04(611)-9948 covering the period 1 July 1964 through 28 February 1967. This study was conducted for the Air Force Rocket Propulsion Laboratory, Edwards, California. The program structure number is 750G and the project number is 3058. The Rocketdyne internal report number is R6959. Classified information has been extracted from (asterisked) documents listed under References.

(U) This technical report has been reviewed and is approved.

Roy Silver
Project Engineer
Air Force Rocket Propulsion
Laboratory
Edwards, California

ABSTRACT (VOLUME I)

(U) Investigations of the aerodynamic spike nozzle concept
are discussed in this report. These investigations
include experimental cold-flow testing of high-area
ratio aerospikes, aerospike nozzles with various
combustor configurations and various size segments
of aerospike nozzles and parametric analytical
application studies for the nozzle concept. One
cold-flow test series investigated the performance
of very high area ratio (ϵ = 150) short length aero-
spike nozzles using helium as the test fluid. A
ten percent length contoured nozzle and a six percent
length conical nozzle were tested. Theoretical and
experimental performance results are presented. The
second cold-flow test series determined the performance
of a series of aerospike nozzles having various combustor
configurations. The effect of nozzle base bleed and
intermodule bleed on performance was investigated.
Combustor configurations consisted of shrouded and
unshrouded continuous annular (toroidal) combustors
and multichamber configurations with eight and
sixteen discrete conventional combustors clustered
around a common spike. Spacing between chambers,
spike length, and engine shrouding were varied for
the multi-chamber configurations. All nozzles had
an area ratio of 50. Theoretical and experimental
performance results are presented. A third cold-flow
test series investigated the relative nozzle wall and
base pressures for 45, 90, and 180 degree segments of
an aerospike nozzle compared to a full annular aero-
spike. Experimental results are presented. Analytical
and design studies were made to determine effective
methods of utilizing toroidal and multichamber construc-
tions for aerodynamic spike configurations over a wide
range of thrust level, chamber pressure, and nozzle
area ratio. Design layouts at several thrust levels
of interest are presented. Heat transfer studies
establishing cooling feasibility and parametric weight
studies are described. Combustor effects on nozzle
performance are discussed.

ABSTRACT (VOLUME II)

(C) Three hot-firing aerodynamic spike nozzle programs are described. One
program had as its objective to obtain a large background of parametric
hot-firing aerospike performance data. Performance data were obtained
over a range of pressure ratio from approximately 350 down to 22.
Thirty 8-second each duration firings, 10 at near sea level conditions
and 20 over a range of high pressure ratio, were conducted. Secondary
flowrate was varied from zero to 5 percent of primary flowrate and
supplied by a gas generator utilizing N_2O_4/UDMH-N_2H_4 (50-50) propellants.
GG mixture ratio was varied from approximately 0.10 to 0.18 at 3 percent
secondary flowrate to determine the effect of secondary gas energy level.
The 12 percent length aerospike thrust chamber had an area ratio of
26 and generated approximately 7400 pounds of thrust at design altitude
and 300 psia chamber pressure. Gains in nozzle efficiency were noted
with the use of up to 3 percent secondary flowrate. A high degree of
altitude compensation was noted with this engine down to a pressure
ratio equal to approximately 12 percent of design pressure ratio
(approximately 300). A complete tabulation of performance is given.
For the second program, the nozzle section of the above engine was
lengthened to 25 percent (of an equivalent 15 degree conical nozzle)
and modified to incorporate liquid (N_2O_4) side injection TVC capability.
Thirty-three firings of 6 seconds each duration were conducted at
altitude to determine liquid injection TVC performance trends with
variations in injection parameters. Results are compared with theory
and applied to typical applications. LITVC performance with N_2O_4 was
generally low and other injection fluids and techniques are recommended.
A third hot-firing test program was conducted to determine the influence
of external flow on in-flight nozzle performance. An aerospike thrust
chamber using H_2O_2 propellants was enclosed by a simulated vehicle
body. The engine generated 400 pounds of thrust at a chamber pressure
of 200 psia. The 20 percent length aerospike nozzle had an area ratio
of 25 and was tested over a range of pressure ratio from 30 to 470 and
at slipstream Mach numbers of 0, 0.55, 0.90, 1.20, 1.40, 1.80 and
2.2. Fifty-seven firings of 1 minute each duration were accomplished.
Still air nozzle efficiency was very high and significant performance
improvement was obtained with the addition of secondary flow. Nozzle
performance was relatively unaffected by slipstream in the nozzle
operating region of practical interest for booster engine application.

TABLE OF CONTENTS

▼

ILLUSTRATIONS

ILLUSTRATIONS (Continued)

ILLUSTRATIONS (Continued)

ILLUSTRATIONS (Continued)

ILLUSTRATIONS (Continued)

ILLUSTRATIONS (Continued)

ILLUSTRATIONS (Continued)

xiii

ILLUSTRATIONS (Continued)

ILLUSTRATIONS (Continued)

ILLUSTRATIONS (Continued)

ILLUSTRATIONS (Continued)

TABLES

NOMENCLATURE

a	Speed of sound
A	Area
a^*	Speed of sound at $M = 1$
A^*	Aerodynamic throat area
A_b	Aerospike base area
A_e	Nozzle exit area
A_t	Primary throat area
a_t	Module throat area
C^*	Characteristic velocity
C_D	Nozzle discharge coefficient
C_F	Thrust coefficient of performance, $F/P_c A_t$
C_{Fb}	Base thrust coefficient
$C_{F_{drag}}$	Thrust coefficient loss from drag
$C_{F_{int}}$	Primary nozzle thrust coefficient
$C_{F_{opt}}$	Maximum C_F referenced to pressure ratio
C_{F_p}	Primary nozzle thrust coefficient
$C_{F_{pi}}$	Ideal thrust coefficient based on primary fluid properties
C_p	Heat capacity at constant pressure
C_T	Nozzle Efficiency
d	Toroidal tube diameter in the throat region
D	Toroidal tube diameter in the chamber region
D_{CL}	Multichamber envelope diameter
D_e	Module exit diameter
f	Weight flow function, $\dot{W} \sqrt{T_o}/P_o A_t$
F	Thrust
F_b	Thrust contribution from aerospike base

F_{int}, F_p	Primary nozzle thrust
F_{opt}, F_{pi}	Ideal thrust based on primary fluid properties and pressure ratio
g_c	Dimensional constant, 32.174 ft-lb$_m$/lb$_f$-sec^2
G	Mass velocity
g	32.2 ft/sec^2
H, h	Enthalpy
h_c	Coolant-side film heat transfer coefficient
h_g	Gas-side film heat transfer coefficient
I_s	Specific impulse
$I_{s_{pi}}$	Ideal specific impulse based on primary fluid properties and pressure ratio
J	Conversion factor, 778.26 ft-lb$_f$/Btu
K	1000 pounds thrust
K_1	Empirical base pressure factor
k	Thermal conductivity
L^*	Characteristic length
L_m	Projected axial length from module throat to module exit
L_N	Total nozzle axial length from throat
L_p	Length of multichamber plug from module exit to plug exit
$\dot{m}$	Mass flow
M	Mach number
M_{es}	Mach number of secondary fluid at base exit plane
N	Number of modules per cluster
P	Pressure
P_a	Ambient pressure
P_b	Base pressure
P_c	Primary chamber pressure

P_{cowl}	Average pressure acting on nozzle cowl
P_{max}	Maximum pressure in recompression region
P_r	Pressure at the flow reattachment point
P_w	Primary nozzle wall pressure
P.R.	Pressure ratio, P_c/P_a
$q, Q/A$	Heat flux
$\bar{R}$	Universal gas constant
R^*	Equivalent aerodynamic throat radius, $\sqrt{A^*/\pi}$
R_B	Base radius at nozzle exit
R_c	Toroidal combustion chamber radius
R_t	Equivalent geometrical throat radius, $\sqrt{A_t/\pi}$
S	Entropy
s	Length
T	Temperature
T^*	Temperature at $M = 1$
T_{AW}	Adiabatic wall temperature
T_B	Coolant bulk temperature
T_{WC}	Coolant-side wall temperature
T_{WG}	Gas-side wall temperature
T_p	Primary gas total temperature
T_x	Reference temperature
T_∞	Free stream temperature
V, v	Velocity
V_∞	Free stream velocity
$\dot{w}_p$	Primary fluid flowrate
$\dot{w}_s$	Secondary fluid flowrate
X	Axial distance along sting from nozzle exit plane
x	Wall thickness

GREEK SYMBOLS

α	Shroud half angle measured from shroud tilt angle β
β	Shroud tilt angle
$\tilde{\gamma}$	Ratio of specific heats
δ	Gap between modules or toroidal tubes
$\epsilon, \epsilon_e \epsilon_o$	Nozzle area ratio
ϵ_b	Base area ratio
ϵ_c	Module contraction ratio
ϵ_{CL}	Multichamber geometric area ratio
ϵ^*_{CL}	Multichamber geometric area ratio referenced to A*
ϵ_{cowl}	Cowl area ratio
ϵ_M	Module area ratio
ϵ^*	Nozzle area ratio referenced to A*
ϵ_{total}	Nozzle area ratio including cowl and base areas
θ_c	Module contraction half angle
θ_T	Module tilt angle
μ	Viscosity
μ_∞	Free stream viscosity
ρ	Density
ρ_∞	Free stream density
ρ^*	Density at M = 1
ϕ	Heat transfer enhancement factor from curvature effects
φ	Heat transfer enhancement factor from chemical dissociation

SUBSCRIPTS

a	Ambient conditions
b	Base

c	Chamber conditions
e	Exit conditions
i.s.	Intersegmental (between modules)
M	Individual module
Mod	Model
o	Stagnation conditions
p	Primary flow
s	Secondary flow
v	Venturi flowmeter
w	Wall
∞	Free stream conditions

SECTION I

INTRODUCTION AND SUMMARY

(U) During recent years, various new thrust chamber configurations have been introduced. The ultimate objective of these advanced concepts has been to provide efficient nozzle performance with short, light-weight structures. One promising approach to this goal is referred to as the aerodynamic spike nozzle concept. Figure 1 shows a model of an aerodynamic spike nozzle with an advanced (toroidal) combustion chamber along with a similar thrust conventional engine. In this configuration, the nozzle, as we know it today, is virtually eliminated.

(C) The aerodynamic spike was readily envisioned as a method of shortening the spike (plug) contour. High pressure gases are exhausted from an annular-type combustion chamber with low-pressure gases coming out of the central portion. By this action an interface, similar to a nozzle, is formed between the flows. The thrust contribution normally attributed to a nozzle is obtained by the pressure of the secondary gases acting over the base region. Outwardly, this configuration looks much like a short length plug. However, the introduction of secondary gases produces flow fields (Fig. 2) and performance comparable with much longer plug nozzle types. This secondary flow has proven to be of benefit to nozzle performance.

(C) Performance of the aerodynamic spike nozzle is a function of various nozzle geometric parameters, of the amount of secondary flow, of the manner in which this secondary flow is introduced and of the relative energy between the primary and secondary streams. Investigation of these parameters was initiated under North American Aviation independent research studies in 1959. Since that time, the aerodynamic spike nozzle has been evaluated both experimentally and theoretically. Study

1
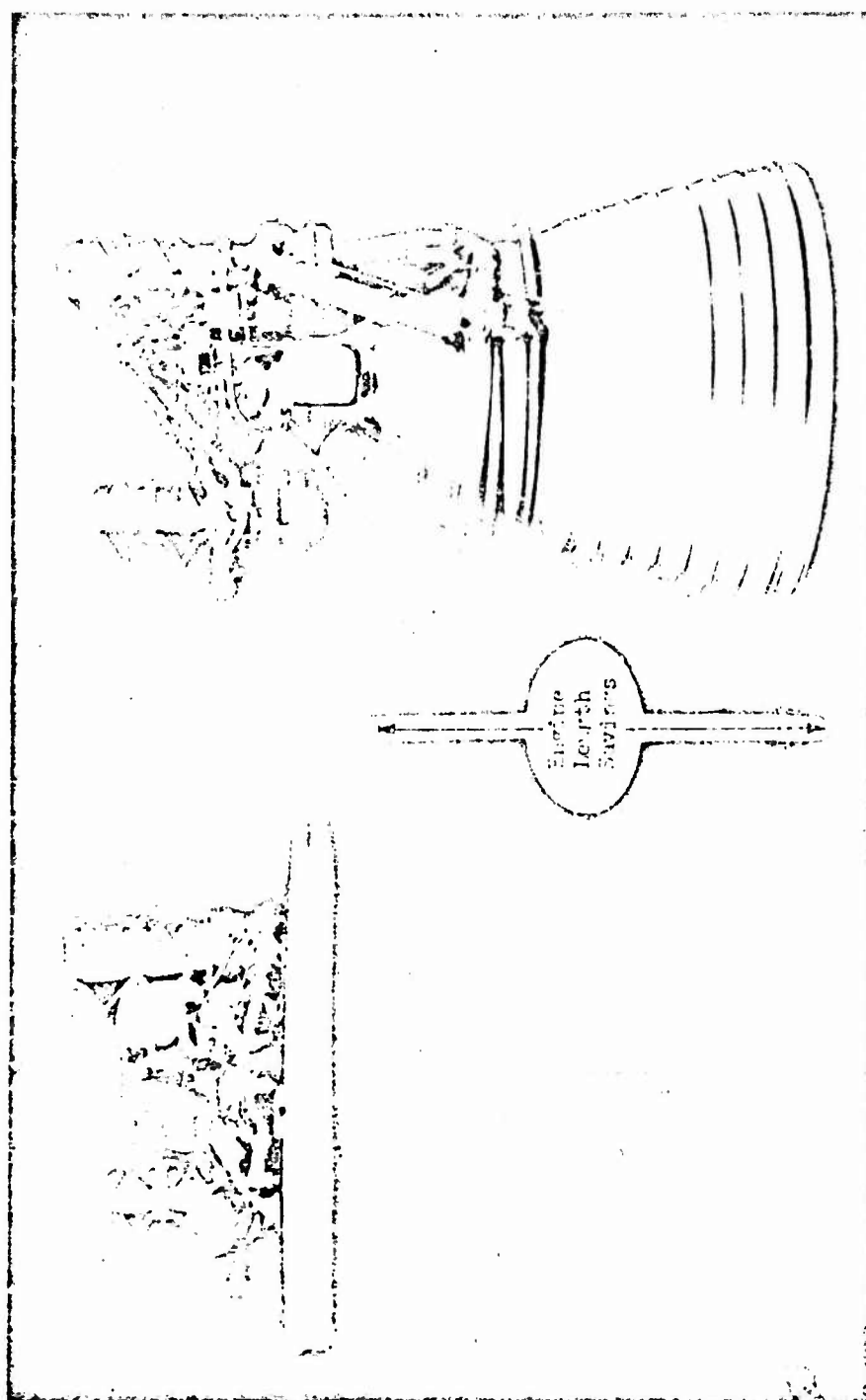
Figure 1. Aerodynamic Spike Engine With Conventional Engine of Similar Thrust

Conventional Spike Nozzle

CONFIDENTIAL

Aerodynamic Spike Concept

Figure 2. Spike Nozzle Concepts

3

programs have systematically investigated the various performance
parameters and evaluated their influence on nozzle efficiency. The
result of this continuous effort is a comprehensive knowledge and
understanding of the aerodynamic spike concept.

(c) Investigations have shown that the use of the aerodynamic spike con-
figuration reduces engine length, weight, and cooling surfaces
exposed to primary combustion products. These short nozzles exhibited
very high nozzle efficiencies, equal to and in most cases superior
to the performance of the conventional 80 percent length optimally
contoured bell nozzle. In addition to the high nozzle efficiency at
design pressure ratios, the aerodynamic spike nozzle provides an
extremely high degree of altitude compensation. The requirement for
low pressure secondary flows also provides a convenient high perform-
ance method of utilizing turbine exhaust gases.

(U) Although verification of these potential gains had been achieved,
several aspects of the aerodynamic spike nozzle concept had not been
explored. In order to further the development of this concept, the
Advanced Aerodynamic Spike Configurations Study was initiated in
July 1964 under contract AF04 (611)-9948. It was the goal of this
study to: (1) evaluate its performance characteristics at high area
ratios, (2) compare methods of applying the concept to advanced
vehicle configurations, and (3) demonstrate nozzle performance
capabilities in a comprehensive hot-firing test series.

(U) In December 1965 the scope of the program was broadened to include:
(1) a hot-firing investigation of thrust vector control characteristics
of an aerodynamic spike nozzle using liquid side-injection, (2) a hot-
firing investigation of aerospike performance when operating in a

typical flight environment, (3) an analytical investigation of nozzle base bleed configurations and a hot-firing demonstration of a promising configuration, and (4) a cold-flow investigation of aerospike nozzle segment performance.

(U) All areas of investigation have been completed. Volume I presents the results of the cold-flow test programs and the analytical and design studies. Volume II presents the results of the hot-firing test programs. The contents of Volume I are summarized in the following paragraphs.

(C) A cold-flow test program was conducted to evaluate aerodynamic spike nozzle performance at high area ratio. A 10-percent-length nozzle contoured for maximum primary thrust and with a 150 area ratio and a 45 degree conical nozzle 6 percent in length with an area ratio of 130 were tested using helium as the primary and secondary fluid. A nozzle efficiency of 99.6 percent was achieved with secondary flow with the 10-percent length, contoured nozzle. The effect of the quantity and method of introduction of secondary flow was investigated. Measurements were made of the pressure distribution in the wake of the nozzles. Good agreement was obtained between theoretical performance predictions and experimental data and the wake measurements verified the analytical flow models used.

(U) A second cold-flow test series investigated the effect of combustor configuration on aerodynamic spike nozzle performance. The specific goal was to couple closely the effects of nozzle contour, combustor shape and the use of secondary gas. To accomplish this, a group of multichamber and annular aerodynamic spike nozzles were tested. These particular cold-flow data combined with available data for various

toroidal configurations may be utilized to evaluate the potential performance of combustor and nozzle designs. An additional cold-flow model which was tested, was a scaled version of a 10,000-pound thrust hot-firing thrust chamber. A direct comparison of cold-flow and hot-firing performance was made (Volume II) with these geometrically similar nozzles.

(c) Analytical and design studies were made to determine effective methods of utilizing toroidal and multichamber constructions for aerodynamic spike configurations. Design layouts were completed at thrust levels of 40,000 pounds, 350,000 pounds, 656,000 pounds, and 2,000,000 pounds. Heat transfer studies establishing cooling feasibility and parametric weight studies were conducted. A comparison of the relative reliability, cost and versatility of toroidal and multichamber aerospike and conventional engine systems was made.

(U) A cold-flow test program was undertaken to determine the performance of segments of an aerospike nozzle. A full 360 degree cold-flow aerospike model was fitted with splitter plates to obtain nozzle segment test configurations of 45 degrees, 90 degrees, and 180 degrees. The nozzle wall and base pressures obtained for the segmented nozzles are compared to the full annular values.

(U) The first section of this report contains a qualitiative description of the principles of operation and the flow regimes for the aerodynamic spike nozzle concept. This should serve to quickly familiarize the reader with the concept and more readily grasp the detailed results presented in the following sections.

SECTION II

THE AERODYNAMIC SPIKE NOZZLE CONCEPT

(c) The aerodynamic spike nozzle concept is based upon the fact that, by suitable design, an ideal, maximum-efficiency spike nozzle can be truncated to a small fraction of its initial length with only a small loss in efficiency. As the spike contour length decreases, the nozzle base area increases and the pressure acting on the base pressure area provides a performance contribution compensating, in part, for the diminishing performance of the primary (isentropic) flow field. In addition, the proper use of secondary mass bleed into the base region of a truncated spike nozzle increases the base pressure contribution, compared to a zero-bleed system, and results in a relatively short nozzle with the high overall performance.

FLOW FIELD BEHAVIOR

(c) An understanding of the primary flow field behavior and the base pressure phenomenon is essential to the formulation of an analytical model of the aerodynamic spike nozzle. The phenomenon is depicted in Fig. 3 for a highly simplified model of uniform flow over a backward-facing step. Reattachment and simultaneous change of direction of the potential flow field produces a recirculating flow in the base which is instrumental in establishing the base pressure. The recirculating fluid consists of low-energy, boundary-layer flow, which is turned back by the increasing pressure gradient in the region of reattachment. This process is viscous in nature.

(c) During operation at high pressure ratios (chamber pressure-to-ambient pressure), the characteristics of the primary flow field upstream of the base, shown as Region 1 in Fig. 4, are determined only by the
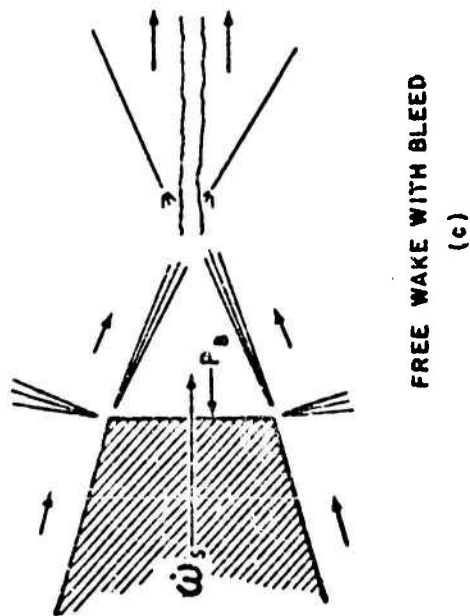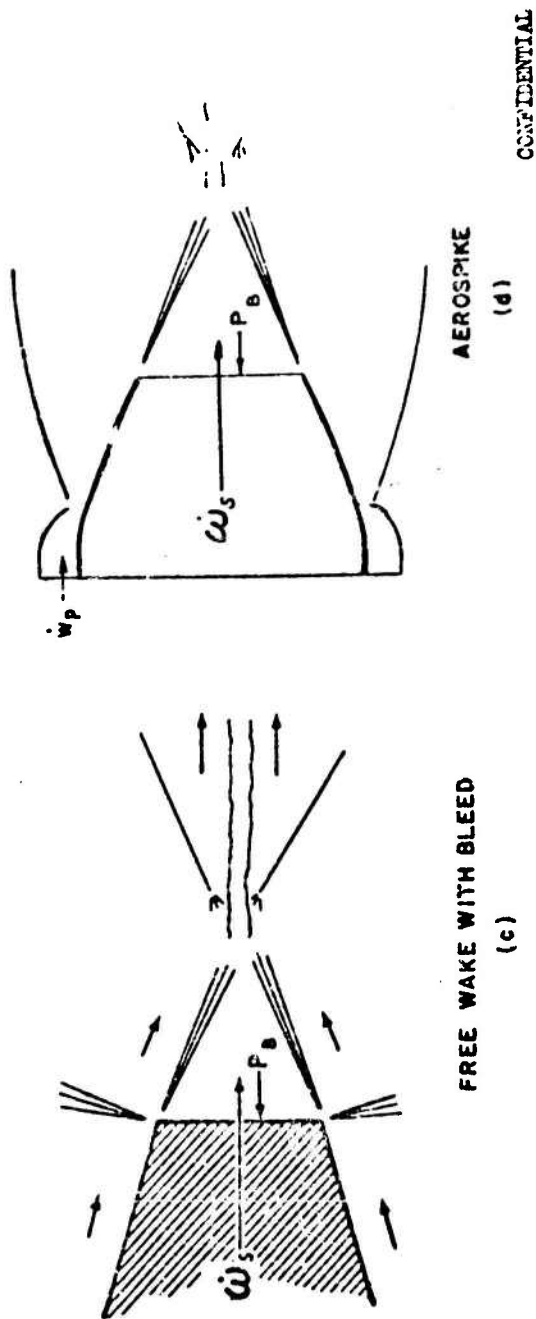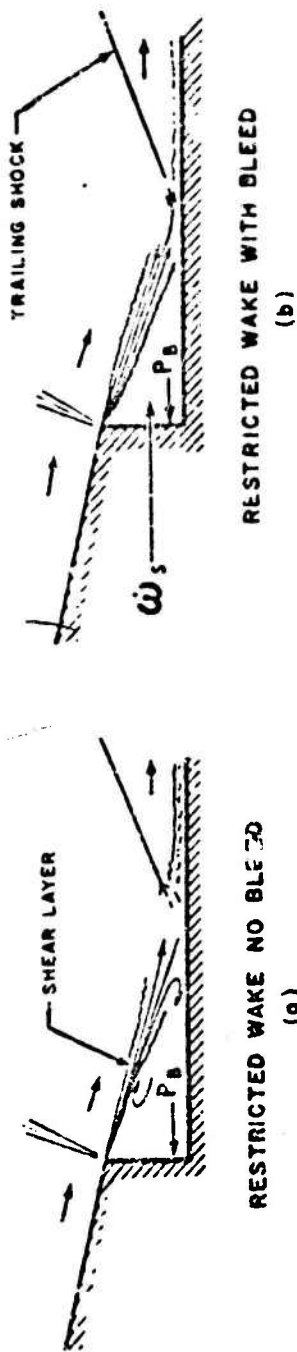
Figure 3 . Aerospike Nozzle Principle of Operation

CONFIDENTIAL

RECOMPRESSION SHOCK (TRAILING SHOCK)

REATTACHMENT REGION

WAKE ⑤

INITIAL BOUNDARY LAYER

BASE CORE

SHEAR LAYER

②

③

LIP

④

INVISCID FLOW FIELD ①
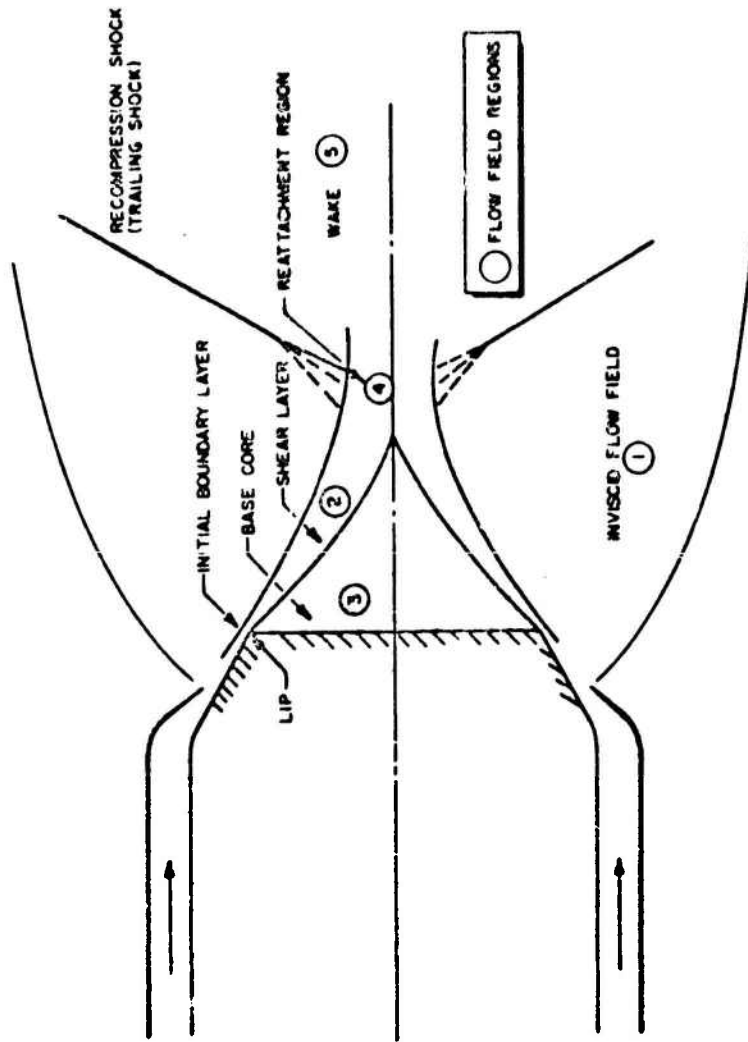
○ FLOW FIELD REGIONS

Figure 4. Aerospike Flow Field Model

9

throat and contour geometry. In Region 2, the flow expands around the
lower lip of the model and detaches, forming a free shear layer which
separates the external flow from a region of subsonic recirculating
gases in the base. The inner free-jet boundary is not affected by
ambient pressure waves from the outer-jet boundary, and thus is inde-
pendent of pressure ratio. The flow along the inner-jet boundary
and its adjacent shear layer impinges on the centerline where it
reattaches and recompresses through a trailing shock. This condition
is referred to as closed-wake flow, and the base pressure is constant
and higher than ambient so that a positive thrust acting on the base
is developed. Ambient pressure effects are not felt on the nozzle
contour or base. The basic mechanism governing the base pressure in
this regime is flow reattachment.

(c) When a small amount of secondary flow is introduced into the base
(at a constant ambient pressure) and the base pressure increases, the
inner free-jet boundary of the primary stream still impinges on the
centerline; however, the angle of impingement becomes shallower as the
base pressure increases (Fig. 5). Schlieren photographs of a
typical configuration are shown in Fig. 6 , for increasing secondary
flowrates at the design pressure ratio. Higher base pressures result
because the secondary flow modifies the shear layer characteristics,
i.e., increases the viscous entrainment region between the primary
and secondary flow regions. The modification of the shear layer is
accompanied by a change in the flow in the reattachment region (Region 4)
resulting in increased base pressure.

(C) As the amount of secondary bleed increases, the base pressure also
increases until a condition is reached where the inner boundary of the
primary flow no longer impinges on the axis. Some of the base bleed
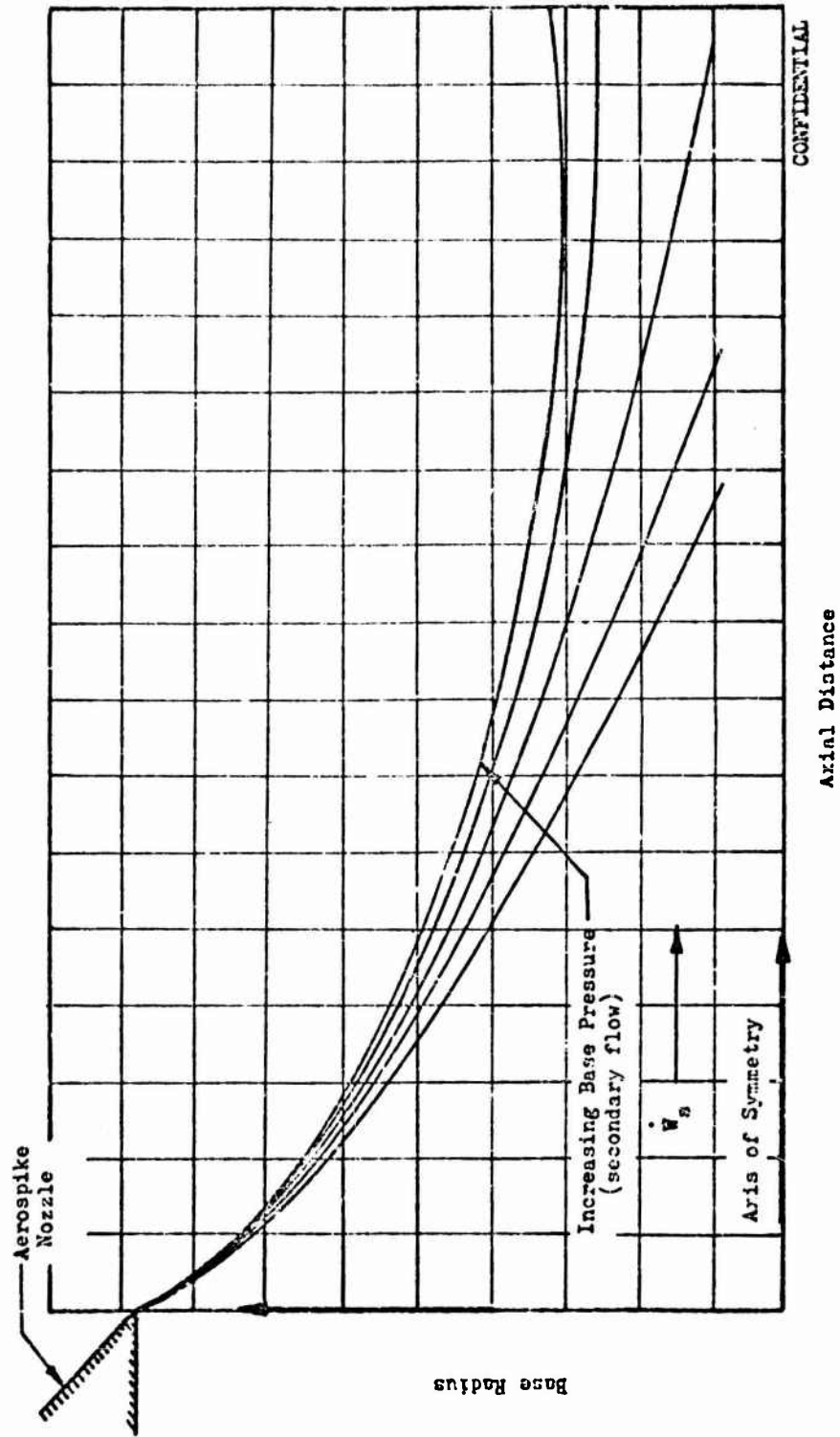
Figure 5. Typical Solution of Aerodynamic Spike Free Jet Boundary with Various Secondary Flows

(a) $\dot{W}_s/\dot{W}_p$ = 0 percent
PR = 1162

(b) $\dot{W}_s/\dot{W}_p$ = 0.48 percent
PR = 1176
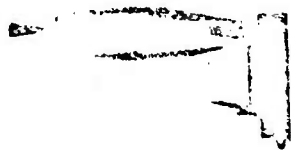
(c) $\dot{W}_s/\dot{W}_p$ = 1.02 percent
PR = 1164
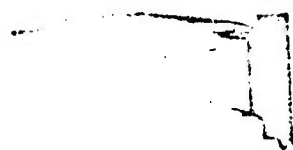
(d) $\dot{W}_s/\dot{W}_p$ = 1.56 percent
PR = 1176   CONFIDENTIAL

Figure   6. Optimum Nozzle (12-Percent Length) With Increasing
Secondary Flowrate, Schlieren Photographs

then is transmitted into the wake region through a central core; this core grows as the secondary bleed rate continues to increase. A decreasing pressure gradient then exists in the base region, and the secondary flow is accelerated by pressure as well as viscous forces.

(c) As the pressure ratio decreases, the nature of the flow field changes considerably. The intersection of the envelope shock and the inner free-jet boundary moves upstream toward the reattachment point as the pressure ratio decreases. This can be observed in the series of Schlieren photographs in Fig. 7. When the reattachment point (Fig. 7b and 7c) is reached, the wake starts to open. The base region then begins to feel the influence of the higher ambient pressure. When the wake opens, the base pressure no longer remains constant (at a constant secondary flowrate), but increases with increasing ambient pressure (decreasing pressure ratios). This open-wake base pressure is, in many cases, greater than ambient pressure. Further decreases in pressure ratio will cause the envelope shock to impinge finally on the nozzle contour (Fig. 7f), causing recompression of the primary flow. The recompression phenomenon yields increased wall pressures at high ambient pressures, eliminating overexpansion losses common to conventional high-area-ratio nozzles operating at low altitudes. Thus, base pressure and nozzle recompression compensate for the ambient condition, and are responsible for the altitude compensating feature of the aerospike nozzle. The wall pressures due to recompression can be considerably higher than ambient or base pressures. Conventional bell nozzles cannot experience recompression nor adjusting nozzle exit pressure (comparable to aerospike base pressure) since the primary flow field is internal to the nozzle hardware. The aerospike nozzle, therefore, exhibits a performance advantage over a convent. al nozzle since the recompression and base pressure phenomena result in good low-altitude performance for a high-area-ratio nozzle without compromising design point performance.

(a) PR = 899

CLOSE WAKE (P_b = CONST.)

(b) PR = 397

OPENING WAKE (TRANSITION)

(c) PR = 279
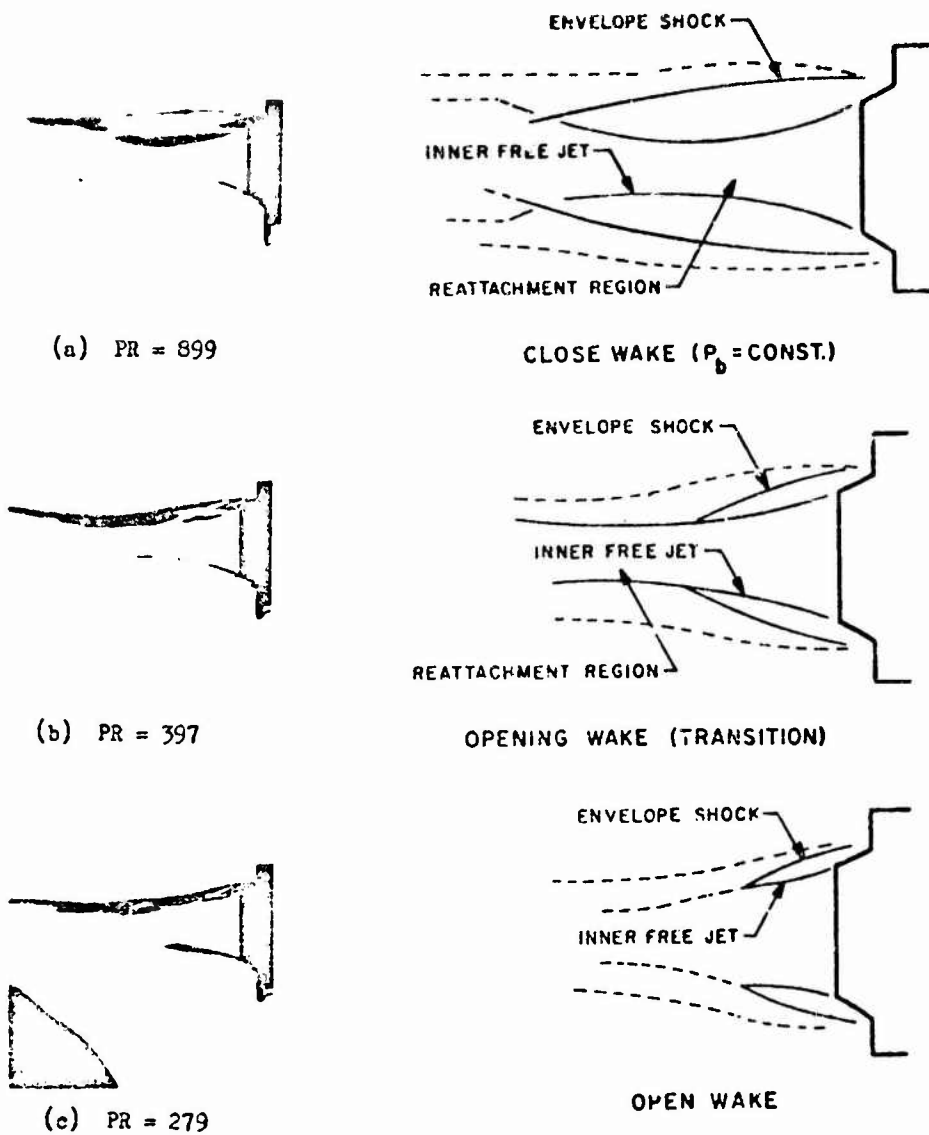
OPEN WAKE

CONFIDENTIAL

Figure 7. Flow Field Behavior With Pressure Ratio, Schlieren
Photographs, Shrouded Ideal Contour (ϵ = 45,
L = 15 Percent, γ = 1.4, $\dot{w}_s$ = 1 Percent)
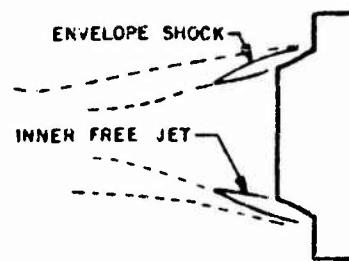
14

ENVELOPE SHOCK

INNER FREE JET

(d) PR = 200

~r. ` WAKE

ENVELOPE SHOCK

INNER FREE JET

(e) PR = 100

OPEN WAKE

ENVELOPE SHOCK

OPEN WAKE

IMPINGEMENT ON
NOZZLE SURFACE,
RECOMPRESSION

(c) PR = 50

Figure 7. Concluded

25
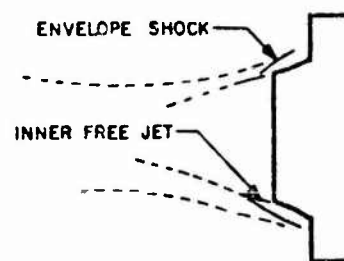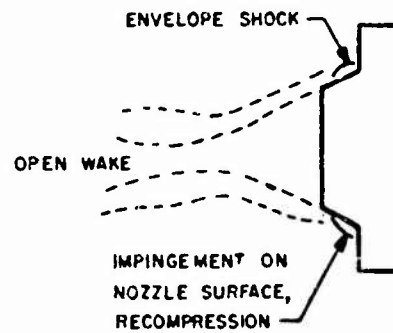
SECONDARY FLOW EFFECTS

(c) Introduction of a secondary flow into the base region improves the base
pressures developed as shown in Fig. 8 . As the secondary flow
increases from the no base bleed case, the nozzle efficiency will
increase due to the increase in base pressure although the total flow-
rate increases. There is a limit to the gain in efficiency and an
optimum flowrate exists for each configuration. This can be determined
by observing the design efficiency with increasing secondary flowrate,
Fig. 9 . Normally, efficiency improvements over the no secondary
flow case are achieved with secondary flows which are a small percentage
of the primary flow. Secondary flows also eliminate rapid decrease in
efficiency with pressure ratio (Fig. 10) and improve altitude com-
pensation.

(c) Nozzle length and secondary flowrate are interrelated in that the
performance gain with secondary flow and the optimum secondary flowrate
are increased for shorter centerbody lengths (Fig. 11). Each aerospike
configuration can be designed such that the secondary flow and length
requirements are balanced to produce a configuration with an optimum
efficiency versus altitude curve.

16
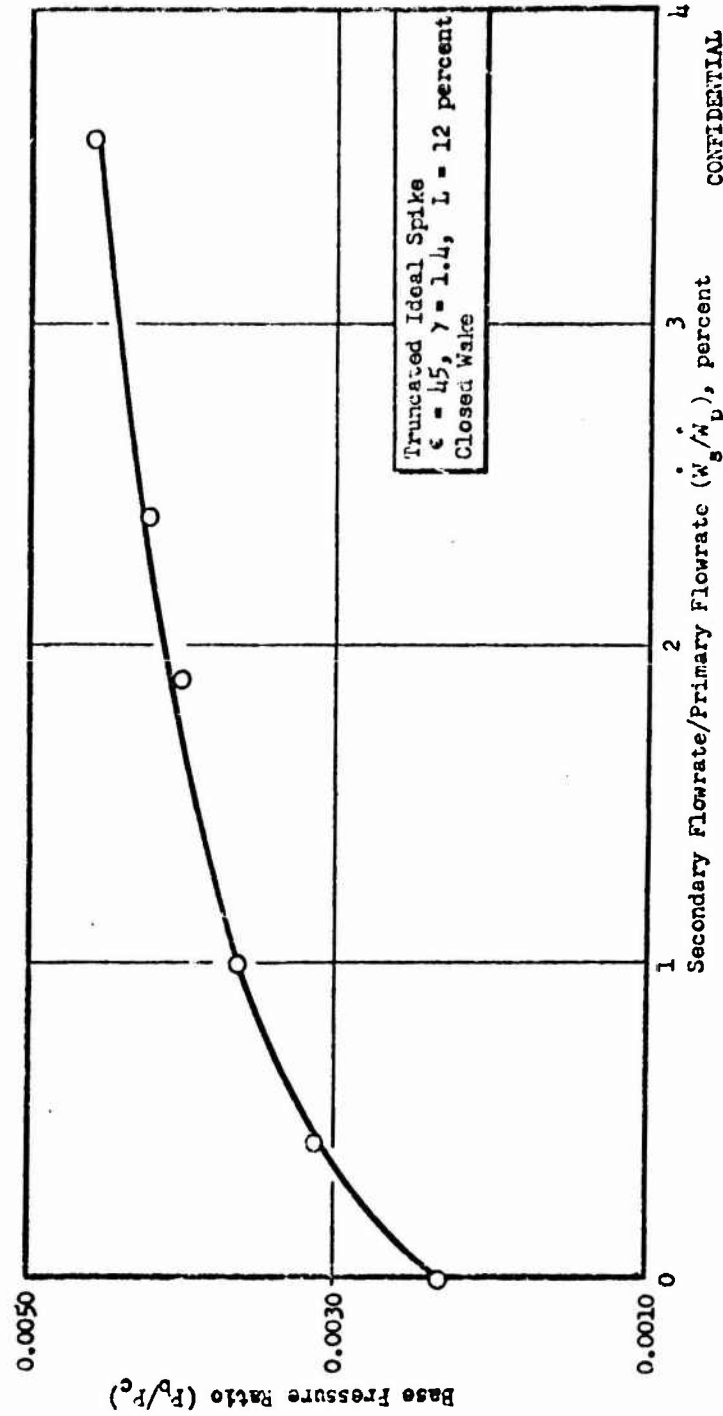
Figure 8 . Base Pressure vs Secondary Flowrate
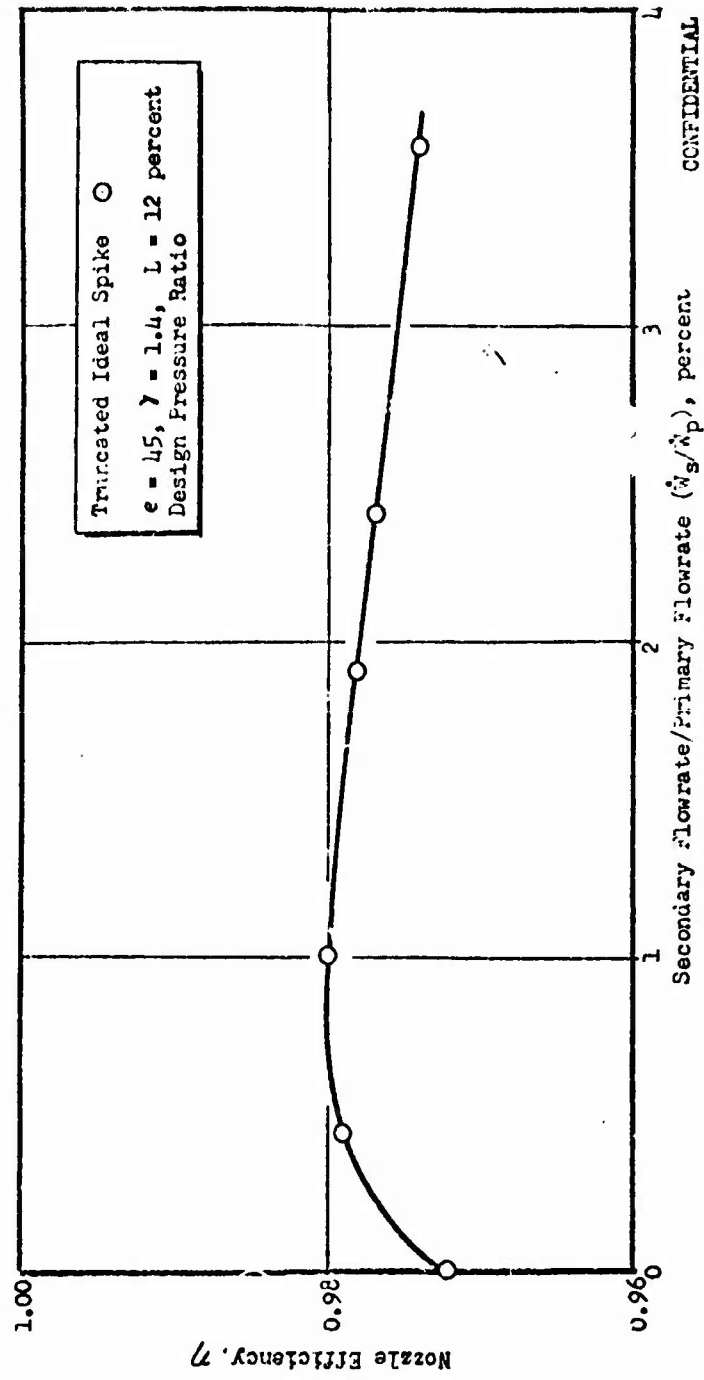
Figure 9. Nozzle Efficiency vs Secondary Flowrate, 12-percent Length.

18
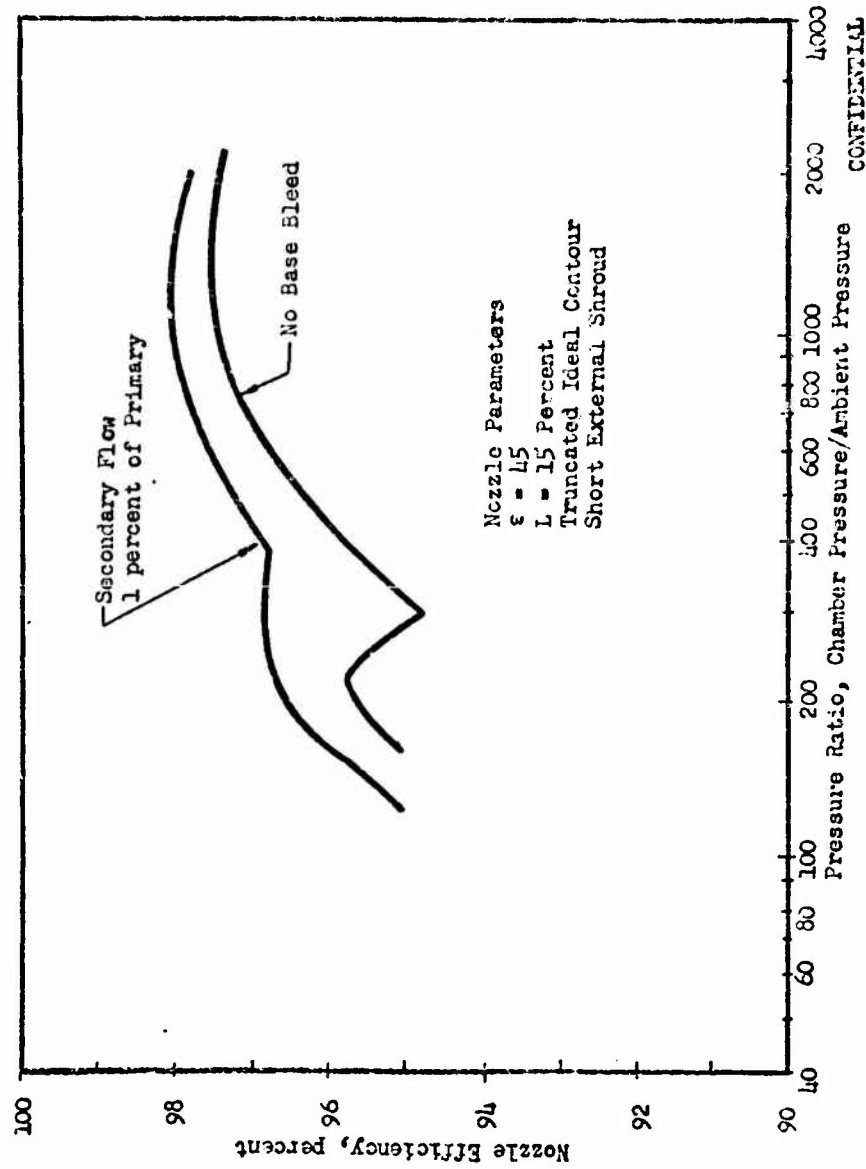
Figure 10. Nozzle Efficiency vs Pressure Ratio with Secondary Flow
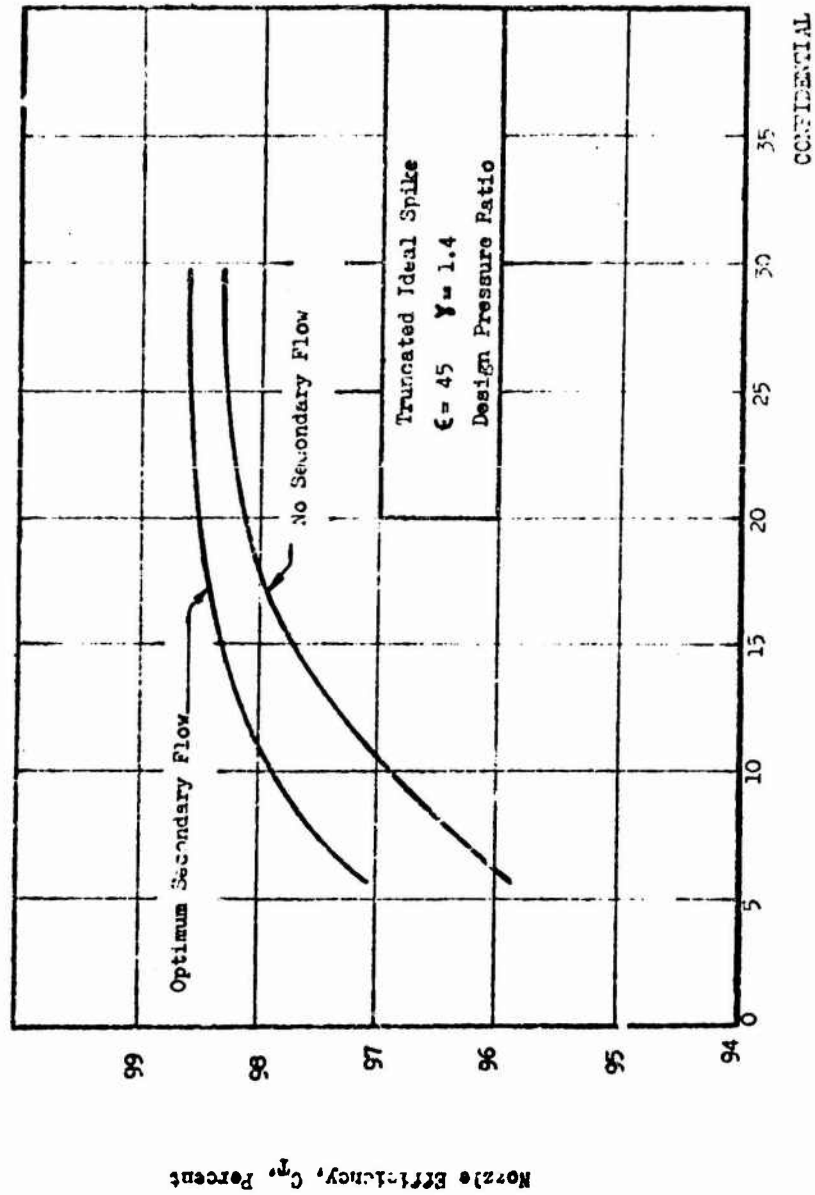
Figure 11. Variation of Nozzle Efficiency With Length

SECTION III

HIGH-AREA-RATIO NOZZLE STUDY

(U) Analytical and experimental studies of the aerodynamic spike nozzle with expansion area ratios as high as 53 have shown this concept to be capable of achieving high performance efficiency over a wide range of pressure ratios with a short nozzle length. In this program, a test series was designed to investigate aerodynamic spike nozzle performance at much higher area ratios ($\epsilon = 150$). The major objectives of this cold flow program were:

    1. To determine potential aerodynamic spike performance at high area ratios ($\epsilon = 150$).

    2. To evaluate theoretical methods of analyzing high-area-ratio aerodynamic spike nozzles.

(U) The models selected for testing were a contoured nozzle with 10 percent (of a 15 degree conical nozzle) axial length and a 45 degree conical nozzle with 6 percent axial length (Fig. 12). Both models were tested with various secondary flows to augment performance. Helium was used for both the primary and the secondary flows.

(U) The test program concentrated on the evaluation of the high performing contoured model for pressure ratios from 160 to 79,000 and secondary flowrates from 0 to 5 percent of the primary flowrate. Several base injection configurations were tested. A total of 45 data points were obtained with the contoured model. Testing of the 45 degree conical model was conducted in the high pressure ratio regime to evaluate theoretical methods of analyzing aerodynamic spike nozzles with high exit flow angles. A total of 15 data points were obtained with the conical model.
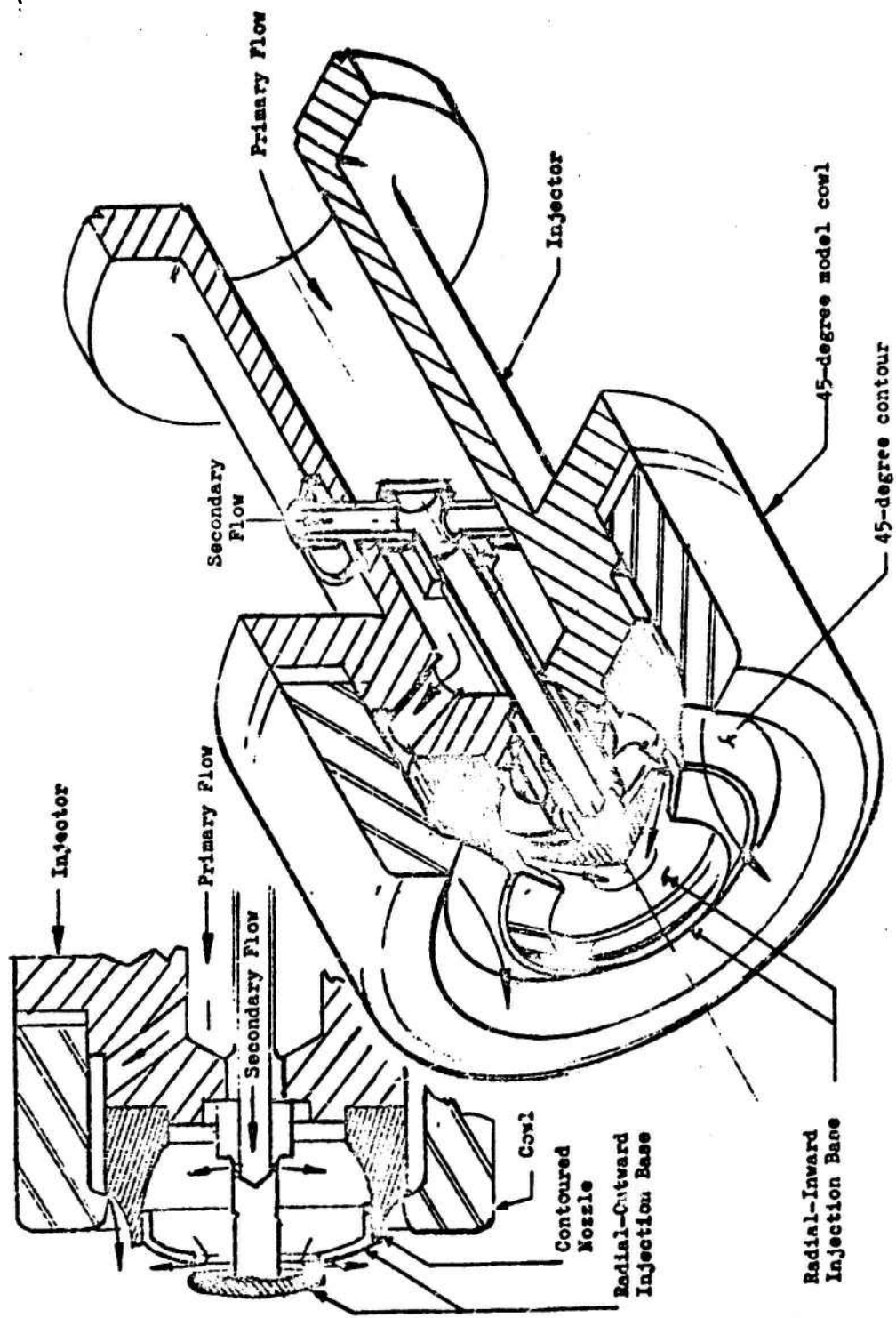
Figure 12. High-Area-Ratio Models

A detailed discussion of the models, instrumentation, test method, and test facility was presented in Ref. 1.

PERFORMANCE DEFINITION

(U) In the following sections the performance of the models has been evaluated in terms of nozzle efficiency, C_T (see Appendix 1). The efficiency, C_T, is equal to

$$C_T = C_F/C_{F_{opt}} \ (1 + \dot{W}_s/\dot{W}_p)$$

(U) C_F can be broken down as follows:

$$C_F = C_{F_{int}} - C_{F_{drag}} + \frac{P_{cowl}}{P_c} \ \epsilon_{cowl} + \frac{P_b}{P_c} \ \epsilon_b - \frac{P_a}{P_c} \ \epsilon_{tot} \qquad (1)$$

The areas of the nozzle upon which the forces represented by these terms act are indicated in the sketch of the aerodynamic spike nozzle control surface in Fig. 13 .

(U) The intrinsic thrust coefficient $C_{F \ int}$ is defined as the sum of the momentum and the pressure forces acting on the primary nozzle throat and the nozzle contour, divided by the term $P_c A^*_t$. The $C_{F_{drag}}$ term is the thrust coefficient loss caused by boundary layer drag in the primary nozzle. The primary thrust coefficient $(C_{F \ int} - C_{F_{drag}})$ acts on the annular area between points 2 (the outer expansion point) and 3 of Fig. 13 . The term $(P_{cowl}/P_c) \ \epsilon_{cowl}$ is the thrust coefficient increment caused by the pressure on the outer contour of the primary nozzle; and it acts on the annular region between points 1 and 2. The term $(P_b/P_c) \ \epsilon_b$ is the thrust coefficient increment caused by base pressure, which acts on the area between points 3 and 4. The $(P_a/P_c) \ \epsilon_{tot}$ term represents the loss in thrust coefficient caused by ambient pressure acting on the nozzle over the area between points 1 and 6.

23

A^*_t = Aerodynamic Throat Area

$\epsilon_{tot} = A_{tot}/A^*_t$

$\epsilon_e = A_e/A^*_t$

$\epsilon_b = A_b/A^*_t$

$\epsilon_p = (A_e - A_b)/A^*_t$

$\epsilon_{cowl} = (A_{tot} - A_e)/A^*_t$
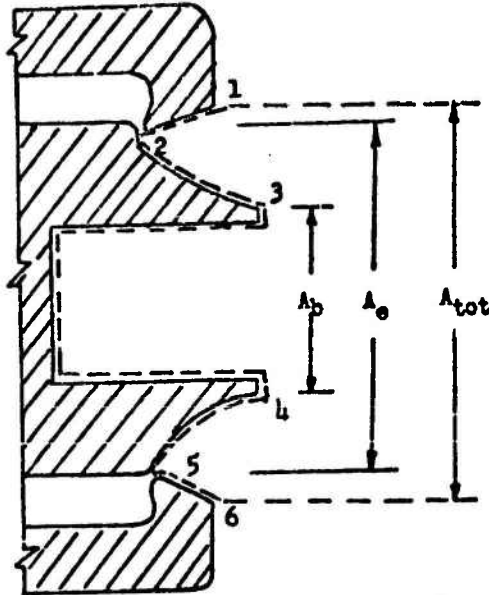
Figure 13. Aerodynamic Spike Nozzle Control Surface

(U) The test data used in the following discussions of the test results
are given in Appendix 2. Note that the efficiencies, C_T, are pre-
sented with and without the thrust contribution of the outer cowl.
The primary flow was attached to the outer cowl surface and produced
a small thrust contribution $\left[(P_{cowl} - P_a)/P_c\right] \varepsilon_{cowl}$ at high pressure
ratios; and the flow separated from the surface and produced a small
drag at low pressure ratios. It was considered best to discuss the
data neglecting the cowl contribution to simplify the comparison
between the experimental data and the predicted performance. There-
fore, the results presented in the following discussions do not include
the $\left[(P_{cowl} - P_a)/P_c\right] \varepsilon_{cowl}$ term; and the effective exit area of the
nozzle becomes A_e. Then the breakdown of nozzle thrust coefficient is

$$C_F = C_{F_{int}} - C_{F_{drag}} + \frac{P_b}{P_c} \varepsilon_b - \frac{P_a}{P_c} \varepsilon_e \tag{2}$$

THE CONTOURED AERODYNAMIC SPIKE MODEL

(U) A contoured aerodynamic spike with an axial length 10-percent that of
an equivalent 15 degree cone and an expansion area ratio of 150:1 was
designed to determine potential performance at high area ratios. A
summary of the 45 data points obtained with this model is given in
Table 1. The model was tested with an open base cavity with secon-
dary flow introduced through an orifice recessed in the cavity. Flow
emerges radially through eight holes in the orifice. Base configura-
tions which injected secondary flow radially inward and outward at the
base exit plane were also tested to determine the effect of these
methods of secondary flow injection on performance.

TABLE 1

HIGH-AREA-RATIO TEST PROGRAM SUMMARY, CONTOURED MODEL

Base Geometry	Secondary Flow, percent $\dot{w}_p$	P_c/P_t	Area Ratio A_e/A^*_t	Percent Length	Number of Tests
Open Cavity	0	160-69,000	147.5	9.39	19
	0	66,400	156.8	9.87	1
	1-5.1	73,000	147.5	9.89	5
	1.1-4.75	1124-9935	147.5	9.89	8
Radial-Inward (Large Gap)	0, 1.5	60,000	147.5	9.89	2
	1.39, 1.72, 2.73	60,000	156.8	9.87	3
Radial-Inward (Small Gap)	2.04	55,000	156.8	9.87	1
Radial-Outward	0-2.05	50,000	156.8	9.87	3
Instrumented Sting (1/4 inch diameter)	0, 4.79, 4.83	60,000	156.8	9.87	3
					45

(U) During testing of the contoured model the model was disassembled once. Reassembly of the model reaulted in an approximately 0.0006 inch change in the model aerodynamic throat gap which changed the model area ratio from 147.5 to 156.8. The change in area ratio is indicated in the table summarizing the tests with this model. However, it causes a difference of only 0.04 percent in the thrust coefficient. In view of this small difference it is reasonable to neglect the change in area ratios in the analysis of the model.

Experimental Performance

(U) The contoured model was tested with an open base cavity and with no secondary flow over a pressure ratio range of 160 to 70,000. It was also tested with secondary flow at a high pressure ratio of approximately 73,000 and at several intermediate pressure ratios from 1100 to 10,000. A photograph of this model is shown in Fig. 14 . In these tests the secondary flow was introduced into the base cavity using the radial-outward injection orifice which can be seen in the photograph.

(c) The efficiencies from the tests without secondary flow over the pressure ratio range from 160 to 70,000 are presented in Fig. 15 . The cure through these points indicates peaks in efficiency at pressure ratios of approximately 1600 and 25,000 (design pressure ratio). For comparison, a fully-expanded, fixed-flow nozzle is also shown on the figure. The base pressures corresponding to these tests are plotted versus pressure ratio in Fig. 16 .
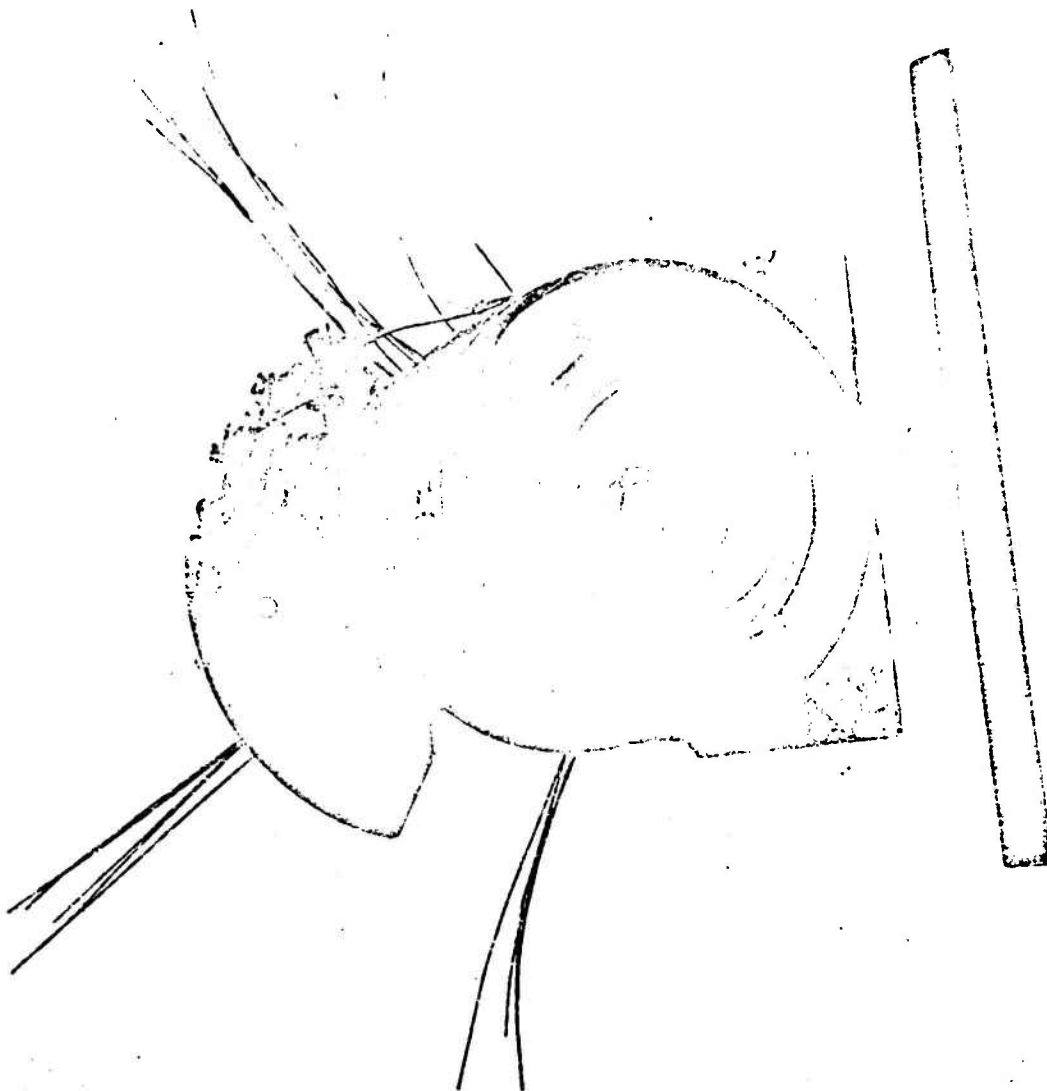
Figure 14. Contoured Aerodynamic Spike Nozzle, Open Base Cavity
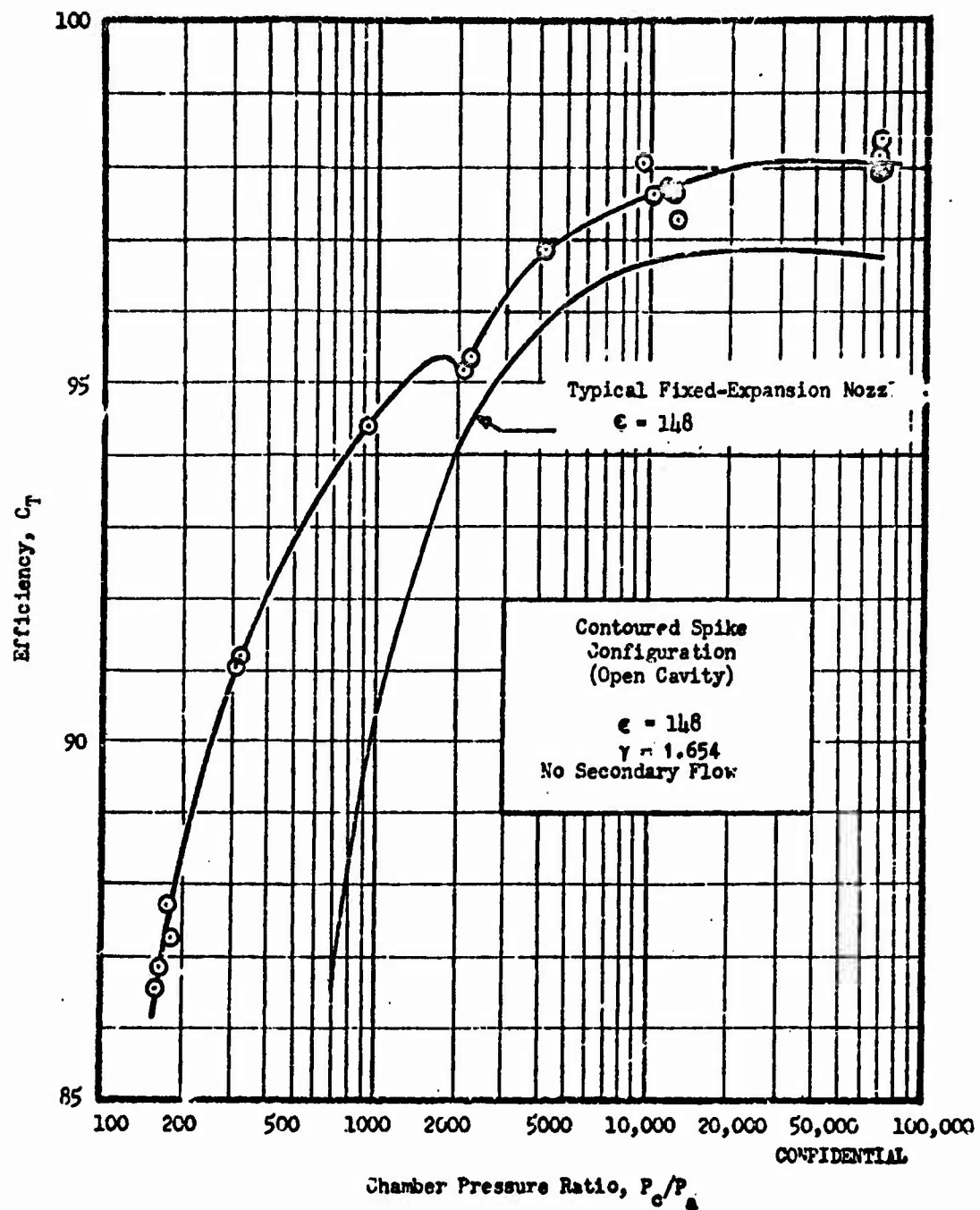
Figure 15. Efficiency vs Chamber Pressure Ratio, Contoured Aerodynamic Spike Nozzle

29

Contoured Spike Model
Open Base Cavity

$\epsilon = 148$
$\gamma = 1.654$
$\dot{w}_s = 0$

P_a/P_c

Data

Chamber Pressure Ratio, P_c/P_a

Base Pressure Ratio, $P_b/P_c \times 10^{-3}$
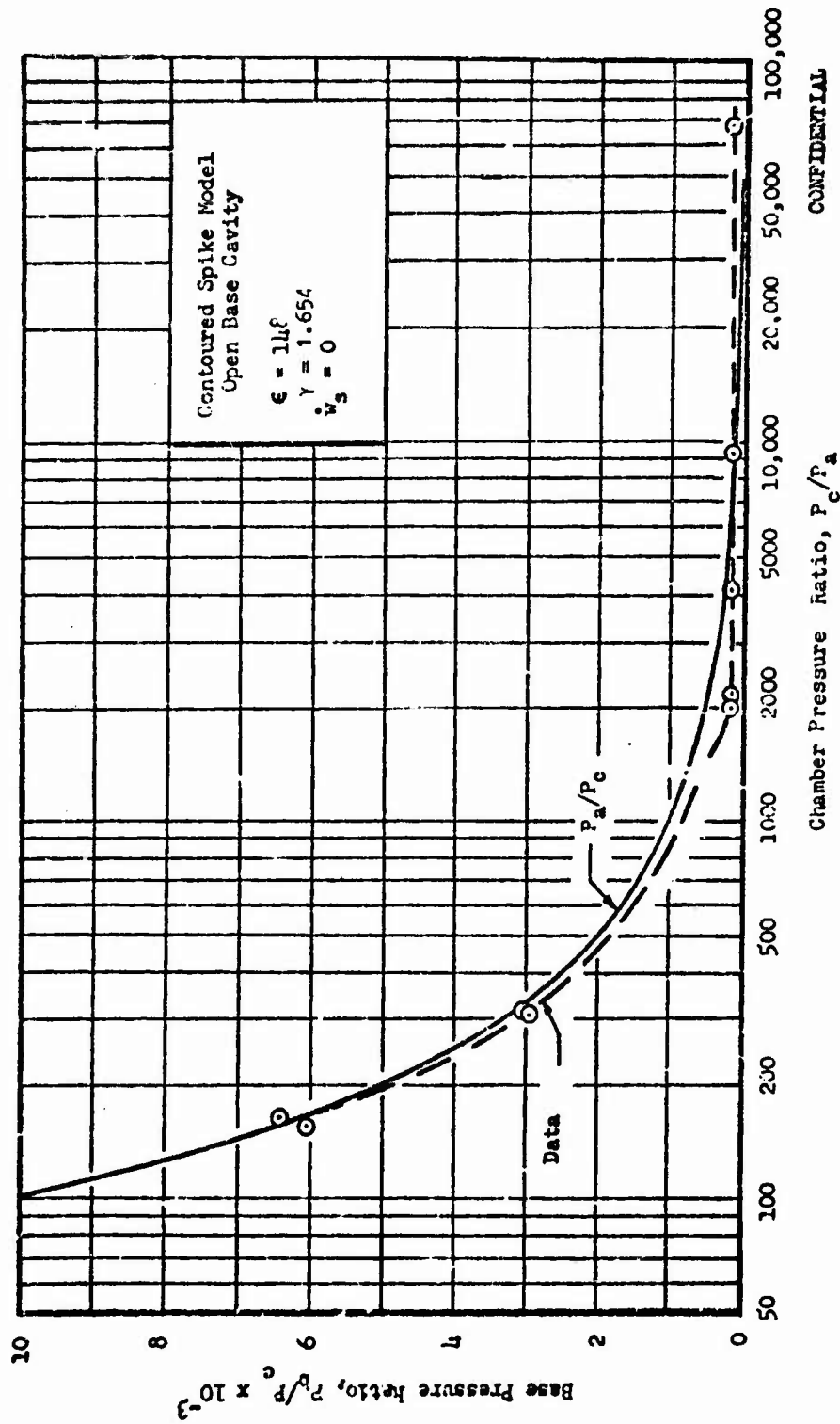
Figure 16. Base Pressure Ratio vs Chamber Pressure Ratio. Contoured Aerodynamic Spike Nozzle Configuration

(C) In the low pressure ratio range from 150 to 1600, the wake of the contoured spike nozzle was open and the base pressure was slightly less than ambient pressure. In this region, C_T rises to over 95 percent and is much greater than that which would be expected from a 148:1 area ratio, fixed-expansion nozzle. The efficiency is comparable to that of a nozzle of lower area ratio. This can also be deduced from an inspection of the components of aerodynamic spike performance. If Eq 2 is further broken down by separating the $(P_a/P_c) \epsilon_e$ term into its components $(P_a/P_c) \epsilon_b$ and $(P_a/P_c) \epsilon_p$, where ϵ_p or $(\epsilon_e - \epsilon_b)$ is the area ratio of the primary nozzle expansion surface, the factors contributing to performance are:

$$C_F = C_{F_{int}} - C_{F_{drag}} + \frac{P_b - P_a}{P_c} \epsilon_b - \frac{P_a}{P_c} \epsilon_p$$

(U) When the base pressure of the spike nozzle is equal to ambient pressure the term $\left[(P_b - P_a)/P_c \right] \epsilon_b$ is equal to zero (as shown in Fig. 16); the remaining equation is equivalent to that of a fixed-expansion nozzle,

$$C_F = C_{F_{int}} - C_{F_{drag}} - \frac{P_a}{P_c} \epsilon_p$$

(C) Thus, if the aerodynamic spike nozzle is compared to a fixed expansion nozzle of the same area ratio as the primary nozzle of the spike, the performance of the two nozzles can differ only by the differences in their intrinsic performance and the drag losses of their primary flow fields. In the case of the 148:1 spike the primary nozzle area ratio is 42:1; therefore, since the base pressure is almost equal to ambient pressure at low pressure ratios, the efficiency of the spike nozzle is

(C) In the low pressure ratio range from 150 to 1600, the wake of the contoured spike nozzle was open and the base pressure was slightly less than ambient pressure. In this region, C_T rises to over 95 percent and is much greater than that which would be expected from a 148:1 area ratio, fixed-expansion nozzle. The efficiency is comparable to that of a nozzle of lower area ratio. This can also be deduced from an inspection of the components of aerodynamic spike performance. If Eq 2 is further broken down by separating the $(P_a/P_c) \epsilon_e$ term into its components $(P_a/P_c) \epsilon_b$ and $(P_a/P_c) \epsilon_p$, where ϵ_p or $(\epsilon_a - \epsilon_b)$ is the area ratio of the primary nozzle expansion surface, the factors contributing to performance are:

$$C_F = C_{F_{int}} - C_{F_{drag}} + \frac{P_b - P_a}{P_c} \epsilon_b - \frac{P_a}{P_c} \epsilon_p$$

(U) When the base pressure of the spike nozzle is equal to ambient pressure the term $\left[(P_b - P_a)/P_c \right] \epsilon_b$ is equal to zero (as shown in Fig. 16); the remaining equation is equivalent to that of a fixed-expansion nozzle,

$$C_F = C_{F_{int}} - C_{F_{drag}} - \frac{P_a}{P_c} \epsilon_p$$

(C) Thus, if the aerodynamic spike nozzle is compared to a fixed expansion nozzle of the same area ratio as the primary nozzle of the spike, the performance of the two nozzles can differ only by the differences in their intrinsic performance and the drag losses of their primary flow fields. In the case of the 148:1 spike the primary nozzle area ratio is 42:1; therefore, since the base pressure is almost equal to ambient pressure at low pressure ratios, the efficiency of the spike nozzle is

very closely related to that of a 42:1 area ratio, fixed-expansion
nozzle in this regime. However, at low pressure ratios, the occurance
of recompression in the primary nozzle of aerodynamic spike nozzles
can result in further increases in performance.

(c) In the high pressure ratio region from a pressure ratio of 2100 to
70,000 the contoured nozzle efficiency with no secondary flow increases
from 95.? percent to 98.1 percent. In this region, the wake is closed;
and the base pressure does not change with pressure ratio. The differ-
ence between ambient and base pressure becomes less as pressure ratio
increases until the two are equal at a pressure ratio of approximately
8000. Then, as pressure ratio is increased further, the base pressure
is increasingly greater than ambient pressure and produces a positive
thrust. The nozzle efficiency in this region is higher than that of
the fixed-expansion nozzle with an area ratio of 148. At design
pressure ratio (25,000), the efficiency peaks at approximately 98.13
percent.

(c) The difference between the closed wake and open wake conditions can
be visualized by an inspection of Schlieren photographs of the contoured
nozzle being tested in the low and high pressure ratio regions. Two
such photographs are presented in Fig. 17 . In Fig. 17a the photo-
graph shows the nozzle wake at a pressure ratio of 936. At this
pressure ratio the wake is open and the base pressure is approximately
equal to ambient pressure. In Fig. 17b, the photograph shows the
nozzle wake at a pressure ratio of 69,000 which is well above the
pressure ratio at which the wake closes. At this pressure ratio the
flow is fully expanded; the base pressure is greater than ambient
pressure and does not change with pressure ratio.
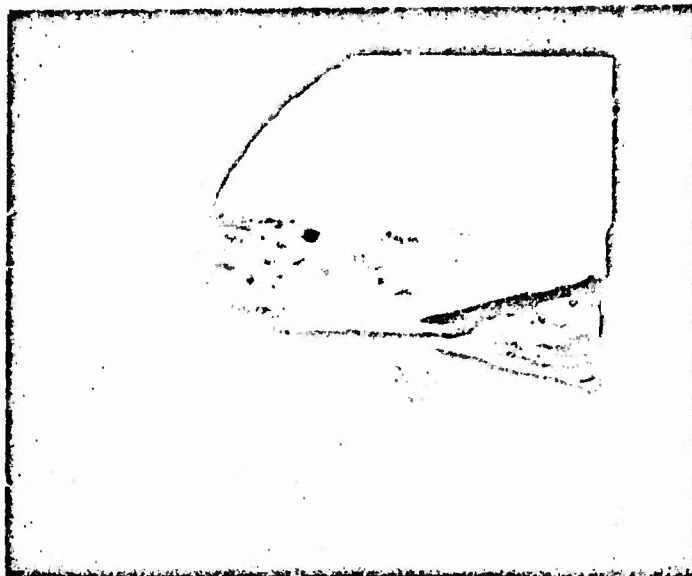
a. Open Wake, Pressure Ratio = 936
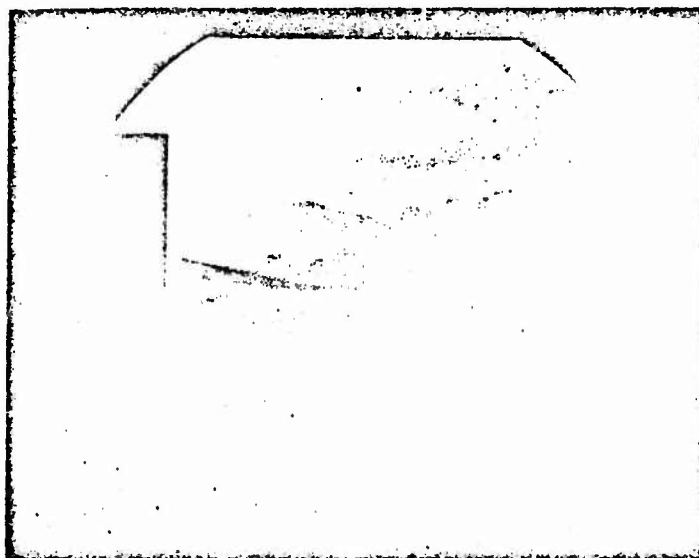
b. Closed Wake, Pressure Ratio = 69,000

Figure 17. Contoured Nozzle Flow Fields

33

(C) Secondary flow was injected into the base region with the recessed orifice to augment performance. Several secondary flowrates were tested at high pressure ratios to determine the maximum efficiency that could be obtained. The pressure ratio varied from 66,800 to 79,100 during these tests. An average value, 73,000, is referred to when the efficiencies are compared. Since the difference in pressure ratio could theoretically make only a 0.02 percent difference in the performance, the data was not normalized to one pressure ratio. The efficiencies for these tests are presented versus secondary flowrate in Fig. 18 . A maximum efficiency of 98.6 percent was obtained with a secondary flowrate of 1.4 percent of the primary flow, an increase of 0.5 percent over the case with no secondary flow. Performance equal to or in excess of the zero secondary flow case is achieved with secondary flows up to four percent of the primary; and performance was higher than that of a comparable area ratio bell nozzle for all secondary flowrates tested.

(C) The base pressures for these tests are plotted versus secondary flow in Fig. 19 . Base pressure increases with the addition of secondary flow. A change in the rate of increase occurs at a secondary flow of 1.4 percent. This change in slope occurs at the same secondary flowrate for which maximum efficiency was obtained.

(C) The efficiencies resulting from the addition of secondary flow in the intermediate pressure ratio range are plotted versus pressure ratio in Fig. 20 . The addition of secondary flow allows a high efficiency to be maintained throughout the tested pressure ratio range. A C_T greater than 96.5 percent is achieved at all pressure ratios greater than 8 percent of design pressure ratio. The gains in efficiency achieved with secondary flow at various pressure ratios are compiled
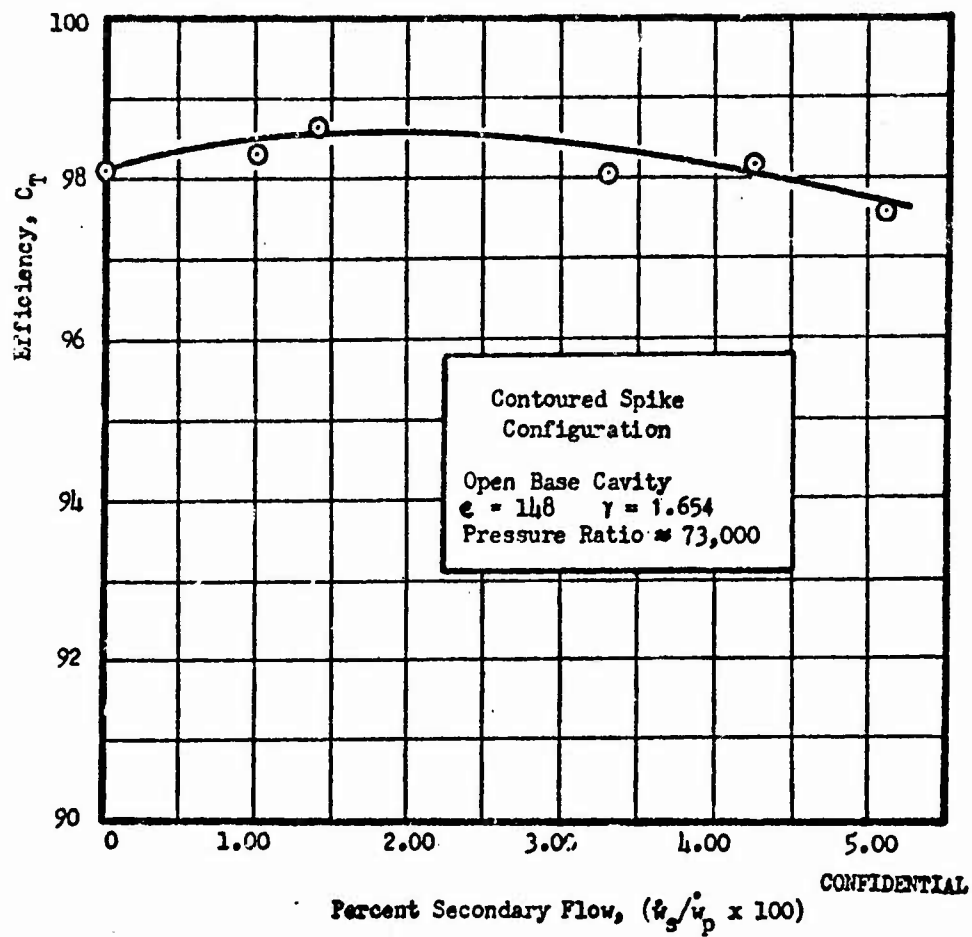
Figure 18. Efficiency vs Secondary Flow
Contoured Aerodynamic Spike Configuration
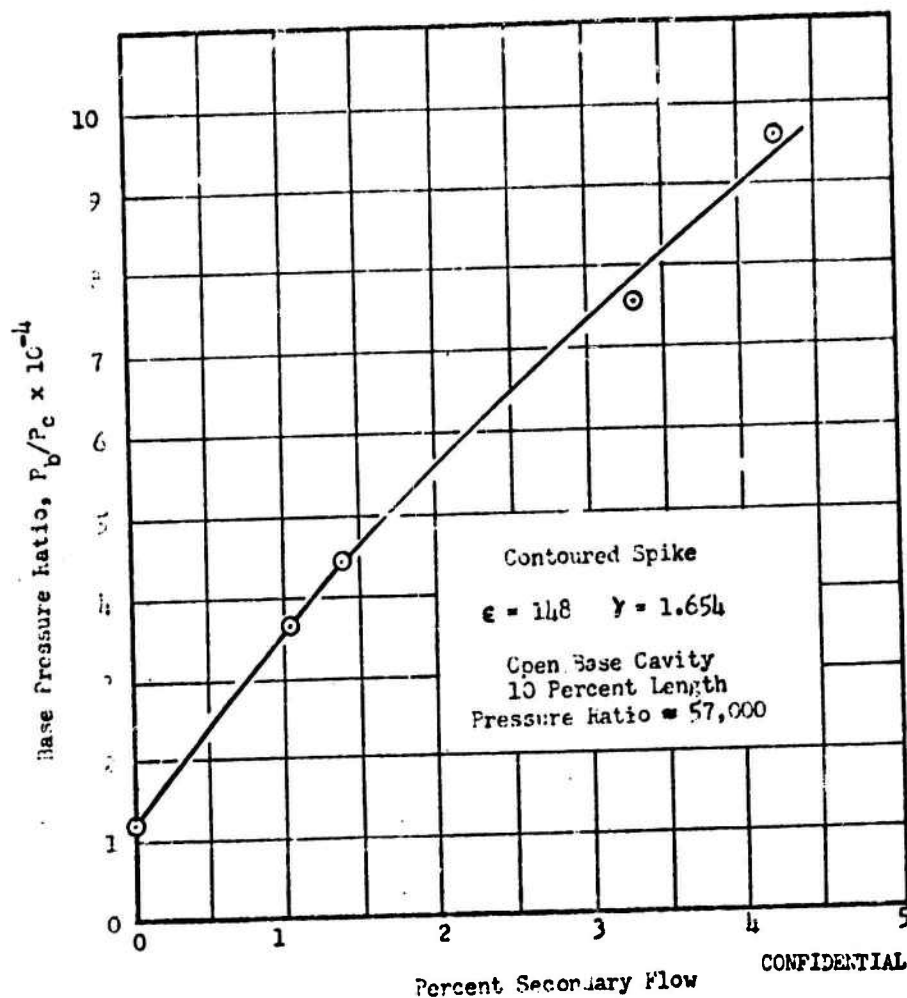
Figure 19. Base Pressure Ratio versus Secondary Flow, Contoured Spike Model

36
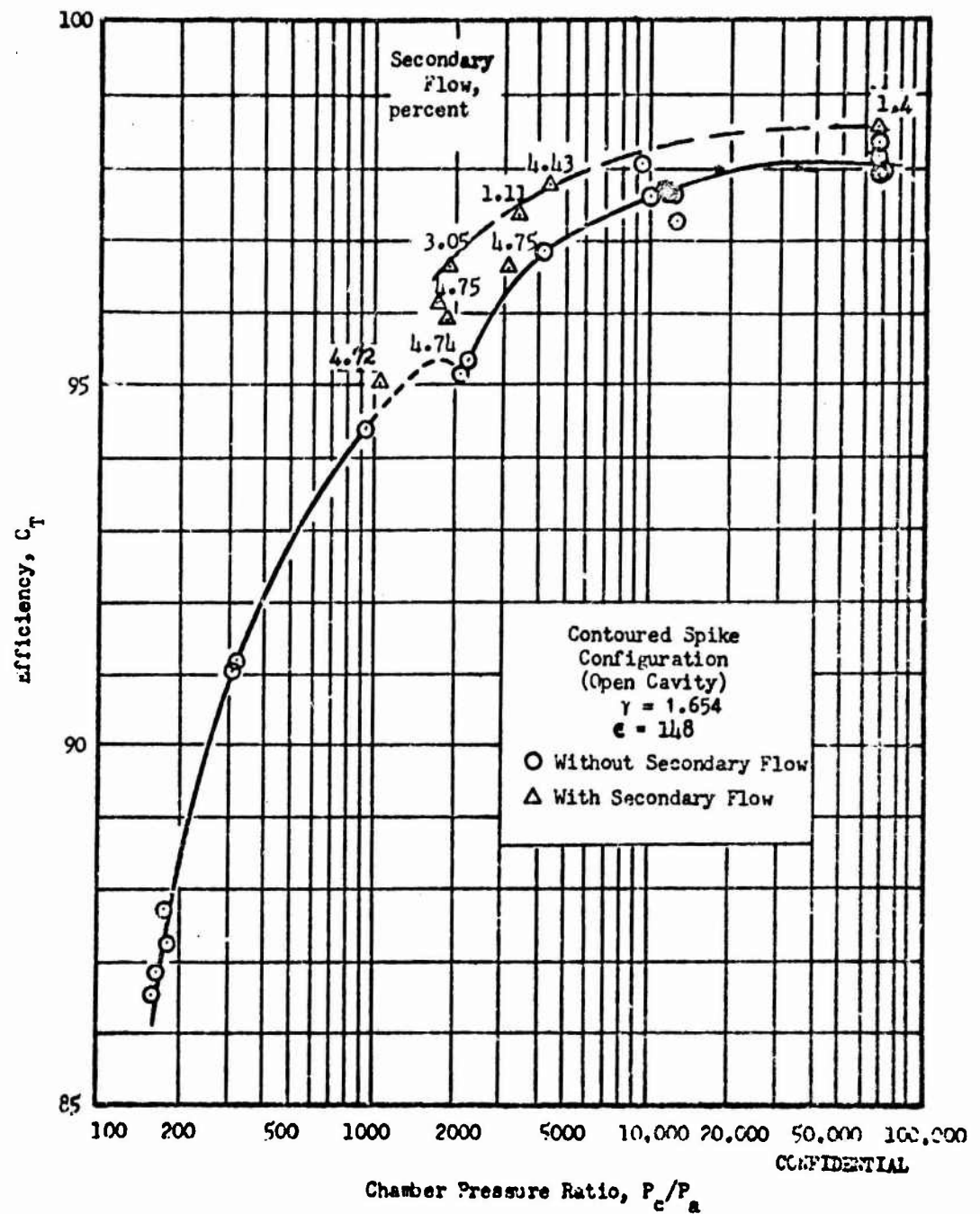
Figure 20. Efficiency vs Chamber Pressure Ratio
Contoured Aerodynamic Spike Nozzle

in Table 2. Note that these secondary flowrates do not necessarily represent those with which maximum efficiency would be attained; they do indicate the performance potential with secondary flow in the tested pressure ratio range.

TABLE 2

Efficiency Increases Achieved from Secondary Flow

P_c/P_a	w_s/w_p, percent	ΔC_T, percent
1850	3.05	+1.3
3300	1.11	+1.1
4200	4.43	+1.1
73,000	1.40	+0.5

(c) The base pressures are plotted for several pressure ratios with secondary flowrates of 1.0 and 4.75 percent of primary flow in Fig. 21. It can be seen that secondary flow increases the base pressure at all pressure ratios tested. Also, in the intermediate pressure ratio region around 2000 a secondary flow of 4.75 percent will increase base pressure above ambient pressure.

Comparison with Theoretical Predictions, Closed-Wake Regime

(C) The theoretical efficiency of the contoured model was predicted prior to testing and presented in Ref 1 . The closed-wake performance predicted for the zero-secondary-flow case is compared with the experimental data in Fig. 22 . The predicted efficiency at design pressure ratio was 98.2 percent; the experimental value was 98.1 percent.
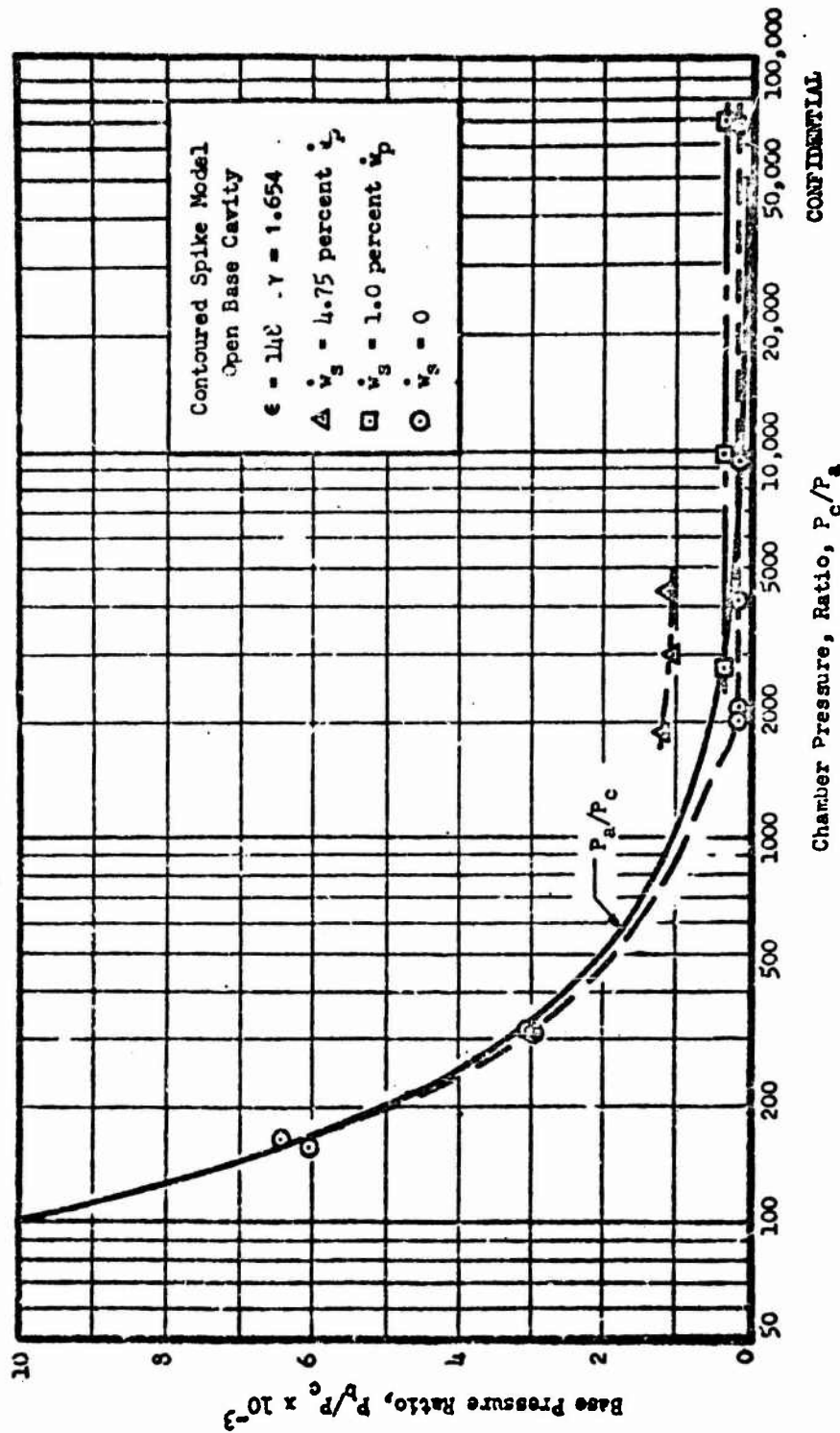
Figure 21. Base Pressure Ratio vs Chamber Pressure Ratio. Contoured Aerodynamic Spike Nozzle Configuration
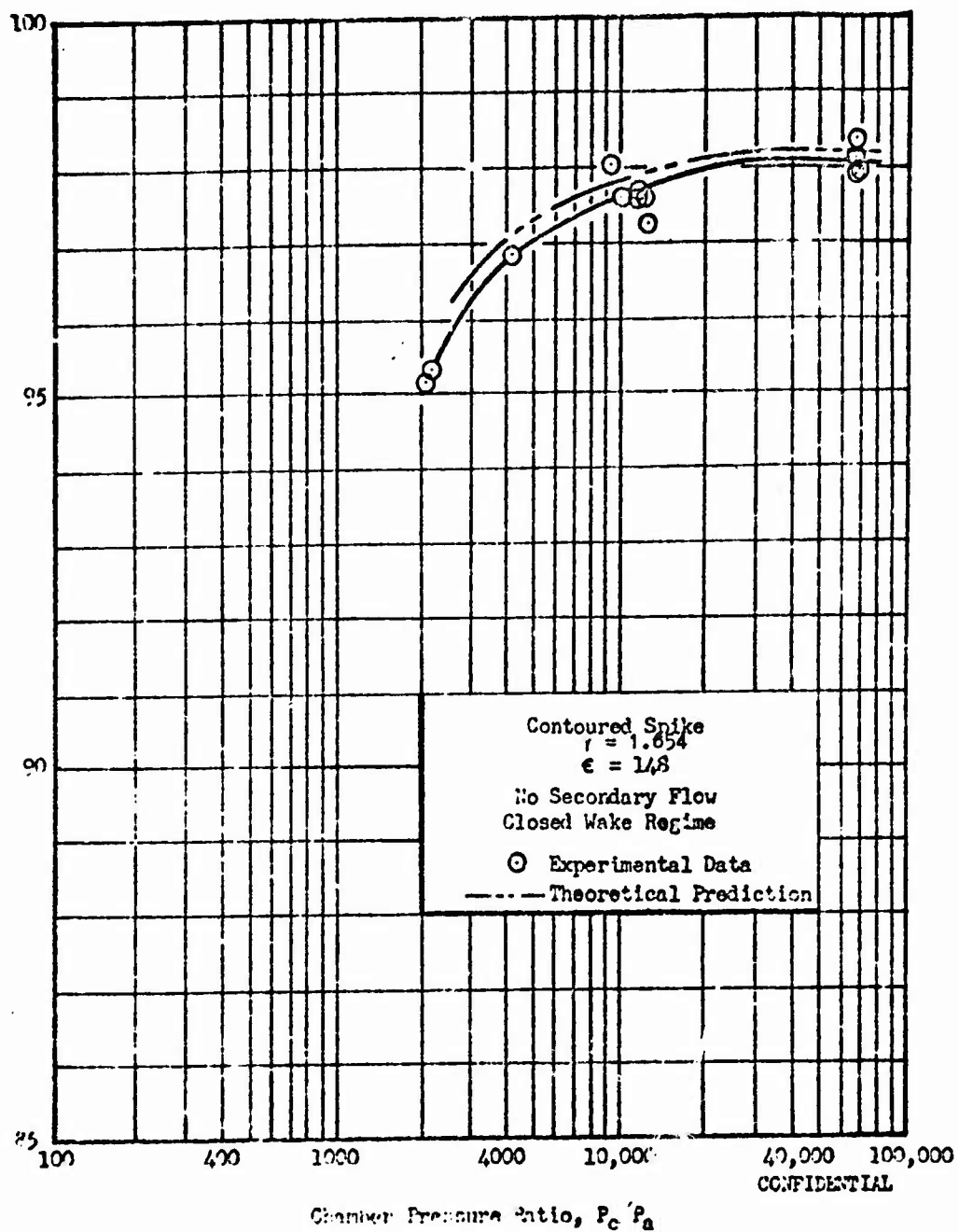
Figure 22. Experimental and Theoretical Efficiencies of Contoured Model versus Pressure Ratio, Closed Wake Regime

40

(c) The experimental wall pressures were measured and are compared with the theoretical values in Fig. 23. The experimental values are lower than the predicted values near the model throat and higher along the rest of the nozzle wall.

(c) In theoretically predicting the base pressure of the models, many of the ideas advanced by Korst and Nash were adopted for use, the most important aspect being the fact that the wake recompression phenomena controls the base pressure. The theoretically predicted base pressures for zero secondary flow are compared with the average measured base pressures in the closed-wake regime in Fig. 24. The theoretically predicted base pressure with no secondary flow was $P_b/P_c = 0.000158$; the average measured value was $P_b/P_c = 0.00012$.

(c) The base pressure of the contoured model was predicted for bleed rates up to $\dot{w}_s/\dot{w}_p = 1.16$ percent. Furthermore, it was predicted that the small bleed regime would end at this point. The theoretical base pressures are plotted with the experimental results in Fig. 25. It can be seen that the theoretically predicted end of the small bleed regime occurs near the change in slope in the experimental curve. It is approximately at this change in slope where the maximum efficiency is achieved from the addition of secondary flow. The theoretically predicted efficiency with 1.16 percent secondary flow was 98.7 percent at the design pressure ratio as compared to the measured value of 98.6 percent.

Comparison with Theoretical Predictions, Open-Wake Regime

(c) The nozzle efficiency predicted in Ref 1 for the open-wake regime is compared with the experimental data in Fig. 26, along with the closed-wake regime results. In this regime the difference between theory and

Contoured Spike Model

⊙ Experimental Pressures, $\epsilon = 148$
$\gamma = 1.654$

—— Theoretical Pressures $\epsilon = 152$
$\gamma = 1.6667$

0.06

0.04

0.02

0.01

0.008

0.006

0.004

0.003

Wall Pressure Ratio, P_w/P_c

0   0.1   0.2   0.3   0.4   0.5   0.6   0.7   0.8
Axial Distance from Throat Outer Expansion Point, Inches
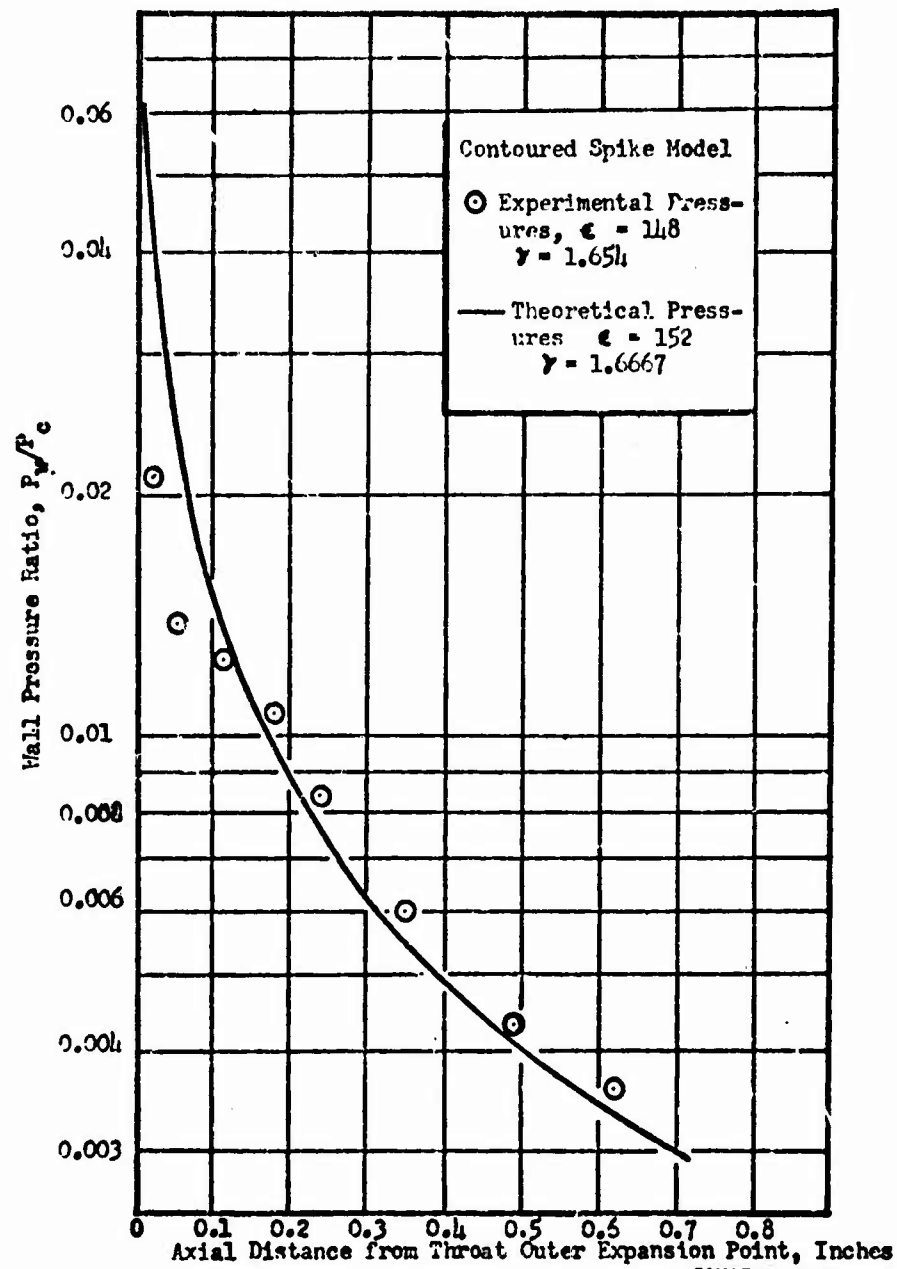
CONFIDENTIAL

Figure 25. Theoretical and Experimental Wall Pressure Profiles, Contoured Spike Model
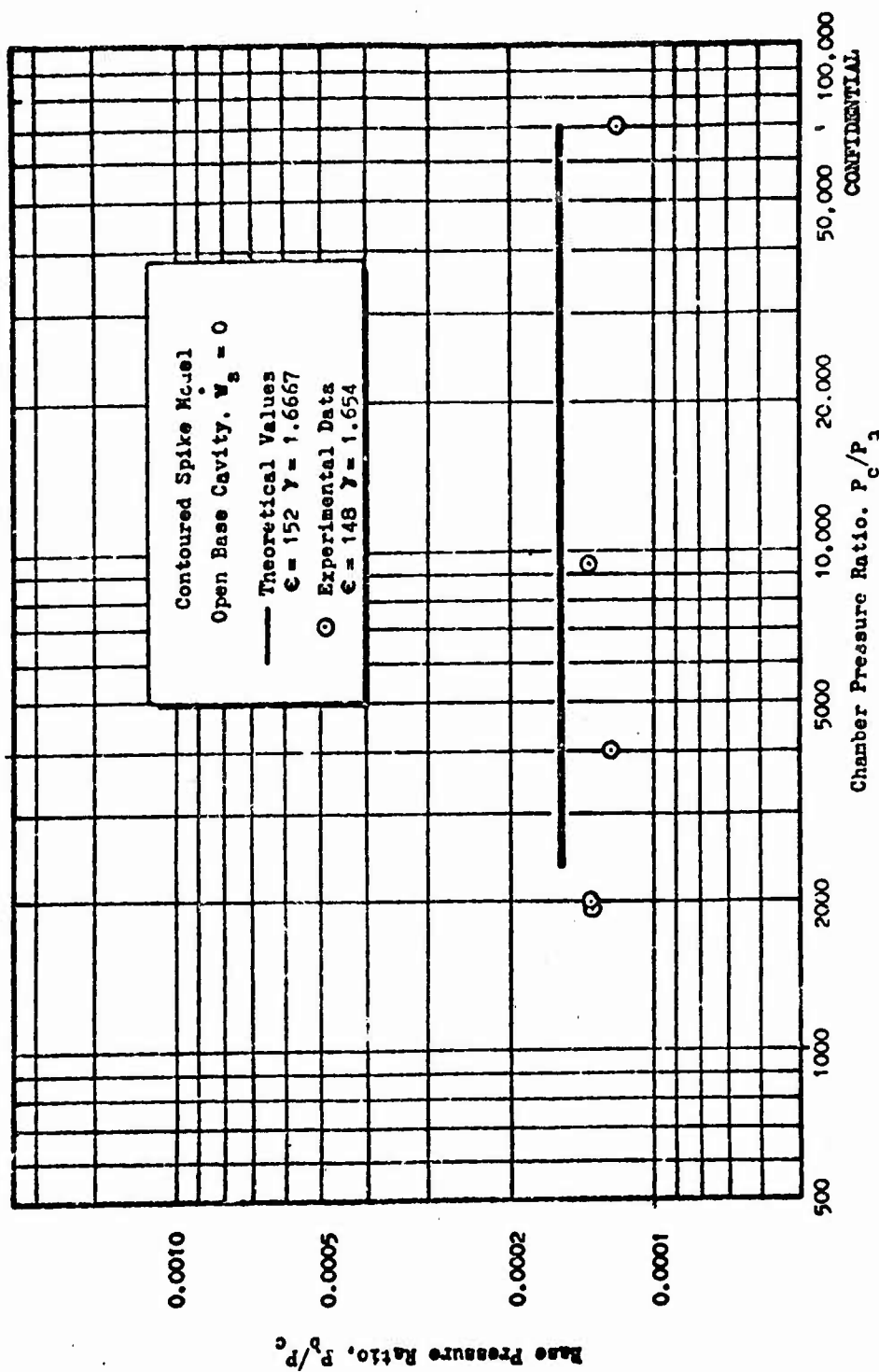
Figure 24. Comparison of Theoretical and Experimental Base Pressure. Closed Wake Regime
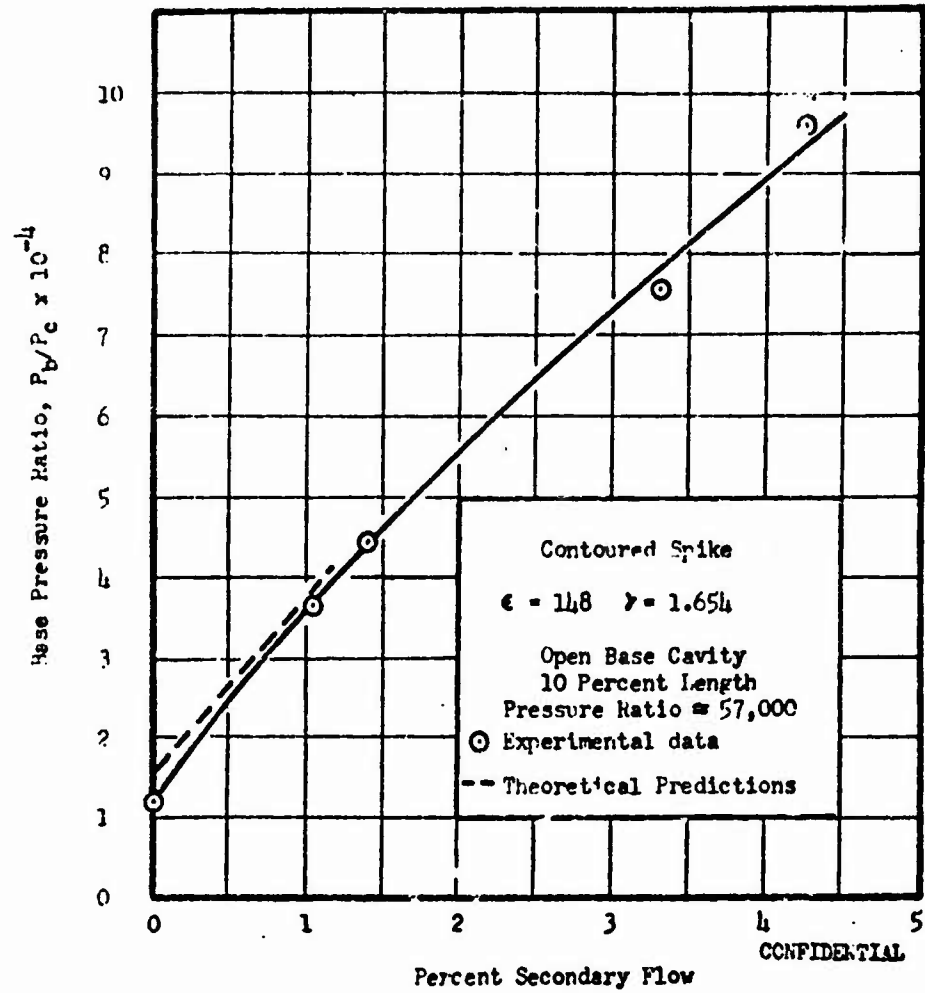
Figure 25. Comparison of Theoretical with Experimental Base Pressures, Small Secondary Flows

44
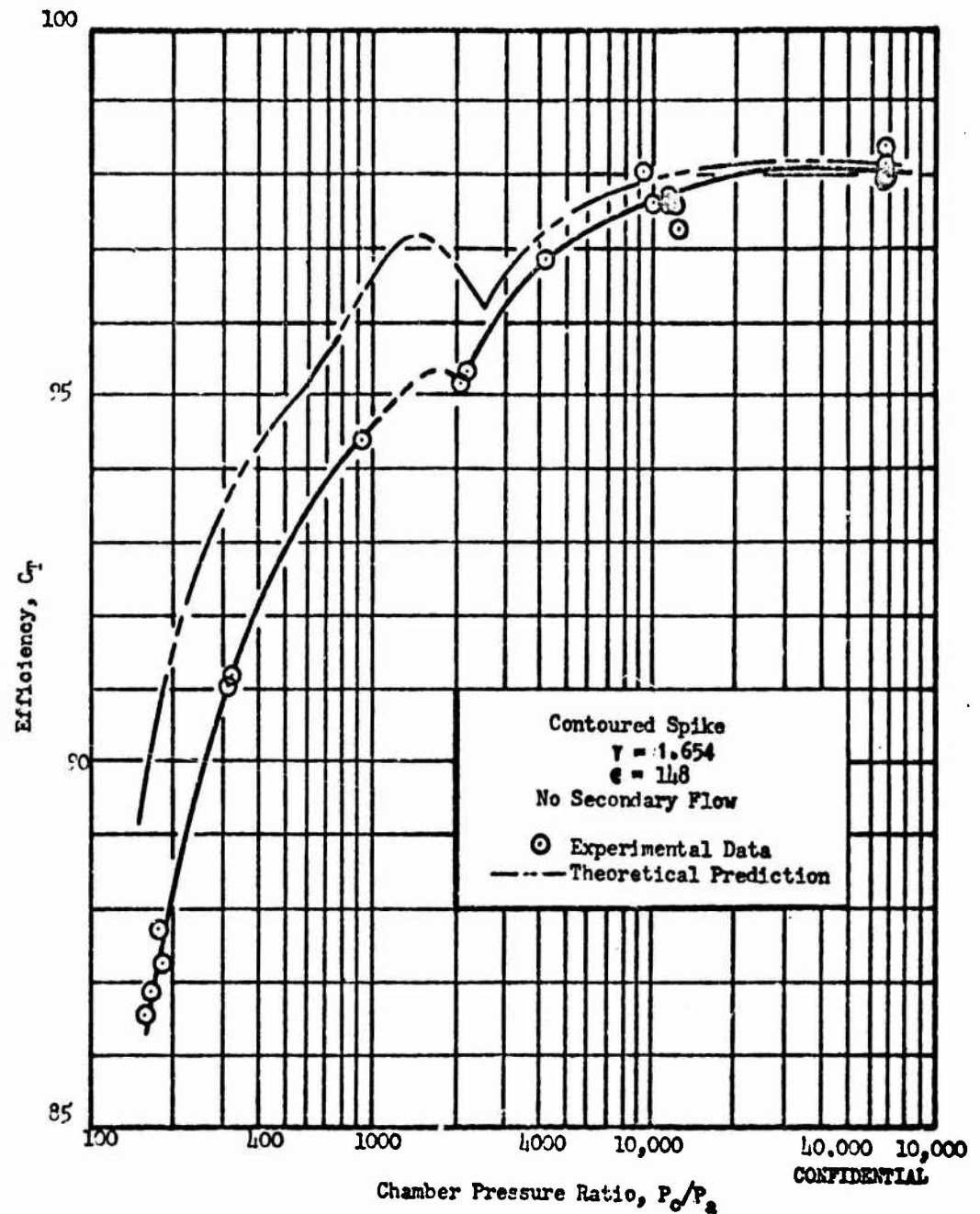
Figure 26. Experimental and Theoretical Efficiencies of Contoured Model Versus Pressure Ratio

45

experiment varies from 1.5 to 3 percent. The experimental base pressures
are plotted with the predicted values in Fig. 27 . The difference
between experiment and prediction in the open wake region are small.
Therefore, the difference between the theoretical and actual perfor-
mance was attributed almost entirely to the analysis of the primary
performance.

(c) The theoretical primary nozzle pressure profiles were predicted for
the open-wake regime in Ref [1] . The methods used in the analysis
had previously produced satisfactory results for cold-flow $(\gamma = 1.40)$
and hot-firing $(\gamma = 1.23)$ models. Recompression which occurred at a
pressure ratio of 160 is indicated by the experimental wall pressures
which are plotted in Fig. 28 . These data are compared with the pre-
dicted recompression for a pressure ratio of 150. The difference
between the actual and predicted recompression is partially caused by
the variance between the actual primary nozzle geometry and the
geometric assumptions used in the theoretical flow-field analysis.
The theoretical calculation assumes a Prandtl-Meyer point expansion at
the outer cowl lip (also the throat location) to find the position of
the free jet boundary; whereas the actual expansion point has a finite
radius and the expansion is influenced by the cowl pressure (slightly
lower than ambient). Further, if a choked flow condition occurs before
the assumed throat location, overexpansion would occur before the cowl
exit point is reached. All of these factors tend to delay and reduce
recompression. Further investigations of the analytical solution for
the primary flow field is also warranted. To obtain high computational
accuracy at this area ratio it be mea increasingly important to main-
tain an extremely fine flow net.

46
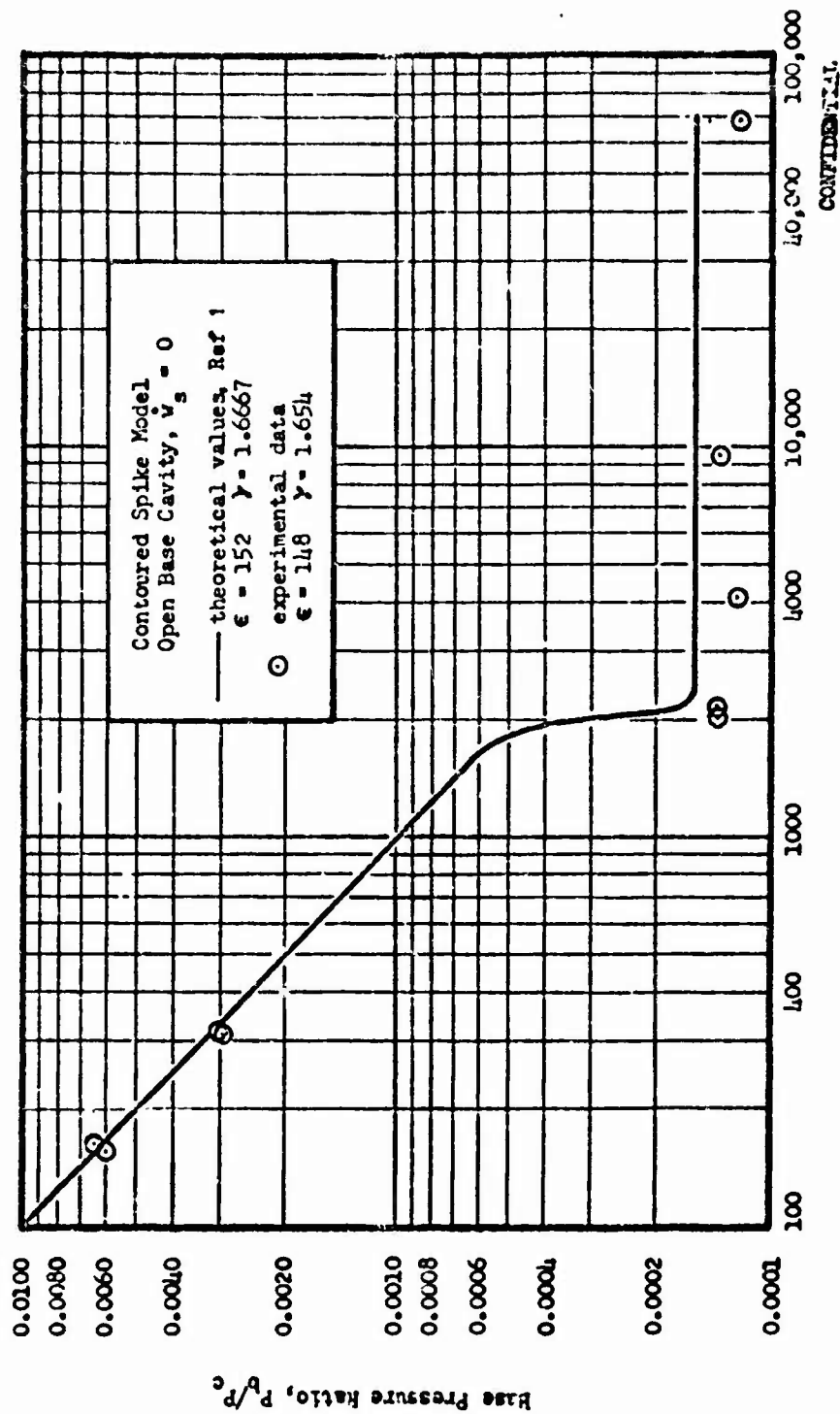
Figure 27. Comparison of Theoretical and Experimental Base Pressures

Axial Distance from Throat Outer Expansion Point. Inches
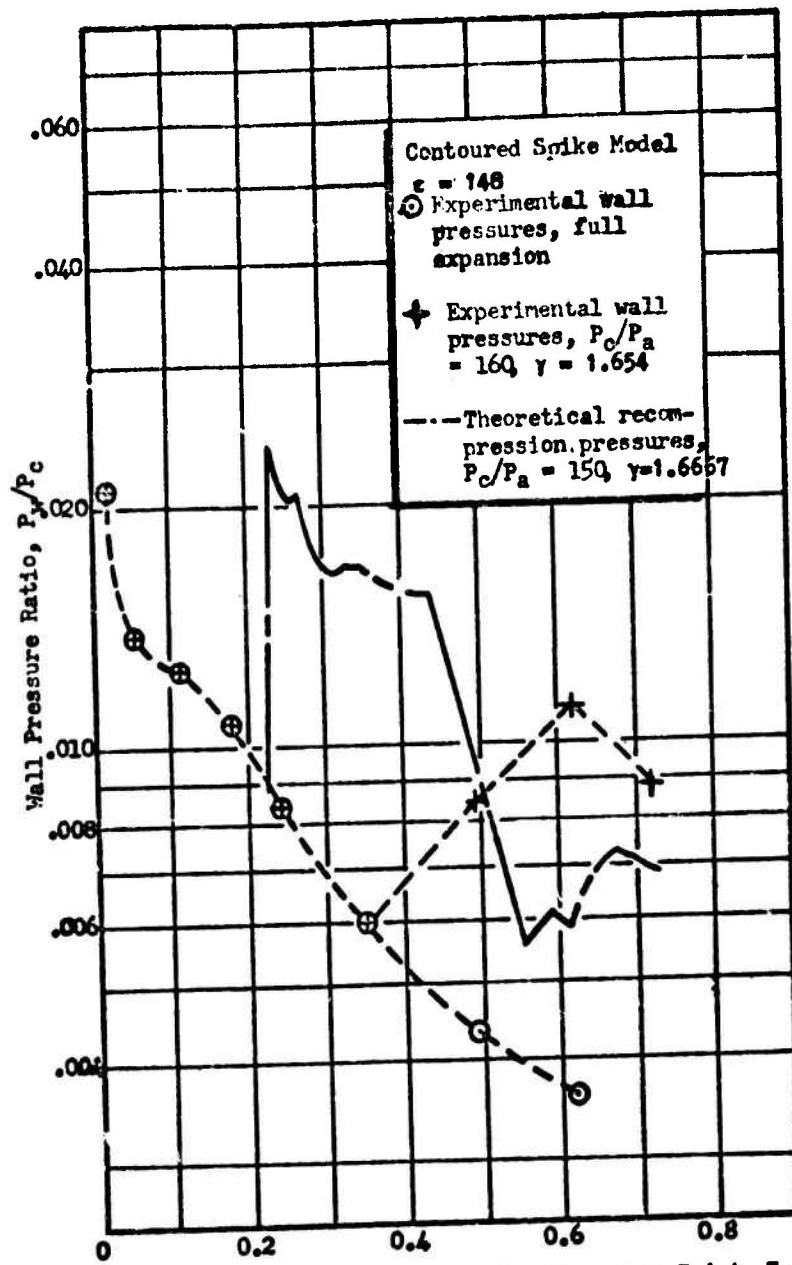
Figure 28. Theoretical and Experimental Wall Pressures with Recompression, Contoured Spike Model

Base G· etry Study

(C) It was postulated from base-pressure theory that methods of secondary flow injection that introduce the secondary flow with no axial momentum and at a low Mach number would result in the most efficient use of secondary flow to increase base pressures. A radial-inward and a radial-outward secondary flow injector (Fig. 29 and 30 , respectively) were designed and fabricated to evaluate this postulate. The radial-inward fixture was designed to allow two annular gap spacings so that the Mach number at which a secondary flow was introduced could be changed.

(C) The base pressures with these secondary flow injection methods in a pressure ratio range of 44,000-69,800 are plotted versus secondary flowrate in Fig. 31 . The base pressures with the recessed orifice are also plotted for comparison. Because the base pressures are a small part of the total thrust for this configuration, a large change in base pressure produces only a small change in efficiency. Also, the base pressures are not a complete indication of the effect of secondary flow on thrust with these methods of injection. The geometrical limitations of the base area did not allow designs of the base plates which would result in pure radial-inward and pure radial-outward secondary flow injection; there was some axial momentum to the secondary flow in the base exit plane in both cases. This axial momentum contributes to the thrust and the nozzle efficiency.

(C) The model performance with the tested methods of secondary flow injection is shown or Fig. 32 . The results indicate that the large-gap radial-inward injection method was not as efficient as the recessed orifice method; however, the large-gap was slightly better than the small-gap,
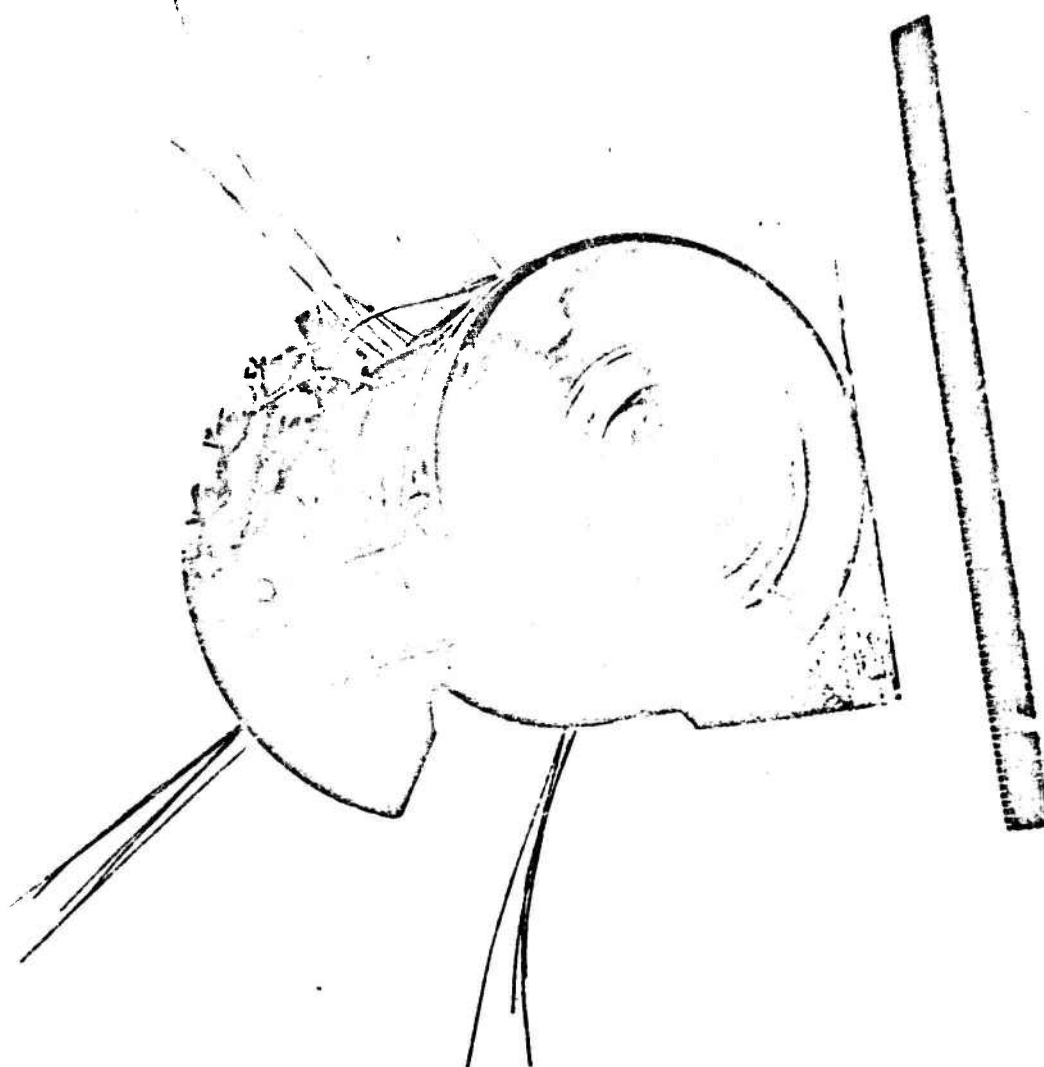
Figure 29. Radial-Inward Secondary Injection Configuration Mounted on the Contoured Nozzle
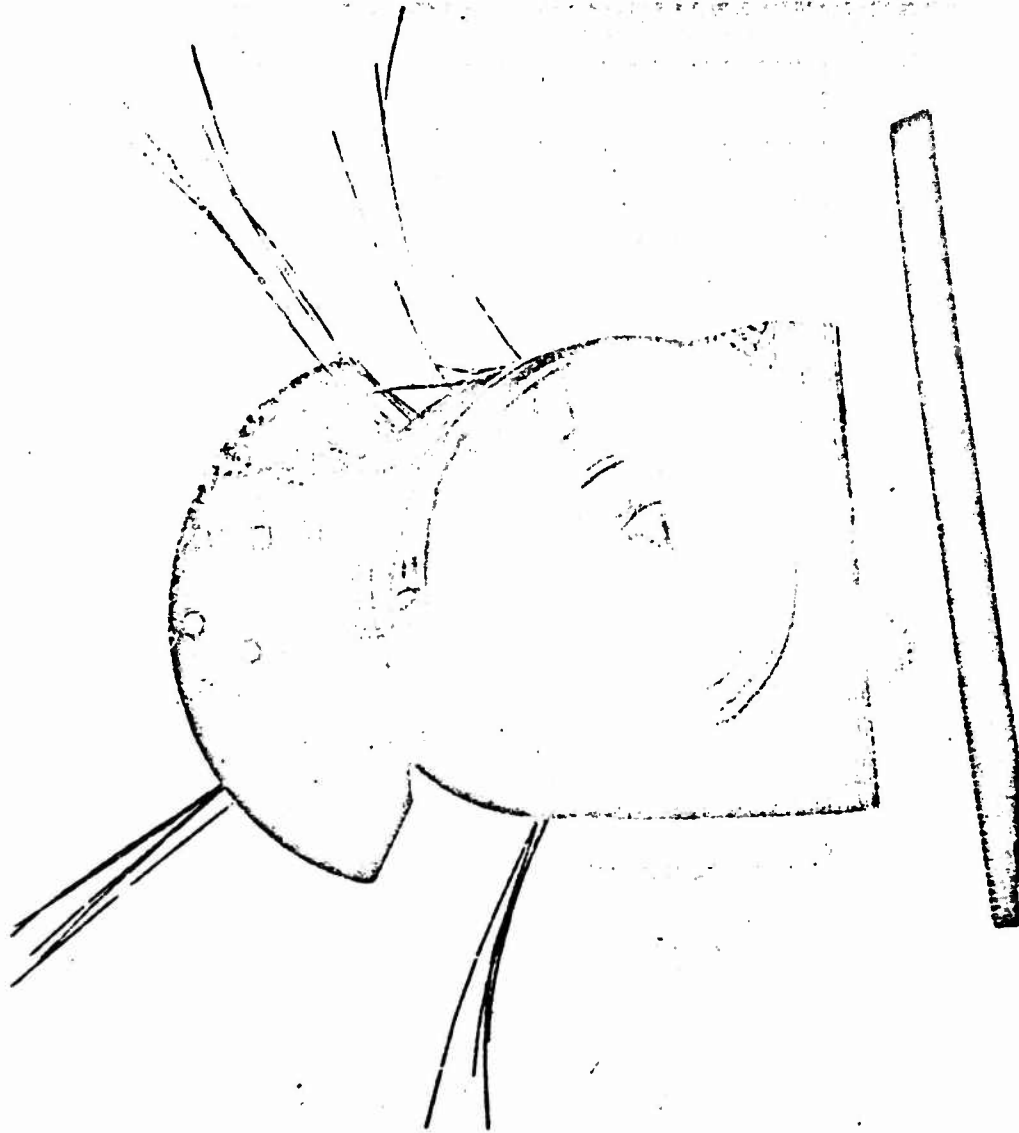
Figure 30. Radial-Outward Injection Configuration Mounted on the Contoured Nozzle
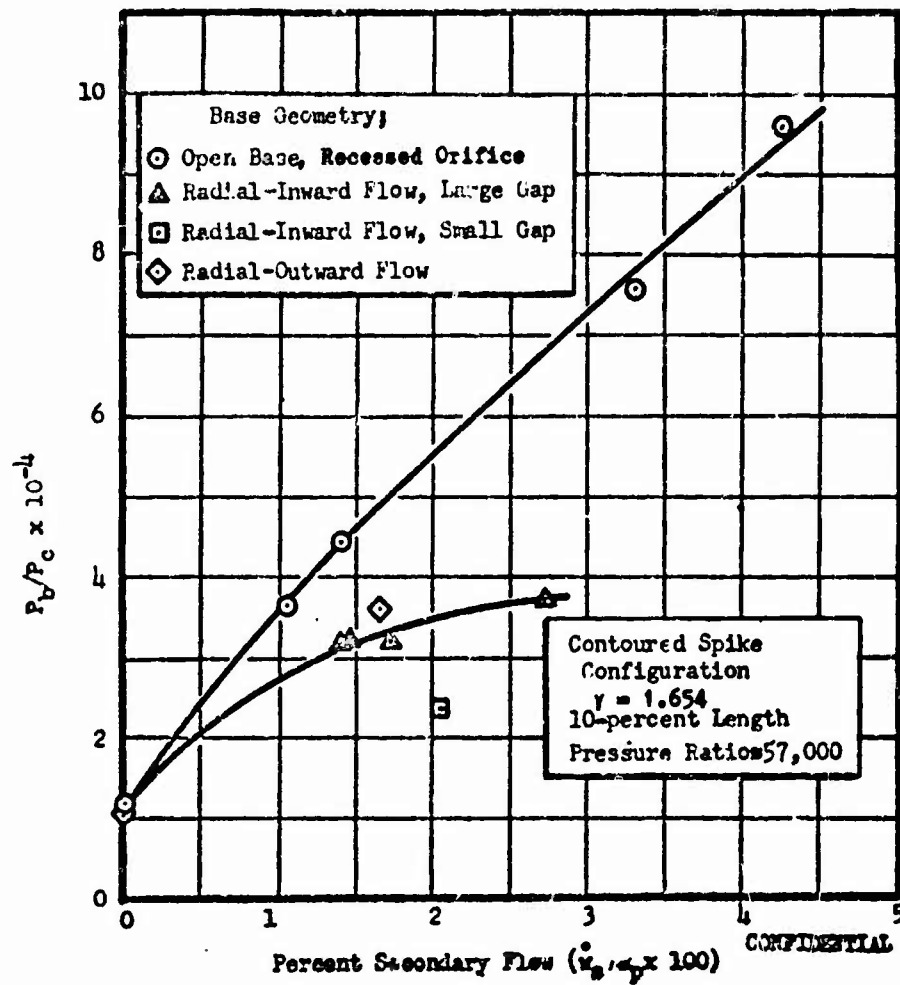
Figure 51. Base Pressure Ratio vs Secondary Flowrate
Contoured Aerodynamic Spike
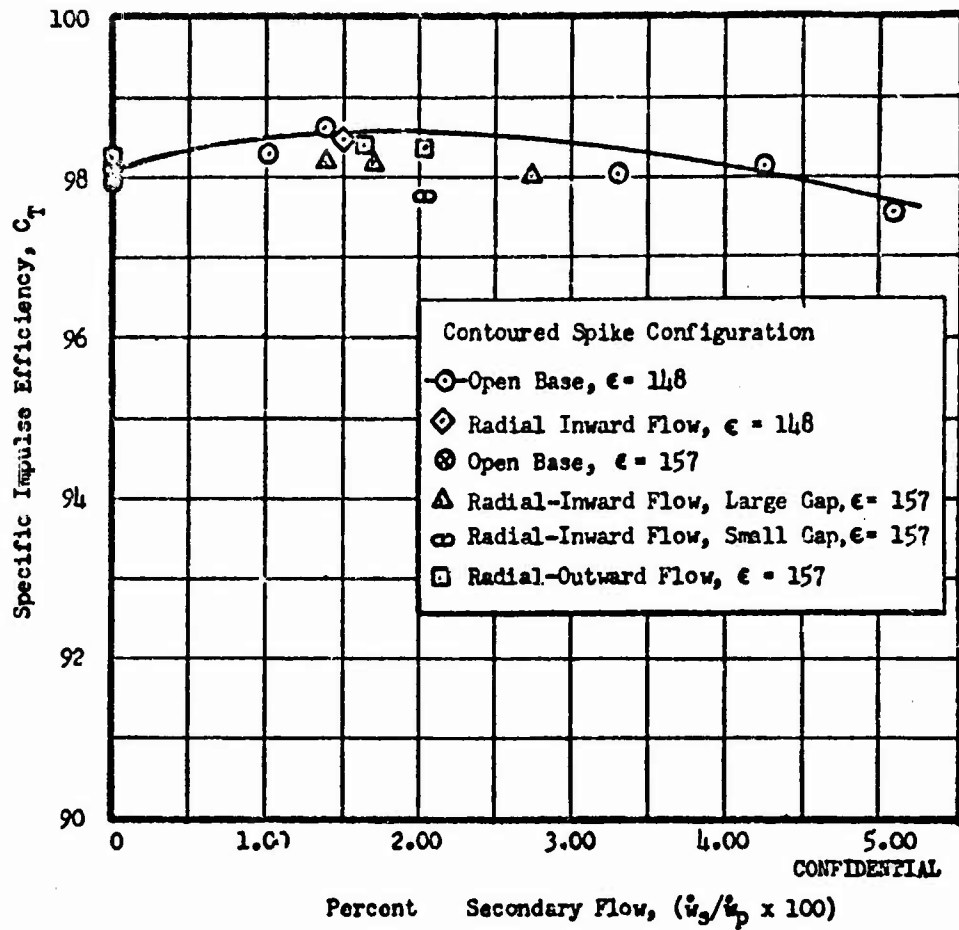
Figure 32. Specific Impulse Efficiency vs Secondary Flow,
Contoured Aerodynamic Spike Configuration,
Pressure Ratio ≈ 57,000.

radial-inward injection method. The secondary flow was injected sub-
sonically for the recessed orifice and the large-gap radial-inward
methods; however, it was injected supersonically in the small-gap
radial-inward method. This indicates that the secondary flow should
be introduced into the base region at a low velocity when it is intro-
duced radially inward. The base pressures also indicate that the radial-
out injection method is slightly better than the large-gap radial-inward
method. The maximum efficiency for the large-gap radial-inward
injection method occurred at a secondary flowrate of 1.4 percent. A
change in the slope of the base pressure versus secondary flow curve
also occurs at this point.

(c) The efficiency and base pressure of the radial-outward injection method
are slightly higher than that of large-gap radial-inward method. This
is contrary to what would be expected from the fact that the secondary
flow of the radial-outward method is supersonic and that of the radial-
inward method, subsonic. The higher base pressure appears to be the
result of the different secondary flow-primary stream interaction.
The Schlieren photographs of the wakes indicate that the radially-out-
ward method affects the wake differently than the two other methods.
The Schlierens for these methods of injection with approximately 1.5
percent secondary flow and at a closed-wake pressure ratio are shown
in Fig. 33 . In contrast to the wakes of the recessed ori-
fice and the radial-inward methods of injection (Fig. 33a and 33b),
a distinct disturbance of the primary flow field caused by secondary
flow is seen near the outlet of the radial-outward configuration.

THE CONICAL AERODYNAMIC SPIKE MODEL

(U) A 45 degree, conical aerodynamic spike with an axial length 6 percent
of an equivalent 15 degree cone and an expansion area ratio of 130:1
was tented.
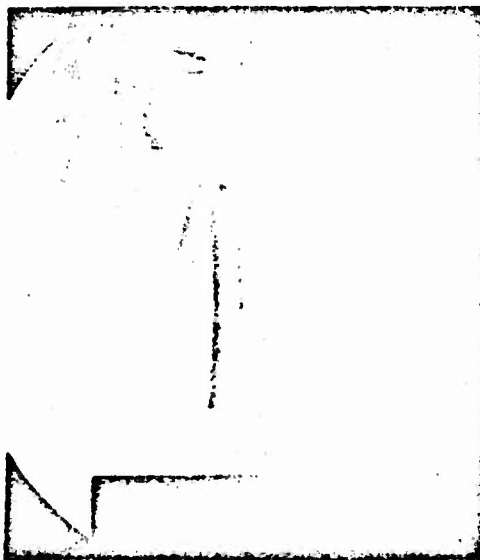
a. Recessed Orifice Injection,
   P.R. = 68,700 $\dot{w}_s/\dot{w}_p$ = 1.4 %
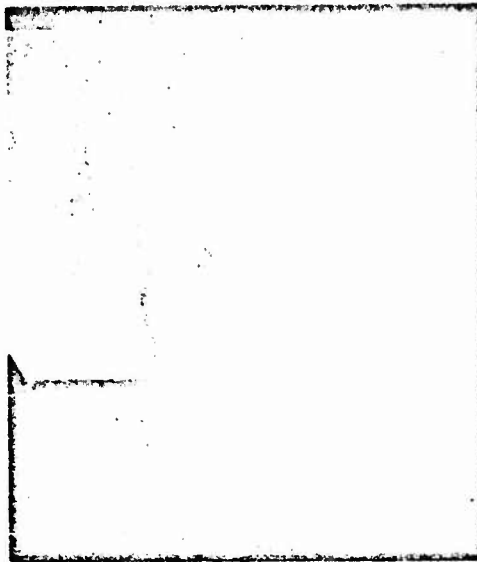
b. Radial-Inward Injection, P.R. = 58,300
   $\dot{w}_s/\dot{w}_p$ = 1.5 %
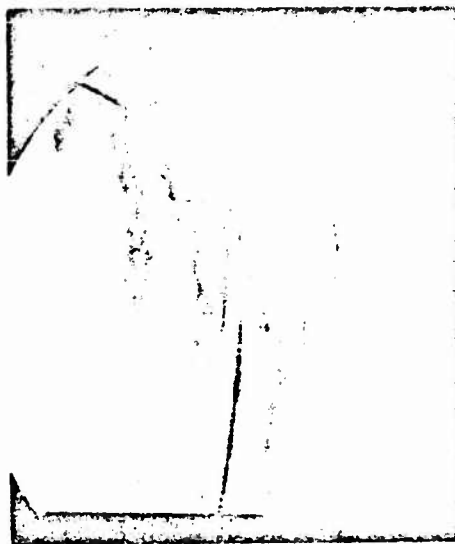
c. Radial-Outward Injection, P.R. = 44,000
   $\dot{w}_s/\dot{w}_p$ = 1.66 %

CONFIDENTIAL

Figure 33.   Flow Fields with Recessed Orifice Radial-Inward, and Radial-Outward Injection Configurations

(U) A summary of the 15 tests completed with this model is given in Table 3. The model was tested with an open base cavity and the recessed orifice method of secondary flow injection. A photograph of this model is presented in Fig. 34 .

Experimental Performance

(c) The conical model was tested over a pressure ratio range of 48,000 to 61,000 with secondary flows from 0 to 3.1 percent of the primary flow. The difference in pressure ratios results in a maximum theoretical difference of only 0.04 percent in C_T, so it was considered reasonable to neglect this difference in comparing the efficiencies. The efficiencies of these tests are presented versus secondary flow in Fig. 35 . A maximum efficiency of 96.2 percent was realized with a secondary flowrate of 2.03 percent; an increase of 1.2 percent in efficiency over the no secondary flow case. The base pressures for these tests (Fig. 36) indicated a change in slope when $\dot{w}_s/\dot{w}_p = 1.6$ percent.

Comparison with Theoretical Predictions

(U) The efficiency was not predicted for the conical model in Ref 1 ; however, base pressure and primary flow field analyses were subsequently completed.

(c) The base pressure was predicted using the same recompression criteria that were applied to the contoured model. The base pressure resulting from this nozzle wake analysis was $P_b/P_c = 0.00071$ and the experimental base pressure was $P_b/P_c = 0.00066$. The difference between the predicted and the experimental base pressures is equivalent to a difference of 0.25 percent in the overall efficiency.

TABLE 3

HIGH-AREA-RATIO TEST PROGRAM SUMMARY, CONICAL MODEL

Base Geometry	Secondary Flow, Percent $\dot{w}_p$	P_c/P_a	Area Ratio	Percent Length	Number of Tests
Open Cavity	0-3.08	60,000	129.9	5.9	5
	0	2600-9400			2 (dynamic tests)
	0-5	60,000			2 (dynamic tests)
Instrumented Sting (1/4 inch diameter)	0	50,000	129.9		4
	3.9	47,664			1
Uninstrumented Sting (0.049 inch diameter)	0	50,000	129.9		1
					—
					15
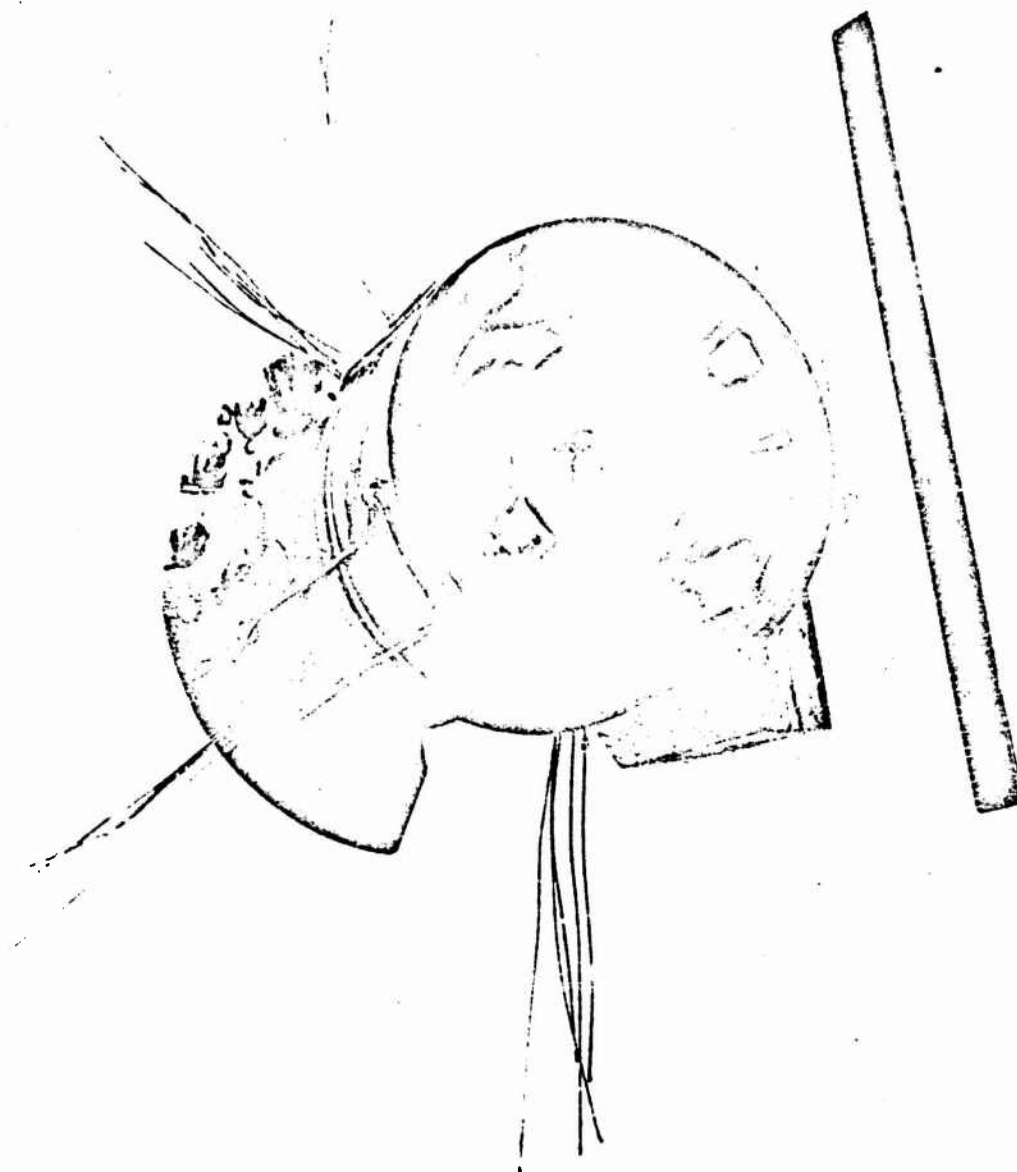
Figure 34. Recessed Orifice Injection Configuration, Conical Nozzle
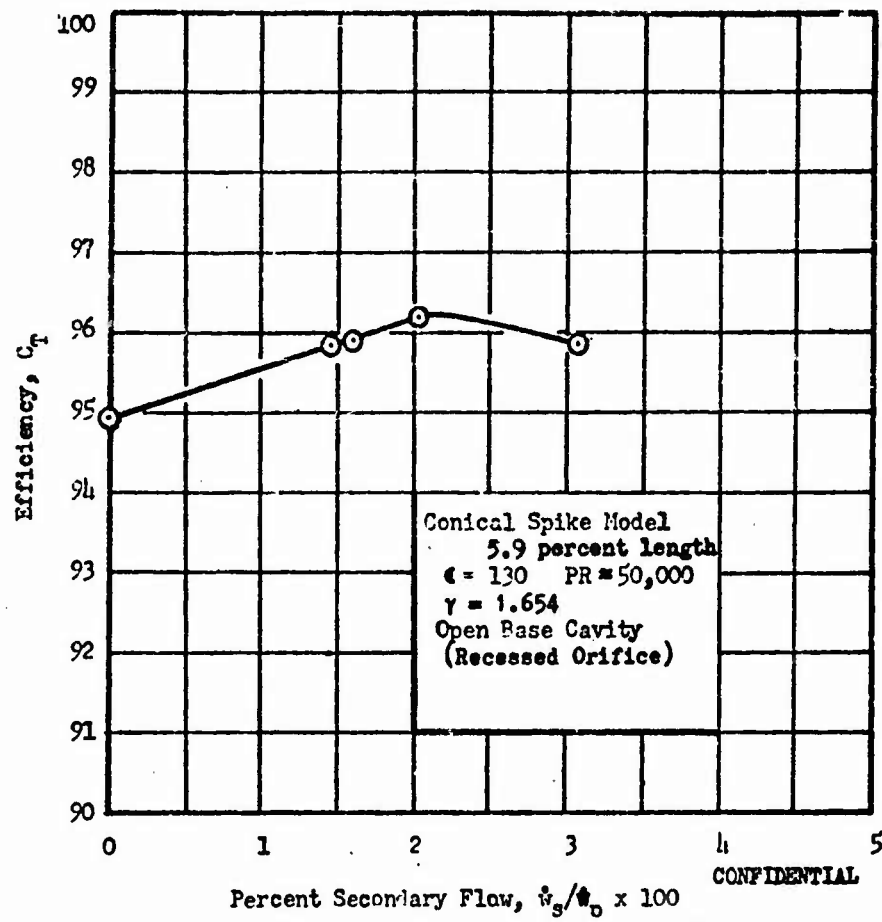
Figure 93. Efficiency Versus Secondary
Flowrate, Conical Aerodynamic Spike
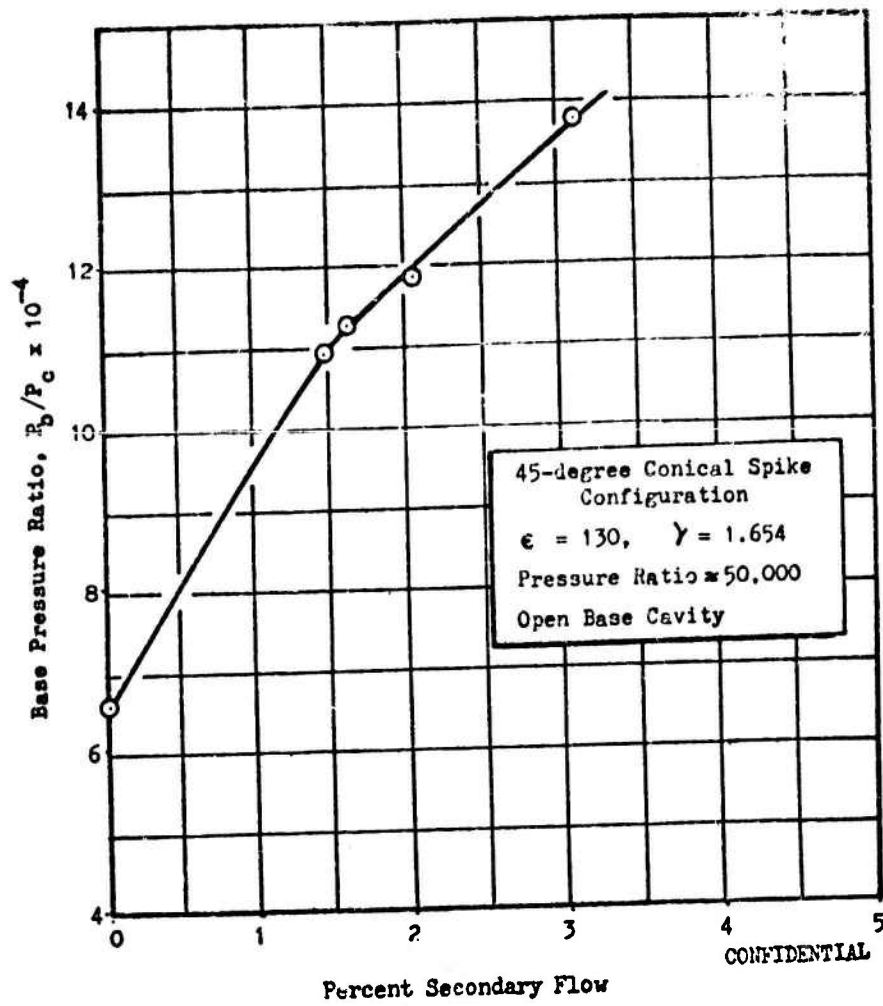
Figure 36. Base Pressure Ratio vs Secondary Flowrate,
45-degree Aerodynamic Spike

(C) To satisfy the recompression criteria it was necessary for the flow to separate from the primary nozzle wall before it reached the end of the nozzle. The base pressure analysis thus led to the prediction that the primary flow should separate from the nozzle wall at a point about 0.17 inch from the throat outer expansion point. The primary nozzle experimental pressures plotted in Fig. 37 indicate that the primary did in fact separate from the nozzle wall at approximately the predicted point. The fact that the separation point was determined by the base pressure solution shows that separations are influenced by the wake recompression phenomena. This makes the base pressure theory a very powerful tool in uncovering unusual flow situations of this sort.

(c) Further confirmation of the interrelation of base pressure and flow separation was gained by comparing the nozzle pressure profiles for various amounts of secondary flow (varying base pressure). These data are indicated in Fig. 38 . The variance in the separation point and the influence of base pressure on the nozzle wall pressures in the separated region is evident.

(c) CONCLUSIONS

1. The high performance $(C_q = 98.6$ percent) of a contoured, high area ratio aerodynamic spike model with secondary flow has been demonstrated.

2. The theoretical prediction of nozzle performance in the closed wake regime agreed within 0.1 percent of the experimental data.

3. Additional analytical and experimental effort is required to obtain a better understanding of high area ratio nozzle recompression phenomenon.

61
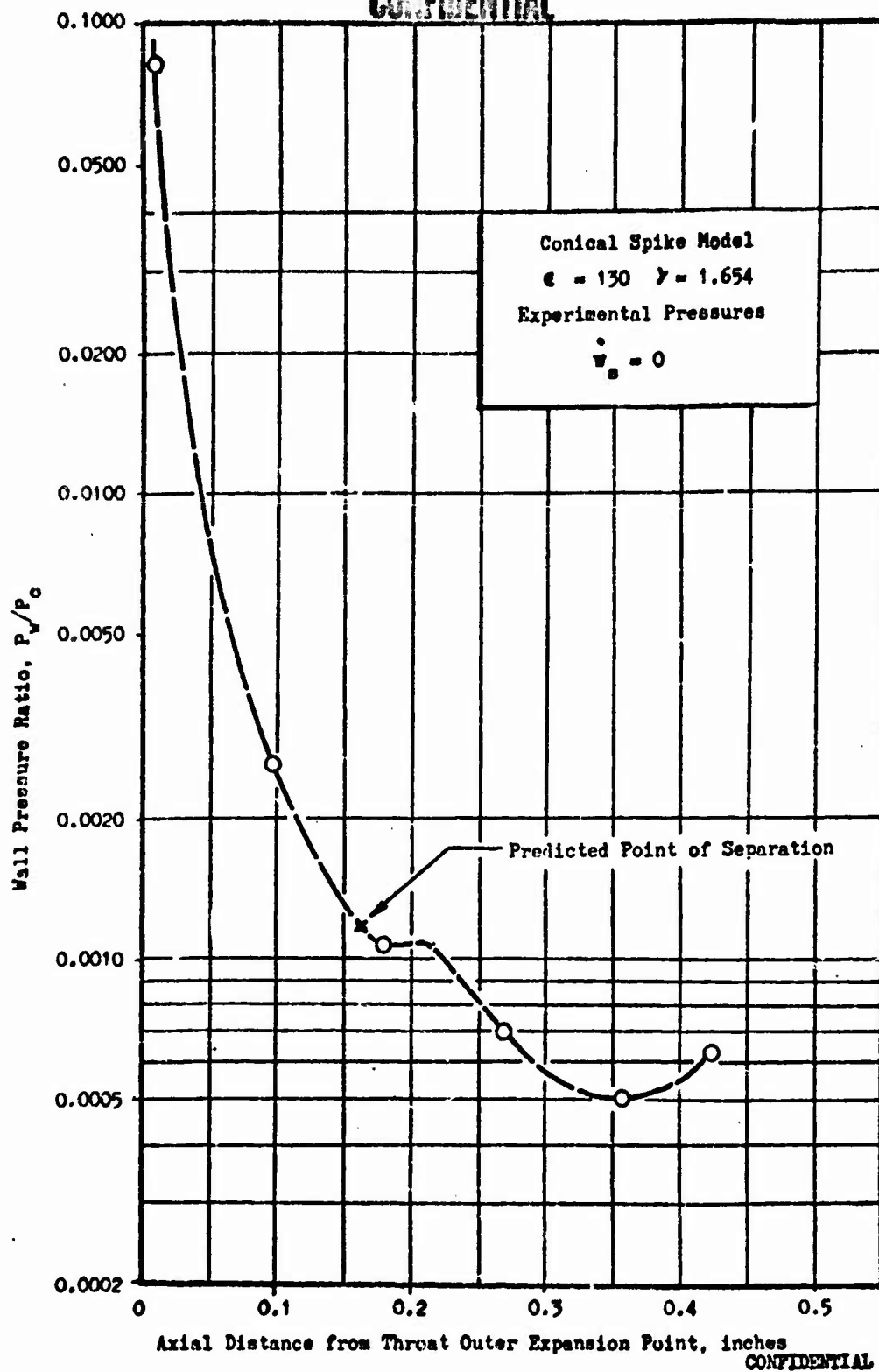
Figure 57. Experimental Wall Pressure Profile Without Secondary Flow. Conical Spike Model

Figure 58. Experimental Wall Pressure Profile with and without Secondary Flow, Conical Spike Model

CONFIDENTIAL

63

4. The most efficient method of injecting secondary flow that was tested is the recessed orifice method. However, low Mach number radial-in and radial-out injection methods, also provide effective means of injecting secondary flow.

5. Primary flow separation effects were theoretically determined for the 45 degree conical aerodynamic spike nozzle. The method used should be of value for analysis of other aerospike contours.

EXPERIMENTAL INVESTIGATION OF THE WAKE

(U) A number of experimental tests were devoted to surveying the aerodynamic spike wake. An instrumented wake probe or "sting" was mounted in the center of the model's base along the centerline of the aerospike wake flow field. The contoured model, fitted with the wake probe, is shown in Fig. 39 . The sting was equipped with six small static pressure taps along the surface of the probe. These taps enabled the reading of wake centerline pressures during any given run.

(C) As noted in the first quarterly progress report (Ref.1), there are three basic secondary flow regimes of interest in the closed-wake aerospike base pressure problem, (1) the no bleed regime, (2) the small bleed regime, and (3) the large bleed regime. The wakes of these three regimes were investigated for the conical and contoured spike models.

(C) The first regime investigated was the no bleed regime at high pressure ratios. In Ref. 1 , it was stated, (referring to Fig. 40) upstream of the base (Region 1) the flow is determined by the body shape and aerospike throat, and details can be obtained from a characteristic solution. In Region 2, the flow expands around the lower lip of the model and separates forming a free shear layer with constant pressure mixing (subregion b) which separates the external flow (subregion c)

64
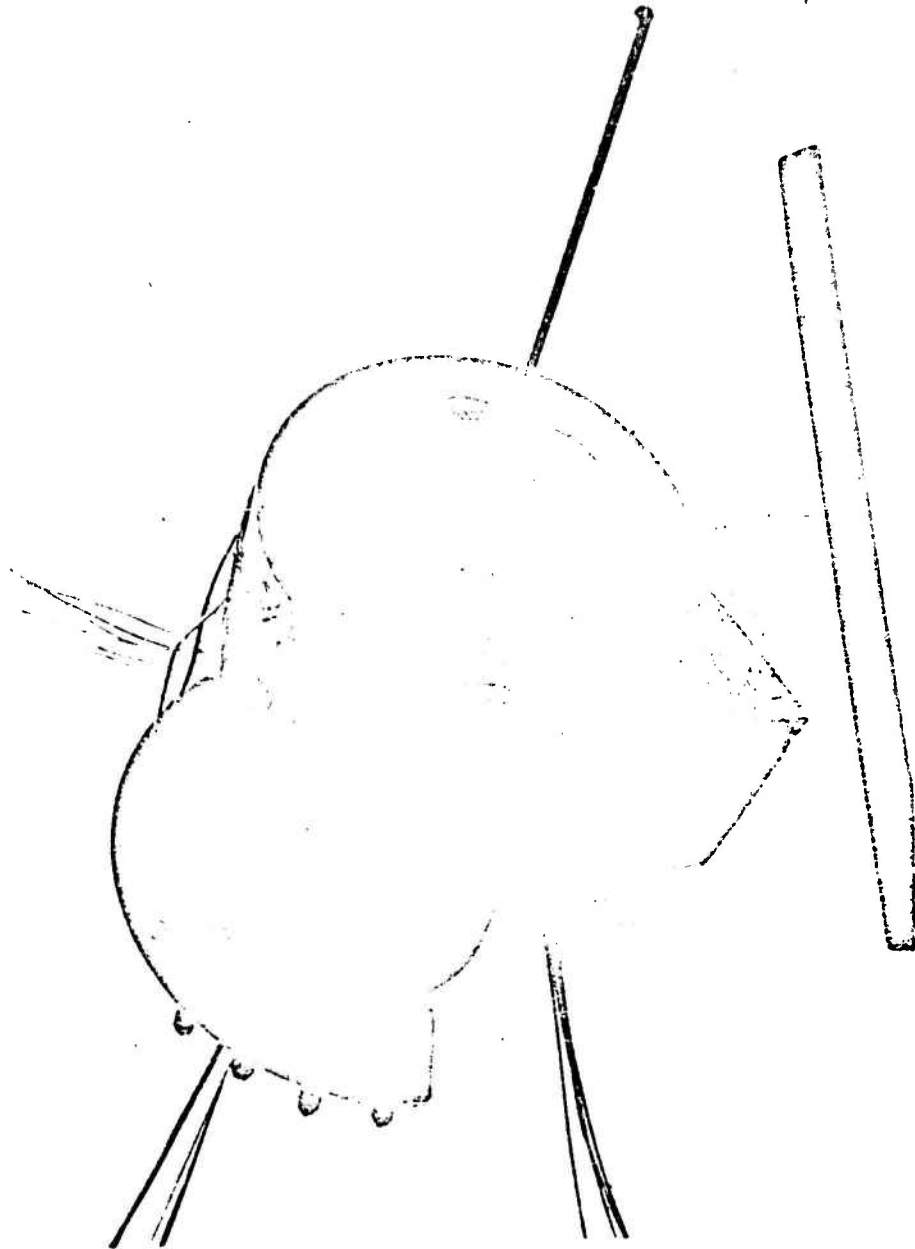
Figure 39. Instrumented Wake Probe Mounted on the Contoured High-Area-Ratio Aerodynamic Spike Nozzle

65
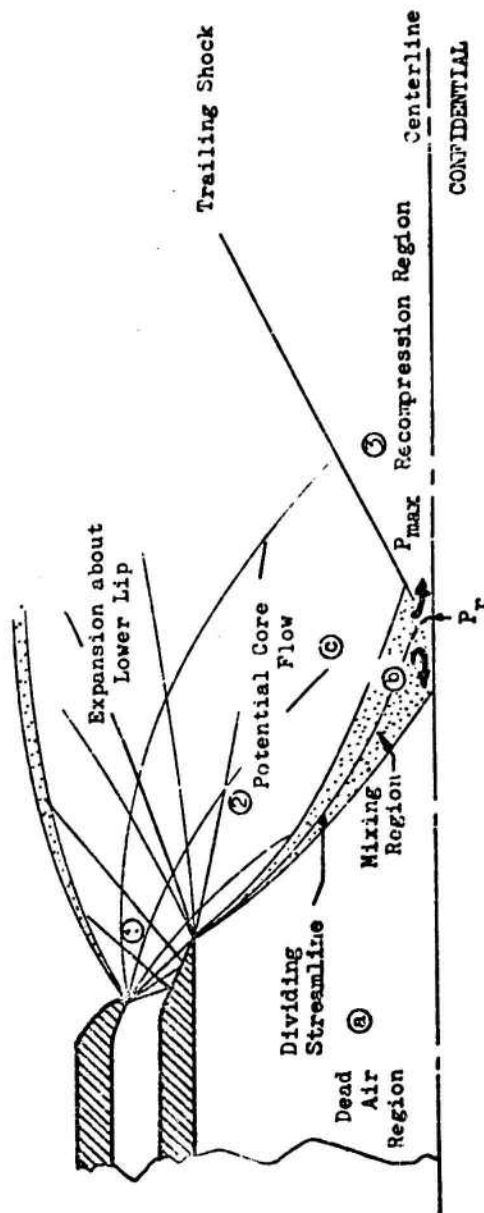
Figure 40. Aerospike Flow Field Model, No-Bleed Regime, Closed-Wake

66

from a "dead air region" of recirculating flow (subregion a). The free jet boundary and its adjacent shear layer then impinges on the centerline core where the flow reattaches and recompresses through a trailing shock separating regions 2 and 3 .

(C) The first objective of the wake probe experiments on the aerodynamic spike was to define the centerline wake pressure profile for the no bleed case and determine P_{max}/P_b. The results of the sting pressure measurements for the contoured and conical models is shown in Fig. 41 and 42 . Within the base cavity the centerline pressure is equal to the base pressure. Near the point on the axis where the shear layer of the free jet begins to impinge (see Fig. 40), the pressure rises rapidly to a maximum. This occurs at the point where the inviscid jet boundary as calculated from the characteristics program, impinges on the axis. The maximum pressure corresponds to the pressure immediately following the trailing shock. This shock is produced by the turning of the incident flow field back to a direction parallel to the centerline of the model. The pressure drops rapidly after P_{max} due to the diminishing strength of the trailing shock caused by the primary expansion waves.

(C) When a small amount of bleed (4.5 percent) was added to the base of the conical spike, the base pressure increased and the centerline maximum pressure, as seen in Fig. 42, decreased from a value of $P_{max}/P_c = 0.012$ to a value of $P_{max}/P_c = 0.0020$.

(C) This decrease in P_{max} is due to the fact that the angle of impingement of the free jet boundary has decreased because of the higher base pressure. A lower turning angle for the primary stream means a smaller pressure rise through the trailing shock. Since P_{max}, in this

67
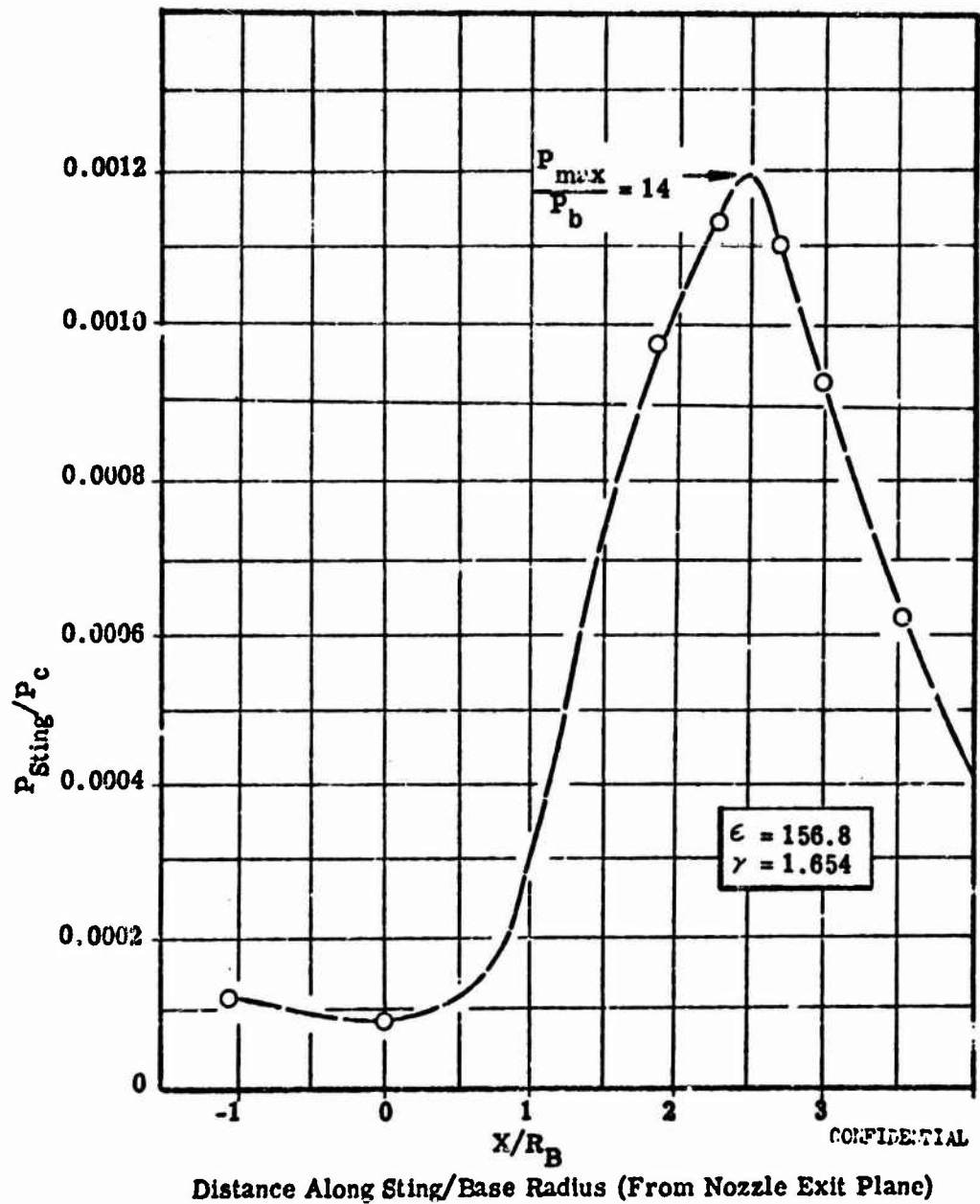
Figure 41. Centerline Wake Pressure Profile Contoured Spike Configuration, No Bleed

68
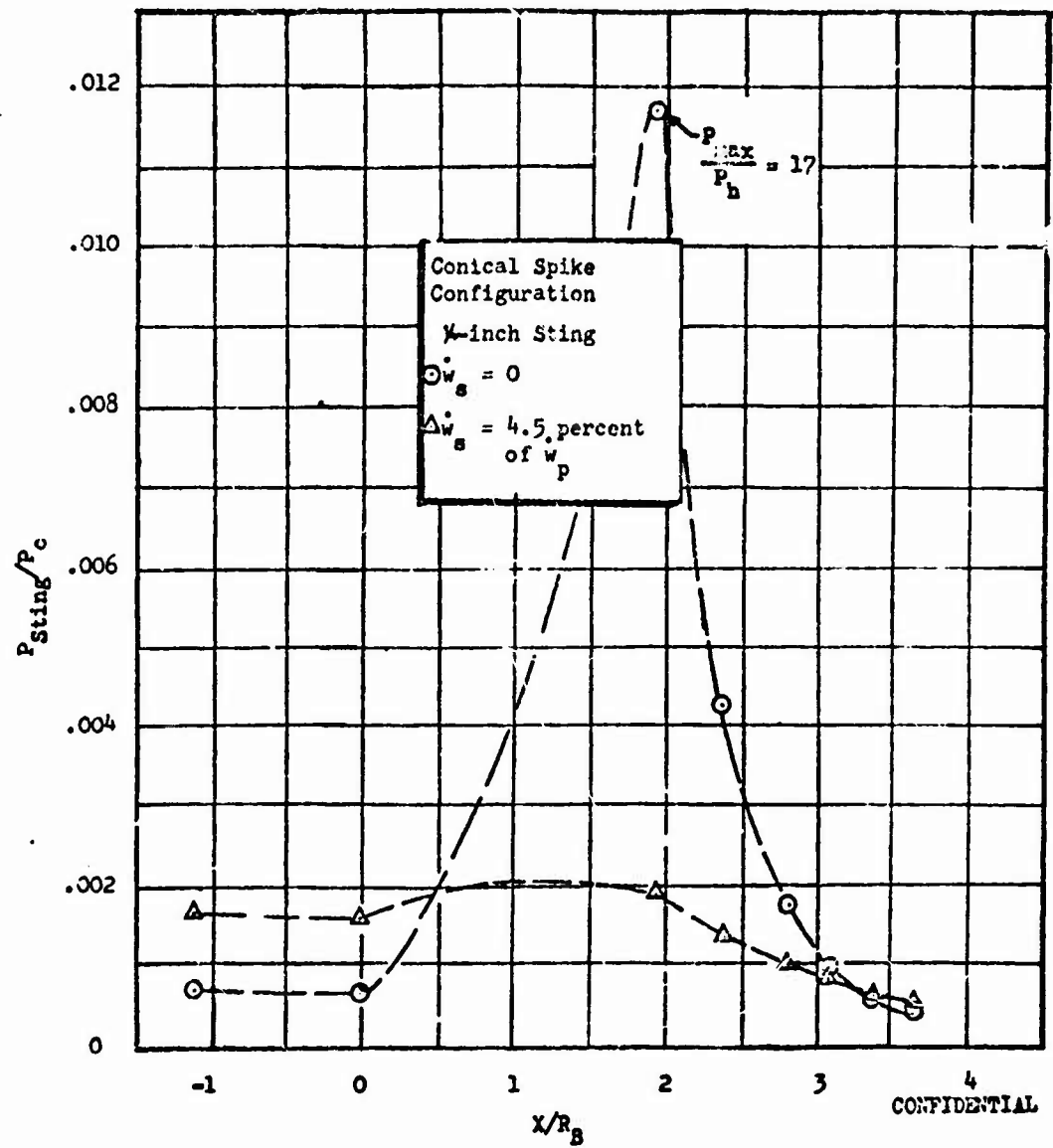
Figure 42. Centerline Wake Pressure Profile, Conical Spike

case, is still higher than P_b, this indicates that the wake is still
in the small bleed regime, where some recompression still occurs. It
should be noted that while 4.5 percent can be considered a "small
bleed" rate for the conical model, it definitely is not "small" for the
contoured model. This flowrate pushes the contoured model base pressure
into the high bleed regime, i.e., where no recompression pressure rise
above P_b is noted.

(C) A picture of the contoured model with sting, operating in the high
bleed regime is shown in the Schlieren photograph of the model operating
at a pressure ratio of 58,000, (see Fig. 43). The inner primary jet
boundary first dips down, then up, forming a continuous boundary between
primary and secondary. In Addy's thesis on ejectors (Ref 2), he
hypothesizes that a stable solution for the base pressure in this regime
is guaranteed by the criteria of choking of the secondary stream at its
minimum area. Thus, the object of testing the aerospike with large
bleed was to determine if Addy's criteria is valid. If so, it then
would be useful in obtaining a large bleed base pressure theory.

(C) The wake survey of the large bleed flow field for the contoured model
is shown in Fig. 44 . A monotonically decreasing centerline pressure
is noted outward along the sting axis. This profile is indicative of
flow in a choked nozzle. The choked pressure ratio corresponding to a
secondary throat is found for helium to have a value $P/P_b = 0.49$.
From the sting pressure measurements, the choked pressure ratio occurs
at a distance, measured from the end of the model, of $X/R_B = 1.6$.
From the Schlieren of Fig. 43 , the minimum area occurs approximately
at the same distance. Thus, it may be concluded that Addy's hypothesis
is valid in the large bleed regime, i.e., choking of the secondary does
occur at the minimum wake area and may be used as a necessary condition
for a stable base pressure solution.
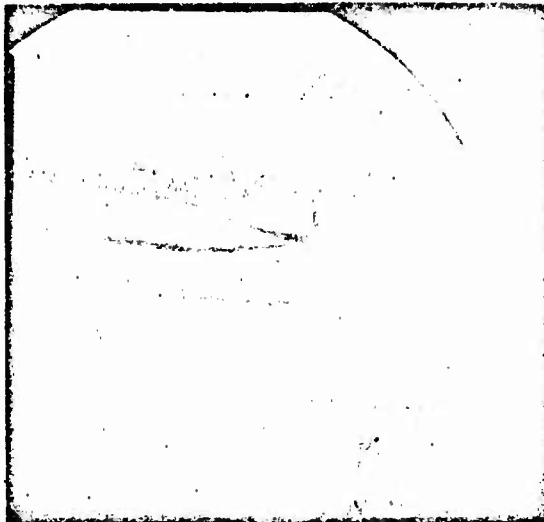
Figure 43. Wake-Flow Study for Contoured
Nozzle, High Bleed Rate
P. R. = 58,000

71
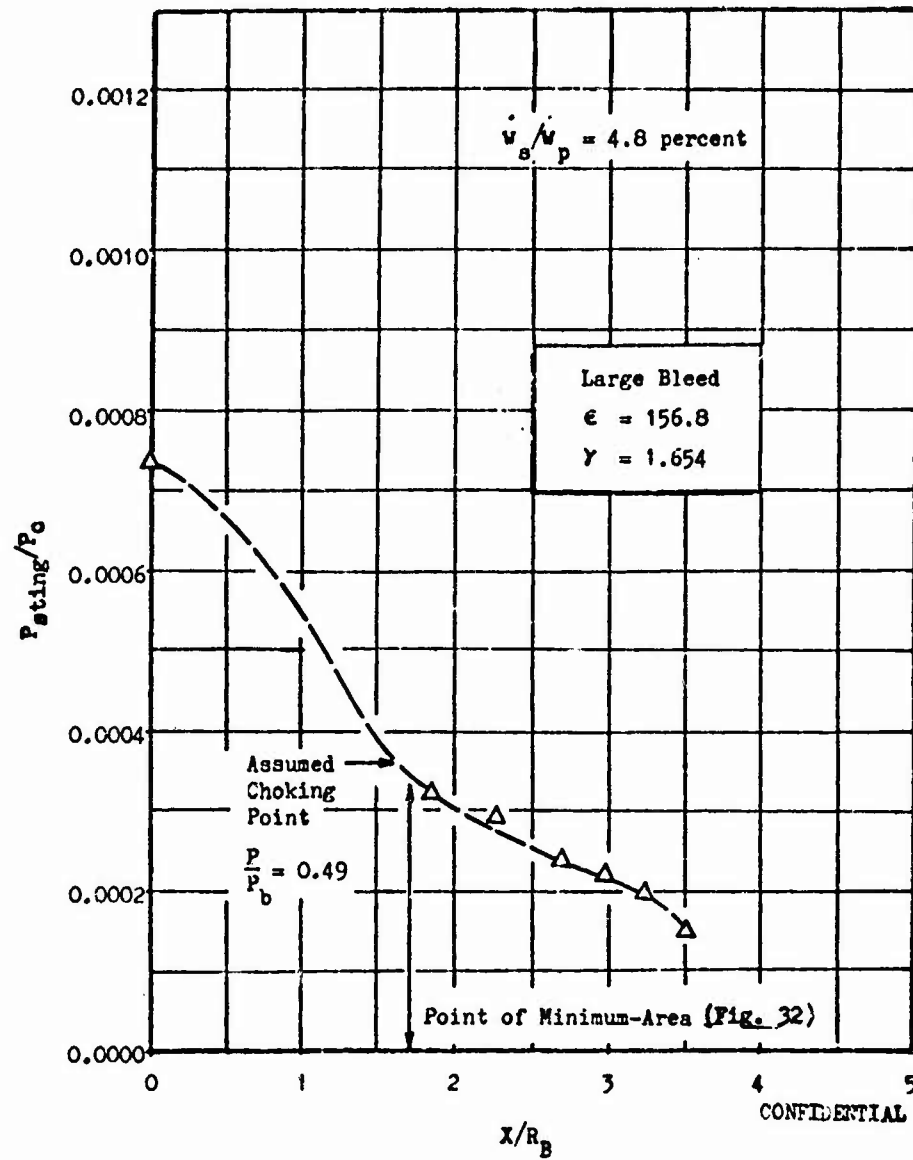
Figure 44. Centerline Wake Pressure Profile Contoured Spike
Configuration. Large Bleed

72

(c) In summary, several significant conclusions can be drawn from this wake study.

1. The wake survey with the 1/4" sting in the no bleed regime demonstrated the sharp pressure rise at reattachment which wake theoretical models qualitatively predict.

2. The centerline pressure profile in the small bleed regime for the conical nozzle was found to diminish considerably in magnitude from the no bleed case but a small pressure rise was still noticeable, justifying the present analytical methods and flow model for this distinct regime.

3. Choking of the secondary flow was shown to occur in the large bleed regime. Use of this evidence has been made in constructing a base pressure solution for the large bleed regime.

73/74

SECTION IV

COLD-FLOW TESTING OF COMBUSTOR CONFIGURATIONS

(U)   The main purpose of this cold-flow test program is to obtain experimental data for aerodynamic spike nozzles having various combustor configurations. The specific goal is to couple closely the effects of nozzle contour, combustor shape, and the use of secondary gas. To accomplish this, a group of multichamber and annular aerodynamic spike nozzles was tested. The models were designed to achieve maximum performance representative of the combustor configuration so that a comparison of relative performance could be made. In addition, a cold-flow model scaled from the hot-firing model was tested to obtain a direct comparison between hot-flow and cold-flow data for geometrically similar models. A total of 256 tests were achieved. A description of the models tested and of the test results is presented herein.

MODEL SELECTION

(U)   The models tested in this program are listed in Table 4. A cold-flow nozzle geometrically scaled from 10,000 pound thrust hot-firing aerospike nozzle was evaluated using various methods of introducing secondary flow into the nozzle base region. These models are designated as Group I, Nos. 1 through 5.

(U)   The models in Groups II and III were all of the same area ratio (50) and, except for model 9, of the same total length. These models were used to investigate the effect of combustor configuration on aerospike nozzle performance. The Group II models have continuous annular throats whereas the Group III models are aerospike nozzles with clustered conventional bell chambers forming the combustion chamber and initial expansion surface.

(U)   Table 5 gives a length comparison for all of the models referenced to both percent length of a 15 degree half angle conical nozzle and an ideal spike nozzle. Module area ratios are given for comparison to overall cluster area ratio of the multichambers. The models are discussed in the following pages.

TABLE 4
COLD-FLOW MODEL DESCRIPTION

Group	Number	Description
I	-	Scaled duplicate of the hot-firing model, $\epsilon_e = 25$
	1	Radial-inward secondary flow
	2	Recessed radial-outward secondary flow
	3	Open base
	4	Supersonic axial secondary flow
	5	Porous plate
II	-	Annular reference models (continuous throats, $\epsilon_e = 50$)
	6	Point expansion nozzle
	7	Shrouded nozzle
III	-	Multichamber models, $\epsilon_{CL} = 50$, circular exit chambers
	8	Eight touching chambers, $\epsilon_M = 30.2$, no shroud, no centerbody
	9	Eight touching chambers, $\epsilon_M = 30.2$, no nozzle extension
	10	Eight touching chambers, $\epsilon_M = 30.2$
	11	Eight chambers with spacing between chambers of 1/3 the exit diameter, $\epsilon_M = 20.7$
	12	Sixteen touching chambers, $\epsilon_M = 20.7$

76

TABLE 5

AEROSPIKE NOZZLE LENGTH COMPARISON

Model Number	N	ϵ_M	δ/D_e	θ_T	Relative Nozzle Lengths			
					Measured From Throat, L_N		Measured From Module Exit, L_p	
					Percent of 15 deg.cone	Percent of Ideal Nozzle	Percent of 15 deg.cone	Percent of Ideal Nozzle
1-5	–	–	–	–	12	9	–	–
6	–	–	–	–	30	16	–	–
7	–	–	–	–	30	16	–	–
8, 9	8	30.2	0.01	5.4	22	12	0	0.0
10	8	30.2	0.01	5.4	30	16	8	.0
11	8	20.7	0.31	9.5	30	16	12	6.5
12	16	20.7	0.02	9.5	30	16	18	10

Scaled Hot-Firing Model

(U)   A geometrically scaled version of the 10,000-pound thrust hot-firing
      model evaluated in this program was designed and tested. This model
      was selected to provide a direct comparison of data between geometrically
      similar hot-firing and cold-flow models and to provide additional design
      information with regard to efficient methods of introducing secondary
      flow into the base region. The nozzle is an ideal (isentropic) contour
      ($\gamma = 1.25$) truncated to a length which is 12 percent of a 15-degree
      conical nozzle with an ϵ_e of 25. The model is shown schematically in
      Fig. 45 with the radial-inward base configuration mounted. Other base
      injection methods tested include: a recessed radial-outward injection
      configuration which is obtained by placing the circular plate (2) flush
      with the nozzle exit and recessing plate (1) within the cavity; open
      base injection with the base plates removed; and two conical nozzles
      replacing the injection orifice (3) which inject secondary flow super-
      sonically into the base region. The assembled model is shown in Fig. 46
      with the various secondary gas injection devices displayed to the right
      of the model. The two components at the top are the supersonic nozzles.
      Below these nozzles are two 8-hole orifices for controlling the secondary
      flow for all configurations other than the supersonic nozzles. The
      second row from the bottom contains the two components required for
      either the radial-inward or radial-outward configuration. The spacer
      required for the radial outward configuration is at the bottom right of
      the photo. A flat porous plate (rigimesh) mounted flush with the
      nozzle exit was also used. This plate is at the bottom left of the
      group.
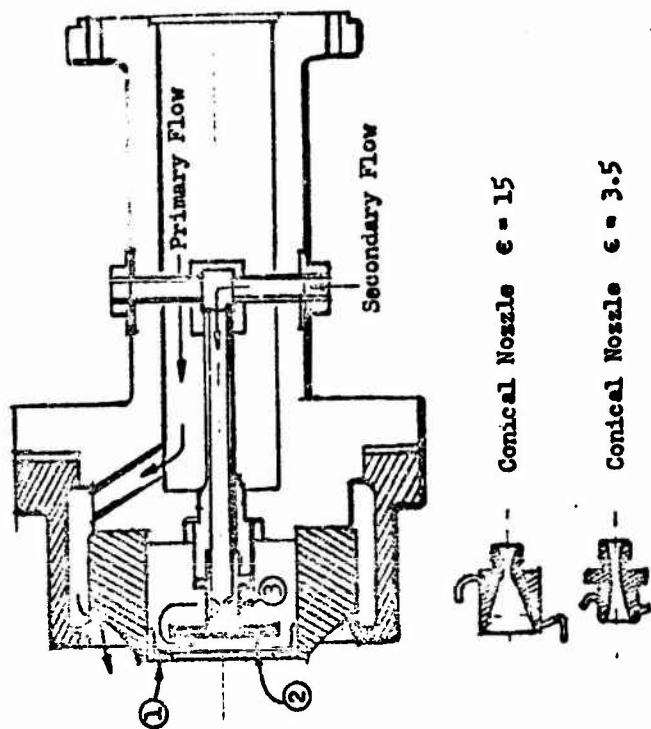
Figure 45. Cold-Flow Model. Scaled Version of 10,000 Pound Thrust Hot-Firing Chamber

79
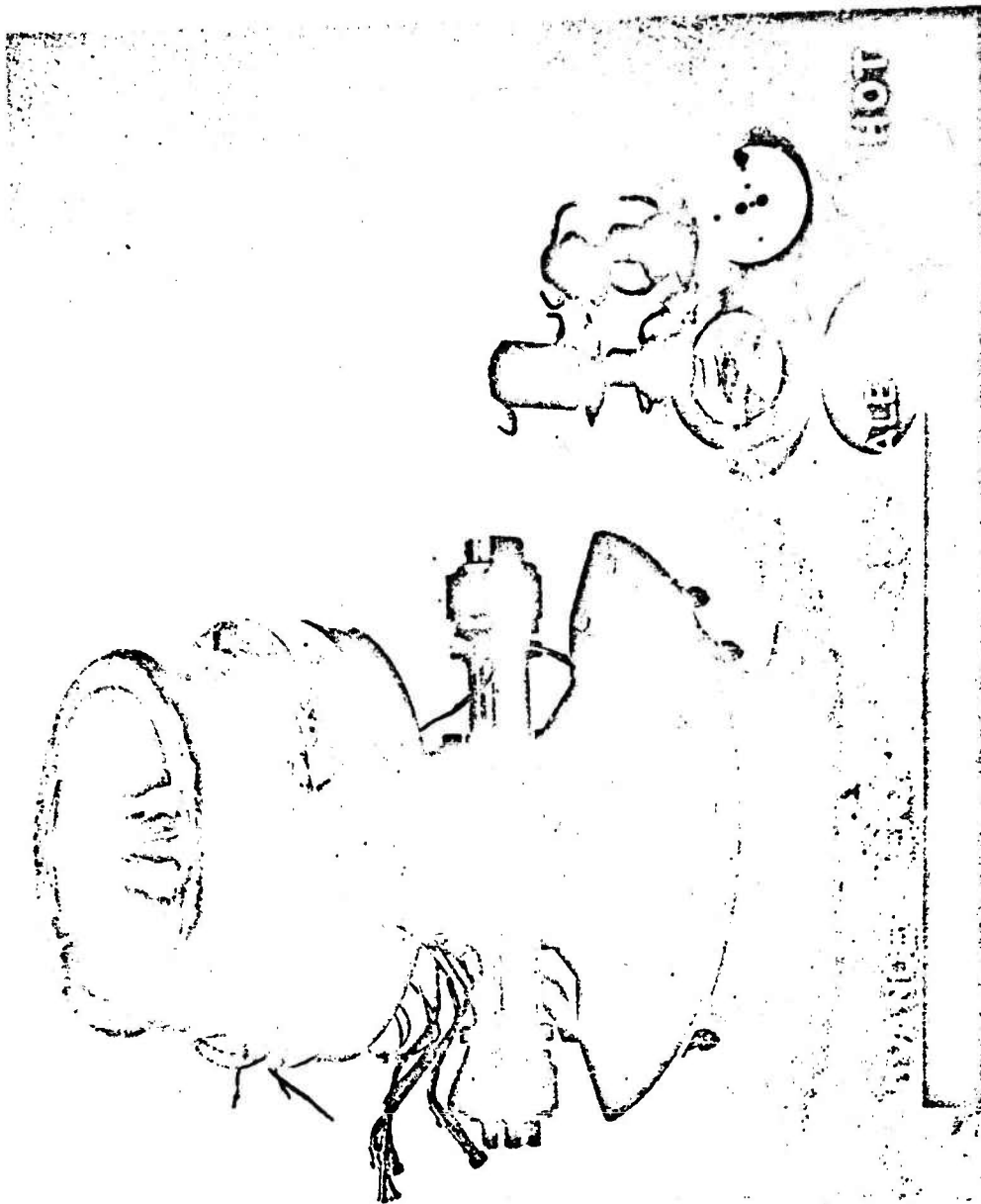
Figure 46. Sealed Hot-Firing Model

80

Annular Reference Models

(U)   Two continuous-throat annular reference models were tested; one is a "point expansion" design and the other is "shrouded". They are illustrated in Fig. 47. The assembled point expansion nozzle is shown in Fig. 48 and the shrouded nozzle assembly is shown in Fig. 49. Each of these models was designed for an area ratio of 50 and an axial length from the outer-throat expansion point equal to 30 percent of a 15-degree conical nozzle of the same area ratio. The contour for the point-expansion nozzle was developed by generating an ideal spike contour with an area ratio of 50 and a γ of 1.4 and subsequently truncating it to 30 percent length.

(U)   The shrouded annular nozzle was designed to approximate the type of shroud for a typical hot-firing nozzle using storable propellants. Proper shrouding of annular nozzles will provide expansion conditions which are favorable for maintaining chemical equilibrium (shifting equilibrium). The selected shroud was an annular cone shape with a 10 degree divergence half angle. The nozzle was shrouded to an area ratio of 3 and the centerbody was designed to give good primary flow field and base pressure characteristics.

(U)   The design of shrouded spike contours is different from the point expansion spike nozzle. For the point expansion nozzle the outer flow perimeter freely expands at the throat to ambient conditions. For the shrouded nozzle the expansion of the outer flow perimeter is contained from the throat by a physical surface of short axial length. The shrouded spike design procedure generates spike contours based on a selected shroud inclination angle and shroud configuration. The steps followed to design the shrouded nozzle were (refer to Fig. 50):

     a) A shroud inclination angle β for the 10 degree half angle cone shroud was selected based on previous work (Fig. 50a).

81
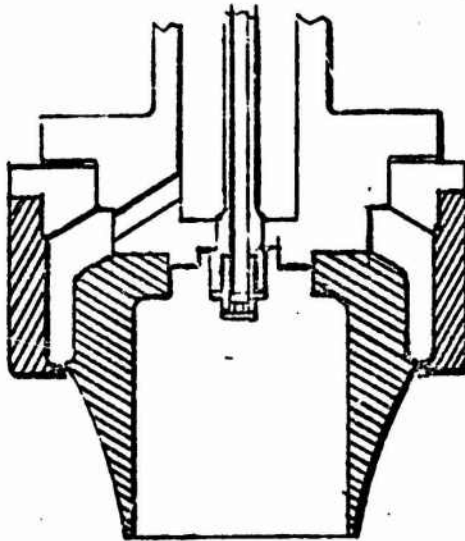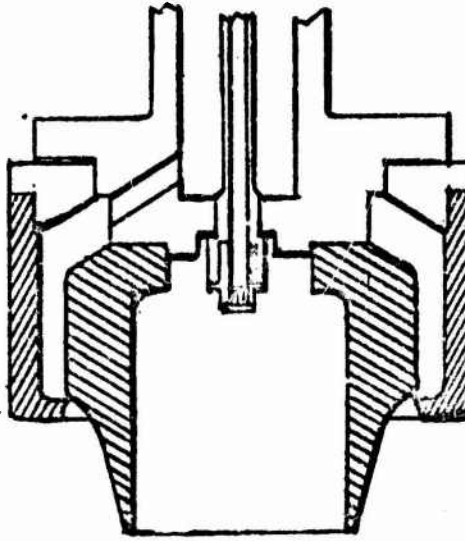
b. Point Expansion Nozzle

a. Shrouded Nozzle

Figure 47. Annular Reference Models
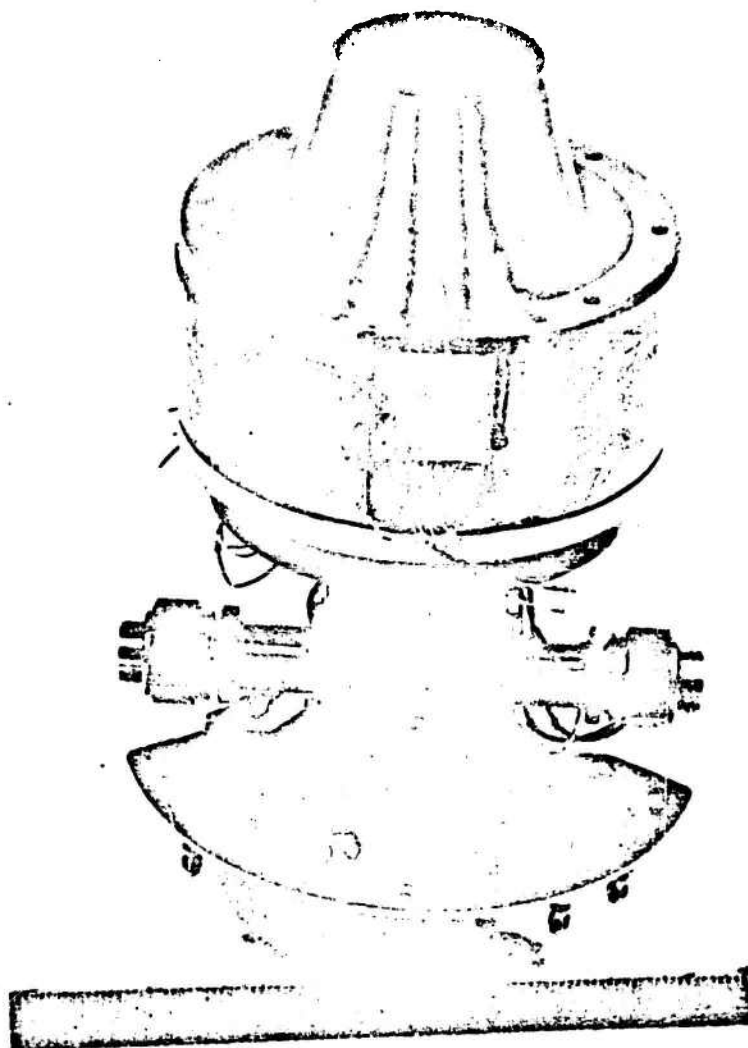
Figure 48. Point Expansion Annular Reference Model, $\epsilon_2 = 50$
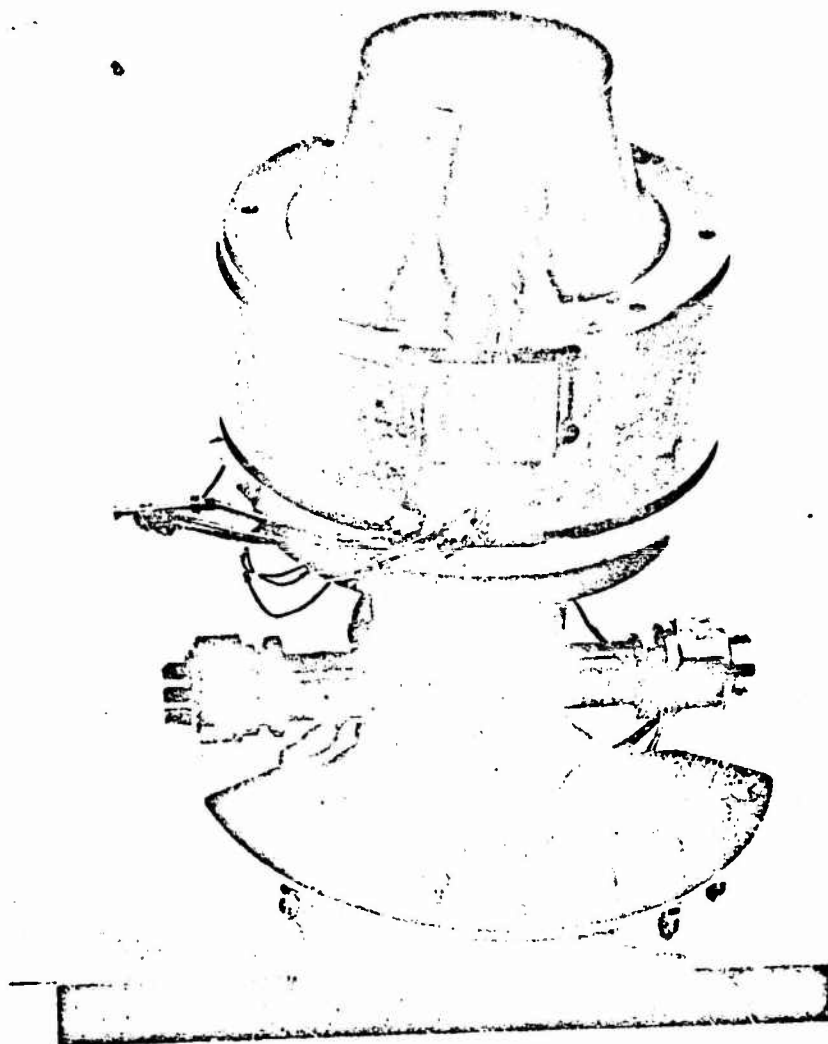
Figure 49. Shrouded Annular Nozzle, $\epsilon = 50$

84

(b) Shroud Flow Field

Characteristic
Net Solution

Input Line

Optimum Contour
Control Surface

Optimum Contour

(d) Contour Design

$\beta = -30°$

$\alpha = 10°$

(a) Shroud Parameters

Prandtl-Meyer Expansion
About Outer Lip

Last Left Running Characteristic
from Shroud Part of Contour
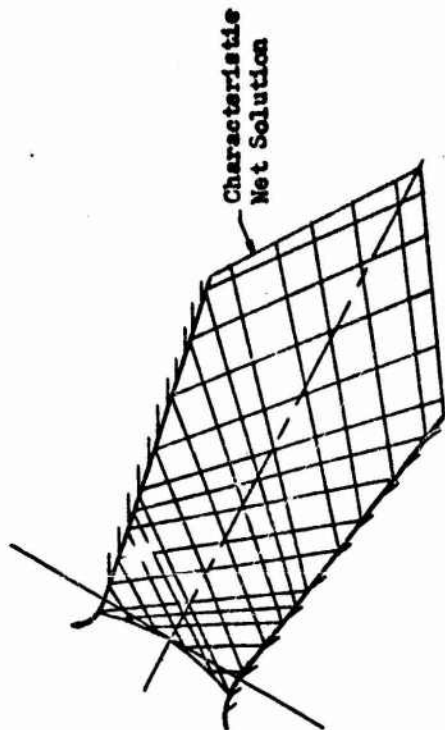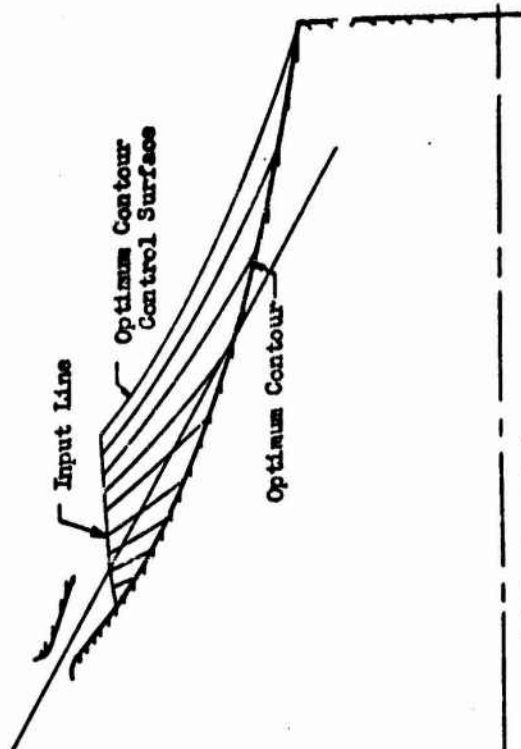
(c) Point Expansion at Outer Lip

85

b) The flow net (Fig. 50b) was computed to the end of the shroud using the method of characteristics for axisymmetric flow.

~) The left characteristic line (input line) from the point on the contour corresponding to the end of the shrouded portion of the contour was extended by turning the flow about the end of the shroud in an expansion fan (Fig. 50c).

d) The extended left characteristic line was used to generate a series of optimum (maximum thrust) control surfaces, each surface defining a nozzle of different length. By computing the characteristic net between the control surface and the input line, the nozzle contour was developed.

(U) The above design procedure can produce a set of contours (various lengths) for a selected shroud inclination angle. The inclination angle may be varied arbitrarily within certain limits, with a different set of contours resulting for each β angle selected. The best inclination angle is determined by designing contours for several inclination angles and selecting the angle that gives highest performance. In this case the results of a previous study indicated that a good β angle for these conditions was -30 degrees.

(U) A different nozzle length results for each different point on the input line selected to generate a design. The shrouded annular nozzle contour selected consisted of an 80 percent length optimum nozzle truncated to 30 percent length. This nozzle was selected from a series of contours of various lengths as the contour yielding the best combination of primary performance and base pressure.

Multichamber Models

(U) Three basic multichamber models were tested, the 8 touching, 8 spaced and 16 touching models (listed in Table 4). The 8 touching models had two basic configurations, i.e., zero centerbody length and a spike centerbody extended to 30 percent length. Two configurations were tested for the 16 touching model; one with open spaces between the modules and one with a filler plate between modules.

86

(U)   The typical model assembly is illustrated in Fig. 51. Each model has an
overall cluster area ratio of 50 (determined by D_{CL} in Fig. 52), and
utilizes 80 percent length individual bell chambers in its respective
cluster. A cylindrical shroud tangent to the individual chamber exits
encloses to multichambers. Each bell was designed for maximum thrust
with air. Assemblies of the 8 chambers touching, 8 chambers spaced and
16 chambers touching multichamber models are shown in Figs. 53, 54, and
55.

(U)   All of the configurations except models Number III-8 and III-9 have spike
centerbodies of sufficient length to provide an overall length, L_M,
equal to 30 percent of a 15-degree conical nozzle. Figure 53 shows
model III-10 with the 30 percent spike installed and the model III-9
centerbody (no spike extension) in the lower right hand corner of the
photo. Model III-8 is a stripped down version of model III-9 and is
shown installed in the RNTF in Fig. 56. The procedure used to design
the multichamber models will be discussed below.

(U)   The following equation (derived in Ref. 3) which describes the inter-
relationship of the clustering geometric variables was used to design
the multichamber models.

$$\frac{\epsilon_{CL}}{\epsilon_N} = \frac{1}{N} \left[\frac{(1 + \delta/D_e) \cos \theta_T}{\sin \left(\text{Arctan} \cos \theta_T \tan \frac{180}{N} \right)} + \cos \theta_T \right]^2$$
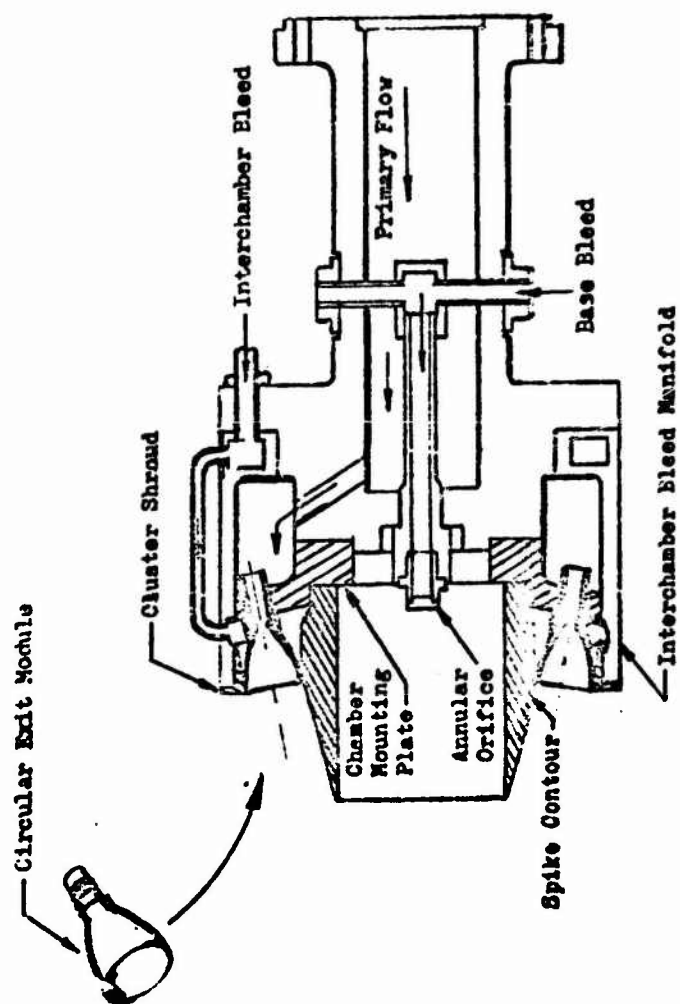
Figure 51. Multichamber Model Configuration
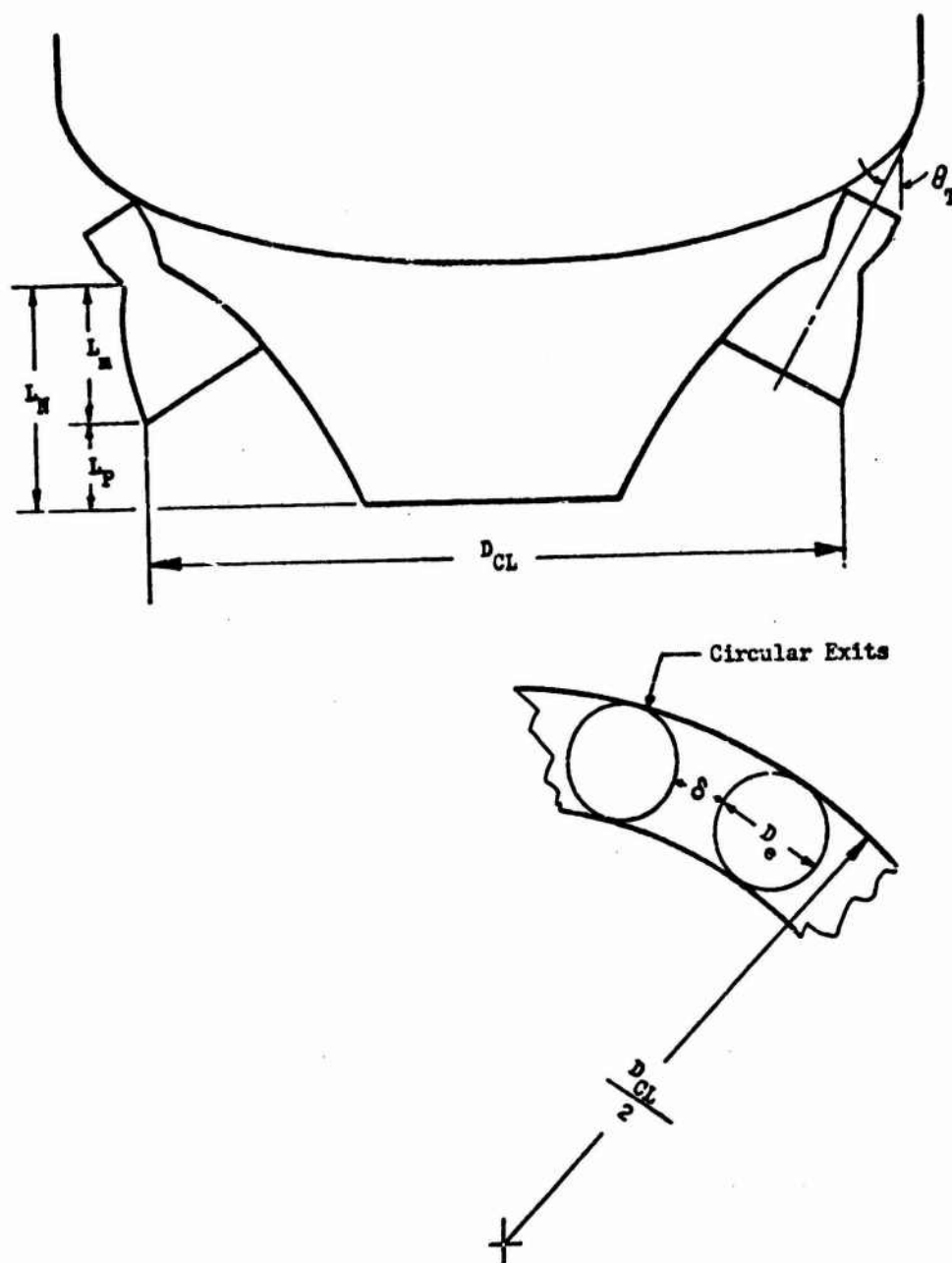
Figure 52. Multichamber Nomenclature

89
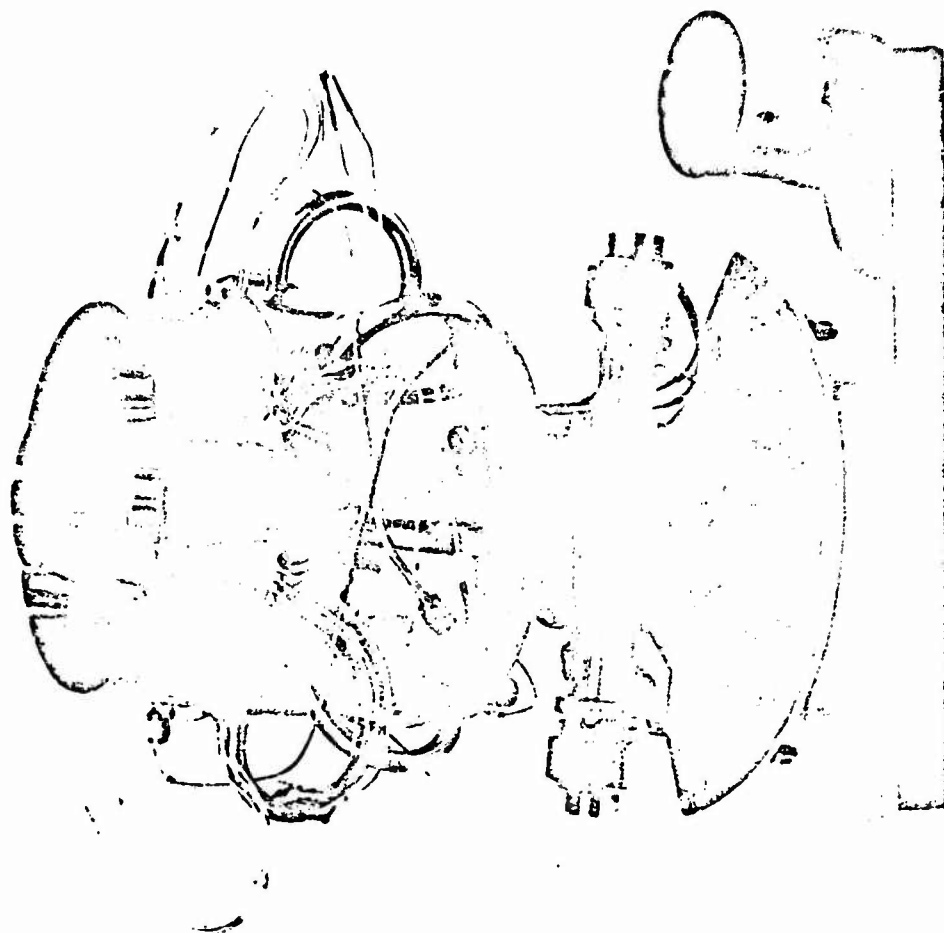
Figure 53. Eight Chambers Touching Multichamber, $\epsilon_{CL} = 50$
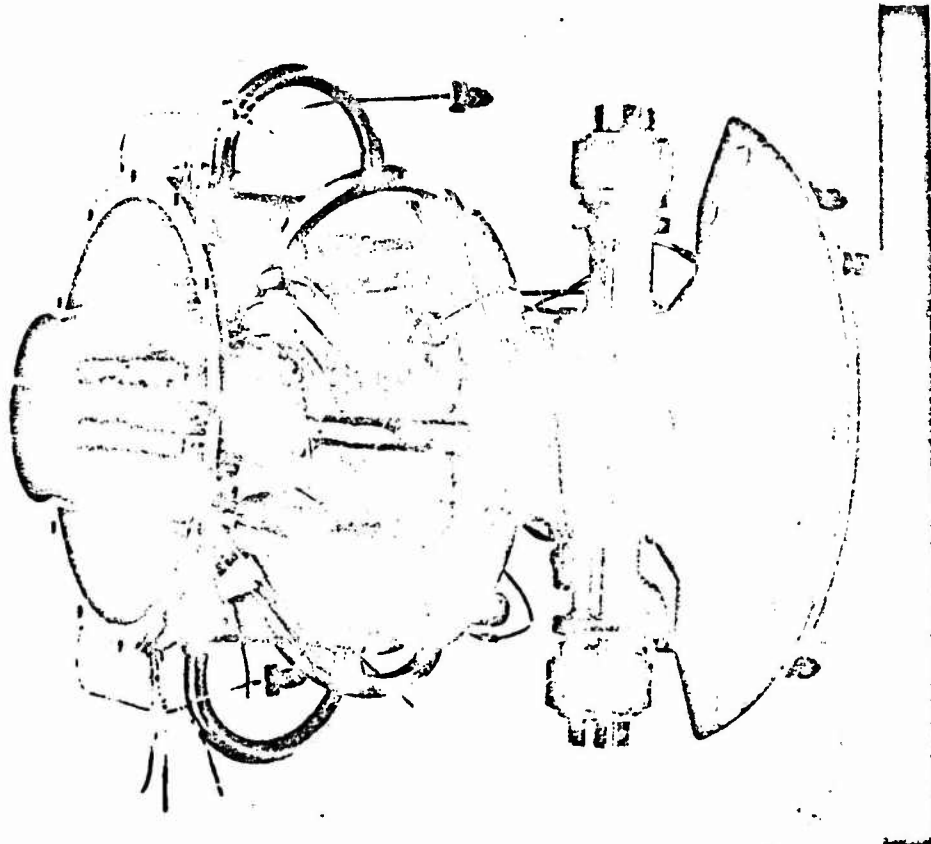
Figure 54. Eight Chambers Spaced Multichamber, $\epsilon_{CL} = 50$
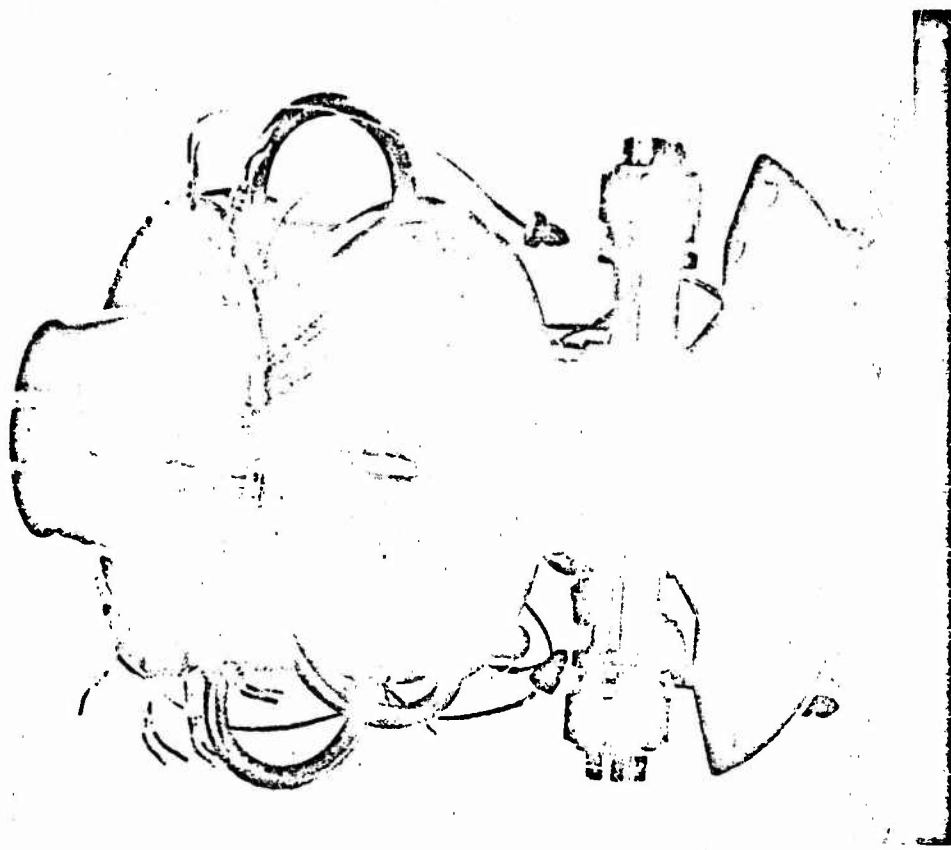
Figure 55. Sixteen Chambers Touching Multichamber, $\epsilon_{CL} = 50$
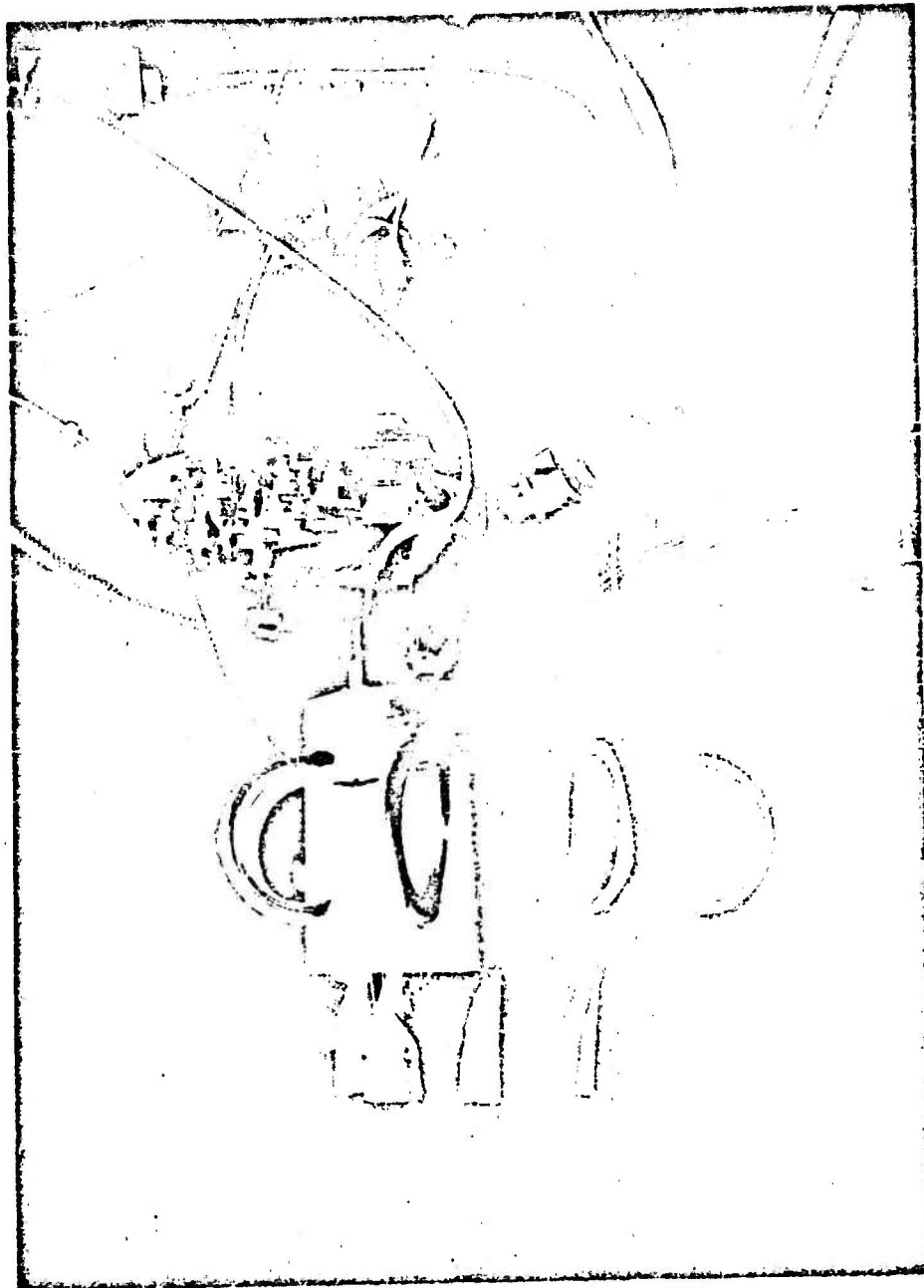
Figure 56. RNTF Installation of Stripped Down Version of Eight Chamber Touching Multichamber.

93

(U) Referring to Fig. 52, the first step in designing a multichamber
     model is to select independently the number of chambers N, the gap
     spacing δ, and the overall area ratio ϵ_{CL}. Two quantities must then
     be determined simultaneously, the modular exit area ratio ϵ_M and the
     tilt angle θ_T. To do this, a module exit area ratio is first assumed.
     The tilt angle is then determined from the difference between Prandtl-
     Meyer angles corresponding to the cluster or overall area ratio
     ($\epsilon_{CL} = 50$ in this case) and the module area ratio. Now that the tilt
     angle is known a new module exit area ratio can be calculated from the
     above equation. The process is repeated until sufficient accuracy is
     obtained.

(U) The tilt angle and module area ratio have now been fixed and the radial
     dimension of point a (Fig. 57) is determined. An ideal spike is
     designed for the same area ratio as the overall or cluster area ratio
     of the multichamber as if it had a point expansion about point c.
     Point b is then selected at the same radial distance as point a and
     the ideal contour is translated axially so that point a and b coincide.
     The ideal contour is then truncated at the desired length. This gives
     a relatively good match in angle between the module and the spike at
     point a.

(U) This process was carried out for all of the multichamber nozzles with
     spike extensions. For the two models with 8 chambers the theoretical
     contours were approximated by conical spikes, the difference in per-
     formance being only 0.01 percent.

94

Ideal Spike Contour

Shift

b

Ideal Contour
After Shift

c

a

Bell Module
Exit
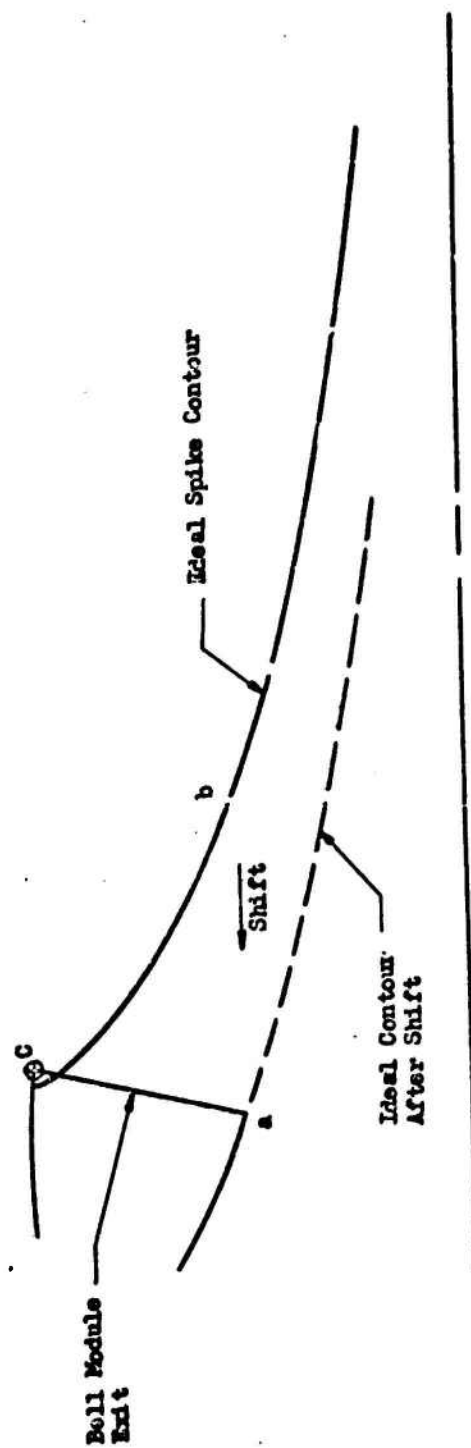
Figure 57. Design of Spike Contour for Multichamber Models

95

TEST PROGRAM

(U) A total of 256 tests were conducted during a 6-week period. All of the configurations were tested over a pressure ratio range approximating sea level to design pressure ratios. The effect of secondary flow was investigated for all configurations over the entire pressure ratio range. Intersegmental (i.s.) bleed was used for the multichamber configurations in addition to secondary flow.

(U) Model I-3, the scaled hot-firing model, was tested using both air and CF_4 gas. Several secondary-flow injection methods were investigated for the scaled hot-firing model.

Performance Calculations

(U) Primary flow field theoretical performance was calculated for the annular models using the method of characteristics (Ref 4 and 5) for the potential flow and the integral momentum equation for the drag losses (Ref 6 through 9). Solutions for both the potential flow field and drag loss have been developed on electronic computer programs used at Rocketdyne. Overall performance was then predicted by adding the contributions from experimental base pressure and ambient drag loss. Total nozzle performance is obtained by a summation of all contributing factors which are listed as follows:

96

1. Potential flow (intrinsic nozzle performance)
2. Boundary layer drag loss
3. Base pressure contribution
4. Ambient drag

$$C_{F_{tot}} = C_{F_{int}} - C_{F_{drag}} + C_{F_b} - C_{F_{Amb.}}$$

(U) With the aid of the figure below, these terms are defined as follows:
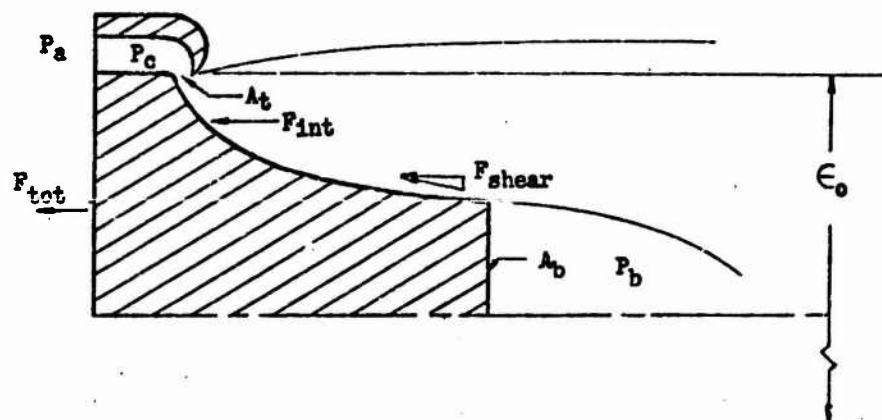
$C_{F_{tot}}$ = overall nozzle performance, $\dfrac{F_{tot}}{P_c A_t}$

$C_{F_{int}}$ = potential flow field performance, $\dfrac{F_{int}}{P_c A_t}$

$C_{F_{drag}}$ = boundary layer drag, $\dfrac{F_{shear}}{A_t P_c}$

C_{F_b} = base pressure contribution, $\dfrac{P_b}{P_c} \dfrac{A_b}{A_t} = \dfrac{P_b}{P_c} \epsilon_b$

$C_{F_{Amb.}}$ = ambient drag, $\dfrac{P_a}{P_c} \epsilon_o$

97

(U)   Nozzle efficiency, C_T , is then calculated by comparing $C_{F_{tot}}$ to the
ideal C_F at a given pressure ratio, P_a/P_o.
$$C_T = \frac{C_{F_{tot}}}{C_{F_{opt}}}$$

where

$$C_{F_{opt}} = \sqrt{\frac{2\gamma^2}{\gamma-1}\left(\frac{2}{\gamma+1}\right)^{\frac{\gamma+1}{\gamma-1}}\left[1-\left(\frac{P_a}{P_c}\right)^{\frac{\gamma-1}{\gamma}}\right]}$$

(U) $C_{F_{tot}}$ is obtained in a slightly different manner for the experimental
data.

$$C_{F_{tot}} = \frac{F_{tot}}{P_{c_{Mod}} A^*_{Mod}}$$

$$A^*_{Mod} = \sqrt{\frac{T_{c_{Mod}}}{T_{c_V}}} \; \frac{P_{c_V}}{P_{c_{Mod}}} \; \frac{f_V}{f_{Mod}} \; A_{t_V} C_{D_V}$$

$$C_{F_{tot}} = \frac{F_{tot}}{P_{c_V} A_{t_V} C_{D_V} f_V} \; f_{Mod} \sqrt{\frac{T_{c_V}}{T_{c_{Mod}}}}$$

in which

F_{tot} = total measured force

P_{c_V} = flowmeter chamber pressure

A_{t_V} = flowmeter throat area

C_{D_V} = flowmeter throat discharge coefficient

T_{c_V} = flowmeter chamber temperature

$T_{c_{Mod}}$ = model chamber temperature

f_V = flowmeter weight flow coefficient

f_{Mod} = model weight flow coefficient

(U) Since $A^*_{Mod} = C_D A_t$ all experimental performances are presented with respect to A^*_{Mod}, the aerodynamic throat area, rather than A_t, the geometrical throat area. A^*_{Mod} was also used in calculating theoretical performance in order to be consistant.

(U) Critical data for all of the models is tabulated in Appendix 3.

Scaled Hot-Firing Model – Air Tests

(U) The principal objectives of the tests with this model were:

1. Determine the overall nozzle performance, with and without secondary flow over an altitude range from sea level to design altitude.
2. Test several base configurations and evaluate secondary-flow injection methods.
3. Determine nozzle performance and base pressures using a gas, CF_4, having a ratio of specific heats which approximates that of hot-firing gases. Compare these CF_4 data with the air data and the data to be obtained in the hot-firing program.

(U)   The open-base model was first tested with air over a pressure ratio range from 20 to 600 (design pressure ratio is approximately 515) without secondary flow. A reference performance with secondary flow was then obtained with the same model by varying the secondary flow rate at pressure ratios of 35, 170, and 540. The secondary flow giving maximum efficiency at each pressure ratio was determined. Secondary flow was introduced using an 8-hole orifice recessed within the open base (Component 3 in Fig. 45,p.79).This configuration (Model I-3, Table 4, p.76) is used as a reference for comparison with the other base configurations and injection methods.

(U)   Tests were then performed with air using the other base injection methods. These were the radially-in, radially-out, porous plate and supersonic nozzle configurations (see Table 4,p.76). The supersonic nozzle configuration consisted of secondary flow being injected through each of two conical nozzles of area ratio 3.5 and 15 respectively. Each configuration was tested at pressure ratios of 35, 170, and 540 using the optimum secondary flowrate determined from the open-base configuration tests.

(C)   The results of the RNTF (Rocket Nozzle Test Facility) tests are shown in Fig. 58 and are tabulated in Appendix 3. Near design pressure ratio $(P_c/P_a = 540)$ the thrust efficiency was 96.5 percent with the open base configuration and no secondary flow. For the open base configuration secondary flow (air) was varied from 0 to 3 percent of primary flow with a resulting nozzle efficiency peak of 97.6 percent (see Fig. 59) occurring at 2 percent secondary flow. These efficiencies with air are lower than usually expected because the contour is designed for $\gamma = 1.25$.
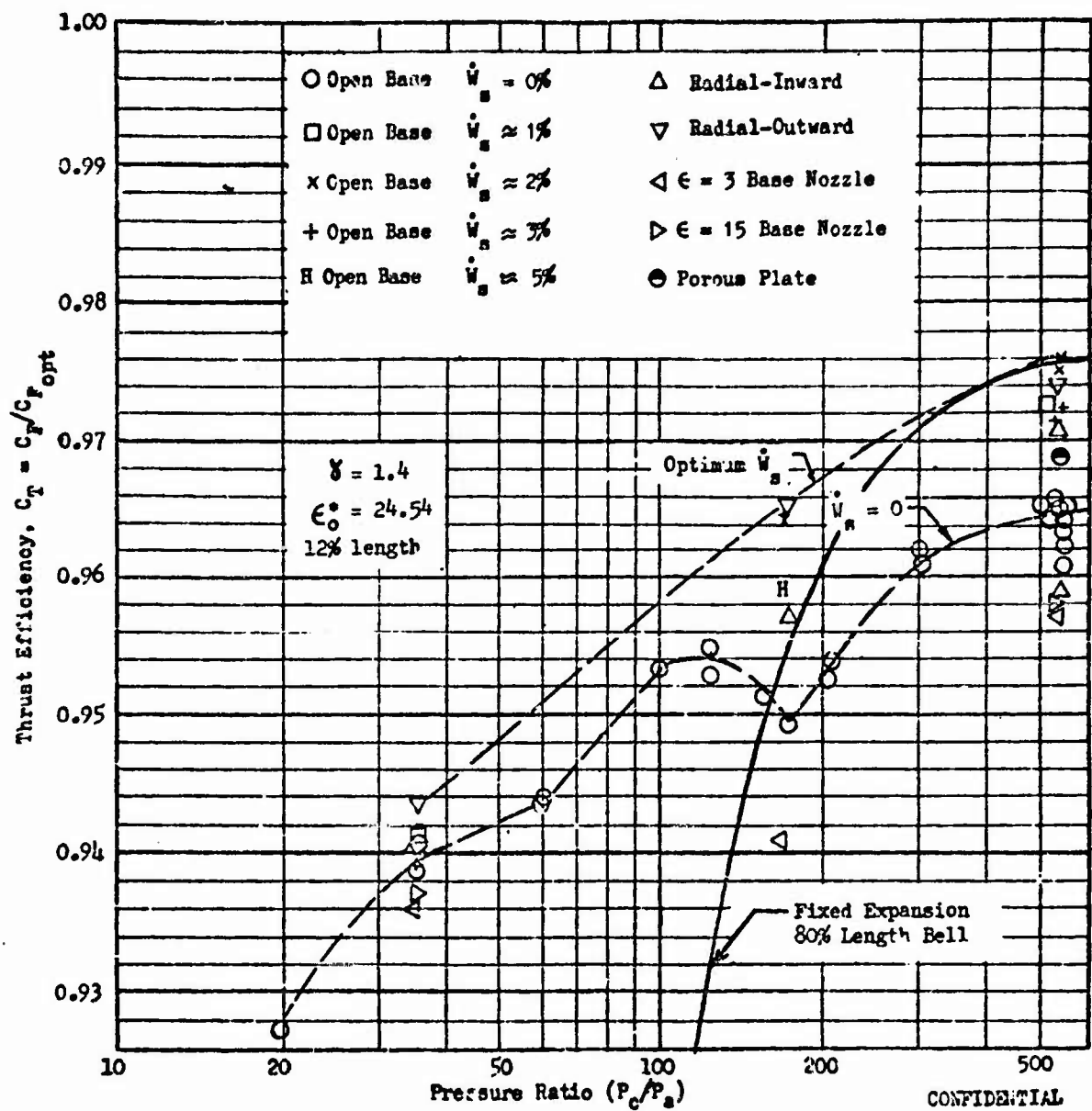
Figure 58. Performance vs Pressure Ratio, Scaled Hot-Firing Model
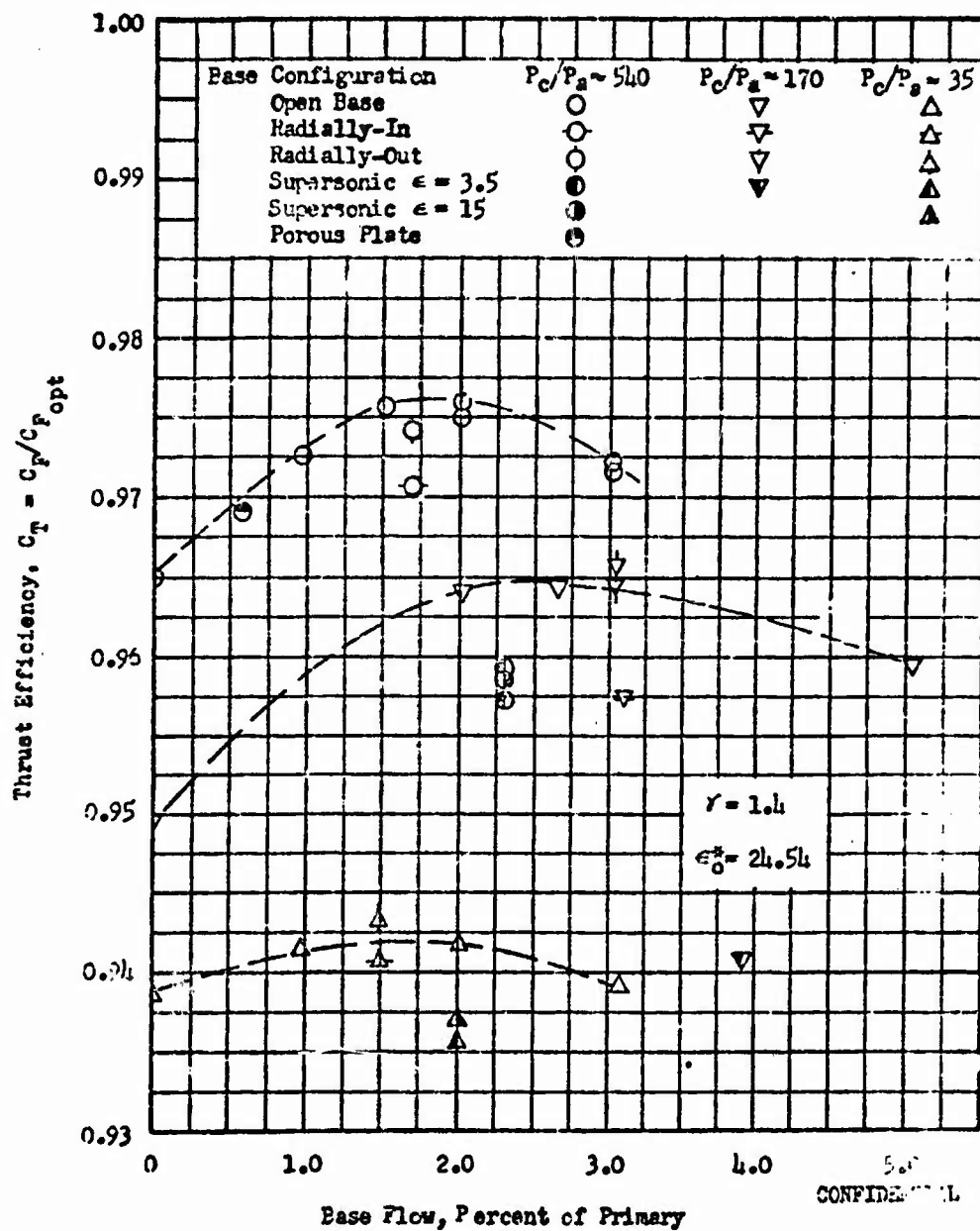
Figure 59. Performance vs Base Flow Rate, Scaled Hot-Firing Model

(C) Figure 59 shows that the porous plate base gives essentially the same performance as the open cavity. The radially-out base gives very nearly the same performance as the open cavity showing slightly lower performance at design pressure ratio but slightly higher performance at the lower pressure ratios. A significant drop in performance is exhibited by the radially-in base at design pressure ratio and the wake closing point (pressure ratio 170). Both base supersonic nozzles exhibit low performances throughout the operating range.

(C) Figure 60 presents Schlieren photographs of tests with the various base configurations at approximately the same secondary flow. The only configuration exhibiting a perceptably different base flow field was the supersonic injection model where the supersonic secondary flow field shocks are readily seen.

(C) Referring to the efficiency curve, Fig. 58, it can be observed that a performance dip occurs at a pressure ratio of approximately 170, the point at which the base flow changes from the closed to the open-wake regime. This point is further verified by observing the base pressure vs pressure ratio plot, Fig.61 , where the base pressure remains steady above a pressure ratio of 170. Introduction of secondary flow at this pressure ratio gives substantial performance increases for the open, radially-out and radially-in base configurations. Both the open base and the radially-out base give a performance increase of about 1.5 percent.

(C) At a pressure ratio of about 35, small gains in efficiency were noted with addition of base bleed with all base configurations except the supersonic injection. For all pressure ratios the optimum secondary flow appears to be between 1.5 and 2.5 percent of primary flow.

a) Open Base
$P_c/P_a = 540$, $\dot{W}_s = 1.5\%$
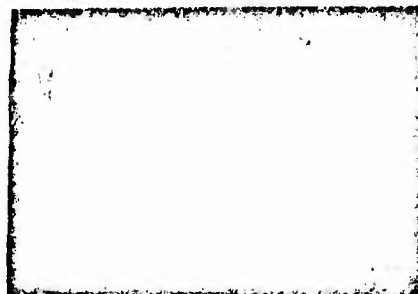
b) Open Base
$P_c/P_a = 539$, $\dot{W}_a = 3.0\%$
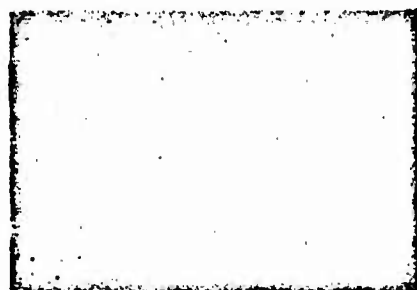
c) Radially-Inward Base
$P_c/P_a = 536$, $\dot{W}_s = 1.7\%$
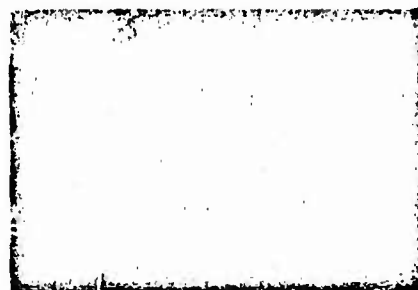
d) Radially-Outward Base
$P_c/P_a = 540$, $\dot{W}_s = 1.7\%$
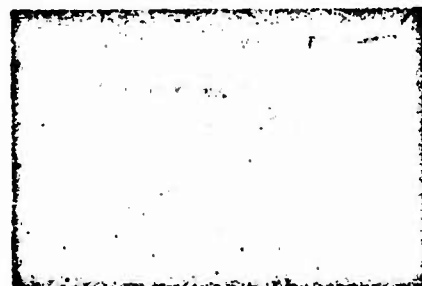
e) Supersonic Base, $\epsilon = 3.5$
$P_c/P_a = 536$, $\dot{W}_s = 2.1\%$

f) Porous Plate Base
$P_c/P_a = 525$, $\dot{W}_s = 2.2\%$

Figure 60. Schlieren Photographs of Various Base Configurations,
$\epsilon_o = 25$, Scaled Hot-Firing Model

104
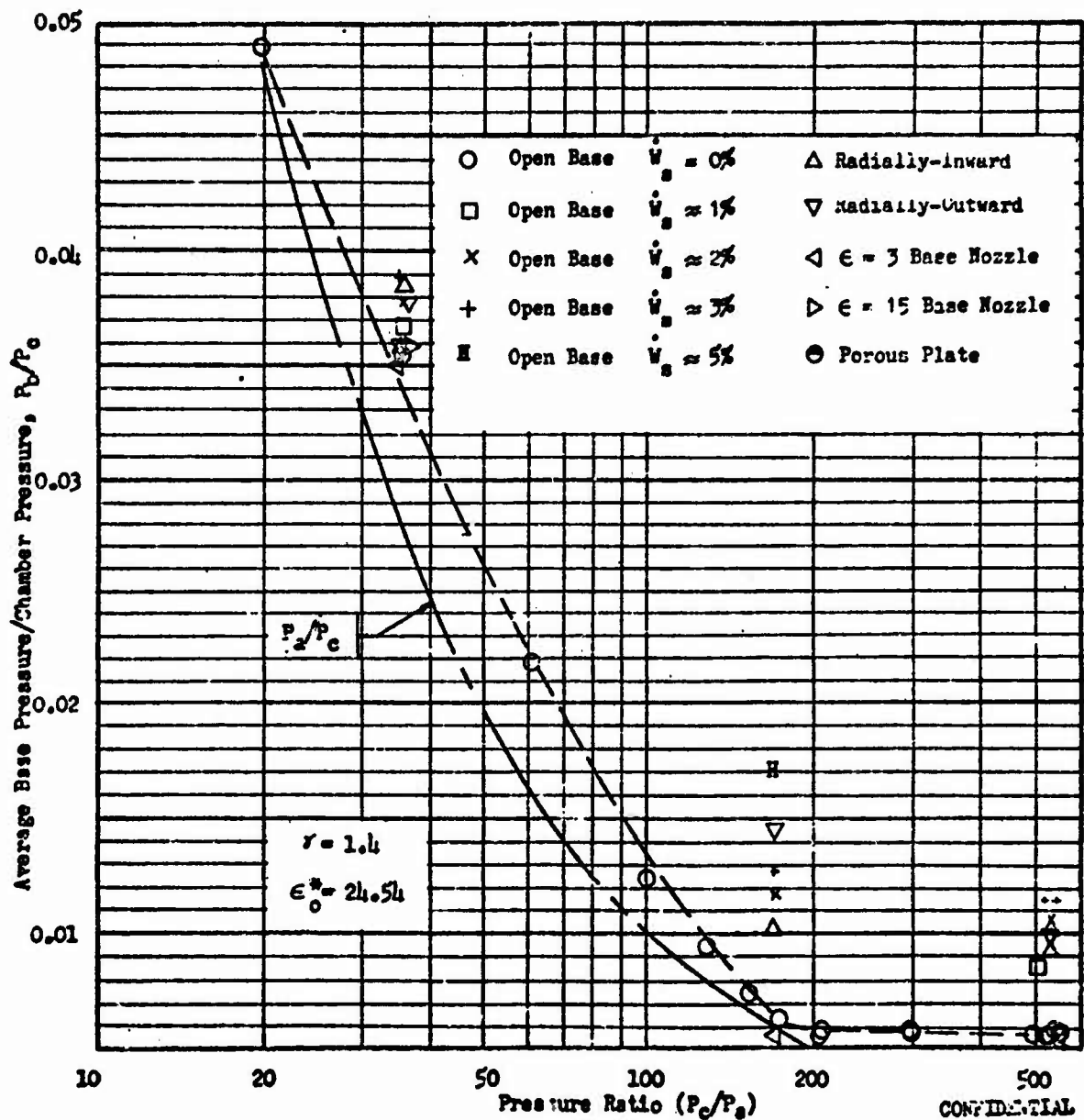
Figure 61. Base Pressure Curve for Scaled Hot-Firing Model

(C) The performance of a fixed expansion, 80 percent length bell of 24.54 area ratio is shown for comparison in Fig. 58 . The bell performance was computed using a nozzle vacuum efficiency of 98.56 percent and a constant drag loss equal to 0.9 percent of the theoretical vacuum thrust coefficient. These values were determined from bell nozzle theoretical efficiency curves and theoretical drag computations for a 27.5 area ratio J-2 cold flow model of the same size and operating at the same chamber pressure.

(C) The efficiencies of the bell and the aerospike are the same at design pressure ratio even though the bell nozzle length is 6.6 times greater than the aerospike. At a pressure ratio of 100 (~20 percent of design) the fixed expansion bell has an efficiency of 91.3 percent compared to 95.8 percent for the altitude compensating aerospike. At a pressure ratio of 50 (10 percent of design pressure ratio) the fixed expansion bell efficiency has dropped to 78.7 percent compared to 94.8 percent for the aerospike. It should be noted that advanced booster engines initially operate at 10 to 15 percent of design pressure ratio. A 16 percent length aerospike designed for air was tested with air under NASA contract (Ref. 11) and yielded design efficiencies of 98.4 percent with secondary flow and 97.2 percent without secondary flow demonstrating design efficiencies substantially higher than a comparable 80 percent length bell. This comparison clearly demonstrates that a short aerodynamic spike nozzle is at least comparable in performance to an 80 percent length bell at design pressure ratio and has considerably higher performance than the bell at lower than design pressure ratio.

(C)   The open base, radially-in, radially-out and the porous plate base plates all showed relatively good base pressure increases with introduction of secondary flow (see Fig. 61). This resulted in net increases in efficiencies. However, the supersonic base injection showed very little or no increase in base pressure in most cases. Thus, when the performance was charged with the additional mass flow for the base, a performance loss resulted.

(C)   Theoretical and experimental wall pressures for this nozzle are presented in Fig. 62 . Near the throat $(X/R^* \approx 0)$ agreement between data and theory is not as good as further down the nozzle contour. This occurs because the pressure gradient near the throat is steep and even small diameter pressure taps cover a significant portion of the actual pressure range.

(C)   The pressure profils down to a pressure ratio of 61 was constant. Below 61 a pressure rise was noted along the contour due to nozzle recompression. Since at low pressure ratios these pressures did not change with secondary flowrate, it can be concluded that the flow did not separate from the contour. This is also evidenced by observing the Schlieren photographs (Fig. 63).

Scaled Hot-Firing Model - CF$_4$ Tests

(U)   Ten tests were conducted using CF$_4$ gas as the test fluid. All tests were performed with the open base configuration. In addition to achieving high performance, this configuration allows a more reliable determination of average base pressure. The base pressure is relatively uniform across the face of the cavity and a good average base pressure is easily obtained.
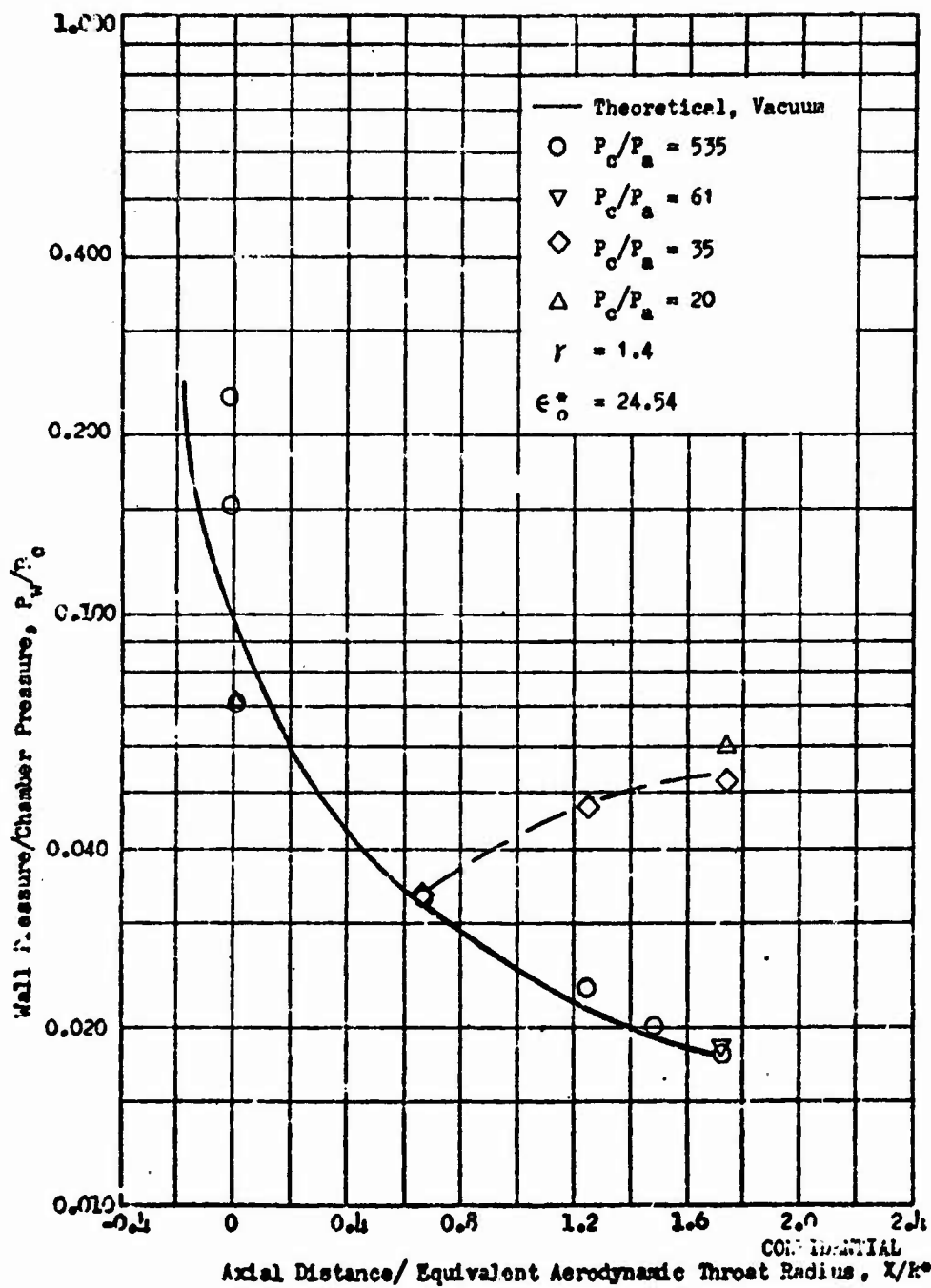
Figure 62. Wall Pressure Profile for Scaled Hot-Firing Model, $\dot{V}_a = 0$
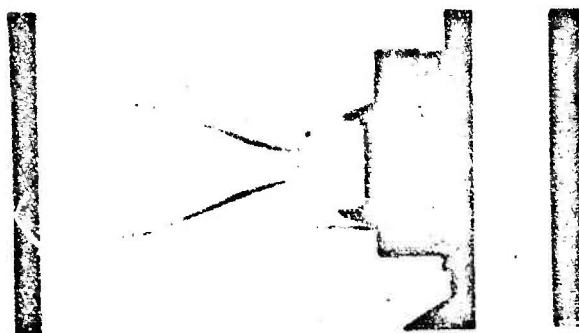
(a) P_c/P_a = 524

$\dot{W}_s$ = 0%
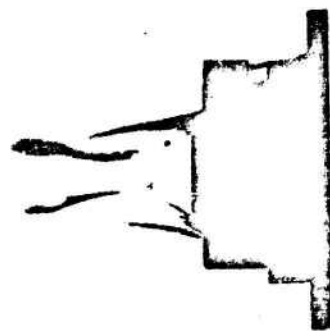
(b) P_c/P_a = 173

$\dot{W}_s$ = 0%
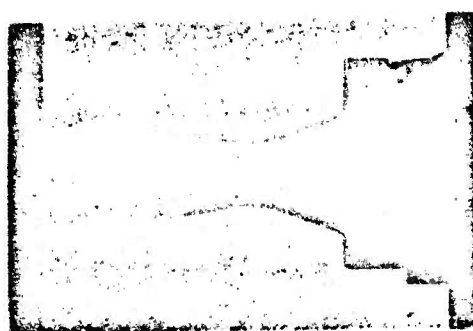
(c) P_c/P_a = 30

$\dot{W}_s$ = 0%
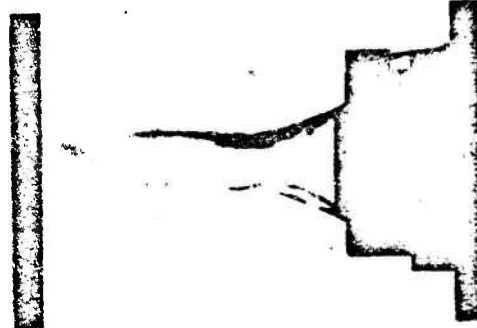
(d) P_c/P_a = 35

$\dot{W}_s$ = 2%

Figure 53. Schlieren Photographs on Scaled Hot-
Firing Spike Nozzle, γ = 1.4 , Open Base

(U) In the initial phase of the CF_4 testing, it was necessary to determine if, and under what conditions, condensation of CF_4 would occur in the flow field. This was found necessary since examination of a pressure-enthalpy diagram (see Fig. 64) for CF_4 indicated that in the expansion process, the pressure and temperature could fall inside the saturation region. For example, starting at a chamber pressure of 150 psia at a temperature of 70 deg F and isentropically expanding over the design pressure ratio of 253, the process end point (the dashed line in Fig. 64) falls just inside the saturation region. Since condensation could affect the base pressure values, initial tests at chamber pressures of 50, 100, and 150 psia were conducted to determine the operating conditions required to avoid condensation. An ultraviolet light was projected across the flow field to detect droplet formation. Polaroid photographs were taken and visual observations were made for each test.

(C) At a chamber pressure of 150 psia, condensation was observed to occur about two-thirds of an exit diameter downstream of the exit of the nozzle (foggy region to the left of the nozzle in Fig. 64). When the chamber pressure was reduced to approximately 100 psia (a more favorable expansion as shown on the pressure-enthalpy diagram) no condensation was observed. All further CF_4 testing was performed at or below a chamber pressure of 100 psia. The values of P_b/P_c were 0.0066, 0.0066 and 0.0067 for P_c values of 50, 100 and 150 respectively. Thus it appeared that condensation had negligible effect on base pressure. In all, eight tests were performed with no secondary flow over a pressure ratio range of 35 to 290 and two tests were performed with secondary flow near design pressure ratio. Data for these tests is tabulated in Appendix 3 and summarized in Figs. 65 and 66.

Figure 64. Pressure-Enthalpy Diagram For Carbon Tetraflouride (CF_4)

111

(C)   Figure 65 shows the performance of the $\epsilon_o^* = 24.26$ nozzle using CF_4. Maximum performance attained at design pressure ratio (253) was 95.6 percent. This was increased to 96.8 percent by addition of 1.7 percent CF_4 base bleed. Examination of the base pressure curve, Fig. 66 , shows the value of P_b/P_c to remain at 0.0067 down to a pressure ratio of approximately 120. At this point the base pressure starts to rise because the wake opens.

(C)   One of the principle reasons for testing with CF_4 was to have a cold-flow gas with a γ similar to that of the hot-firing model. Upon examining several gases CF_4 appeared to be the most reasonable gas to use. It had the necessary low γ and could be expanded to a low enough pressure without changing state. The equivalent γ for the hot-firing model is 1.25. At the time of selection of CF_4, available information indicated that the γ of this gas would be close to 1.25. Since this is a relatively new gas available on a commercial basis, relatively little physical data was available until some time after the model was tested. The data shows that γ has a very wide variation from the chamber condition to the ambient condition. For example at $P_c = 100$ psia and $T_c = 530$ degrees Rankine, $\gamma = 1.18$. Expanding to $P_a = 0.2$ psia isentropically results in a $\gamma = 1.30$. This makes it quite difficult to arrive at an equivalent constant γ to use in an analysis involving the assumption of a perfect gas.

(U)   A parallel effort was simultaneously conducted at Rocketdyne evaluating the properties of CF_4 gas. In this effort it was found that it would be necessary to arrive at an ideal thrust coefficient $(C_{F_{opt}})$ for a given expansion process by considering the actual enthalpy change of the gas rather than calculating the ideal thrust coefficient from the

112
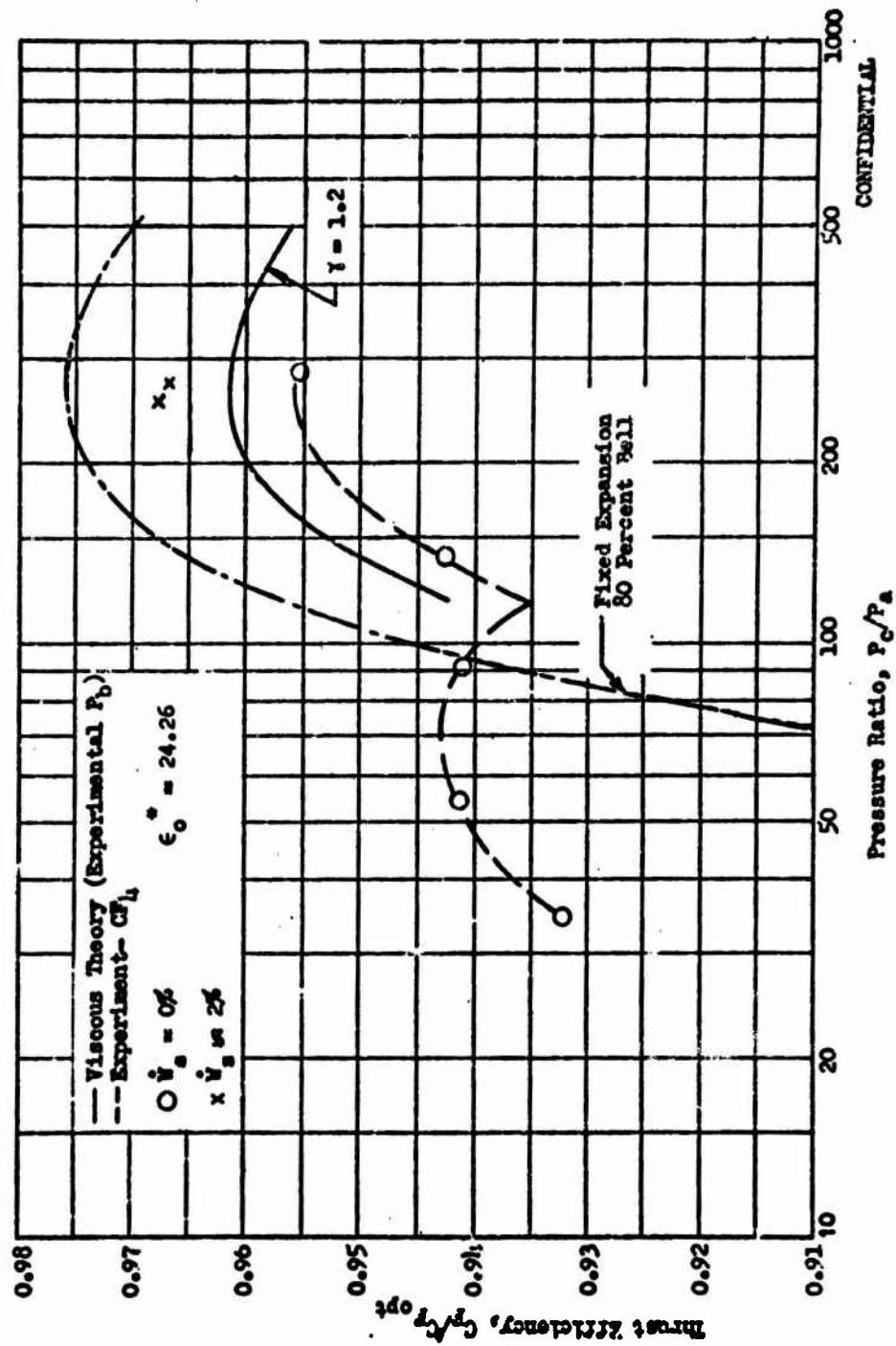
Figure 65. Performance vs Pressure Ratio, Scaled Hot-Firing Model, CF_4 Tests
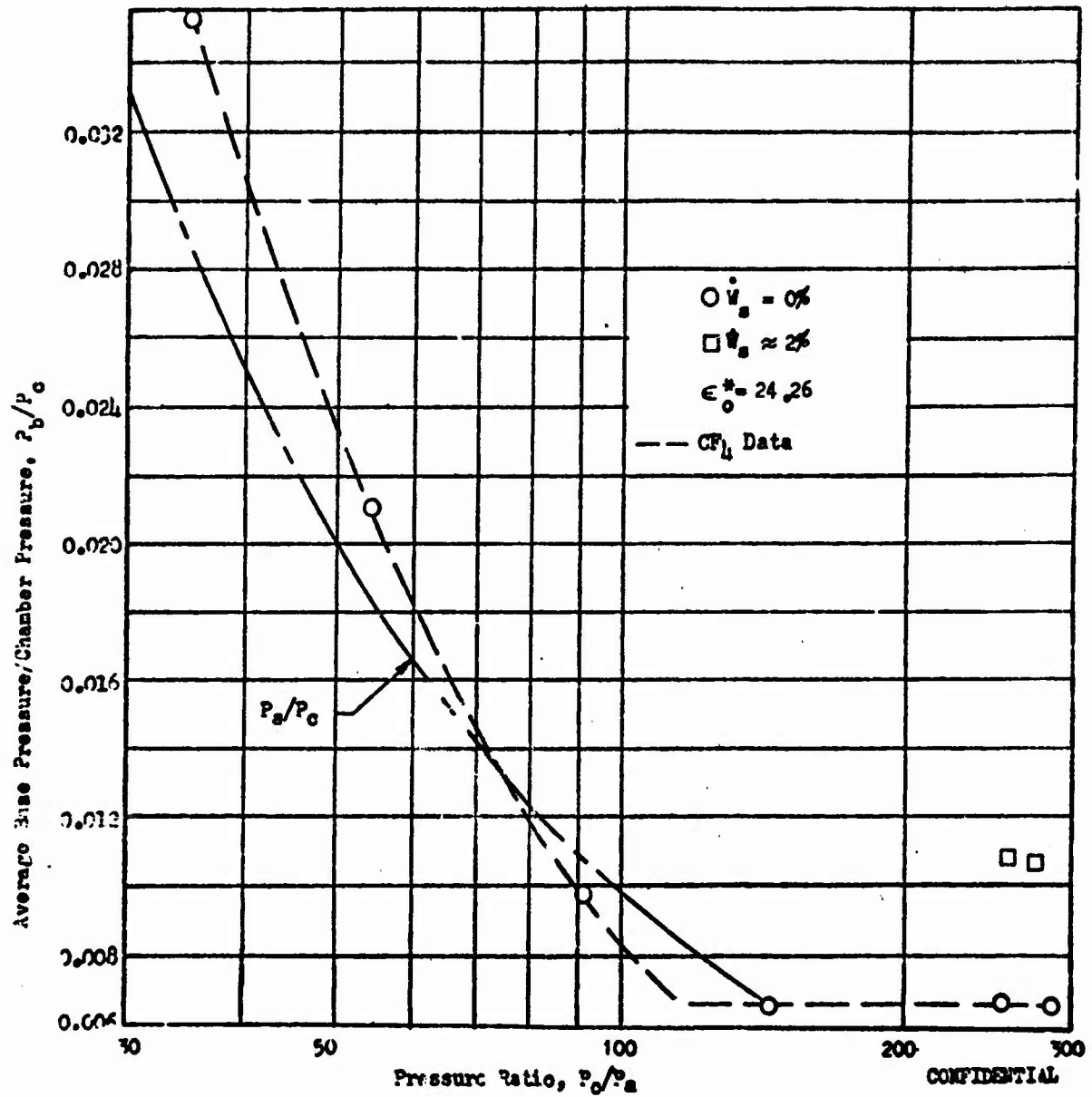
Figure 66. Base Pressure vs Pressure Ratio, Scaled Hot-Firing Model, CF_4 Tests

usual one-dimensional ideal gas equations assuming a constant γ and
pressure ratio. The method arrived at is summarized in Appendix 4.
Using the real gas properties a $C_{F_{opt}}$ is arrived at for a particular
set of conditions (P_c, T_c, P_a, $\Delta S = 0$) and is used in calculating
nozzle efficiency.

$$C_T = \frac{C_{F_{experimental}}}{C_{F_{opt}} \Big|_{\substack{real \\ gas}}}$$

(C) These are the experimental values shown in Fig. 65. In this figure
is also shown the theoretical performance curve (using experimental
base pressures) for the $\epsilon_o^* = 24.26$ nozzles. The analysis for $\gamma = 1.2$
fell above the experimental curve. The amount of deviation is approx-
imately 0.6 percent. This deviation could be caused by the accuracy
limitations of the CF_4 properties. Reference 10 indicates that accuracy
is limited by the equation of state used.

(U) A representative value of γ for the operating range over which the
nozzle was tested was found to lie somewhere between 1.20 and 1.21
(from the CF_4 properties). The representative γ is calculated from
the real gas $C_{F_{opt}}$ from

$$C_{F_{opt}} = \sqrt{\left[\left|\frac{2}{\gamma - 1}\right| \left|\frac{2}{\gamma + 1}\right|^{\frac{\gamma + 1}{\gamma - 1}}\right]\left[1 - \left|\frac{P_a}{P_c}\right|^{\frac{\gamma - 1}{\gamma}}\right]}$$

The real gas $C_{F_{opt}}$ and the pressure ratio are substituted in the above
equation and the equation is solved for γ. This value of γ is called
the process γ.

(c) The performance of a fixed expansion, 80 percent length bell of 24.26 area ratio is shown for comparison in Fig. 65. The bell performance was computed using a nozzle vacuum efficiency of 98.56 percent and a constant drag loss equal to 0.8 percent of the theoretical vacuum thrust coefficient. These values were determined from bell nozzle theoretical efficiency curves and theoretical drag computations for a similar cold flow bell nozzle.

(c) The efficiency of the 80 percent length bell nozzle at design pressure ratio is 97.6 percent compared to 96.8 percent measured for the 12 percent length aerospike. The 0.8 percent lower performance for the aerospike tends to indicate that for lower γ gases somewhat longer aerospike lengths are required to achieve efficiencies equal to a bell at design pressure ratio. However, the theoretically predicted C_m (using measured base pressures) for the aerospike is also 0.6 percent higher than the measured values. Usually this type of theoretical prediction agrees with experimental data within 0.25 percent. If the theoretical values are more nearly correct the aerospike with secondary flow is only 0.2 percent lower performing at design pressure ratio than the bell. Theoretical analysis of this aerospike nozzle indicates that a gain of approximately 1.1 percent in efficiency at design pressure ratio would be achieved by increasing the aerospike length from 12 percent to 25 percent (both 12 percent and 25 percent lengths will be tested in the hot-firing phase of this program). This would result in design efficiencies between 97.9 and 98.5 depending on whether the gain is added to the experimental or to the theoretical aerospike performance curve.

(C)   At a design pressure ratio of 100 (40 percent of design pressure ratio) the bell performance is approximately 0.5 percent higher than the experimental aerospike performance without secondary flow. Based on the similar effect of secondary flow on performance for this model with air and CF_4 it is expected that CF_4 secondary flow would increase performance between 1.0 to 1.5 percent at a pressure ratio of 100 bringing the experimental aerospike performance from 0.5 to 1.0 percent above the bell. The previous comments about the uncertainty of the experimental performance and the performance effects of a longer nozzle length also apply at this pressure ratio and would further increase the performance advantage over the bell to approximately 2.0 to 2.5 percent.

(C)   At a pressure ratio of 50 (20 percent of design pressure ratio) the fixed expansion bell performance is 84.4 percent compared to 94.1 percent for the experimental aerospike without secondary flow.

Base Pressure Calculations

(C)   Theoretical and empirical methods of determining base pressures have been developed (Ref 11) and are in use at Rocketdyne. The theoretical methods are sub-grouped into three separate flow regimes; (1) small bleed, closed-wake, (2) large bleed, choked flow through the wake recompression zone, and (3) open-wake, low pressure ratio. Regimes (1) and (2) are at high nozzle operating pressure ratios, preventing ambient pressure from communicating with the base. Regime (3) is at low pressure ratios, giving a large base flow core which is not choked.

(C)   The essential difference between the small bleed and large bleed theories is in the recompression mechanism where the wake coalesces. For small bleed there is a recirculation of the base flow from the recompression zone back into the base flow region. As the bleed rate increases the amount of recirculation is reduced until no recirculation occurs but outflow from the base region through the recompression zone is the prevailing mode. The exact transition point is not easily determined but corresponds roughly to the maximum performance point in a performance vs base bleed curve (See Fig. 59).

(C)   Data of the hot-firing model for the open cavity base has been re-plotted in Fig. 67 , 68 and 69 along with the theoretical predictions of base pressure for this nozzle. For the air tests, the transition from small to large bleed is shown to occur at $\dot{W}_s/\dot{W}_p$ = 1.55 percent. This compares to a maximum efficiency point on Fig. 59 of $\dot{W}_s/\dot{W}_p$ = 2.0. The same theory applied to the CP_4 gas tests is shown in Fig. 68. Agreement in both cases is good.
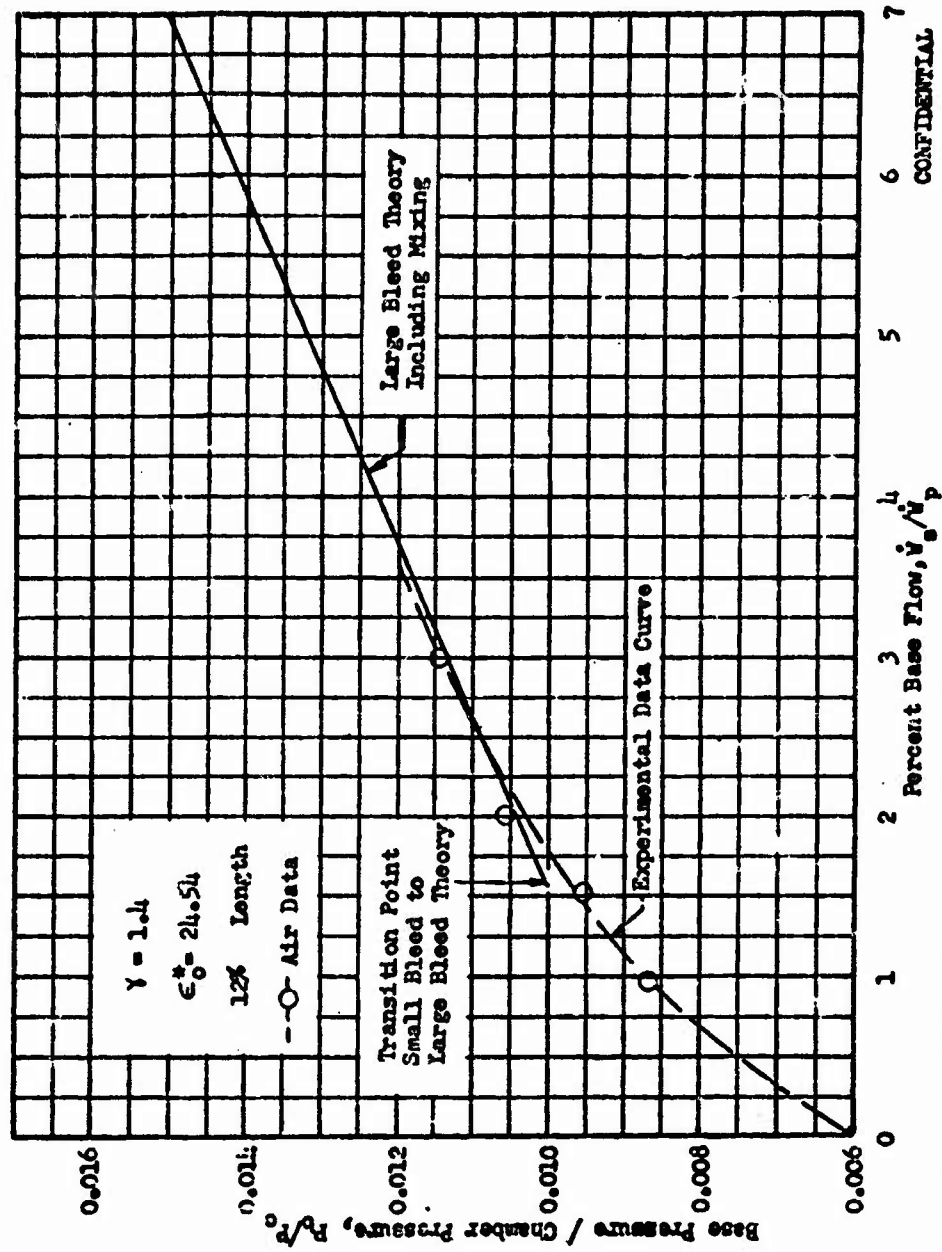
Figure 67. Base Pressure vs Percent Base Bleed for Closed-Valve Flow, Scaled Hot-Firing Model, Air.
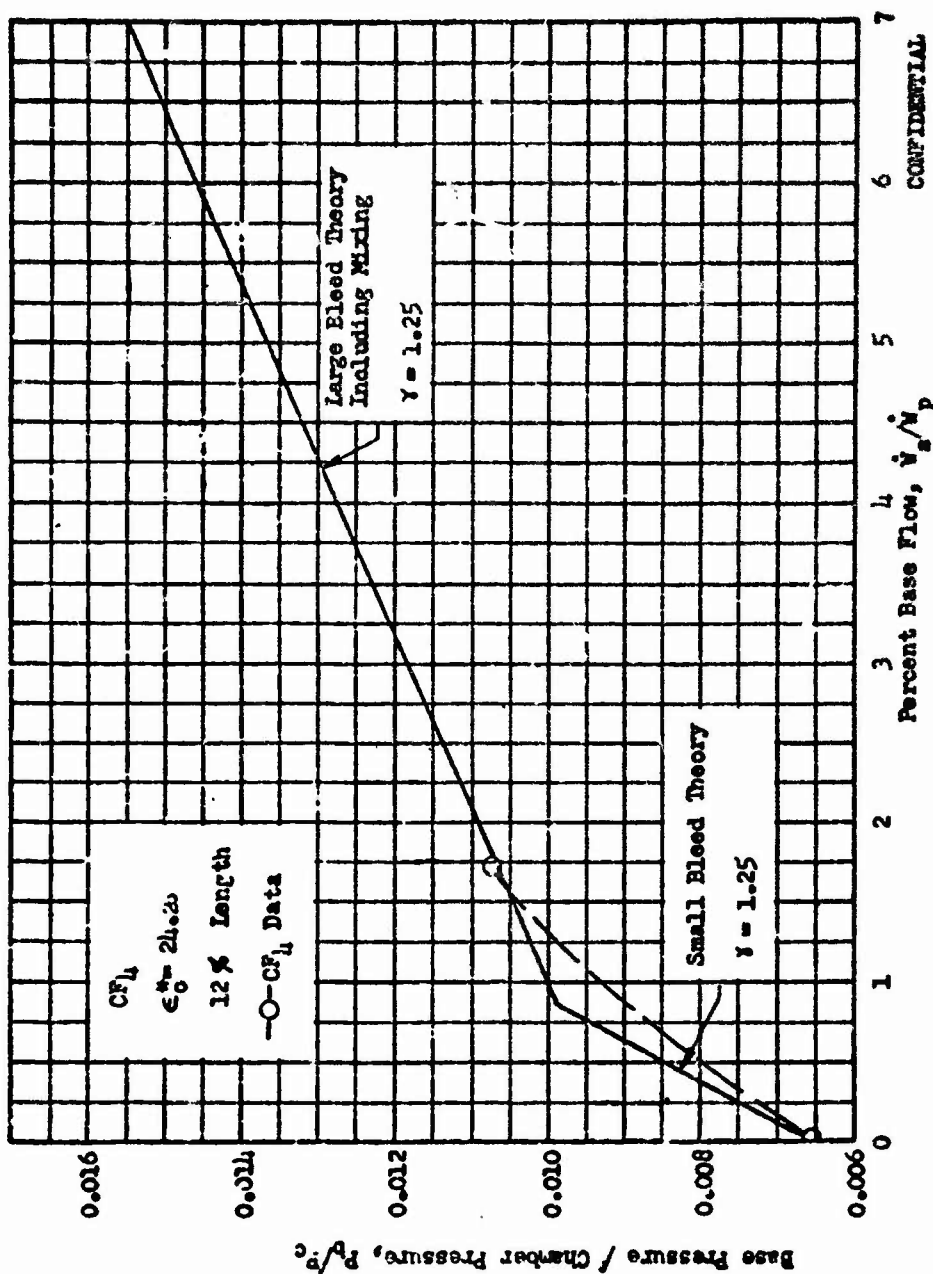
Figure 68. Base Pressure vs Percent Base Bleed for Closed-Wake Flow, Scaled Hot-Firing Model, CF_4 Tests

(C) The open-wake theory was applied to the same nozzle at a pressure ratio
of $P_c/P_a = 61$. In this case the theory predicted pressures slightly
higher than the data (Fig. 69).

Annular Reference Models

(U) The principal objectives of testing the continuous-throat annular
reference models ($\epsilon_o = 50$) were:

1. Determine performance for both shrouded and unshrouded
continuous-throat aerodynamic spike nozzles over a wide
pressure ratio range with and without secondary flow for
comparison with the multichamber performance.

2. Record base pressures for comparison with multichamber base
pressure values.

3. Determine the ambient pressure compensating characteristics
of these nozzles.

(U) These models were tested (with air) over a pressure ratio range   from
100 to 1500 and a secondary flow (air) range   from 0 to 3 percent
of primary flow. Secondary flow was introduced from an annular orifice
recessed within the centerbody. An open-cavity base configuration was
used throughout the tests. Fifty-six tests were accomplished with
these models.
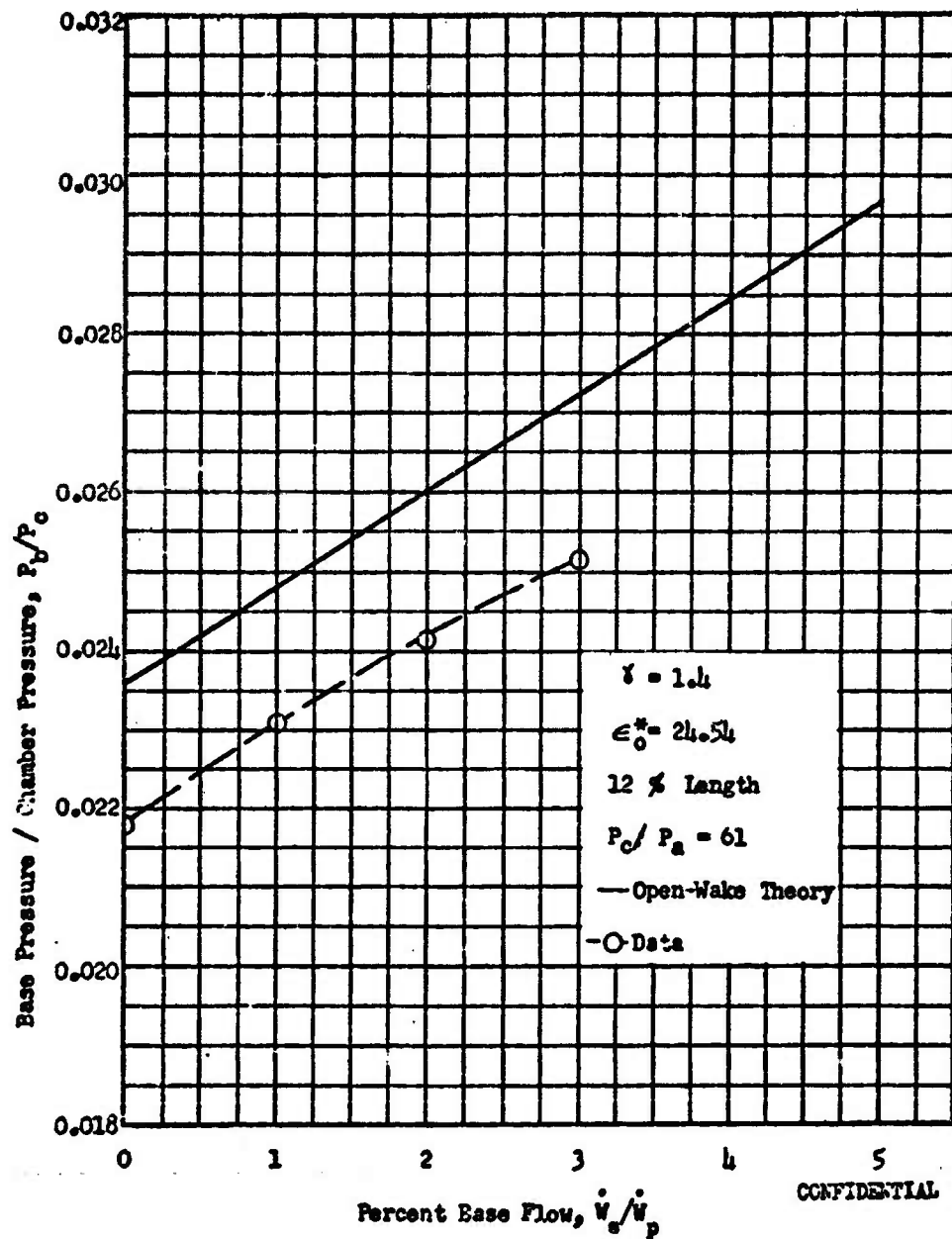
Figure 69. Base Pressure vs Percent Base Bleed for Open-Wake Flow, Scaled Hot-Firing Model

Point Expansion Model

(C) Performance results of cold-flow testing of the point expansion model (model II-6, Table 3), are shown in Fig. 70 and in Appendix 3. Experimentally, the nozzle efficiency reached a value of 98.6 percent at a pressure ratio of 1375 and no secondary flow.

(C) The performance at design pressure ratio (1375) peaked at 98.8 with the addition of 0.9 percent secondary flow (See Fig. 71). Efficiency gains were small since the nozzle (30 percent length) already has a high efficiency without secondary flow, leaving little margin for improvement. However, when secondary flow is available this configuration still provides a high performance means of utilizing it.

(C) The performance curve at a pressure ratio of 490, becomes discontinuous, corresponding to the transition from closed to open base wake flow (See also Fig. 72 showing the transition in base pressure at a pressure ratio of 490). Adding secondary flow to the base at this point increased the nozzle efficiency from 97.3 with no secondary flow to 97.8 with 1.0 percent secondary flow (See Fig. 71). As normally occurs at the transition point, an appreciable increase in performance can be realized with the proper addition of secondary flow.

(C) Secondary flow was added to the base at a pressure ratio of 150. Figure 71 shows that substantial efficiency gains were obtained raising the zero secondary flow efficiency from 94.8 to 96.0 percent at the optimum secondary flowrate of 1.8 percent.
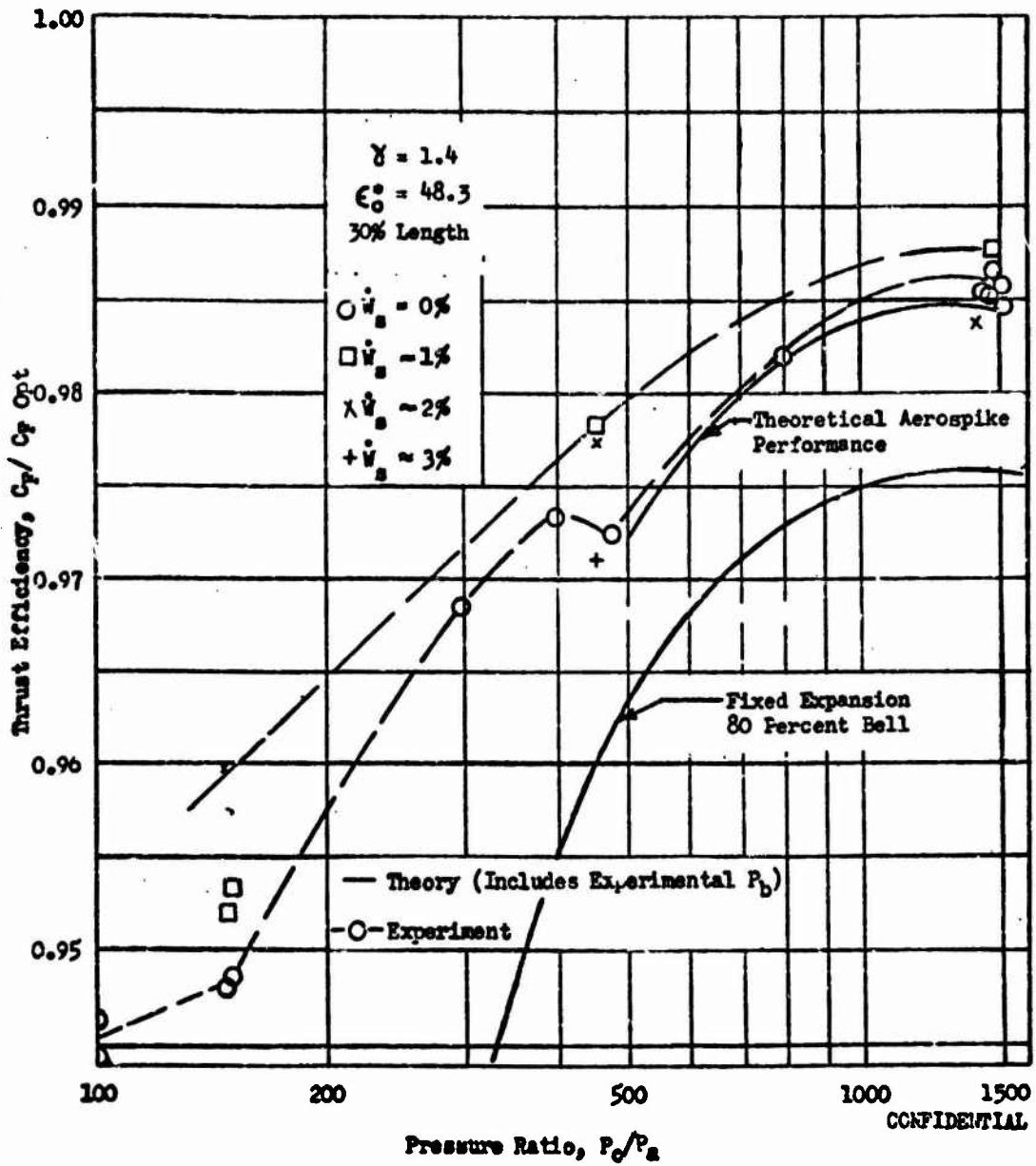
Figure 70. Thrust Efficiency vs Pressure Ratio, Point Expansion
Spike Nozzle

124
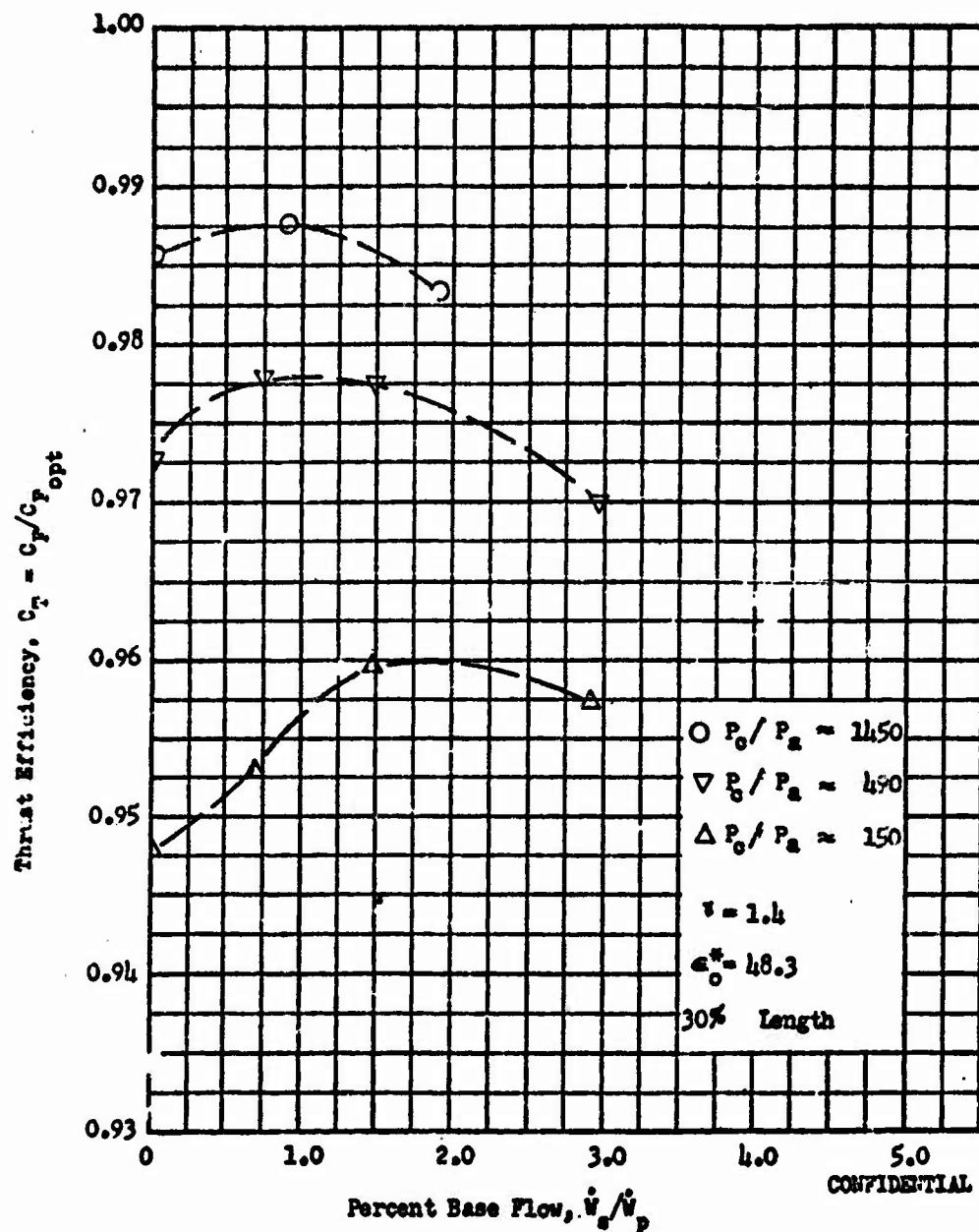
Figure 71. Thrust Efficiency vs Percent Base Flow,
Point Expansion Spike Nozzle
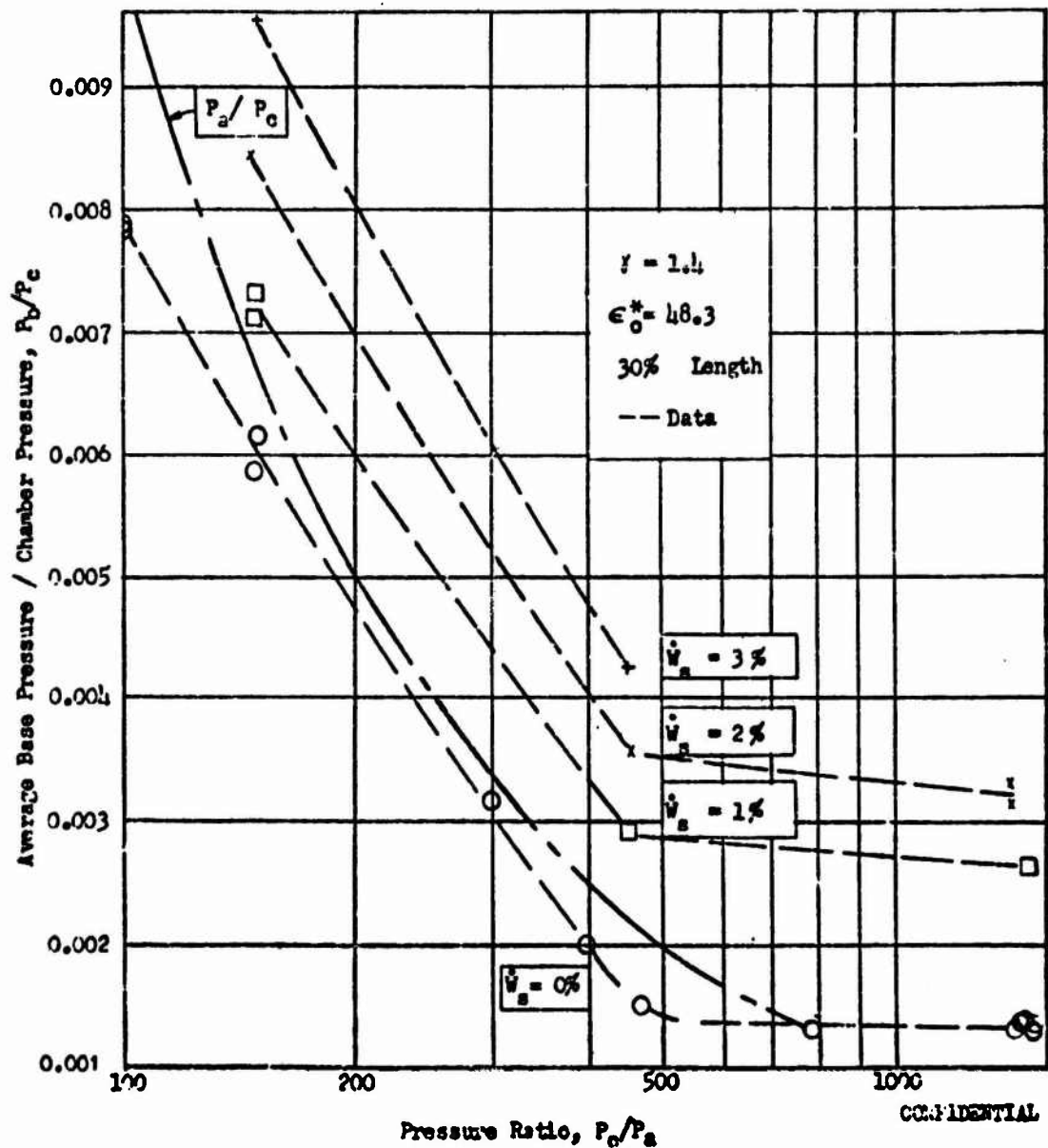
Figure 72. Base Pressure vs Pressure Ratio for Point Expansion
Spike Nozzle

126

(C)   The performance of a fixed expansion, 80 percent length bell of 48.3 area ratio is shown for comparison in Fig. 70. The bell performance was computed using a nozzle vacuum efficiency of 98.65 percent and a constant drag loss equal to 1.0 percent of the theoretical vacuum thrust coefficient. These values were determined from bell nozzle theoretical efficiency curves and theoretical drag computations for a similar cold flow bell nozzle.

(C)   The efficiency of the 80 percent length bell nozzle is 97.6 percent at design pressure ratio compared to 98.8 percent for the 30 percent length aerospike. At a pressure ratio of 500 (36 percent of design pressure ratio) the bell nozzle efficiency is 96.3 percent compared to 98.0 percent for the aerospike. At a pressure ratio of 150 (11 percent of design pressure ratio) the fixed expansion bell efficiency is 86.4 percent compared to 96.0 percent for the aerospike.

(C) Using the method of characteristics for axially symmetric flow, the point expansion nozzle was analyzed for primary flow field performance. The experimental base pressure performance contribution was then added to the inviscid performance. Shear stress and friction drag were calculated and the drag loss was subtracted from the inviscid theory. This resulted in the viscous theory curve shown in Fig. 70 which agrees very well with experimental results.

(C) Experimental and theoretical contour pressure profiles are shown in Fig. 73 . Again, agreement is very good between theory and experiment. Recompression is shown to occur below a pressure ratio of 300.

(U) Schlieren photographs for tests at both high and low pressure ratios with and without secondary flow are shown in Fig. 74 .

Shrouded Annular Model

(C) Design expansion area ratio for the shrouded annular spike model was the same as the point expansion spike. As built and flow checked, the area ratio, ε_o^*, was 48.6. Efficiency for this model was, in general, 0.5 percent lower than for the point expansion model, although, since this model was designed, techniques of designing shrouded nozzles have improved and experience shows that it is possible to achieve shrouded nozzle performance comparable with point expansion nozzles.

(C) At peak performance (Fig. 75) for no secondary flow the shrouded nozzle efficiency was 98.0 percent. Essentially no efficiency increase was noted (Fig. 76) with the addition of secondary flow at design pressure ratio.
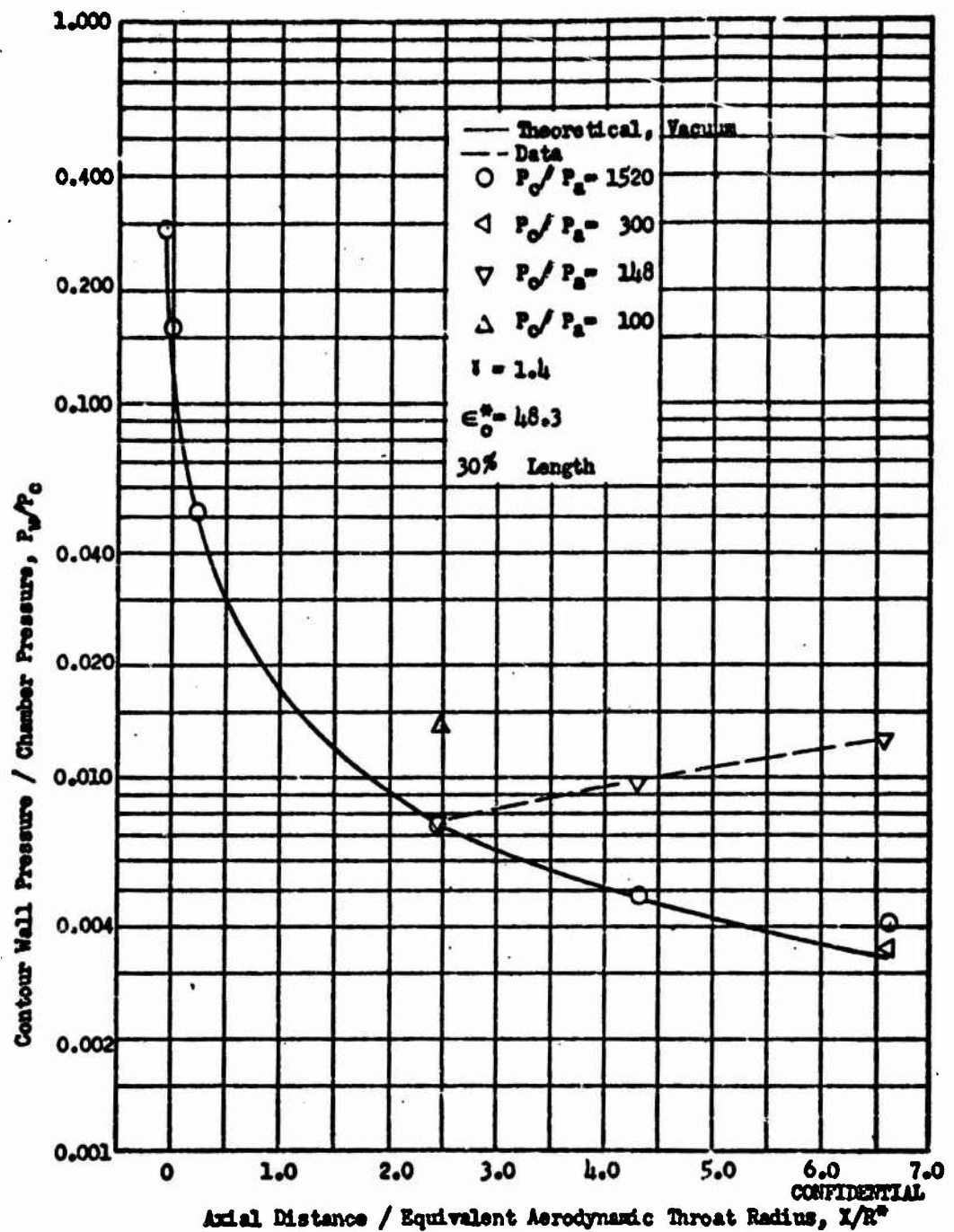
Figure 73. Contour Pressure Profile, Point Expansion Spike Nozzle

129

(a) P_c/P_a = 1467

$\dot{W}_s$ = 0%

(b) P_c/P_a = 151

$\dot{W}_s$ = 0%

(c) P_c/P_a = 1412

$\dot{W}_s$ = 2%

(d) P_c/P_a = 147

$\dot{W}_s$ = 2%

CONFIDENTIAL

Figure 74. Schlieren Photographs of Point
Expansion Model Spike Nozzle
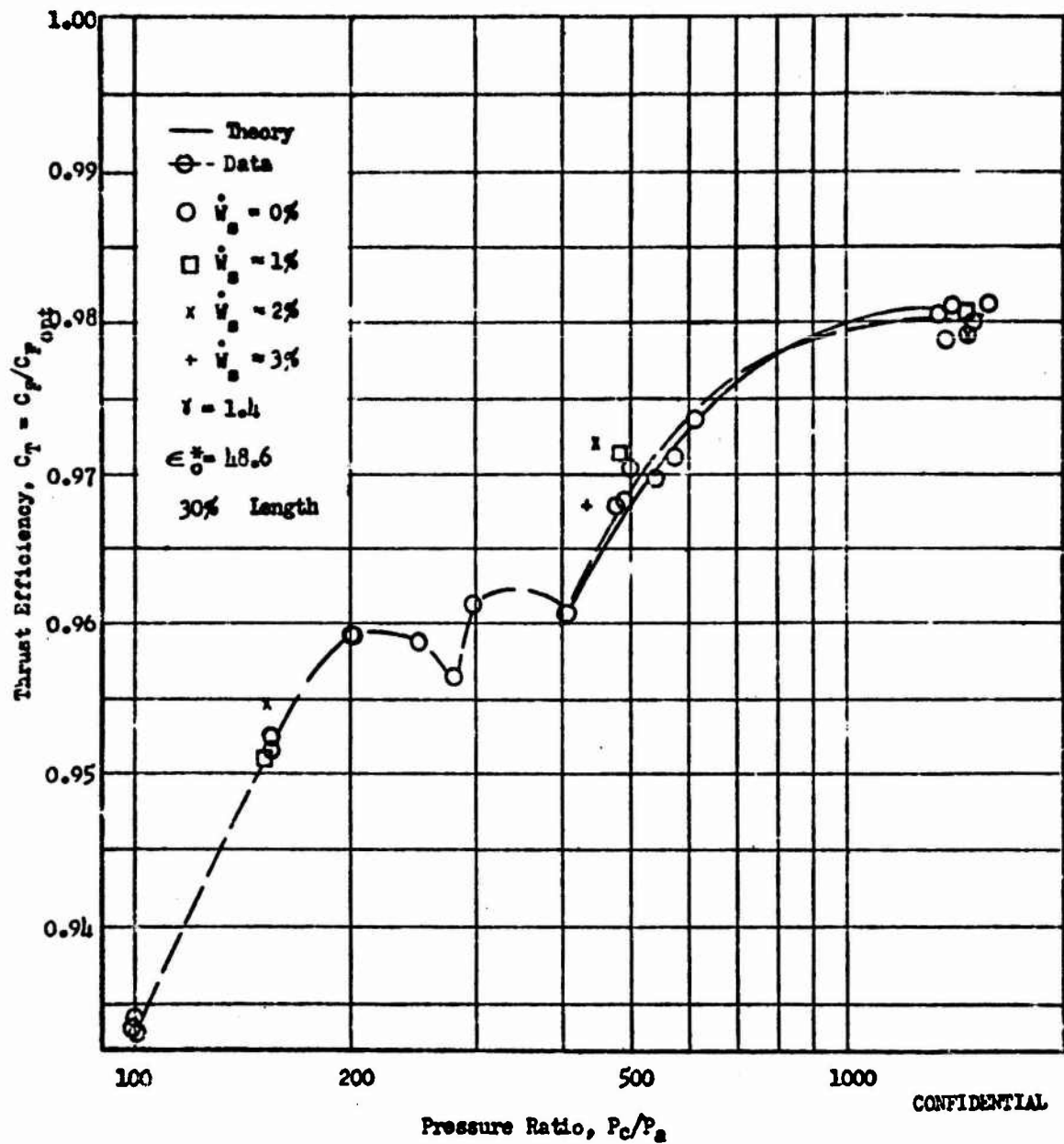
Figure 75. Thrust Efficiency vs Pressure Ratio, Shrouded Spike Nozzle

CONFIDENTIAL

151
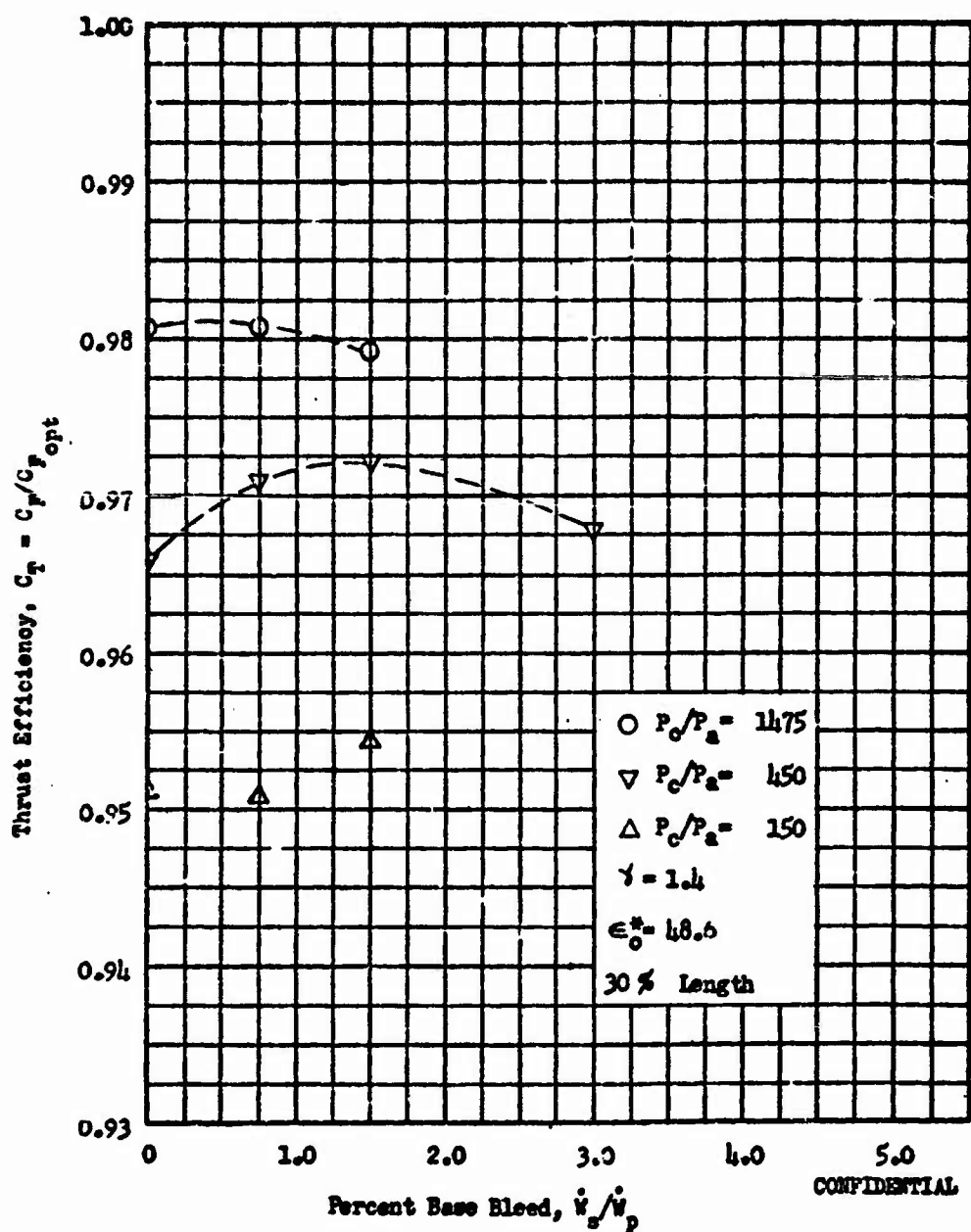
Figure 76. Thrust Efficiency vs Percent Base Bleed, Shrouded
Spike Nozzle

(C)   Two dips in the performance curve can be observed; one at a pressure
ratio of 400 and the second at a pressure ratio of approximately 290.
The base pressure curve (Fig. 77) shows that the transition from closed
to open wake occurred at a pressure ratio of 400. No unusual base
pressure trends can be noted at a pressure ratio of 290. Therefore, this
second dip must be caused by some other condition. At a pressure ratio
of 290 the contour pressure profile (Fig. 78) is the same as for high
pressure ratios. Shroud pressures (not shown) are also the same as for
high pressure ratios. When the pressure ratio is reduced to 200 wall
pressures at the end of the contour increase (Fig. 78) indicating
either nozzle recompression or separation from the contour. In the
characteristic solution to the primary flow field this pressure ratio
(290) corresponds approximately to the pressure along the last character-
istic line from the end of the shroud to the end of the contour. This
suggests that below a pressure ratio of 290 recompression waves between
the shroud and inner contour are causing an increase in contour pressure
(down to a pressure ratio of 200) which is not completely offset by
the increase in ambient pressure force in the opposite direction.
Examination of the Schlieren photographs, Fig. 79 shows that the flow
does not appear to be separating from the contour and compression waves
are impinging on the contour at pressure ratios around 250.

(C)   Secondary base bleed was added near a pressure ratio of 400 (Fig. 76).
At a pressure ratio of 450 performance increased from 96.6 percent at
zero bleed to 97.2 percent at 1.5 percent bleed. At the low pressure
ratio end $(P_c/P_a = 150)$ of the performance curve, efficiency was increased
from 95.1 percent to 95.5 percent with 1.5 percent bleed.

(C)   Theoretical performance (including drag losses) and wall pressure
(vacuum) profiles agree very well with the data for this nozzle
(Fig. 75 and 78).
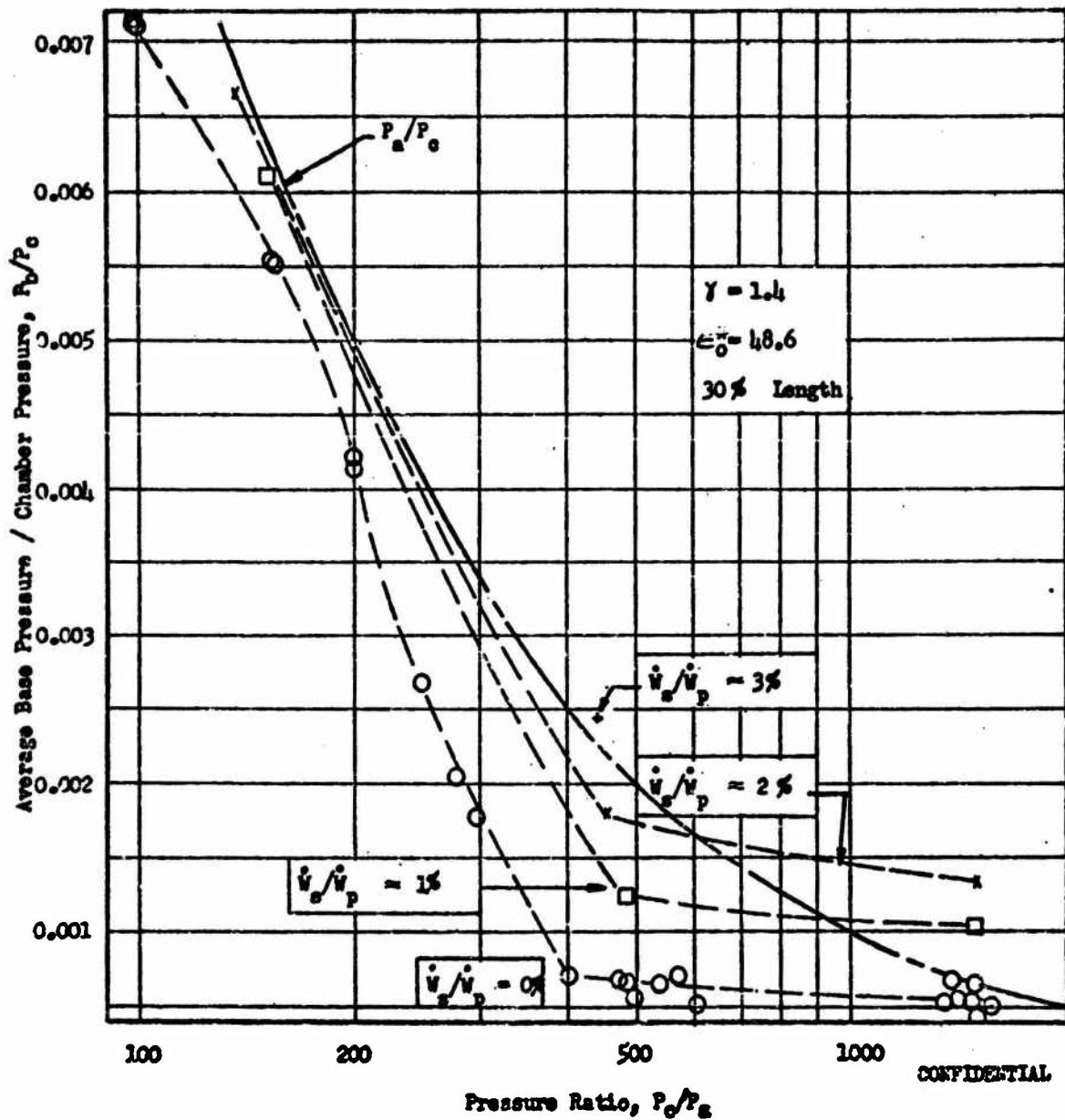
Figure 77. Base Pressure vs Pressure Ratio for Shrouded Spike Nozzle

164
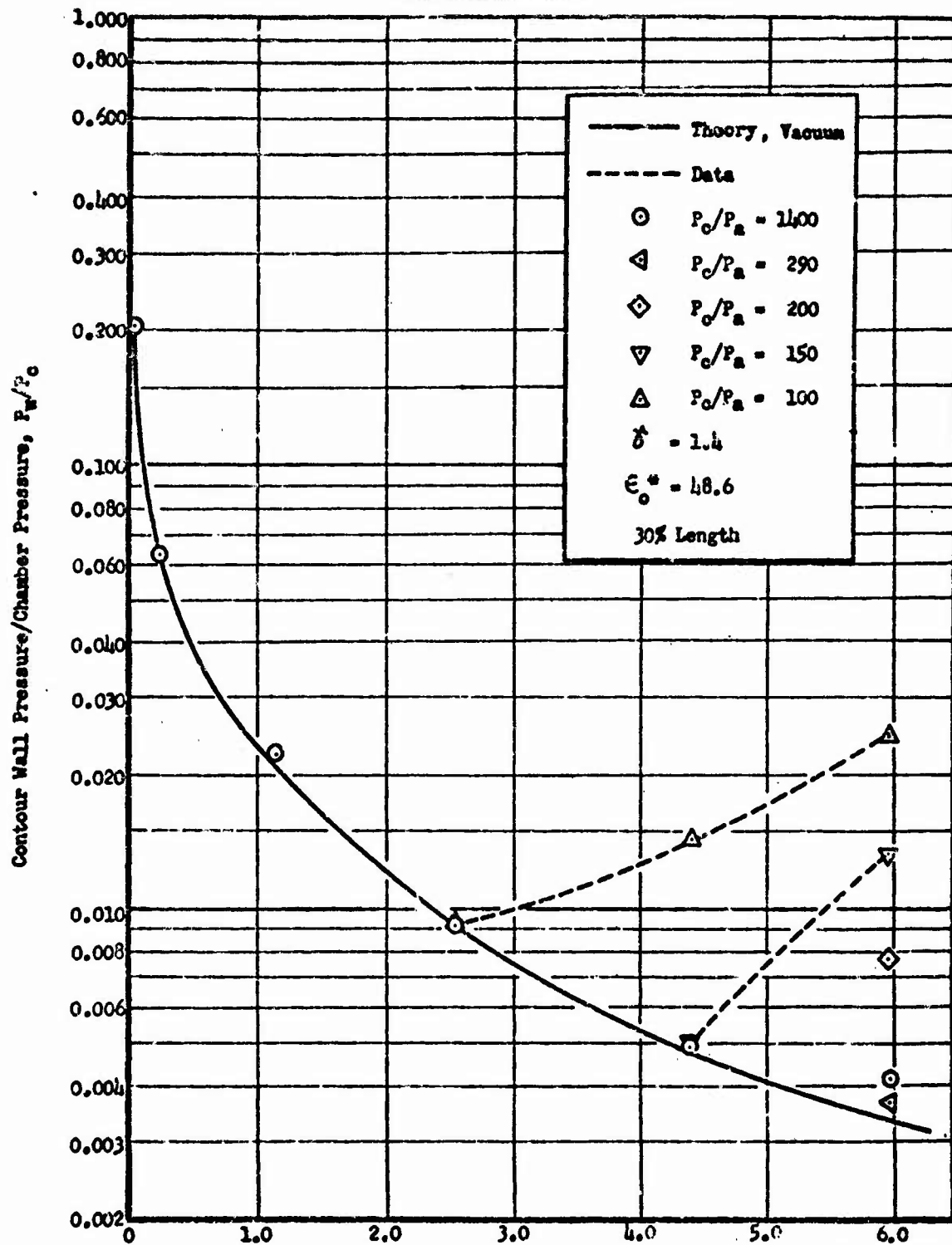
Figure 78. Contour Pressure Profile, Shrouded Spike Nozzle.

(a) P_c/P_a = 1525

$\dot{W}_s$ = 0%

(b) P_c/P_a = 248

$\dot{W}_s$ = 0%

(c) P_c/P_a = 155

$\dot{W}_s$ = 0%
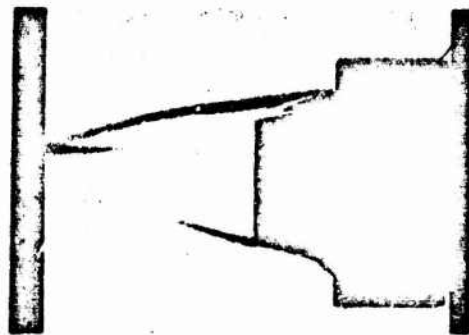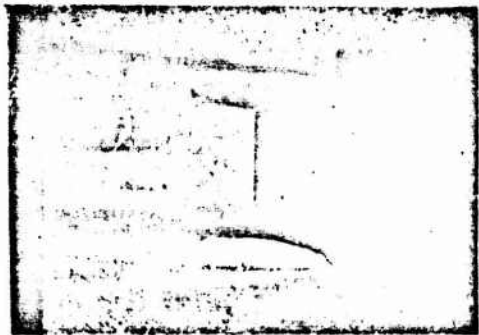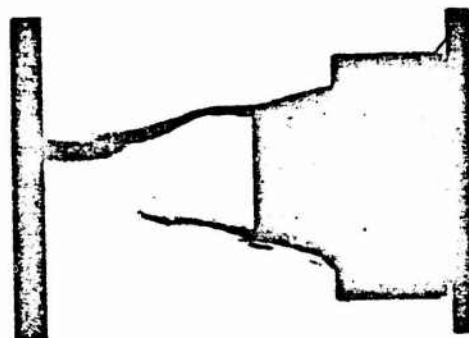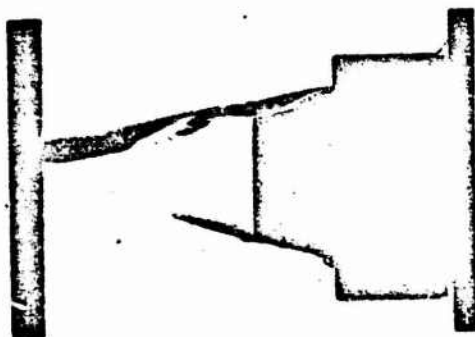
(d) P_c/P_a = 101

$\dot{W}_s$ = 0%

Figure 79. Schlieren Photographs of Shrouded
Annular Spike Nozzle

136

Multichamber Models

(U) Although the performance of multichamber spike nozzles has previously
been investigated in considerable detail, data are lacking for the
effects of secondary gas flow on performance for this combustor nozzle
configuration. The purpose of this test series was to obtain performance
data for multichamber spikes with secondary flow. Secondary flow was
introduced into both the centerbody region $(\dot{W}_e)$ and the region between
the individual chambers $(\dot{W}_{i.e.})$ in an effort to obtain maximum overall
performance. The principal test objectives are as follows:

1. Determine the maximum performance achievable through the use of
   secondary flow with the multichamber configurations and compare
   the data with the data from the reference models.
2. Determine whether secondary flow alters the relative effects on
   performance of the multichamber variables such as nozzle length,
   spacing, primary chamber area ratio and number of chambers.
3. Record and evaluate intersegmental and centerbody base pressures
   with and without interchamber and base bleed.
4. Determine the effect of interchamber bleed on the nozzle pressure
   profiles along the primary chamber centerline and between
   chambers.
5. Perform tests with one nozzle of the cluster plugged to simu-
   late engine-out performance.

(U) A total of 141 tests were accomplished with the multichamber con-
figurations. The eight touching chamber models (Models III-9 and III-
10) were tested over a pressure ratio range of from 100 to 1500 (design
pressure ratio for $\epsilon_{CL} = 50$) with intersegmental and base bleed rates

157

from 0 to 3 percent of the primary flowrate. Engine-out tests were performed by plugging one of the nozzles of Model III-9. Several tests were performed on a stripped down version (Model III-8). The cluster outer shroud and the spike contour (see Fig.56 p.93) were removed to obtain this configuration which simulated engines extending considerably beyond a vehicle external fairing and tank bottom.

(U)   Model III-11 (Fig.54 p.91) consists of eight individual 80-percent length bell nozzles with an area ratio of 20.7. The lower individual nozzle area ratio (compared to $\epsilon_M = 30.2$ for Models III-9 and III-10) for this eight chamber configuration results in a spacing between the module exits. The distance between module exits (δ) is 0.31 times the module exit diameter D_e. This model was tested over the same range of pressure ratios, intermodule and centerbody bleed flowrates that were used with the eight touching chamber configurations. However, testing with intersegmental bleed was limited to design pressure ratio.

(U)   Model III-12 consists of 16 touching chambers of ϵ_M equal to 20.7 placed around a central spike, giving an overall 30 percent length nozzle with a cluster area ratio of 50. This model is shown installed in the Rocket Nozzle Test Facility in Fig. 80 . Tests were conducted with this model over a pressure ratio range   from 100 to 1800 with intersegmental and centerbody bleed rates to 3 percent of primary flow.

(U)   To see if an improvement in performance with intersegmental bleed could be obtained, the intersegmental area in the region between the tangent points of the touching chambers and the outer shroud was blocked off using the scalloped plate shown in Fig. 81 . The scalloped plate served to isolate the interchamber region from ambient conditions. Tests were

138

Figure 80. Sixteen Nodule Multichamber Installation in Rocket Nozzle Test Facility, $\epsilon_{CL} = 50$
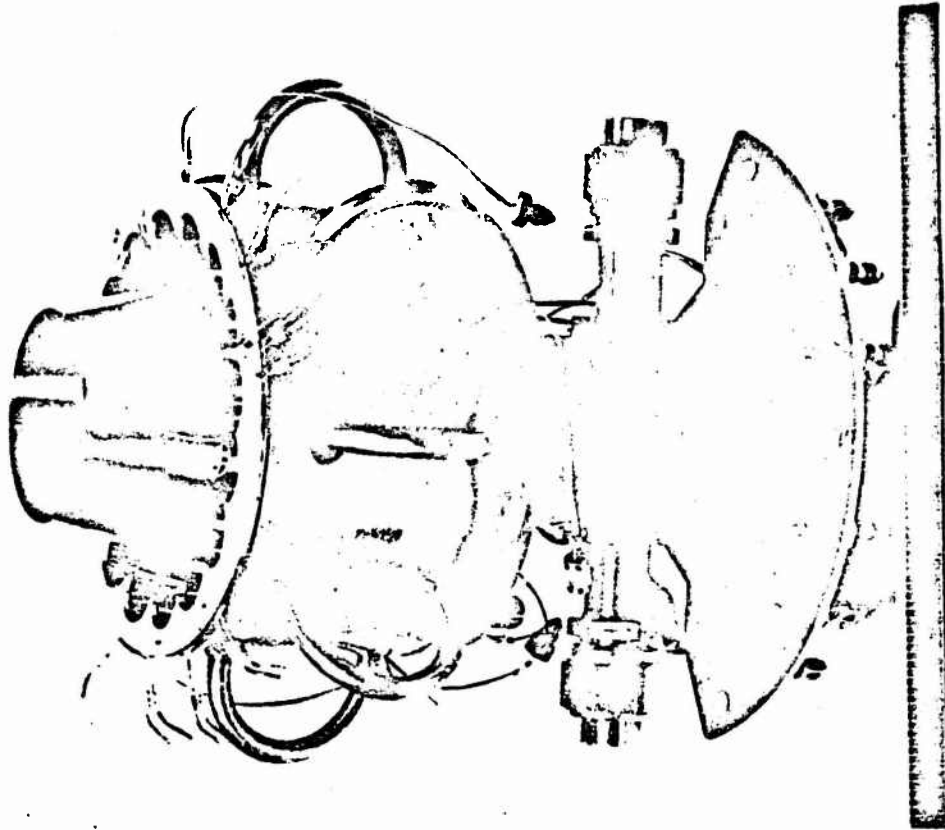
Figure 81. Sixteen Chamber Assembly with Interchamber Scallop

140

conducted with this scalloped 16-chamber configuration over a pressure ratio range from 150 to 1400 with interchamber and centerbody bleed rates to 4 percent of primary flow.

8 Touching Chambers - No Spike

(C) The first of the multichambers tested was model III-9, 8 touching chambers with no spike. Figure 82 shows the experimental performance for this model. Peak performance was 96.7 percent at a pressure ratio of 1400 although the performance curve is relatively flat from pressure ratios of 600 to 1400. Base bleed was introduced into the base region via a radial bleed orifice deep in the base cavity (see Fig. 51). Bleed rates were varied from 0 to 1.5 percent of primary flow rate. As shown in Fig. 83 no improvement in performance was obtained with base bleed at the high pressure ratio.

(C) A performance curve dip occurs at a pressure ratio of 280 which is also the corresponding break in the base pressure curve (Fig. 84), indicating the wake closing point in the base region. Performance with no secondary bleed at this pressure ratio was 94.2 percent. Figure 83 shows a performance increase to 94.8 with 0.7 percent secondary bleed.

(C) A sharp point of inflection in the base pressure curve for zero base bleed is observed at a pressure ratio of 240. A similar point of inflection is noted in the pressure curve for tap 3 (Fig.85) at a pressure ratio of 240. This tap is located on the cylindrical centerbody which forms the inner envelope of the modules and is midway between the exits of adjacent modules. Thus it records the pressure which is acting on the jets of adjacent nozzles.
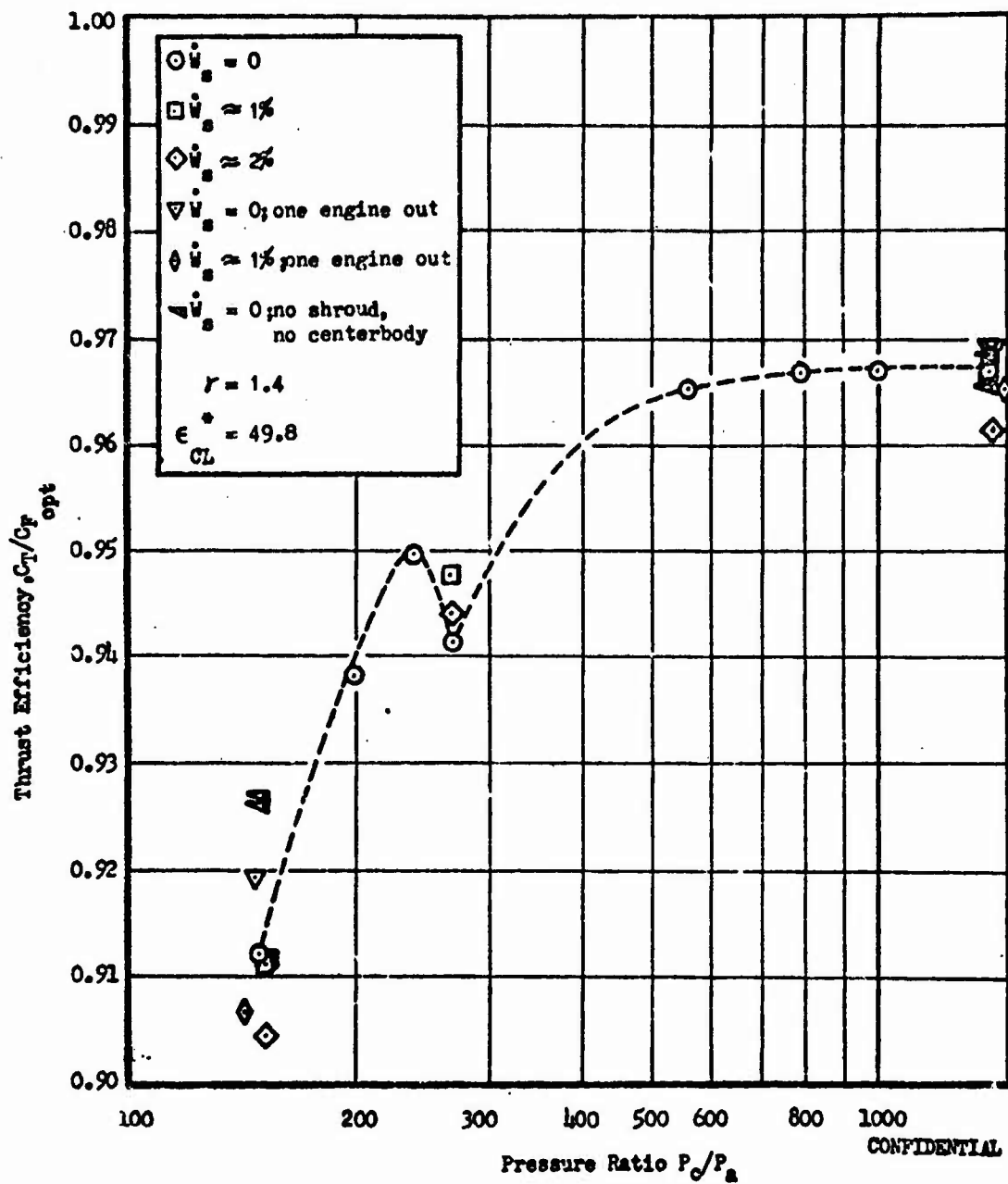
Figure 82. Thrust Efficiency vs Pressure Ratio,
8 Module Touching Multichamber, No Spike

142
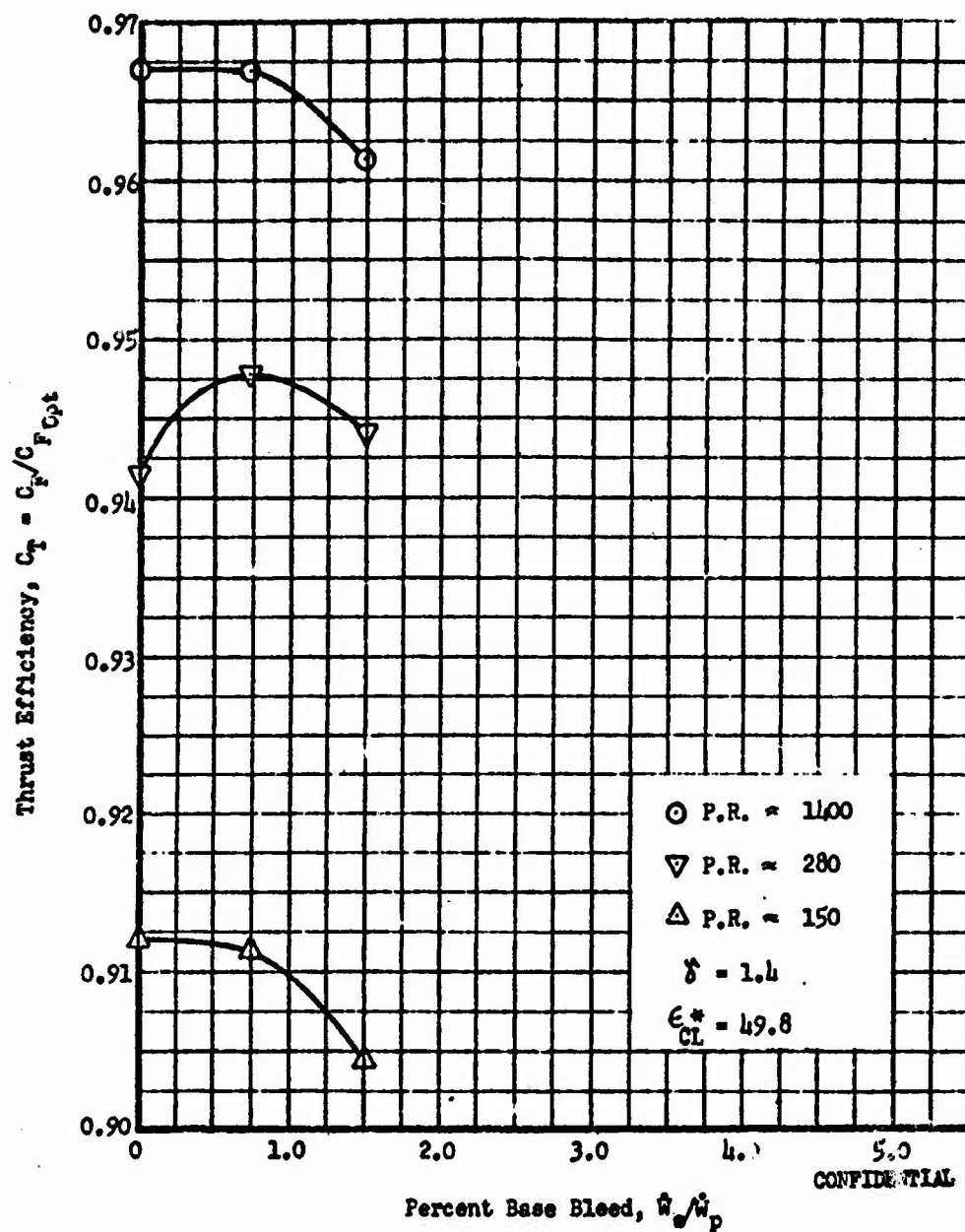
Figure 83. Thrust Efficiency vs Percent Base Bleed, 8 Module Touching Multichamber, No Spike

143
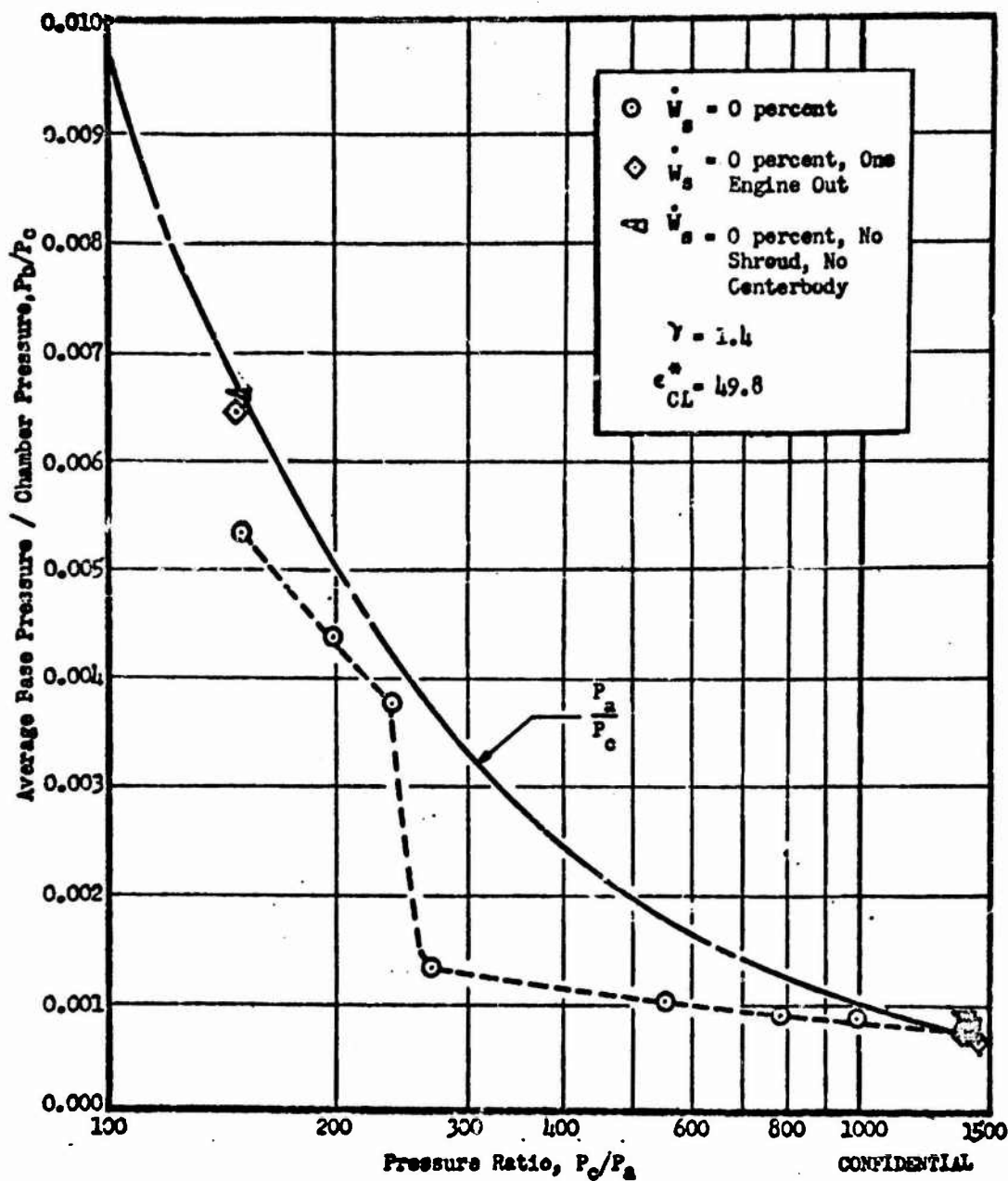
Figure 84 . Base Pressure vs Pressure Ratio, 6 Module Touching
Multichamber, No Spike
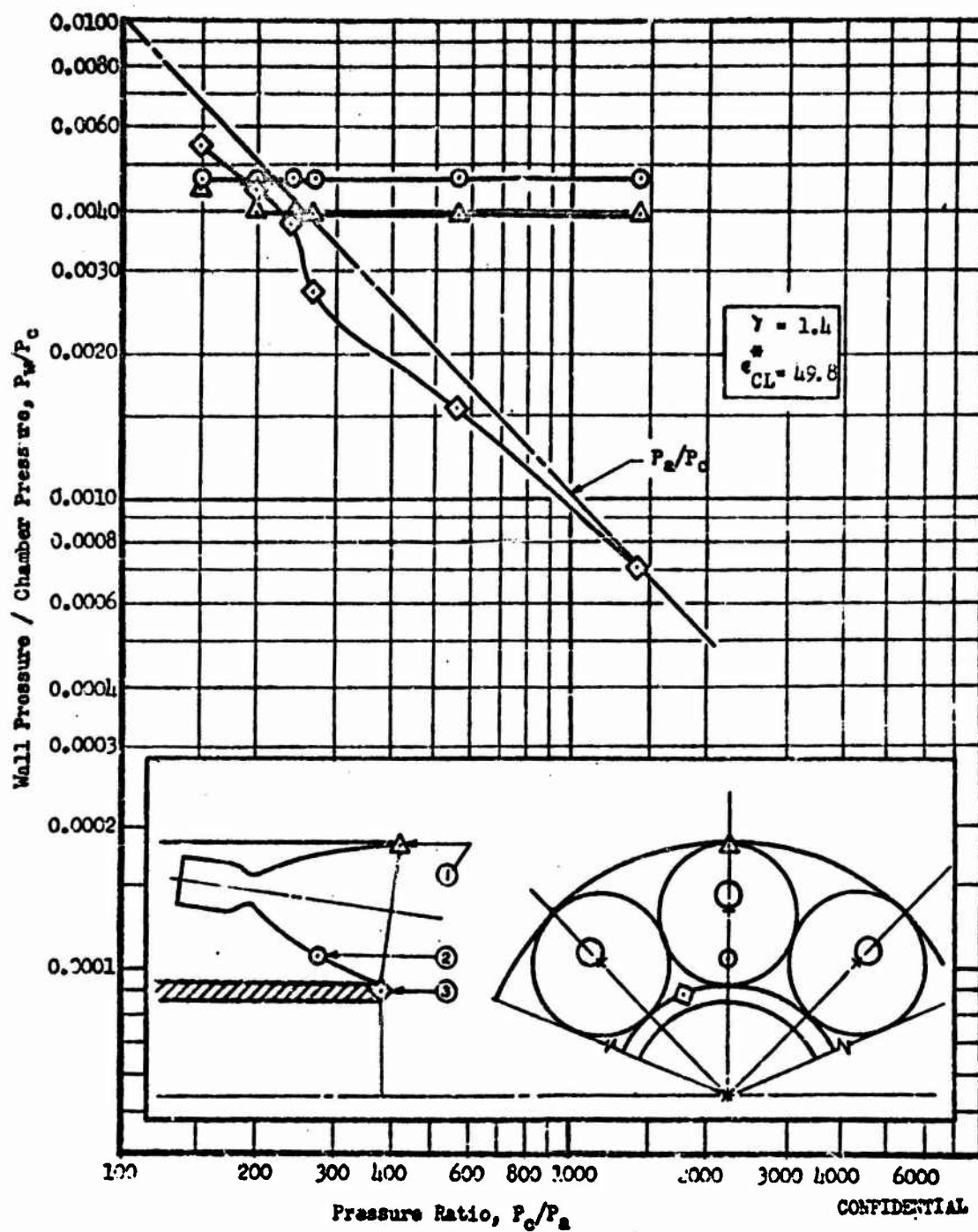
Figure 85 . Wall Pressure vs Pressure Ratio, 8 Module Touching Multichamber
No Spike

(c) Noting the trends in base pressure and pressure at tap 3, the following postulation is made to explain the base pressure trends of Fig. 84 for the zero base flow case. When the nozzle is operating at a high pressure ratio (above 300) the module jets will impinge on each other and coalesce into a common (but complex) flow field. This impingement pattern terminates olose to the module exits exposing a small flow area for ambient air to enter the base region from between the modules (see Fig. 86a). At a pressure ratio of 1400, $P_a = P_b$ (see Fig. 84) and no net flow occurs into the base. As P_c/P_a is decreased, P_a rises more rapidly than P_b and flow into the base region results. When P_c/P_a reaches 500, $P_b/P_a \approx 0.5$ and flow into the base should be choked.

(c) Further increases in P_a can not be communicated to P_b, however flow into the base will increase in proportion to P_a. Somewhere between a pressure ratio of 280 and 240 the increase in base bleed from the ambient causes the wake to open resulting in a steep rise in P_b because; 1) open wake flow allows better communication of ambient pressure to the base and 2) the module wakes coalesce much further downstream, as shown in Fig. 86 b and allow a larger area for ambient flow to bleed into the base region. The pressure ratio P_b/P_a is now much greater than 0.5 and choking of the flow into the base does not occur. This allows P_b to closely follow P_a (see Fig. 84 for $P_c/P_a < 240$).

(c) At a pressure ratio of 150 the performance with no secondary flow was 91.2 percent and showed no increase with the addition of secondary flow (see Fig. 83). The pressure profile curve of Fig. 85 shows a rising pressure near the module exit, indicating flow separation from the module.
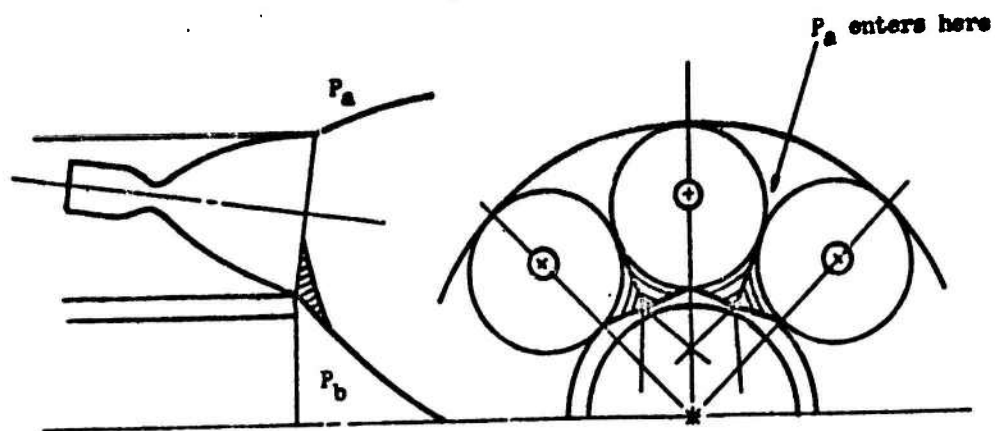
a) Module Jets Coalescing at High Pressure Ratio
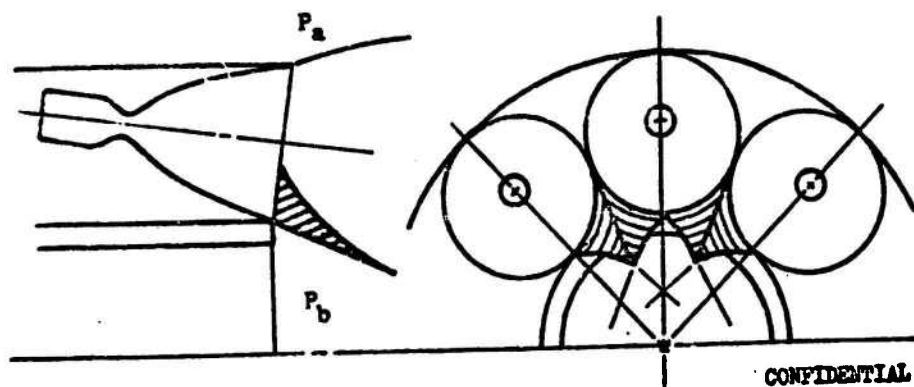
b) Module Jets Coalescing at Intermediate Pressure Ratio

Figure 86. Module Jet Structure, 8 Module
Touching Multichamber, No Spike

(C)   In the closed wake regime the base pressure is not as constant as in the nozzles with spike extensions. This is most likely due to the fact that the base region is never completely isolated from the ambient in this nozzle. Ambient pressure is felt from the region behind the modules through the intermodule wakes where the base can be communicated to the ambient.

(C)   Base bleed had very little beneficial effect on this model. Essentially no increase in performance was noted at design pressure ratio or at low pressure ratios for any bleed rates. Small gains were noted at the curve dip point.

Engine-Out Tests

(C)   Flow through one chamber of Model III-9 was stopped by inserting a plug in the throat of the chamber. Surprisingly no decrement in performance was noted over the symmetrically flowing case with or without secondary flow (see Fig. 82). In fact at a pressure ratio of 150 a small increase (approximately 0.8 percent) in performance was noted for the no bleed case. Again, this is likely due to the fact that with one engine off, ambient was allowed to communicate more readily with the base. This is verified by the base pressure curve, Fig. 84 , which shows an increase in base pressure for the engine out, compared to the symmetrically flowing case, especially at low pressure ratios. At a pressure ratio of 1400, performance and base pressure were approximately the same with one engine out as with no engines out.

Stripped Model

(U)   A version of Model III-9 was tested with no centerbody duct or outer cluster shroud (see Fig. 86). This was called Model III-8.

(C)   Essentially this was simply an open cluster of 8 engines. Referring to Fig. 82 , performance at high pressure ratios was slightly lowered but at low pressure ratio, performance was increased about 1.0 percent due to higher overall base and intermodule pressures at zero secondary flow (see Fig. 84).

(U)   Schlieren photographs of Models III-8 and III-9 are shown in Fig. 87 .

(a) Model III-9

P_c/P_a = 1467

$\dot{W}_s$ = 0%

(b) Model III-9

P_c/P_a = 249

$\dot{W}_s$ = 0%
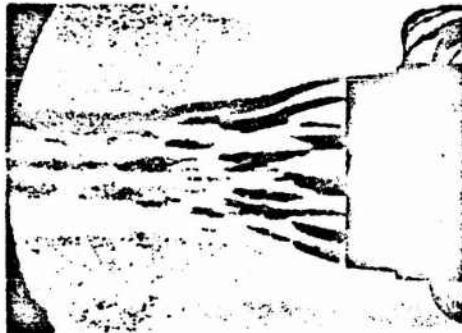
(c) Model III-9

P_c/P_a = 150

$\dot{W}_s$ = 0%
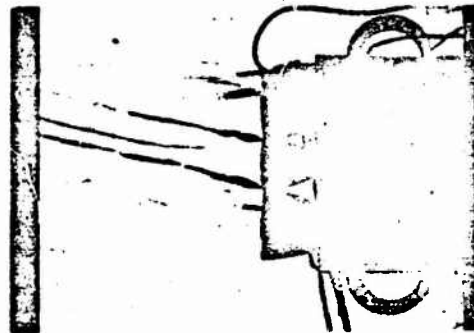
(d) Model III-8

P_c/P_a = 1387

$\dot{W}_s$ = 0%

CONFIDENTIAL

Figure 87. Schlieren Photographs for 8 Module
Touching Multichamber, No Spike

8 Modules Touching With Spike Centerbody

(U) Model III-10, Fig.53 , has 8 modules touching with a spike center-
body extending the nozzle length, L_N, to 30 percent of a 15 degree cone
of ϵ = 50. The nominal cluster area ratio is 50 and the model is
essentially model III-9. with the spike replacing the short cylindrical
centerbody.

(C) This model has provisions for bleeding flow into the spaces between the
modules (intersegmental bleed, $\dot{W}_{i.s.}$) in addition to base bleed, $\dot{W}_s$.
With the combination of intersegmental bleed and base bleed at various
bleed rates, a variety of possible combinations of $\dot{W}_{i.s.}$ and $\dot{W}_s$ could
be used. However, a systematic approach to the testing can reduce the
number of tests required to obtain significant data. The approach used
was to first optimize the intersegmental bleed at zero base bleed and
then, using the optimum $\dot{W}_{i.s.}$ optimize the base bleed. As it turned
out the best nozzle performance was obtained with $\dot{W}_{i.s.}$ = 0. An
explanation will be given for this result later in this section.

(C) Referring to Fig. 88 and the data in Appendix 3 , the performance of this
nozzle is shown for a pressure ratio range from 150 to 8000. At zero
intersegmental and base bleed rates the performance reached a maximum
value of 97.1 percent at a pressure ratio of 1450. Referring to Fig.89
it can be seen that the addition of either intersegmental or base bleed
did not increase performance at high pressure ratios. Examination of
the base pressure curve, Fig. 90 , shows that intersegmental bleed
does not improve the base pressures at high pressure ratios. While
introduction of intersegmental bleed increased the intersegmental pressure
(see data in Appendix 3). the resulting increase in thrust for the
additional mass flow was low, causing a drop in overall efficiency.
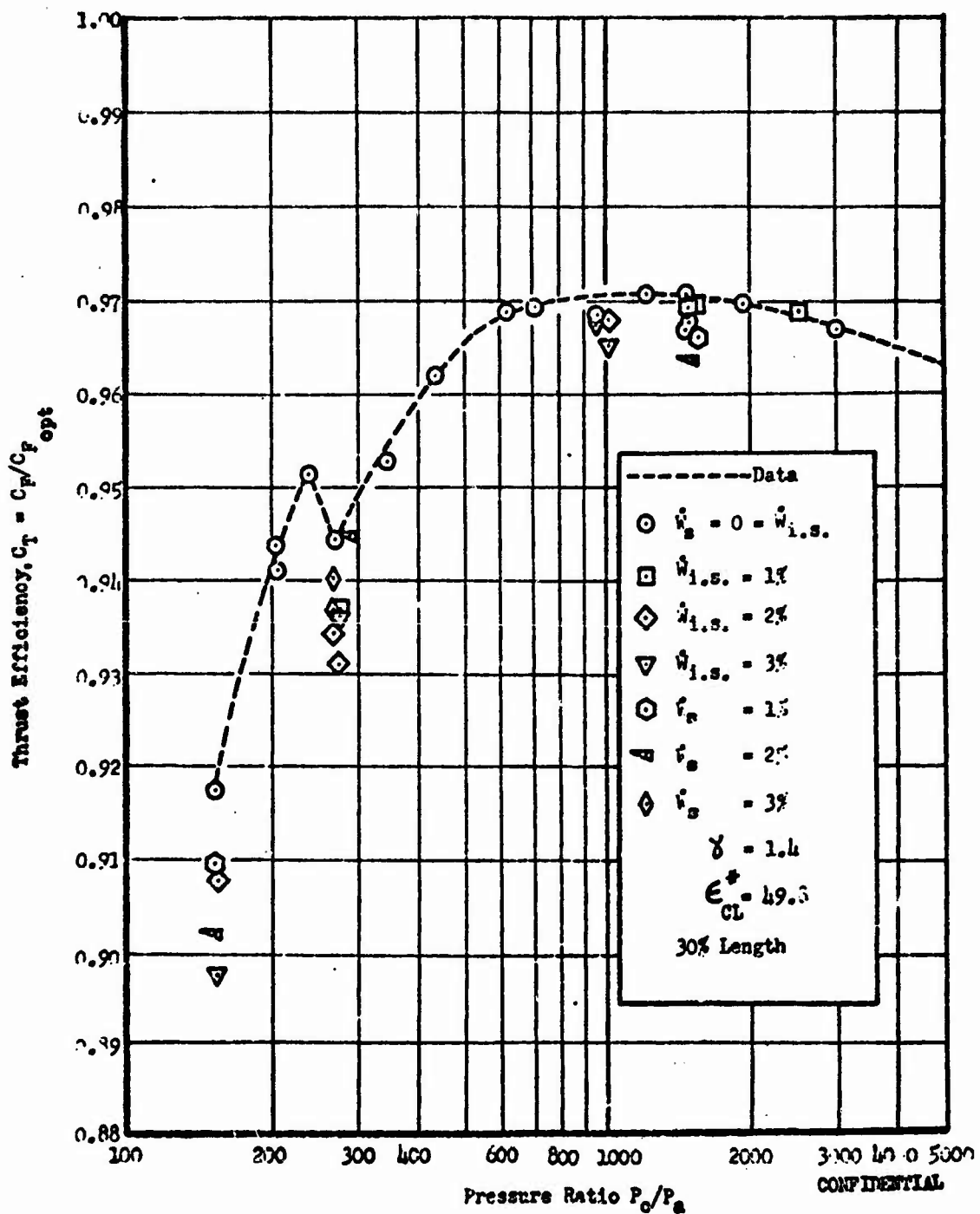
Figure 86. Thrust Efficiency vs Pressure Ratio, 8 Modules
Touching Multichamber, 30 Percent Length
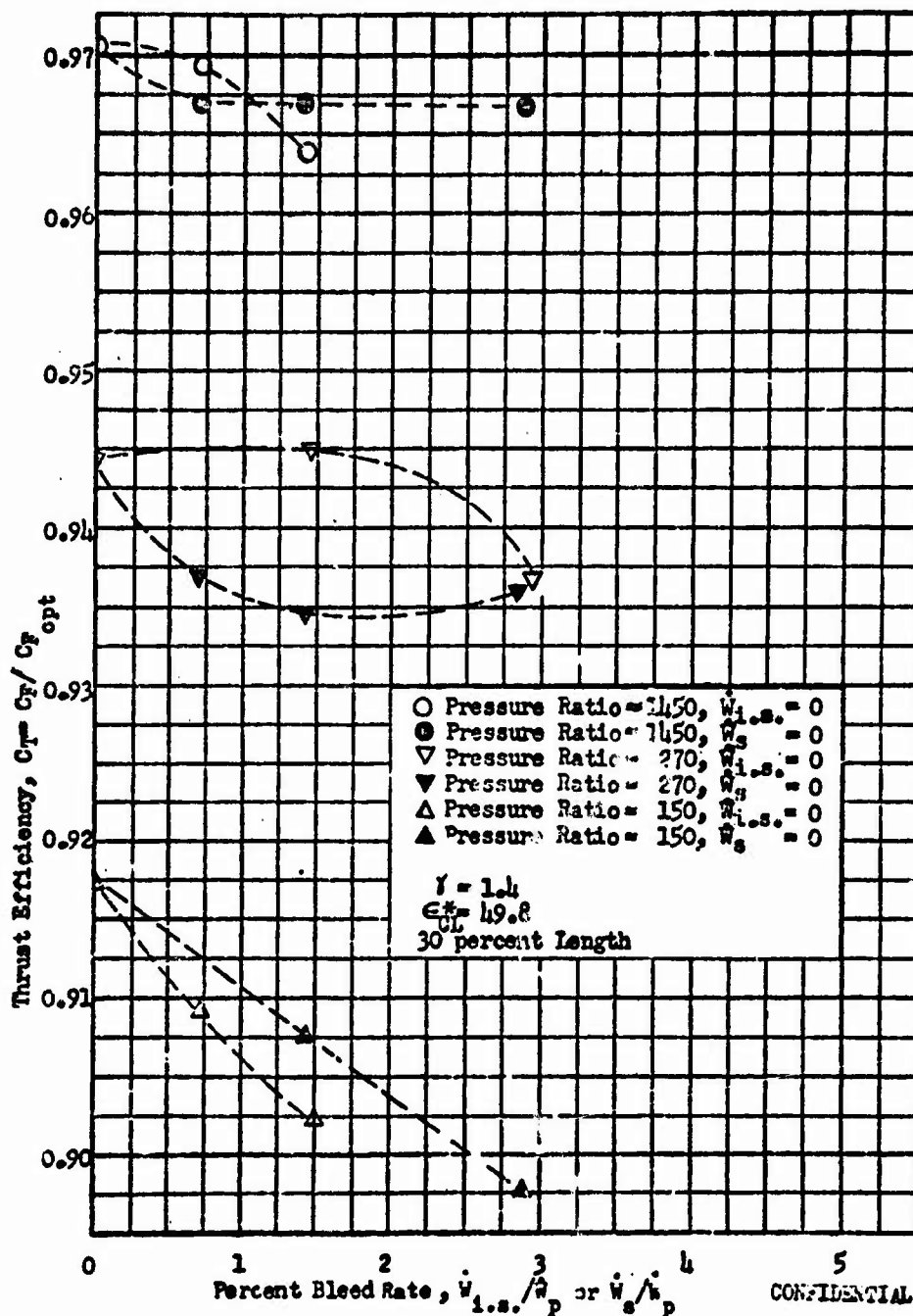
Figure 89. Thrust Efficiency vs Bleed Rate, 8 Module Touching
Multichamber, 30 percent Length
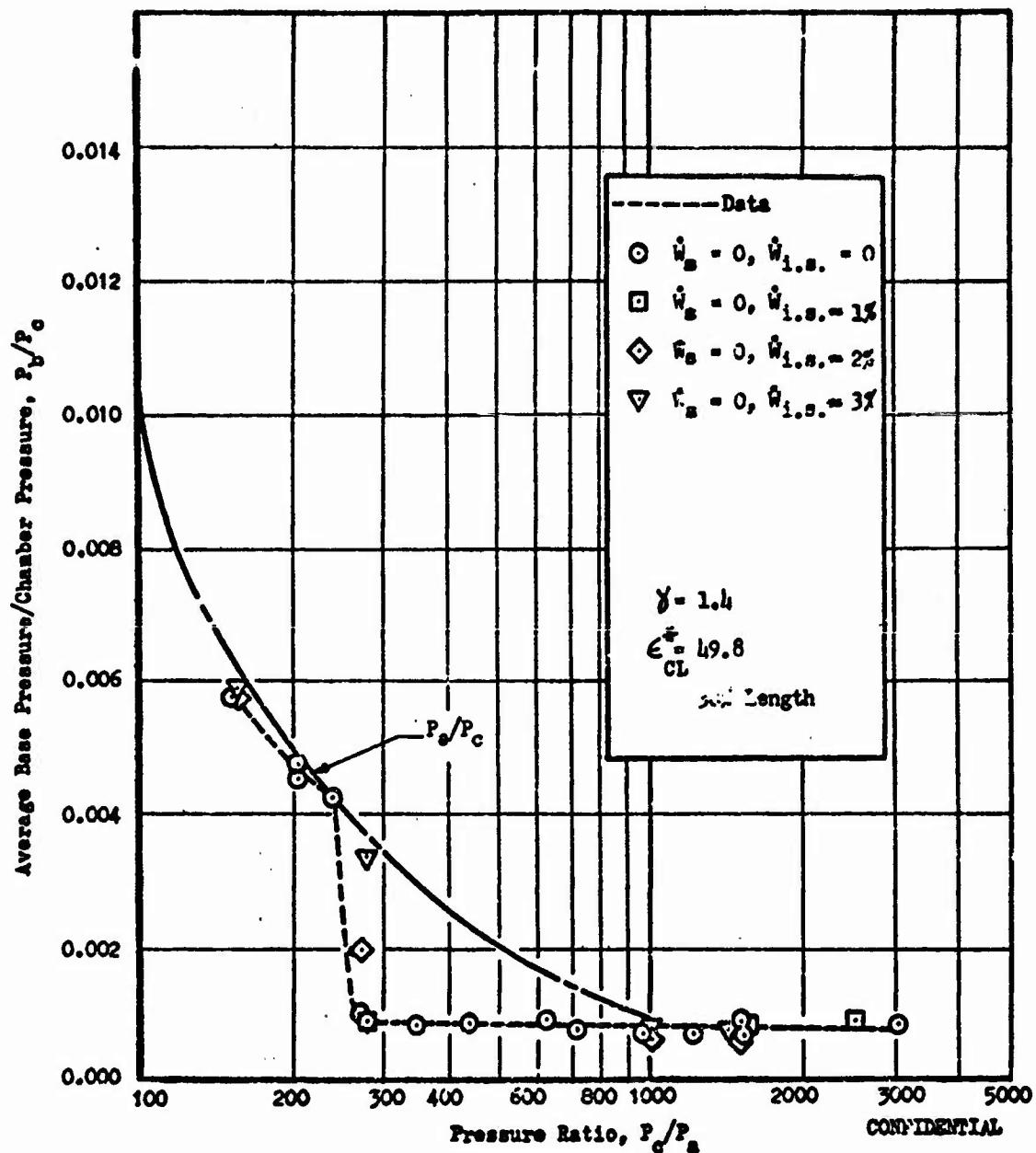
Figure 90. Base Pressure vs Pressure Ratio, 8 Modules
Touching Multichamber, 30 Percent Length

154

(C) Bleed addition apparently causes the following phenomenon to occur:
Referring to the efficiency vs base bleed curve (Fig. 71) for the point
expansion annular nozzle, it is worth noting that for small bleed rates,
base pressures and nozzle efficiencies increase. However, for larger
bleed rates the efficiencies decrease. These are known as the small
bleed and large bleed regimes of the base flow. It is also known
that mass bleed can be replaced by an equivalent boundary layer or
momentum thickness in the approach section. Two reasons can be given
for the formation of a large momentum thickness in the multi-chamber
nozzle. First, a series of shocks are caused by the coalescing of the
primary flow fields from the modules. The action of these shocks
intercepting the contour may well cause a thickening of the boundary
layer and an increase in the momentum thickness along the contour.
Second, bleed from the spaces between the modules can easily be
entrained in the boundary layer along the contour, whether or not
intermodule bleed is introduced. This is because of the large openings
to the ambient behind and above the module. Both conditions may cause
a considerable increase in the equivalent momentum thickness, along
the contour and thus at the end of the centerbody, over the annular
nozzle case.

(C) Referring to the plot of Fig. 91, two curves are shown for performance
vs bleed rate. The performance curve for the annular nozzle shows the
normal increase in performance for small base bleed rates and decrease
for large bleed rates. The multichamber curve shows the same trend
but a lower efficiency due to primary flow field shock losses. Both
curves of Fig. 91 assume the same momentum thickness at the end of
the contour. If it now can be assumed that the mass bleed between the
modules causes an increase in entrained air in the boundary layer along

155
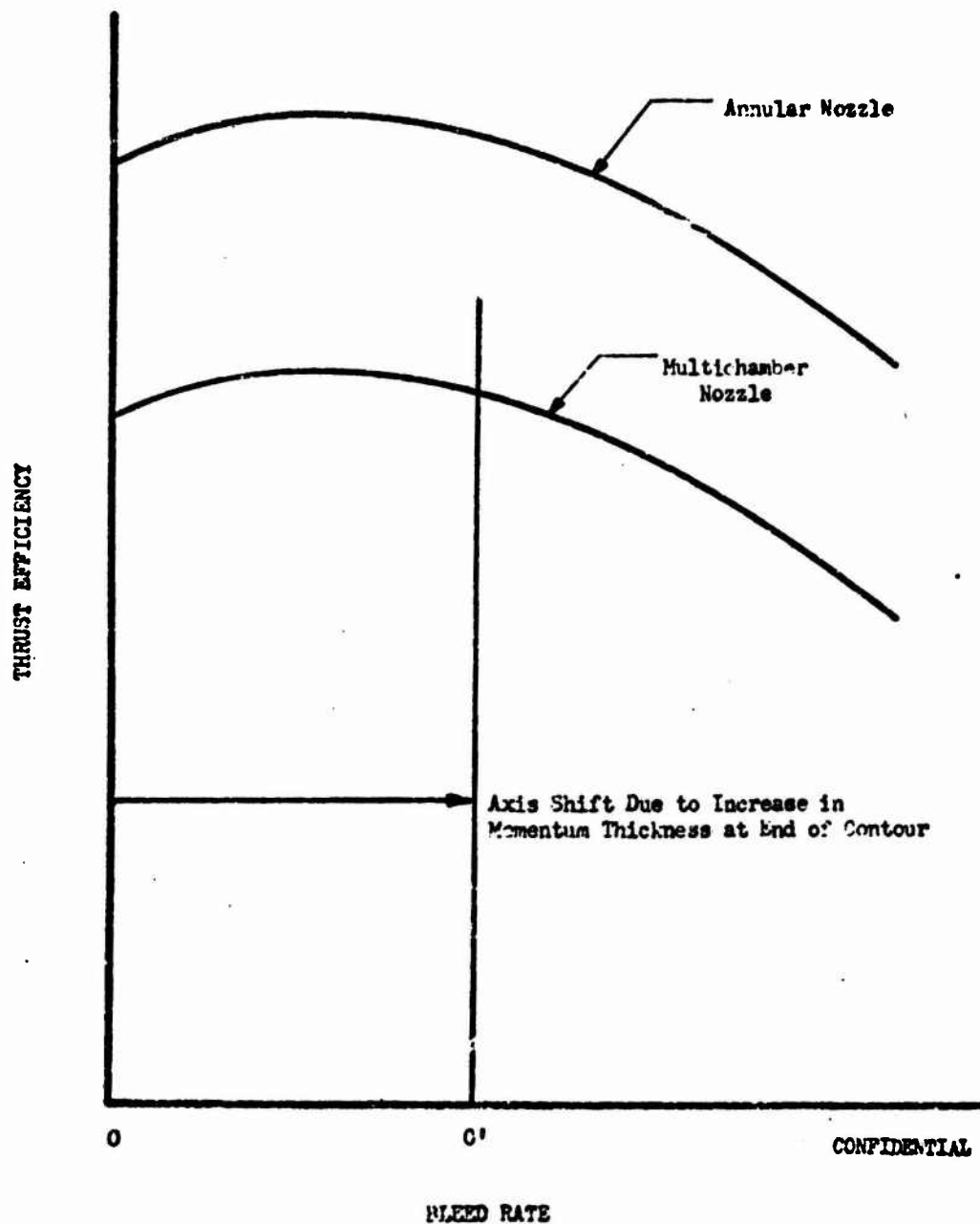
Figure 91. Thrust Efficiency vs Bleed Rate
for Annular and Multichamber Nozzle

the contour, an increase in momentum thickness occurs for the multi-
chamber nozzle. This increase in momentum thickness for the multi-
chamber can now be equated to some positive base bleed rate and one
can obtain the efficiency vs actual bleed rate curve for the multi-
chamber by shifting the zero bleed axis from 0 to 0'. Now note that
the zero bleed point is past the optimum bleed point for the case of
little or no momentum thickness. Thus, no amount of either interseg-
mental or base bleed can increase the performance of this hypothetical
nozzle. This curve is qualitatively similar to the experimental data
shown in Fig. 89 .

(C)   The transition point from closed to open-wake base flow for this nozzle
occurs at a pressure ratio of 270, as shown in Fig. 88 and 90. Again,
no performance improvements are obtained by either intersegmental or
base bleed.

(C)   Base pressure rises sharply at the transition pressure ratio (270) and
then increases at a reduced rate below a pressure ratio of 240. Note
that this condition is very similar to the base pressure curve of
Fig. 84 (p.144) for model III-9. This characteristic base pressure trend
for model III-10 shown in Fig.90 is similar to that of model III- 9.
The same explanation for this phenomenon that was given for model III-9
applies. Choking of flow into the base may be occurring in the region
between pressure ratios of 240 and 500. Evidence for this is the lower
than critical pressure ratio between P_b and P_a. At the lowest pressure
ratio at which the nozzle was tested, P_c/P_a = 150, the same phenomenon
is observed in performance, i.e., at zero intersegmental and base flow
the efficiency was 91.7 percent and as either intersegmental or base
bleed was increased, performance decreased.

(c) Figures 92, 93, 94, and 95 show the pressure profiles for this nozzle. Figures 92 and 93 show the wall pressure profiles for various wall taps versus nozzle pressure ratio. In Fig. 92 the pressure taps are in line with the centerline of the module with two taps located in the module and three taps on the contour. The trends are as anticipated with pressures decreasing with increasing pressure ratios on the taps further on down the contour. In Fig. 93 the taps are located between the modules. The tap near the exit plane of the modules follows the ambient pressure while the last two taps follow ambient only to pressure ratios of 300 to 400. Beyond this point the pressures on the contour rise indicating that the wake between the nozzles is moving back towards the throat. The pressure rise is due to shock interaction. Figures 94 and 95 show the same data but plotted in a different manner. The pressures along the module centerline continually decrease at high pressure ratios; however, the pressure profile curves move up with decreasing pressure ratio indicating that recompression may be occurring on the contour as P_a increases. On the other hand the pressure profiles between the modules show adverse pressure gradients to the nozzle exit because of a complex flow field along this plane.

Eight Modules Spaced

(c) The final 8-module configuration tested, Model III-11, was the model with spacing between the modules and an overall length of 30 percent. This model has the lowest performance of all models tested. Peak performance (shown in Fig. 96) of 96.2 percent occurred at a pressure ratio of 950. This pressure ratio is optimum for a one-dimensional ideal area ratio of 37.4. Since the efficiency maximizes at this point, 950 is considered the design pressure ratio for this nozzle. The addition of base bleed at this pressure ratio caused the overall nozzle performance to decrease (Fig. 97).
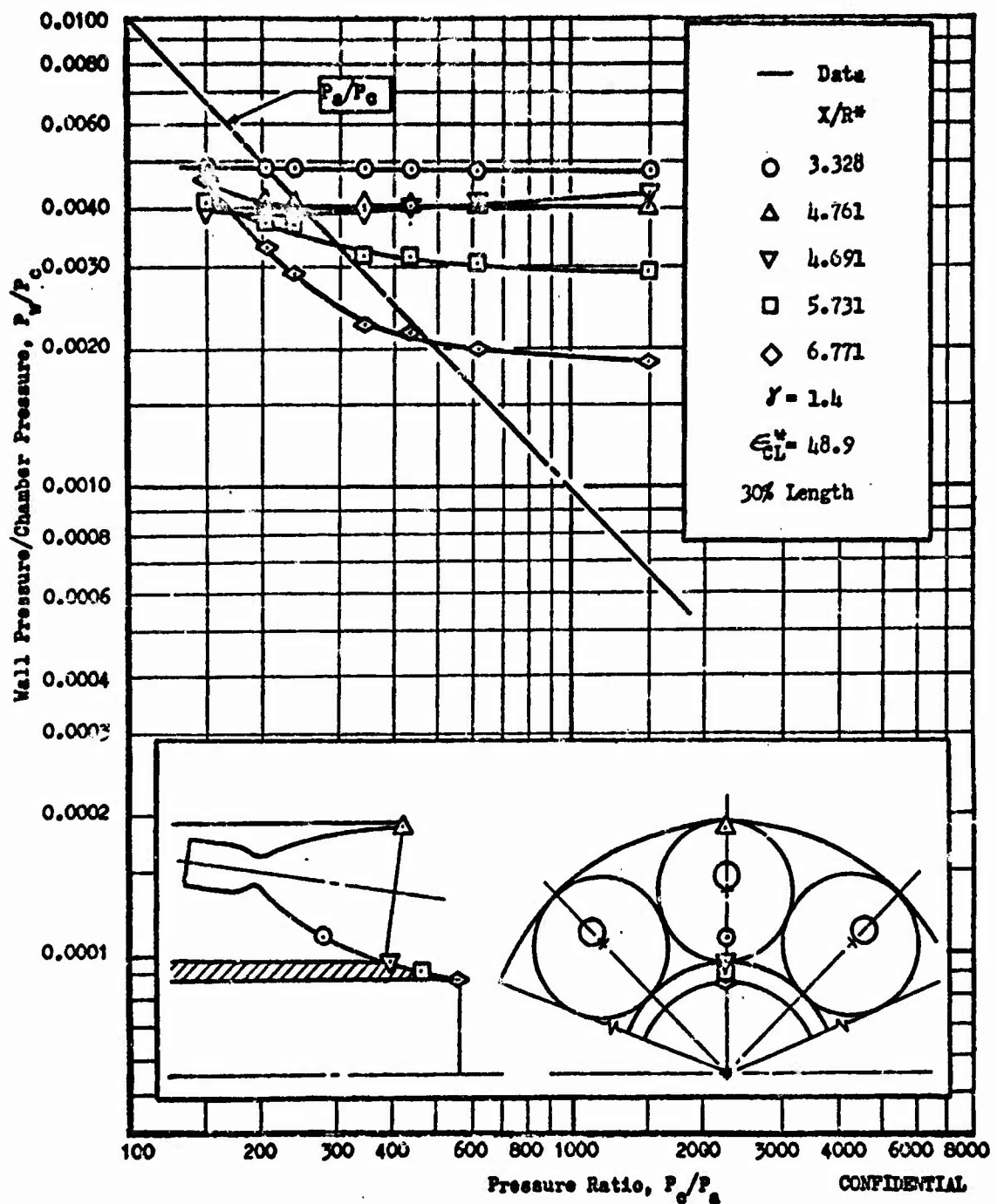
Figure 92. Module Centerline Wall Pressure vs Pressure Ratio,
8 Modules Touching Multichamber, 30 Percent Length
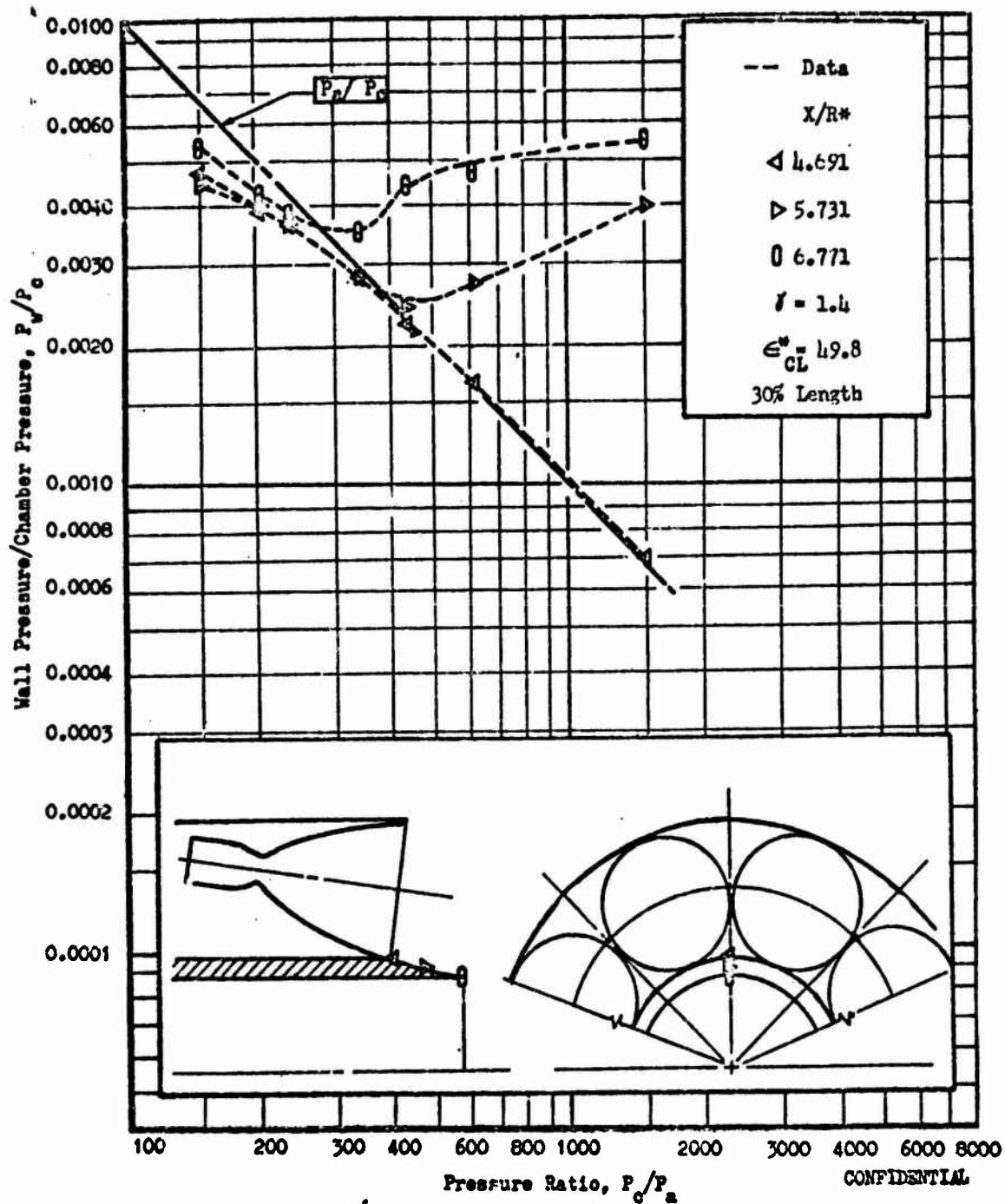
Figure 93. Wall Pressure Between Modules vs Pressure Ratio,
8 Modules, Touching Multichamber, 30 Percent Length

160
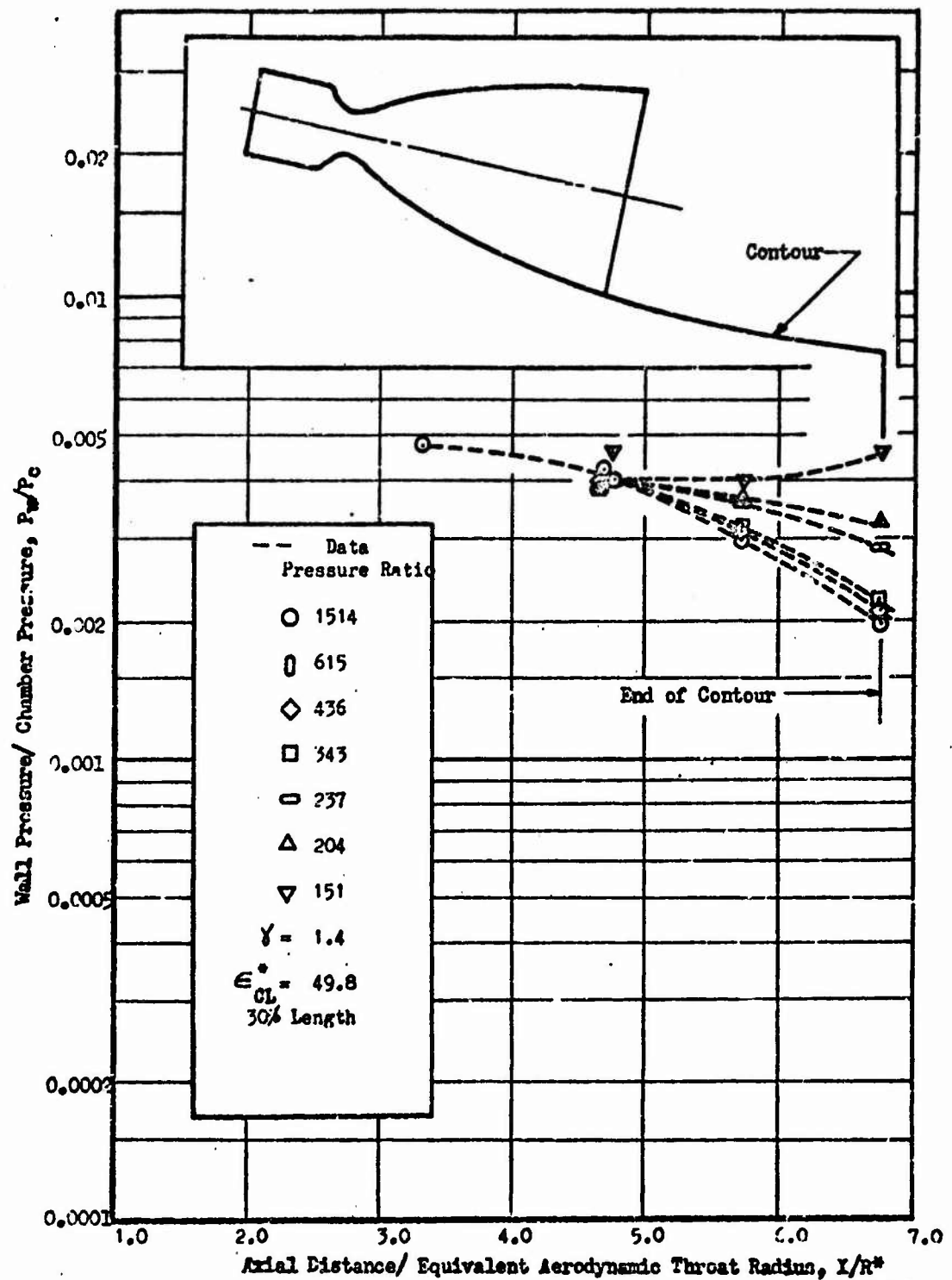
Figure 94. Module Centerline Wall Pressures vs Axial Length,
8 Module Touching Multichamber, 30 Percent Length
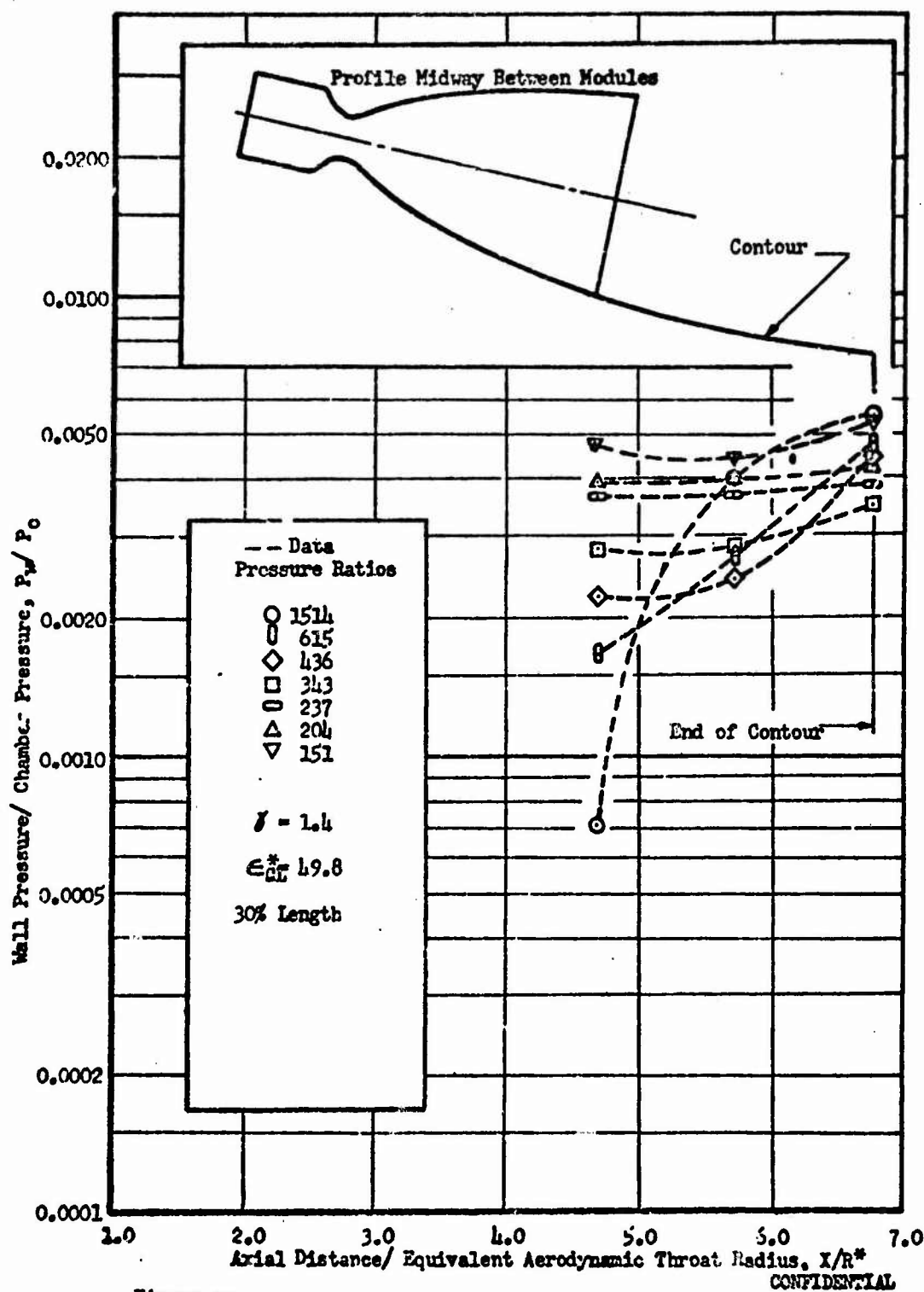
Figure 95. Wall Pressure Between Modules vs Axial Length,
8 Modules Touching Multichamber, 30 Percent Length
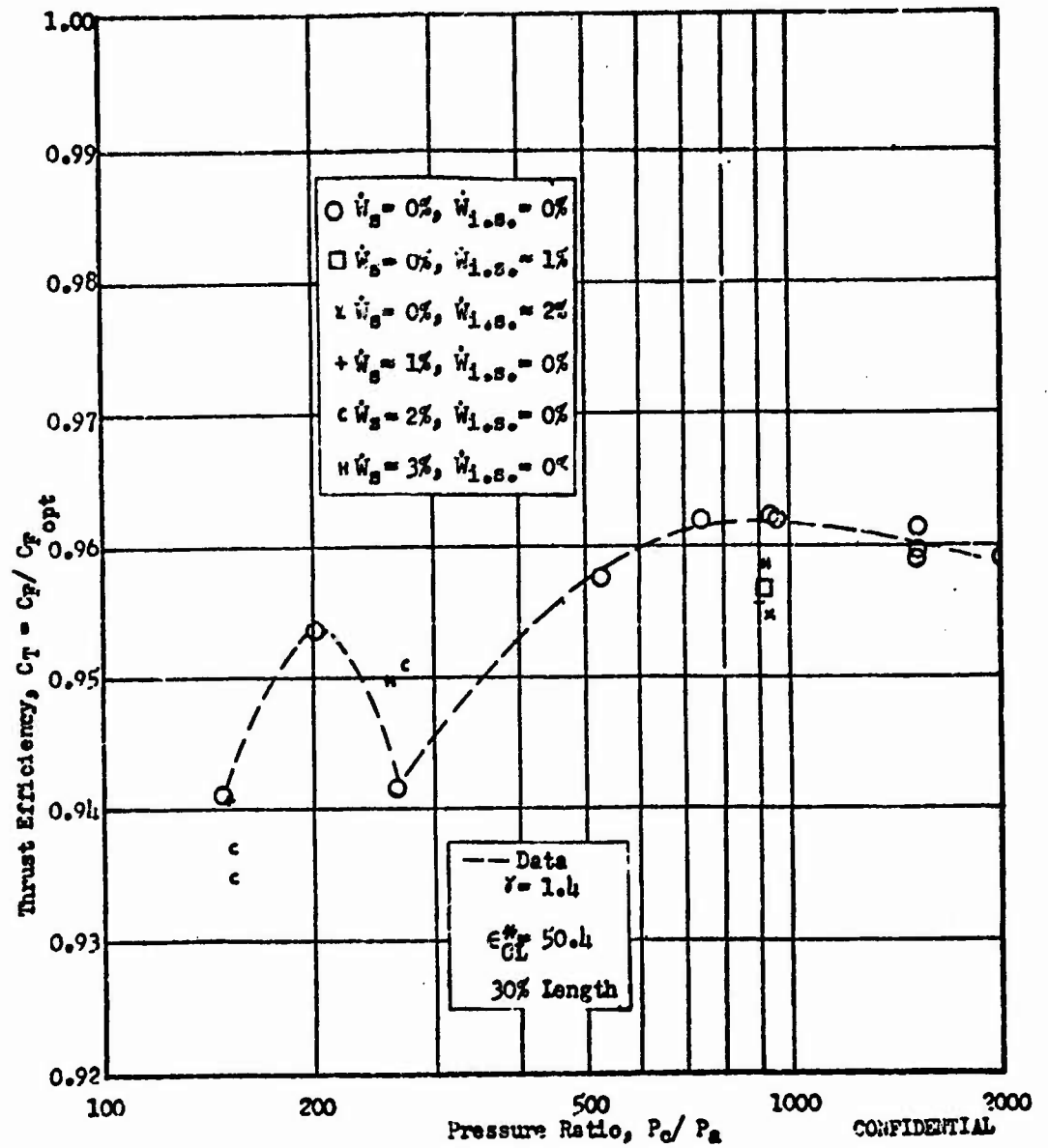
Figure 96. Thrust Efficiency vs Pressure Ratio, 8 Modules
Spaced Multichamber, 30 percent Length

163
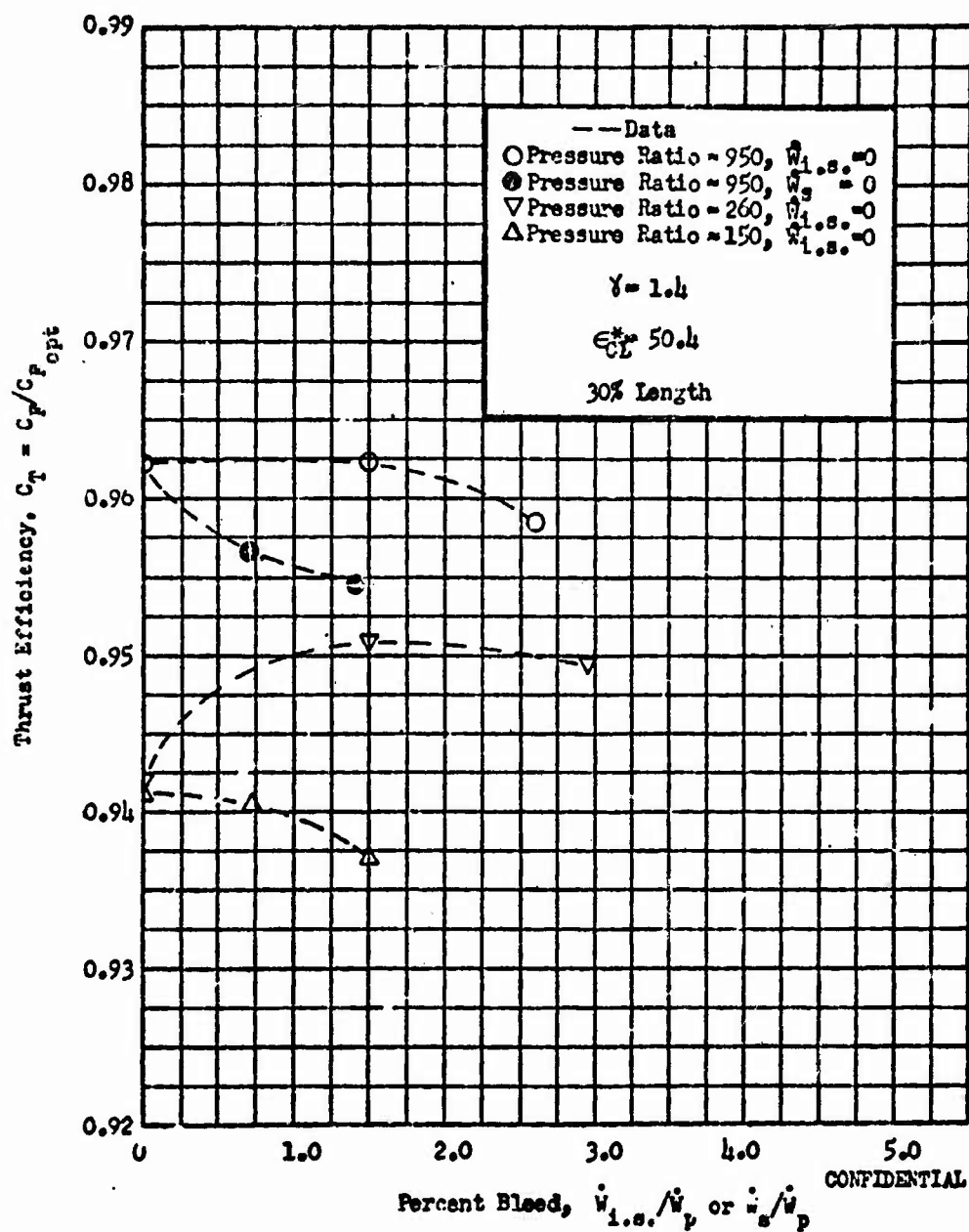
Figure 97. Thrust Efficiency vs Percent Bleed, 8 Module
Spaced Multichamber, 30 percent Length

164

(C)   The transition from closed to open-wake flow occurred at a pressure ratio of 270 (Fig. 98). Addition of base bleed at this pressure ratio increased performance from 94.2 to 95.1 percent at an optimum bleed rate of 1.5 percent. This increase in performance was apparently caused by an increase in wall contour pressures. At zero base bleed the wall pressure, P_w/P_c, at the end of the contour was 0.00196 and increased to 0.00327 for 1.5 percent base bleed. This bleed appears to be causing separation from the contour, resulting in an efficiency increase. In contrast, introduction of base bleed into Model III-10, 8 touching multichamber, did not cause an increase in contour pressure and thus efficiency did not increase.

(C)   A sharp increase in performance occurs at a pressure ratio of 200, due to a rapid rise in base pressure from the closed wake condition. Performance then falls off as pressure ratio is decreased beyond this point.

(C)   The lowest pressure ratio at which tests were conducted on this nozzle was 150. Addition of base bleed caused a loss in performance.

(C)   Use of intersegmental bleed caused a loss in performance at design pressure ratio. The explanation for this loss is similar to that given for the previous multichamber models. The base pressure curve, Fig. 98 , also shows the same trend as the previous model. In addition, this curve verifies the transition point to be near a pressure ratio of 270.

(C)   The module and plug wall pressure profiles of Fig. 99 , 100, 101 and 102 show the same trend as for model III-10.
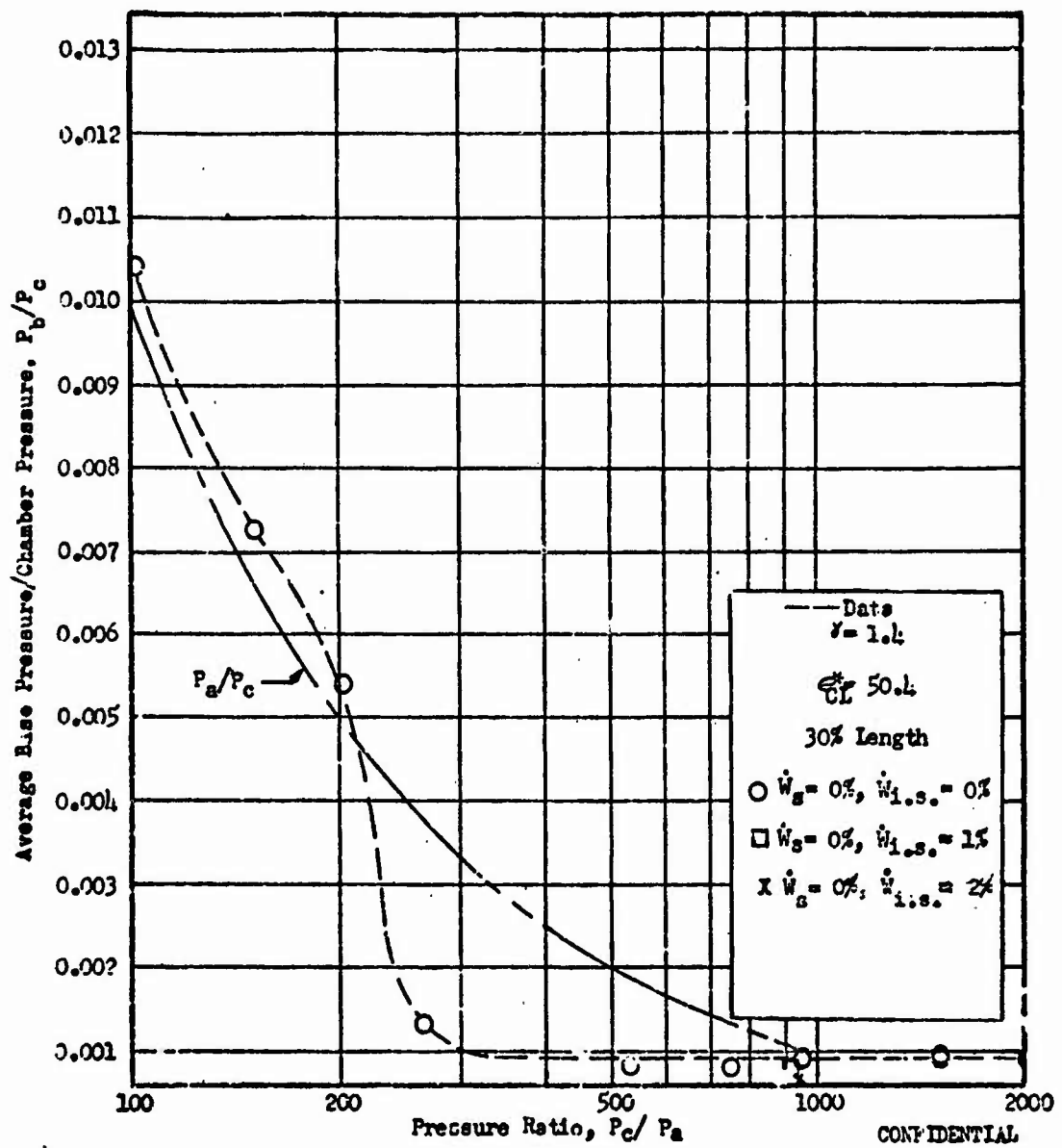
Figure 98. Base Pressure vs Pressure Ratio, 8 Module Spaced Multichamber, 30 percent Length
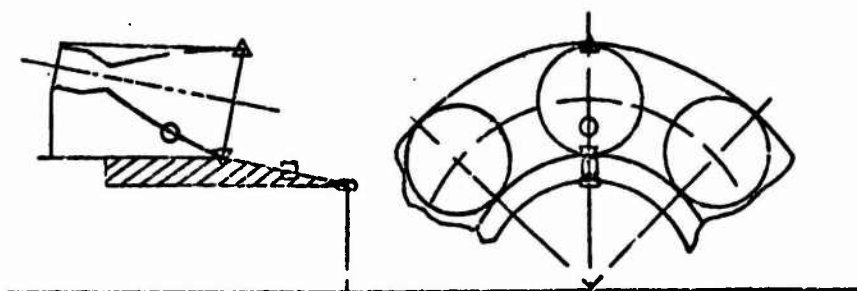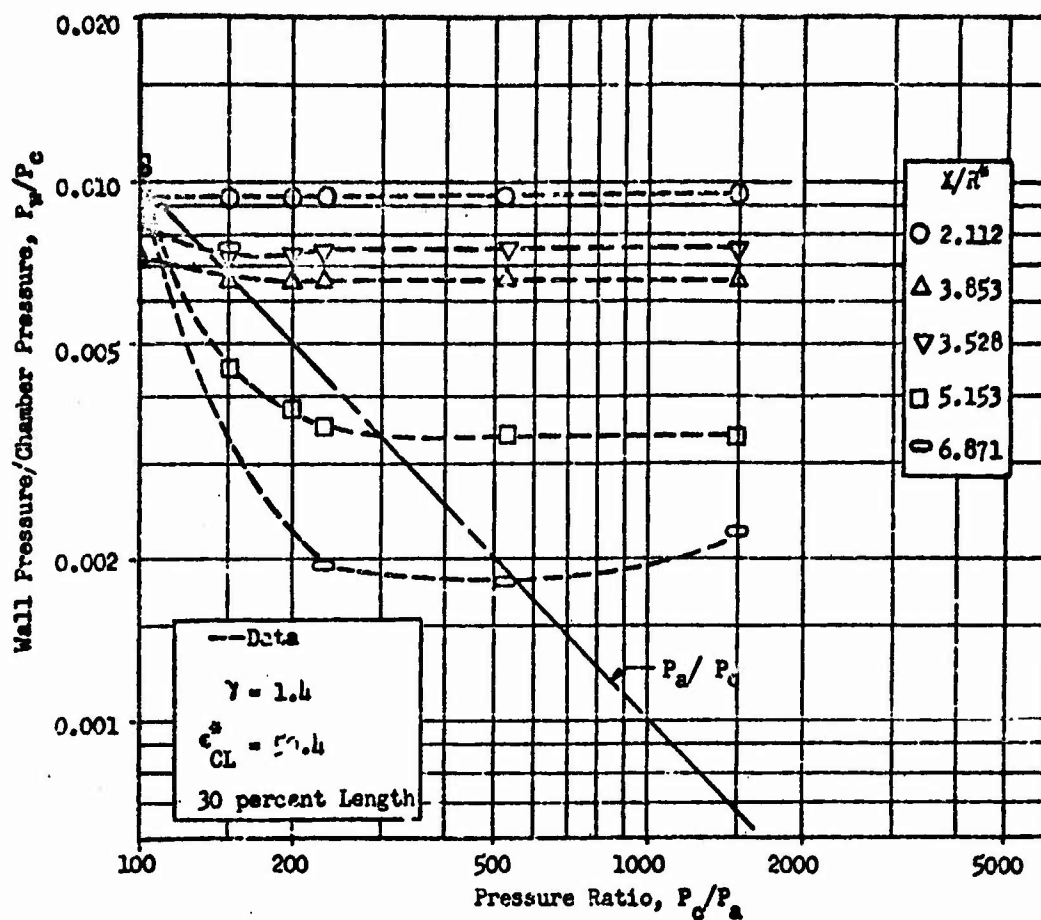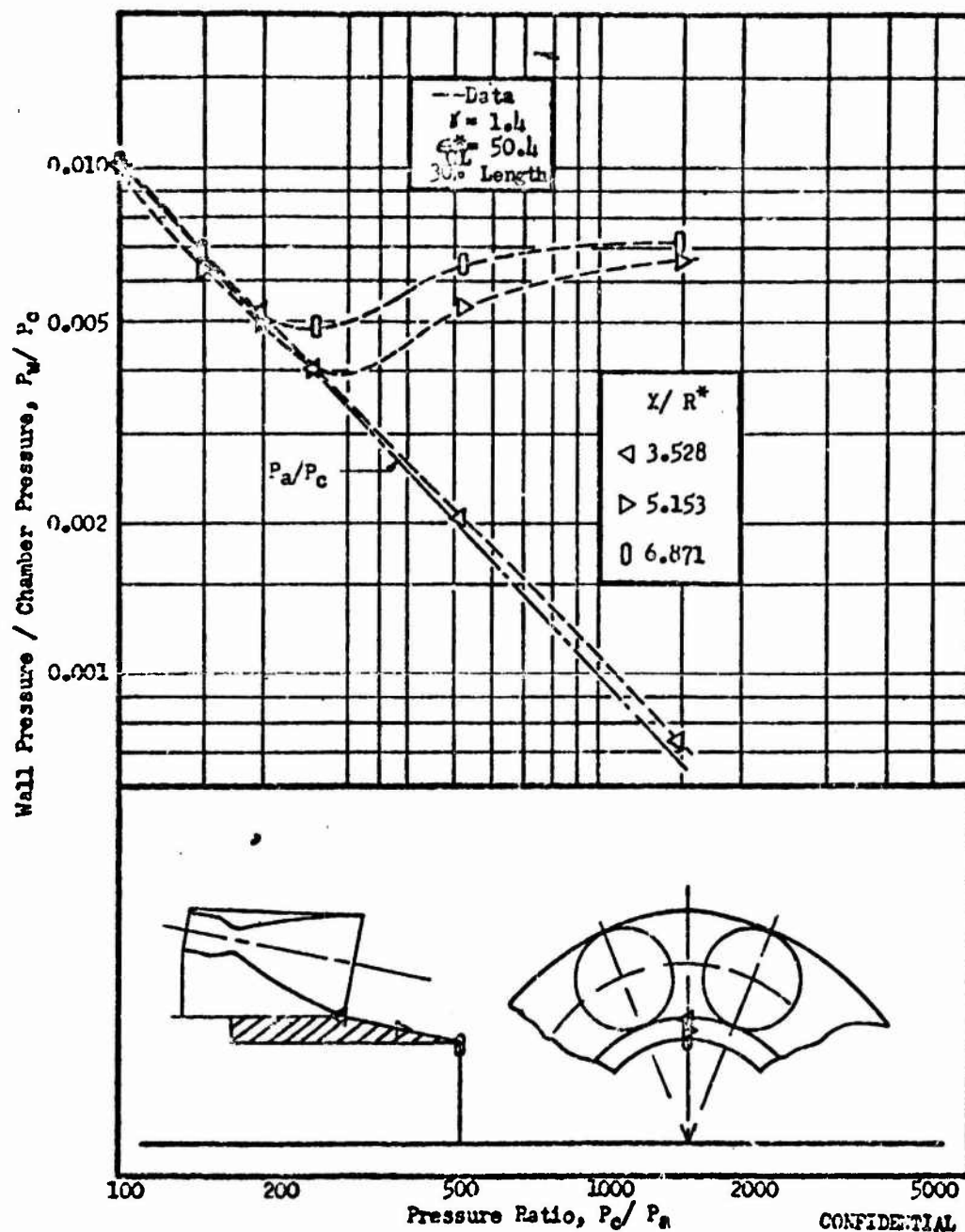
Figure 99. Module Centerline Wall Pressure vs Pressure Ratio, 6 Module Spaced Multichamber, 30-percent Length

167

Figure 100. Wall Pressure Between Modules vs Pressure Ratio, 8 Modules Spaced Multichamber, 30 Percent Length

168
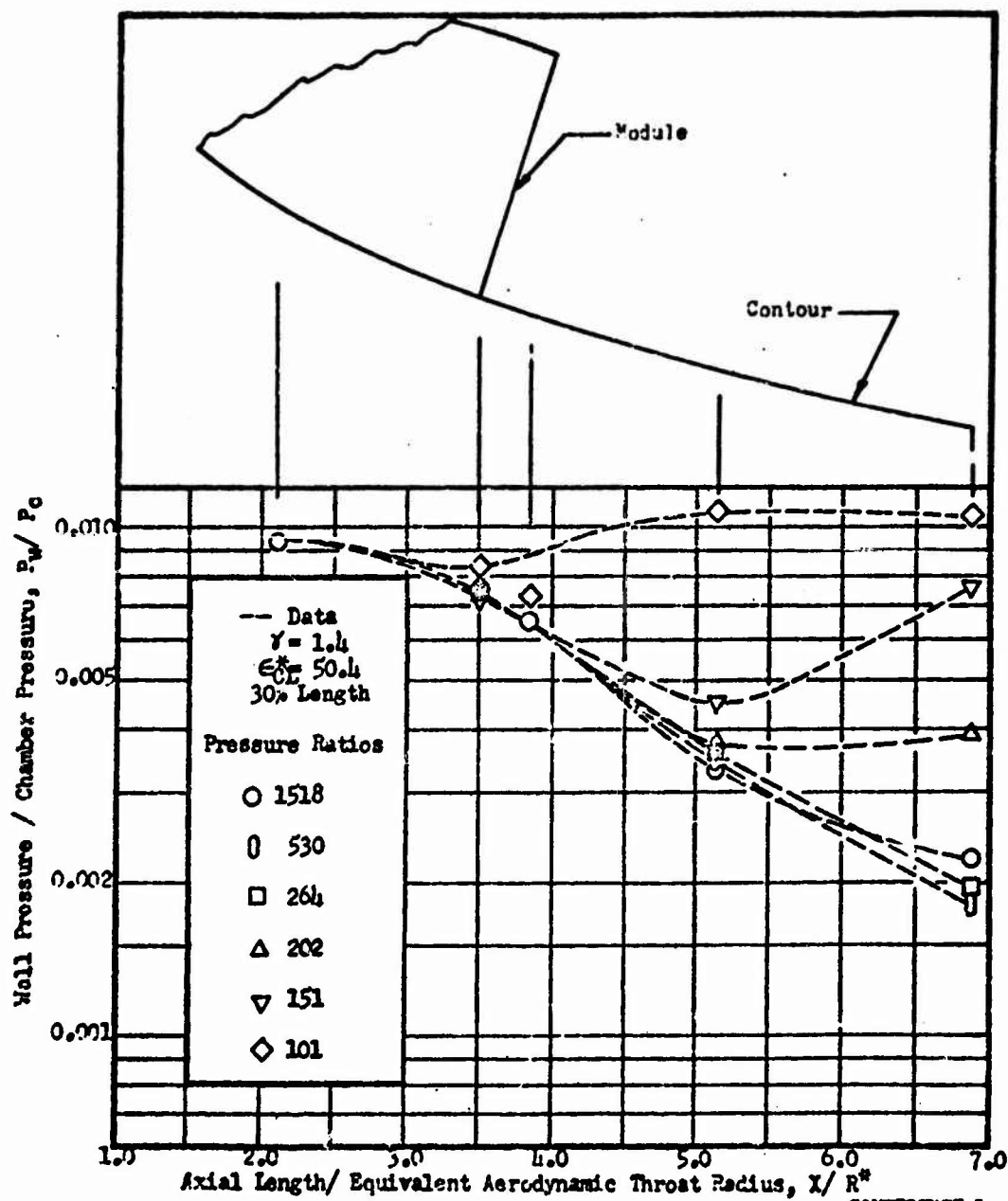
Figure101. Module Centerline Wall Pressure vs Axial Distance,
8 Modules Spaced Multichamber, 30 percent Length
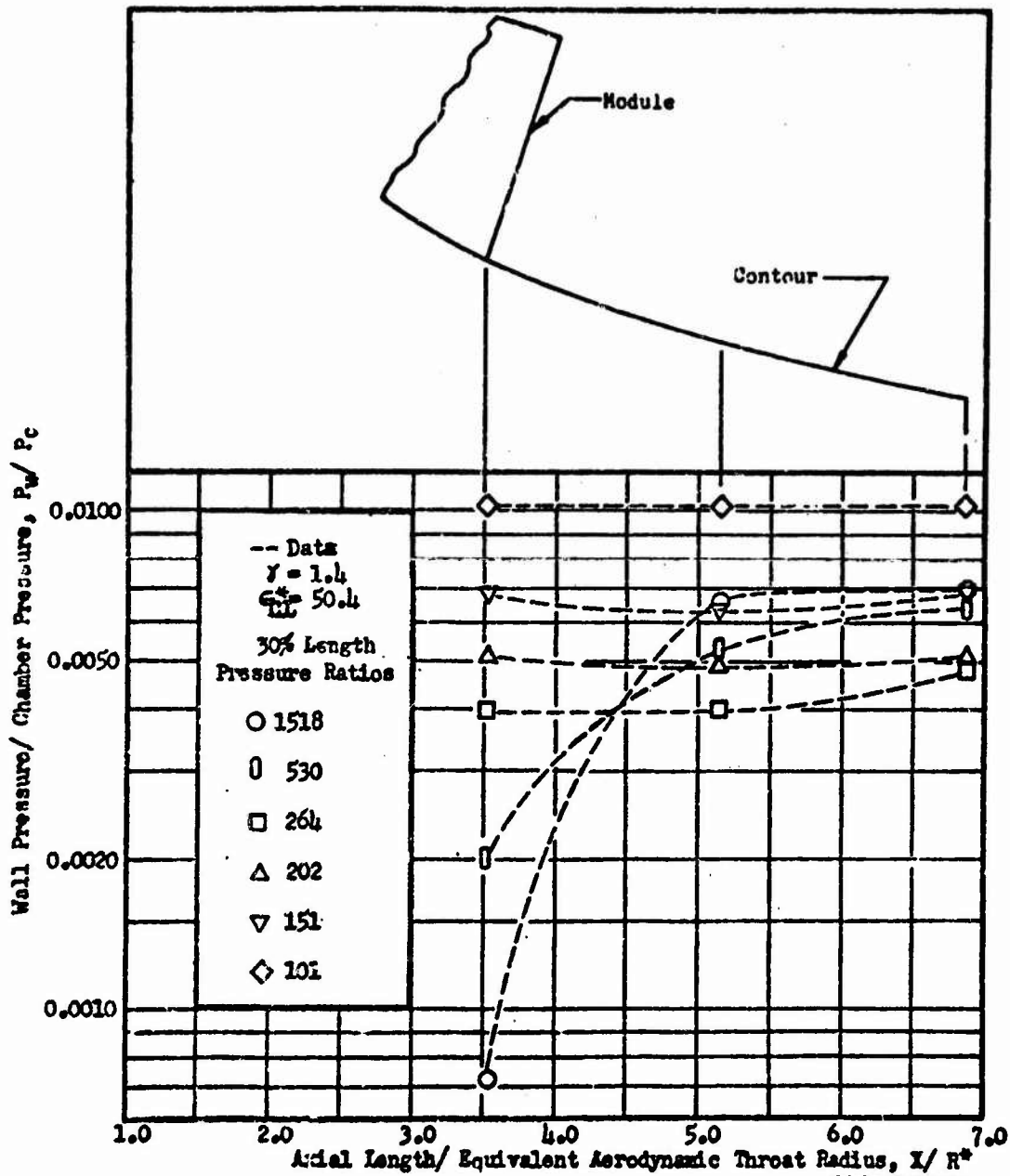
Figure 102. Wall Pressure Profile Between Modules vs Axial Distance,
2 Module Spaced Multichamber, 30 Percent Length

Sixteen Module Multichamber

(C)   The final multichamber model tested was model III-12, the 16 touching modules with the centerbody spike extension. Performance for this model is shown in Fig.103 . The highest performance attained with no base or intermodule bleed (See Fig. 103) was 96.7 percent at a pressure ratio of 1200. The base flow transition point from closed to open-wake occurred at a pressure ratio of 370, (See also base pressure curve Fig. 104).

(C)   As shown by Fig. 103 and 105 , no performance gains were noted with any of the intermodule bleed rates used.

(C)   At design pressure ratio (1200) and the transition point, performance increases were obtained at 0.7 percent base bleed. Due to the fact that this model was designed with 16 modules, the primary flow more closely approximates an annular nozzle, the shocks are weaker and the spaces between the modules are smaller. All these factors tend to reduce the momentum thickness and therefore the bleed performance curves, Fig. 105 , more closely approximate the annular nozzle case.

(C)   The pressure profile curves, Fig. 106 , 107, 108 and 109 are similar to those for the 8 module chambers.

(C)   In an attempt to improve the intersegmental pressures a filler plate was placed in the exit plane of the modules to help keep up the intersegmental pressures (Fig. 81). The performance results of this are shown in Fig. 110. At the high pressure ratio end, P_o/P_a = 1300, the performance with no intersegmental bleed was 96.6 percent as opposed to 96.7 percent for the no filler plate model. Since this is within the accuracy of the data scatter, essentially no performance
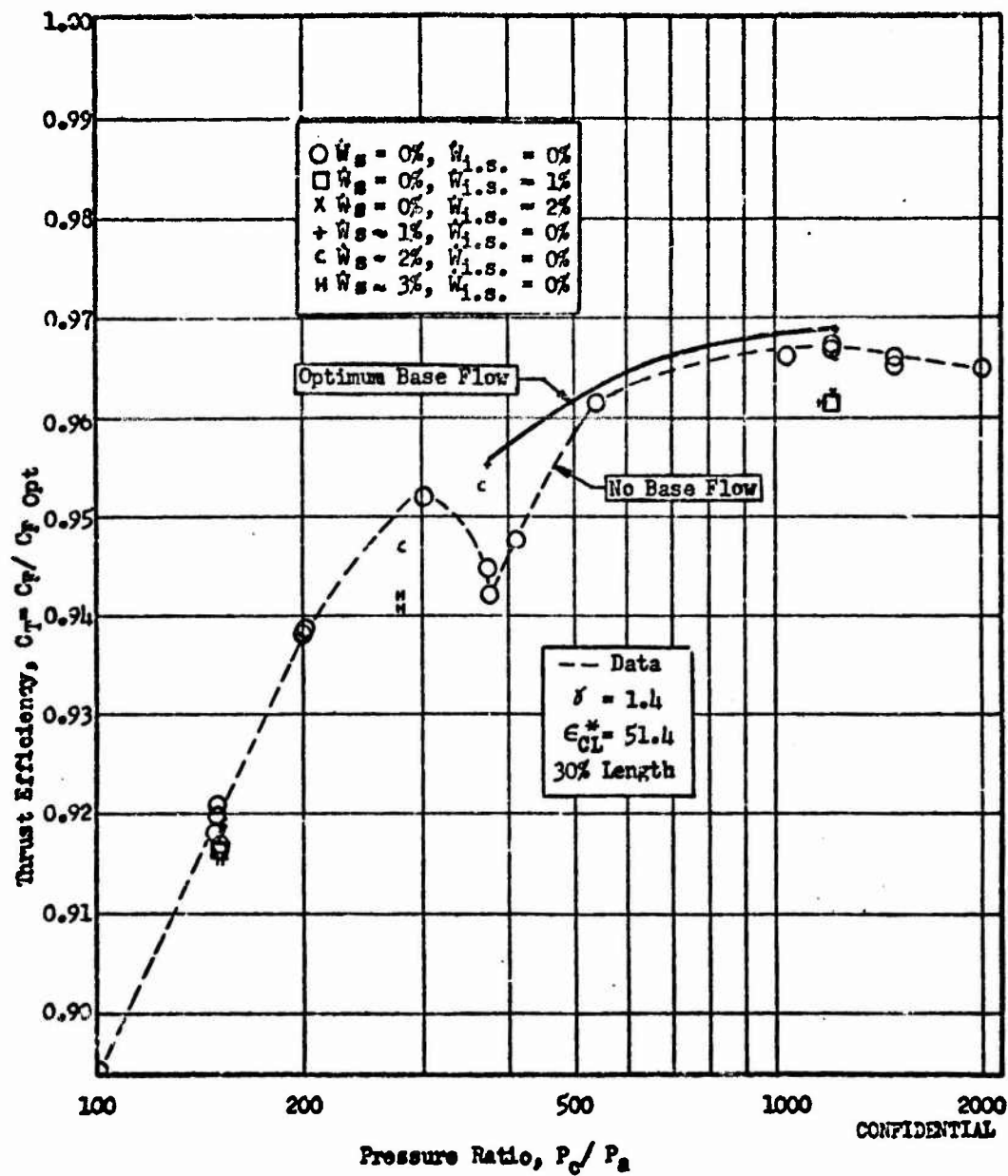
Figure 103. Thrust Efficiency vs Pressure Ratio,
16 Module Multichamber, 30 percent Length

172
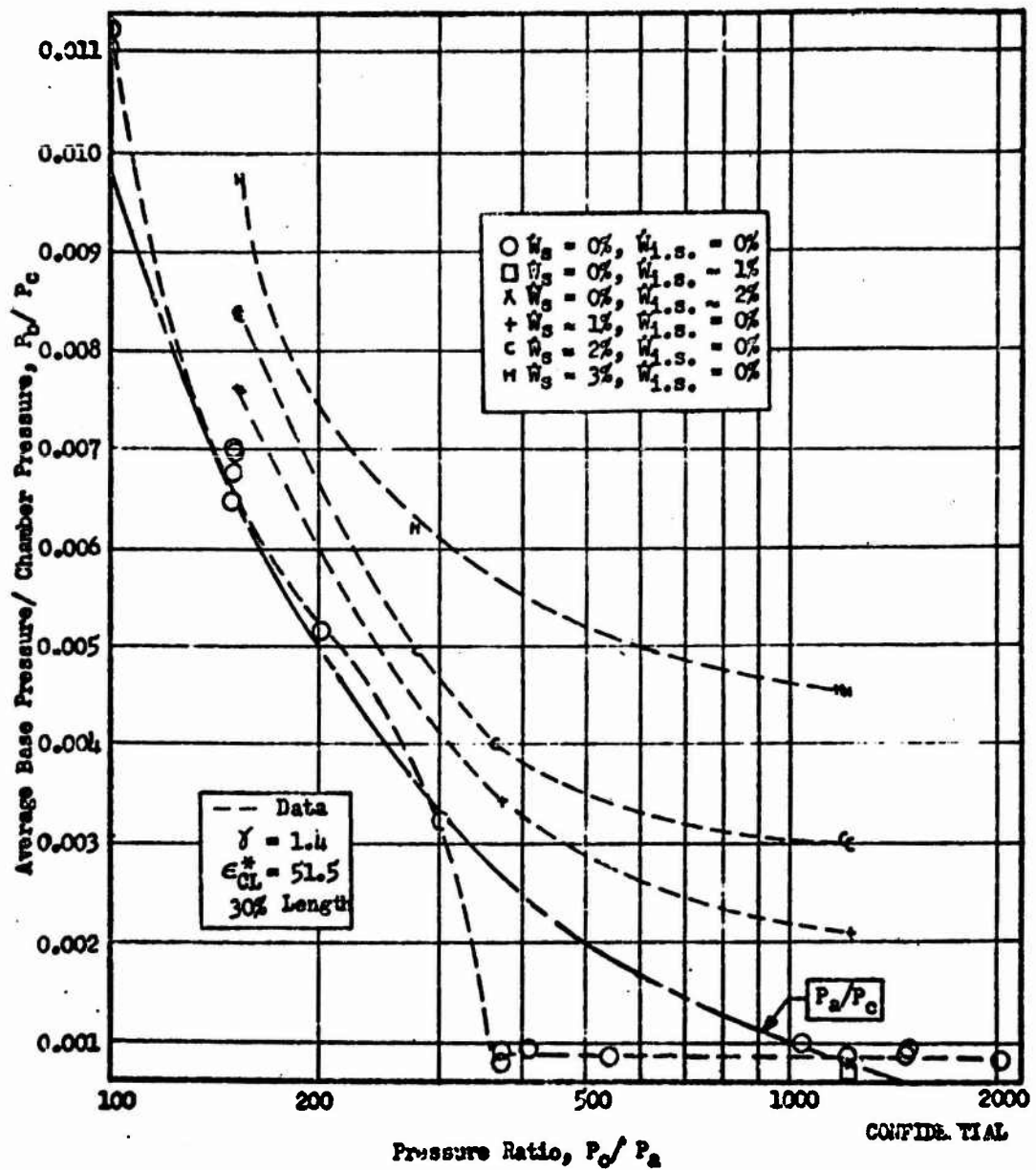
Figure 104. Base Pressure vs Pressure Ratio,
16 Module Multichamber, 30 percent Length
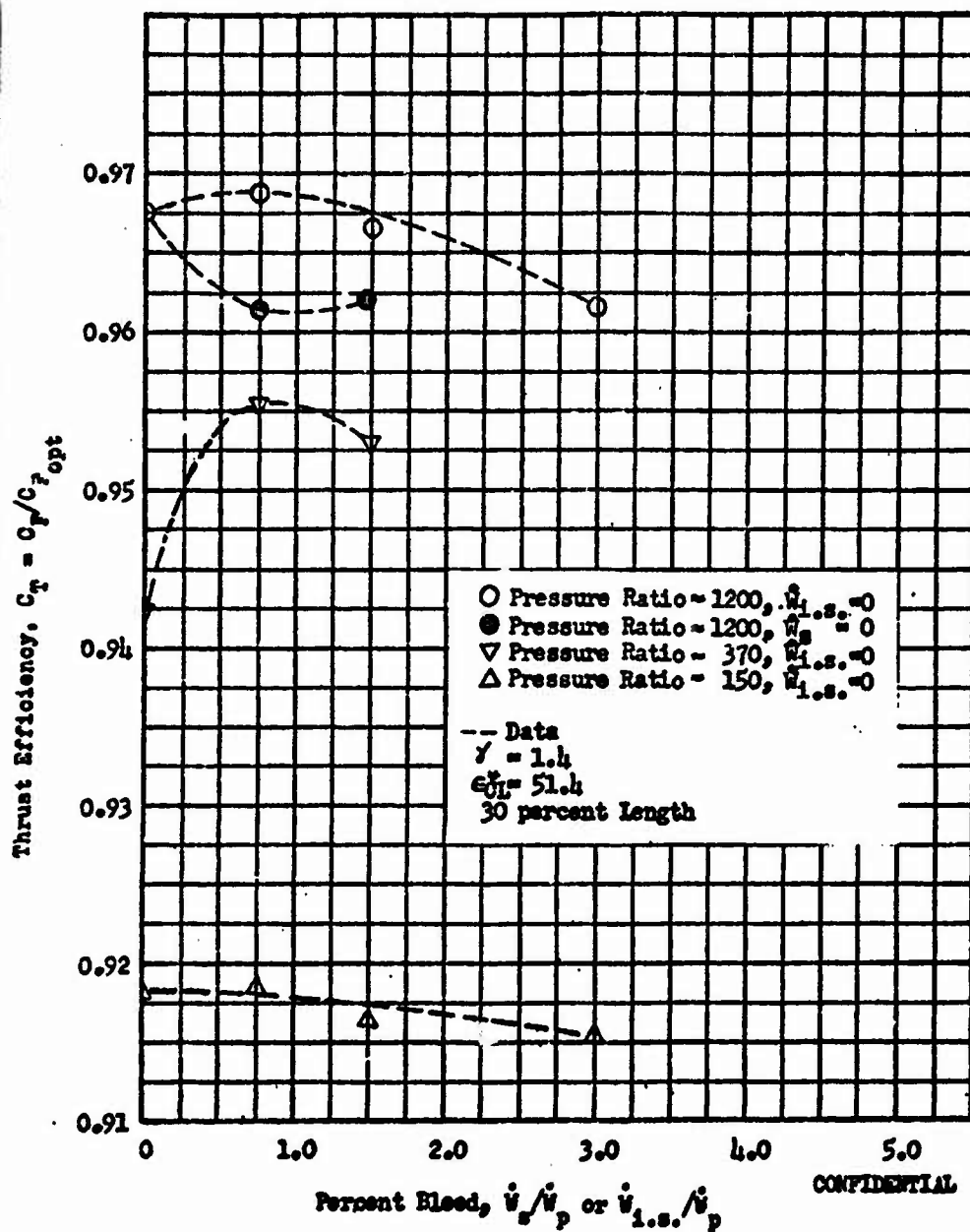
Figure 105. Thrust Efficiency vs Percent Bleed,
16 Module Multichamber, 30 percent Length
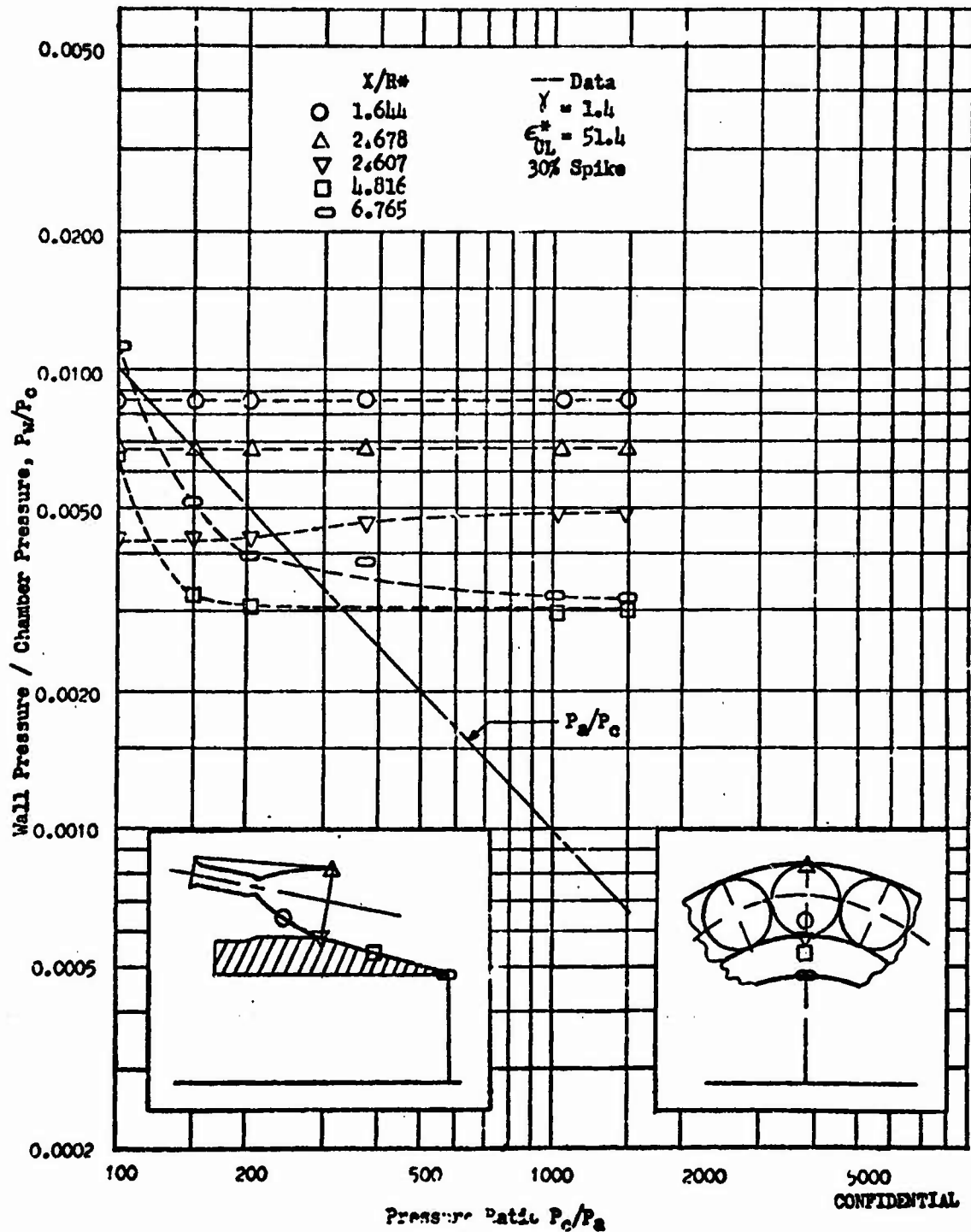
Figure 105. Module Centerline Wall Pressure vs Pressure Ratio, 16 Module Multichamber 30 percent Length
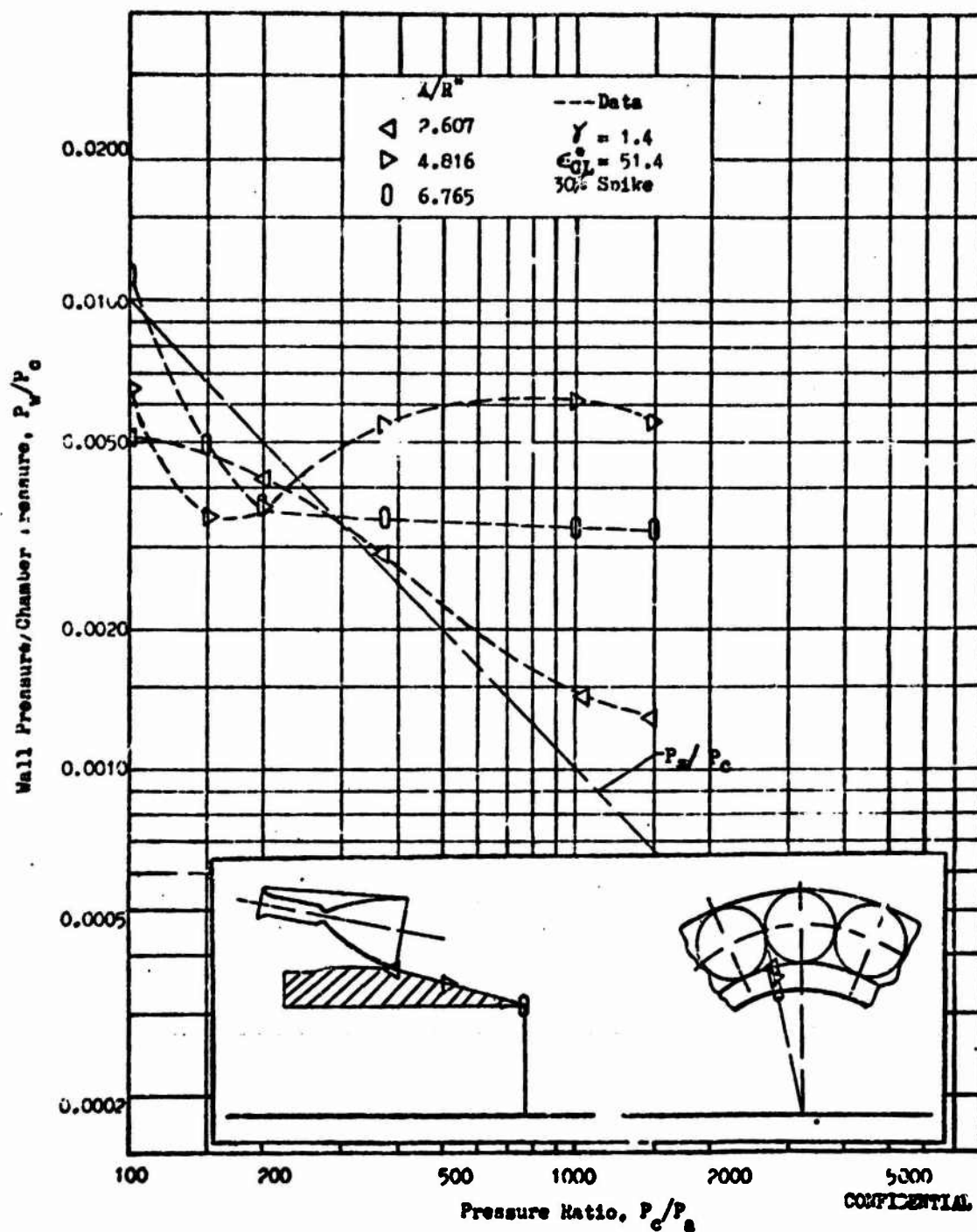
Figure 107. Wall Pressure Between Modules vs Pressure Ratio,
16 Module Multichamber, 30 Percent Length

176
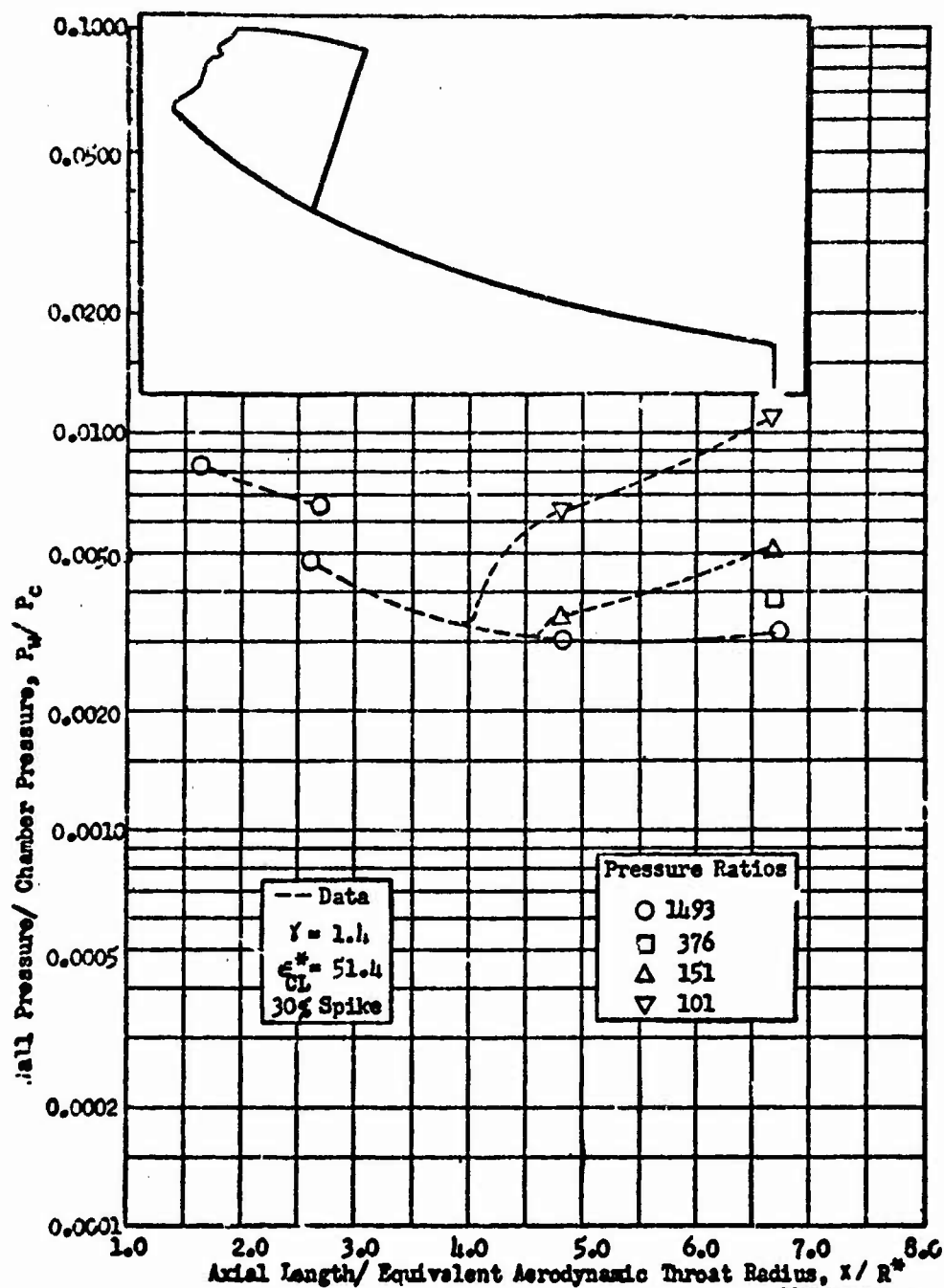
Figure 108. Module Centerline Wall Pressure vs Axial Length, 16 Module Multichamber, 30 percent Length
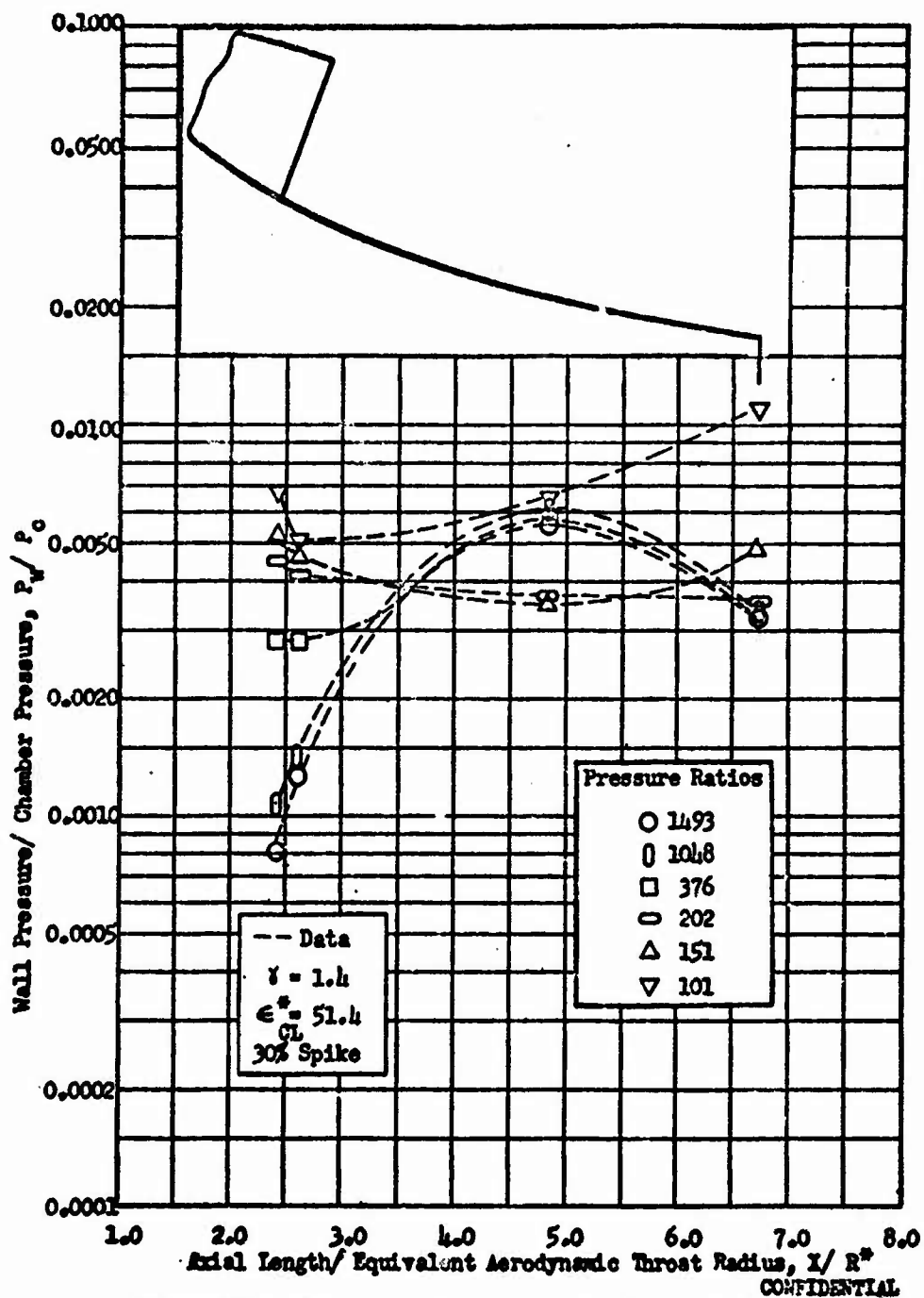
Figure 103. Wall Pressure Between Modules vs Axial Length, 16 Module Multichamber, 30 Percent Length
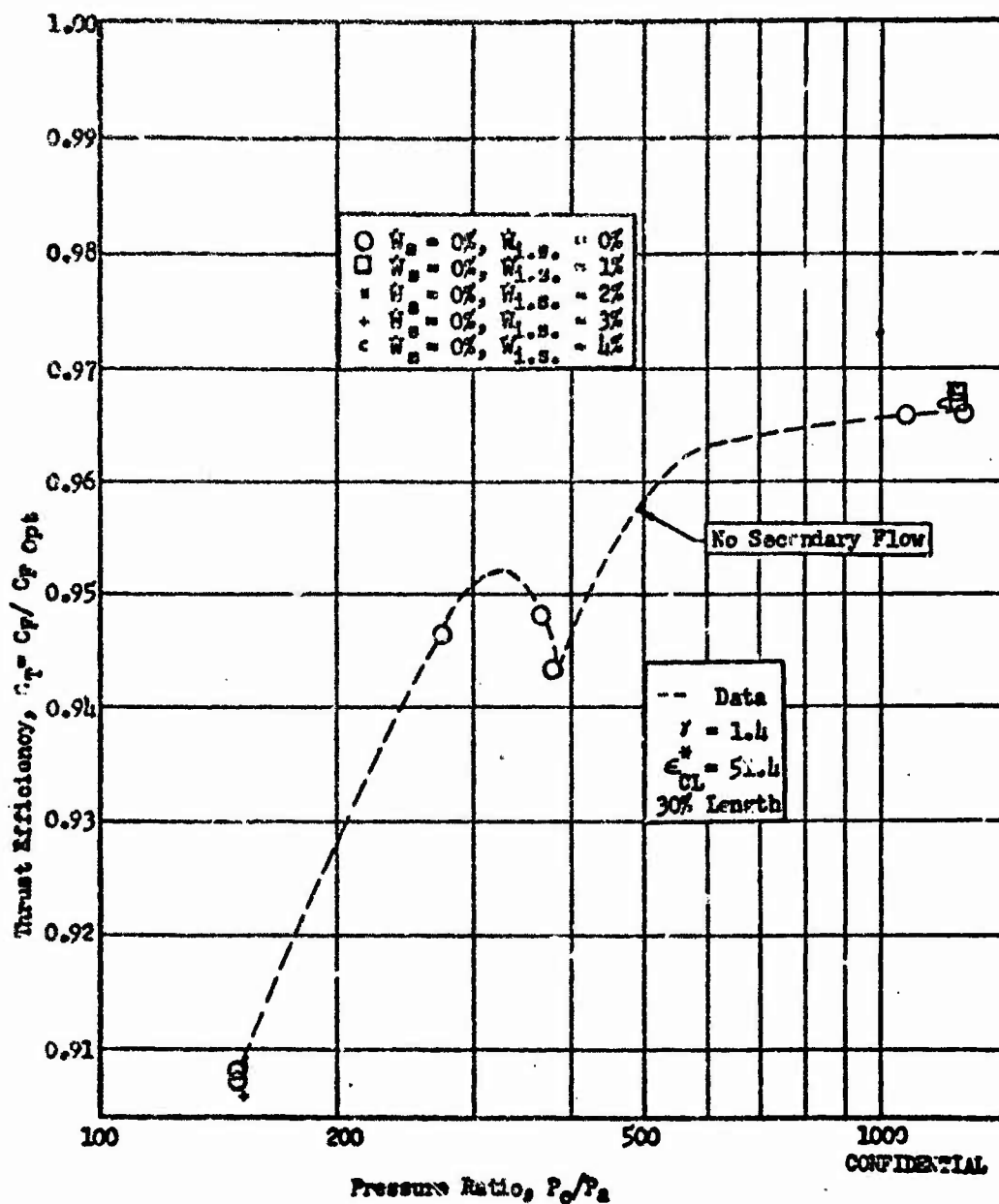
Figure 110. Thrust Efficiency vs Pressure Ratio, 16 Module Multichamber with Intersegmental Filler Plate

179

change resulted by addition of the filler plate. One factor here was that there was no actual seal between the filler plate and the modules and ambient could still bleed into the spaces behind the modules. Performance improved about 0.2 percent with the introduction of 1-2 percent intersegmental bleed, as compared to a decrease of approximately 0.5 percent for the same model without the filler plates. Use of intersegmental bleed at a pressure ratio of 150 resulted in a slight decrease in performance. The combined use of intersegmental and base bleed resulted in approximately 0.5 percent decrease in efficiency at both low (150) and high (250) pressure ratios. Base pressures for this model are shown in Fig. 111. While intersegmental bleed at high pressure ratio had no effect on centerbody base pressure for the model without the filler plate (Fig. 104), it significantly increased base pressure for the model with the filler plate. The performance curve dip point occurs at about the same place in both configurations but at low pressure ratios (150) there is a loss in efficiency of over 1 percent for the nozzle with the filler plate. The reason is that flow behind the modules is restricted resulting in lower intersegmental pressures.

DISCUSSION OF RESULTS

ε = 25 Models

(C) The test results show the following characteristics for this nozzle:

    1. Good performance can be attained with this nozzle over a pressure ratio range from sea level to design altitude with the proper base bleed and base configuration.
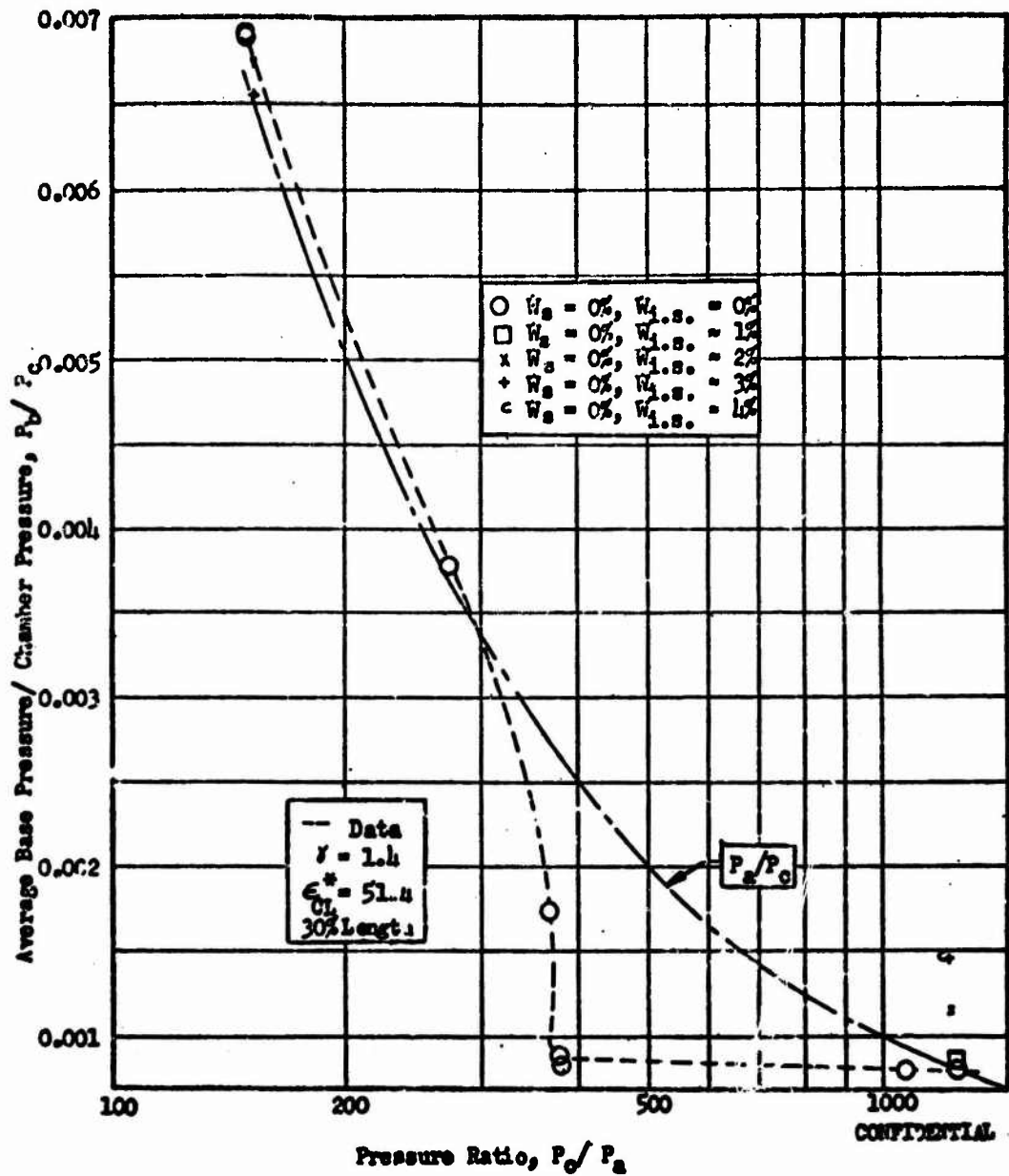
Figure 111. Base Pressure vs Pressure Ratio, 16 Module Multichamber with Intersegmental Filler Plate

2. The best performing base configurations were the open cavity, the radially-outward base, and the porous-plate base.

3. Supersonic injection into the base causes a loss in performance.

4. Optimum secondary flowrate is between 2 and 2.5 percent of primary flow over the test range for this nozzle.

5. Theoretical computations of the effect of secondary flow on base pressure agreed well with the data.

6. Base pressures were higher for CF_4 than for air. Based on these results, hot firing base pressure predictions for zero secondary flow would be higher than the air. Correlation of the data with hot-firing data will be conducted later in the program.

(C) A summary of the performance for the $\epsilon_o = 25$ nozzle is given in Table 6. The performance is based on values achieved at design pressure ratio with zero and the optimum value of secondary flow. Secondary flow for the porous plate was limited to 0.6 percent due to flow restrictions in the plate and pressure restrictions in the base cavity.

$\epsilon = 50$ Annular Models

(C) The $\epsilon = 50$ group of models was tested primarily for the purpose of evaluating different combustor configurations. For the purpose of comparison a point expansion truncated ideal spike was tested as the reference for all of the $\epsilon = 50$ models. Figure 112 shows the performance of this nozzle to be the highest of all models tested at all

TABLE 6

SUMMARY PERFORMANCE OF ϵ_e = 25 NOZZLE

Nozzle	[1] Pressure Ratio P_c/P_a	[2] Base Flow Percent W_s/W_p	Performance $C_{F_{measured}}/C_{F_{opt}}$	Base Pressure P_b/P_e
ϵ_o = 25, Air Open Base	540 540	0 2.0	96.5 97.6	.0060 .0105
ϵ_o = 25, Air Radially-Out Base	540	1.7	97.4	.0010
ϵ_o = 25, Air Radially-In Base	540	1.7	97.1	.0093
ϵ_o = 25, Air ϵ_o = 3.5 Base Nozzle	540	2.3 2.3	95.9 95.9	.0053 .0050
ϵ_o = 25, Air ϵ_o = 15 Base Nozzle	540	0.6	96.9	-
ϵ_o = 25, Air Porous Plate Base	290 280	0 1.7	95.6 96.8	.0067 .0108
ϵ_o = 25, CF_4 Open Base				

1. Design pressure ratio
2. Approximately optimum base bleed for all configurations except the porous plate
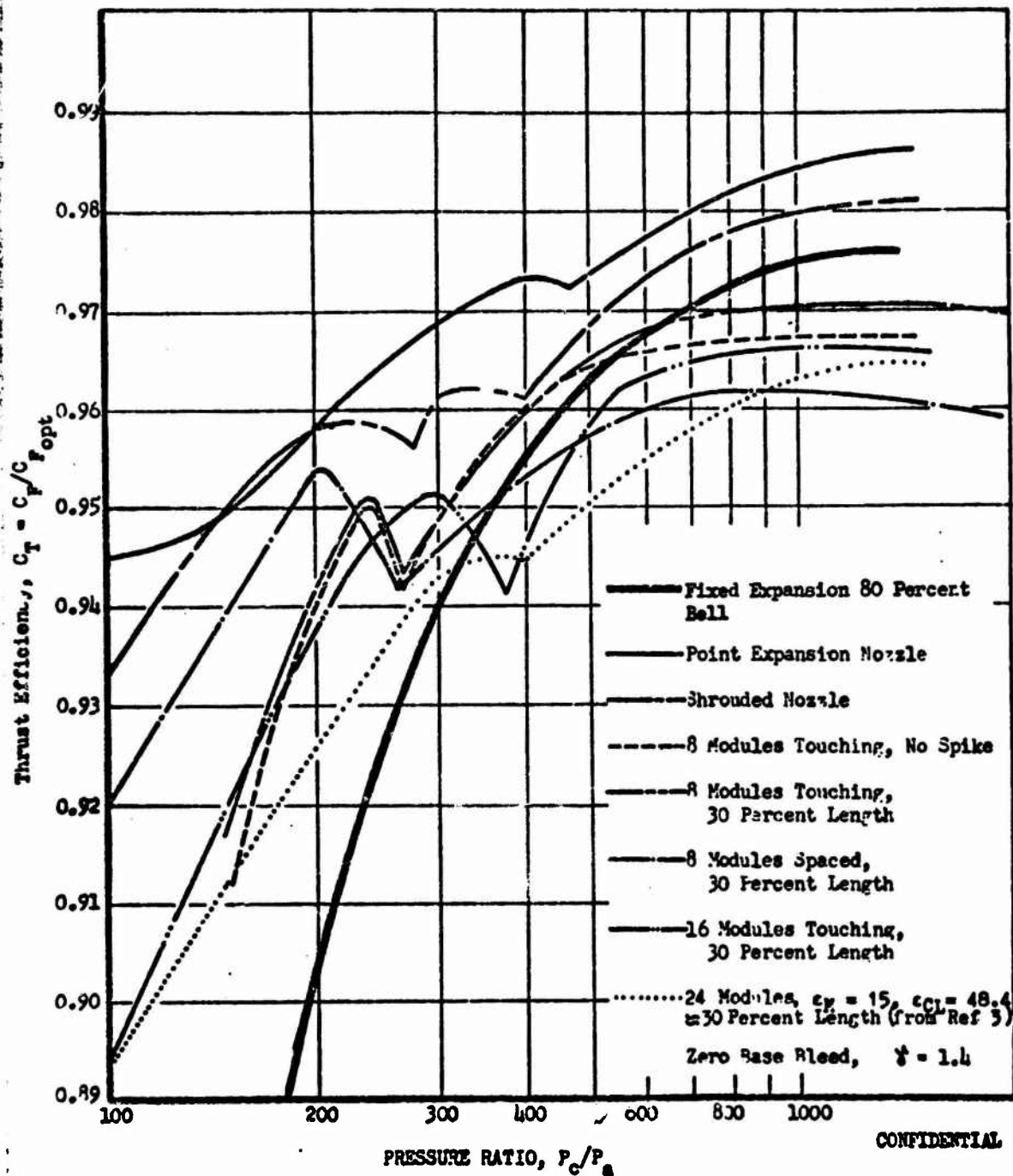
Figure 112. Comparison of Experimental Performance of $\epsilon_{CL} = 50$ Annular and Multichamber Nozzles

Legend:

—— Fixed Expansion 80 Percent Bell

—— Point Expansion Nozzle

—·— Shrouded Nozzle

——— 8 Modules Touching, No Spike

——·— 8 Modules Touching, 30 Percent Length

—— 8 Modules Spaced, 30 Percent Length

—— 16 Modules Touching, 30 Percent Length

········· 24 Modules, $\epsilon_N = 15$, $\epsilon_{CL} = 48.4$ ≈30 Percent Length (from Ref 3)

Zero Base Bleed, $\gamma = 1.4$

Thrust Efficiency, $C_T = C_F/C_{F_{opt}}$

PRESSURE RATIO, P_c/P_a

pressure ratios. This is the usual case when testing with a non-reacting gas since chemical kinetics are not involved and ideal potential flow is the sole contribution to primary performance. However, when hot reacting gases are considered as the propellant, the chemical kinetics of the gases play a significant role in primary performance. As previously explained the shrouded spike nozzle was tested as a representative design for a hot gas nozzle. The air tests do not reveal any chemical kinetic performance benefits but only the difference in non-reacting gas performance between the nozzles. Figure 112 shows that for the particular shroud design selected the potential performance loss was approximately 0.5 percent from the reference model over the major portion of the operating range. Since the shrouded nozzle was designed, more recent experience and technology has shown that improved shrouded nozzle designs are possible. In most cases it is theoretically possible to reduce the shrouded nozzle potential flow loss to a very small value.

(C) Table 7 is a summary of performance and base pressure values for these nozzles. Referring to Table 7 and Fig 112 the following observations can be made concerning these two nozzles:

1. Performance is high for both nozzles with the point expansion nozzle having slightly over 0.5 percent greater performance throughout the pressure ratio range of 300 to 1500.

2. At very low pressure ratios the shrouded nozzle shows better altitude compensating characteristics and has performance equal to the point expansion model.

TABLE 7

SUMMARY PERFORMANCE OF ε = 50 NOZZLES

Nozzle	[1] Pressure Ratio P_c/P_a	[2] Base Flow Percent $\dot{W}_s/\dot{W}_p$	Performance $C_{V\,measured}/C_{V\,opt}$	Base Pressure P_b/P_c
$\epsilon_0 = 50$ point expansion	1450 1450	0 0.9	98.6 98.8	0.00. 0.0026
$\epsilon = 50$ shrouded	1475 1475	0 0.7	98.0 98.1	0.0006 0.0011
$\epsilon_{CL} = 50$ 8 modules touching no centerbody extension	1400 1400	0 0.7	96.7 96.7	0.0008 —
$\epsilon_{CL} = 50$ 8 modules touching spike centerbody	1400 1400	0 0.7	97.1 96.9	0.0008 —
$\epsilon_{CL} = 50$ 8 modules spaced spike centerbody	950 950	0 1.5	96.2 96.2	0.0009 —
$\epsilon_{CL} = 50$ 16 modules touching spike centerbody	1200 1200	0 0.7	96.7 96.9	0.0009 0.0021
$\epsilon_{CL} = 50$ 16 modules touching with filler plate spike centerbody	1300 1300	0 2.0 $(\dot{W}_{ic}/\dot{W}_p)$	96.6 96.8	0.0008 0.0013

1. Pressure ratio at which maximum efficiency occurs
2. Approximate optimum $\dot{W}_s$ $(\dot{W}_{ic} = 0)$ or $\dot{W}_{ic}$ $(\dot{W}_s = 0)$

3. Secondary flow improves performance by only a small amount for both nozzles. This is primarily because nozzle performance without secondary flow is already high.

4. From design pressure ratio down to the open wake transition point, the point expansion nozzle has about twice the base pressure as the shrouded nozzle (See Fig. 72 and 77). However, below the transition point the base pressure of the shrouded nozzle rises more rapidly than the base pressure of the point expansion nozzle. This accounts for the improved altitude compensating characteristics of the shrouded nozzle. Nevertheless, even though the compensation is better the shrouded nozzle only matches but never exceeds the performance of the point expansion model.

5. If chemical kinetics are considered and it can be shown that the shrouded nozzle has a higher I_{SP} (close to full shifting) performance for hot gases, then the shrouded nozzle could give the higher overall performance at all pressure ratios. The amount of chemical equilibrium achieved during expansion depends chiefly upon the propellants, mixture ratio, chamber pressure, thrust level, and shroud design.

ϵ= 50 Multichamber Models

(U) Three basic multichamber models were tested, the 8 touching, 8 spaced and 16 touching models (listed in Table 7). The 8 touching model had two basic configurations, i.e., zero centerbody length and a spike

centerbody extended to 30 percent length. Two configurations were tested for the 16 touching model; one with open spaces between the modules and one with a filler plate between modules.

(C) Of all the multichamber models, the 8 touching model had the highest performance in zero and extended centerbody lengths. Figure 112 shows that addition of the centerbody improved the performance of this model about 0.4 percent over the range of operation. Referring to the discussion of the test results on these two nozzles, the following comments can be made:

1. Performance for this model was in general 1-2 percent below that of the reference model (point expansion).

2. Addition of either base bleed or intersegmental bleed did not in general increase the performance of either configuration of this model.

3. No performance degradation was noted for one engine out at either design pressure ratio or at very low pressure ratios. This result is applicable to this configuration only. Other test results (Ref 3) indicate performance losses are obtained with engine out configurations.

(C) When the module area ratio of the 8 module multichamber was reduced to 20.7, spaces resulted between the nozzles. A comparison of the performance of the 8 spaced multichamber unit to the other models tested is made in Fig. 112. At high pressure ratios the performance of the 8 spaced model is lower than the other models. This can be attributed to: (1) a basically low module area ratio, and (2) shock losses in the primary flow field because of the spacing.

(C) At low pressure ratios the performance for this nozzle is higher than any of the other multichambers. The spacing is beneficial at pressure ratios below 240. Inspection of Appendix 3 shows that the intersegmental pressures are higher for the 8 spaced models than they are for the 8 touching model at low pressure ratios. This configuration had the lowest effective area ratio of the models tested. Peak efficiency occurred at a pressure ratio of 950 compared to 1200 to 1400 for the other models. When it is further noted that the basic module area ratio is low (thus module design pressure ratio is low) it is easy to see why this model has good performance at low pressure ratios.

(C) Figure 112 shows that the model with the 16 touching modules had a slightly lower performance level than the 8 chamber model. The wake closure point occurred at a somewhat higher pressure ratio and low pressure ratio compensation was about as good as the 8 modules touching models. Although increasing the number of modules is usually associated with increasing the performance, this was not so for the given ground rules for these multichambers. The ground rules were: (1) the cluster area ratio shall remain constant, and (2) for a given number of modules the modules shall touch. With these restrictions the module area ratio is fixed. Thus, the module area ratio for the 8 chamber touching model was 30.2 and for the 16 chamber was 20.7. This means that the basic primary flow field performance for the modules was greater for the 8 module unit than for the 16 module. Although the shock and intermodule pressure losses are less for the 8 module model this did not make up for the basically greater performance of the higher area ratio 8 module touching units. This infers that there is an optimum number of modules which will maximize the module performance-shock-intermodule pressure trade-off. An additional factor which may have

influenced the relative performance of these models is the spacing ratio, δ/D_e. The value of δ/D_e was 0.020 for the 16 chamber model compared to 0.012 for the 8 chamber model. This would tend to cause relatively higher transition losses for the 16 chamber model. However, data from Ref 12 indicates that this difference in δ/D_e should result in less than 0.1 percent difference in efficiency between the models.

(C) For comparison purposes a multichamber spike nozzle tested and reported in Ref 3 was included in Fig. 112 . This model consisted of 24 touching modules of area ratio 15 spaced around a spike centerbody. The cluster area ratio, ϵ_{CL}, was 48.4 and the overall length was approximately 30 percent of a 15 degree conical nozzle of the same area ratio. This model corresponds closely to the 16 chamber configuration tested in this program. Data from this reference appears to agree well with the 16 chamber data, particularly with respect to efficiencies ($\dot{W}_e = 0$) at design pressure ratio, the transition pressure ratio and low pressure ratio. The wake transition point pressure ratio is approximately 400 for the 24 chamber model compared to 370 for the 16 chamber model which is consistant with the general trend toward higher transition point pressure ratios as the continuous throat configuration is approached.

SECTION V

INVESTIGATION OF AEROSPIKE SEGMENT TESTING CONCEPT

(U) One of the advantages in the development of the annular combustion chamber of aerospike nozzles is the capability of testing full-scale but partial thrust segments rather than the full annular combustor. See Fig. 113.

(C) Experience and analysis have shown that segments can be developed at considerably lower cost and time than full annular or conventional combustors to achieve a given level of performance and reliability. Cost reduction with segment testing is characterized by the smaller hardware and associated smaller experimental facilities which lead to lower propellant costs, reduced size of support equipment, easier handling and transportation, and general lower manpower requirements. Development time is reduced because of higher test frequencies associated with units of lower thrust levels.

(C) The simultaneous development of combustion chamber segments and investigation of full annular engine performance can be achieved with modules equipped with splitter plates or solid surfaces placed at a given segment angle to contain the expanding flow of gases. A typical experimental test set-up for an aerospike module and splitter plates is shown in Fig. 114.

(C) To obtain full annular nozzle performance from segment tests it is necessary to duplicate the pressure profiles both on the primary expansion and base surfaces under conditions simulating the full annular nozzle operation. A cold flow test program was undertaken to investigate the difference in pressure profiles both on the

191
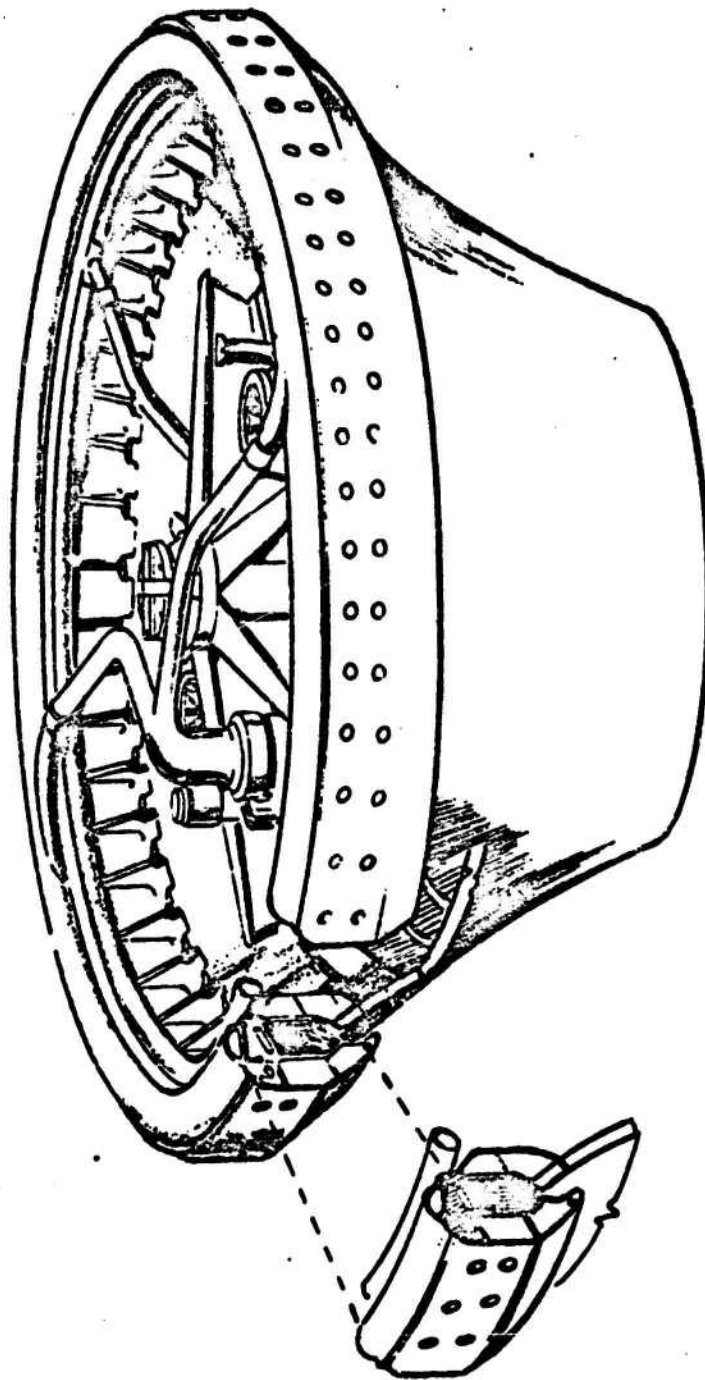
Figure 115. Aerospike Segment Testing Development Approach.
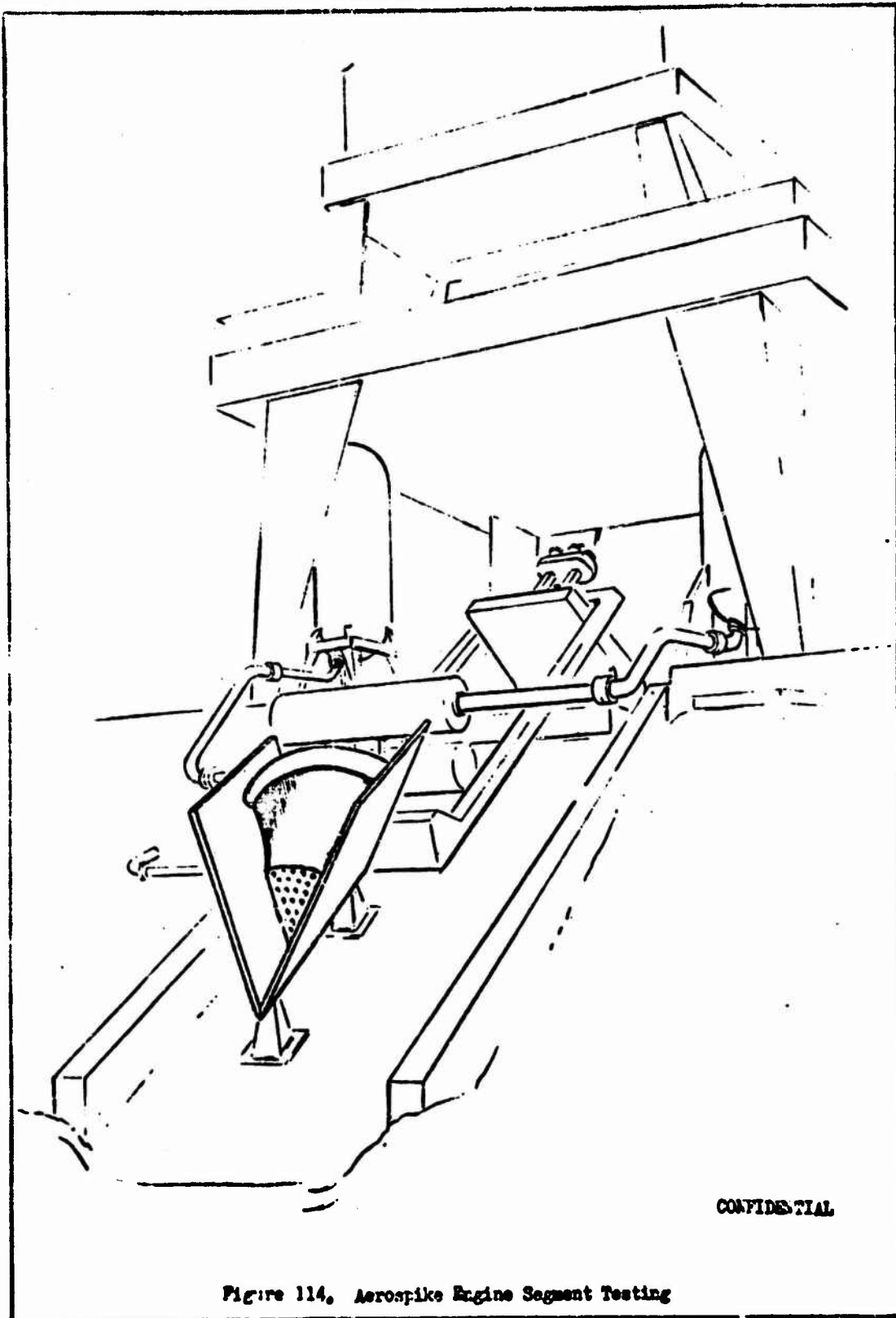
CONFIDENTIAL

Figure 114. Aerospike Engine Segment Testing

primary expansion surface and base between nozzle segments and a full annular aerospike nozzle. The test program objectives were as follows:

1) Obtain pressure distributions on the primary expansion surface

2) Determine the effect of segment sector angle on base pressure for open and closed wake conditions, with and without secondary flow.

DESCRIPTION OF COLD FLOW TEST PROGRAM

(U)   A full annular aerospike nozzle model was fitted with two splitter plates as shown in Fig.115, and tested with air in the Rocket Nozzle Test Facility. The nozzle had an area ratio of 44:1 and an axial length equal to 20 percent of the length of a 15 degree conical nozzle of equivalent area ratio. The model was tested at a nominal stagnation pressure of 200 psia at pressure ratios of 120 and 1200 (corresponding to open and closed wake conditions), both without secondary bleed and with a ratio of secondary to primary flow of approximately .85 percent. Secondary injection was achieved through radial-out orifices located in the base cavity. For all of the above test parameters the included angle between splitter plates was set at 45, 90, and 180 degrees. With the splitter plates in the 45 and 90 degree positions, only that portion of the nozzle throat between the splitter plates was left open, the remainder of the throat was sealed to prevent flow. For the splitter plates in the 180 degree position, one series of tests was made with half the throat sealed off, another with full open throat, i.e., flow on both sides of the splitter plates. See Fig. 116 for arrangement of splitter plates on the aerospike model. In

194
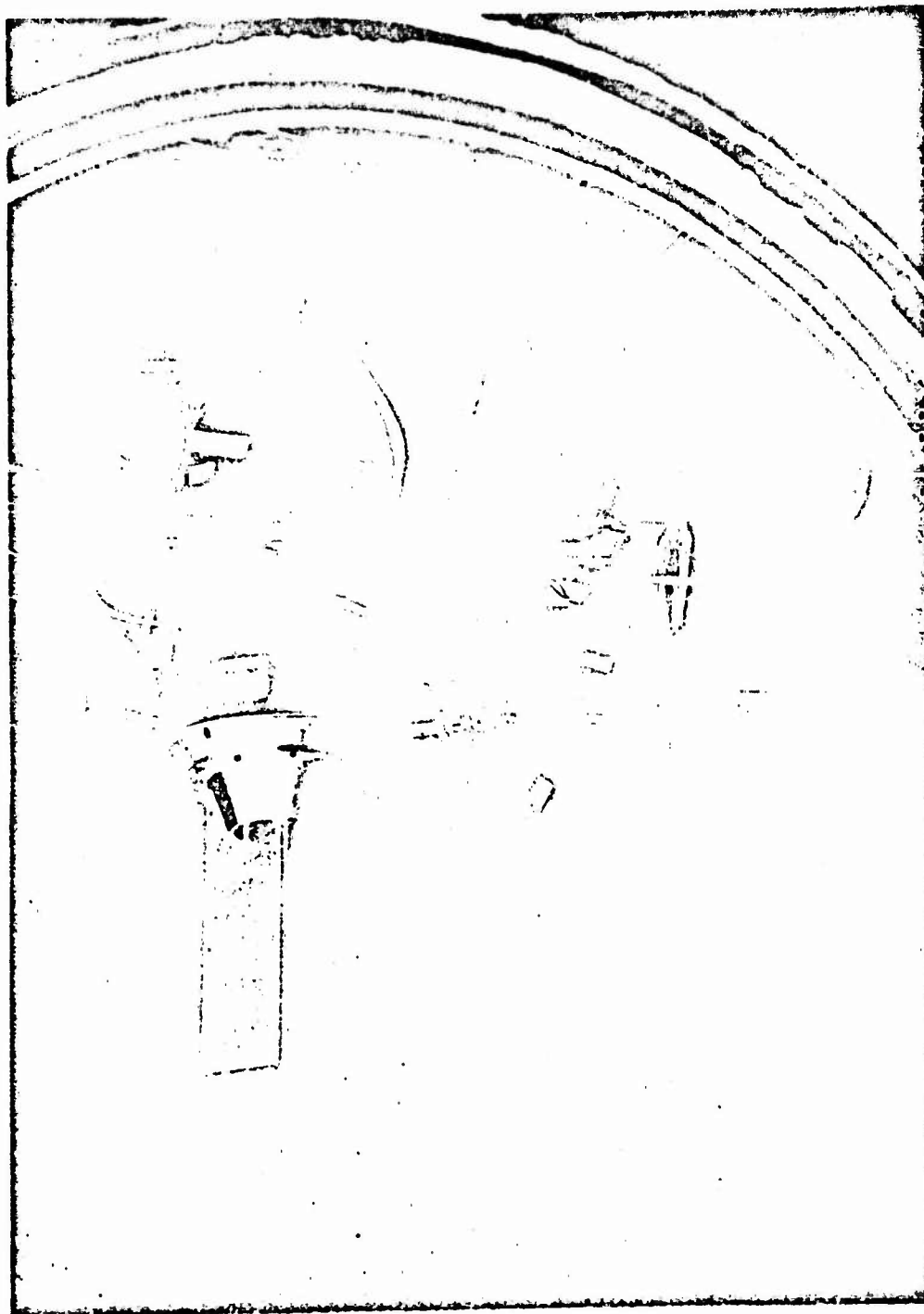
Figure 115. RNTF Installation of Aerospike Nozzle ($\epsilon = 441$, 20 percent length) with Splitter Plates

195

Figure 116. Instrumentation Drawing, Separation Plates, Annular Model

addition to the above tests, the full annular nozzle without splitter plates was tested for reference purposes. During all tests pressure profile measurements were taken along the primary expansion surface and in a radial direction on the base surface. A summary of tests and the average (area weighted) measured base pressure is given in Appendix 5.

Discussion of Results

(C) 1) The wall pressure distribution along the primary expansion surface is given in Figs.117 and 118 for nozzle operating pressure ratios of 120 and 1200 respectively. The differences in wall pressure profiles between the reference model (no splitter plate) and the model with splitter plates is due to the non-axial symmetry of the flow field. One reason for the flow field distortion is the growth of a boundary layer along the splitter plate causing recompression in the supersonic flow. The consistency of the deviation with splitter plate angular variation can be attributed to the constant relation between one side of the splitter plate and the primary wall pressure taps as shown on Fig. 116.

(C) Despite the influence of the splitter plates on the wall pressures, the net effect on nozzle axial force is small because the pressure deviations are small and occur in a region of the nozzle where the wall angles with respect to the axis are relatively shallow.

(C) 2) The variation of base pressure with splitter plate angle is shown on Figs.119 and 120 for nozzle pressure ratios of 120 and 1200 respectively. In general, the curves indicate that the segment base pressures approach the full annular nozzle base pressures for low and high segment angles, with maximum deviation for a 90 degree
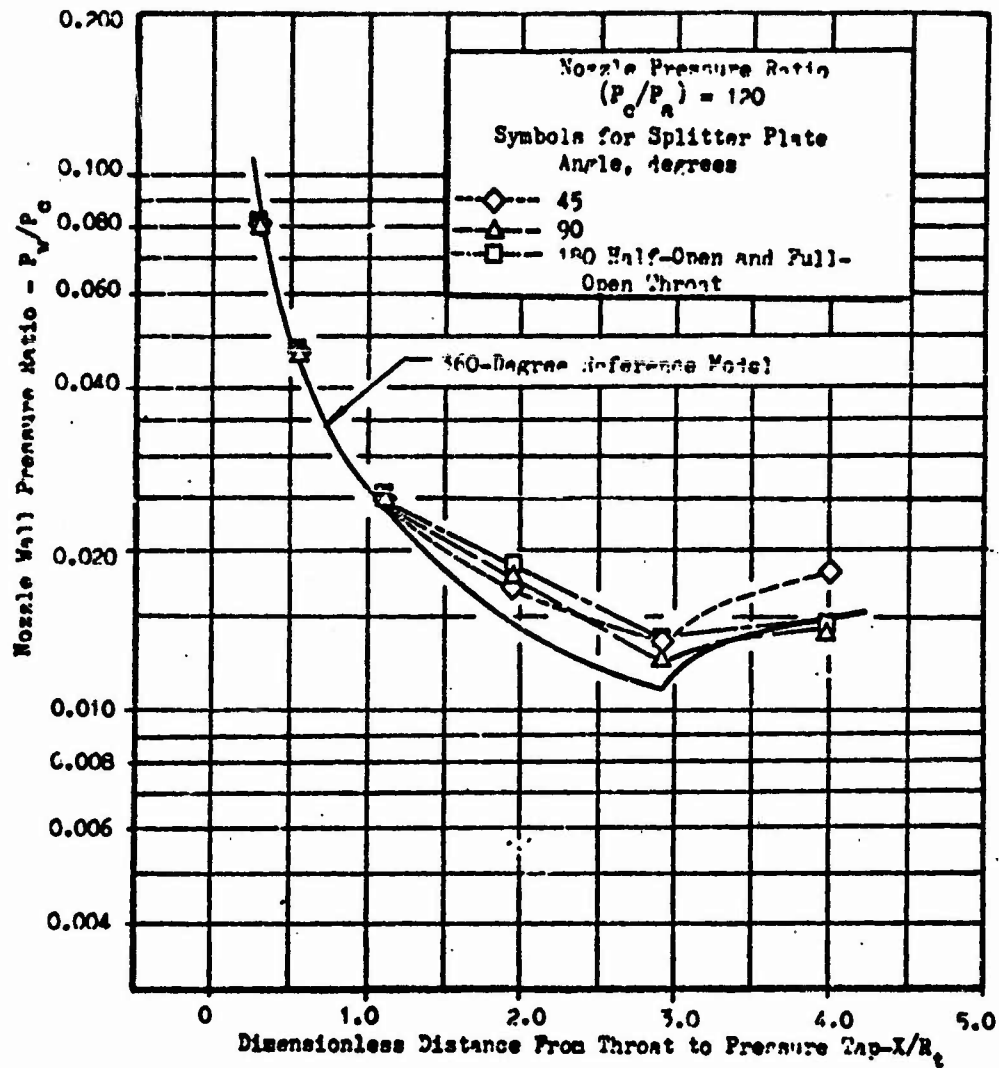
Figure 117. Primary Wall Pressure Profile, $P_c/P_a = 120$
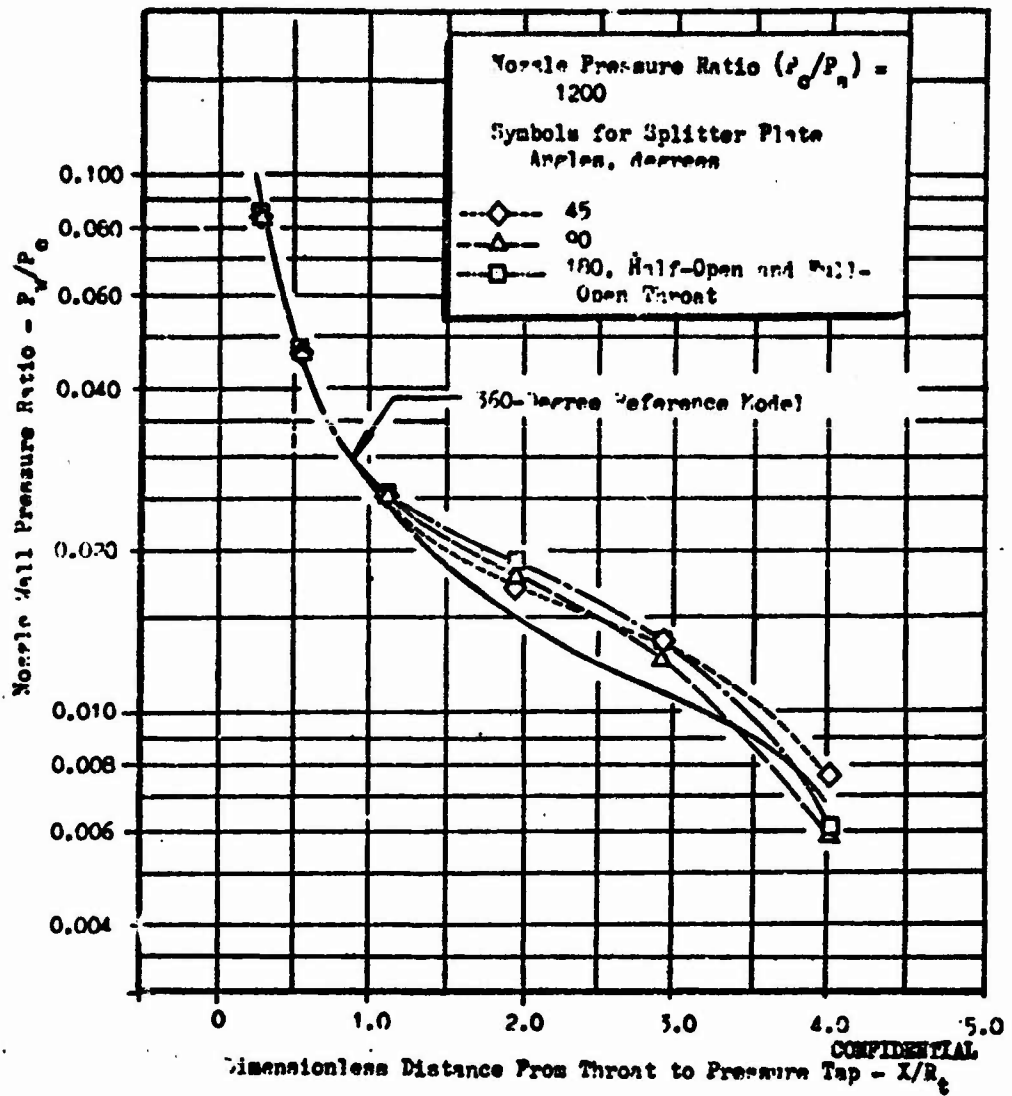
Figure 118. Primary Wall Pressure Profile, P_o/P_a = 1200

199
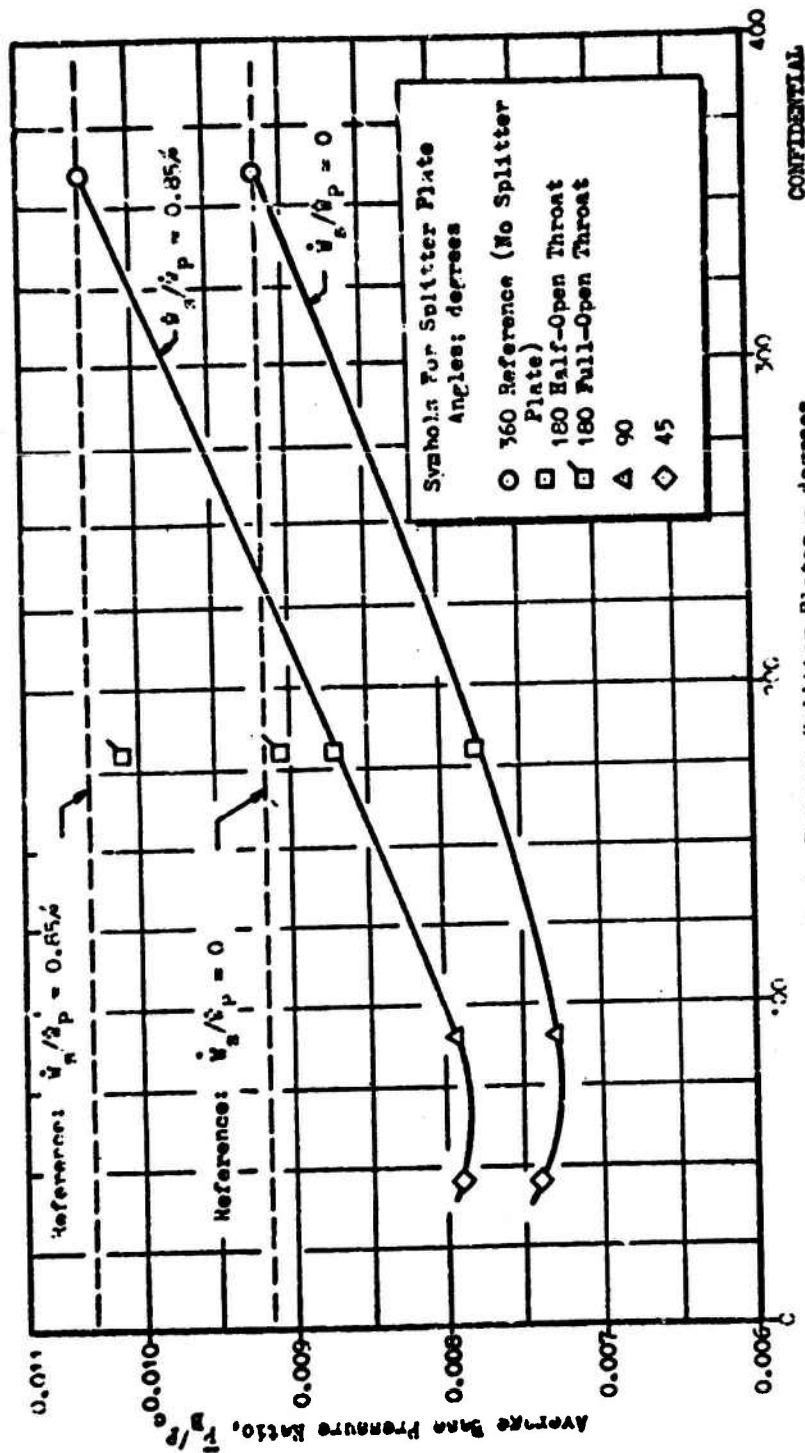
Figure 119. Average Base Pressure vs Splitter Plate Angle, Pressure Ratio $(P_c/P_a) = 120$
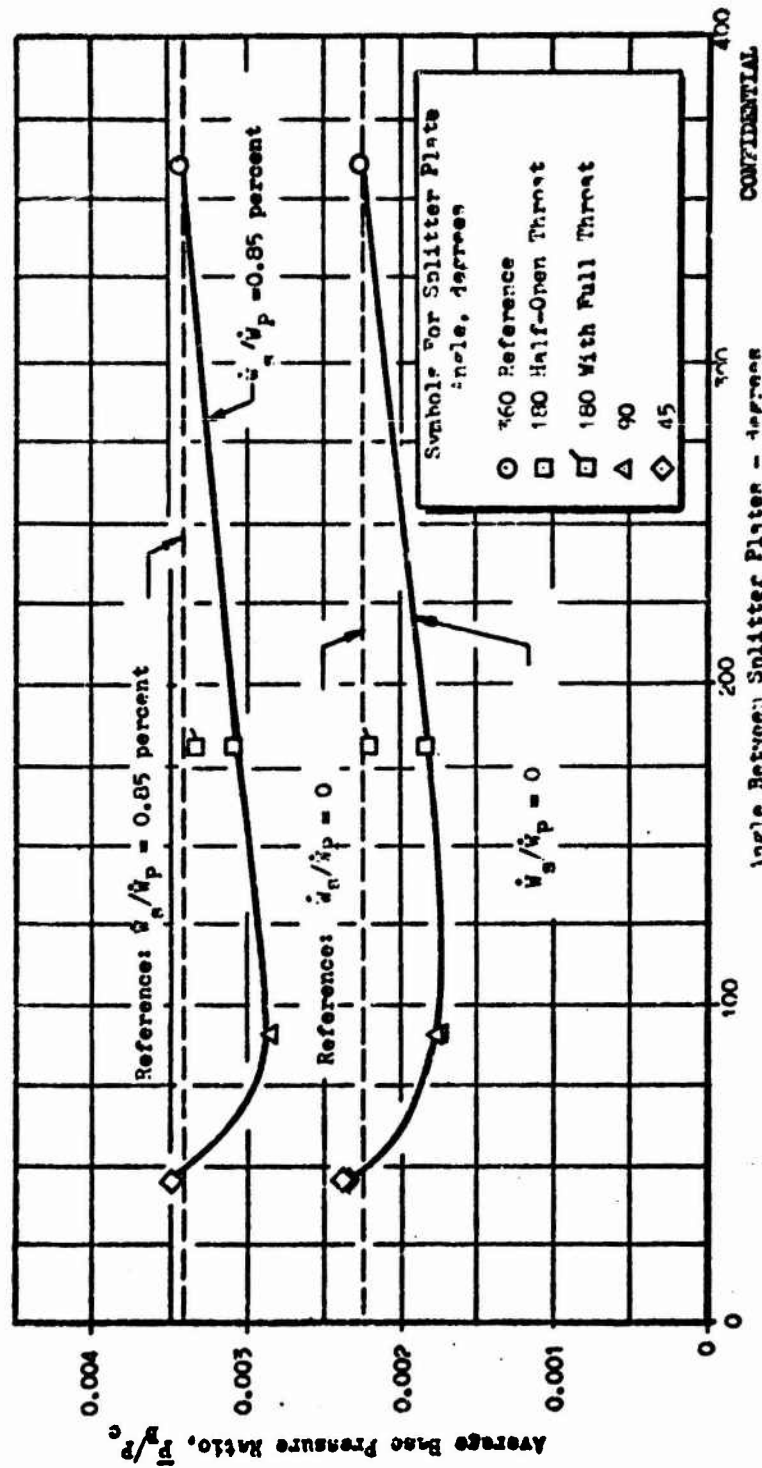
Figure 120. Average Base Pressure vs. Splitter Plate Angle Pressure Ratio $(P_o/P_1) = 4200$

segment angle. These trends are the same irrespective of nozzle pressure ratio and secondary bleed. For "locked-in" wake conditions (high pressure ratios), the full annular base pressure is duplicated with a 45 degree nozzle segment, whereas decreasing the nozzle pressure ratio results in a lower base pressure (25 to 30 percent) when compared to full annular nozzle base pressure.

(C) It is interesting to note that in the case of the 180 degree segment with flow on both sides of the splitter plates, the base pressure was increased to the reference level when the splitter plates were completely removed. This would indicate the possibility of either (1) pressure feedback at the end plane of the splitter plates, or (2) pressure leaks at the junction of the splitter plates and aerospike model. For this series (180 degree sector with flow on both sides) there was no sealing between the plates and the model. Additional testing would permit an experimental check of either hypothesis.

CONCLUSIONS AND RECOMMENDATIONS

(C) 1) For the particular aerospike nozzle model tested with air, full annular aerospike performance is attained with a 45 degree segment when operating at the "locked-in" base pressure condition.
2) When operating in the "open-wake" region, all nozzle segments had base pressure ratios lower than the full annular aerospike.
3) Further experiments are needed to study the performance influence of splitter plate length, fluid properties, and nozzle area ratio.

SECTION VI

ANALYTICAL AND DESIGN STUDIES OF AEROSPIKE COMBUSTORS

(C) Analytical design studies were performed to investigate various engine/
vehicle configurations incorporating the aerodynamic spike nozzle.
Combustor concepts that were considered included several types of
toroidal combustors and cylindrical combustors (multichambers) with
discrete circular throats and various shaped expansion sections.
Associated with the integration of the various combustor concepts into
vehicle systems, consideration was given to envelope requirements, nozzle
cooling, nozzle performance, engine weight, versatility, reliability,
cost, upper and lower stage, plumbing, turbomachinery, controls, and
methods of thrust vector control. The range of engine parameters
considered were

Chamber pressures from 300 to 3000 psia
Thrusts from 20,000 to 2,000,000 pounds
Expansion area ratios up to 150
N_2O_4/UDMH-N_2H_4 (50-50) Propellants

SUMMARY

(C) Ideally the objective of these studies was to determine which type of
combustor could be utilized most effectively with an aerodynamic spike
nozzle at a particular operating point in the parameter range of
interest. The normal criteria for selection of a particular combustor
would include detailed consideration of engine performance, engine
weight, nozzle cooling, turbomachinery, design complexity, fabrication
technique and cost, development time and costs, engine reliability and
overall cost effectiveness. The scope of this study was such that
only a few of the aforementioned items could be treated in any detail.
Therefore only a limited number of general conclusions were obtained
in this study.

(C)   Specific items which were treated in this work included the following.
Investigations were made to establish the geometric effects of various
multichamber exit shapes and to determine the relative envelopes of
engine and vehicle configurations. A summary of toroidal combustor and
multichamber effects on nozzle performance is presented. Also included
is a brief description of multichamber and toroidal aerospike performance
programs which were developed partially utilizing data generated in this
program. A parametric weight comparison was made of single bell, multi-
chamber and toroidal chamber aerospike engines of 2,000,000 pounds
thrust over a wide range of chamber pressure and area ratio. A review
of previous studies of relative versatility, reliability and cost of toroidal
aerospike, multichamber and conventional engine systems was made and the
pertinent results are discussed.

(C)   The two most heavily emphasized studies were in the areas of nozzle
heat transfer and system design. Detailed heat transfer studies were
made to establish limits of regenerative cooling feasibility for
multichamber and toroidal chamber aerospikes utilizing N_2O_4/UDMH-N_2H_4
(50-50) propellants. The studies were conducted over a wide range
of chamber pressure, area ratio, and thrust level. Design layouts were
made for typical single bell, multichamber, and toroidal aerospike
engines at four specific thrust levels of interest. The features of
the configurations are described along with advantages, disadvantages,
and potential problem areas.

(U)   A summary of major conclusions covering the analysis and design section
is presented at the end of this section.

COMBUSTOR DESCRIPTION

(C) Two basic types of combustor seem suitable for use with the aerodynamic
spike nozzle. These are the toroidal combustor and the multichamber
combustor. There are many variations of each of these basic concepts
and each has it own advantage and disadvantages. The geometric
relationships for throat area, area ratio, etc. are also unique for
each concept. This section presents an introduction to these combustor
concepts and their geometric characteristics.

Toroidal Combustor Configuration

(C) The chief feature of the toroidal combustion chamber is that it provides
a continuous or near continuous annular throat which is the most
desirable type to achieve maximum performance from the annular aerodynamic
spike nozzle. Disturbances to the sonic and supersonic flow caused by
structural members in the flow field or discrete combustors result in
nozzle performance losses.

(C) Three variations of the toroidal combustor concept are shown in Fig. 121
The sonic tube combustor is the simplest type in that the combustor
is formed and self-supported by rows of individual, formed tubes which
may be regeneratively cooled or film cooled. The throat is formed by
swaging the tubes. The cooling circuit is simple and a minimum of
external structural support is used. The chief disadvantages of this
configuration are high heat flux is encountered at the throat, high
stresses must be sustained by the tubing, and flow disturbances result
from expansion around the throat structure. These flow disturbances
can be minimized by using aerodynamic shaped tube trailing edges.

(C) The subsonic tube configuration alleviates all the problems of the sonic tube. An efficient structural member is placed in the subsonic region of the combustor where disturbances to the flow are negligible, and where the peak heat load is less than at the continuous annular throat. The disadvantages of this concept are increased weight and complexity of the structure and cooling system.

(C) The full baffle annular combustion chamber is the highest performing configuration and the peak heat flux is minimum. A continuous annular throat is formed with rows of thin walled tubing. Structural support is provided by cooled baffles and a variety of external structure types. This chamber type is the heaviest of the three but it is relatively simple in construction concepts.

(C) Many variations of these basic designs have been considered and are continually being improved upon at Rocketdyne. It should be noted that the complete annular engine may be formed by a number of independent straight or curved combustor segments or as a continuous single circular unit. The building block engine concept has many advantages which become more important as the total engine size increases.
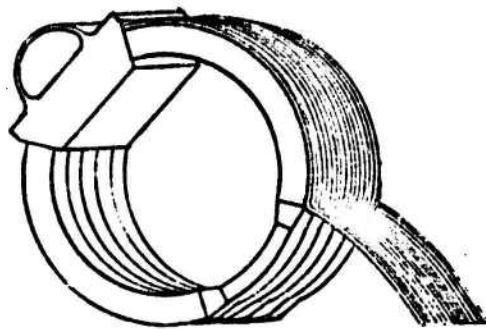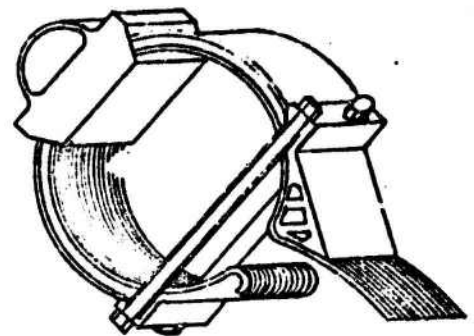
SONIC TUBE   SUBSONIC TUBE
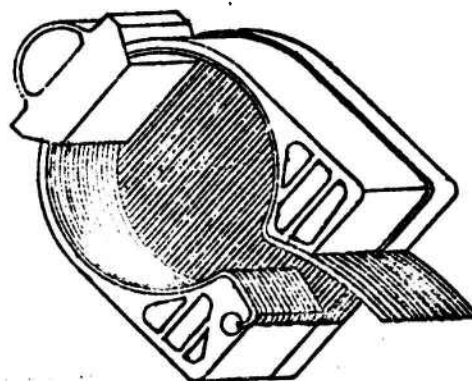
FULL BAFFLE ANNULAR   CONFIDENTIAL

Figure 121. Toroidal Combustor Configurations

Toroidal Combustor Geometry

(C) The toroidal aerospike engine is geometrically unique from the multi-chamber configuration or the conventional engine in that the nozzle area ratio is determined by the throat geometry. This can be seen by the equations below which are applicable to a circular continuous annular throat. The symbols are illustrated in the sketch below.
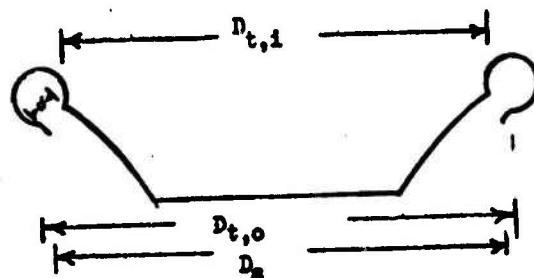
Shrouded Aerospike Geometry

$$A_t = \pi \delta (D_{ti} + D_{to})/2 \longrightarrow \pi \delta D_{to}/2$$

$$A_e = \pi D_s^2/4 \longrightarrow \pi D_{to}^2/4$$

$$\epsilon = A_e/A_t \longrightarrow D_{to}/2\delta$$

(C) At a given thrust level and chamber pressure (A_t) the area ratio and throat gap are determined by the throat (engine) diameter. More exact relationships for various toroidal configurations (e.g. sonic tube throats and straight chamber segments) may be found in Ref. 17 .

Multichamber Configurations

(C) There are probably as many variations of the multichamber concept as there are of the toroidal concept. The basic theme of this configuration is to utilize existing engine technology in the construction of an advanced annular engine. This concept consists of conventional combustion chambers clustered around a central aerospike nozzle as shown in Fig. 122 .

(C) This configuration provides some of the altitude compensating characteristics of aerospike nozzles while allowing a conventional approach to the design of those components of the engine which produce a major portion of the total thrust. The principal disadvantage to this concept is that performance is considerably below that which can be achieved with a continuous annular throat. To achieve the desired high performance annular flow configuration, the nozzle portion of the conventional chamber may be modified in various degrees as shown in Fig.123 . As the nozzle exits approach the annular shape, the nozzles approach a two-dimensional configuration. The advantages of the flat exit modules are that flow impingement losses are minimized and that (this will be discussed in the next section) a high engine area ratio can be achieved with a low module area ratio. This allows the flow to be exposed to ambient pressure sooner and hence a higher degree of altitude compensation capability is achieved. The major disadvantages of the two-dimensional module are (1) long length is required to achieve a high theoretical thrust efficiency, (2) frictional losses are increased by the large module surface area, (3) performance losses are caused by rotational flow in the module, and (4) structural requirements are severe.
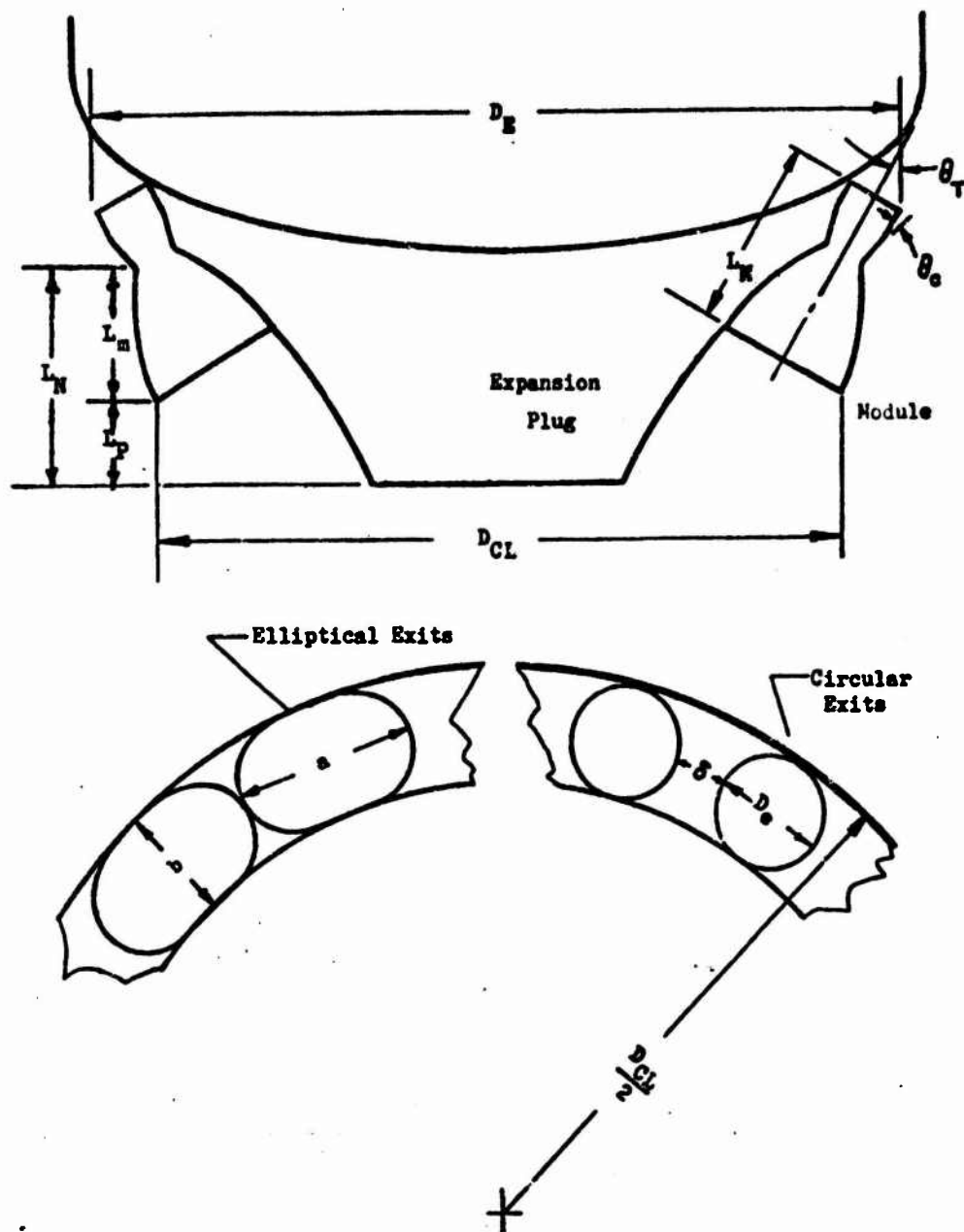
Figure 122, Multichamber Nomenclature
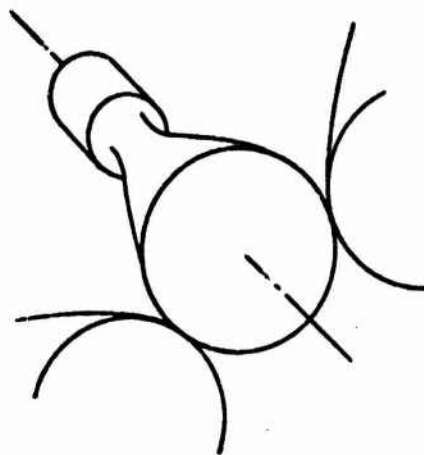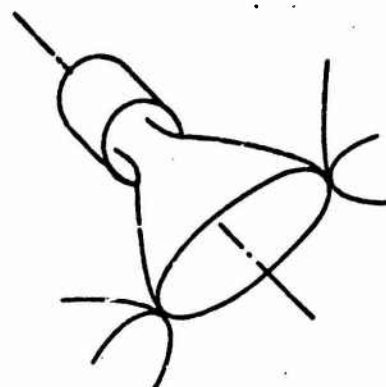
Circular Exits   Conventional Elliptical Exits
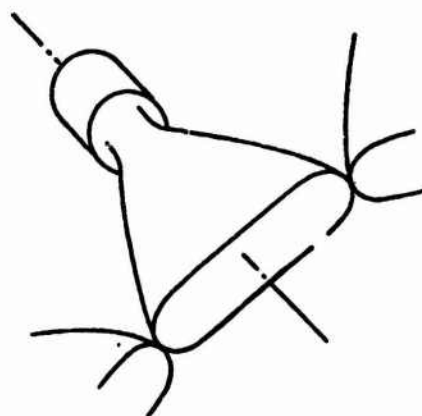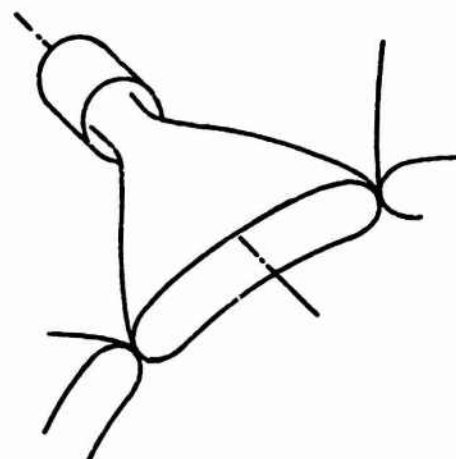
Straight Elliptical Exits   Curved Elliptical Exits

Figure 123. Advanced Modular Exit Shapes

211

Multichamber Combustor Geometry

(C) The principal characteristics of multichamber systems are the number of modules, the module expansion area ratio, and the system geometric area ratio, the latter being equal to the circular area enclosing the module exit (i.e., $\pi D_{CL}^2/4$ in Fig. 122) divided by the total throat area. These parameters are, in turn, governed by the shape of the module exits, the spacing between modules, and the inclination or "tilt" angle of the individual modules.

(C) The relationship between the modules and the overall system is generally expressed in terms of an "amplification factor," representing the ratio of the system area ratio to the module area ratio. For circular module exits, this factor is

$$\frac{\epsilon_{CL}}{\epsilon_M} = \frac{1}{N} \left[\frac{(1 + d/D_e) \cos \Theta_T}{\sin\left[\text{arc tan} (\cos \Theta_T \tan \frac{180}{N}) \right]} + \cos \Theta_T \right]^2$$

Where N = number of modules
ϵ_{CL} = system geometric area ratio
ϵ_M = module area ratio
d, Θ_T are as indicated in Fig.

(C) The variation of amplification factor with gap spacing and numbers of modules for circular exit modules with Θ_T = 20 and 10 degrees is shown in Figs. 124 and 125. Tilt angle has only a small effect on amplification factor; these data are therefore representative over the general range of interest, from approximately 5 to 30 degrees. The curves illustrate
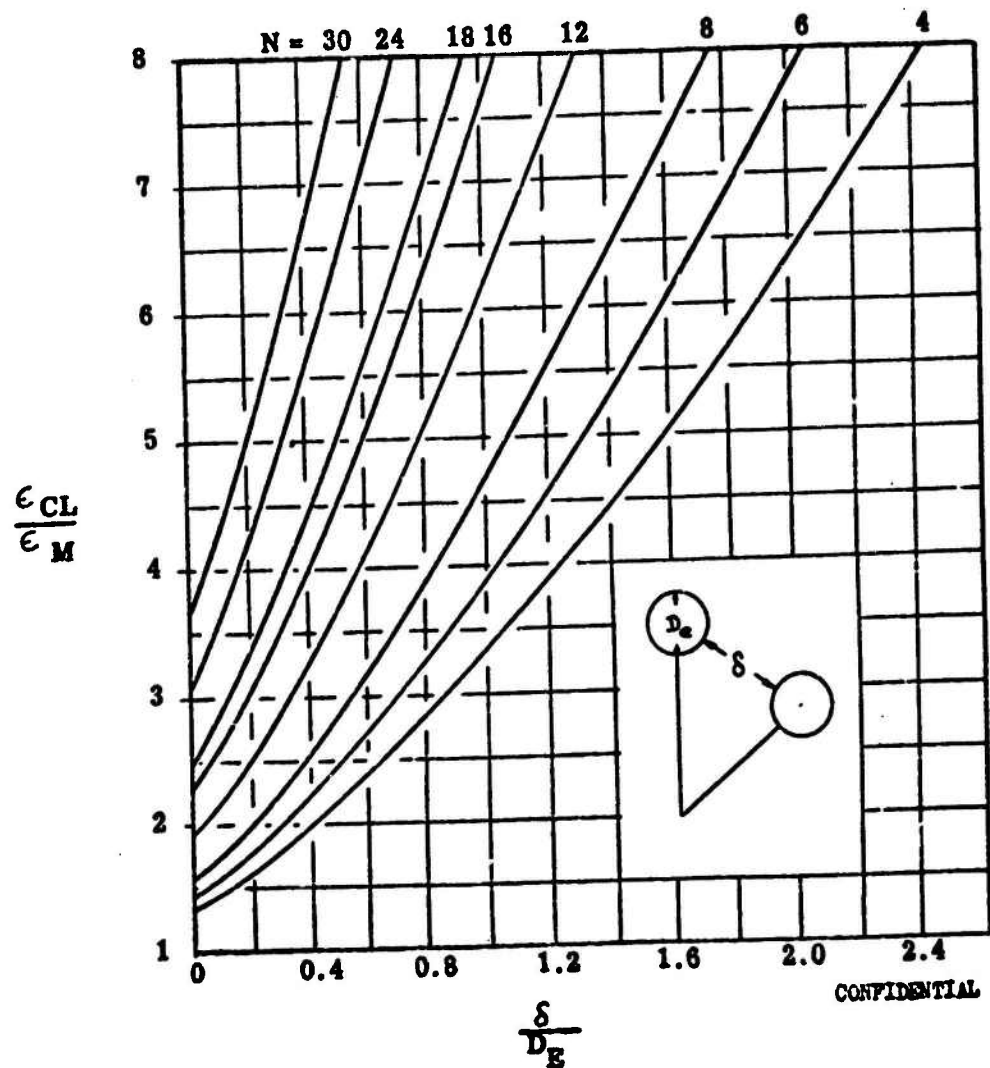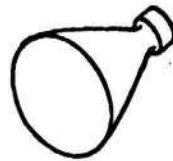
Figure 124. Geometric Amplification Factor as a Function of Circular Gap Spacing Ratio and Number of Modules

213
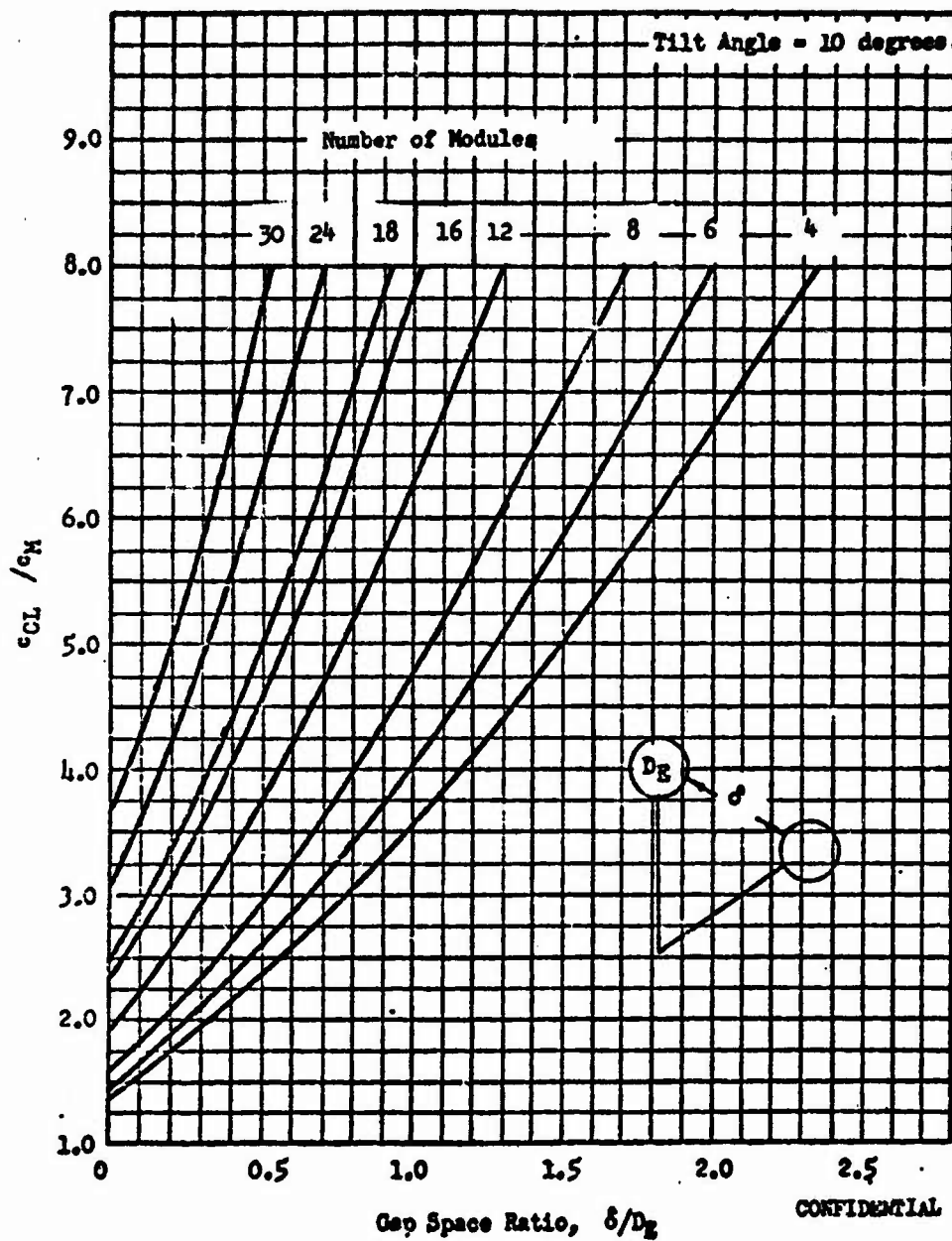
Figure 125 Geometric Amplification Factor as a Function of
Circular Gap Spacing Ratio and Number of Modules

214

that high amplification factors may be achieved by either increasing
the number of chambers or increasing the spacing between chamber exits.

(C) Amplification factors for the non-circular exit shapes shown in Fig.123
are presented in Fig.126 as a function of the slenderness ratio, a/b,
and number of modules. The governing equations for these systems are
shown below.

Conventional Elliptical Exit Shape

$$\frac{\epsilon_{CL}}{\epsilon_M} = \frac{1}{N}\left[\sqrt{\frac{a}{b}}\cot\frac{180}{N} + \sqrt{\frac{b}{a}}\cos\theta_T\right]^2$$

Straight Elliptical Exit Shape

$$\frac{\epsilon_{CL}}{\epsilon_M} = \tan\frac{180}{N}\left[\frac{a/b}{\tan\frac{180}{N}} + \cos\theta_T\right]^2 \Bigg/ 4(a/b-1) + \pi$$

Curved Elliptical Exit Shape

$$\frac{\epsilon_{CL}}{\epsilon_M} = \frac{\frac{1}{\pi}(\frac{a}{b})^2 N^2 + 2\frac{a}{b}N\cos\theta_T + \cos^2\theta_T}{\pi N\left[1 + \frac{4}{\pi}(\frac{a}{b}-1)\right]}$$

(C) It is important to note that although amplification factors for the
non-circular systems are higher than for corresponding circular-exit
configurations, system studies such as Ref. 12 have indicated that the
disadvantages cited previously tend to offset the potential benefits
of non-circular systems.

Tilt Angle = 20 degrees Modules Touching

Conventional Exit (Ellipse) —— Curved Exit (Ellipse) ----- Straight Exit (Ellipse) —·—
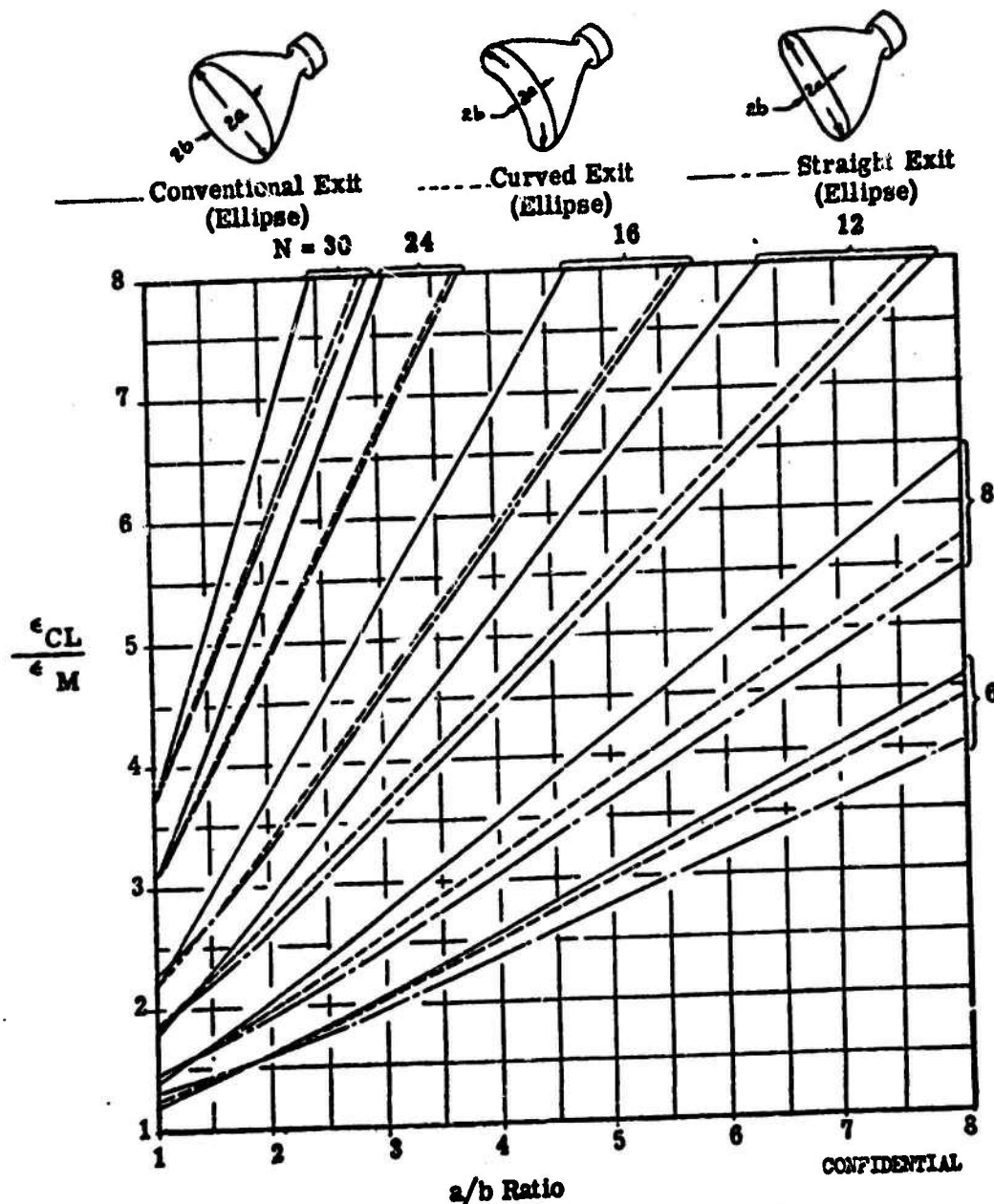
Figure 126. Amplification Factor as a Function of Ellipse Ratio and Number of Modules

216

ENGINE AND VEHICLE ENVELOPE REQUIREMENTS

(C) The range of chamber pressure (500 psia to 3000 psia), thrust level (20K to 2000K), and area ratio (to 150) investigated in this study encompasses a wide range of engine and vehicle diameters. Therefore some approximate dimensional studies were made to gain some initial insight into the relative engine and vehicle sizes being considered and the effect of chamber pressure, area ratio, and thrust level on relative engine and vehicle envelope.

(C) Figure 127 shows the relative engine and combustor dimensions to scale for a group of toroidal engines of 150 area ratio over the thrust range from 20,000 to 2,000,000 pounds. The same relative dimensions are approximately applicable to multichamber configurations. The combustion chamber diameters are sized to be a minimum of six inches and/or provide a chamber characteristic length greater than 30 inches. It can be seen that at low thrust levels, high chamber pressures and high area ratios, the combustor dimensions become a significant fraction of the engine diameter.

(C) The diameters of a number of existing vehicles and preliminary design vehicles utilizing $N_2O_4/UDMH-N_2H_4$ (50-50) propellants were correlated with thrust as shown in Fig. 128 . The straight lines represent a variation of vehicle diameter with the cube root of engine thrust which is an approximate relation in frequent use. These correlation lines were superimposed on plots of toroidal engine diameter vs. chamber pressure shown in Fig. 129 , 130 , and 131. These curves are also roughly applicable to multichamber engines. The data indicates that for the range of area ratios, chamber pressures, and thrust levels considered it is unlikely that a vehicle envelope will seriously restrict the selection of optimum engine operating pressure and area ratio. A comparison of the trends of vehicle and engine diameter with thrust level does indicate that the selection of area ratio and chamber pressure tends to become more restricted as thrust level increases.
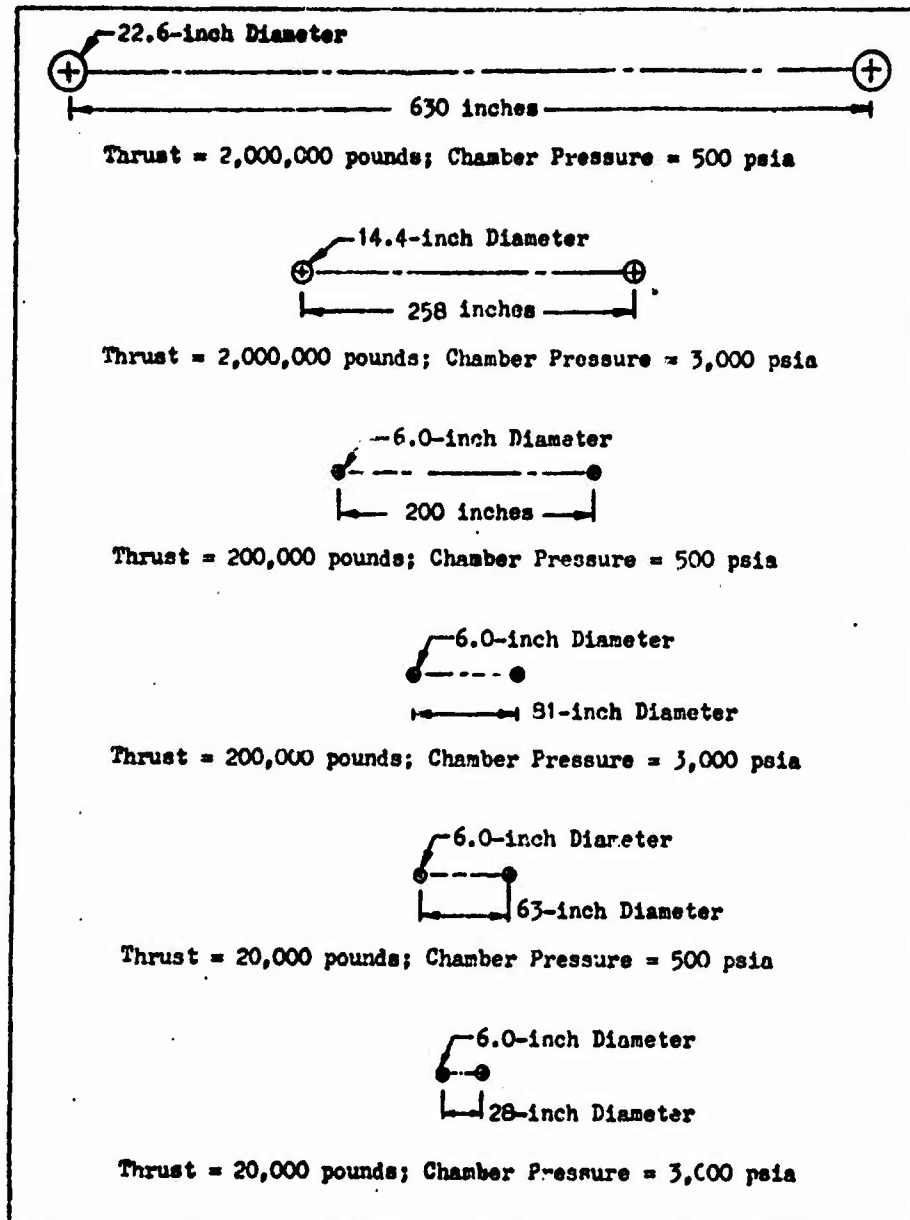
Figure 127. Limit Combustor Dimensions, $\epsilon = 150$
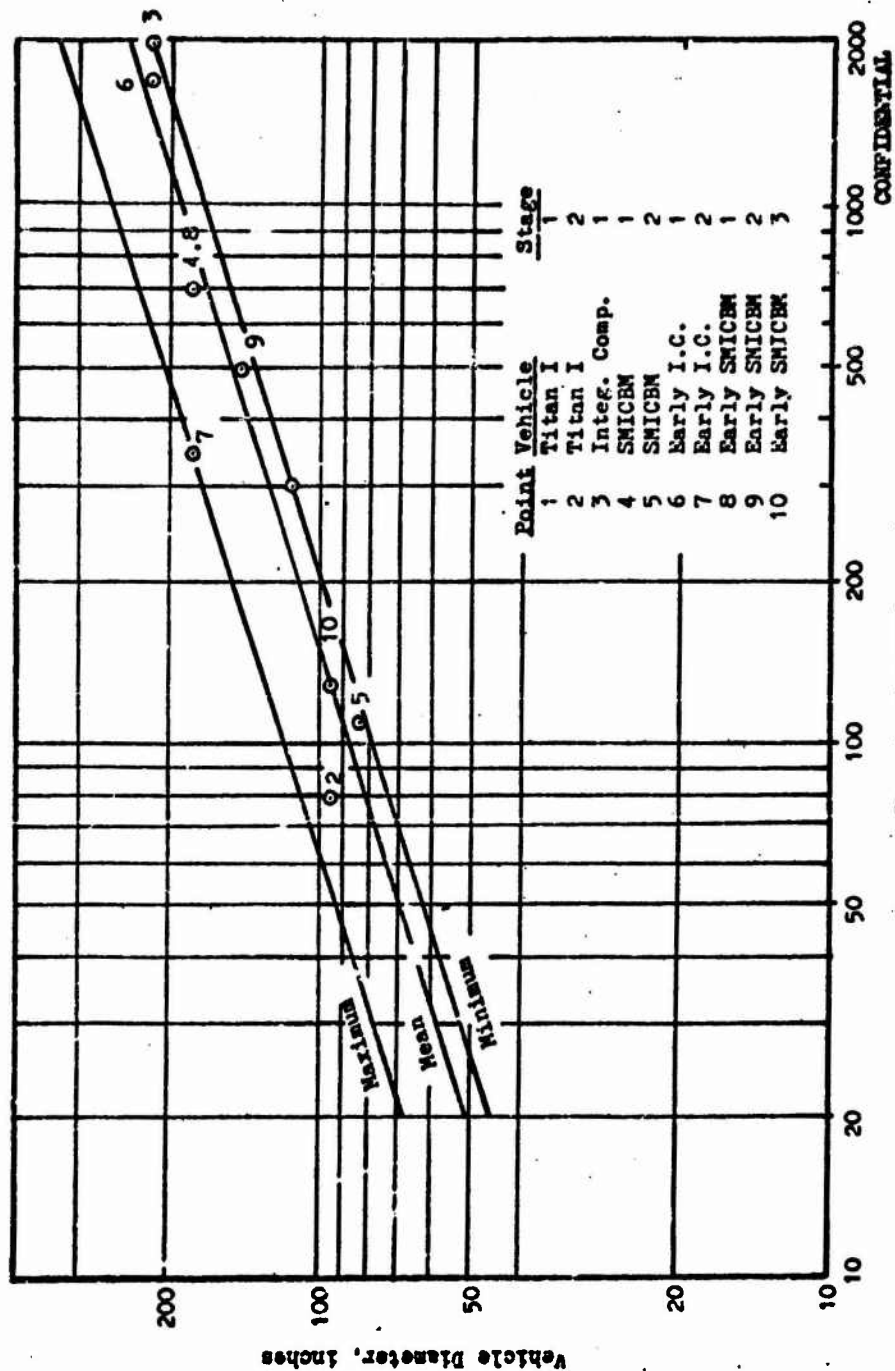
Figure 128 Vehicle Diameter Correlation with Stage Thrust
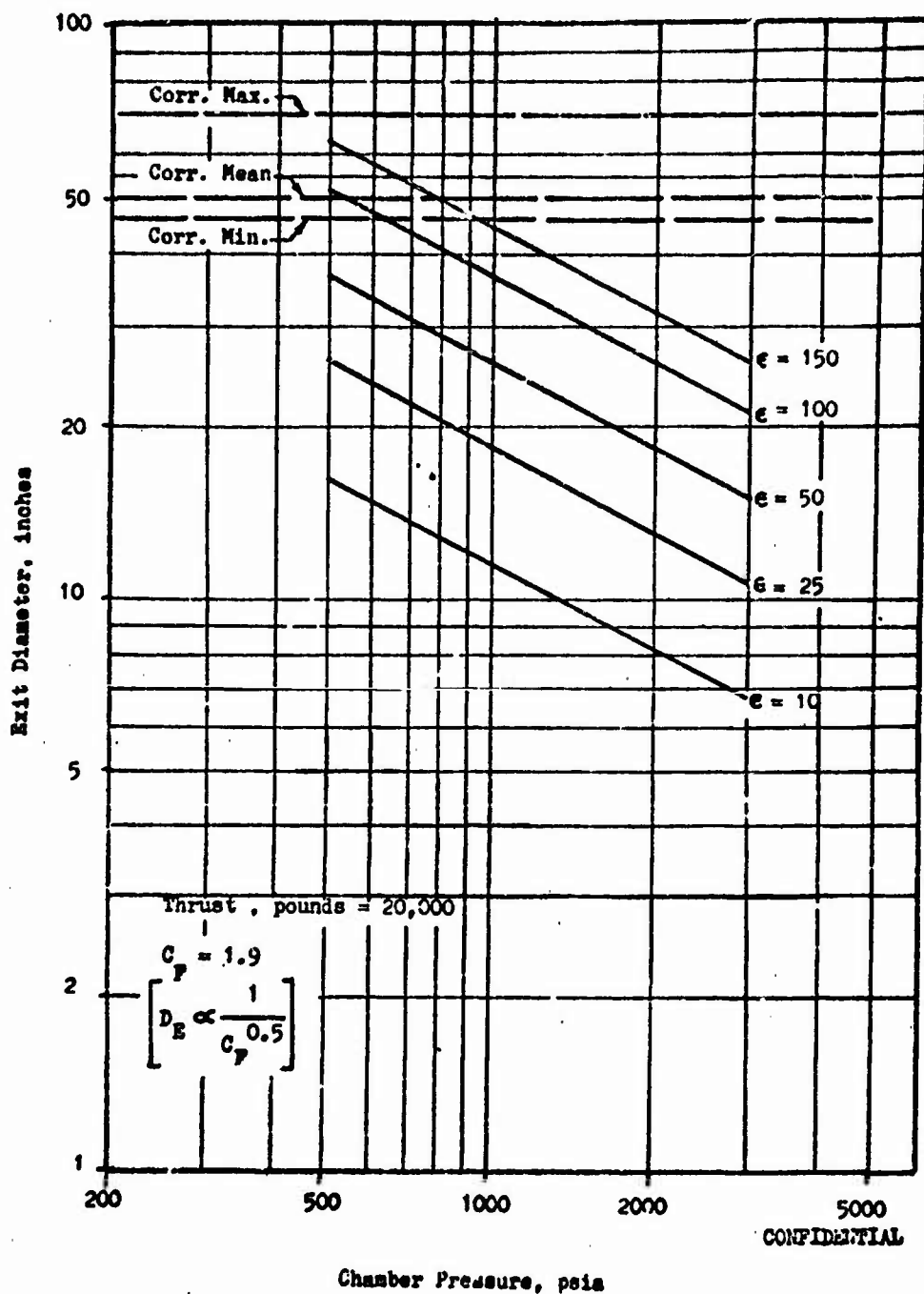
Figure 129. Toroidal Engine Envelope(F ~ 20,000 pounds)

220
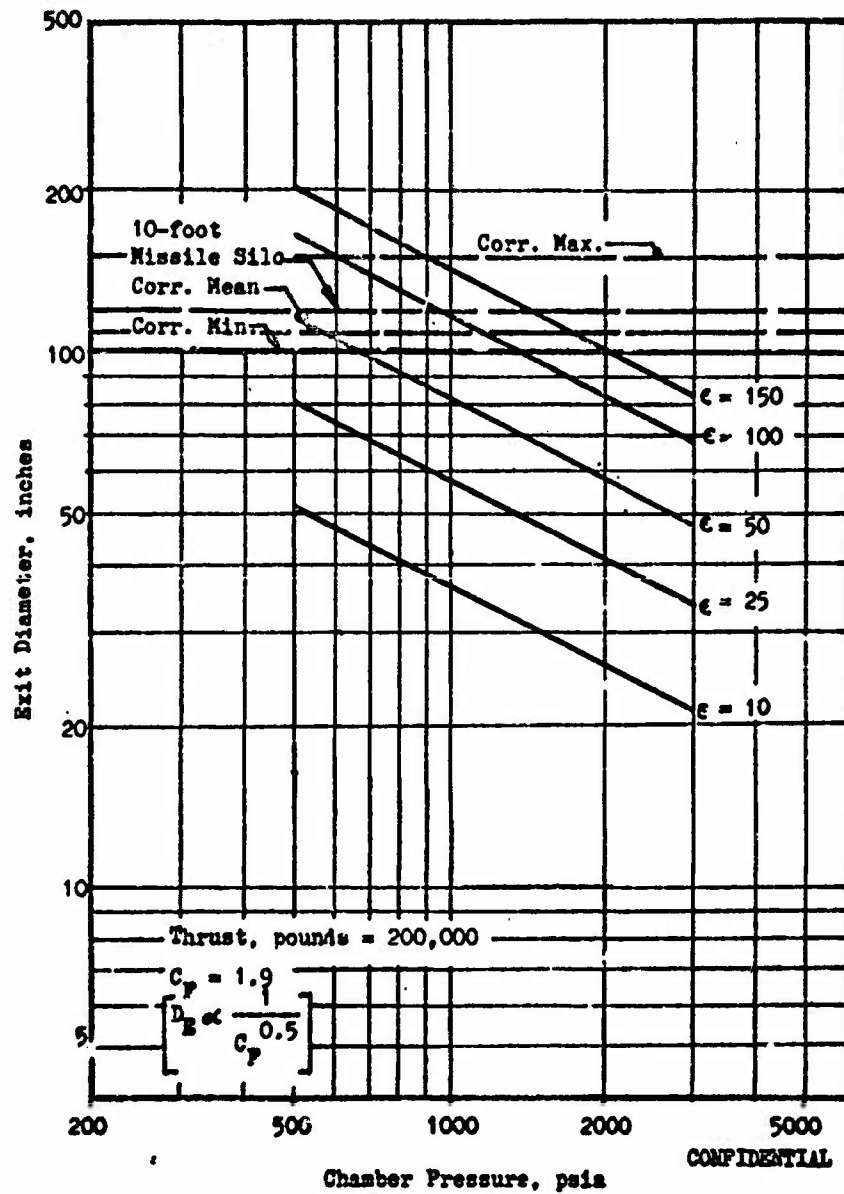
Figure 130. Toroidal Engine Envelope(F = 200,000 pounds)

221
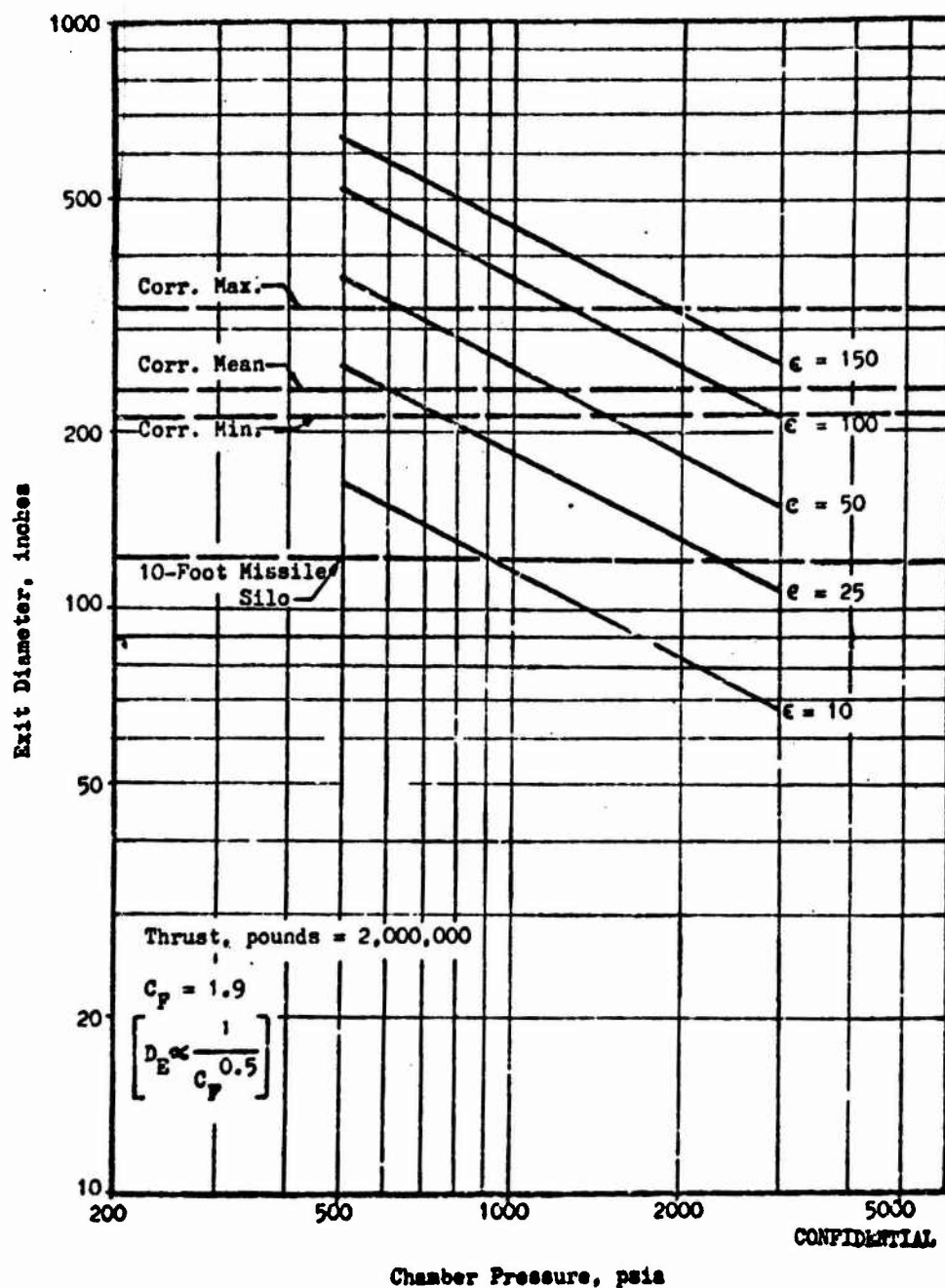
Figure 131. Toroidal Engine Envelope(F = 2,000,000 pounds)

PERFORMANCE

(U) In this section, the effects of geometrical nozzle and combustor parameters
upon advanced aerodynamic spike configurations are discussed. The discussion
is limited to the partial effects of each of these parameters established
from empirical and analytical studies conducted under this and other
contracts. The interrelationship of these parameters and their optimization
through system or mission studies was outside the scope of this study. A
review of current performance analysis techniques is also presented.

Combustor Geometry Effects

(C) The combustor geometry affects the combustion and gas expansion perfor-
mance of the thrust chamber. The combustion efficiency (η_{c*}) is chiefly
a function of the injector design and is affected by the combustor
geometry to a lesser degree. In the present discussion, it is assumed
that it is the expansion efficiency η_{CF} (or C_T) that is mainly
affected by combustor geometry, and that the combustor concepts considered,
toroidal and multichamber, have been designed (or developed) to attain
equal combustion efficiencies.

(C) Toroidal Configurations. Four configurations of the toroidal combustion
chamber concept as shown in Fig. 121 have been examined in detail; the
sonic tube, the subsonic tube, the full baffle annular, and the annular
configuration. In the first three configurations structural members
(inserts) are allowed to extend across the combustion chamber introducing
disturbances in the flow of the gases. Proper shaping of the insert
surface is possible in all cases to minimize the disturbance introduced.

223

(C) The expansion efficiency losses for the annular toroidal configuration
are only those caused by friction drag on the nozzle wall and by streamline
divergence losses at the nozzle exit plane. There is no disturbance of
the potential flowfield in the combustion chamber.

(C) The circular-type subsonic tube toroidal configuration disturbs the
potential flowfield, but because this disturbance occurs in the subsonic
region of the flow, and because the spacing between tubes is larger
(than for sonic tubes), the losses sustained by this configuration are of
relatively small magnitude. Five tenths of one percent decrease in C_T
was experienced in testing of a 240-subsonic-tube unit of tube spacing-to-
tube diameter ratio (δ/d) of approximately one. These losses are caused
by friction and pressure drag developed on the tube surface, and by
disturbance of the throat flow (sonic line) which affects the pressure
on the nozzle wall and the base pressure. Larger spacings (δ/d) lead
to reduction of all four forms of performance degradation. Proper
contouring of downstream tube surfaces, as will be shown for the case of
the sonic tube, lead to further reduction of performance losses.

(C) The higher expansion performance losses are experienced by the circular-
type sonic tube toroidal configuration. The disturbance in the flow for
this configuration takes the form of increased boundary layer surface
area, separation of the flow behind the tubes, shocks, and disturbance
of the sonic line. Theoretical work on this configuration has shown
that increasing the tube spacing leads to reduction of expansion performance
losses, and that for any tube spacing, the performance losses can be
reduced to tenths of one percent through incorporation of ideally
contoured trailing edges in the space immediately behind the tubes.

(C) These trailing surfaces prevent flow separation with associated shock
disturbances, thereby reducing the pressure drop, and the shock stagnation
pressure losses. Though surface area is increased, the reduction in
pressure drag and stagnation pressure losses noticeably offset the increase
in friction drag.

(C) The lower losses in performance of sonic tube configurations are obtained
through the incorporation of a full-length ideally contoured trailing edge.
Heat transfer and fabrication considerations, however, dictate the allowable
length for the trailing edge. The ideally contoured baffle length can be
truncated in a manner depicted in Fig.132 , without an excessive sacrifice
in performance. This latter point is illustrated in Fig. 133, a graph nozzle
expansion efficiency $\eta_{C_{T_V}}$ as a function of nozzle area ratio for the ideally

contoured trailing surface at various degrees of truncation. Even for the most
severe degree of truncation considered, h/D_t of 0.103, the performance loss is not
higher than 0.35 percent for a tube spacing δ/d_t of one, and gas specific heat
ratios of 1.15 to 1.25. The loss indicated is the sum of divergence and
pressure drag losses incurred in the combustion chamber through deformation
of the inviscid flow field. This net loss is a function of the tube and
throat geometry and constitutes a fixed loss in thrust coefficient which
is not recoverable in the supersonic portion of the nozzle, but is rather
dissipated into the shock and viscous flow structure downstream of the tubes.
As the value of this loss is fixed, an increase in overall expansion area
ratio makes it a diminishing fraction of the overall thrust coefficient.

(C) Friction drag losses for the toroidal combustion chamber using tapered
sonic tubes have been shown to be nearly equal to losses in the annular
toroidal combustion chamber. This equality concept may be arrived at from
the following observations: drag upstream of the geometric throat (subsonic
flow region) of either configuration is negligible, tapered sonic tubes
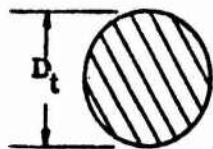
Circular

20° Conical

15° Conical

Figure 132. Toroidal Throat Tube Contour Shapes
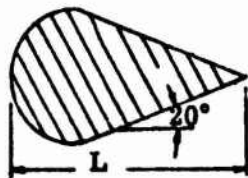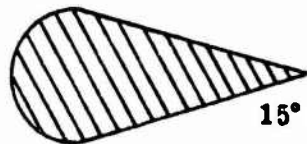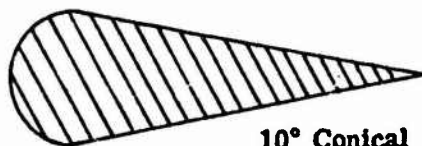
10° Conical
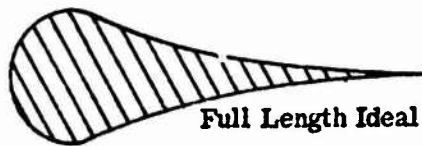
Full Length Ideal Isentropic
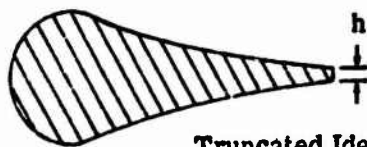
Truncated Ideal - $h/D_t = 0.052$
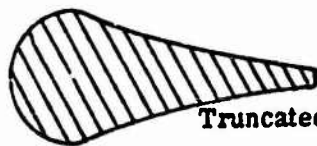
Truncated Ideal - $h/D_t = 0.077$

Truncated Ideal - $h/D_t = 0.103$

Tube Length - L/D_t

226
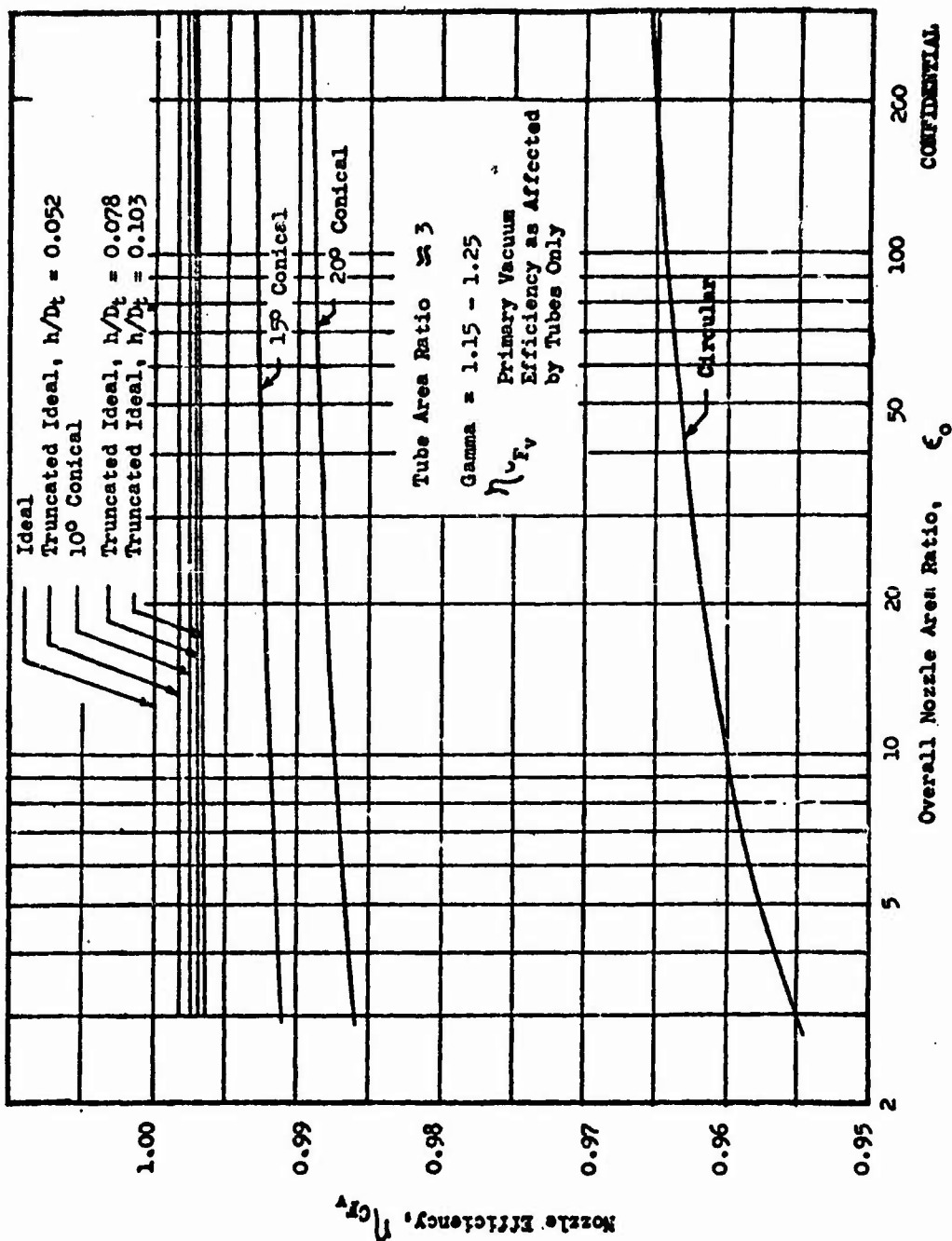
Figure 133. Effect of Sonic Throat Tube Shapes on Vacuum Efficiency

present a large wetted surface area (drag is directly related to surface area) but allow a significant reduction in nozzle axial length when expanding to equal flow conditions. The result is that drag losses for equivalent annular and tapered sonic tube toroidal configurations are essentially equal. Typical values calculated for LOX-H_2 annular and sonic-tube toroidal systems with overall expansion area ratio of 6 are shown in the table below.

TABLE 8

COMPARISON OF TOROIDAL CHAMBER DRAG LOSSES

	Annular	Tube - 15° Conical Trailing Surface
Tube Area Ratio (ϵ_t)	0	2.96
Overall Area Ratio (ϵ_o)	6.00	6.00
Ideal Thrust Coefficient (C_F)	1.6811	1.6811
Contour Drag Loss (ΔC_{F_D})	0.0170	0.0064 (from ϵ = 2.96 to 6.00)
Tube Drag Loss (ΔC_{F_D})	0	0.0113
Total Friction Drag (percent Ideal C_F)	1.01	1.05

(C) From the above discussion, it follows that the differences in performance indicated in Fig.133 between the ideal and the various toroidal tube configurations also represent the differences between toroidal-tube and full-annular toroidal combustion chambers including drag losses.

(C) For comparison, the losses to be expected for a circular-type sonic tube and for tubes having conical trailing edges have also been included in Fig.133. Even a 20-degree conical trailing edge achieves a significant gain in performance over the circular sonic type (on the order of 2.5 percent).

(C)   For equal combustion chamber conditions and equal insert cross-sectional
      area, the performance loss caused by pressure drag per structural member
      is of the same magnitude for both the untapered sonic tube (circular) and
      the baffled annular combustor configurations. Because of increased surface,
      the friction drag is higher for the baffled annular configuration. The
      number of required baffles are fewer, however, than the sonic tubes or
      even the subsonic tubes, therefore making this configuration the   less
      subject to expansion performance degradation. A 48-baffle unit tested
      in cold-flow conditions with a baffle-to-baffle width ratio d/w of
      100:1 indicated performance losses of approximately 3 tenths of one percent.
      Calculated losses for this configuration were 0.23 percent.

(C)   <u>Multichamber Systems.</u> Module spacing and exit shape are the principal
      combustor variables affecting system efficiency. Experimental data defining
      the influence of these parameters are limited; however, estimates of the gap
      correction factor can be determined on the basis of cold-flow results
      from this program and from data presented in Ref. 3. The data shown
      in Fig. 134 indicate that substantial losses can be incurred in systems
      having sizable gaps between module exits, particularly in systems having
      short plug lengths. The reduction of these losses in longer systems
      indicates that some degree of recovery occurs.

(C)   Performance data for noncircular exit systems indicate no advantage
      relative to ciruclar-exit configurations (Ref 12). These data, however,
      were obtained for modules having circular-throat modules. Probable
      causes of this low performance are increased friction drag on the relatively
      large module surface area and rotational flow in the module induced by
      the transition from a circular throat to a nearly two-dimensional nozzle.
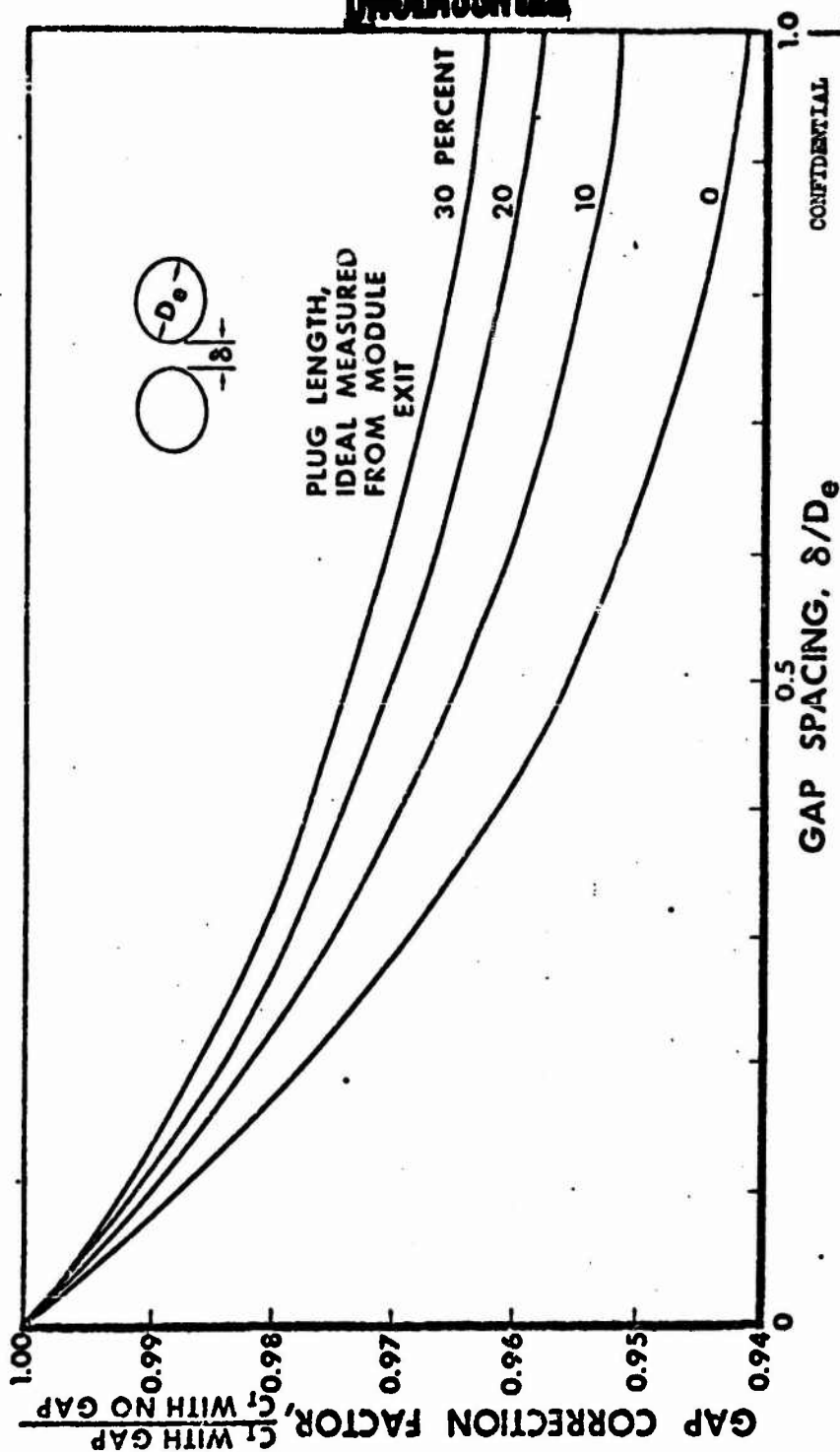
Figure 134. Effect of Module Spacing on Propulsion System Performance

Nozzle Length

(C) As is the case with bell and conical nozzles, increasing the length of
toroidal aerospike configurations increases the nozzle (potential) per-
formance, increases the drag losses, and increases the overall thrust
chamber weight. The rate at which all these quantities increase with
length differs with the nozzle type. The nozzle length required for a
certain application is obtained from mission-optimization studies. In
this section, the effect of nozzle length on expansion performance (C_{T})
without regard to mission or payload is discussed.

(C) Toroidal Configurations. The basic toroidal configuration is the annular.
It has been established through cold-flow testing that the truncated
ideal isentropic spike contour used in conjunction with the annular
toroidal configuration is the highest overall performing of the contour
types. Optimum contours (contours designed for maximum primary thrust
in a given nozzle length) yield higher primary performance, but their
lower base pressure make this configuration perform lower than the
truncated ideal isentropic spike contour. Longer lengths would be
required of optimum contours to achieve total performance equal to the
truncated ideal spike.

(C) To achieve full ideal expansion, an isentropic spike nozzle must have a
full length. This maximum length, expressed in terms of a 15-degree
cone, increases with an increase in expansion area ratio, and with an
increase in specific heat ratio. The same can be said of the truncated
ideal spike nozzle contour. To achieve a given nozzle efficiency, longer
truncated ideal spike contours are required as expansion area ratio
increases, and as specific heat ratio increases. For given expansion
area ratio and specific heat ratio, increasing the nozzle length increases
nozzle efficiency (C_{T}) continuously even when adding the optimum amount

of secondary flow in the base of the aerospike. There is a length, however, beyond which the performance increases are not significant. This can be seen from Fig. 135 a plot of nozzle efficiency with secondary flow versus nozzle length for an expansion area ratio of 45 and a specific heat ratio of 1.4. Beyond a nozzle length of 30 percent (in terms of a 15-degree cone) the performance gains caused by increasing length are extremely small. As length increases, the gains from secondary flow diminish as can be seen by comparing the "no secondary" and "with secondary" performance efficiency curves in Fig. 135. The secondary flow required for optimum performance is also reduced as the gains diminish. At a different area ratio and gamma (with different propellants), the length required for the above trends to repeat however is different.

(c) Multichamber Systems. The aerodynamic performance of multichamber systems increases with increasing length in a manner similar to that noted in annular combustor systems. However, it is important to recognize that the length of a multichamber system is comprised of module length and a plug nozzle length; the plug nozzle length by itself is not an adequate indicator of system aerodynamic efficiency.

(c) The cold-flow data generated in this program and the data presented in Ref. 12 were compiled to ascertain the relationship between design point aerodynamic efficiency, $C_{m_{des}}$ and plug length, and number of modules. The resulting correlation is shown in Fig. 136. A locus of points representing any total system length could be superimposed upon the data in Fig. 136; as shown by the typical example on Fig. 136. The result is a nearly constant C_m, with a gradual decay indicated as the number of modules increases. It is evident that for plug lengths beyond approximately 15 percent (based upon the length of an ideal spike), further increases in performance are small and number of modules has little effect on efficiency.

Truncated Ideal Spike
$\epsilon = 45$ $\gamma = 1.4$
Design Pressure Ratio

No Secondary Flow

Optimum Secondary Flow

CONFIDENTIAL
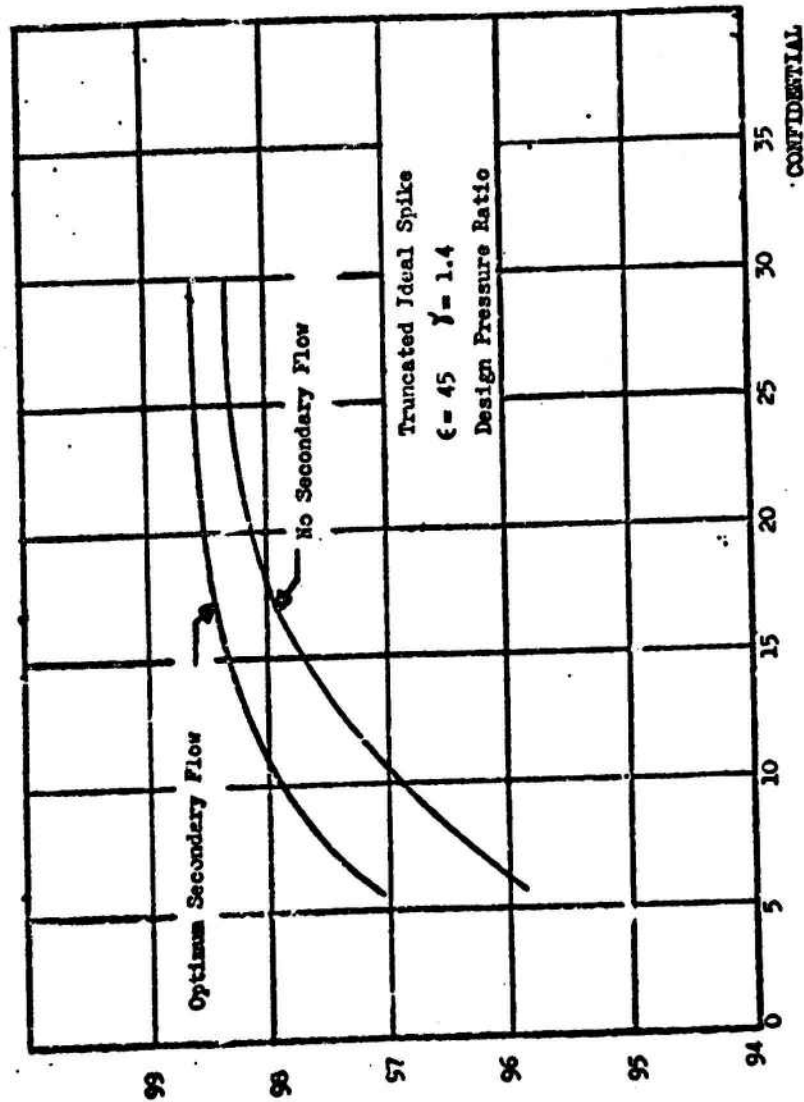
Nozzle Efficiency, C_F, percent

Figure 135. Variation of Nozzle Efficiency With Length
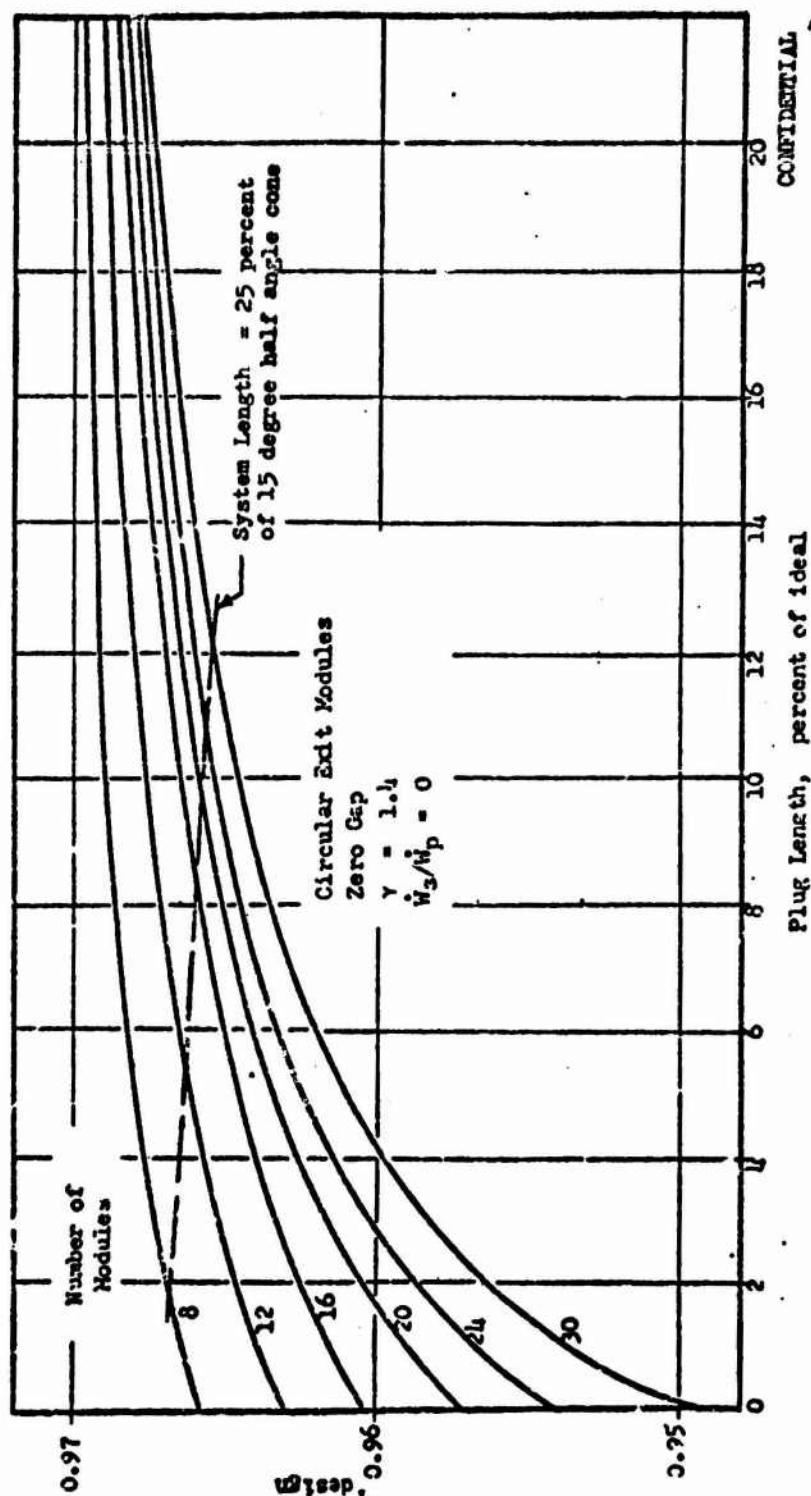
Figure 136. Effect of Plug Length and Number of Modules on Thrust Efficiency

Performance Analysis Techniques

(U) The performance analysis technique, as developed at Rocketdyne for use
with aerodynamic spike configurations, is a collection of theoretical
procedures and refined empirical equations which take into account
inviscid primary performance, viscous primary losses, kinetic losses,
base pressure without secondary flow, the effect of secondary flow and
secondary flow properties on base pressure, and the effect of varying
ambient pressure. Computer programs exist for the complete performance
analysis of the toroidal and multichamber configurations. The main
features of these programs and the techniques employed are reviewed
briefly in the following subsections. For a complete discussion of
these programs, Ref. 18 and 19 are available.

(C) Toroidal Configurations. The computer program for the annular toroidal
aerospike configurations is capable of designing an ideal spike config-
uration for a given thrust or a given throat area utilizing any of the
following three propellants; LOX/H_2, $NTO/50-50$, and LOX/RP; at the
major mixture ratios of interest. The nozzle design is then subjected
to a method-of-characteristics analysis which yields divergence losses
for the primary flow at any operating pressure ratio, and a boundary
layer analysis which yields friction drag losses. From built-in tables,
kinetic losses are evaluated; and from empirical equations, the base
pressures are calculated. These separate contributions are then combined
with the ambient pressure drag to obtain overall nozzle output in the
form of thrust, nozzle thrust coefficient, and/or nozzle efficiency in
vacuum. The basic equations used are:

$$(1) \quad F = P_{c_p} A_t \left[c_{F_{i,v}} - \Delta C_{F_{div.}} - \Delta c_{F_{drag}} - \Delta C_{F_{kin.}} \right] + P_b A_b - P_a A_e$$

$$(2) \quad \dot{W}_T = \frac{P_{o_p} A_{t_p} g}{C_p^*} + \frac{P_{o_s} A_{t_s} g}{C_s^*}$$

$$(3) \quad C_p = \frac{\mathcal{F}}{P_{o_p} A_t \left[1 + \dot{W}_s / \dot{W}_p\right]}$$

(C) Calculated values from use of these three equations can then be utilized to derive nozzle efficiency C_T or specific impulse efficiency η_{I_s} values for any pressure ratio, given a value of the combustion efficiency η_{c*}, and a suitable reference for thrust coefficient and specific impulse; i.e., $C_{p_{opt}}$ and $I_{s_{opt}}$. A flow diagram for the program is shown in Fig. 137. In the region of pressure ratios where the ambient pressures influence the base pressure (open wake), the latter are not calculated in the program. Equations are given in Ref. 19 which will allow the calculation of the base pressure in the open-wake through use of an empirical technique. Reference 19 also gives a detailed description of theoretical and empirical equations used in the design and analysis of the toroidal aerospike overall performance, as well as a description of program operational procedures.

(C) Losses caused by introduction of structural members across the flow are not calculated in the program but can be included into equation (1) through the use of information in Fig. 133, and the equation:

$$C_{p_{pins}} = (1 - \eta_p) C_{p_{i,v}}$$

Where η_p is obtained from Fig. 133.

236
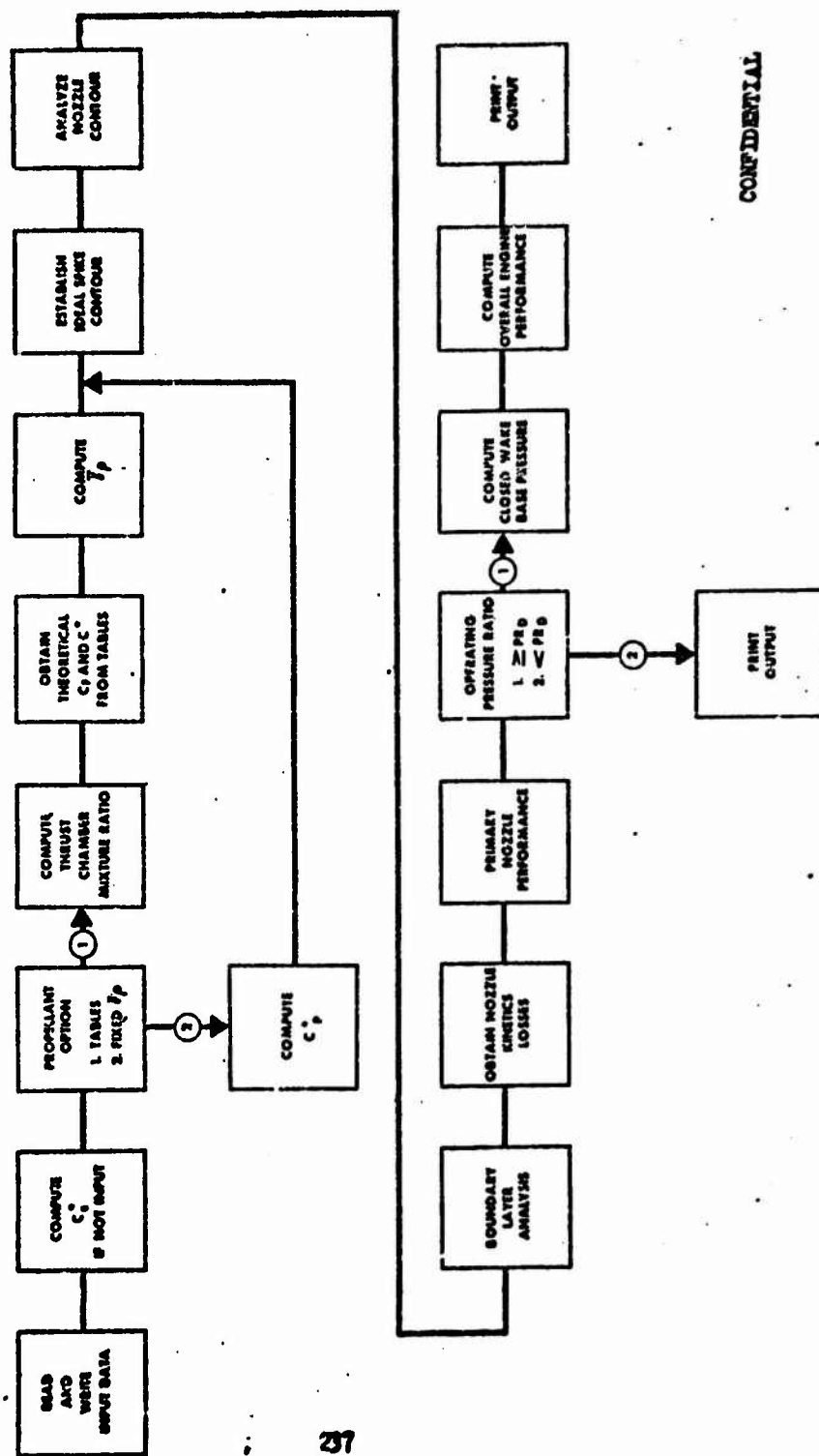
Figure 137. Flow Diagram, Aerodynamic Spike Engine Design Program

(C) <u>Multichamber Configurations:</u> Computer programs developed under
NAS 8-20237 (Multichamber, Plug Nozzle Systems Analysis) are currently
used at Rocketdyne for estimation of multichamber propulsion system
performance.

(C) The basic approach to multichamber system analysis at low altitudes
is similar to the technique used to determine toroidal system performance;
i.e., the summation of an analytically derived primary flow contribution
and empirical estimates for the remaining contributions. The thrust
delivered by tilted bell modules, representing more than 95 percent
of the total thrust at low altitudes, is readily amenable to analysis.
The remaining factors are expansion on the plug nozzle and base pressure;
each of these effects is estimated by empirical correlation of cold-flow
data.

(C) High altitude performance for multichamber systems is obtained by the
technique described in Ref. 29 and illustrated in Fig. 138. In this
instance, cold-flow performance is estimated from a matrix of experimental
C_T vs plug length and number of modules data, and analytical corrections
are applied to translate the performance value to the appropriate gas
properties, system size and base bleed flowrate and properties.

Includes plug nozzle overexpansion and base bleed flow losses
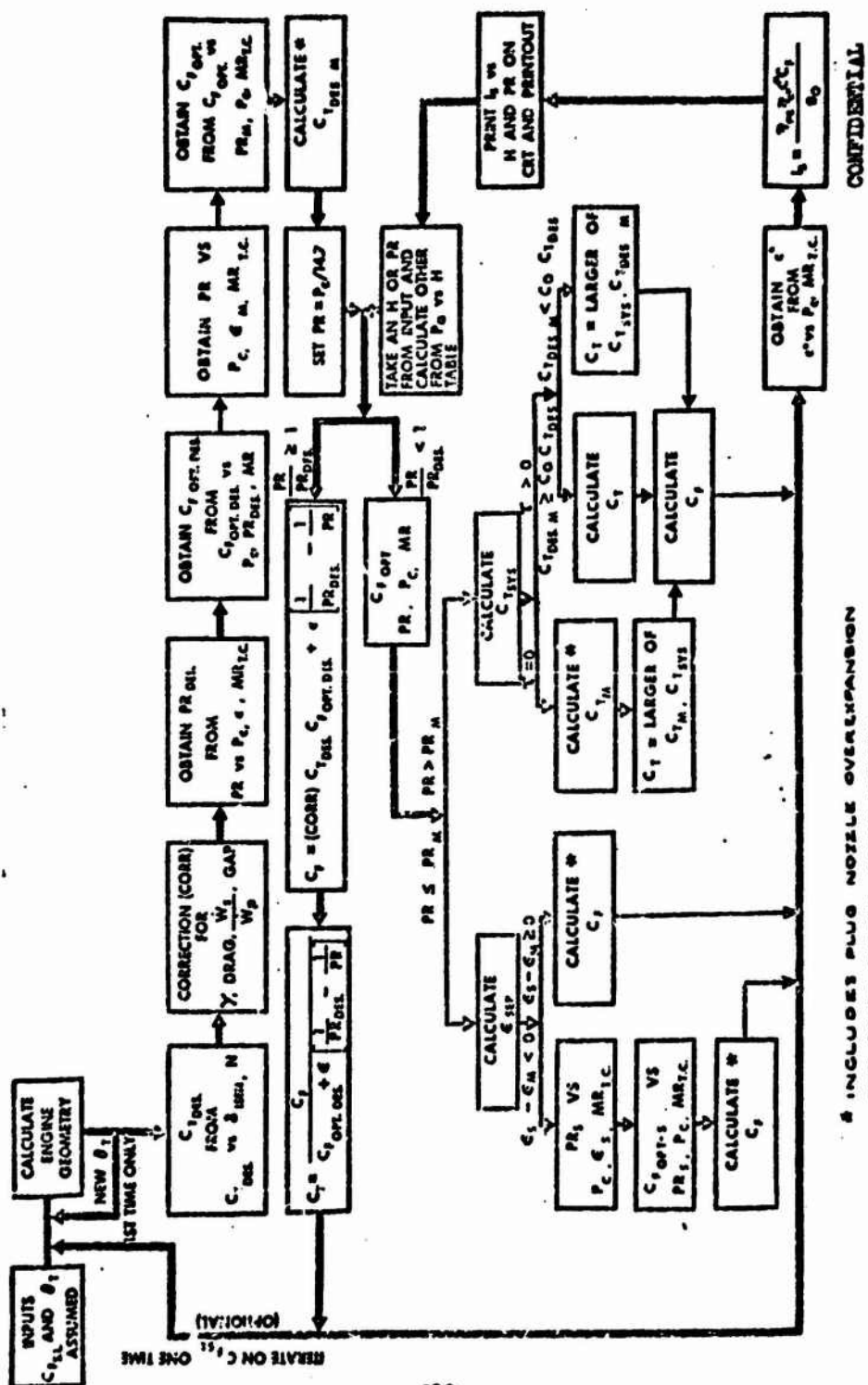
Figure 138. Flow Diagram for Multichamber System Performance Program

(c) The analysis includes a theoretical separation criterion which permits
the analysis to proceed accurately regardless of the degree of over-
expansion. An empirical approach is used in the transition region
between the two methods, with the performance trend dictated by the
presence or absence of base bleed. With no base bleed, the module
performance continues to prevail beyond the module design pressure
ratio, resulting in a "trough" in the delivered C_T curve (see sketch).
Since the general tendency indicated by cold-flow data is for base
bleed to eliminate this trough, a simplified approach was employed,
in which the presence of any quantity of base bleed is assumed to
cause the C_T curve to be horizontal between the module design pressure
ratio and the intersection with the system closed-wake C_T curve.

Overall System C_T With Base Bleed

System (Closed-Wake) C_T

Module Closed-Wake C_T

System (Module) C_T

C_T

P.R.
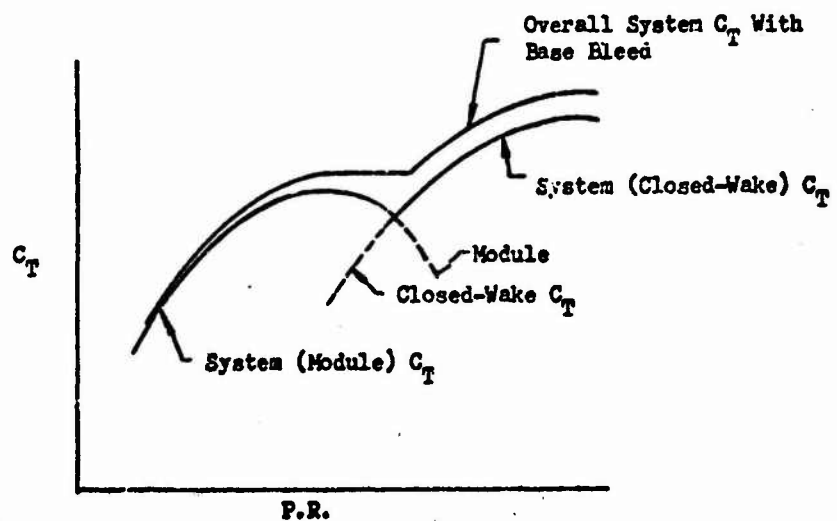
(C)   An important aspect of performance computation became apparent from data generated during the experimental multichamber investigation conducted in this program. From data showing the variation of C_T vs pressure ratio, it was evident that effective expansion area ratio (i.e., design pressure ratio) could be predicted more accurately based on a "scalloped" exit area rather than on the area of the circle enclosing the module exits. As shown in Fig. 139, this factor is significant in systems having relatively few modules. Scalloped area ratio is therefore utilized as the basis for computing system design pressure ratio in the computer program.
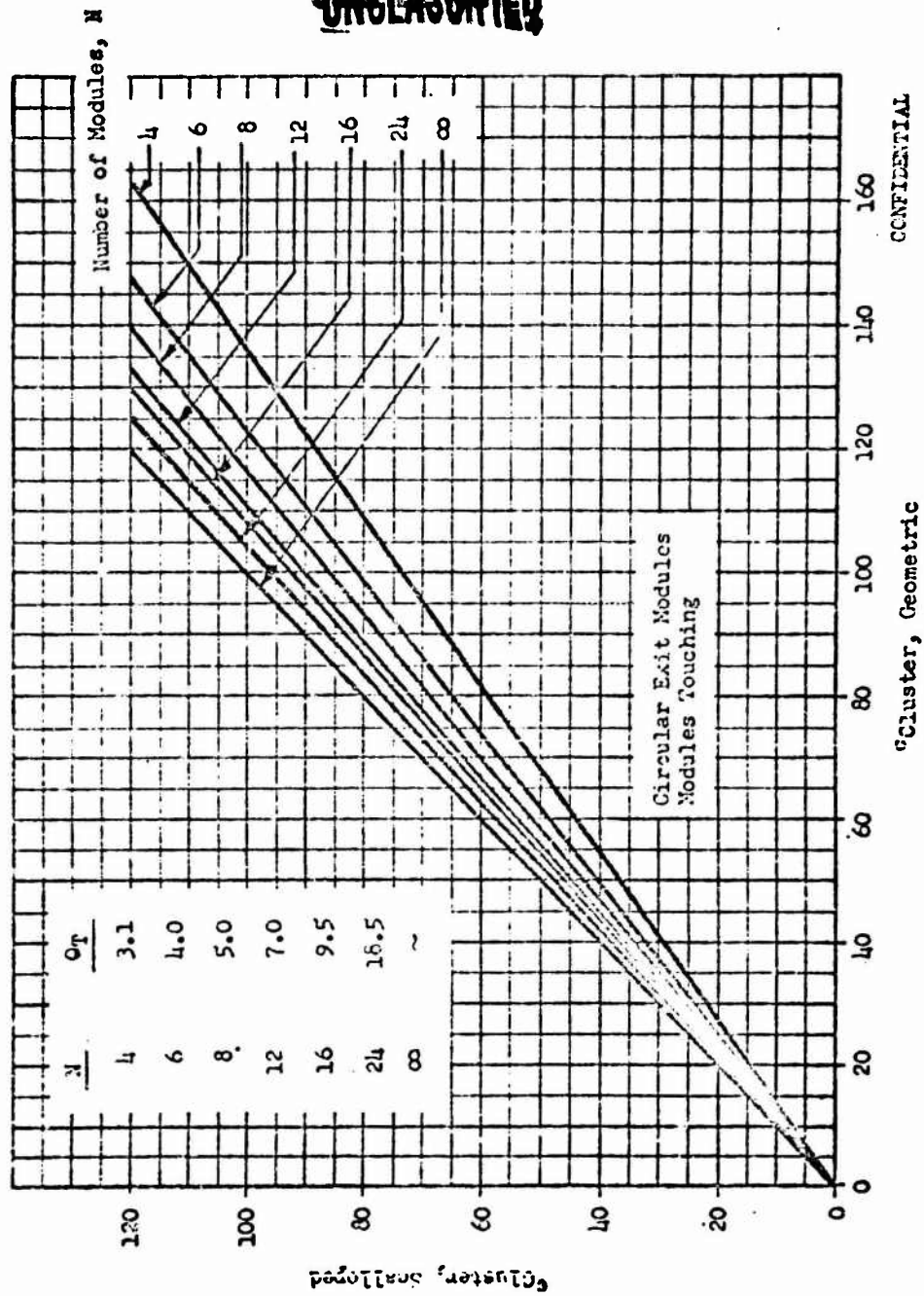
Figure 139 Scalloped and Geometrical Cluster Expansion Area Ratio Exchange Curves

ENGINE WEIGHT COMPARISON

(C) A parametric study was made to compare the weight of toroidal and multichamber aerospikes and conventional single bell engines utilizing N_2O_4/UDMH-N_2H_4 (50-50) propellants. The engines were compared at a thrust level of 2,000,000 pounds over a range of chamber pressures from 1000 psia to 3000 psia and a range of area ratios from 20 to 150. The method of analysis and results are presented in the following paragraphs.

Method of Analysis

(U) Engine weights were computed for multichamber and toroidal aerospike engines and conventional single bell engines. The characteristics of the engines evaluated and the range of parameters investigated are listed in Table 9 .

(C) The study was conducted at a fixed sea level thrust of 2,000,000 pounds. The aerospike engines all had a total length from the throat to the nozzle exit plane equal to 20 percent of a 15 degree conical nozzle. The single bell engines were 80 percent in length. Area ratios from 20 to 150 were investigated for the aerospike engines and from 20 to 100 for the bell engines. Chamber pressures from 1000 psia to 3000 psia were investigated for the aerospike engines and from 1000 psia to 2000 psia for the bell engines.

(C) Three variations of the multichamber configuration were investigated, an eight module configuration with eight sets of individual fuel and oxidizer turbopumps, a sixteen module configuration with sixteen turbopump sets $M_{T/P}$, and a sixteen module configuration with eight turbopump sets. The eight module configurations are approximately 20 percent in length to the exit of the modules and therefore require no spike nozzle extension.

(C) Toroidal aerospike weights were computed using an existing computer program developed for annular nozzle weight analysis. Multichamber weights were

TABLE 9

CHARACTERISTICS OF ENGINE SYSTEMS

F = 2,000,000 Pounds; N_2O_4/UDMH-N_2H_4(50-50)

CONFIDENTIAL

Configuration	Number of Turbopump Sets	Nozzle Length (percent 15 degree cone)	P_c range (psia)	ε Range
8 Module Multichamber	8	20 (no spike)	1000-3000	20-150
16 Module Multichamber	16	20 (8.6 to 10.6 percent spike)	1000-3000	20-150
	8	20 (8.6 to 10.6 percent spike)	1000-3000	20-150
Toroidal	8	20	1000-3000	20-150
Single Bell	1	80	1000-2000	20-150

computed using both an existing bell engine weight computer program and the annular nozzle weight program. Weight relationships for structure supporting the multichamber modules and the multichamber spike were based upon weight analyses of structural drawings of H-1 cluster configurations and large (18 to 30 million pounds thrust) multichamber LO_2/LH_2 aerospike engines (Ref. 18).

(C) The engines were all assumed to obtain their turbine drive fluid by tapping off main combustion chamber gases. All engines were assumed to be regeneratively cooled (with N_2H_4-UDMH below P_c = 1500 and with N_2O_4 at chamber pressure of 1500 psia and above) with supplemental film cooling at 3000 psia chamber pressure. The results of parametric heat transfer studies were used to determine tube pressure drop and consequent pump discharge pressure requirements.

Results

(C) Engine weights for the various configurations are shown vs. area ratio in Fig. 140 through 143. Several trends can be seen from these data. Engine weight increases very rapidly with increasing area ratio, the rate of increase decreases with increasing chamber pressure. The single bell engine system increases in weight more rapidly than the other configurations, however, it is lighter than the sixteen chamber configurations up to area ratios between 60 and 100. The single bell engine is approximately equal in weight to the eight module configuration and the toroidal aerospike at low area ratio but rapidly becomes considerably heavier than the aerospikes as area ratio increases.

(C) The sixteen module configurations are consistantly heavier than the eight module configuration because of the weight of the spike nozzle extension. The use of fewer turbopumps in the sixteen module configuration results in consistantly lower engine weights.
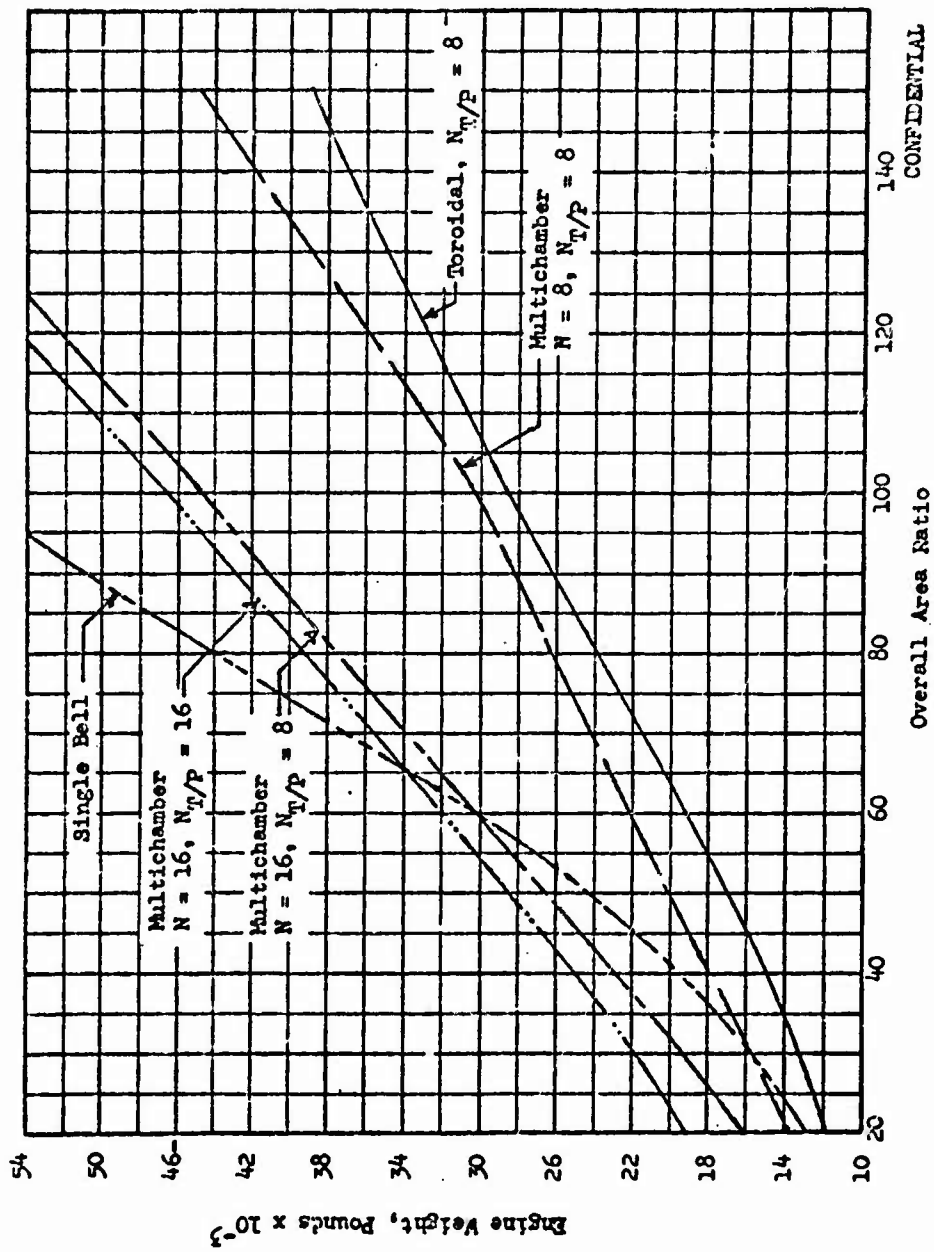
Figure 140. Engine Weight vs Area Ratio - F = 2,000,000; P_c = 1000 psia

CONFIDENTIAL
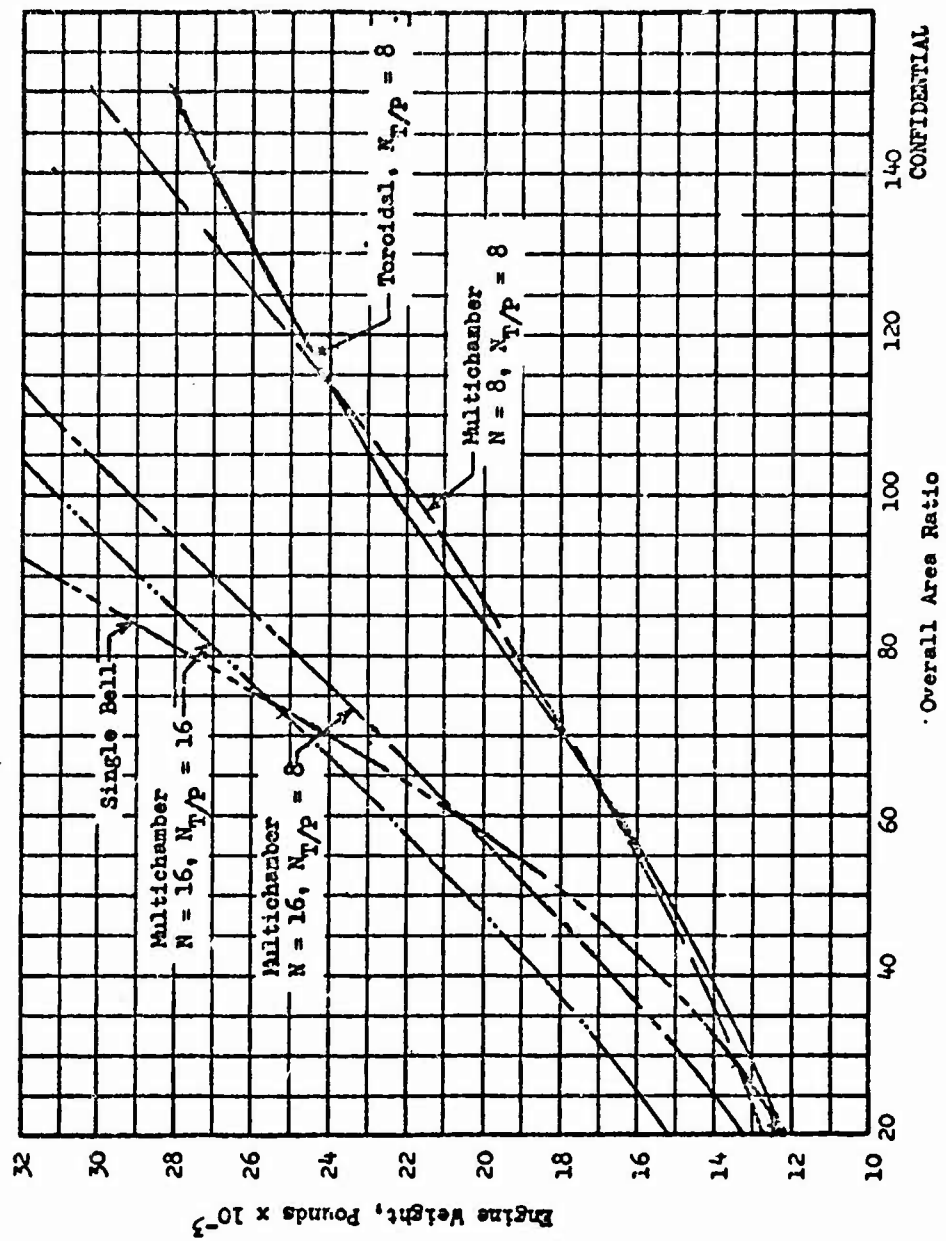
Figure 141. Engine Weight vs Area Ratio – F = 2,000,000 Pounds; P_c = 1500 psia

CONFIDENTIAL
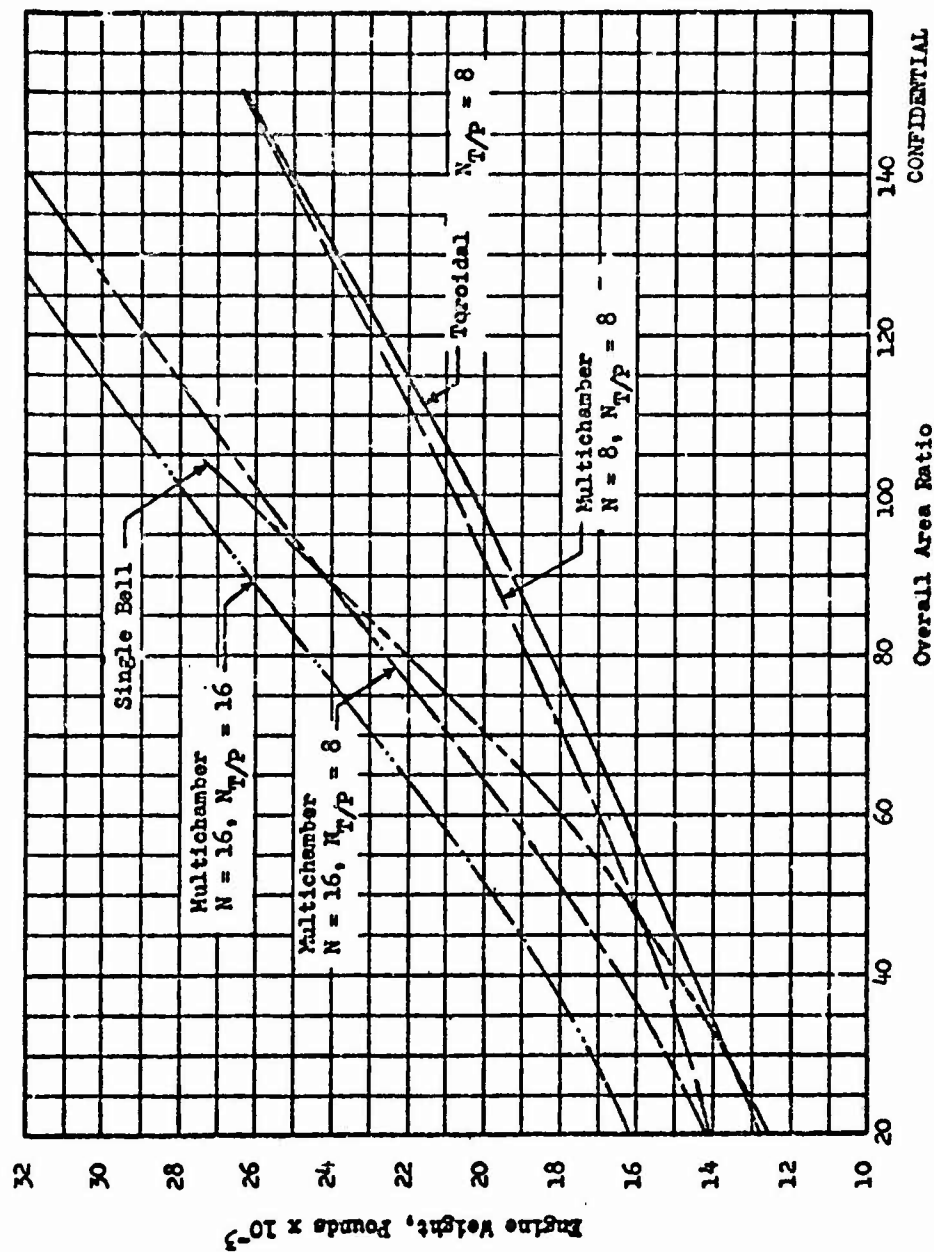
Figure 142. Engine Weight vs Area Ratio — F = 2,000,000 Pounds; P_c = 2000 psia
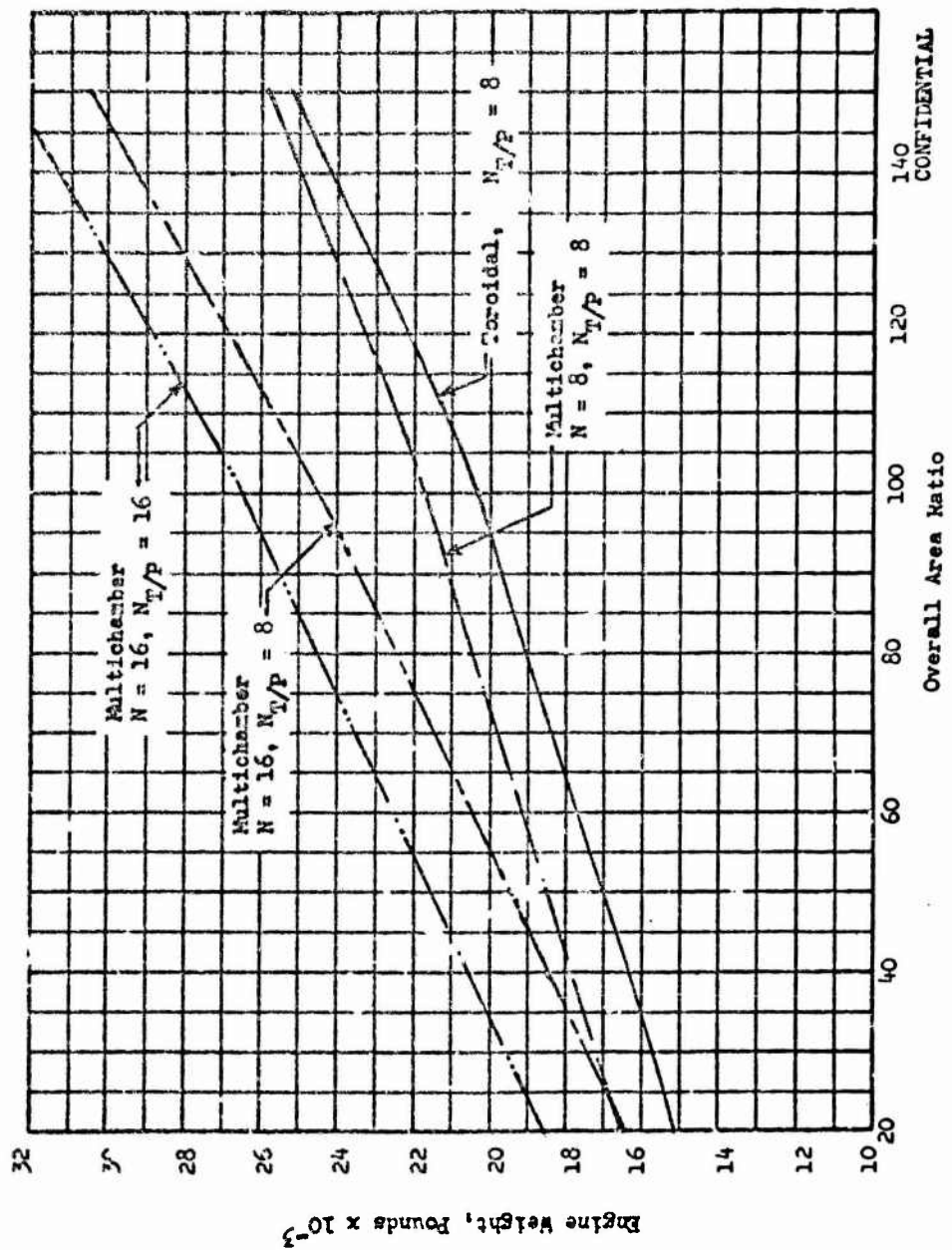
Figure 143. Engine Weight vs Area Ratio - F = 2,000,000 Pounds; P_c = 3000 psia

(C) The eight module multichamber configuration is generally slightly heavier than the toroidal configuration although in certain areas the weights of these two configurations are approximately the same.

(C) The same data is replotted vs chamber pressure in Fig. 144 and 145 for constant area ratios of 20, 50, 100, and 150. The following weight trends can be observed from this type of plot. The engine weights all tend to reach a minimum value with chamber pressure. The chamber pressure at which a minimum weight is achieved increases with increasing area ratio. The single bell engine weights are much more sensitive to chamber pressure than the other configurations at high area ratios and they also achieve a minimum weight at higher chamber pressures than the other configurations. The toroidal configuration weight appears to be the least sensitive to variations in chamber pressure.
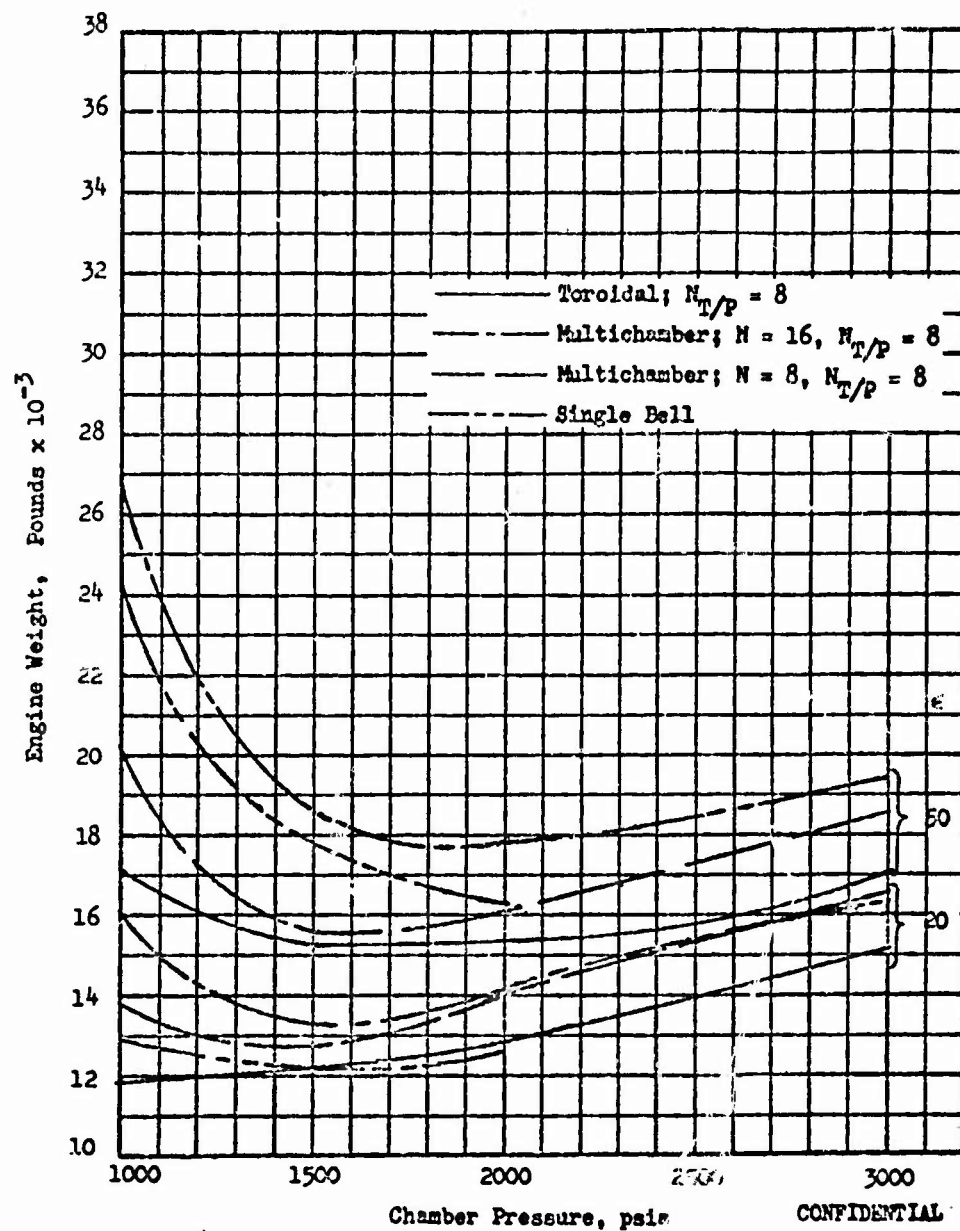
Figure 144. Engine Weight vs Chamber Pressure — ϵ = 20 and 50

251
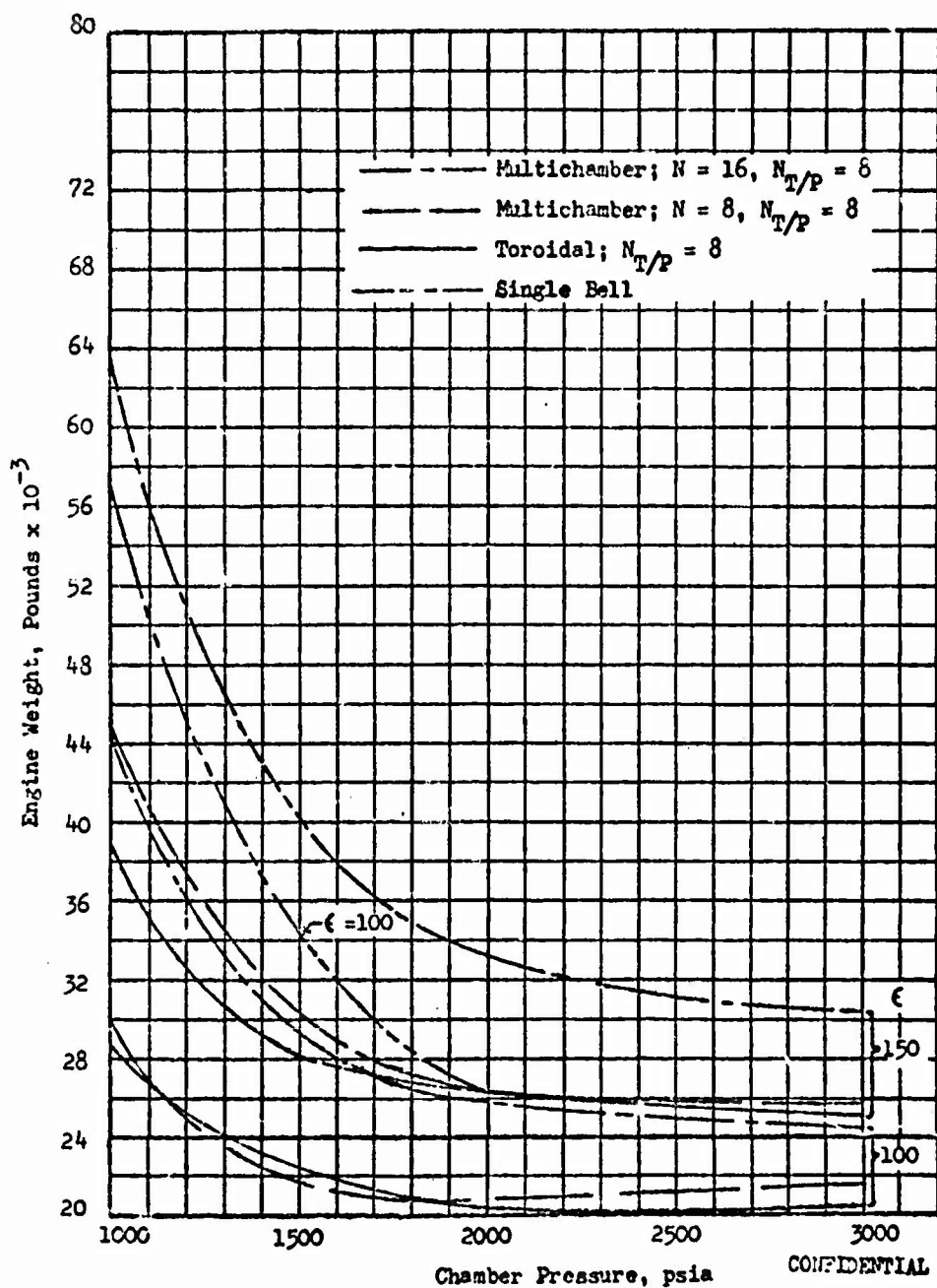
Figure 145. Engine Weight vs Chamber Pressure - ϵ = 100 and 150

HEAT TRANSFER STUDIES

(U) A primary consideration in the selection of a suitable combustor configuration for aerodynamic spike nozzles is regenerative cooling feasibility. Therefore, heat transfer studies were conducted to determine regenerative cooling limits (chamber pressure, area ratio, and thrust) for aerodynamic spike nozzles with toroidal combustion chambers and with clustered conventional chambers.

(C) The engines studied utilize the storable propellants N_2O_4 and N_2H_4-UDMH (50-50). Both propellants were considered for the coolant. The range of thrust investigated varied from 3000 pounds to 300,000 pounds for conventional single chambers and from 10,000 pounds to 2,000,000 pounds for toroidal aerospikes. Other parameters which were investigated included area ratios to 150 and chamber pressures from 300 to 3000 psia.

(U) Practical regenerative cooling limits were established by performing a numerical integration of pressure drop and bulk temperature rise along the coolant flowpath for numerous cases sufficient to cover the desired engine parameter range.

(U) The results are summarized in curves showing the variation in coolant pressure drop requirements with chamber pressure, thrust level, coolant, and (for toroidal combustors) area ratio for aerospike engines using conventional chambers and toroidal combustors.

Relative Cooling Capabilities of the Propellants

(U) Before the coolant pressure drop requirements for thrust chambers utilizing N_2O_4 and N_2H_4-UDMH (50-50) are discussed, it is helpful to analyze the cooling capabilities of the two possible coolants to better understand their characteristics under specific conditions. Therefore, a discussion of the merits of both candidate coolants is presented.

(C) The regenerative cooling capabilities of both candidate coolants depend greatly upon the coolant pressure. Below the critical pressure of N_2O_4 (approximately 1500 psia) UDMH-N_2H_4 is the superior coolant. Above its critical pressure, N_2O_4 is the better coolant. This is primarily because the heat transfer coefficient is increased (approximately doubled) by the endothermic dissociation of N_2O_4 to NO_2 at the coolant tube wall (Ref. 13).

(C) The cooling capabilities of both candidate coolants at subcritical pressures are compared in Fig. 146 Under these pressures, the coolant wall temperature must be kept approximately equal to the saturation temperature of the coolant. If the wall temperature is above the saturation temperature, bulk boiling occurs. This will cause tube burnout.

(C) The wall temperatures shown in Fig. 146 for N_2O_4 are the corresponding saturation temperatures for vapor pressures of 500 psia (T_{wc} = 660 deg. R) and 1500 psia (T_{wc} = 760 deg. R). The wall temperatures shown for
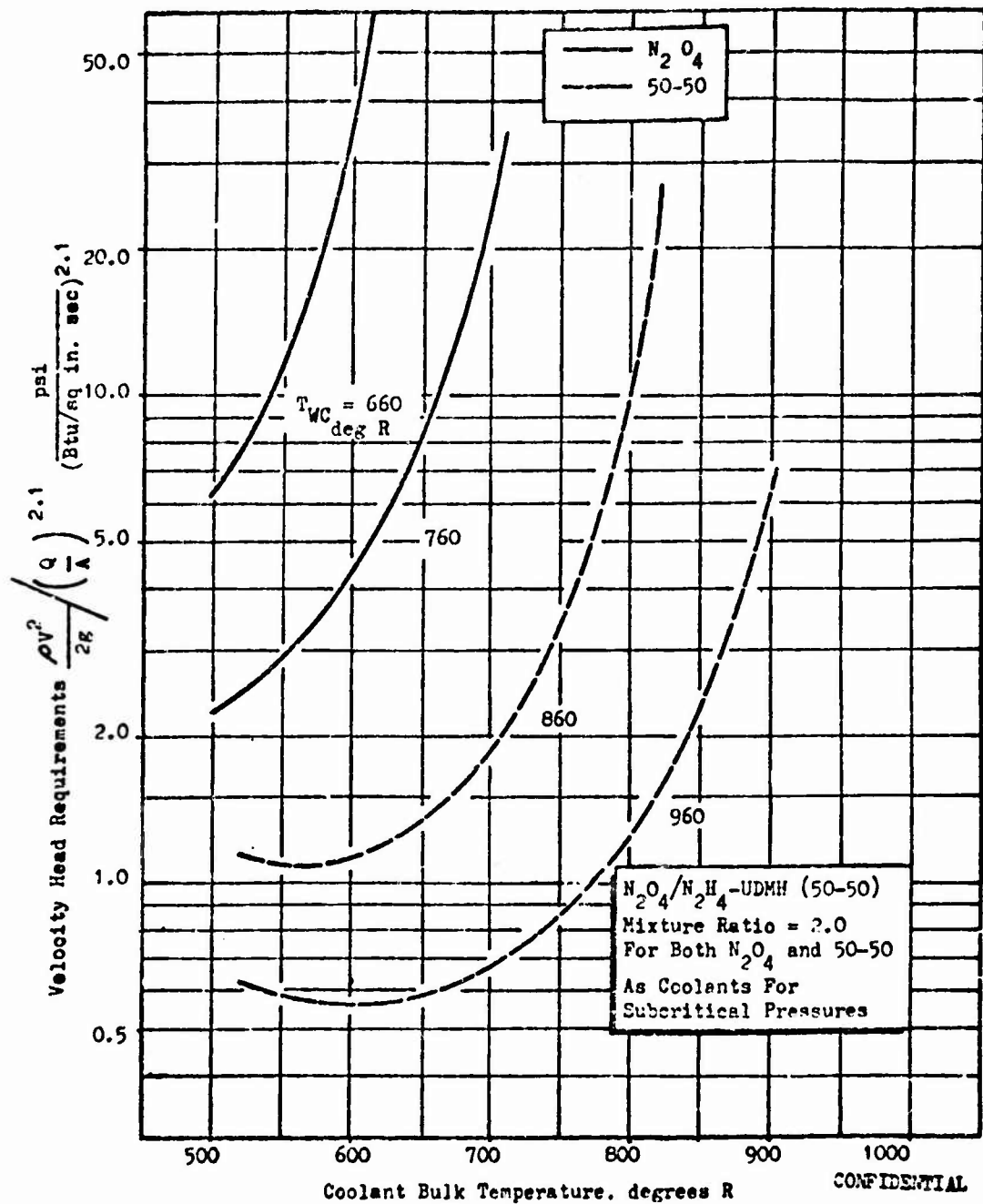
Figure 146. Coolant Velocity Head Requirements vs Coolant Bulk and Wall Temperature

N_2H_4-UDMH (50-50) are the saturation temperature for a vapor pressure of 500 psia (T_{wc} = 860 deg. R) and an experimentally determined upper allowable temperature of 500 deg. F. Above this wall temperature exothermic decomposition of the fuel can occur as reported in Ref. 14. At a vapor pressure of 1500 psia the saturation temperature of 50-50 fuel is above the 500 deg. F wall temperature limit.

(C) A small increase in N_2O_4 bulk temperature sharply increases the coolant velocity head (and pressure drop) requirement. The required velocity head increases by a factor of four when the bulk temperature increases from 500 deg. R to 650 deg. R for a coolant wall temperature of 760 deg. R. For the same vapor pressure of 500 psia and the same bulk temperature of 600 deg. R, the velocity head requirement of N_2O_4 coolant is 30 times as large as the requirement for 50-50 fuel. These results clearly indicate the superior cooling capability of 50-50 fuel at subcritical pressures.

(C) The velocity head requirements for both coolants at supercritical pressures are shown in Fig. 147. The coolant side wall temperatures of 960 deg. R for 50-50 fuel and 1060 deg. R for N_2O_4 are the maximum allowable. A 600 deg. F wall temperature limit appears necessary with N_2O_4 coolant to prevent oxidation of the tube wall. For a coolant bulk temperature range from 500 deg. R to 750 deg. R, the velocity head requirement of 50-50 fuel is approximately six times as large as the requirement for N_2O_4. Thus N_2O_4 is the superior coolant at supercritical pressures.
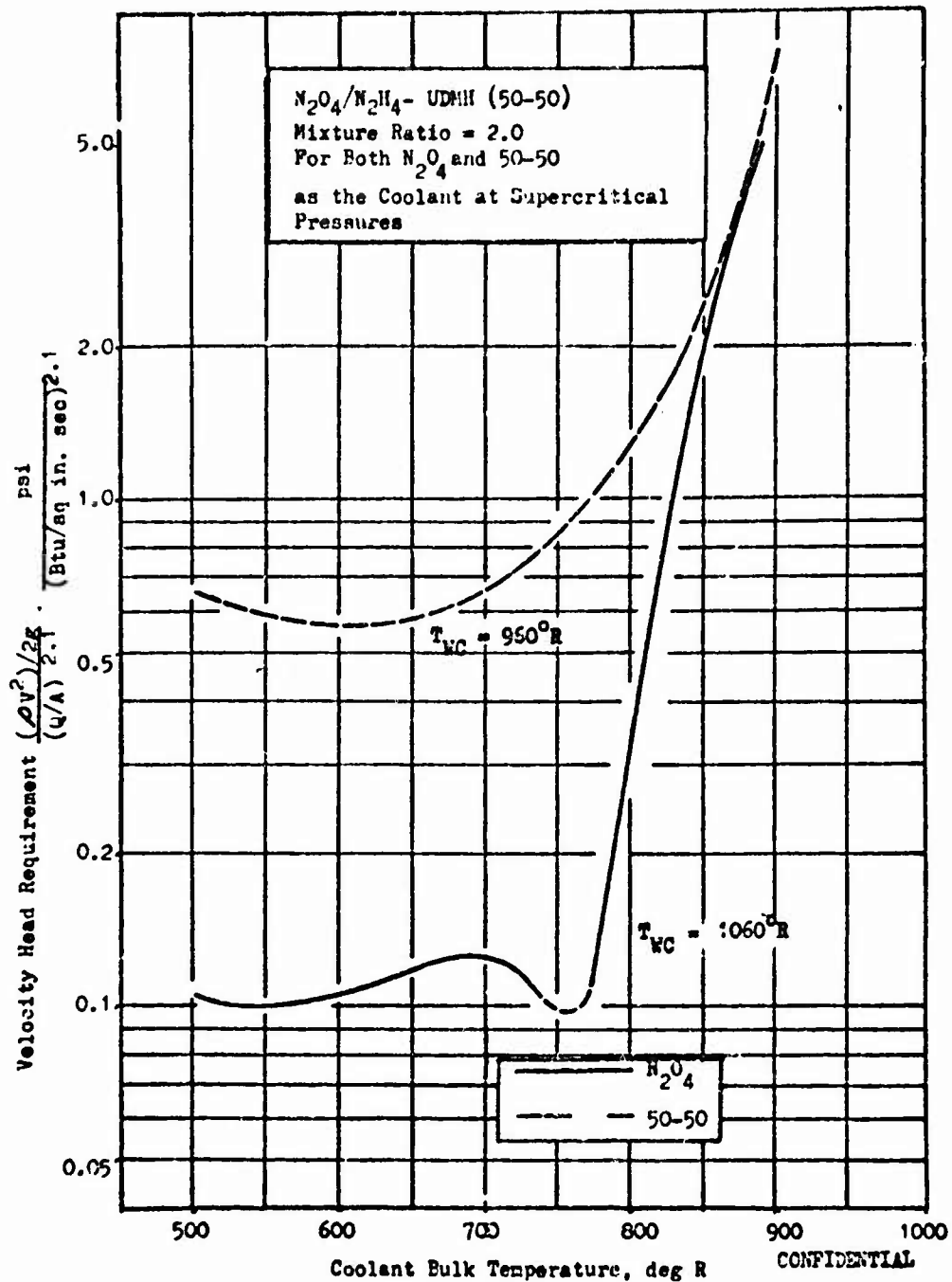
Figure 147. Coolant Velocity Head Requirements vs Coolant Bulk Temperature and Wall Temperature

Regenerative Cooling Limits for Conventional Combustors

(C) To investigate the regenerative cooling limits for multichamber
aerospikes with a total thrust range from 20,000 pounds to 2,000,000
pounds it is necessary to determine the limits for multichamber modules
of much lower thrust level. This is because conventional chambers
clustered in groups of 8 or more comprise a typical multichamber
aerospike configuration. As will be shown these modules become
increasingly difficult to cool regeneratively as the module thrust
level decreases. In this study module thrusts from 3,000 pounds to
300,000 pounds were analyzed to cover the total multichamber engine
thrust range of interest.

(C) The criterion used to judge regenerative cooling feasibility is the
coolant pressure drop. This is the most practical criterion. However,
it is the most difficult to obtain. Each case requires numerical
integration along the coolant flow path using a digital computor
program. In this analysis of conventional chambers N_2H_4-UDMH (50-50)
was used as the coolant at chamber pressures below 1500 psia and N_2O_4
was used at chamber pressures above 1500 psia. The resultant parametric
pressure drop curves and the method of analysis are discussed in the
following paragraphs.

(C) Method of Analysis. For the analysis of conventional thrust chambers
cooled with UDMH-N_2H_4 (50-50) the specific cases analyzed on the IBM
computer were thrusts of 10,000 pounds, 60,000 pounds, and 300,000 pounds
and chamber pressures of 50 psia, 150 psia, 600 psia, and 1200 psia.
The nozzles were assumed to have an area ratio of 100 but were regeneratively

cooled to area ratios of 3, 8, 30 and 30, respectively, at each of the above chamber pressures. The specific cases analyzed are listed in Table 10 .

(C) For the analysis of conventional chambers with N_2O_4 cooling, the operating ranges were chamber pressure from 1500 psia to 3000 psia and engine thrust levels from 3,000 pounds to 300,000 pounds. The nozzles were assumed to be entirely regeneratively cooled with an area ratio of 100. The specific cases analyzed are tabulated in Table 11 .

(C) The thrust chamber utilizes N_2O_4/ UDMH-N_2H_4 (50-50) propellants at a mixture ratio of 2.0. Frozen equilibrium C* performance (100 percent of theoretical) and a nozzle thrust coefficient of 1.8 were assumed. A single downpass coolant circuit was used to obtain the lowest coolant pressure drop conditions.

(U) The local heat flux Q/A which must be dissipated through the chamber wall is given by

$$Q/A = h_g \ (T_{AW} - T_{WG})$$

(C) The gas side film coefficient h_g was determined by the simplified Bartz equation

$$h_g = \frac{0.026}{d_H^{0.2}} \ G^{0.8} \ \frac{C_p \mu^{0.2}}{N_{Pr}^{0.6}} \ \sigma$$

where

$$\sigma = \left[\frac{1}{2} \left[\frac{T_{WG}}{T_{AW}} \right] \left[1 + \frac{\gamma-1}{2} M^2 \right] + \frac{1}{2} \right]^{-0.68} \left[1 + \frac{\gamma-1}{2} M^2 \right]^{-0.12}$$

CONFIDENTIAL

TABLE 10.

SUMMARY OF REGENERATIVE COOLING OF BELL CHAMBERS WITH UDMH-N$_2$H$_4$ (50-50)

Thrust 1000 pounds	Chamber Pressure, psia	Contraction Ratio	Regeneratively Cooled Area Ratio	Number of Tubes	Maximum Coolant Velocity (ft/sec)	Number of Tube Splices	T$_{WC}$ Maximum deg. F	Pressure Drop / Chamber Pressure
10	600	3.0	30	400	275	2	500	4.40
	50	2.0	3	1200	86	0	295	0.50
60	1200	2.0	30	350	387	1	500	2.40
	600	2.0	30	400	189	1	500	1.05
	150	2.0	8	750	90	1	340	0.31
	50	2.0	3	1100	40	0	295	0.02
300	1200	2.0	30	400	294	1	500	1.01
	600	2.0	30	450	152	1	500	0.51
	150	2.0	8	1000	74	0	340	0.15
	50	2.0	3	1200	33	0	295	0.01

TABLE 11

SUMMARY OF REGENERATIVE COOLING OF BELL CHAMBERS WITH N_2O_4 AT SUPERCRITICAL PRESSURE

Thrust, 1000 pounds	Chamber Pressure, P_c psia	Contraction Ratio, ε_c	Combustor Length, inches	Number of Tubes	$(Q/A)_{max}$ $\frac{Btu}{in^2 sec}$	Maximum Coolant Velocity (ft/sec)	Coolant Tube Pressure Drop ΔP (psi)	Bulk Temperature Rise ΔT (deg F)
3	1500	9	6.1	150	35.6	640	2267	328
10	1600	6	8.5	140	33.8	260	469	281
	1750	6	8.4	200	36.6	700	3142	285
50	1900	4	12.1	150	34.0	240	305	234
	2050	4	12.0	200	36.4	460	841	240
	2100	4	12.0	210	37.2	640	1478	243
	2150	4	11.9	250	38.0	970	3958	265
300	2300	3	16.6	200	34.0	210	662	192
	2500	3	16.4	250	36.6	380	1535	195
	2600	3	16.4	280	38.0	600	2940	199

261

and is, simply stated, a function of the properties of the combustion products and the local mass velocity. The adiabatic wall temperature T_{AW} is relatively invariant throughout the nozzle and is nearly equal to the combustion temperature. It is relatively insensitive to all chamber operating conditions except mixture ratio. The gas side wall temperature T_{WG} is a variable dependent upon the maximum operating temperature which a selected tube wall material can sustain while maintaining a satisfactory strength. For this analysis inconel X and 347 stainless steel were used for chambers cooled with fuel and oxidizer, respectively. The maximum useful wall temperature T_{WG} used for these materials was 1600 deg F.

(C) Typical peak heat fluxes encountered at the throat of conventional chambers and continuous annular throat toroidal combustors are shown in Fig. 148. These curves were computed assuming a T_{WG} equal to 1600 deg F and using the equations above for h_g and Q/A. When considering a conventional chamber δ_T is the throat radius, while δ_T is the throat gap for a continuous annular throat toroidal combustor. δ_T may be computed from

$$\delta_{T_{Bell}} = \sqrt{\frac{A_T}{\pi}}$$

$$\delta_{T_{annular}} = \sqrt{\frac{A_T}{4\pi\epsilon}}$$

Most practical applications are within the range of δ_T shown.

(C) For steady state heat conduction the heat flux conducted through the tube wall satisfies the relationship

$$Q/A = \frac{k}{X}(T_{WG} - T_{WC})$$
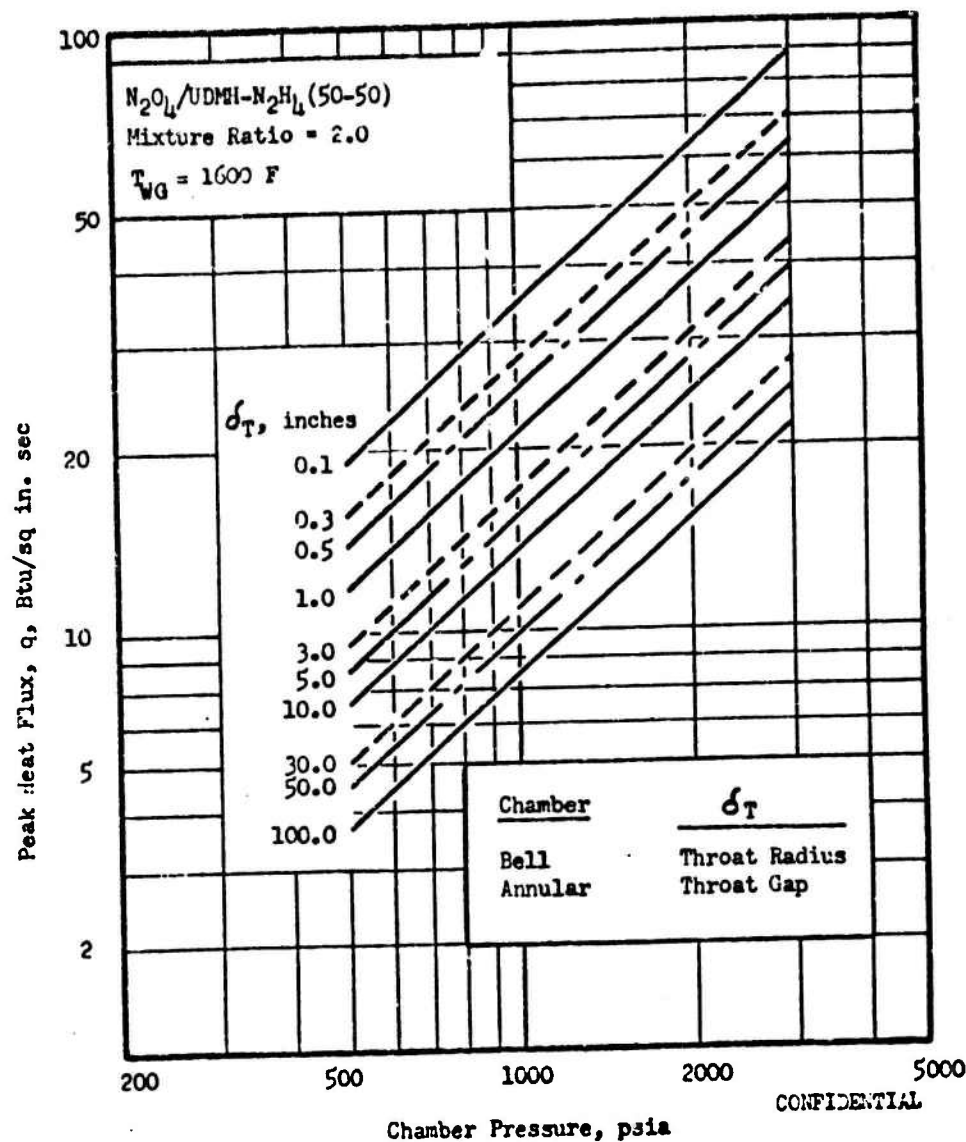
Figure 148. Peak Heat Fluxes for Bell Nozzles and Continuous Annular
Throat Toroidal Combustor

263

where k and X are the material thermal conductivity and wall thickness, respectively, and T_{WC} is the coolant side wall temperature. For this analysis a wall thickness (inconel X) of .012 inch and a maximum coolant side wall temperature of 500 deg. F were assumed with fuel coolant. For chambers cooled with H_2O_4 a wall thickness (347 stainless steel) of 0.01 inch and a maximum coolant side wall temperature of 600 deg. F was used.

(C) Figure 149 shows the maximum heat flux that can be passed through a tube wall. By imposing the maximum possible temperature differential across a given material, the maximum possible heat flux is determined as a function of wall thickness. The results are shown for three selected materials; 347 stainless steel, inconel X, and a molybdenum alloy T2M. Stainless steel and inconel X are materials with a maximum useful temperature of approximately 1600 deg. F. The working temperature of T2M was also assumed to be 1600 deg. F for comparative purposes although its maximum allowable temperature is approximately 2500 deg. F. From the graph the merits of a refractory material can be easily realized.

(C) For a practical tube wall thickness of 0.01 inch, the maximum heat flux which can be passed through a 347 stainless steel tube wall is 41 Btu/sq. in. sec. For 0.012 inch inconel X tubing a peak heat flux of 41 Btu/sq. in. sec. can be passed through the wall. In certain applications where tubing strength is a factor, inconel X is preferable to 347 stainless steel because its strength is much greater.

(C) The local heat flux is absorbed entirely by the coolant according to the following expression which must be satisfied simultaneously with the previous two steady state expressions

$$Q/A = h_c (T_{WC} - T_{BC})$$
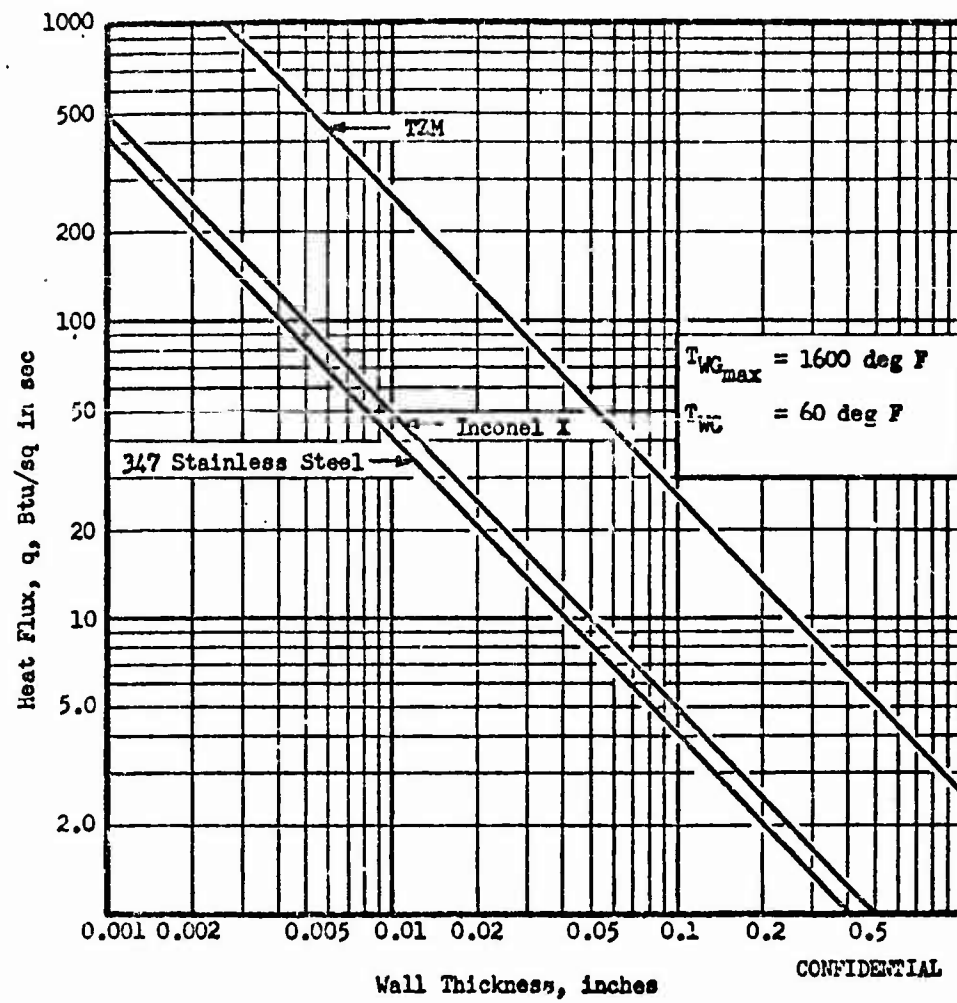
Figure 149. Heat Conduction Limits of Various Materials

where T_{BC} is the coolant bulk temperature and the coolant side film coefficient h_c is computed from an empirical correlation of experimental data developed at Rocketdyne.

$$N_{Nu} = \frac{h_c D}{k} = 0.005 \; Re^{0.95} \; Pr^{0.4} \; \varphi$$

(C) The enhancement factor φ is used for N_2O_4 cooling at supercritical pressure to account for the large increase in its cooling capacity caused by the endothermic dissociation of N_2O_4 to NO_2 at the tube wall.

(C) The relationships described above are programmed for machine computation. The three equations describing the heat flux are solved simultaneously at numerous stations along the thrust chamber using imposed restrictions such as maximum T_{WG}, tube thickness, maximum T_{WC}, etc. Coolant bulk temperature rise, velocity and pressure drop are computed at the same stations and, where applicable, numerically integrated. The cooling feasibility curves discussed in the following paragraphs were generated using this computor program.

(C) Results. The coolant jacket pressure drop with N_2O_4 coolant at supercritical pressures is shown as a function of chamber pressure in Fig. 150. The sharp inflection of the curves clearly defines the maximum feasible operating chamber pressure within a narrow band for a given thrust level. The smallest engine which was regeneratively cooled was approximately 3000 pounds thrust with a maximum chamber pressure limit of 1500 psia. For the maximum thrust level considered of 300,000 pounds, the limiting chamber pressure was approximately 2650 psia. For the intermediate thrust levels of 10,000 pounds and 50,000 pounds, the limiting chamber pressures were approximately 1750 psia and 2150 psia respectively.
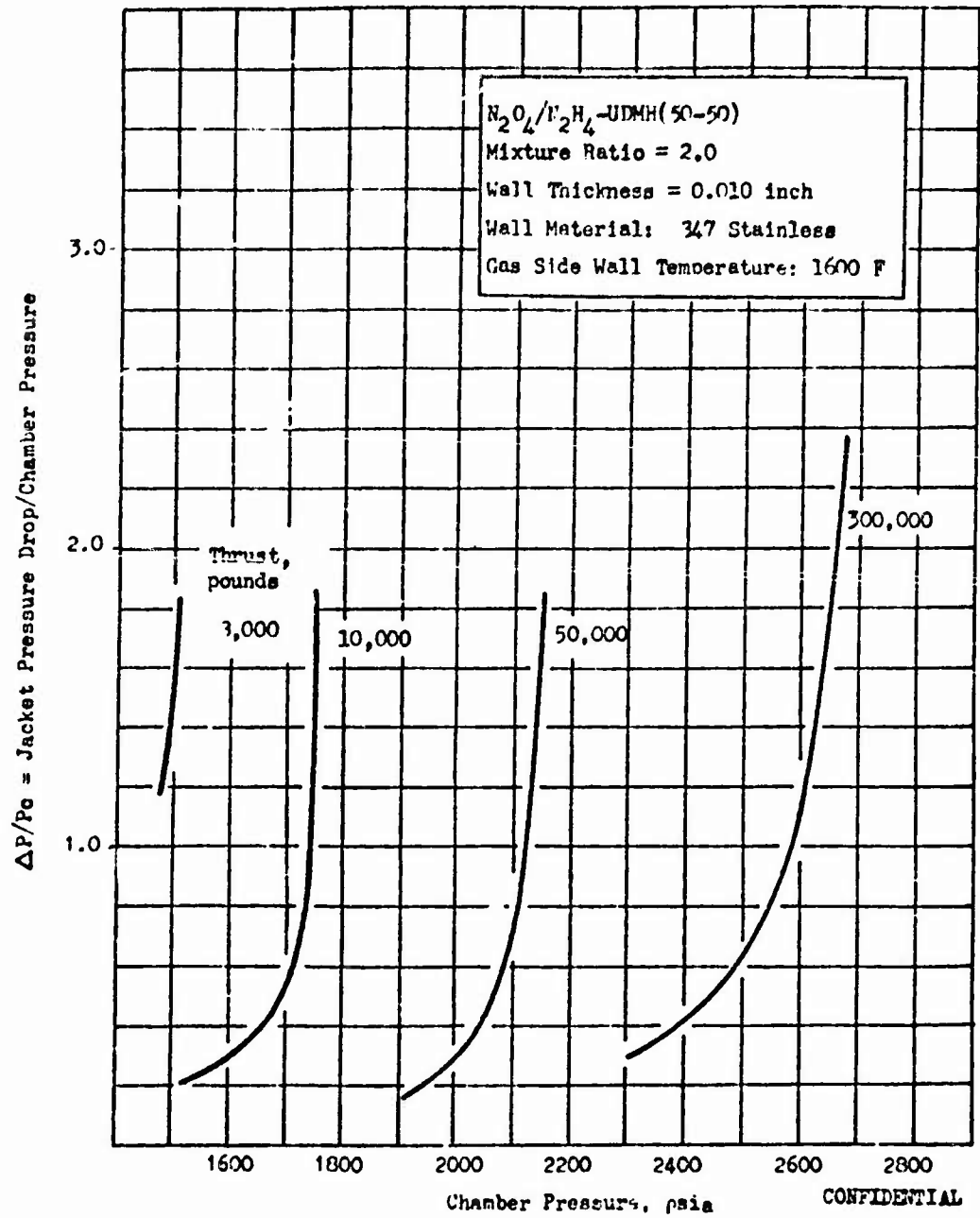
Figure 150. Tube Bundle Pressure Drop vs Chamber Pressure
for Bell Thrust Chamber Using N_2O_4 Coolant

267

(C) The data is replotted in Fig. 151 showing the limiting chamber pressure vs thrust level with ratio of tube pressure drop to chamber pressure as a parameter. Since a very small gain in the maximum operating chamber pressure limit (100 psi to 200 psi) is experienced by increasing the $\Delta P/P_c$ from 0.4 to 1.3 it is more likely that the lower limit curve would be used in an actual engine application.

(C) For use in a multichamber aerodynamic spike nozzle application over a thrust range from 20,000 to 2,000,000 pounds a cluster of 8 chambers would have in..vidual thrusts of from 2500 to 250,000 pounds. The curves indicate that regenerative cooling with N_2O_4 above its critical pressure is feasible for conventional thrust chambers in this thrust range. Extrapolation of the $\Delta P/P_c = 0.4$ curve to 2500 pounds thrust shows a maximum chamber pressure of approximately 1350 psia. The same curve indicates a maximum chamber pressure of approximately 2375 psia for a 250,000 pound thrust engine. A cluster of 16 engines with a total thrust of 2,000,000 pounds and an individual engine thrust of 125,000 pounds has a maximum chamber pressure limit of approximately 2200 psia. Thus for the same total thrust level the use of a larger number of clustered engines will reduce the maximum engine operating pressure a significant amount.

(C) The coolant pressure drop with UDMH-N_2H_4 (50-50) coolant is shown as a function of chamber pressure in Fig. 152. It can be seen that the pressure drop requirements increase gradually over a wide range of chamber pressure making it rather difficult to select a distinct maximum operating chamber pressure. If an arbitrary $\Delta P/P_c$ limit of 2.0 (which is far in excess of the normal design value) is assumed then maximum chamber pressure for thrusts of 10,000 pounds, 60,000 pounds and 300,000 pounds are 250 psia, 1200 psia, and 2000 psia, respectively.

(C) The data are replotted in terms of maximum chamber pressure as a function of thrust level in Fig. 153. Using the $\Delta P/P_c = 2.0$ curve for a module thrust of 2500 pounds an eight-module, fuel cooled, multichamber configuration
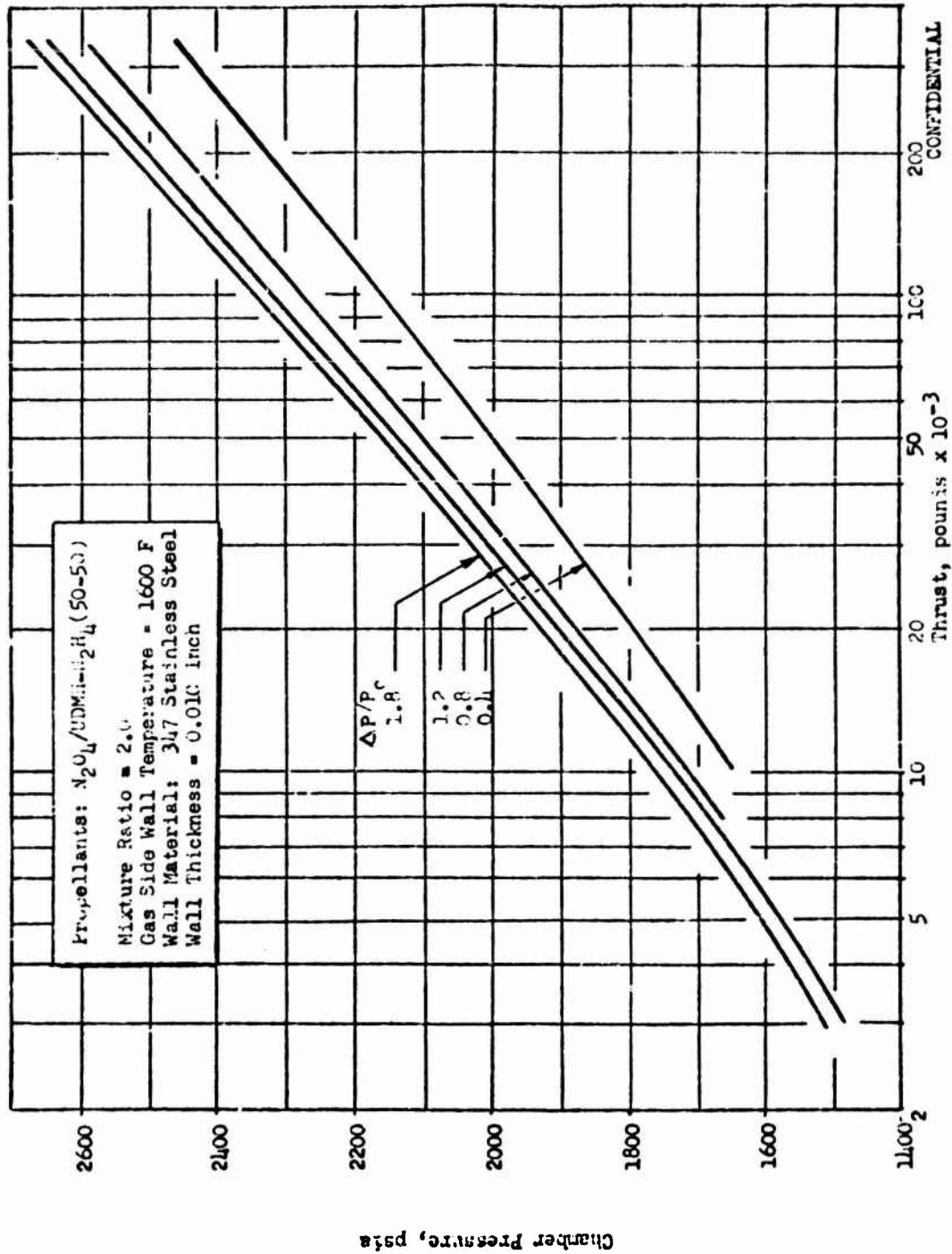
Figure 151. Regenerative Cooling Limits for Bell Thrust Chambers, Using N_2O_4 Coolant
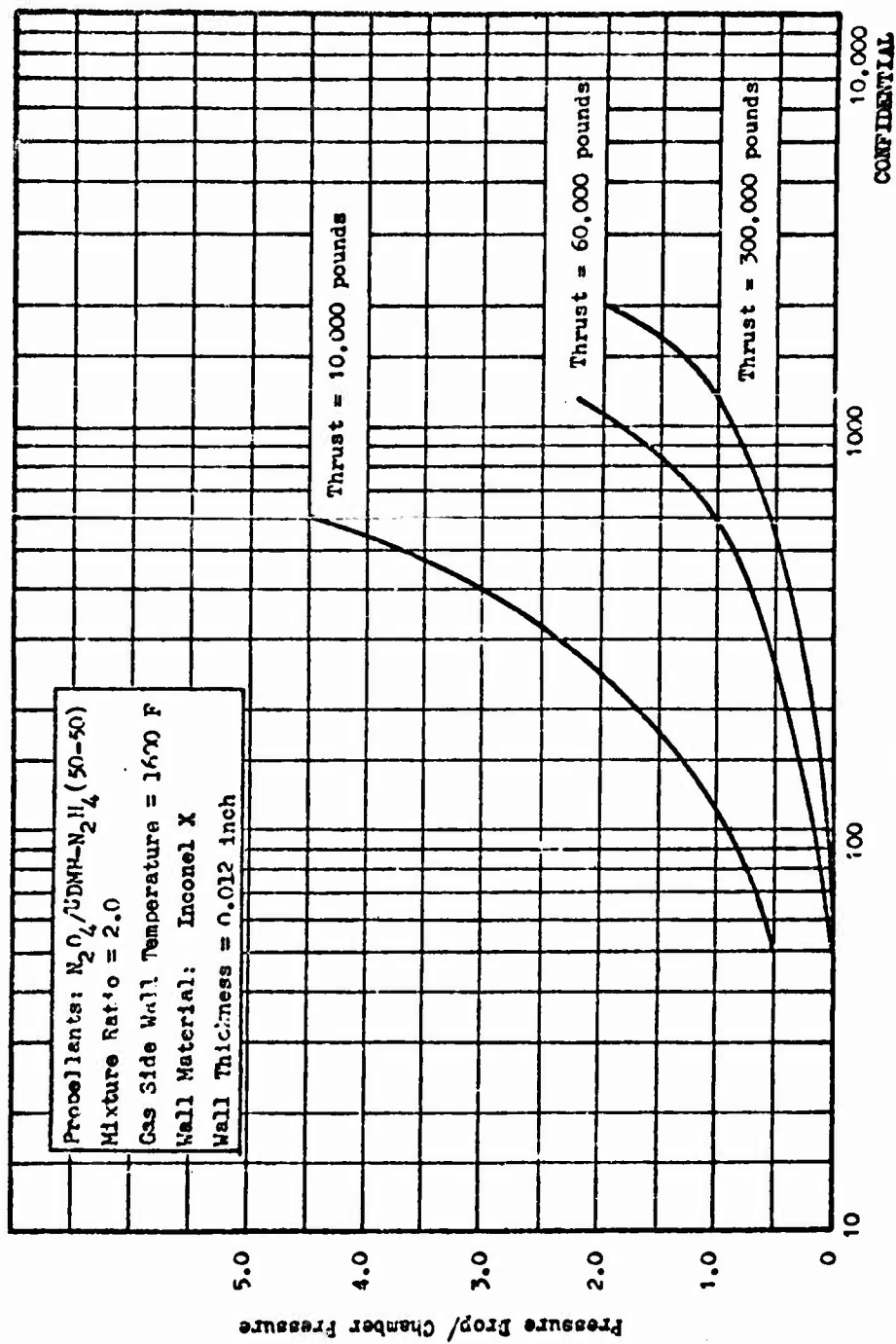
Figure 152. Pressure Drop/Chamber Pressure vs Chamber Pressure for Bell Thrust Chambers Using UDMH-N_2H_4 (50-50) as Coolant
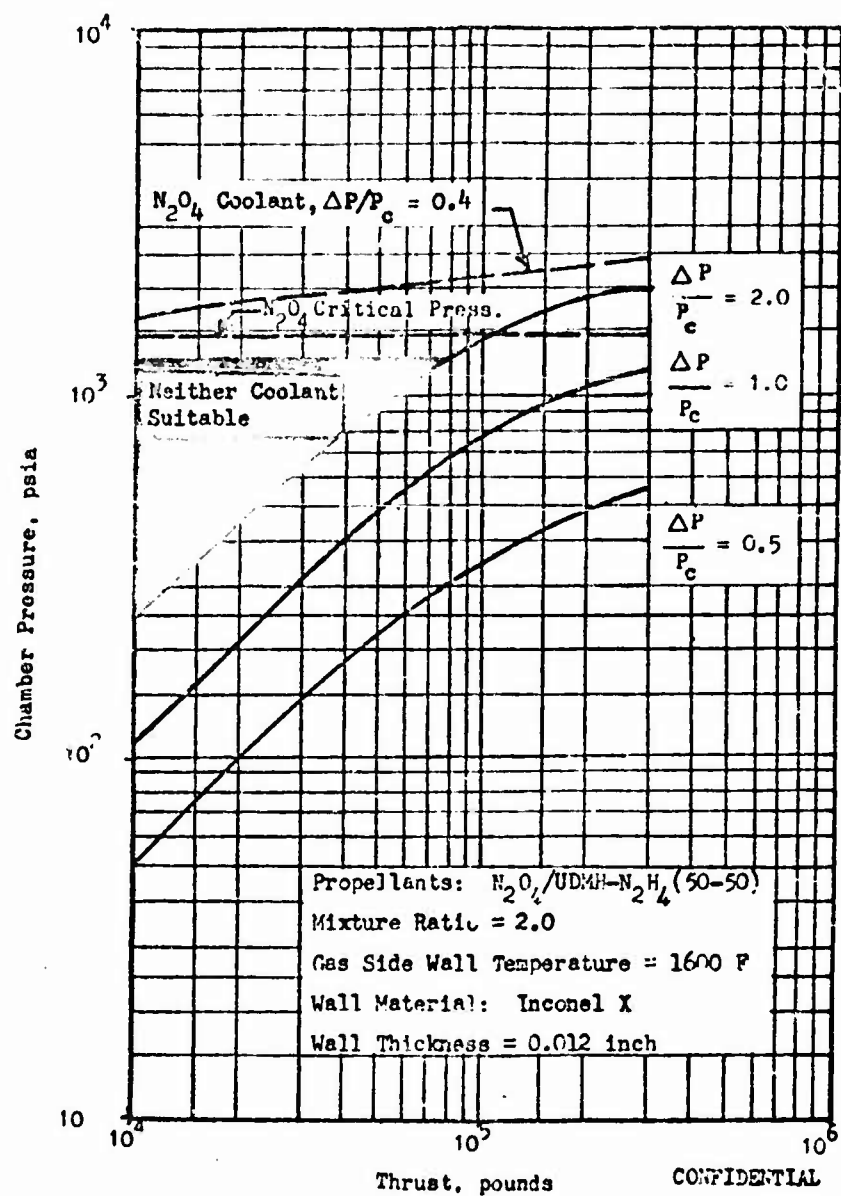
Figure 153. Regenerative Cooling Feasibility Limits for Bell Thrust Chambers Using UDMH - N_2H_4 (50-50) as Coolant

271

would have a maximum chamber pressure of approximately 70 psia. With N_2O_4 coolant at supercritical pressure this same module size could operate at 1350 psia with a $\Delta P/P_c = 0.4$. At this thrust level there is therefore a large range of chamber pressure (approximately 70 to 1250 psia) over which neither coolant is satisfactory. This occurs because cooling with N_2O_4 at subcritical pressure results in tube pressure drops higher than with fuel coolant and cooling with supercritical N_2O_4 requires that the coolant exit the tubes at approximately 1500 psia, regardless of the chamber pressure. Since a nominal injector pressure drop is 10 to 20 percent of the chamber pressure, the excess of the tube exit pressure over the required injector inlet pressure is wasted. From Fig. 153 it appears that this awkward region (between $P_c = 1250$ psia and the $\Delta P/P_c = 2$ curve) where neither coolant is entirely satisfactory at intermediate chamber pressures extends to a module thrust level of approximately 80,000 pounds or an eight-module multichamber thrust level of 640,000 pounds. The range of undesirable chamber pressures decreases, however, as the thrust level increases.

(C) The maximum chamber pressure with fuel cooling for an eight-module multichamber configuration of 2,000,000 pounds thrust is approximately 2,000 psia ($\Delta P/P_c = 2.0$ curve) compared to approximately 2400 psia for chambers cooled with N_2O_4.

Regenerative Cooling Limits for Toroidal Combustors

(C) Maximum chamber pressure limits with full regenerative cooling were determined for aerodynamic spike thrust chambers using a toroidal type chamber construction. Machine computation of pressure drops and bulk temperature rise were conducted assuming a continuous annular throat configuration. The results also represent upper limits for other types of toroidal chamber construction such as the subsonic tube and the sonic tube shown in Fig. 121.

272

The chambers were analyzed using UDMH-N_2H_4 (50-50) coolant and N_2O_4 coolant at both subcritical and supercritical pressure. The results are presented in parametric curves of maximum chamber pressure as a function of the ratio of engine thrust to engine diameter and of area ratio.

(C) Method of Analysis. The method of analysis for toroidal chambers is similar to that described for the conventional chamber with one major difference. A boundary layer approach (Ref. 15 and 16) was employed to calculate the gas side convective coefficients of the annular nozzles.

(C) The conventional tube material selected for the study was 347 stainless steel with a tube thickness of 0.010 inch. The material was assumed to have a maximum allowable temperature of 1600 deg. F. The hoop radius of the combustion chamber was three inches with the engine having an ϵ equal to 100 and a 20-percent length nozzle. For the overall area ratio, a thrust coefficient of 1.8 was assumed.

(C) At the subcritical pressures, the coolant-side wall temperature was assumed equal to the saturation temperature. This saturation temperature is determined by the allowable coolant vapor pressure. The coolant vapor pressure must be less than the coolant static pressure to prevent a bulk boiling condition. Above the critical pressure, the coolant-side wall temperature was taken as 500 deg. F for 50-50 fuel. Above this temperature, the capability of 50-50 fuel was found to be limited because of tube failure apparently caused by rapid thermal decomposition at the wall. With N_2O_4 as the coolant, the limiting wall temperature was 600 deg. F. Above this wall temperature, oxidation occurs which limits the cooling design. As the chamber pressure is increased from the critical pressures for either coolant, the coolant wall temperature is forced down because of the limitation placed on the gas side wall temperature. When the coolant wall temperature is decreased, the weight flow requirement per tube increases. In

order to meet the weight flow requirement per tube, multiple-pass cooling circuits were necessary. The number of passes varied for the different operating conditions that were analyzed.

(C) A multipass configuration is illustrated in Fig. 154 . The coolant flow circuit begins at the injector, proceeds to the nozzle skirt exit, and continues back through another set of tubes to the injector. This consittutes a 2-pass cooling circuit. For other cooling circuits, the pattern will be similar but with more passes.

(C) A similar-type cooling circuit was assumed for the shroud part of the toroidal thrust chamber. The total coolant flowrate was split, half of it cooling the nozzle part of the thrust chamber and the other half cooling the shroud part. It was assumed that the pressure drop and temperature rise were the same in either section.

(C) The pressure drop evaluation was conducted for continuous annular throat toroidal thrust chambers only. Similar computations to include configurations such as the segmented annular throat toroidal chamber, the subsonic toroidal chamber, and the sonic toroidal chamber were not done. However, the limits established by the present study are also applicable as upper limits for the other toroidal combustors. Each of the previously mentioned design configurations have more surface area which must be cooled than its counterpart continuous-throat annular chamber. Thus it would be expected that the former designs will require higher pressure drops and bulk temperature rises.

(C) The study was conducted for engines with a combustor hoop radius of three and an area ratio of 100. But the results are applicable to other hoop dimensions and area ratios. The total heat input in the combustor varies slightly with combustor hoop radius. Thus, the pressure drop is approximately

Shroud Portion

Coolant Flow
Circuit

Second Pass

Nozzle Portion

First Pass
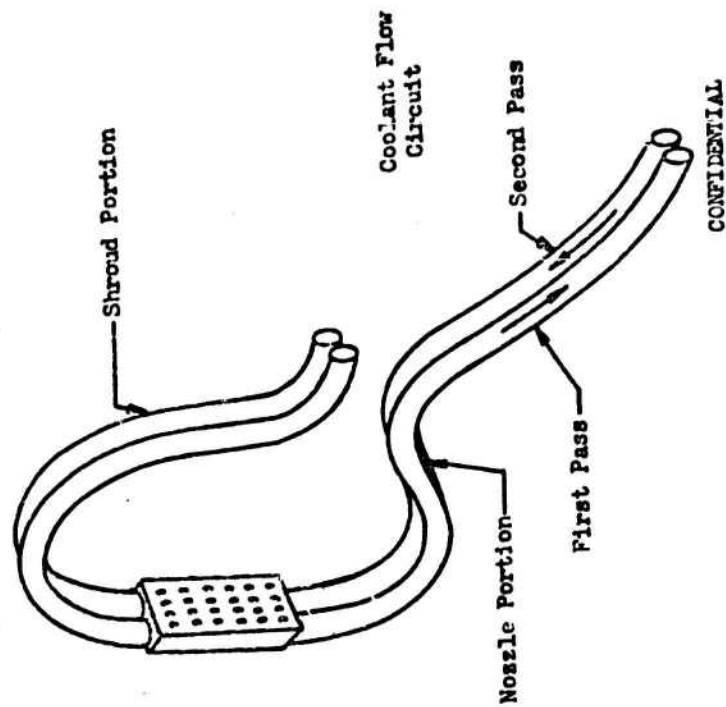
CONFIDENTIAL

Figure 154. Toroidal Combustor

275

the same. For the annular engine the heating conditions at a given chamber pressure normalize as a function of engine thrust to annular throat diameter F/D. From the simplified relationships below for a continuous throat toroidal aerospike it can be seen that specifying the thrust and throat diameter determines the throat gap and area ratio at a given chamber pressure.

$$F = P_c A_t C_F = P_o C_F \pi \delta_T D$$

$$\epsilon = A_e/A_t = D/4 \, \delta_T$$

$$F/D = P_c C_F \pi D/4 \epsilon$$

(C) <u>Results.</u> Pressure drop and gas side wall temperature limit curves for UDMH-N_2H_4 (50-50) and N_2O_4 as coolants are shown in Figs. 155 and 156 . The values are plotted as a function of chamber pressure and the ratio of thrust to engine diameter. The region to the left of the lines of constant T_{WC} is unfeasible since the lines represent a condition where T_{WB} equals T_{WC}. The limit lines of constant T_{WG} also represent a condition where the coolant bulk temperature equals the coolant side wall which in turn assumes an infinite coolant velocity and pressure drop. The limit lines based upon constant values of $\Delta P/P_c$ are more realistic since they show the practical limitations of coolant pressure drop based upon detailed analysis of the engine coolant circuit.

(C) It can be seen that the $\Delta P/P_c$ limit curves correspond closely to the T_{WG} and T_{WC} limit curves for N_2O_4 cooling at supercritical pressures but are considerably below the T_{WG} and T_{WC} limit curves for cooling with fuel and N_2O_4 at subcritical pressure. This is because the velocity head requirement for N_2O_4 above its critical pressure is almost constant for a considerable range of bulk temperature values (Fig. 147) whereas it is not for fuel and N_2O_4 at subcritical pressures (Fig. 146).

276

Figure 155. Cooling Feasibility Limits and Pressure Drops for Continuous
Annular Throat Toroidal Combustors Using N_2H_4-UDMH as Coolant

277
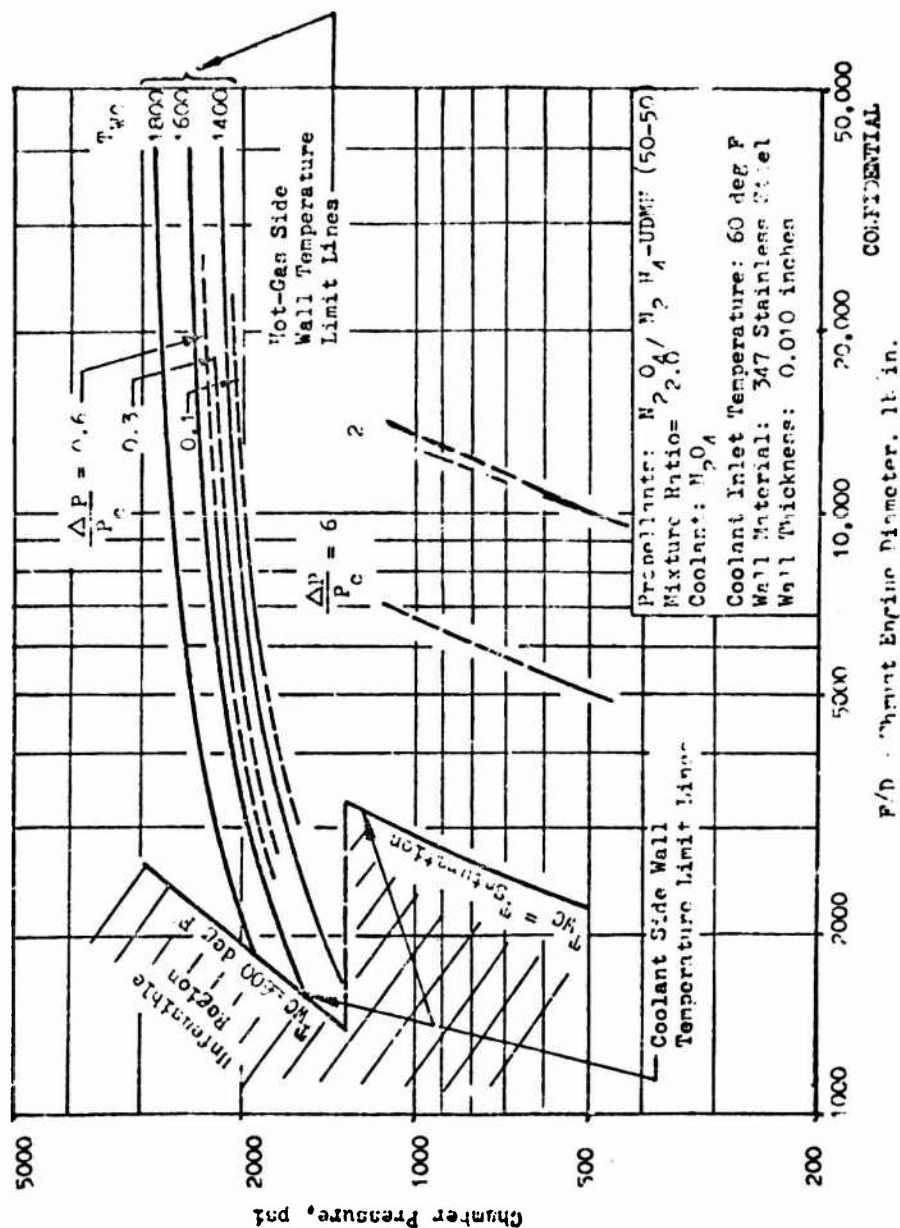
Figure 156. Cooling Feasibility Limits and Pressure Drops for Continuous Annular Throat Toroidal Combustors Using N_2O_4 as Coolant

278

(C) The pressure drop limit curves are replotted in more recognizable terms in Figs. 157 and 158. Figures 157 and 158 show the maximum area ratio as a function of chamber pressure for thrust levels from 10,000 pounds to 2,000,000 pounds. The limit curves for fuel coolant are based upon a $\Delta P/P_c$ value of 2.0. The limit curves for N_2O_4 coolant at subcritical and supercritical pressures are based upon constant $\Delta P/P_c$ values of 2.0 and 0.6 respectively. It should be noted that the bell chamber limit curves were essentially independent of area ratio while the limiting chamber pressure for annular nozzles is a strong function of area ratio.

(C) For both fuel and oxidizer coolant the curves in Figs. 157 and 158 show similar trends. As the thrust level decreases the range of area ratios and chamber pressures which can be regeneratively cooled decreases. For an engine thrust level of 20,000 pounds and intermediate chamber pressures of 300 to approximately 1250 psia, cooling with N_2O_4 below its critical pressure is not feasible while fuel coolant is feasible only to area ratios of approximately 5. However extrapolation and interpolation of the limit curves for supercritical N_2O_4 to 1250 psia chamber pressure and 20,000 pounds thrust indicates that an area ratio of approximately 30 may be regeneratively cooled. This is similar to the situation encountered for conventional chambers of low thrust level.

(C) For the upper thrust level of interest, 2,000,000 pounds, the chamber pressure limit for a nominal area ratio of 40 is approximately 1800 psia with fuel coolant and approximately 2275 for N_2O_4 coolant. These values are comparable with the eight-module 2,000,000 pound thrust multichamber limits of 2000 psia and 2400 psia for fuel and oxidizer coolants, respectively.
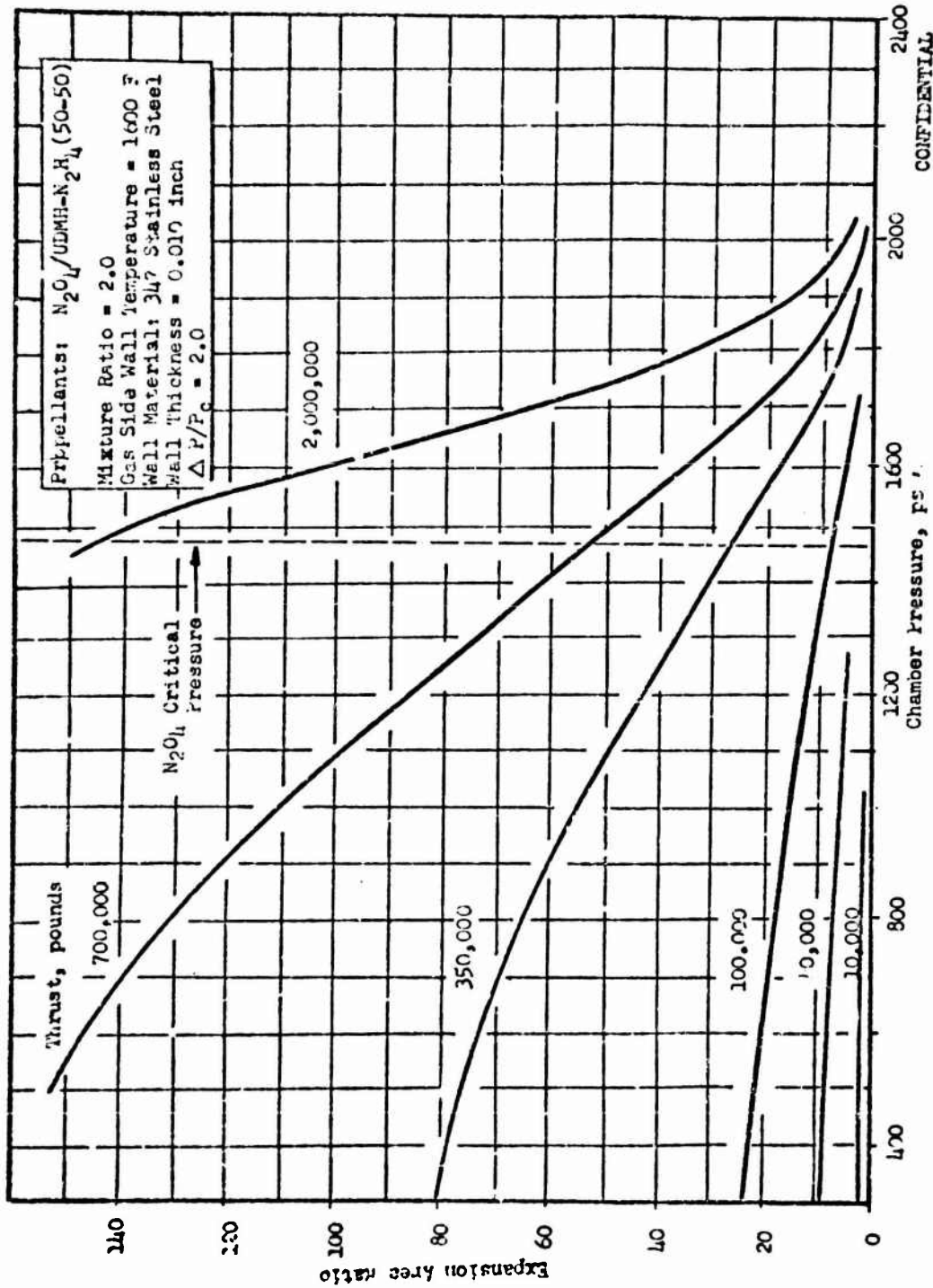
Figure 157. Regenerative Cooling Limits for Continuous Throat Toroidal Combustors Using UDMH-N2H4 (50-50) as Coolant

280
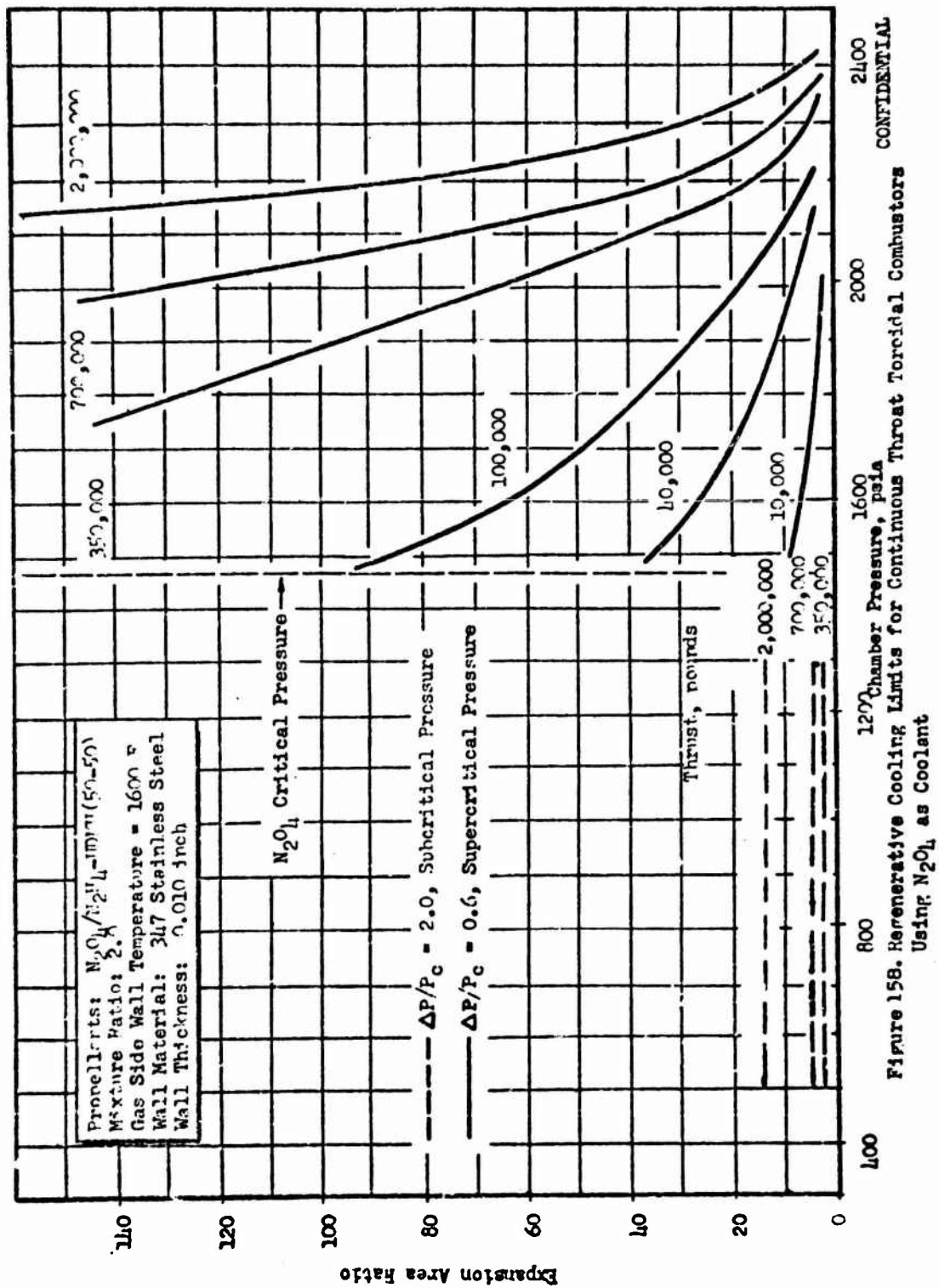
Figure 158. Regenerative Cooling Limits for Continuous Throat Toroidal Combustors Using N_2O_4 as Coolant

Alternate Design Techniques

(C) The effort in this study concentrated on establishing regenerative cooling limits for aerospike combustors using conventional materials. It should be noted however that the region of applicability of these combustor concepts can be extended by alternate design techniques. Thus, marginal designs shown in the figures can be cooled with judicious changes from the set conditions specified in the study. In the subsequent discussion, the above desirable changes will be discussed in conjunction with the aerospike design.

(C) Increase Coolant Wall Temperature. Near the throat region at high chamber pressures, the coolant-side wall temperatures were lower than the maximum allowable value. This was because of the limitation placed on the gas-side wall temperature. Thus by selecting a material which can withstand a higher gas-side wall temperature, an increase in the coolant side wall temperature can be realized.

(C) From the heat conduction equation

$$Q/A = \frac{k}{X} \ (T_{WG} - T_{WC})$$

increase in the conductivity of a selected material will also be beneficial. This will reduce the temperature gradient through the coolant tube walls.

(C) Another property of a selected material is the yield strength. With a higher strength material, the minimum tube thickness can be decreased. This in turn will increase the coolant wall temperature. Thus it would be desirable to select a material which has a higher gas-side maximum allowable wall temperature, higher thermal conductivity, and higher yield strength. Refractory metals will fit the three categories.

(C) <u>Curvature Effects at the Throat Region.</u> The major problem in cooling the aerospike design is the high heat flux located at the throat region. In order to cool this portion of the nozzle, a high coolant mass velocity is necessary. Consequently a high jacket pressure loss is induced (See Fig. 159). One means of decreasing the pressure drop is to utilize the enhancement of the coolant associated with particular tube curvatures. Rocketdyne has investigated curvature effects. An example of the results can be seen in Fig. 160. A definite increase in cooling capability is realized when the coolant undergoes a rapid turning. A considerable amount of theoretical and experimental effort is still necessary to correlate influencing items such as the effect of the ratio of tube diameter to radius of curvature and bulk Reynolds number.

(C) <u>Mass Transfer Cooling.</u> Augmenting the fully regenerative design with mass transfer cooling methods will reduce the heat input to the coolant. Consequently, a lower pressure drop can be realized.

(C) Possible methods are transpiration cooling, film cooling, and ablation cooling. Transpiration cooling involves the introduction through a porous wall. Film cooling is realized by introducing a film of coolant onto the gas-side region through discrete slots or openings. The limiting case of film cooling is transpiration cooling. Ablation cooling is accomplished by utilizing a wall material that will melt, sublime, or decompose when introduced to the hot gas stream. These methods are similar in that the coolant material absorbes heat from the main stream gas and is then injected back into the main stream. Thus the overall heat flux which enters the coolant jacket is reduced. In some cases, this reduction can be considerable. It is quite feasible that ablation cooling may be applicable as a single means of cooling.
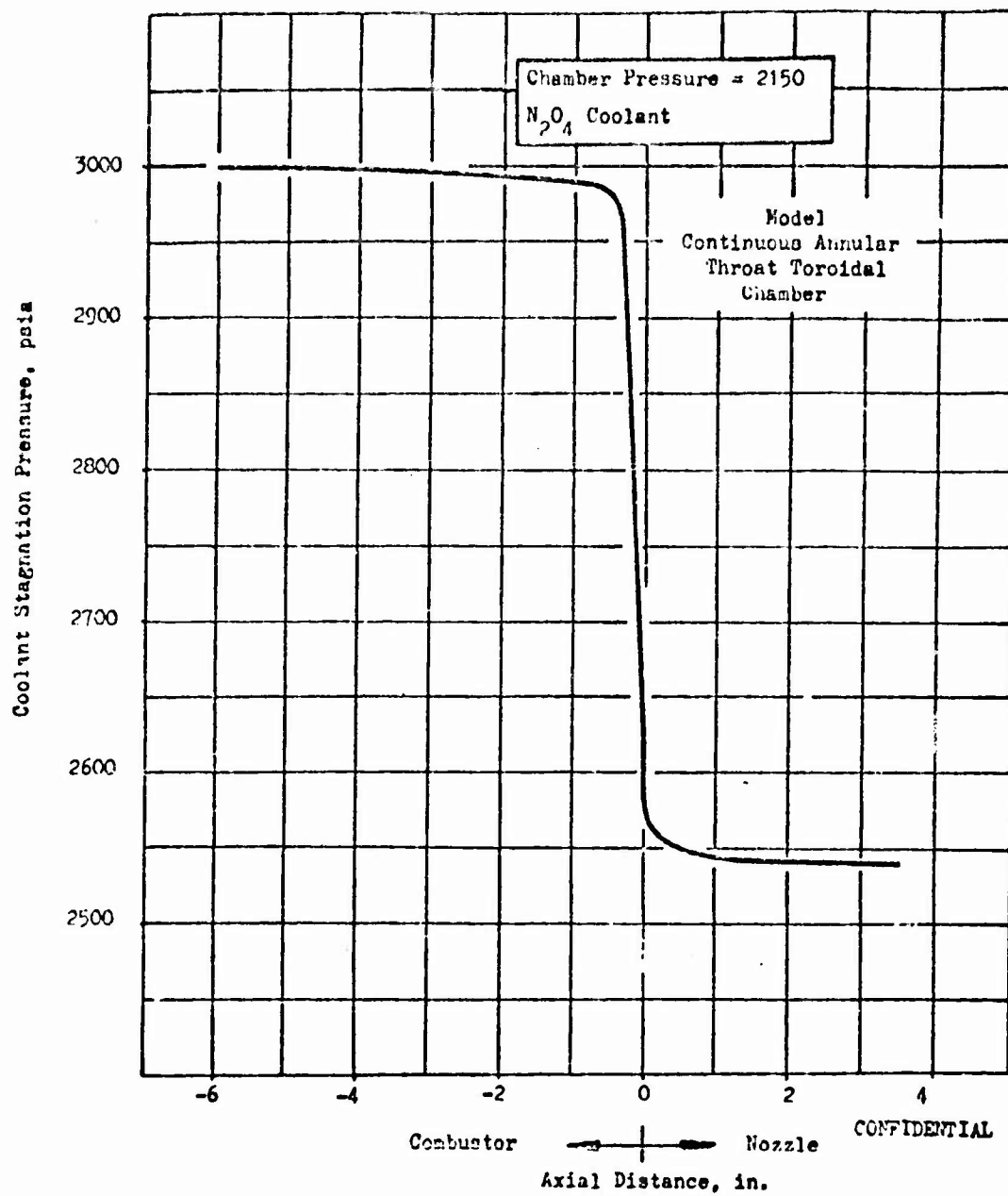
Figure 159. Typical Stagnation Pressure of Coolant
vs. Axial Length

284
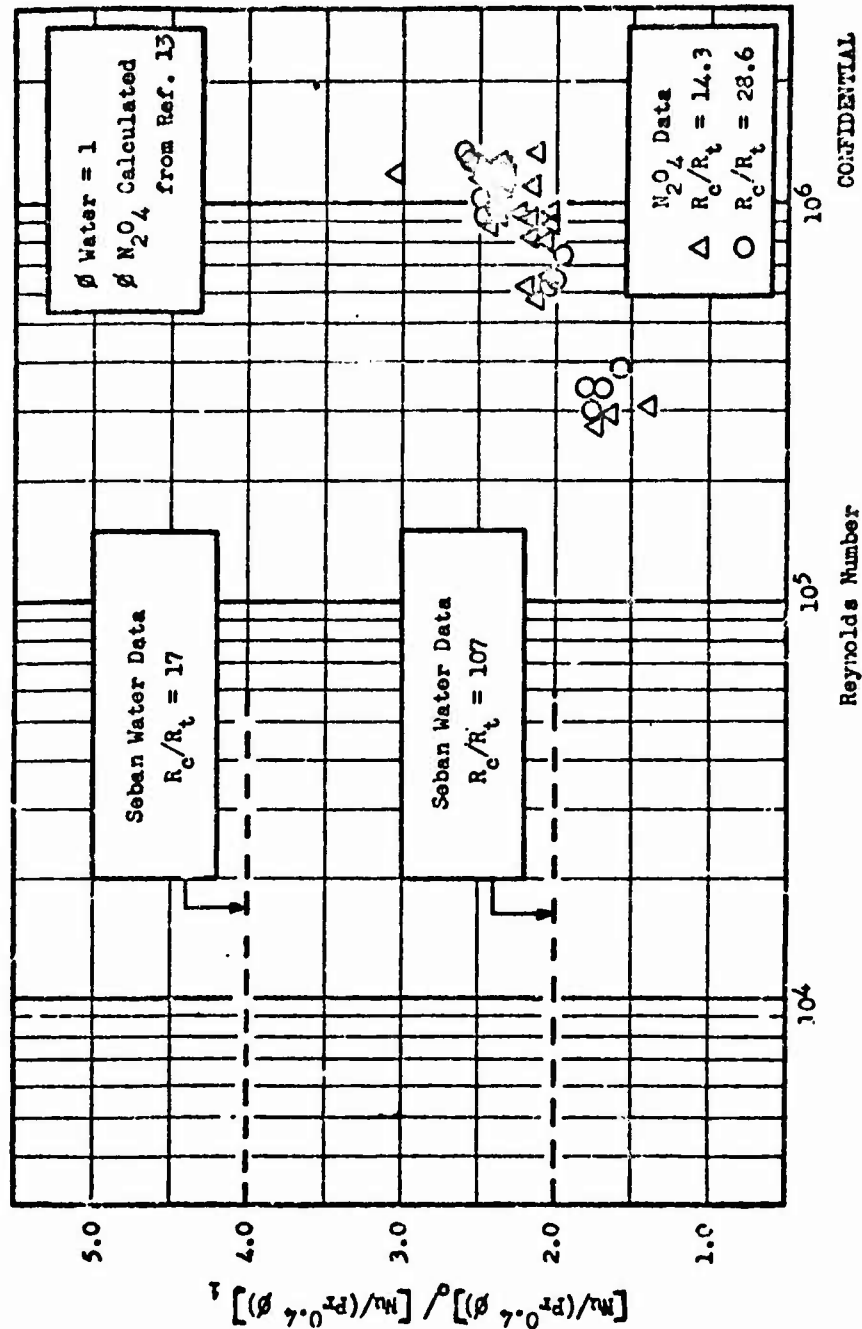
Figure 160. CONCAVE TO CONVEX SURFACE HEAT TRANSFER RATIO FOR CURVED TUBE EXPERIMENTS, CORRECTED FOR DISSOCIATION INFLUENCES

285

Conclusions

(C) Significant conclusions resulting from this study are the following:

1. Regenerative cooling of both multichamber and toroidal chamber aerospikes becomes increasingly difficult as engine thrust level is decreased. At the 20,000 pound thrust level regenerative cooling of either multichamber or toroidal chamber aerospikes appears possible only with N_2O_4 coolant at supercritical pressures. An alternate design approach such as an ablative chamber may be desirable for low thrust moderate chamber pressure applications.

2. For the upper thrust level range of interest, 2,000,000 pounds, the maximum chamber pressures for regenerative cooling attainable with a toroidal aerospike are approximately 200 psi lower than with an eight-module multichamber and are approximately the same as with a sixteen-module aerospike.

3. Regenerative cooling limits for the multichamber engines are relatively insensitive to either the module area ratio or the cluster area ratio. The chamber pressure limits for an annular throat configuration are a strong inverse function of area ratio.

4. N_2O_4 above its critical pressure is a better coolant than UDMH-N_2H_4 (50-50). Below the critical pressure of N_2O_4 the superiority of the coolants is reversed.

5. The range of feasibility of both combustor concepts may be extended from that indicated here by using alternate design techniques such as refractory tubing or coatings and partial or full mass transfer cooling.

286

DESIGN STUDIES

(C) The objective of this portion of the program was to determine effective
methods of utilizing toroidal and multichamber constructions for aero-
dynamic spike configurations. Combustors considered included several
toroidal types and clustered conventional chambers with both circular
and noncircular exits. The studies covered a range consistent with
Air Force propulsion requirements. These requirements include thrusts
from 20,000 pounds to 2,000,000 pounds, chamber pressures from 300 psia
to 3000 psia, and expansion area ratio of 150.

(C) Employing design guidelines presented in the analysis section of this
report, layouts of representative systems which use multichamber or
toroidal aerodynamic spike nozzles were made together with corresponding
conventional single bell engine systems. The design points selected
for each system are shown in Table 12 . These points cover the
parameter range of interest and were selected to take advantage of
previous design investigations at the same operating conditions.

TABLE 12

POINT DESIGN PARAMETERS   CONFIDENTIAL

Thrust (1000 pounds)	Chamber Pressure (psia)	Area Ratio
40	500	100
350	2000	150
658	300	10
2000	2000	50

(C) The purpose of these layouts was to gain insight into the structural
and operational aspects of systems employing the toroidal and multi-
chamber combustor concepts and to appraise the systems size and
complexity relative to the more conventional bell engine system. In
Table 13 the major characteristics of the systems investigated at
each of the four selected design points are presented. When designing
the engine systems, different multichamber configurations (round and
splayed exits, Fig. 161) and different toroidal combustor config-
urations (subsonic tube and baffled annular, Fig. 121) were selected.
The purpose of this was to become familiar with the structural and
functional aspects of the different combustors. The choice of
combustor at a given design point was arbitrary. The aerodynamic
spike nozzle lengths shown were also selected arbitrarily and do not
represent the results of a performance optimization. The paragraphs
that follow describe the design features of each of the selected
systems; advantages, disadvantages, and potential problem areas are
exposed in the process.

Point Designs - 40,000-Pound Thrust Level

(C) Layouts of typical 40,000-pound thrust multichamber and toroidal
chamber aerodynamic spike engines together with a conventional bell
thrust chamber are shown in Figs. 162, 163, and 164. The overall
expansion area ratio of each engine is 100 and the chamber pressure
is 500 psia.

(C) The multichamber configuration consists of a cluster of 12 conventional
regeneratively cooled chambers with tangent chamber exits. With tangent
circular exits, the ratio of the overall area ratio ϵ_{CL} to the module

TABLE 15. DESIGN STUDY SUMMARY

Nozzle Type	Combustor Type	Type Cooling	Propellant Feed (Power Source)	Secondary Gas Source	Thrust (1000 lbs)	Chamber Pressure (psia)	Type TVC	Area Ratio	Nozzle Length from Throat (% cone)
Aerospike	12-Circular Exit Multichamber	Regenerative	Pump Fed (Chamber Tapoff)	Turbine Exhaust	40	500	Gimbal	100	14.0
Aerospike	Subsonic Tube	Regenerative	Pump Fed (Chamber Tapoff)	Turbine Exhaust	40	500	Gimbal	100	29.3
Bell	Cylindrical	Regenerative	Pump Fed (Chamber Tapoff)	—	40	500	Gimbal	100	80.0
Aerospike	8-Splayed Exit Multichamber	Regenerative	Pump Fed (Chamber Tapoff)	Turbine Exhaust	350	2000	Liquid Injection	150	18.9
Aerospike	Baffled Annular	Regenerative	Pump Fed (Chamber Tapoff)	Turbine Exhaust	350	2000	Liquid Injection	150	33.8
Bell	Cylindrical	Regenerative	Pump Fed (Chamber Tapoff)	—	350	2000	—	150	80.0
Aerospike	12-Circular Exit Multichamber	Ablative	Pressure Fed	Chamber Tapoff	658	300	—	11.5	17.3
Aerospike	Baffled Annular	Ablative	Pressure Fed	Chamber Tapoff	658	300	—	8.2	27.8
Bell	Cylindrical	Ablative	Pressure Fed	—	658	300	—	8	80.0
Aerospike	8-Circular Exit Multichamber	Regenerative	Pump Fed (Chamber Tapoff)	Turbine Exhaust	2000	2000	Liquid Injection	60	17.9
Aerospike	Baffled Annular	Regenerative	Pump Fed (Chamber Tapoff)	Turbine Exhaust	2000	2000	Liquid Injection	55	51.6
Bell	Cylindrical	Regenerative	Pump Fed (Chamber Tapoff)	—	2000	2000	—	55	80.0
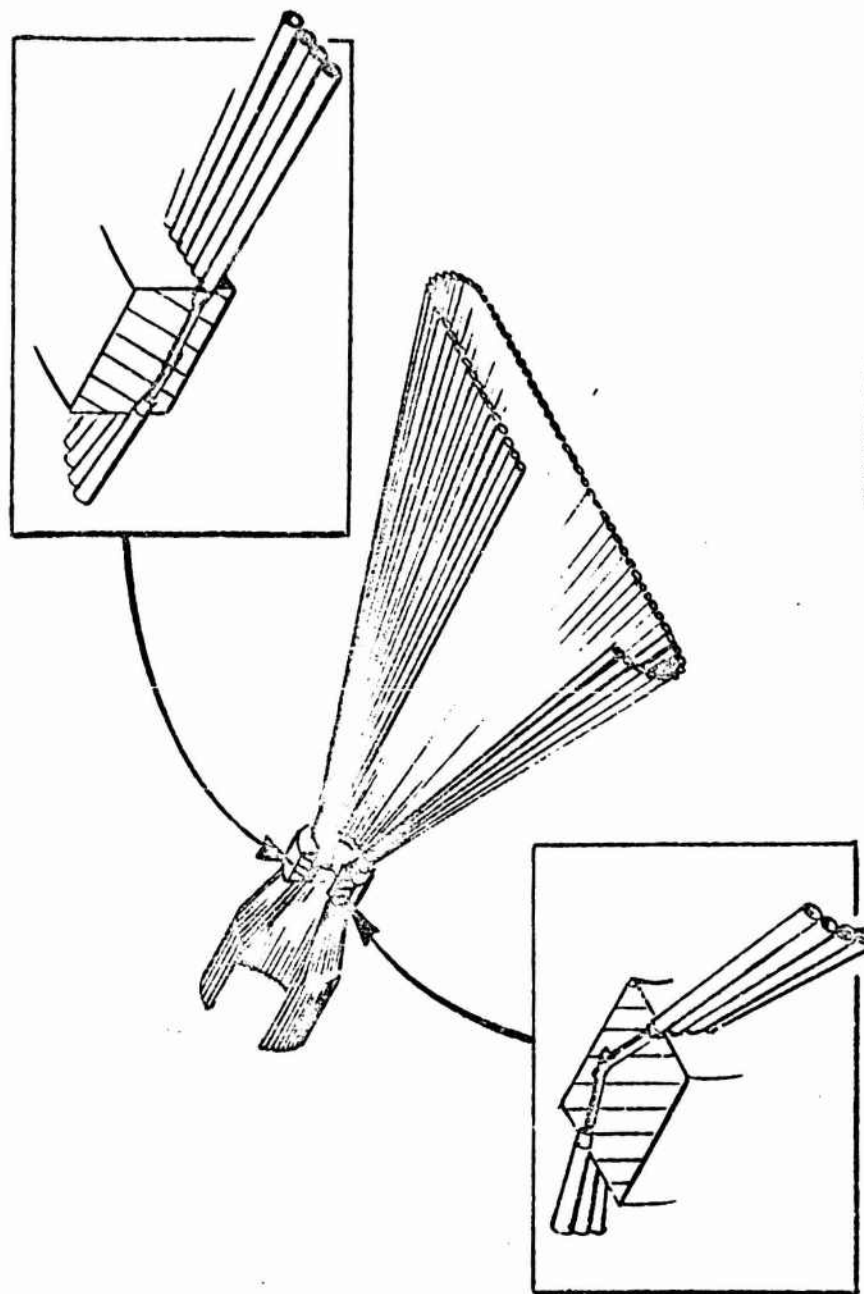
CONFIDENTIAL

Figure 161. Spleyed Exit Multichamber

FUEL INLET

OXIDIZER INLET

120

120

74

59

2

MAJOR SYSTEM PARAMETERS

F = 40,000 LB. (VACUUM)

P_c = 500 PSIA (NOZZLE STAGNATION)

ϵ = 100
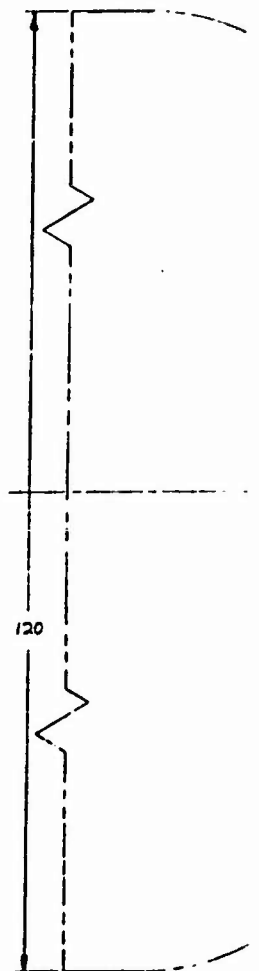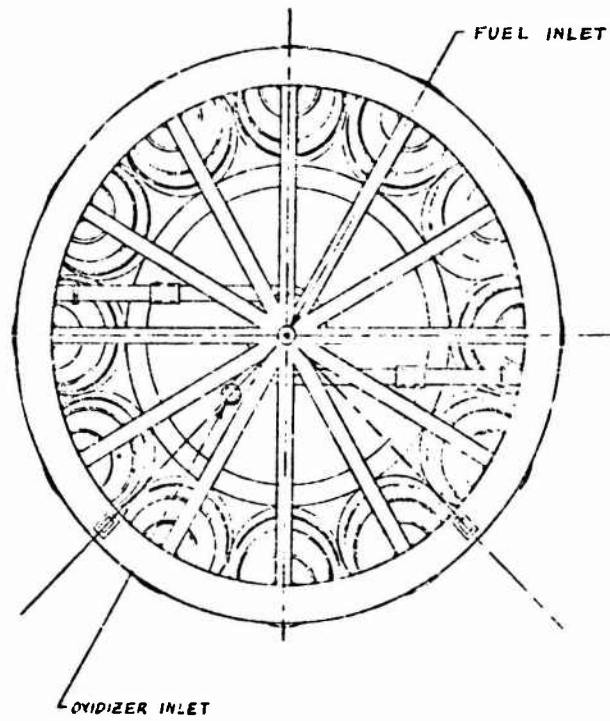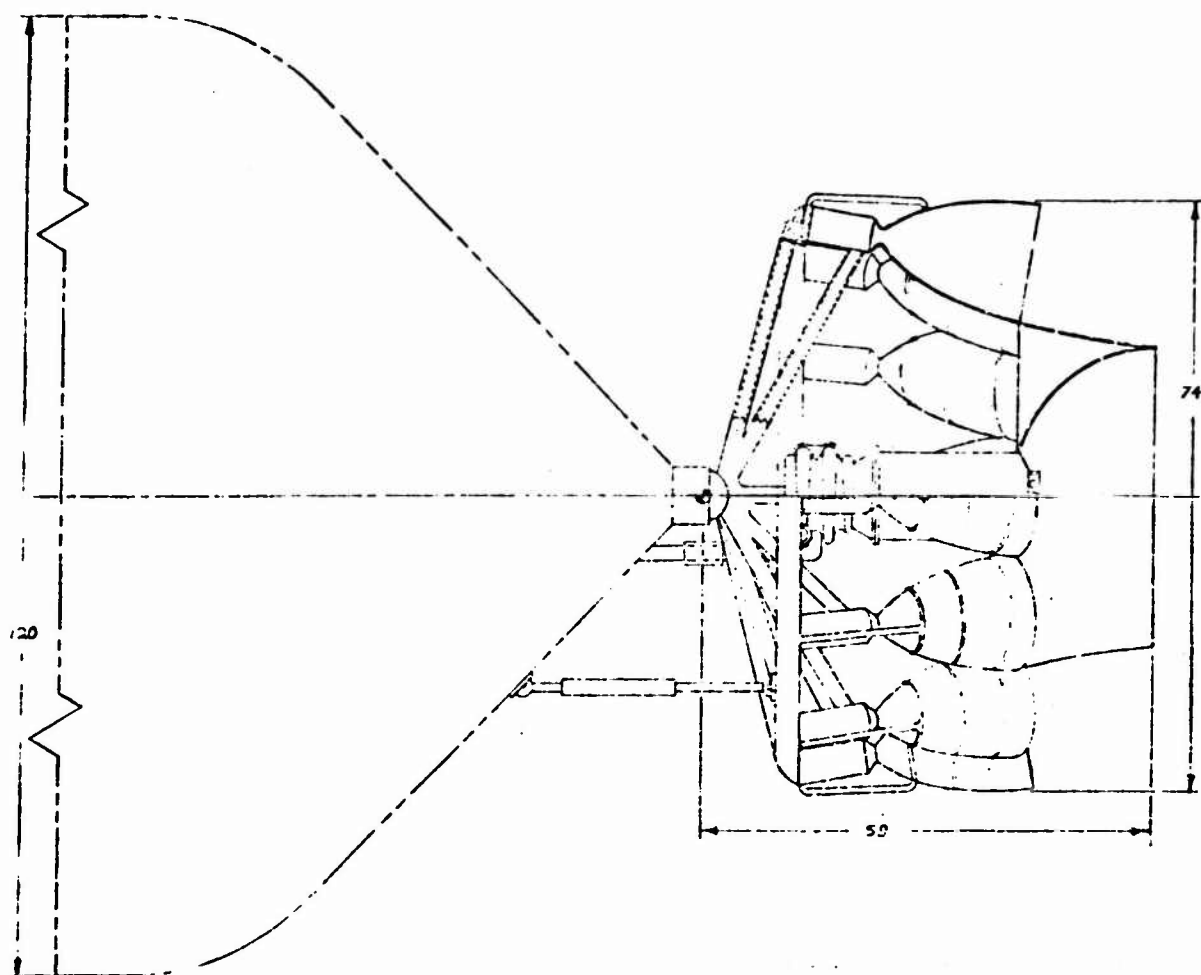
ϵ_M = 51.8

PROPELLANTS = NTO/50-50
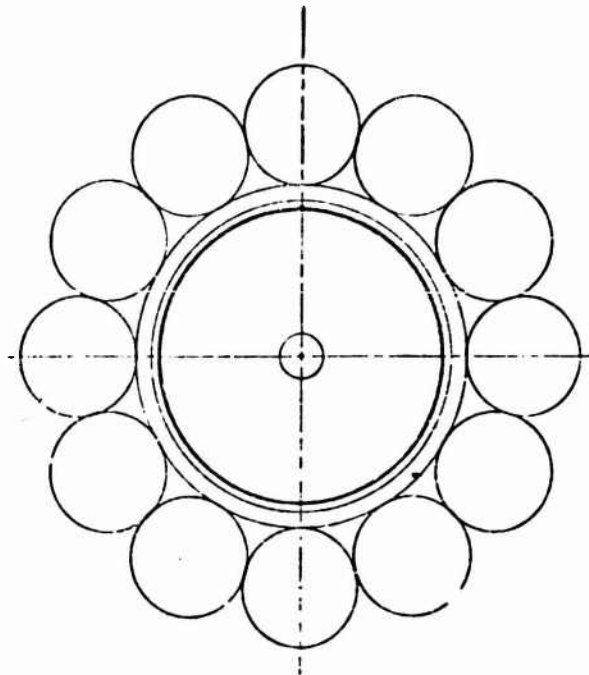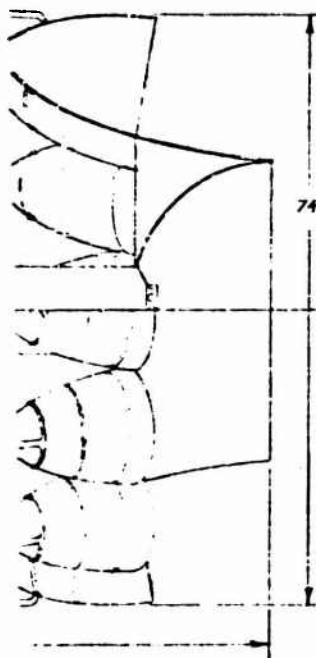
Figure   162. Aerospike Engine System,
              Multichamber, Low Thrust,
              and Low Chamber Pressure
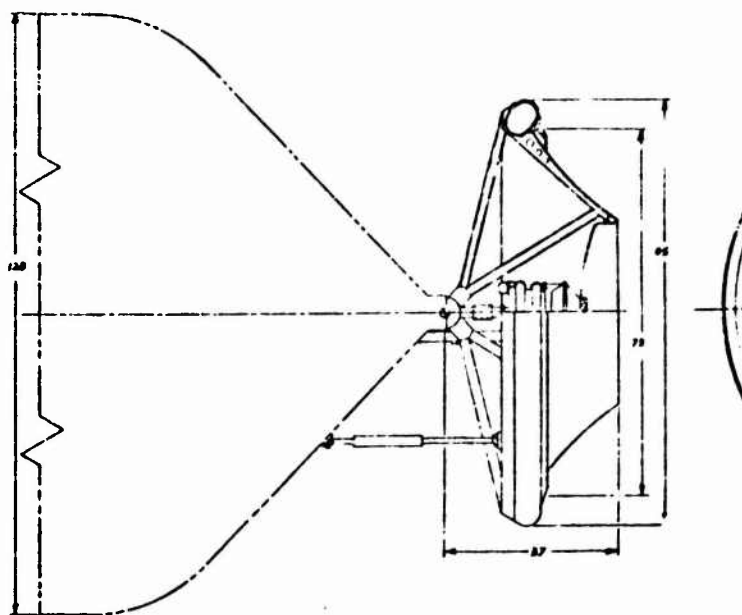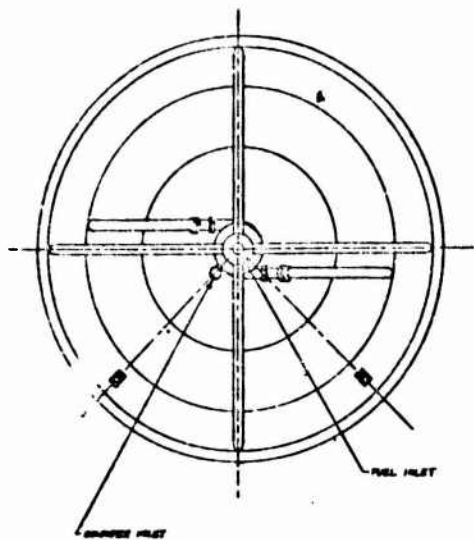
3

FUEL INLET

OXIDIZER INLET

1

GRIDDLE FEED MANIFOLD

2
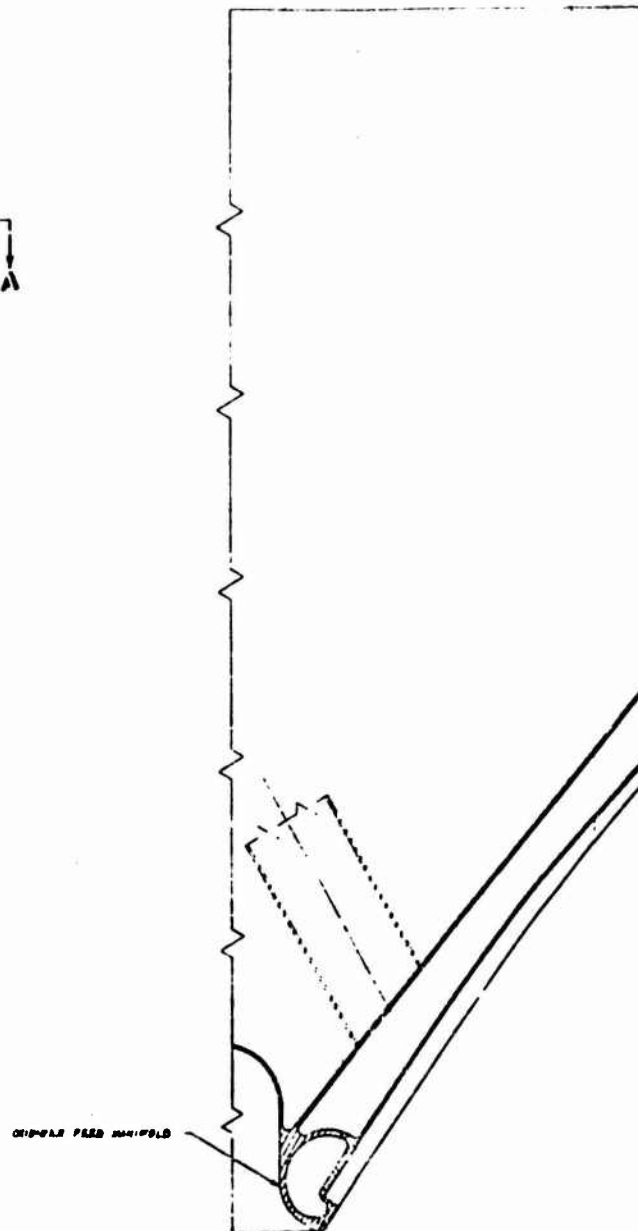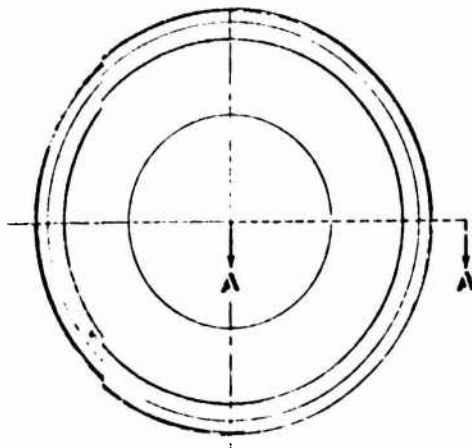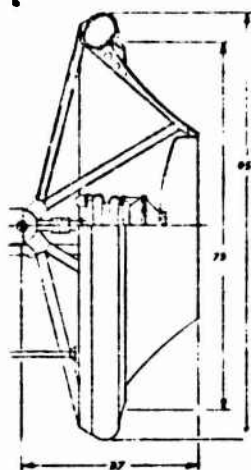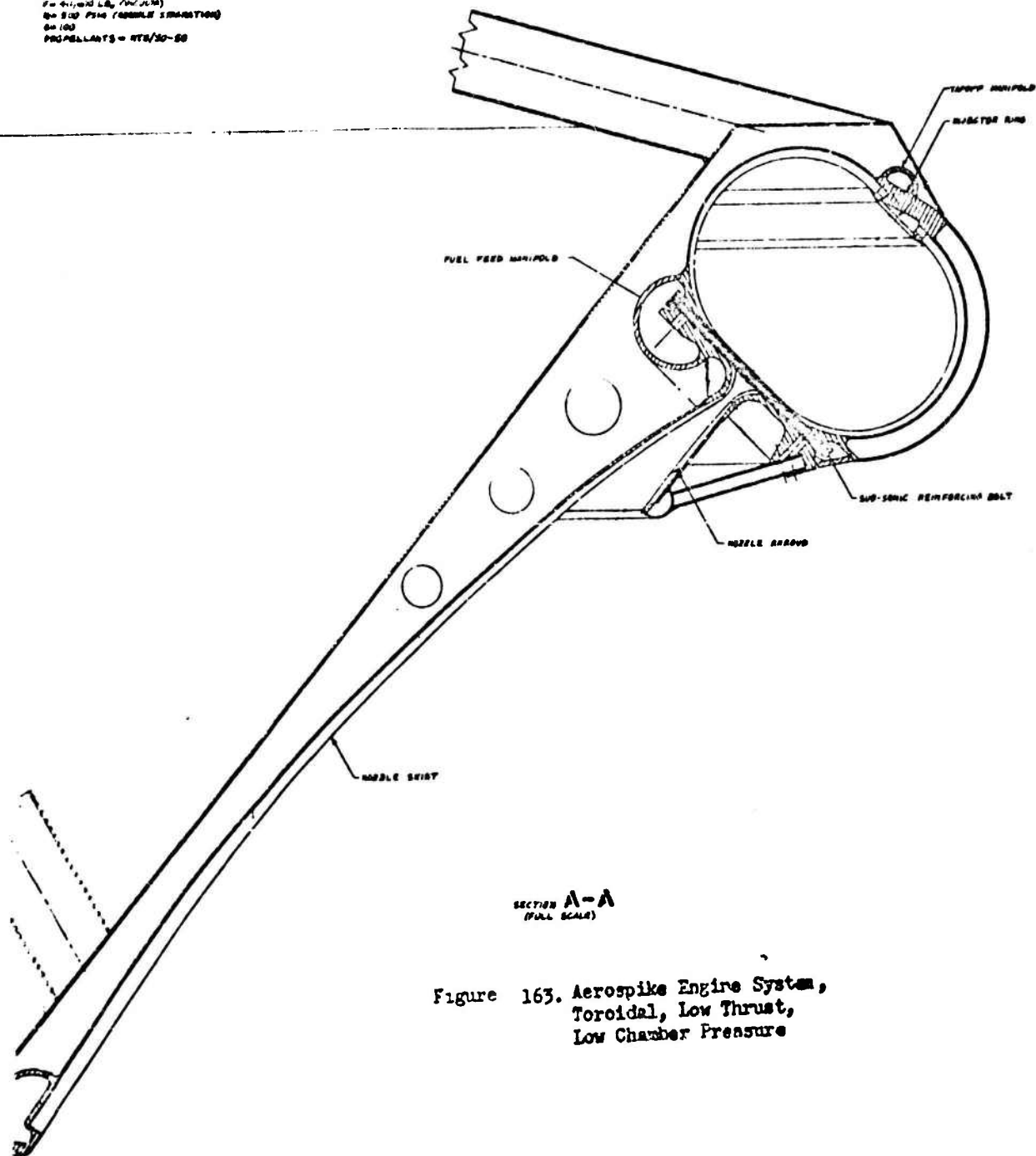
Figure 163. Aerospike Engine System,
Toroidal, Low Thrust,
Low Chamber Pressure

120

73

58

119

2
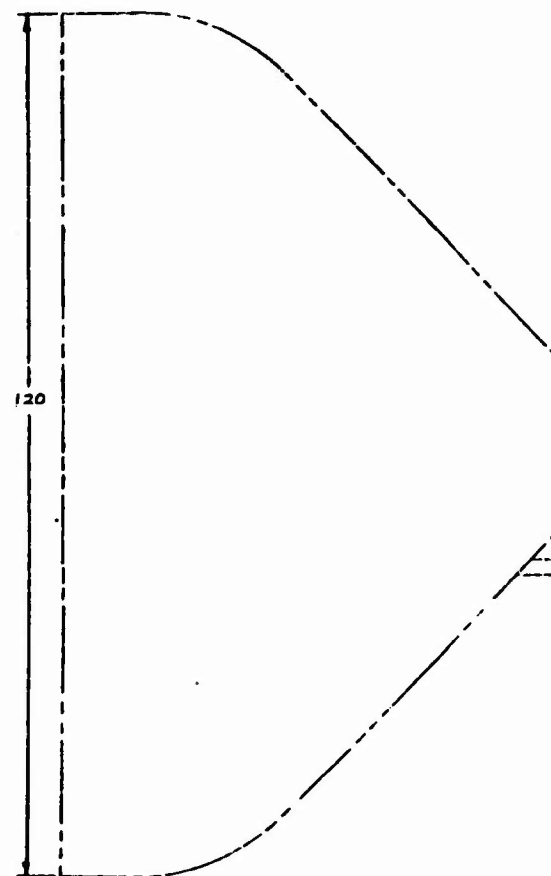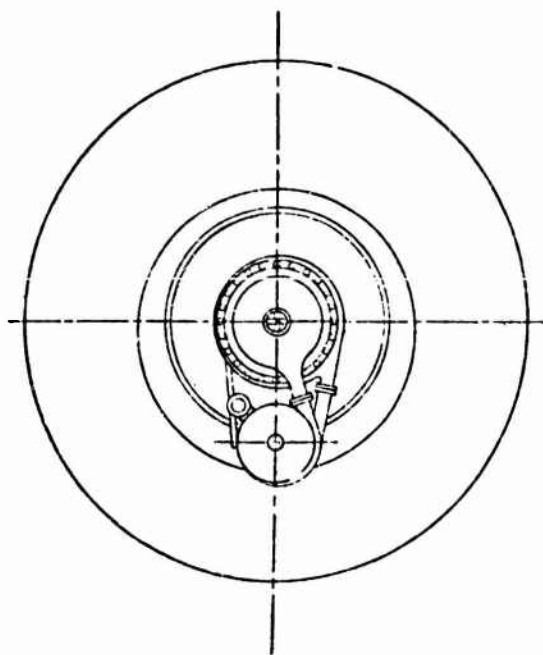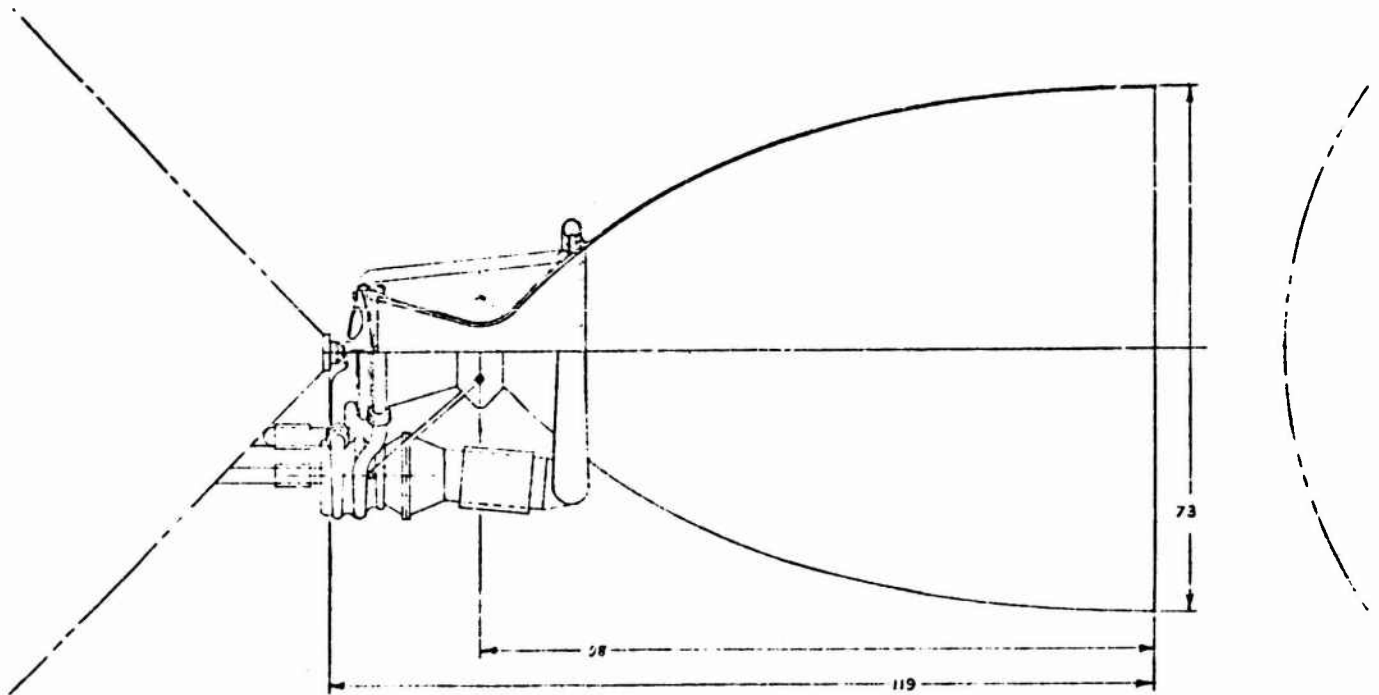
MAJOR SYSTEM PARAMETERS
F = 40,000 LB$_f$ (VACUUM)
P$_c$ = 500 PSIA (NOZZLE STAGNATION)
ϵ = 100
PROPELLANTS = NTO/50-50

73

-119-
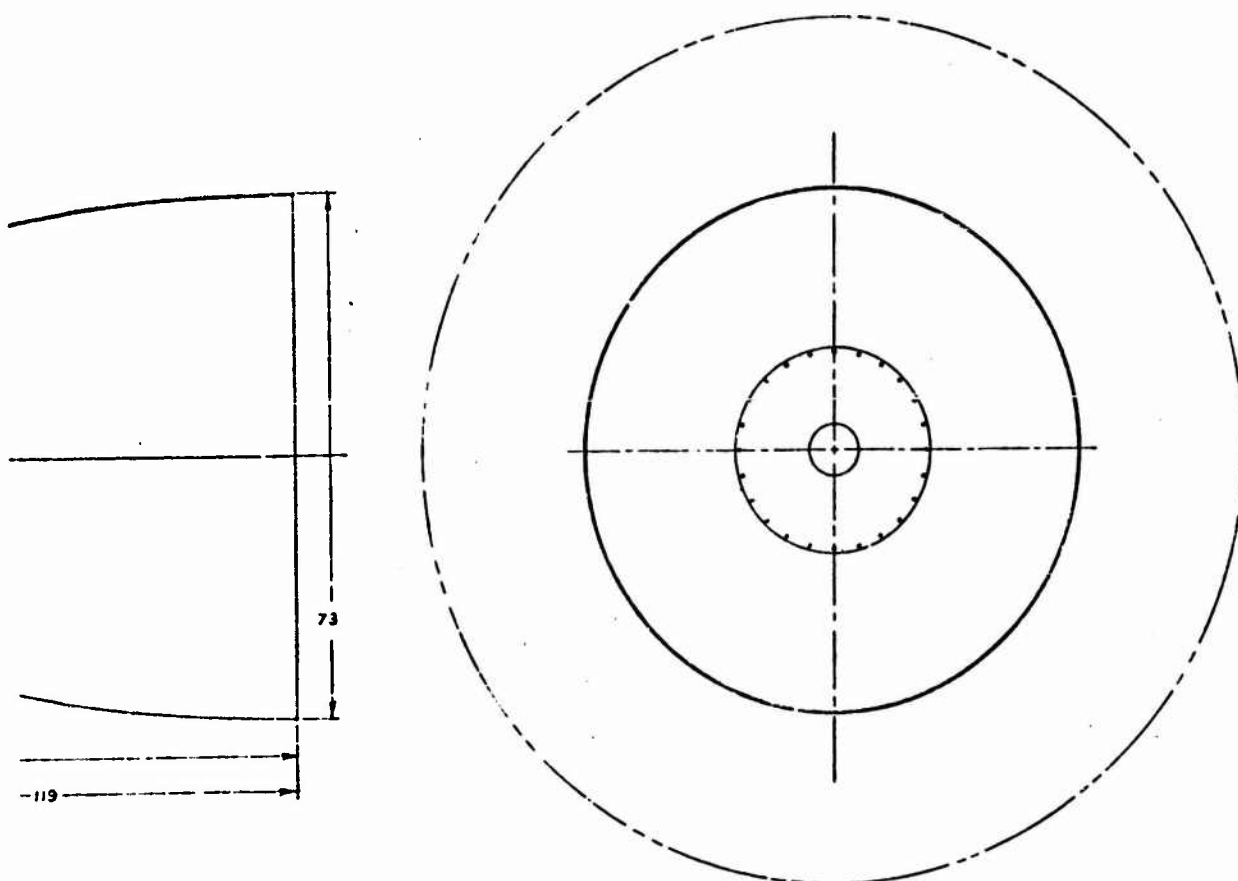
Figure 164. Conventional Ball Engine System,
Low Thrust, Low Chamber Pressure

293

area ratio ϵ_M is essentially (with a weak dependence on module tilt angle, Ref. 3) a function only of the number of clustered chambers. The selection of 12 modules with circular touching exits fixes ϵ_M at 51.8. The overall nozzle length L_N from the module throat to the plug exit (see Fig. 122 on page 210) is 29.3 percent of an equivalent 15 degree conical nozzle. The length to the multichamber exit is 16.8 percent.

(C) A simple point gimbal and conventional hydraulic actuator are employed. The oxidizer inlet duct passes through the center of the gimbal joint. Tubular columns transmit thrust loads to the gimbal block from a structural ring into which the module injector blocks are mounted. The ring also contains the tangential propellant distribution manifolds. Propellants are fed to the modules from a single shaft, back-to-back turbopump. Propellants are routed directly to the tangential distribution manifold. Turbine exhaust provides secondary flow for the plenum chamber type centerbody.

(C) The engine was designed with a single downpass coolant through the modules to a module area ratio of 15. An ablative nozzle extension is used from this point to the module exit. The spike portion of the nozzle is fabricated of radiation cooled material.

(C) The toroidal combustor configuration shown is regeneratively cooled and is supported in the chamber region by regeneratively cooled support tubes passing through the chamber walls. The nozzle length from the throat to the exit is 14 percent of an equivalent 15 degree conical nozzle.

(C) System aspects of the toroidal design are essentially similar to those of the multichamber design. The same gimbal and central turbopump arrangement is used. Thrust mounts should be somewhat simpler and lighter as a uniform circumferential thrust force is applied as opposed to twelve discrete loads.

(C) The combustion chamber was sized to a minimum combustion length of six inches from injector face to throat. This produces a chamber characteristic length (L^* = 186 inches) greatly in excess of that used in conventional combustors (L^* = 30 to 50 inches). Recent experimental data using F_2/H_2 indicates the high combustion efficiencies can be achieved in toroidal combustors with diameters of only 3 inches. Therefore, it is likely that small diameter combustors could be used at this thrust level. The oval combustor contour is used to minimize induced bending moments on the support pins.

(C) Oxidizer enters at the nozzle exit and cools the nozzle and inboard chamber section. Fuel is used to cool the support pin and outboard chamber region. Turbine drive gas is obtained by tapping into the primary combustion chamber through the injector face. Turbine exhaust gases are directed radially outward into the base region.

(C) A conventional single bell engine system is shown for comparison in Fig. 164. The envelope length for the bell chamber is significantly longer than for the aerodynamic spike configurations. The axial length from the outer throat point to the nozzle exit (expressed as percent of a 15 degree cone) is 14 percent, 29.3 percent and 80 percent for the toroidal, multichamber and bell configurations, respectively. The percent axial length to the exit of the multichamber module is 16.8 percent. This factor is of significance because this length can be reduced only by decreasing the module area ratio. Module area ratio can be reduced by increasing the number of modules while maintaining a touching exit condition or by introducing gaps between chamber exits. Increasing the number of chambers increases system complexity and makes cooling more difficult whereas the introduction of gaps between chambers has been shown (Ref. 3) to lower performance.

Point Designs - 350,000-pound Thrust Level

(C) On Figures 165 through Fig. 169 are shown layouts of multichamber and toroidal chamber aerodynamic spike engines and a single bell chamber engine. These engines produce approximately 350,000 pounds thrust at a chamber pressure of 2000 psia and an area ratio of 150.

(C) 350K Multichamber Aerospike. The splayed exit multichamber was investigated at this thrust level. The primary purpose of elongating the exit is to achieve an axisymmetric annular flow field at the module exit plane. The elongated exits also allow low module area ratio to be achieved with a small number of clustered chambers. The engine has eight regeneratively cooled chambers with each chamber exit extending over a 38 degree arc. The module area ratio is 13.8. The reduction in area ratio compared to circular exit clusters is easily seen by comparing this configuration to the 40,000-pound thrust design which has twelve chambers with a module area ratio of 51.8 and a cluster area of 100.

(C) Module length is 57.8 percent of a 15 degree cone whose circular exit area encloses the 38 degree arc subtended by the splayed chamber and 210 percent of a 15 degree cone of 13.8 area ratio. Analytical studies of splayed module performance indicate that even though the module exit area can be reduced with splayed exits, for maximum module thrust the module nozzle length should be a high percentage (70 to 80) of the length of a 15 degree conical nozzle having an exit diameter equal to the exit span of the module. This can be shown from a vacuum performance analysis of a two-dimensional module. Figure 170 shows the maximum vacuum performance of two-dimensional nozzles of various lengths with a square throat of unit dimensions and constant exit dimensions of 7.3 and unity. This module design corresponds to an eight touching module multichamber configuration with a cluster area ratio of 50.
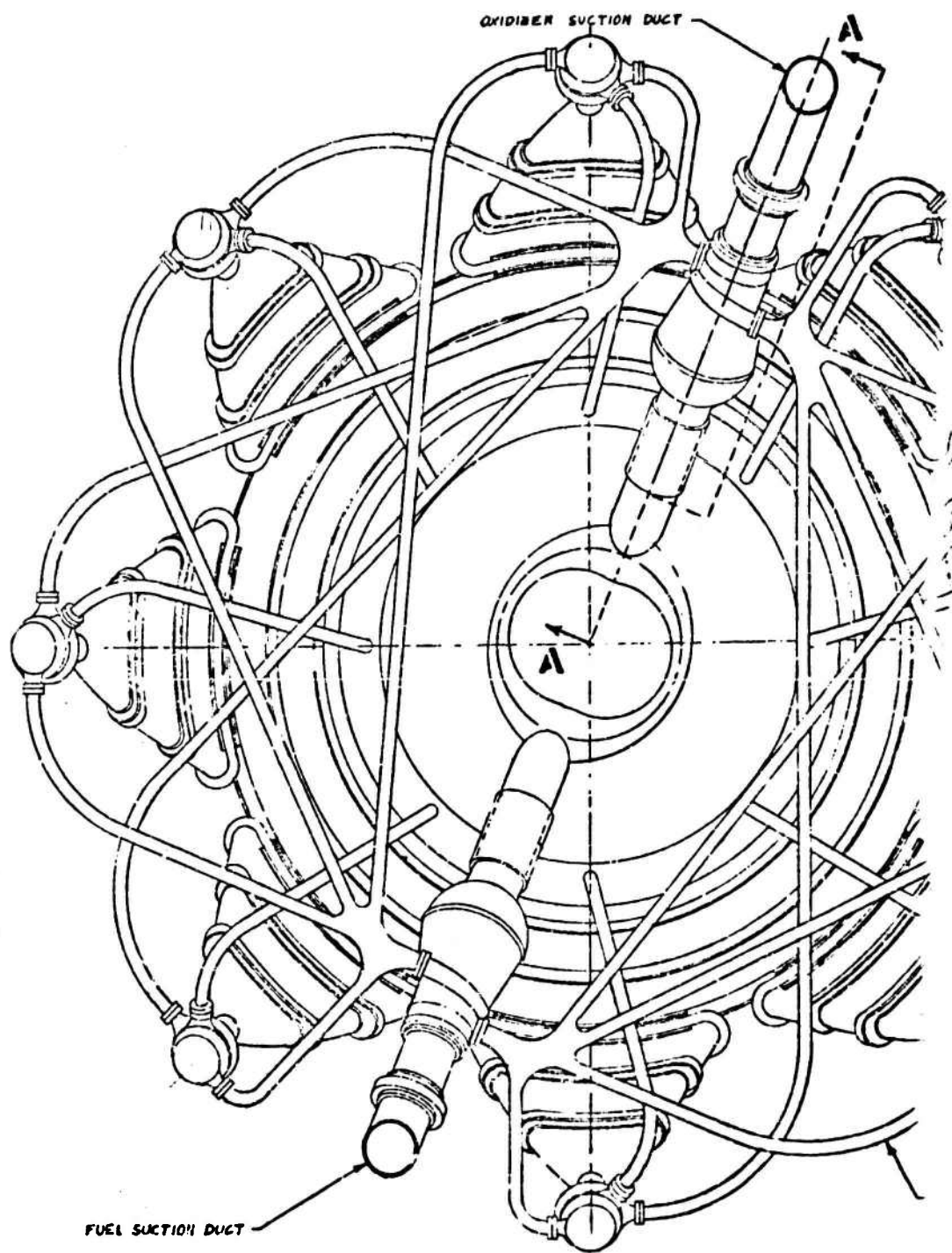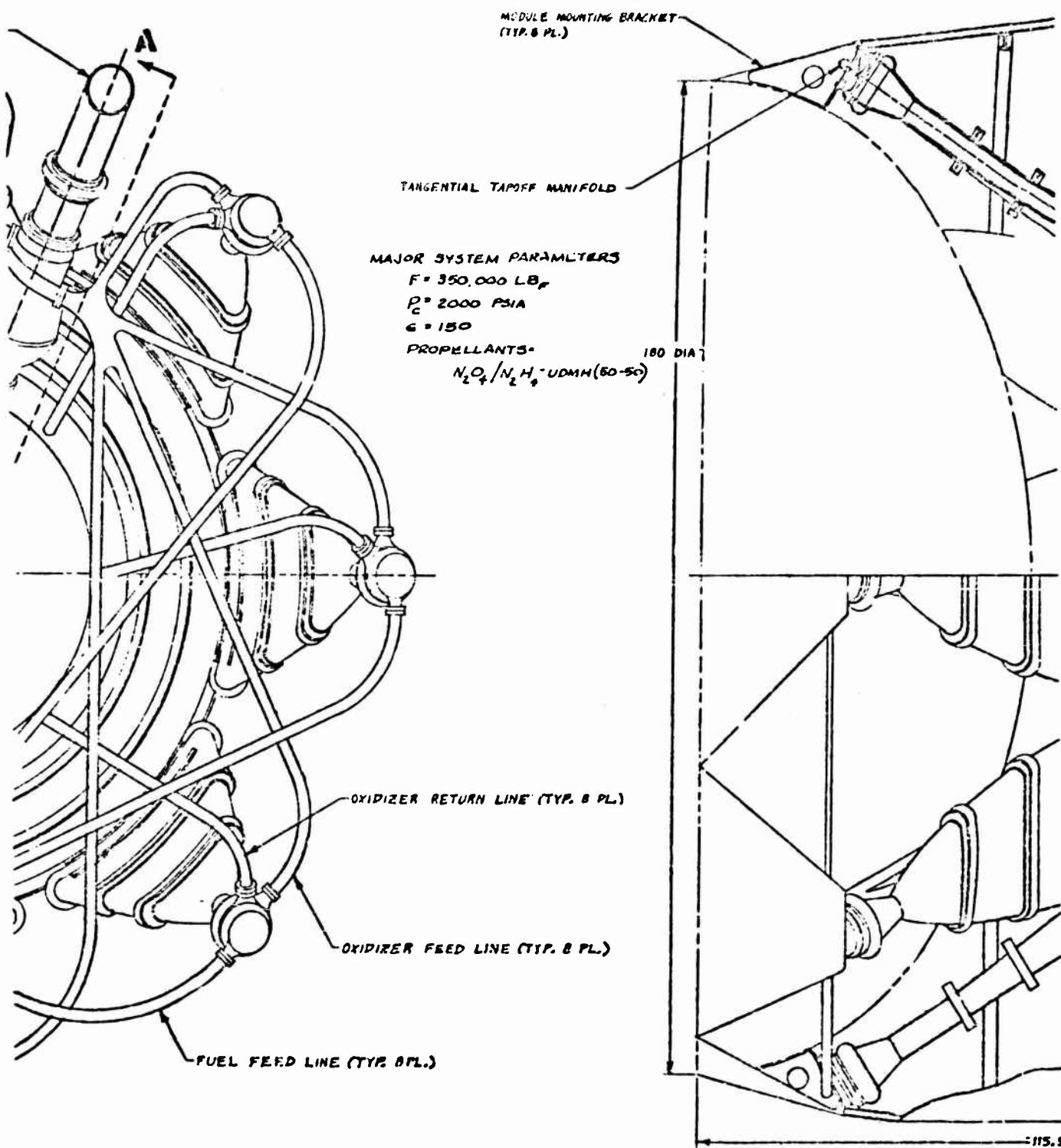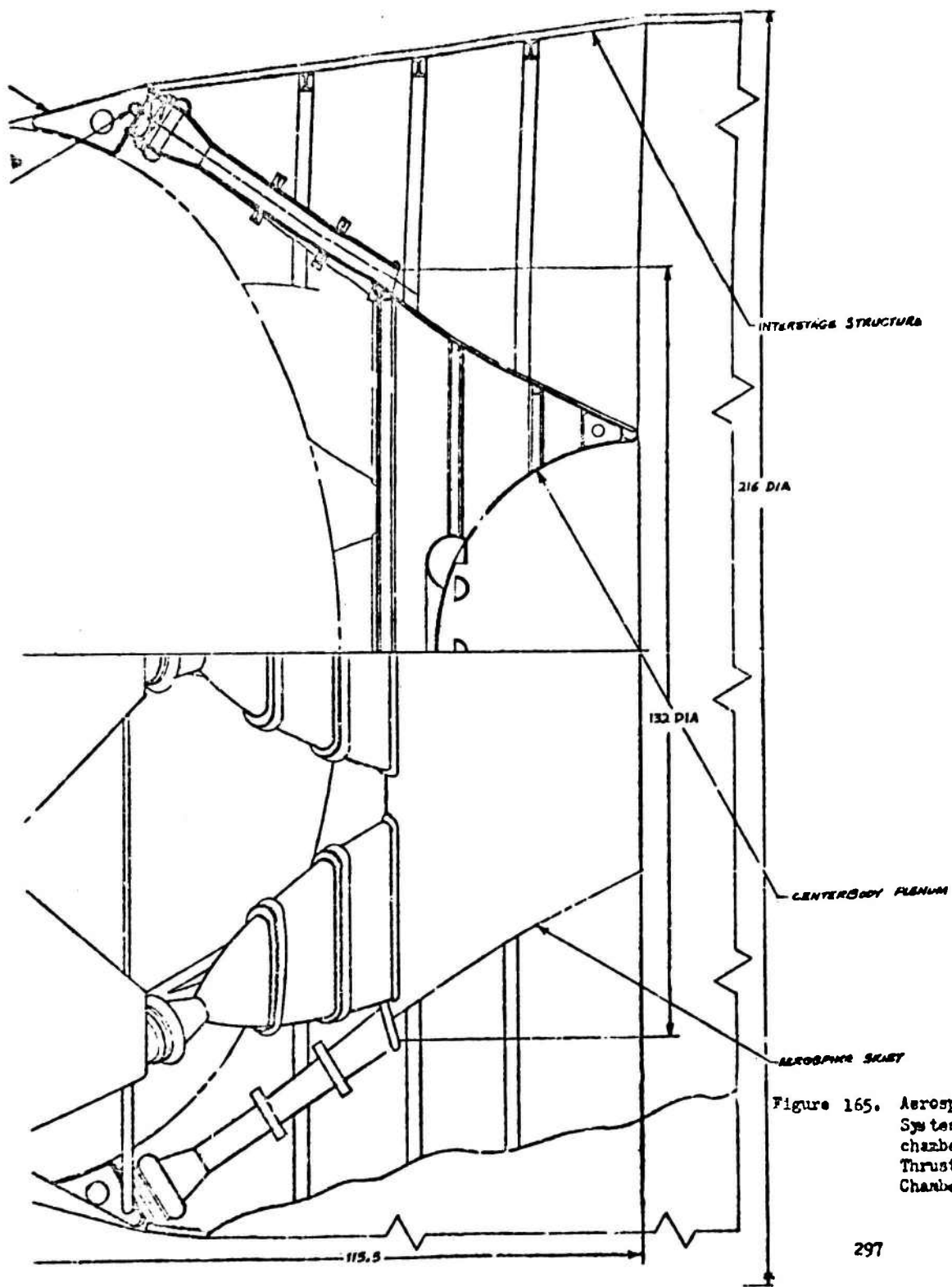
OXIDIZER SUCTION DUCT

A

A

FUEL SUCTION DUCT

A

MODULE MOUNTING BRACKET
(TYP. 6 PL.)

TANGENTIAL TAPOFF MANIFOLD

MAJOR SYSTEM PARAMETERS
$F = 350,000$ LB$_f$
$P_c = 2000$ PSIA
$\epsilon = 150$
PROPELLANTS-
N_2O_4 / N_2H_4-UDMH(50-50)

180 DIA

OXIDIZER RETURN LINE (TYP. 8 PL.)

OXIDIZER FEED LINE (TYP. 8 PL.)

FUEL FEED LINE (TYP. 8 PL.)

115.9

2

INTERSTAGE STRUCTURE

216 DIA

132 DIA

CENTERBODY PLENUM

AEROSPIKE SKIRT

115.5

Figure 165. Aerospike Engine System, Multi-chamber, Medium Thrust, High Chamber Pressure

297
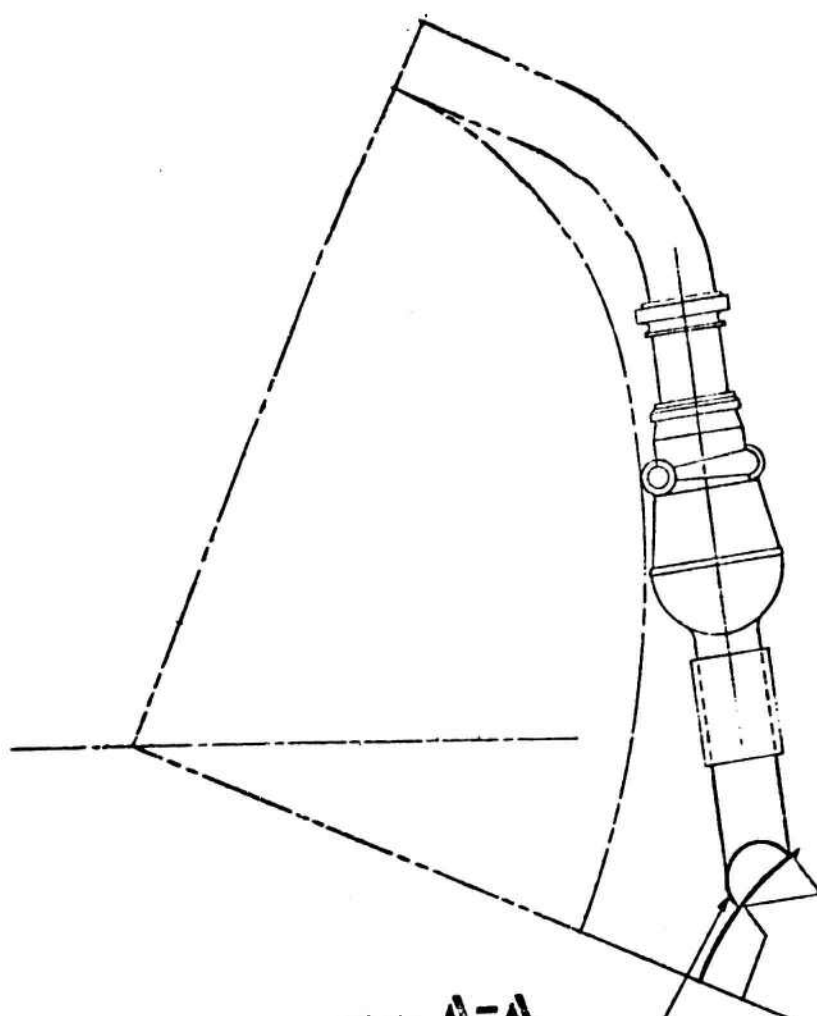
SECTION **A-A**

SECONDARY FLOW DISTRIBUTION
MANIFOLD

NOTE: PLUMBING OMITTED
FROM SIDE AND BOTTOM
VIEWS FOR CLARITY
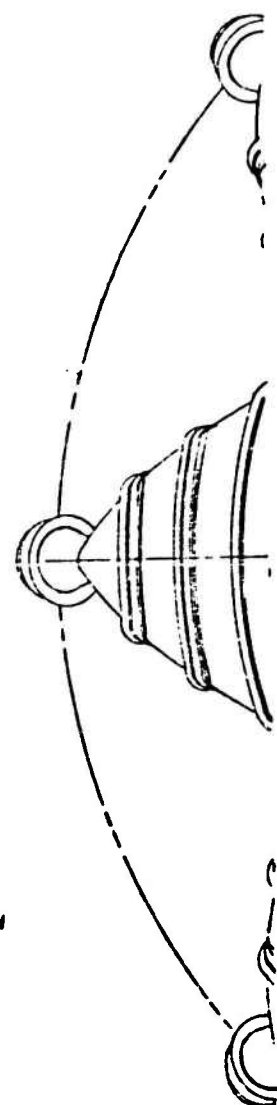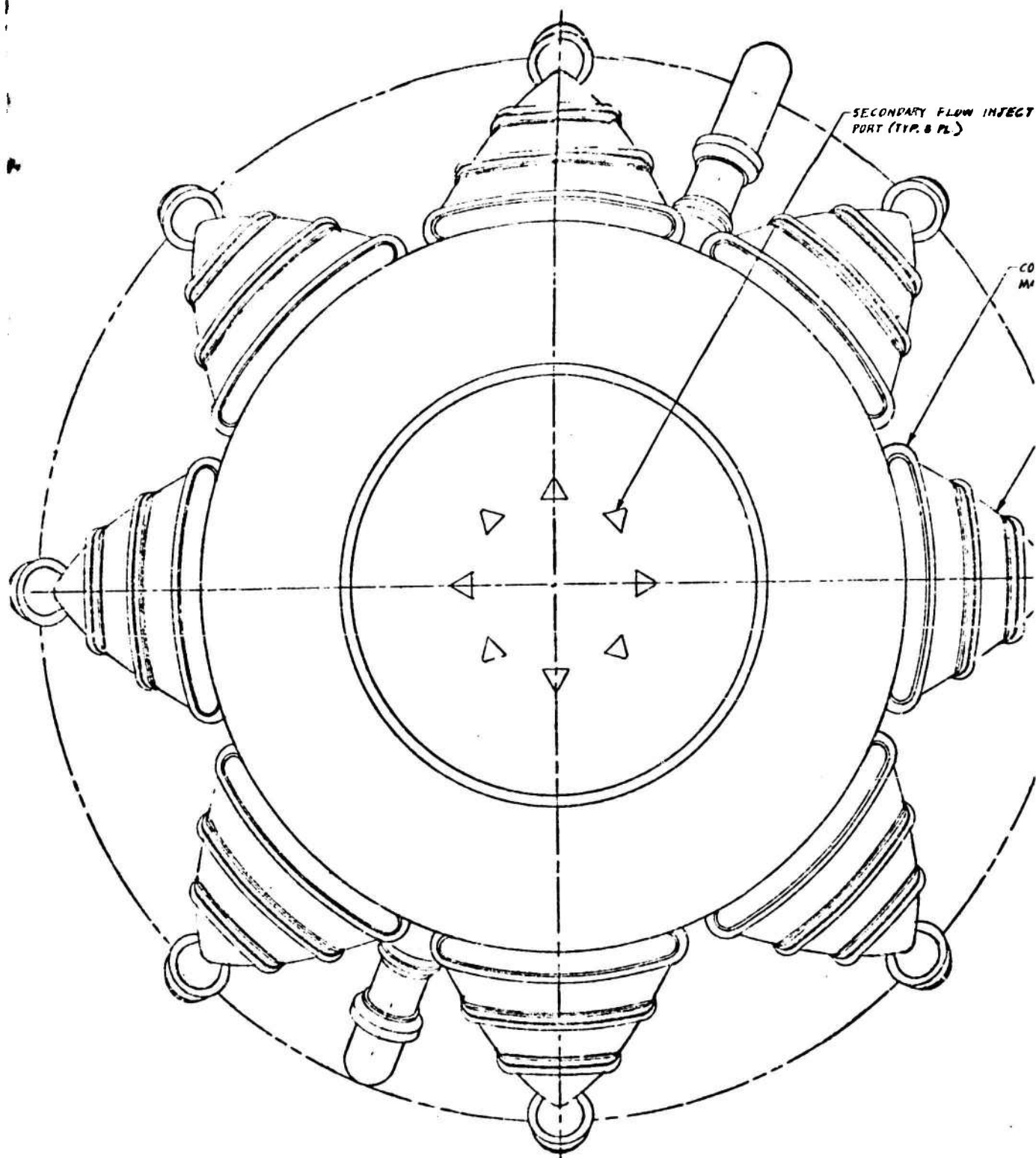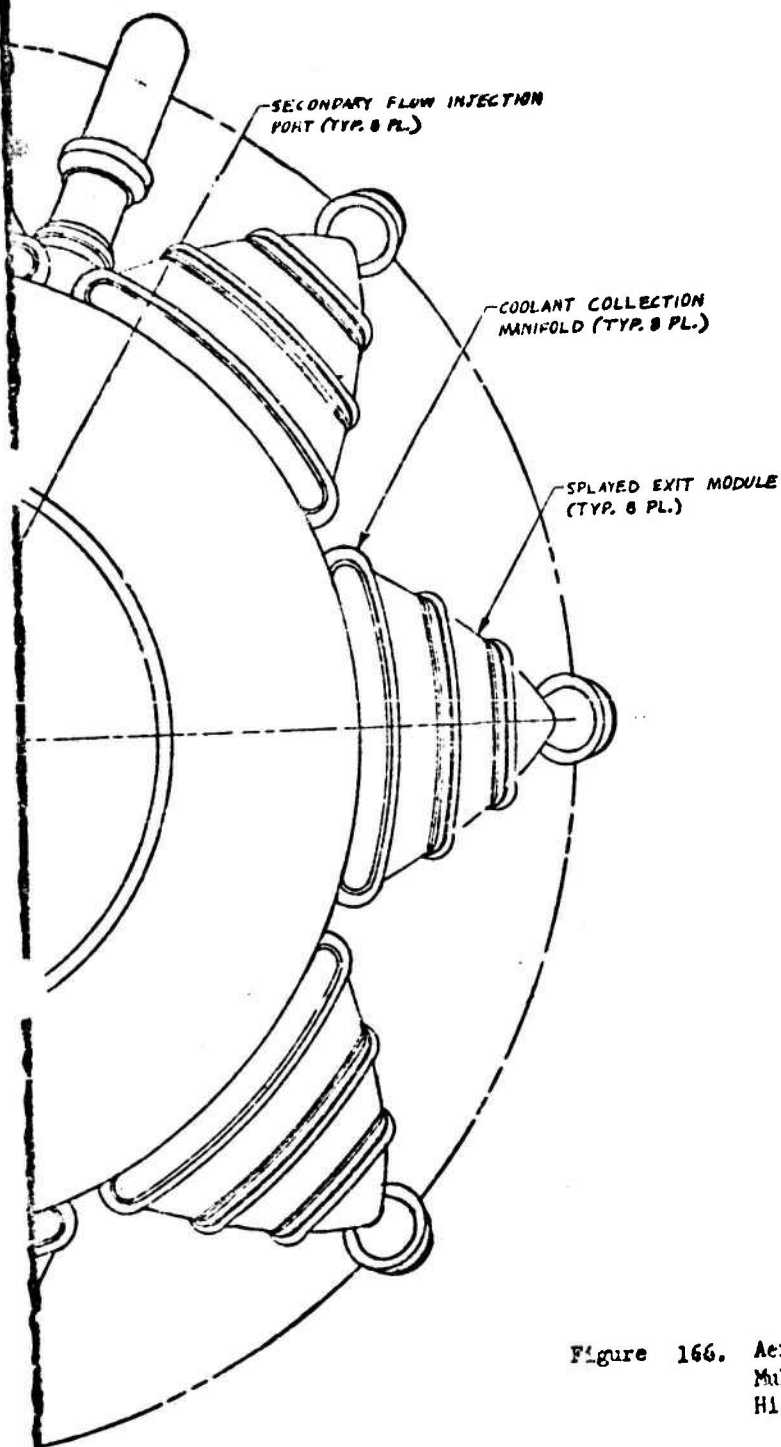
1

SECONDARY FLOW INJECT
PORT (TYP. 8 PL.)

CO
M

2

SECONDARY FLOW INJECTION
PORT (TYP. 8 PL.)

COOLANT COLLECTION
MANIFOLD (TYP. 8 PL.)

SPLAYED EXIT MODULE
(TYP. 8 PL.)

MAJOR SYSTEM PARAMETERS
$F = 350,000\ LB_F$
$P_c = 2000\ PSIA$
$\epsilon = 150$
PROPELLANTS = N_2O_4/N_2H_4-UDMH (50-50)

Figure 166. Aerospike Engine System,
Multichamber, Medium Thrust,
High Chamber Pressure
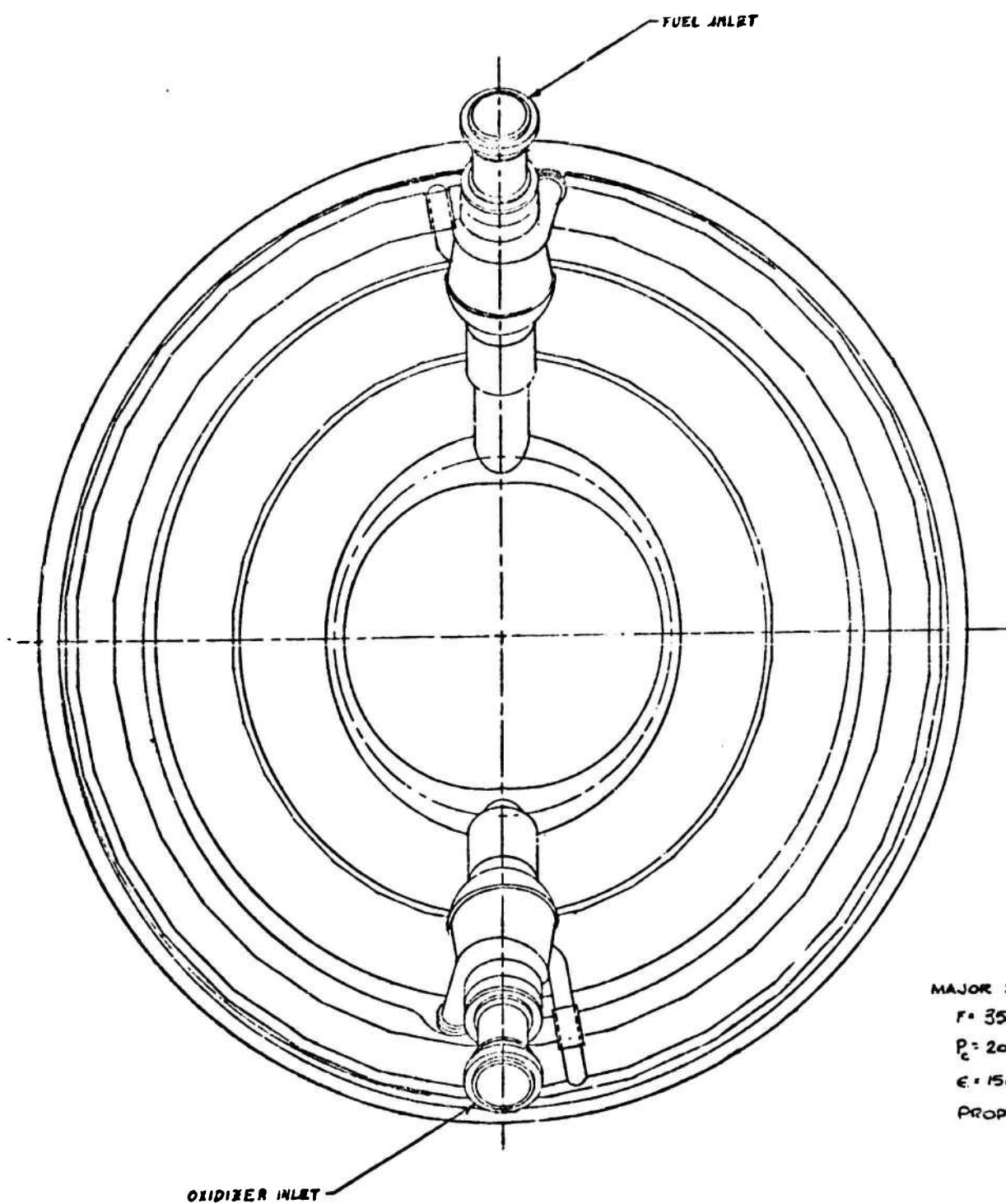
FUEL INLET

OXIDIZER INLET

MAJOR S
F = 35c
P_c = 200
€ = 150
PROPE

2

TAPOFF MANIFOLD

180 DIA

MAJOR SYSTEM PARAMETERS

$F = 350,000$ LB$_F$

$P_c = 2000$ PSIA

$\epsilon = 150$

PROPELLANTS $= N_2O_4/N_2H_4$
UDMH /50-50

FULL
COMBU
(TYP 3

1

2
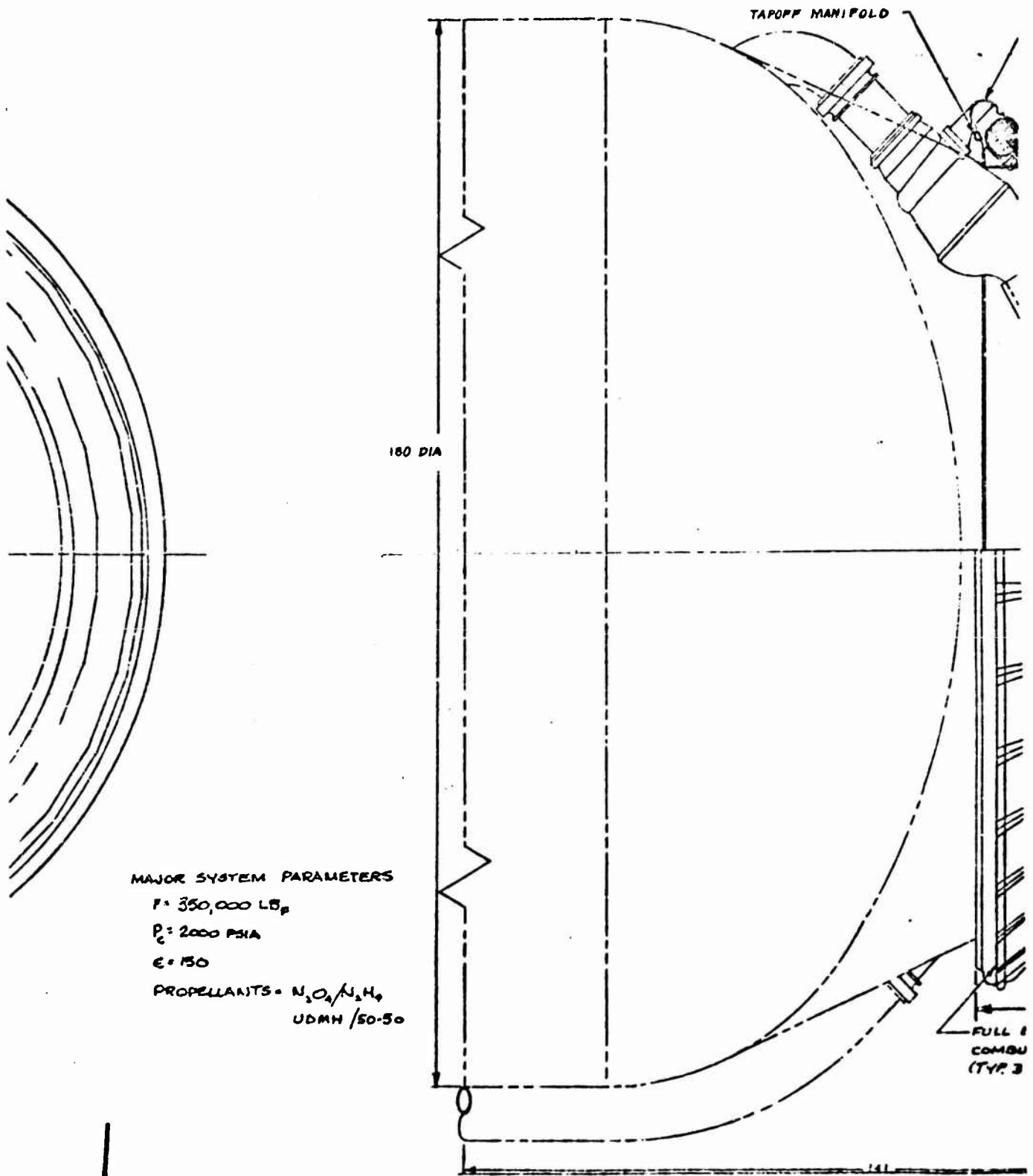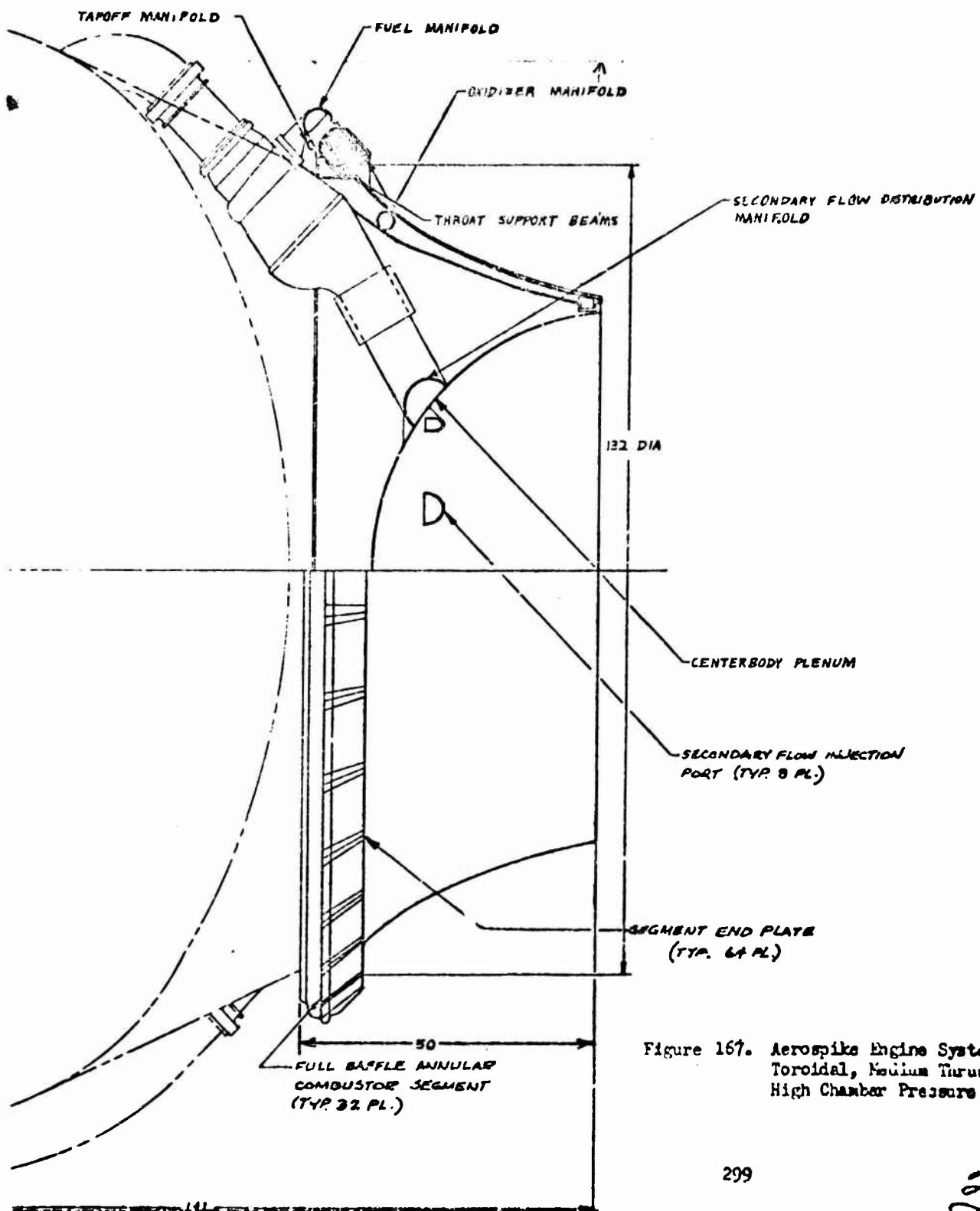
Figure 167. Aerospike Engine System, Toroidal, Medium Thrust, High Chamber Pressure

299

3
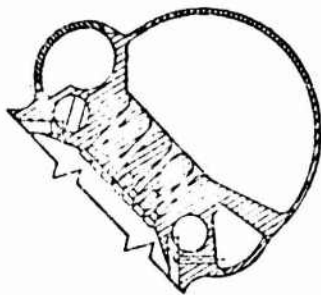
SECTION C-C
(FULL SCALE)

SECTION B-B
(FULL SCALE)

INJECTOR STRIPS NOT SHOWN

INBOARD TURRET SUPPORT
BEAM

INBOARD WALL TUBE

OXIDIZER FEED MANIFOLD

SECTION A-A
(FULL SCALE)

B

2

INBOARD MANIFOLD

B

INBOARD THRUST SUPPORT BEAM

FUEL FEED MANIFOLD

B

OUTBOARD WALL TUBE

OUTBOARD THRUST SUPPORT BEAM

INBOARD WALL TUBE
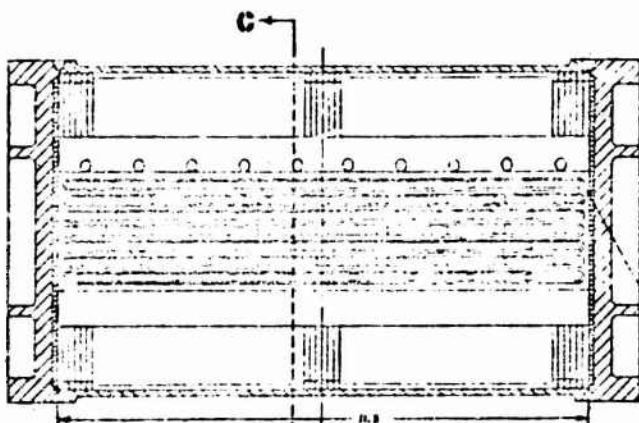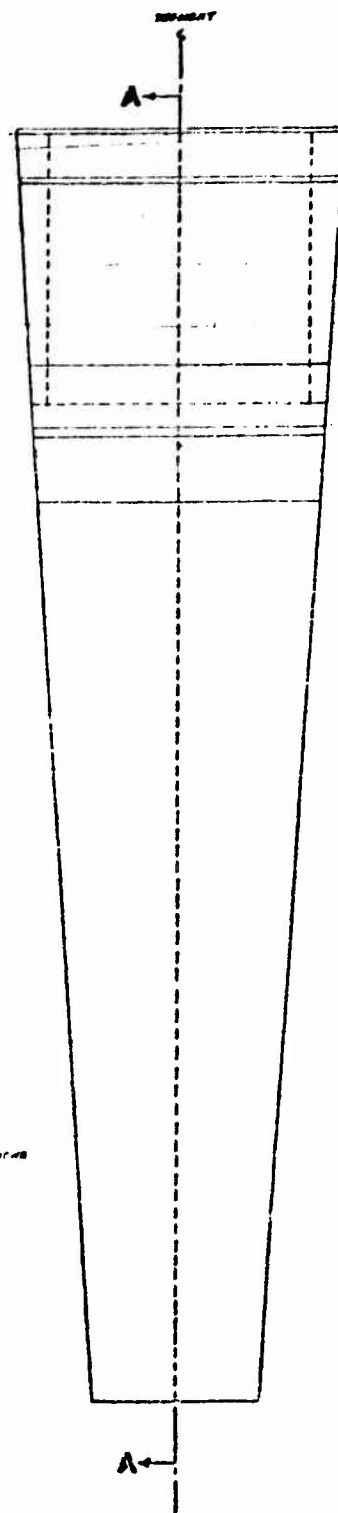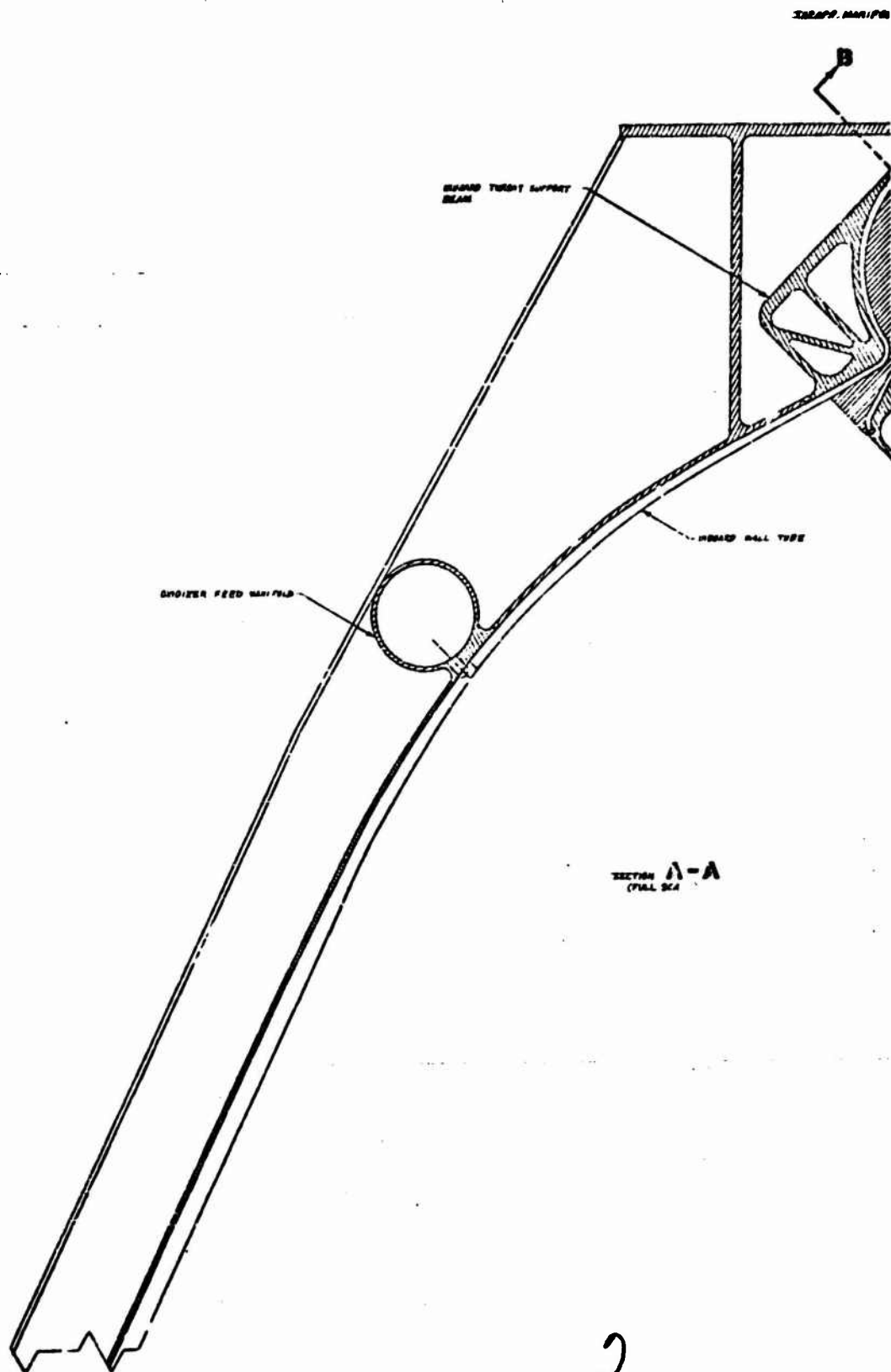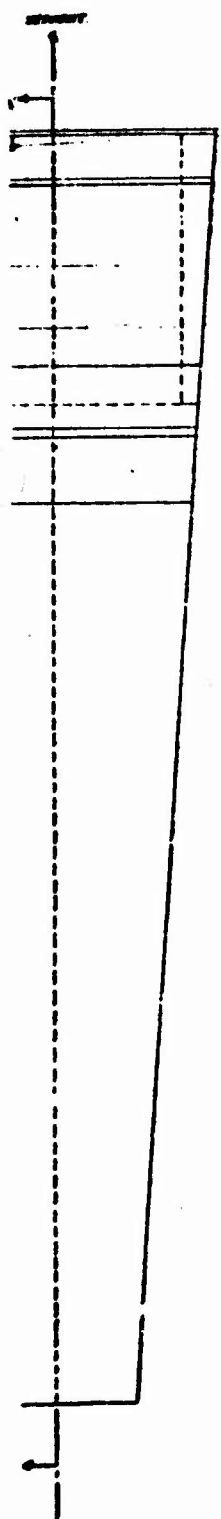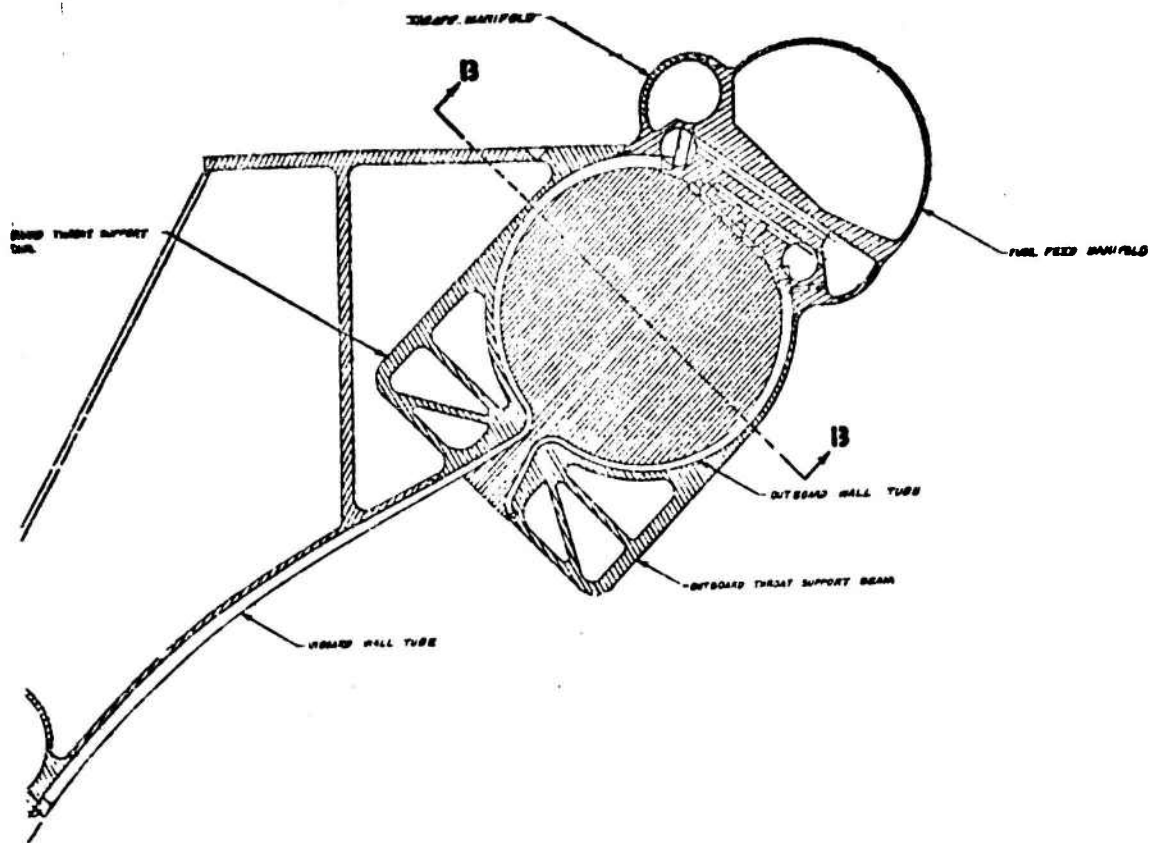
SECTION A-A
(FULL SCALE)

Figure 168. Aerospike Combustor Segment,
             Toroidal, Medium Thrust,
             High Chamber Pressure.

MAJOR
F = 35
P_c = 20
ϵ = 15,
PROPL
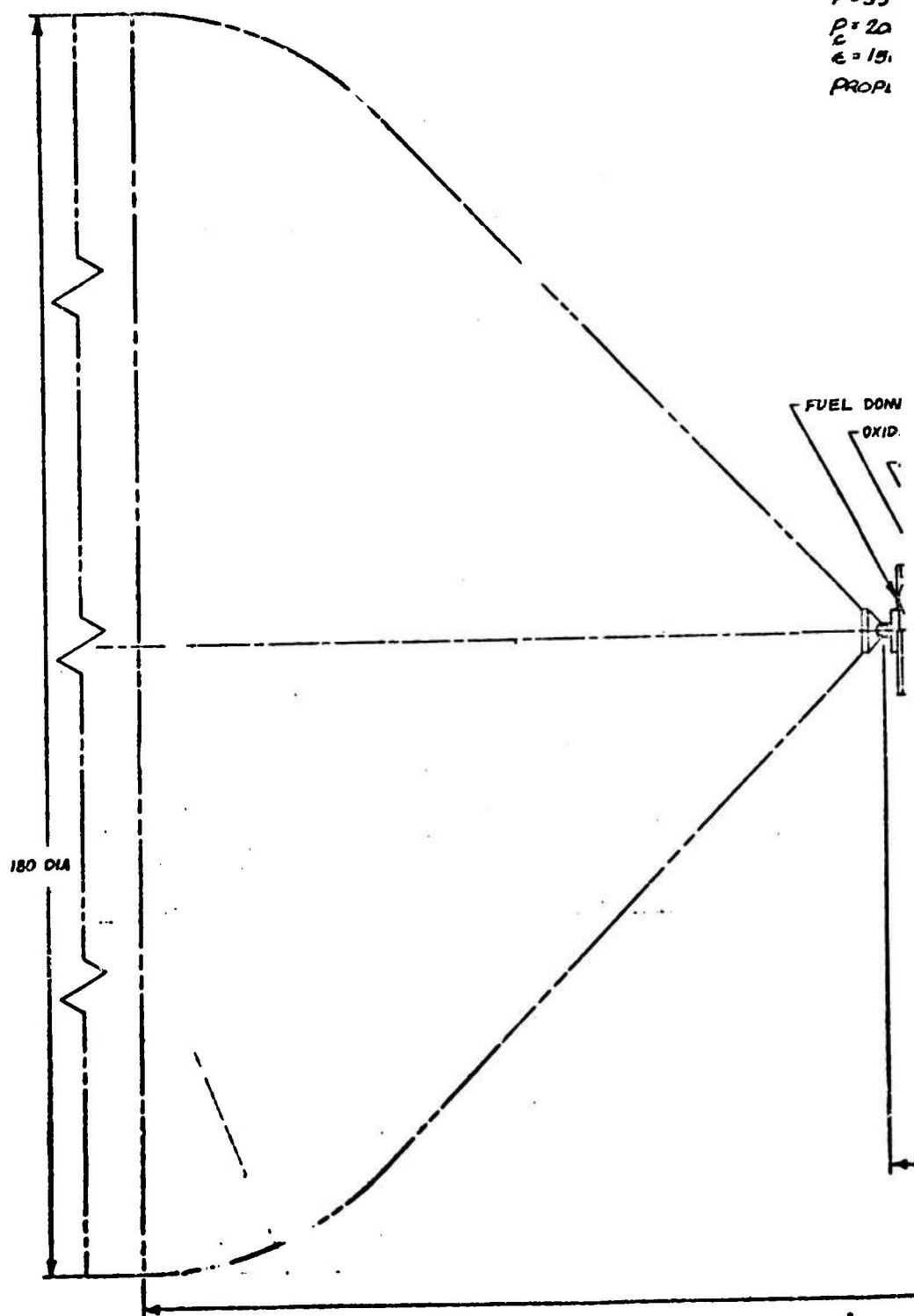
FUEL DOME
OXID.

180 DIA

MAJOR SYSTEM PARAMETERS
 F = 350,000 LB
 P_c = 2000 PSIA
 ε = 150
 PROPELLANTS = N_2O_4/N_2H_4 -UDMH (50-50)
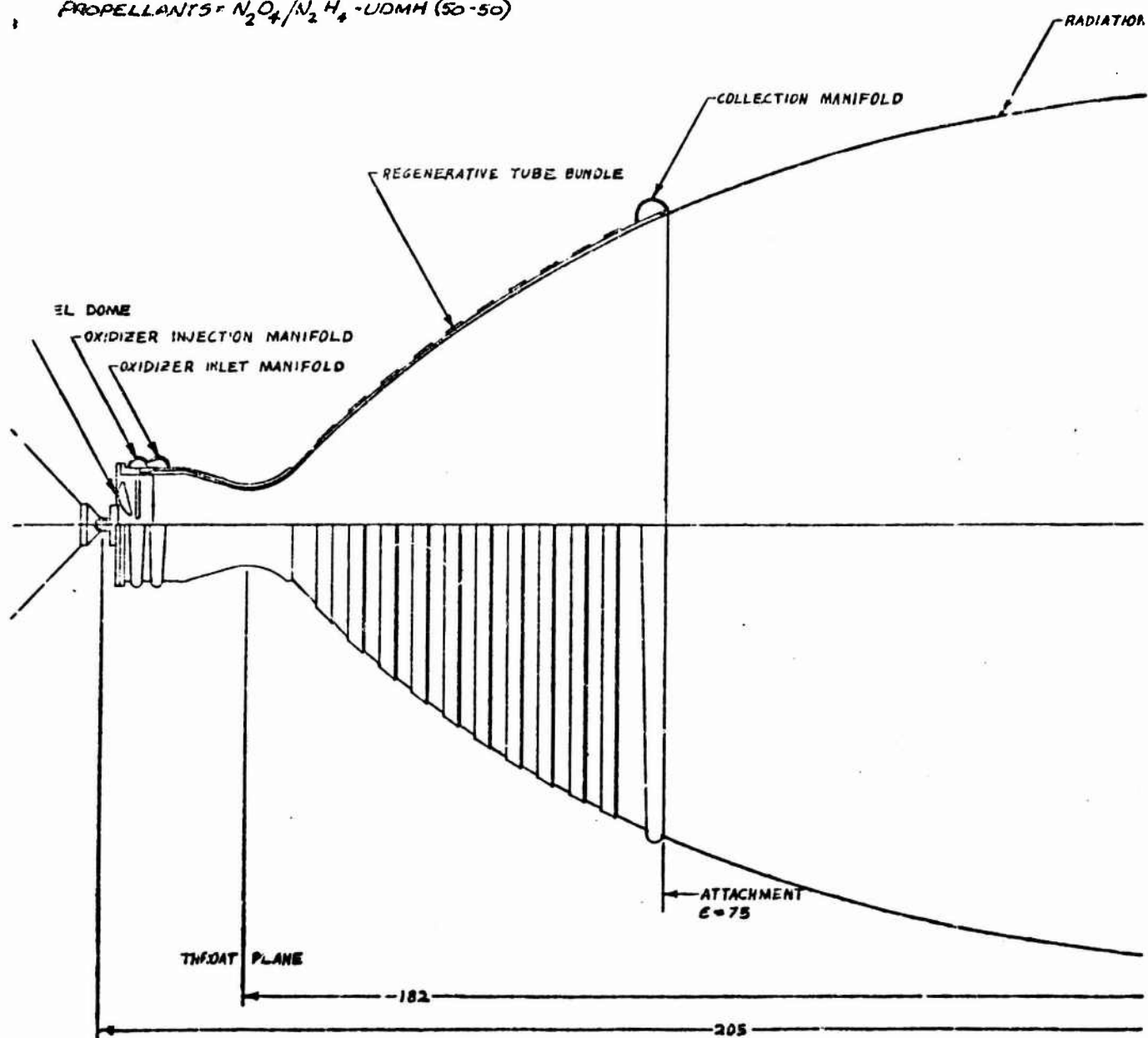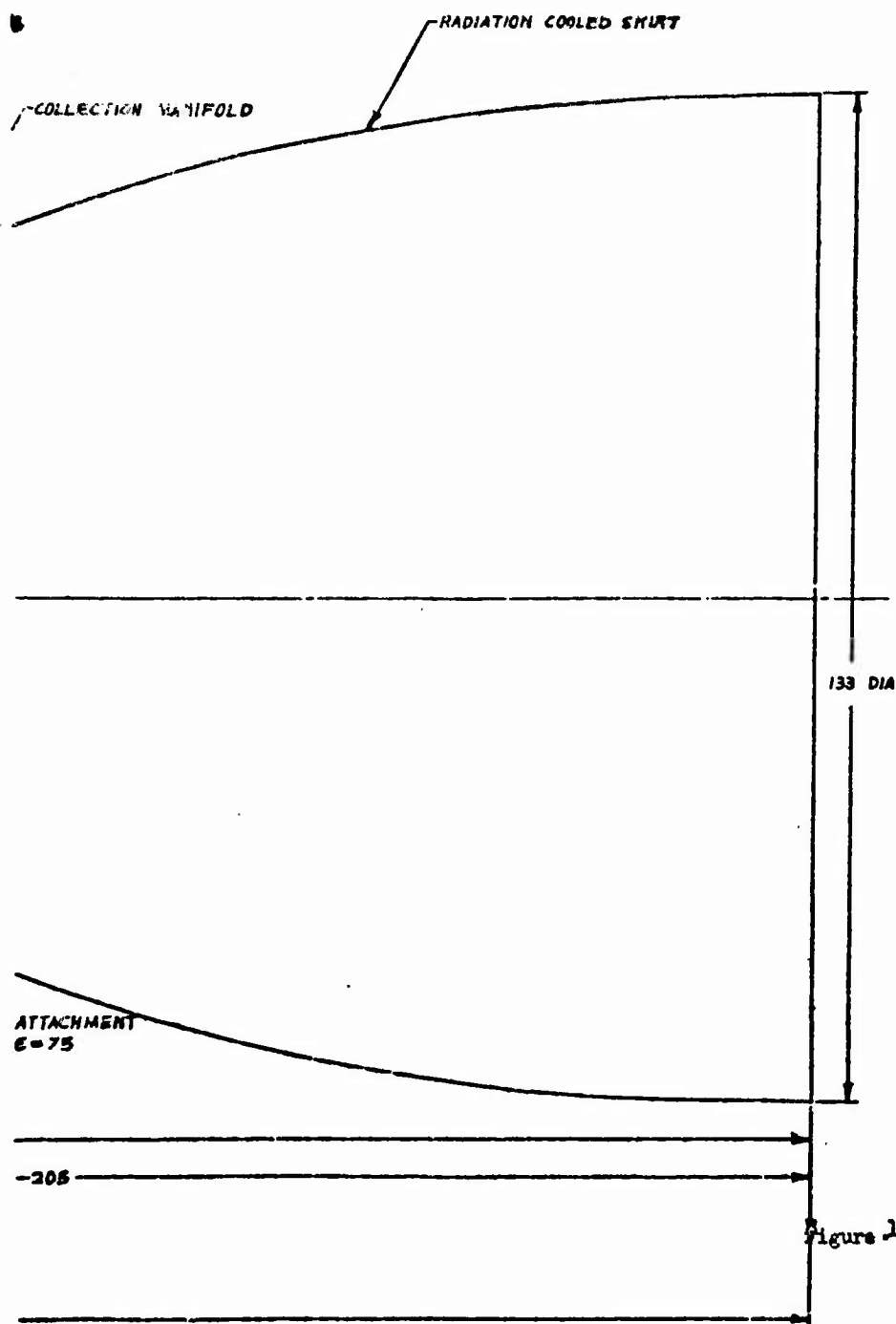
Figure 169. Conventional Thrust Chamber, Bell, Medium Thrust, High Chamber Pressure

RADIATION COOLED SKIRT

COLLECTION MANIFOLD

133 DIA

ATTACHMENT E=75

-205

2   301   3
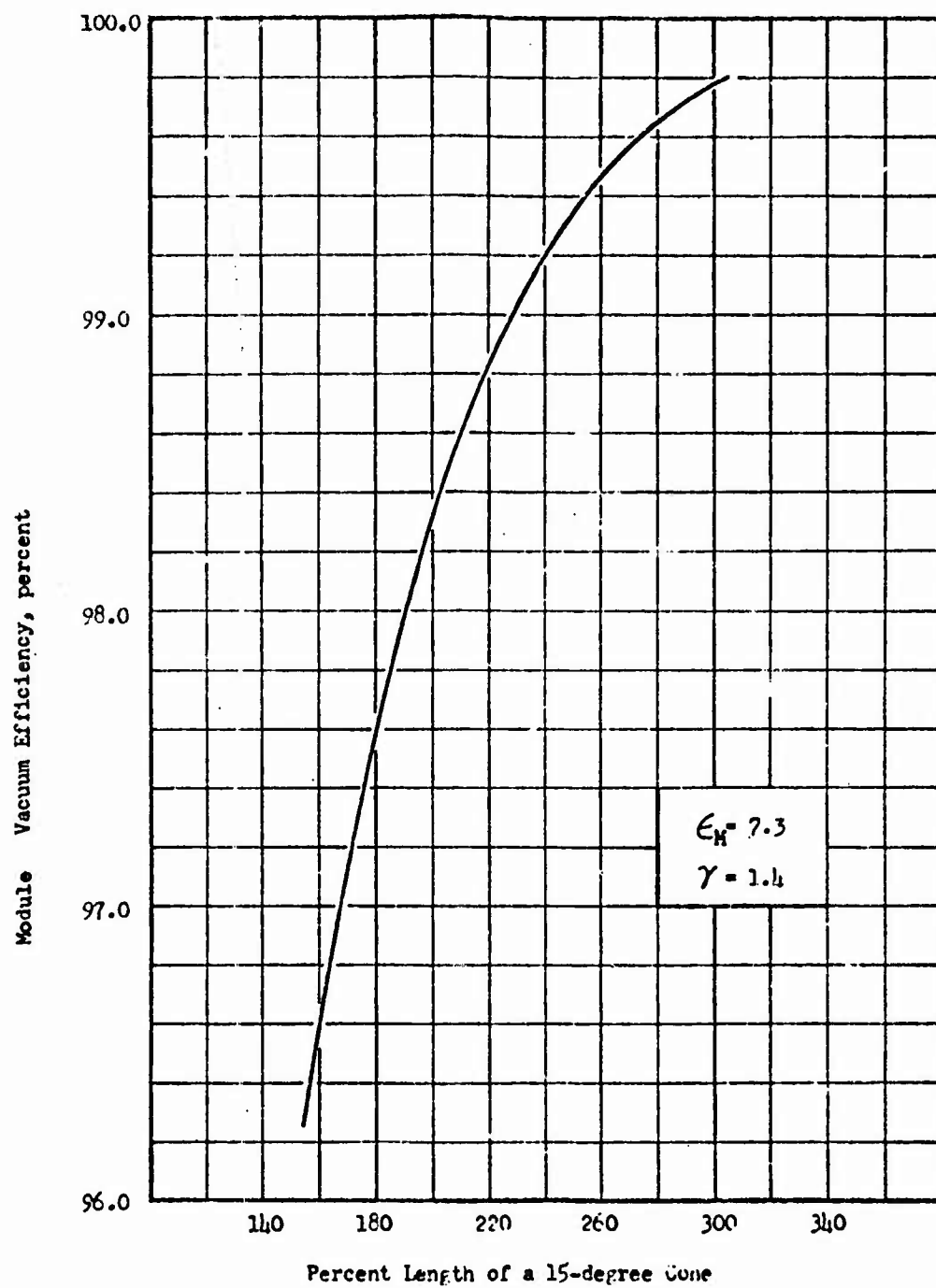
Figure 170. Maximum Performance vs Percent Length for a Two-Dimensional Nozzle

302

(C) A set of two turbopumps, one fuel and one oxidizer, feed propellants through individual lines to each thrust chamber. It can be seen that the use of a pair of pumps (mounted off the engine centerline) with eight chambers requires eight different high pressure ducts for each pump. The shorter ducts would require orificing to match propellant distribution between the ducts.

(C) Simpler options that could be employed if interchangeability contraints are neglected include one set of pumps for every module or feeding each two modules from a pump placed between them. Provision of one pump set per module (single or dual shaft) would facilitate pump fed development testing on a module level and allow direct operation with 2, 4, or 6 modules out. Feeding each two modules from a single shaft, back-to-back pump placed between them would allow operation with 4 modules out in the event of pump failure. Feeding each two adjacent modules from alternate fuel and oxidizer pumps placed between them would not allow module out operation in the event of pump failure.

(C) Feeding all chambers from a central single shaft turbopump would require placing the ambient temperature portion of the machine inside the fuel tank, or dimpling the tank bottom to accommodate it. If these options are unacceptable, a decrease in centerbody plenum depth or an increase in interstage structure length and weight would be necessary.

(C) A major disadvantage of the splayed nozzle multichamber combustor compared to a similar circular exit combustor lies in the difficulty of fabricating regenerative tube bundles in the splayed shape. It is

expected that the fabrication of ablative or radiation cooled nozzles
in this shape would present no problems as serious as those anticipated
in a regenerative bundle. If the splayed bundle exit is curved around
a radius as in the drawing, at most only pairs of tubes in any assembly
would be interchangeable, and in some cases even these pairs would be
right and left hand versions of the same contour, requiring a dif-
ferent forming die for each tube in the bundle. If the exit is made
straight, so that the cluster exit is polygonal, at most groups of
four tubes per bundle could be interchangeable.

(C) An alternate nozzle fabrication method was reviewed which offered
promise of forming the splayed nozzle shape by an assembly of straight
tapered tubes identical in cross-sectional contour but cut off at
varying lengths at the module exit. Figure 161 illustrates the method.

(C) Instead of forming the convergent-divergent contour of the chamber from
continuous tubes which become non-interchangeable aft of the module
throat, the axisymmetric combustion chamber is first formed of one
shape of identical tubes which are brazed into holes in a transition
ring at the module throat. These holes lead immediately into nozzle
tubes that are brazed into the other end of the short ring. The nozzle
tubes in the plane of nozzle divergence enter the ring at the angle of
divergence. Tubes in the non-divergent nozzle plane enter the ring
parallel to the nozzle axis. Intermediate tubes enter at intermediate
angles. Thus, the bending of tubes to various angles is replaced by
the drilling of holes at varying angles. Film cooling of the transition
ring may be necessary.

(C) Modules are cooled with N_2O_4 in a single downpass flow pattern in order
to minimize coolant bulk temperature at the chamber throat. From the
collection manifold, coolant must flow aft to cool the aerospike skirt.

(C)   Several alternative flow transition methods exist. From the standpoint
of structural strength and leak tight coolant sealing a promising pro-
cedure would be to make the inside module nozzle tubes and the skirt
tubes immediately aft of them as one continuous tube (which might in-
clude one or more brazed tube splices). Coolant flow from the outside
module tubes could be either manifolded and ducted back to the module
injector or flow between modules as shown and enter the inner continuous
tubes through slots cut in the sides not exposed to hot gas. This
option has the disadvantage that coolant velocity and pressure drop in
the skirt must be increased to offset the lowered N_2O_4 flowrate. If
the exterior chamber tube flow is utilized for skirt cooling, extra
skirt tubes must be included to fill the gap aft of where it passes
between chambers. A disadvantage of either sort of continuous module-
skirt tube construction was the aspect of including modules and skirt
in one brazed assembly. Apart from severe tolerance requirements, a
replacement of a defective module would be difficult. A construction
method permitting module substitution on a "plug in" basis is
preferable. The module-skirt transition configuration shown in Fig. 165
employs a segment transition manifold to permit removal of the module
from a bolted flange on the skirt.

(C)   Exhaust pressure inside the splayed module nozzles exerts forces tending
to distort the contour into an axisymmetric, circular exit bell contour.
Nozzle banding or other external structure must be fastened around the
brazed tube bundle to resist these loads. A detailed weight comparison
between a circular exit module and a comparable module with a 2:1
elliptical exit shape was made in Ref. 18 . Even with this relatively
moderate ellipse ratio the elliptical exit shaped nozzle was heavier
than the circular exit nozzle by a factor of two. This relative weight
ratio becomes greater as the nozzle approaches a two-dimensional shape.

(C) Chamber thrust lo 's are transmitted into the vehicle shell through brackets which diffuse the point loads into a continuous line load. The chamber injectors are bolted directly to these brackets. Tapoff gases tapped from a port on the axis of each injector pass through a sleeve and into a tangential collection manifold threading through small cutouts in the bracket webs. Turbopump mounts are fastened to two adjacent thrust brackets. Turbine exhaust gas is manifolded and distributed through eight ports in the centerbody plenum.

(C) 350K Toroidal Aerospike. A full combustion zone baffle combustor was chosen to represent the toroidal family of combustion at this design parameter level. A layout of the engine is shown in Fig. 167.

(C) In the full baffle annular toroidal chamber, a rectangular throat slot releases primary gas from a cylindrical combustion volume. Chamber pressure is contained in a structural box formed by an injector bar opposite the throat slot, two chamber half shells, an end plate across each end of the cylinder, and two beams, inboard and outboard of the throat slot which stretch between end plates. The chamber half shells are exposed to the usual hoop and axial tension stresses present in a pressurized cylinder, while bending moments incurred in slitting the cylinder down one side are absorbed in the throat support beams.

(C) The engine pictured is composed of 32 such segments, arranged in a 32 sided polygon. Selection of segment number (N) was constrained primarily by weight tradeoff which determined an optimum end plate separation to be 11.3 inches. With the selection of an end plate separation, and a value of area ratio, the number of segments in the engine was limited to a small range of integers dependent on end plate thickness.

(C) An aerospike skirt length of 19% the length of a 15° half angle cone to an area ratio of 150 is shown in the engine layout. An outboard shroud to an area ratio of 3.5 was used. A hemispheric plenum centerbody was used, with a toroidal manifold to tangentially distribute turbine exhaust from the torbopump outlets.

(C) The combustor segment injector (Fig. 168) provides the following flow scheme; single up pass inboard wall tube, injector face tapoff, and double pass outboard wall tubes. Tapoff gas is tapped from the chamber at the side of the face near the outside fuel injector strip. An insulated sleeve ducts the gas through the end cap feed passage and into the tapoff manifold. Fuel is fed from a manifold on the back of the block through down holes directly into milled grooves in the injector face. The grooves feed face strips which inject the fluid in the selected pattern. Oxidizer is introduced from a tapered toroidal manifold located near the top of the skirt. The coolant is double passed downwards to cool the lower skirt and then flows upwards to the combustion chamber in a single pass. The single pass wall tubes start flattened at the feed manifold, become circular in cross section at the throat, and return to an oval cross section toward the injector to reduce coolant velocity. The wall tube bundle is brazed into a continuous groove in the injector block. The N_2O_4 flows into a deeper groove with holes drilled in the groove bed. These holes cross to a deep drilled hole traversing the injector block lengthwise. The coolant flow splits into two parts, one flowing along the deep drilled hole to cool the end plates, the other passing through cross holes to a third welded manifold which feeds the downpass tubes of the outboard wall bundle. The up pass tubes of this bundle feed a second deep drilled hole containing the return flow from the end plates. Small cross holes then feed oxidizer to the injection strip grooves.

The engine was assumed fixed, with thrust vector control provided by side liquid injection of N_2O_4.

(C) <u>Comparison to 350K Bell Engine</u>. The overall engine length of the 80% bell engine shown in Fig. 169 is 205 inches. On this same basis of length from the exit plane to the forwardmost point on the engine, the multichamber and toroidal engines are 45% and 40% respectively of the bell chamber length. The overall diameters of these engines were 147 percent and 125 percent the diameter of the conventional engine.

(C) A comparison on the basis of physical overall length has questionable validity at this design point, as the degree of engine/vehicle integration varies among the designs. If a comparison is made on the basis of length attributable to the engine over and above that of its associated tank bottom (45 degree cone for bell engine, 0.7 ellipse for aerospikes), the multichamber and toroidal engine lengths are both 26% of the bell length. The provision of a conical tank bottom for the bell engine would further increase the length and weight of interstage structure in this upper stage application.

Medium Thrust Low Chamber Pressure Engine Design

(C) Multichamber, toroidal aerodynamic spike engines and a single bell engine which are suitable as the propulsion system for a medium thrust low chamber pressure application are presented in Fig. 171 through 175. The engines generate 658,000 pounds of thrust at a chamber pressure of 300 psia. Propellants are supplied to the thrust chambers by tank pressure. Area ratio was limited by the 13 foot tank diameter

OXIDIZER DOME

FUEL
INJECTION
MANIFOLD

AERODYNAMIC
BOAT TAIL
SHROUD

ABLATIVE
COOLED
MODULE
(12 REQ'D)

113

80

58

14°

O   O

145 DIA

TAPOFF (SECONDARY FLOW)
DUCT (12 REQ'D)

A

ABLATIVE COOLED SPIKE
EXPANSION NOZZLE

(CONDARY FLOW)
(REQ'D)

145 DIA

157 DIA
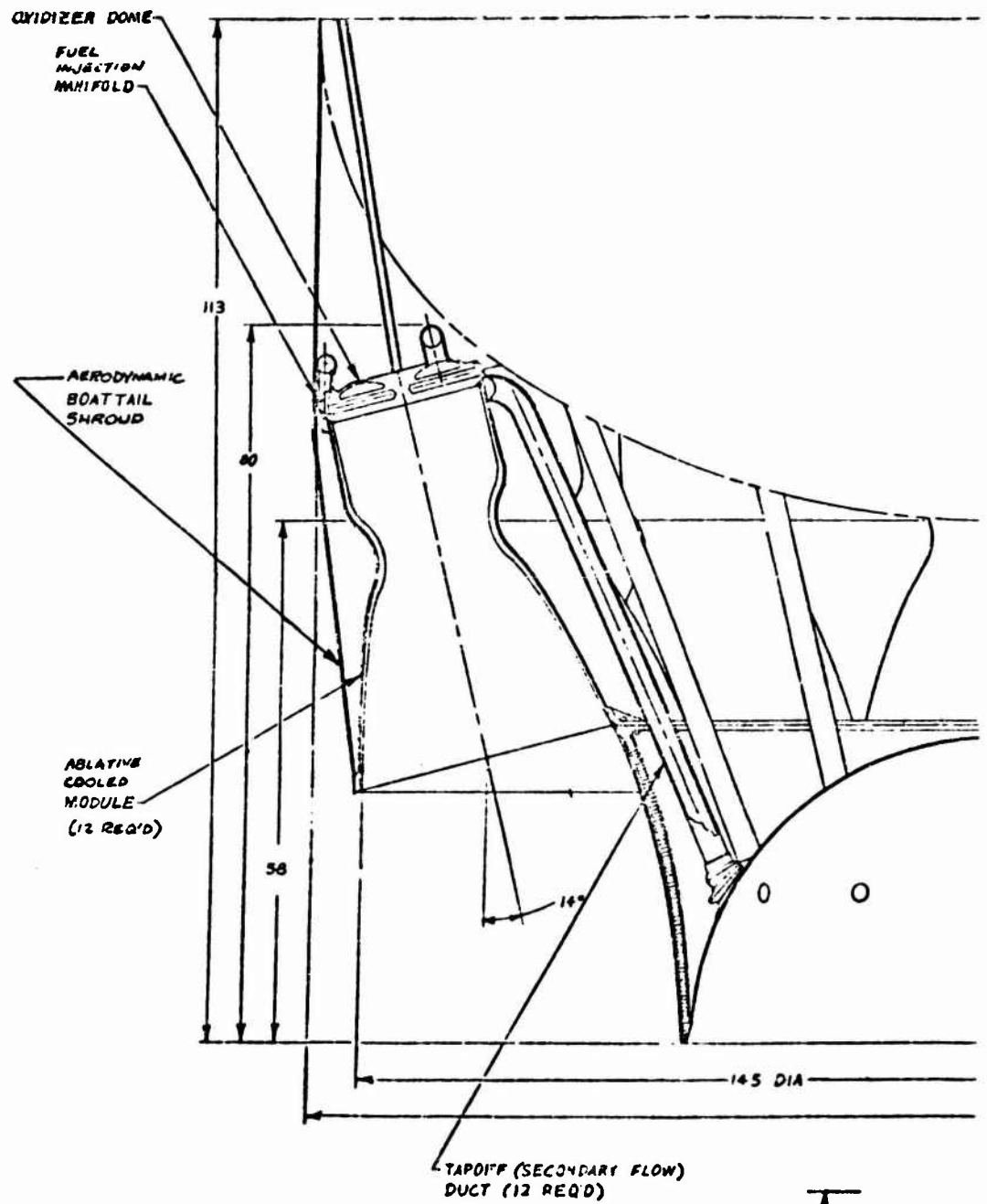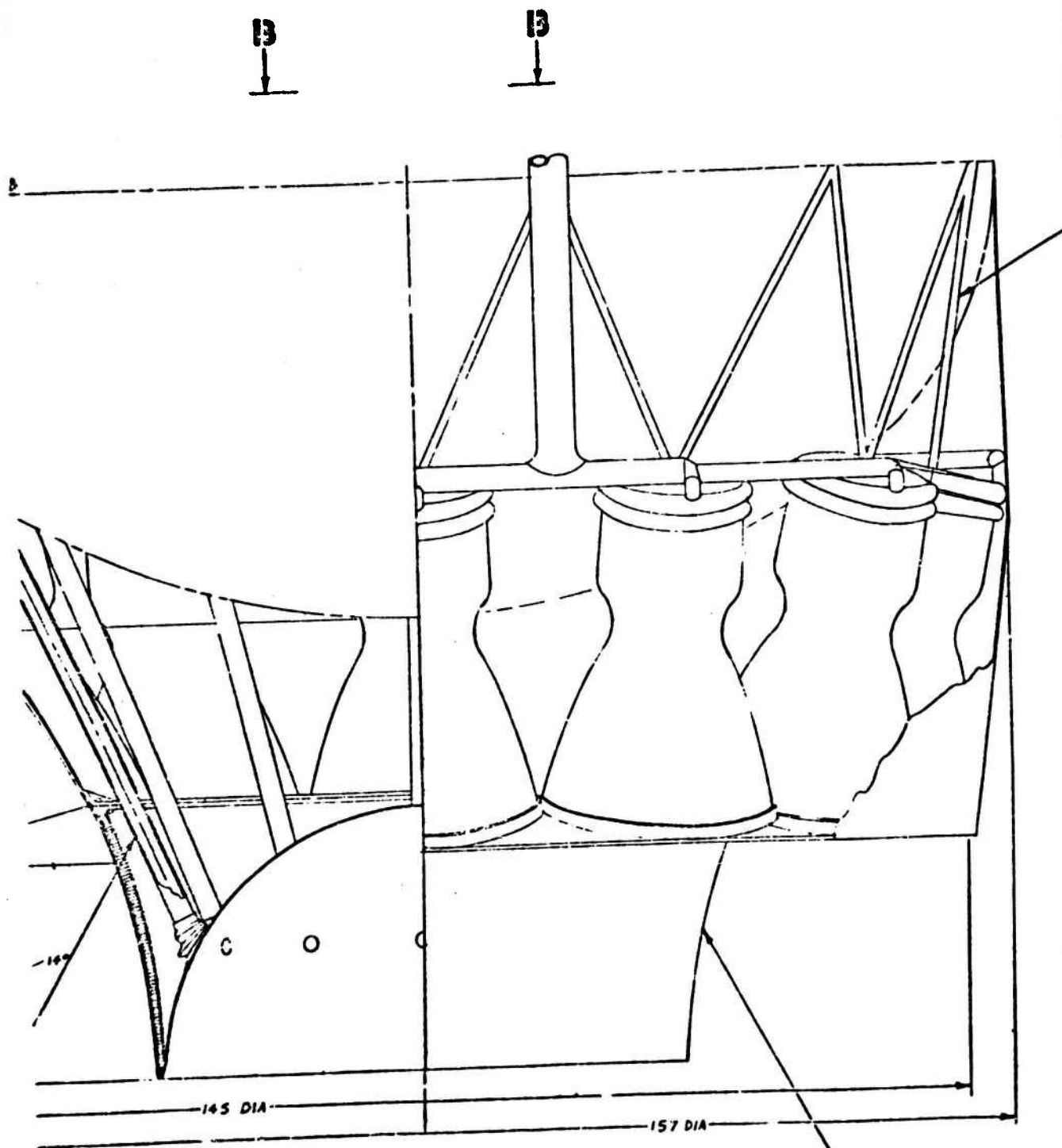
TUBULAR THRUST STRUT
(24 REQ'D)

ABLATIVE COOLED SPIKE
EXPANSION NOZZLE

MAJOR SYSTEM PARAMETERS

F = 657,780 LB$_F$ (SEA LEVEL)
P_c = 300 PSIA (NOZZLE STAGNATION)
ϵ_c = 11.5
ϵ_n = 5.41
N = 12 BELL CHAMBERS
PROPELLANTS = N_2O_4 / N_2H_4 - UDMH (50-50)

NOTE: The area ratio described by the scalloped perimeter of the module exits is 10.0

Figure 171. Multichamber Aerodynamic Spike Engine System. Medium Thrust, Low Chamber Pressure.

VIEW 13-13

OXIDIZER FEED MANIFOLD
(3 REQ'D)

FUEL FEED MANIFOLD
(3 REQ'D)

VIEW B-B

1

2

ABLATIVE-
COOLED INTER-
MODULAR
BAFFLE
(12 REQ'D)

VIEW **A - A**

Figure 172. . Multichamber Aerodynamic Spike
Engine System, Medium Thrust,
Low Chamber Pressure.

TYPICAL
MODULE

140.0

VIEW A·A

FUEL INLET LINE
3 REQD. 5.20 DIA

OXIDIZER TANK

180.0 C

TAP OFF (SECONDARY FLOW)
DUCT (.080A-0.020) 347 CRES
2 REQ.

CENTER BODY
347 CRES - QL

BURST DIAPHRAGM

232

80.0 D

FUEL MANIFOLD
3 REQD

DATA:
1ST STAGE
12 MODULES (3 SEGMENTS/MODULE)
F= 657,780 LB
P_c= 300 PSIA
ϵ = 8.0
MR= 2.0
PROP: N_2O_4/N_2H_4-UDMH (50-50)

2

Figure173. Toroidal Aerodynamic Spike Engine. Medium Thrust. Low Chamber Pressure.

311
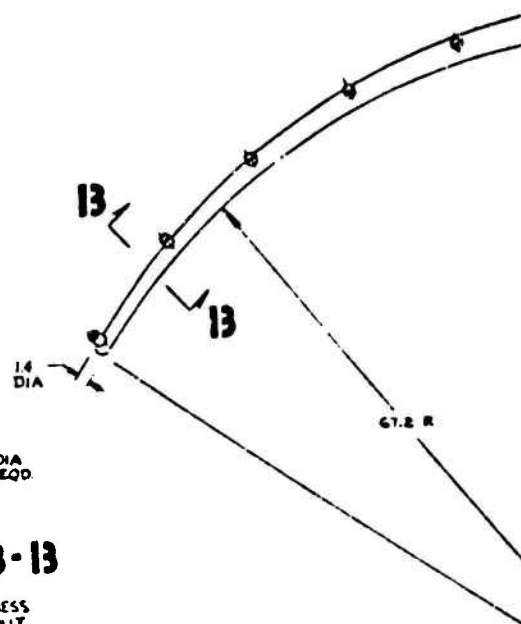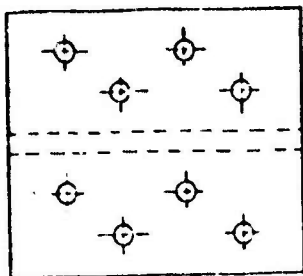
SECTION **B-B**

.032 THICKNESS
THROUGHOUT

.12 DIA
12 REQD.

14
DIA

67.8 R

MODULE END PLATE

.50

.55 DIA
(TYP)
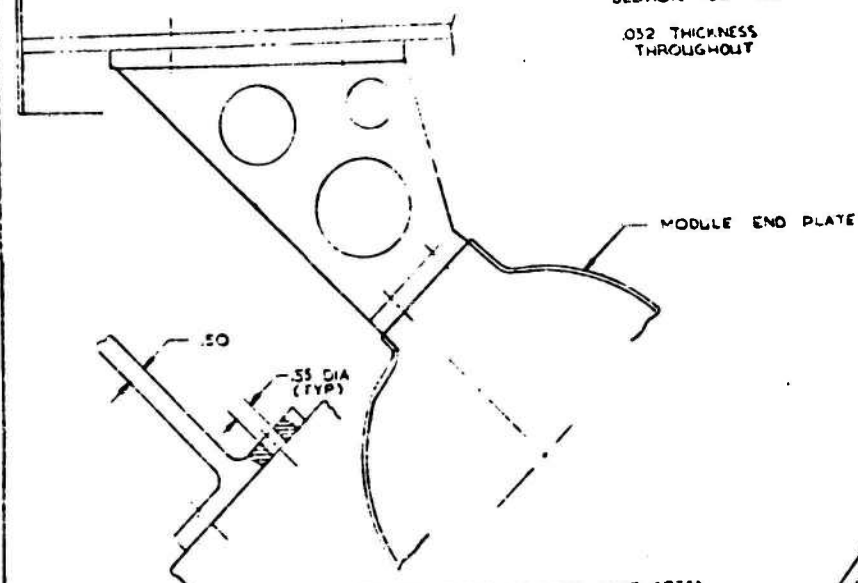
TYPICAL THRUST MOUNT (347 CRES)
1/2 SIZE
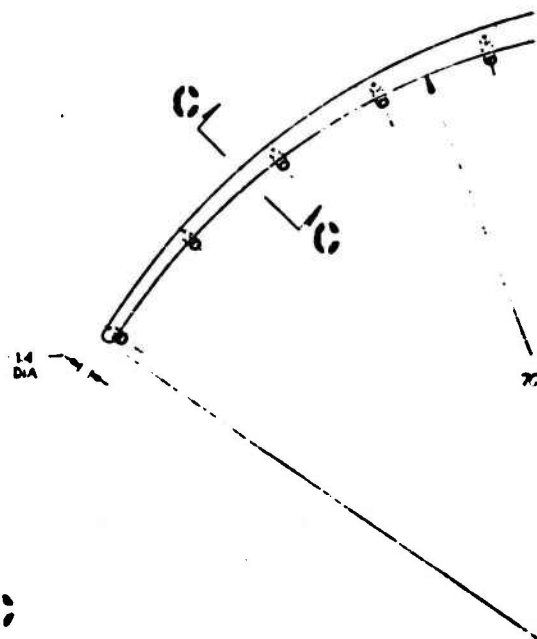
SECTION **C-C**

.032 THICKNESS
THROUGHOUT

.12 DIA
12 REQD

14
DIA

312
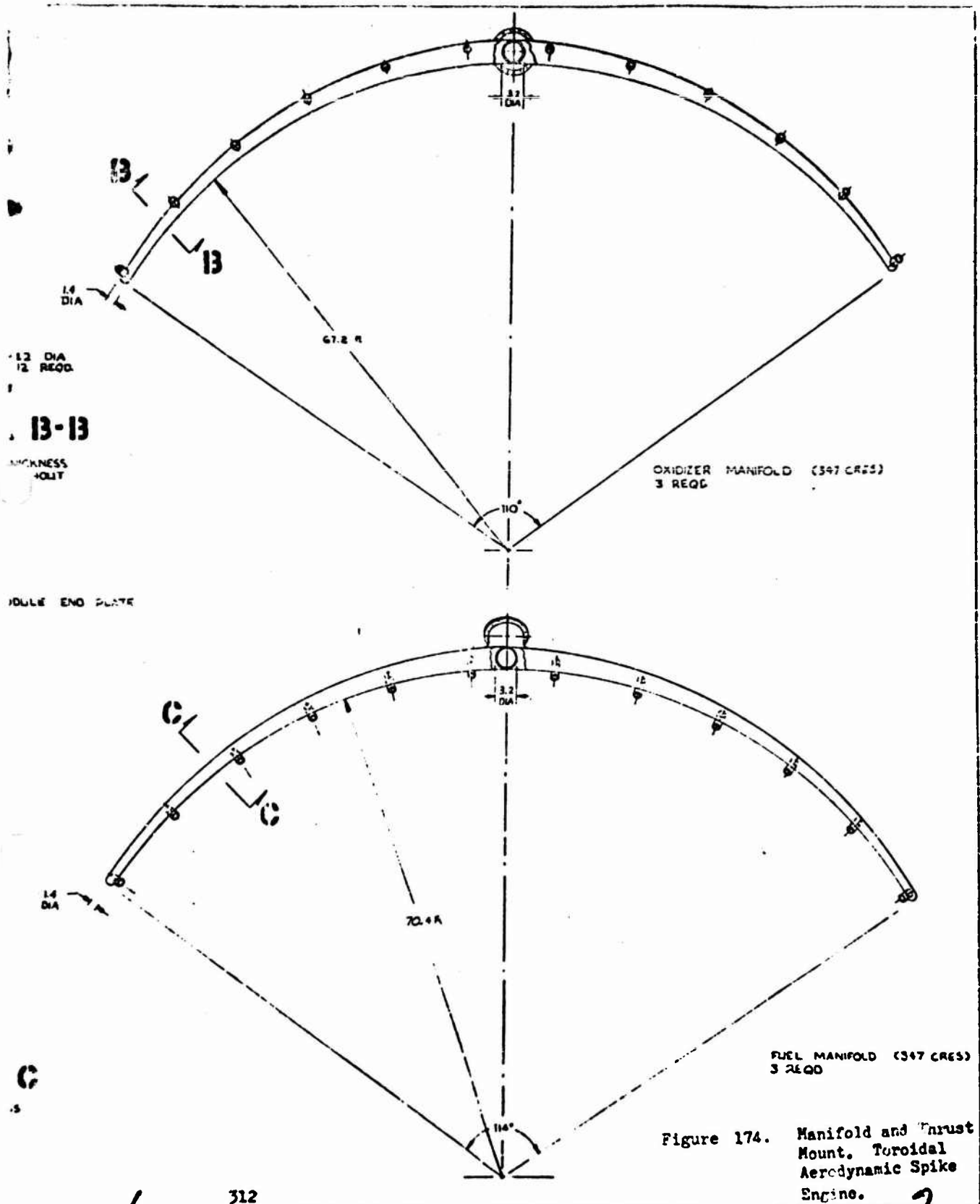
Figure 174. Manifold and Thrust Mount, Toroidal Aerodynamic Spike Engine.

312

MAJOR SYSTEM PARAMET
$F = 657,780$ l.B, (SEA LE
$P_c = 300$ PSIA (NOZZLE S
$E = 8.0$
PROPELLANTS = N_2O_4 /A

156 DIA

THROAT

37

71

BOATTAIL LIMITED ENVELOPE

JET SEPARATION LIMITED ENVELOPE (ε = 8.0)
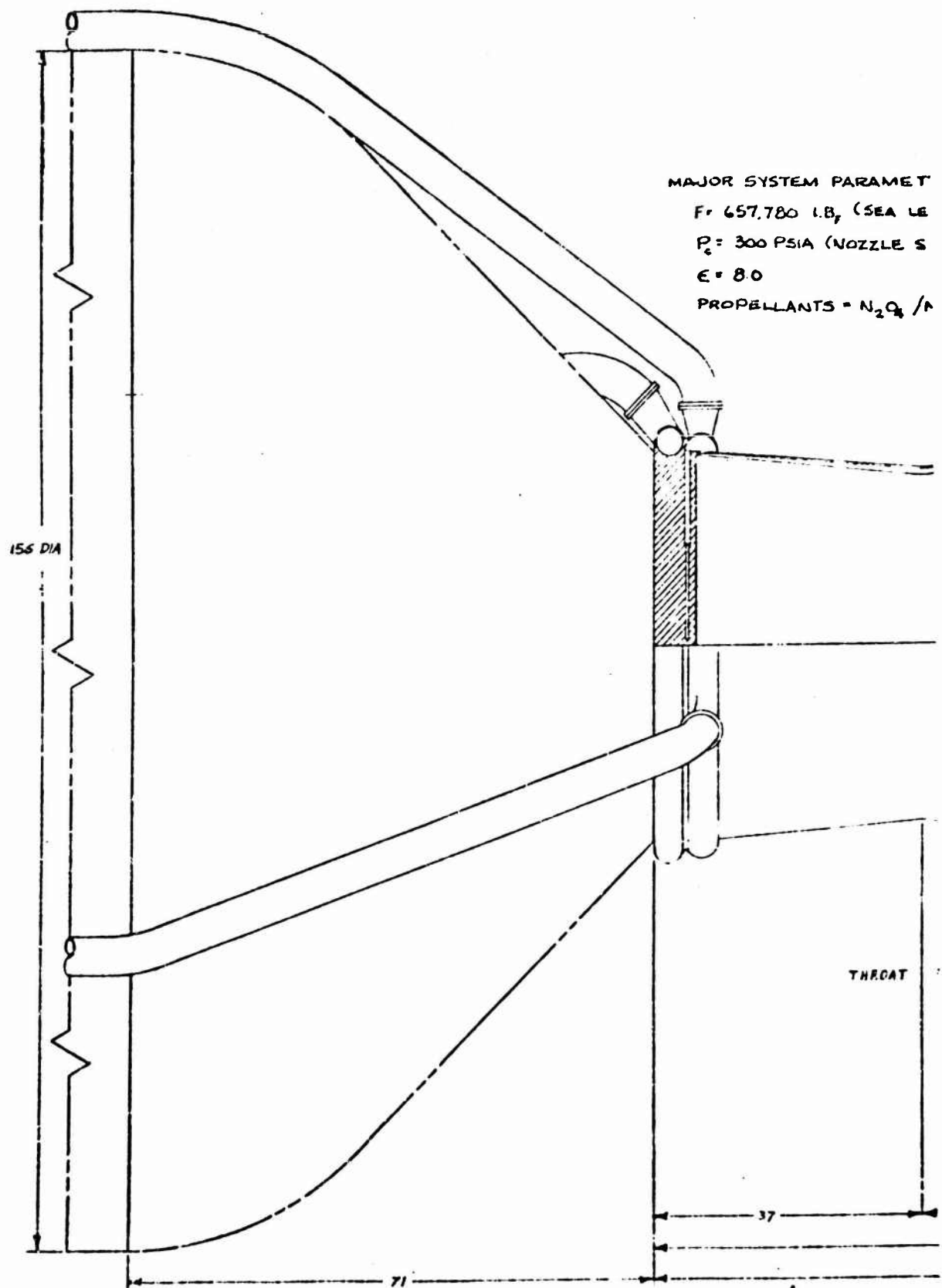
HR SYSTEM PARAMETERS

657,780 LB$_f$ (SEA LEVEL)

= 300 PSIA (NOZZLE STAGNATION)

= 8.0

PROPELLANTS = N_2O_4 / N_2H_4 - UDMH (50-50)
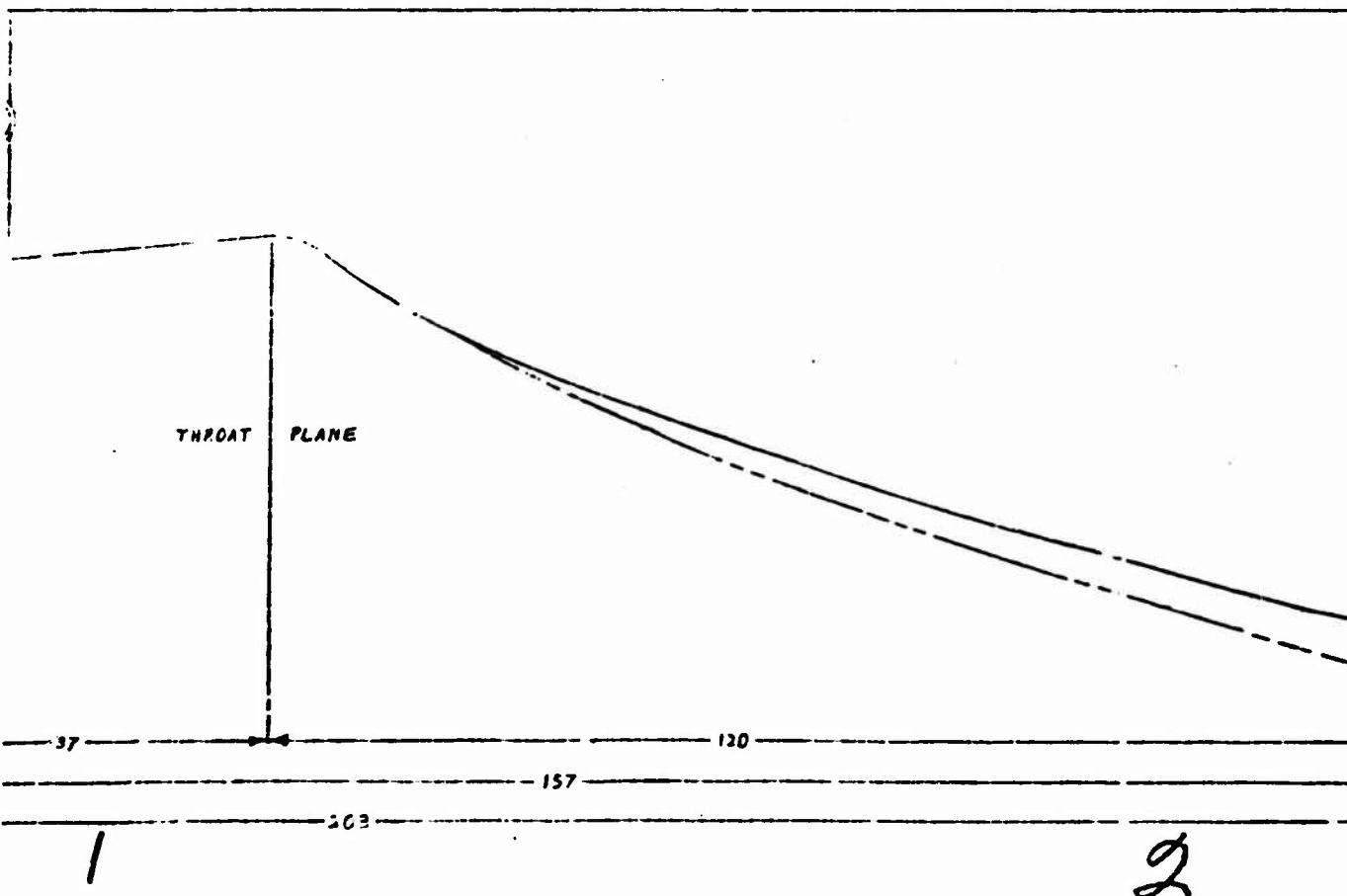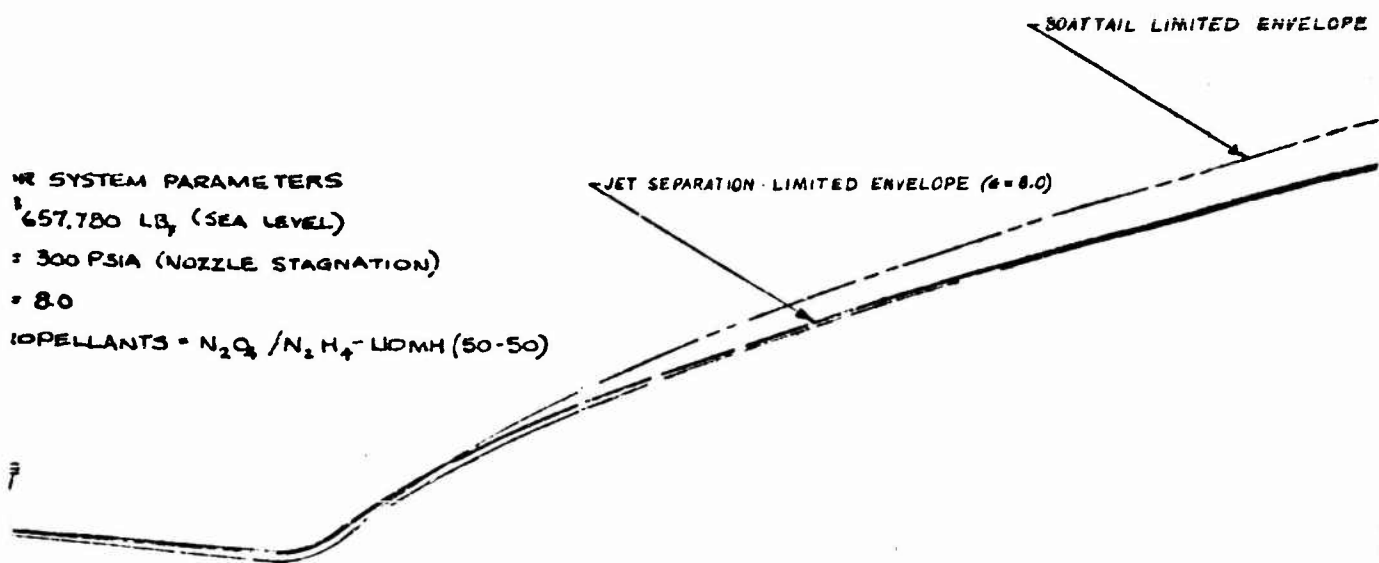
THROAT PLANE

37
120
157
203

1   2

BOATTAIL LIMITED ENVELOPE (ϵ = 12.5)

ENVELOPE (ϵ = 6.0)

124 DIA

155 DIA

Figure 175. Single Bell Engine System.
Medium Thrust, Low Chamber
Pressure.

313

2
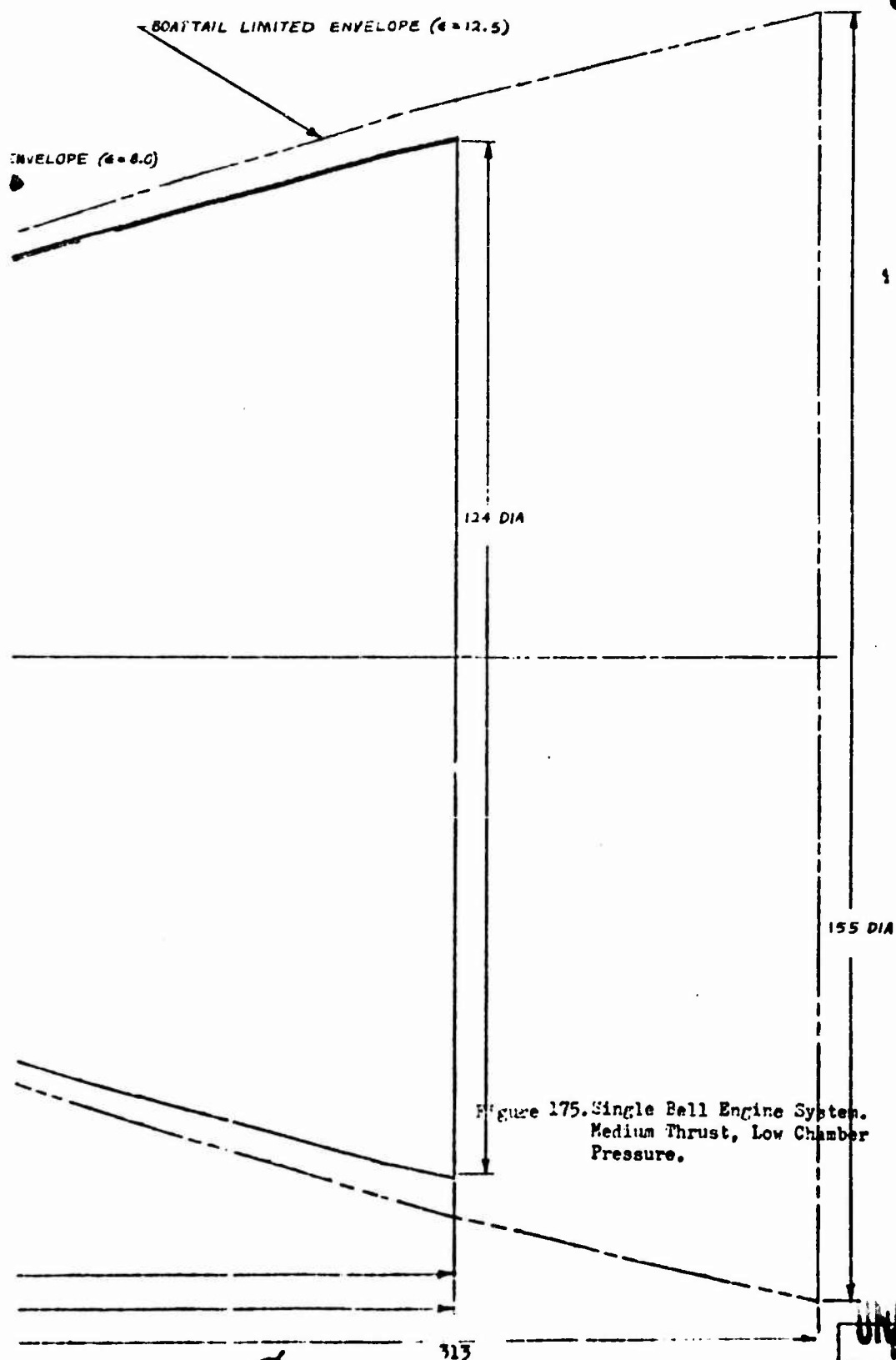
(fixed by a maximum overland transportation envelope) for the toroidal
and multichamber engines and by nozzle separation for the single bell
engine system. Table 14 summarizes the envelopes found for these
booster configurations.

(C) The annular toroidal combustor is divided into thirty-six (36) segments
by full combustion zone baffles. Each group of three segment is plumbed
in common to form twelve (12) modules. The modules are fed in groups
of four from three fuel and three oxidizer ducts, each fitted with burst
diapgragms. Engine start is initiated by pressurizing the propellant
tanks. Cutoff is accomplished by propellant depletion. These sequences
are also practical for the analogous multichamber configuration. The
multichamber design (Fig. 171) employs twelve chambers, each bell
module being analogous to a three segment module of the toroidal config-
uration. The bell modules extend to an area ratio of 5.4 which brings
the exits nearly tangent. A small exit separation is necessary to
accommodate the structural rings and ablative liners.

(C) Although regenerative cooling of a sonic tube toroidal combustor is
feasible for these engine parameters, ablative cooling was employed in
the present study since regenerative pressure drop is reflected directly
as a tank weight increase in pressure fed stages.

(C) Both multichamber and toroidal combustors are cooled by the ablation
of a phenolic refrasil liner which is bonded to the structural shells
with a high temperature adhesive. An ablative liner thickness of 0.63
inch would be required at the throat of either combustor for cooling
over the 91 second burning duration. Char erosion of the throat
dimension may be held to 6 - 8 percent of ablative thickness by in-

Table 14 Engine Envelope Summary

CONFIDENTIAL

Thrust Pounds	Engine Type	Nozzle Length, From Throat, L_N		Engine Length, From Turbopump Inlet		Engine Length, From Elliptic Tank Bottom		Engine Diameter
		inches	Percent of 15 degree cone	inches	Percent of 15 degree cone	inches	Percent of 15 degree cone	inches
653,000	Toroidal	26.5	17.7	41.5	26.4	30.5	17.7	156.0
658,000	Multichamber	54.3	36.2	80.0	51.0	58.0	33.7	156.0
658,000	Single Bell	120.0	80.0	157.0	100.0	172.0*	100.0	124.0
2,000,000	Toroidal	62.6	19.0	98.5	45.0	68.2	26.2	216.0
2,000,000	Multichamber	104.0	30.0	144.5	66.0	100.0	38.5	216.0
2,000,000	Single Bell	202.0	80.0	218.5	100.0	260.0*	100.0	164.0

*This gives an indication of the relative comparison of total vehicle length affected by the engine configuration. The conical tank bottom normally used with the single bell engine requires a longer tank structure. The value shown is measured from the actual bell exit to a fictitious elliptic tank bottom which contains the same quantity of propellant as the conical tank bottom.

jecting approximately 2 percent of fuel film coolant along the chamber walls, based on LEM engine tests. A 8 percent surface regression corresponds to throat area increases of 2 percent, 1.5 percent, and 0.5 percent for the annular toroidal, multichamber, and single bell combustors respectively.

(C) Multichamber combustors should show char and erosion depths slightly less than those experienced in annular combustors under similar surface conditions, since the heat streamlines diverge radially, i.e., the cross sectional perimeter exposed to hot gas is less than the perimeter being charred. This effect is small at the 658K design point, the diminution in heat flux at the char layer amounting to 5 percent when half charred and 9 percent at full char. At lower module thrusts and longer burning times, this effect would become more important.

(C) Thrust load transmission in the toroidal design is accomplished by supporting the centerbody and skirt loads by a honeycomb sandwich shell backing the ablative coolant layer. This shell is welded to the inboard throat support beams of the toroidal segments. Engine thrust is transmitted to the vehicle through twelve thrust mounts welded to the segment end caps bounding each module. The load path in the multichamber configuration is somewhat more complex, as it was assumed here that some weight could be saved by utilizing the outer structural shells of the bell modules as members to transmit expansion nozzle and centerbody components to the module thrust structure. These shells could be built up of welded sections and ablative liners bonded and cured in place. A reinforcement ring was placed around the module exits to distribute the nozzle line load and bending moment into the twelve members. The rings also provide a convenient place to weld

ablative cooled baffle plates which seal the boattail from recirculating gas. A bolted connection is shown at the interface of the spike nozzle and the bell modules. The ablative liners of each module and the spike are case and cured as independent units.

(C) The thrust structure shown in Fig. 171 is composed of twenty-four (24) tubular thrust struts arranged in a lattice. The struts are 17-7PH steel as is the propellant tankage. Welding of 24 such struts into place would be considerably cheaper than the construction of a semi-monocoque or sandwich shell over the same span. A monocoque shell of thickness constrained by compressive yield stress ($t = 0.016$ inch) was found to be unstable in the local buckling mode. Local reinforcement around the strut attachment points will be necessary to diffuse the loads into the membrane. The placement of anti-slosh and anti-vortex baffles on the tank interior would be coordinated with these attach points to minimize the weight of such reinforcement.

High Thrust, High Chamber Pressure Engine Design

(C) The last design point evaluated was for an engine system which operates at high (2000 psia) chamber pressure and delivers 2,000,000 pounds of thrust at sea level. Typical multichamber and toroidal aerodynamic spike engines and a single bell chamber engine which meet these requirements are shown in Figs. 176, 177, and 178. These engines are regeneratively cooled with N_2O_4 at supercritical pressure. Parallel turbines driven by primary combustor tapoff gases are used. Both engines contain eight modules, each fed by its own separate oxidizer and fuel turbopump. The area ratios of the annular engines were limited by an 18 foot vehicle diameter. Jet separation at sea level
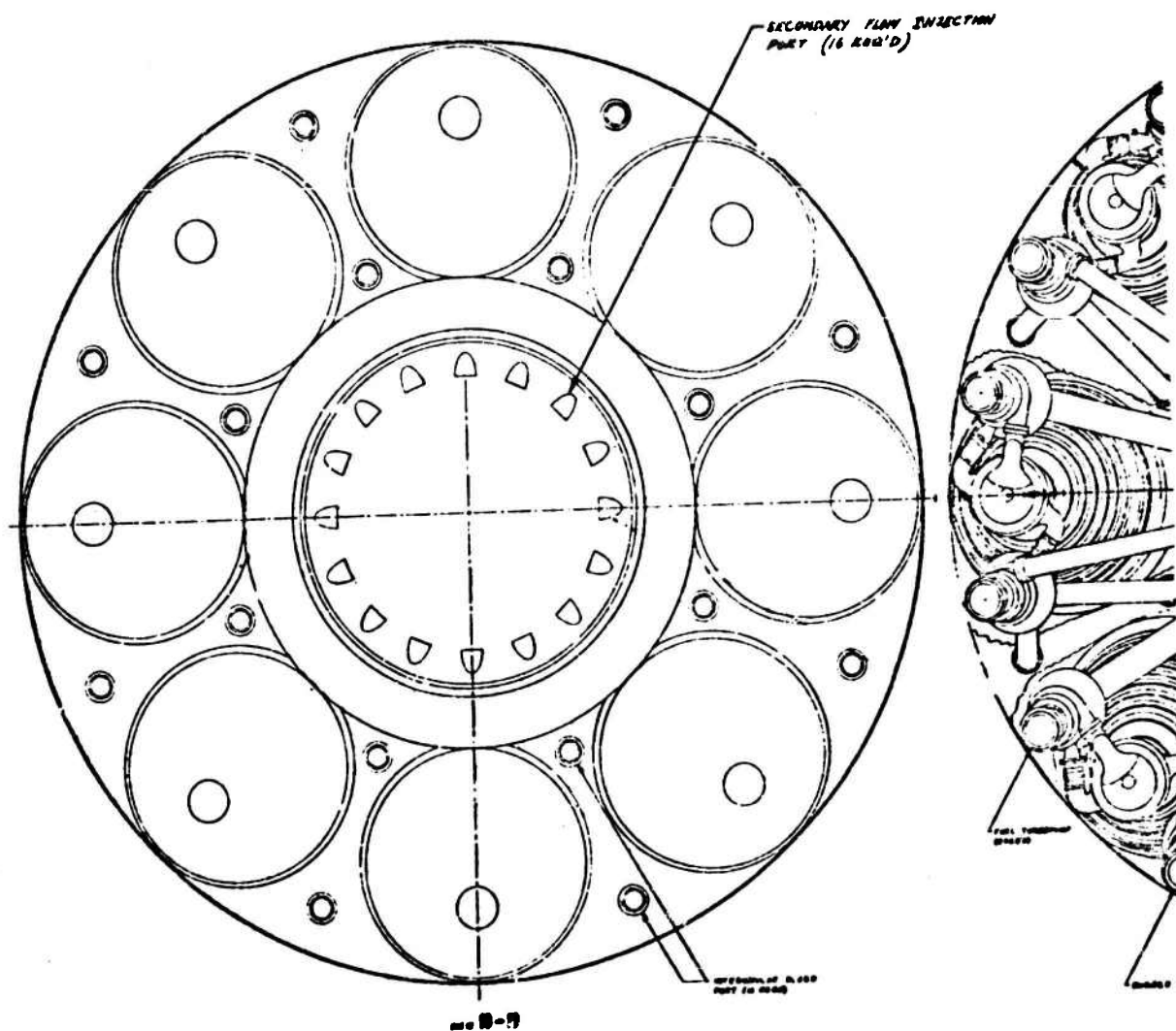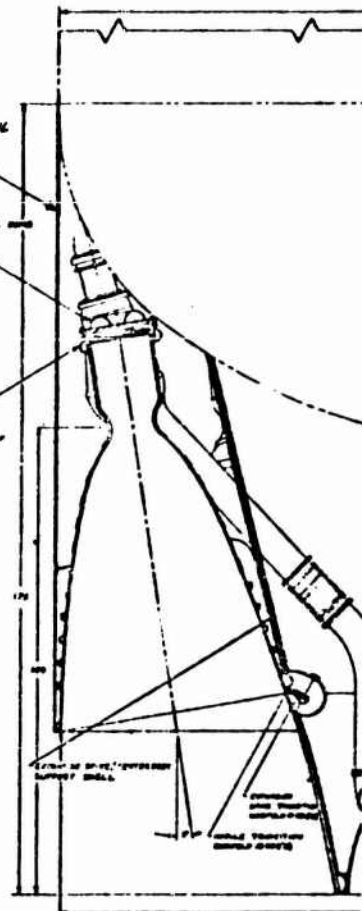
SECONDARY FLOW INJECTION
PORT (16 REQ'D)

FIG 10-7

MAJOR SYSTEM PARAMETERS
F = 2,000,000 LBf (SEA LEVEL)
Pc = 2000 PSIA (NOZZLE STAGNATION)
εₑ = 60
εₘ = 30
N = 8 MODULES
PROPELLANTS : N₂O₄/N₂H₄ - UDMH (50-50)

NOTE: The area ratio defined
by the scalloped perimeter of
the module exits is 50.7.

1

2

Figure 176. Multichamber Aerodynamic Spike Engine System High Thrust, High Chamber Pressure.

318

FUEL FEED MA?

OXIDIZER FEED MAN

OXIDIZER TURBOPUMP (8 P

MODULE TAPOFF DUCT (8 REQL

FUEL TURBO PUMP (8 REQD)

VIEW A-A

1
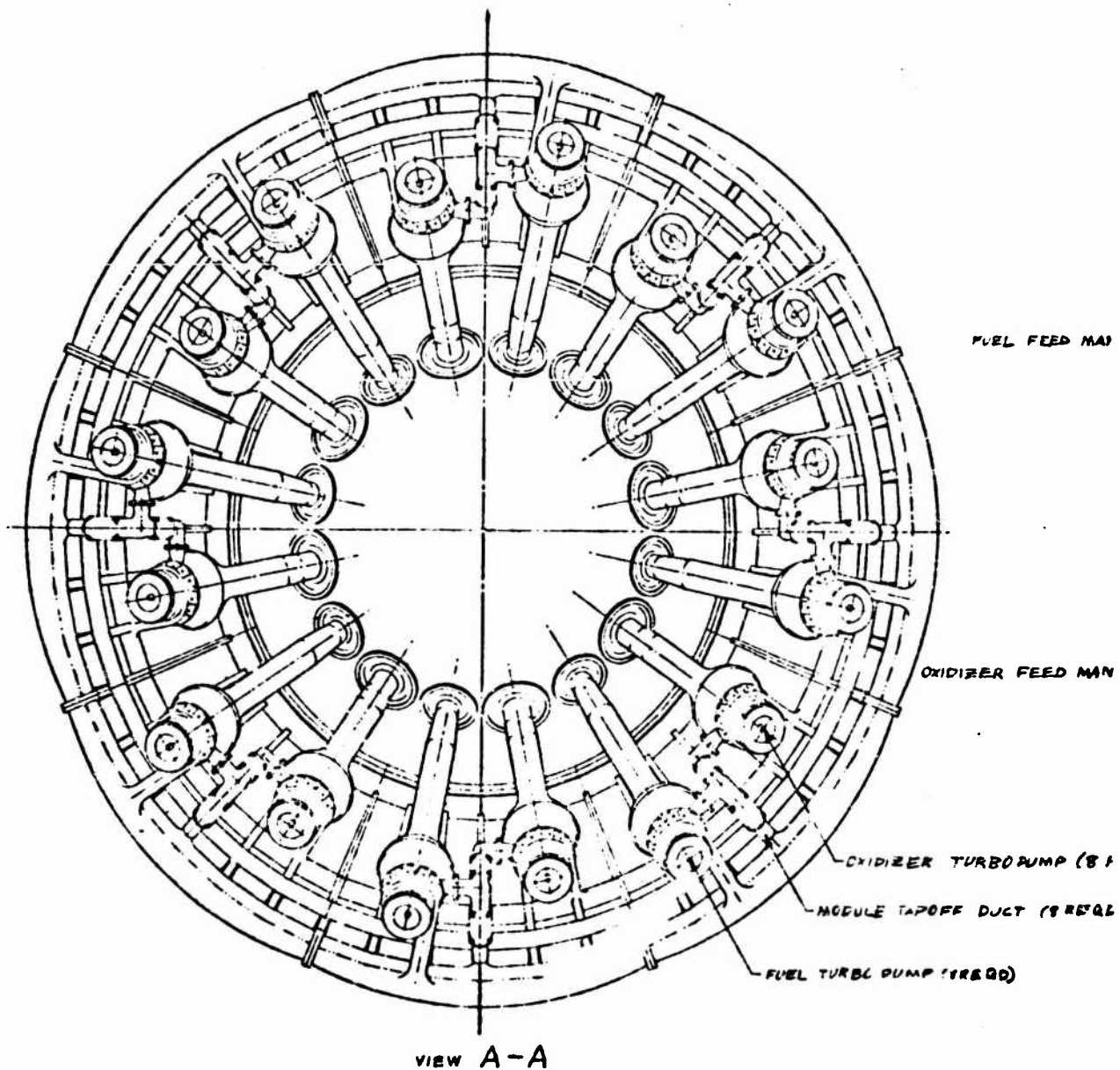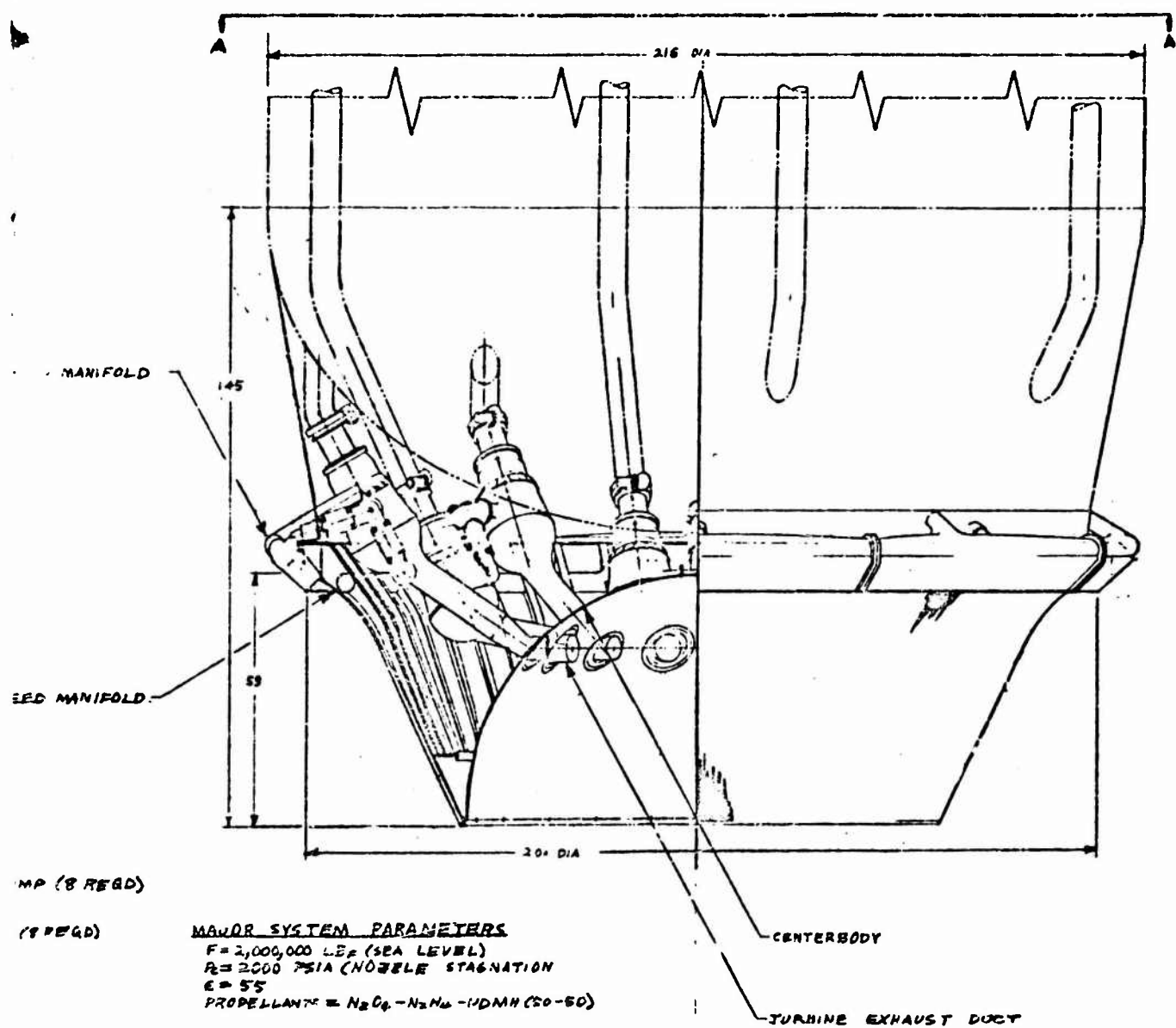
Figure 177. Toroidal Aerodynamic Spike Engine System. High Thrust, High Chamber Pressure.
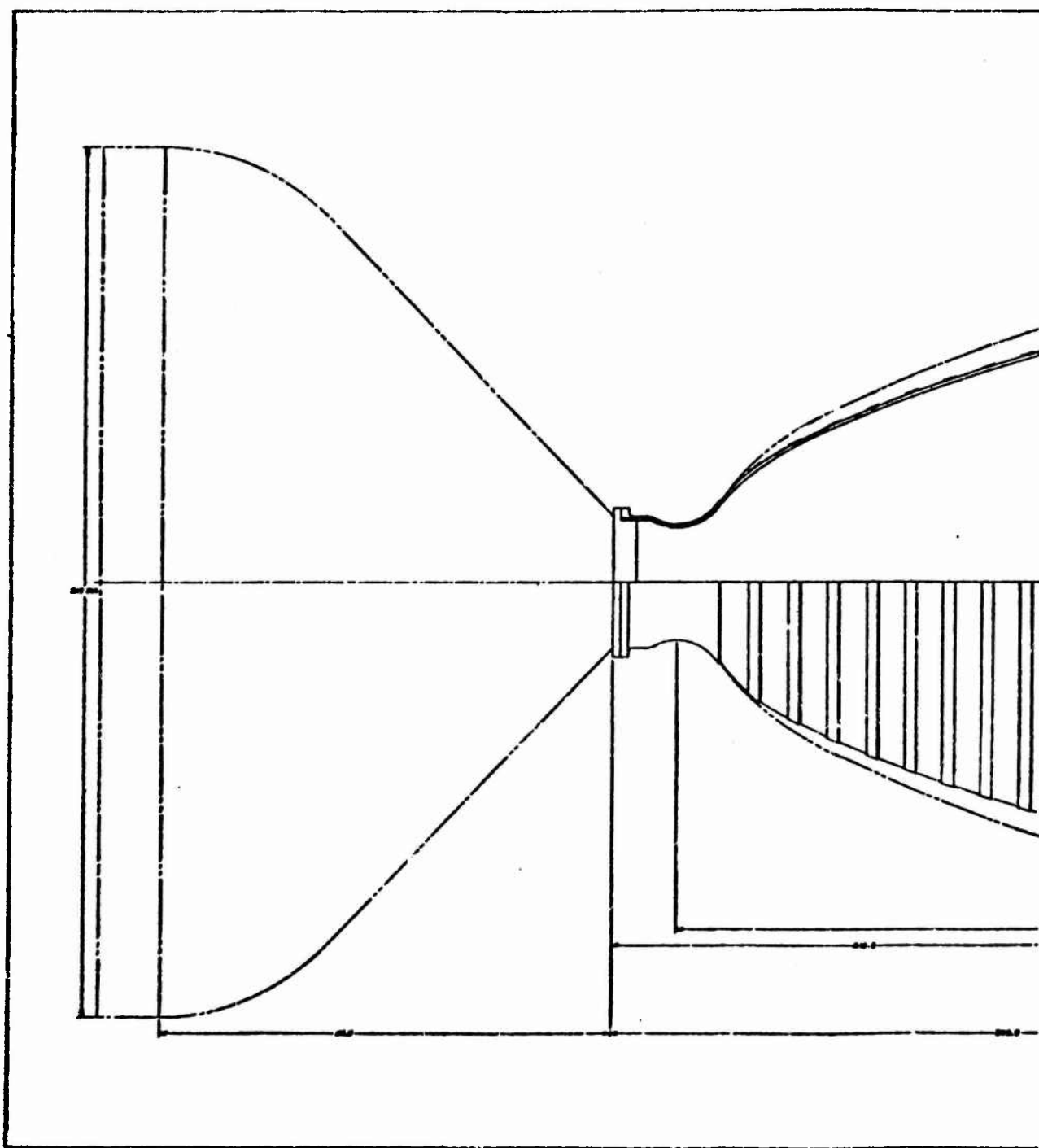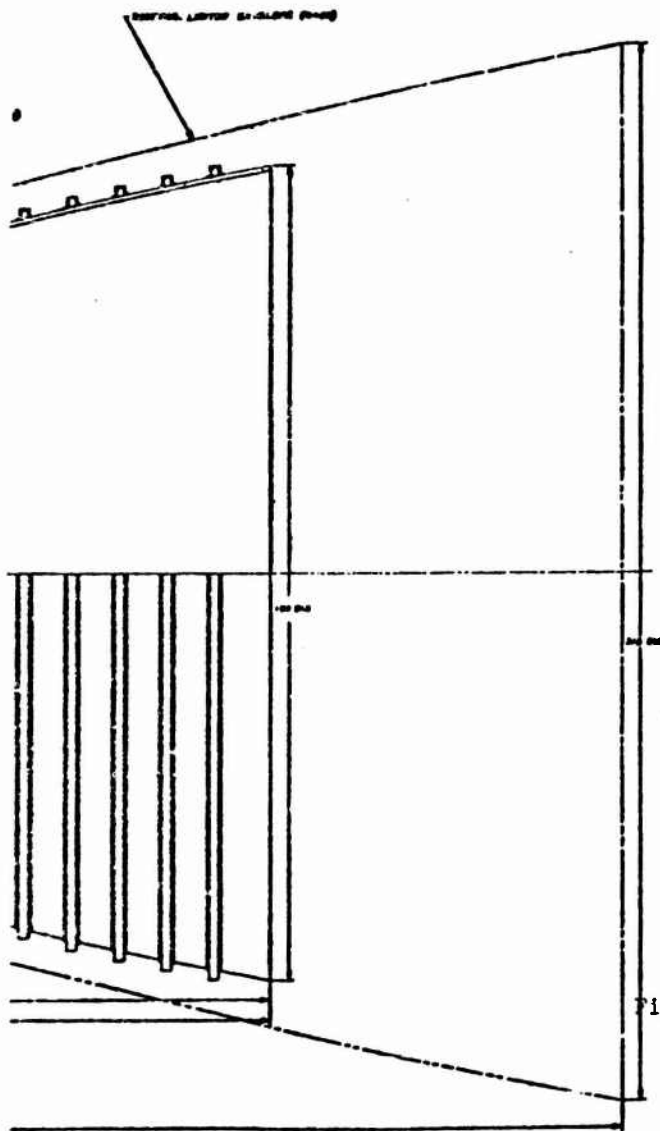
MAJOR SYSTEM PARAMETERS
F = 2,000,000 LB$_F$ (SEA LEVEL)
P$_c$ = 2000 PSIA (NOZZLE STAGNATION)
ε = 55
PROPELLANTS = N$_2$O$_4$ - N$_2$H$_4$ - UDMH (50-50)

MANIFOLD

FED MANIFOLD

MP (8 REQD)

(8 REQD)

CENTERBODY

TURBINE EXHAUST DUCT

216 DIA

145

59

20. DIA

2

1

Figure 173.

Figure 178. Single Bell Engine.
High Thrust High
Chamber Pressure.

constrained the area ratio of the bell thrust chamber to a much lower value of 35. Dimensions for these engine systems are given in Table 14. Multichamber module area ratio was set at 30 to provide nearly tangent exits without sea level separation of the bell modules. The toroidal combustor is shrouded to an area ratio of 3.5 to maintain chemical reaction equilibrium during the initial part of the expansion process. An aerospike nozzle lenth of 19 percent of a 15 degree hald angle cone of equivalent area ratio was selected for the toroidal combustor. An equal percent length multichamber combustor would have had no common spike, as all of this length would be taken by the bell modules. A 30 percent length configuration with a common spike was assumed for layout purposes, as this value corresponded to that of the cold-flow model tested.

(C) Several turbopump mounting positions were considered for the toroidal configuration. The radial inclined position was selected since it (1) had short propellant discharge ducts which were closely coupled to the combustor and supported the turbopumps, (2) packaged within the dimensional confines of a module, (3) made provision for a parallel turbine tapoff system, and (4) minimized the length of hot gas ducting. Mounting the pumps outboard of the toroidal combustor required very long turbine discharge ducting to feed secondary flow to the aerospike centerbody. A common axis turbopump with back-to-back turbines could be packaged within a module if mounted "horizontally" (axis oriented in the circumferential direction perpendicular to the vehicle centerline), but this produced poor exit conditions for the turbine exhaust gases and required elbows ahead of the pump inlets (increased NPSH requirements). This configuration required as much separation between the top of the toroidal combustor polygon and the tank bottom as the radial inclined position and so offered no engine length saving.

(C) Turbopump mounting in the 2000K multichamber aerospike design resolved to a choice between placing the machinery with axes nearly parallel to the vehicle centerline and with discharges opposite the bell module injectors or opposite the module/common expansion spike transition. The former option was chosen as it permits placing the turbomachinery nearer the module thrust structure, at points where the bell modules are comparatively rigid, and where the lengths of oxidizer inlet, fuel discharge, and oxidizer and fuel turbine tapoff lines are minimized. As turbopumps are placed between, rather than inboard of the bell modules, maintenance access to them may be gained after engine/vehicle mating through doors in the non-loadbearing outer shroud. Mounting the oxidizer turbine between chambers also places its discharge in a favorable position for the introduction of intermodular bleed gas, as shown in Fig. 176. This mounting does have the disadvantage of long oxidizer coolant feed ducts.

(C) Coolant transfer between multichamber modules and the expansion nozzle tube bundle was accomplished by placing eight collection manifolds around the expansion nozzle and ducting the flow to eight distribution manifolds around the module exits. The bolted flanges shown could be welded if disassembly for maintenance is not necessary.

(C) Theoretical minimum pressure drop is achieved in regenerative multichamber combustors along a single downpass flow path. This flow path is inconvenient from a systems standpoint as it requires an extra duct to return the coolant to the module injectors.

(C) At high chamber pressures where combustion chamber dimensions are relatively small and at high thrusts where relatively large manifold areas are required for constant manifold velocity, another effect is

observed. Figures 179 and 180 are sketches of a multichamber module
injector sized to the flow requirements of the 2300K design point. It
can be seen that the injector used with the single downpass cooling
path requires four tangential distribution manifolds whose space
requirements become awkward for the manifold velocities assumed. In
contrast, an up pass injector requires two less welded manifolds and
allows the use of a thinner injector block. Additional injector
block thickness is required in the downpass injector as space for the
tapoff manifold. In this configuration, both tapoff ports and coolant
tube feed holes must be located near the injector face. In the up
pass injector, the tapoff manifold may be located aft of the injector
face plane, since the coolant feed manifold does not interfere with
it.

(C) An alternate mounting for the oxidizer pump opposite the module/spike
transition was also considered for this application. A pass-and-one-
half flow circuit was visualized in which oxidizer would flow first
aft and then forward to cool the spike nozzle then transfer to the bell
chamber in a single up pass. The position of the pump discharge
opposite the flow transition was found to offer no significant advan-
tage over the configuration shown in Fig. 176 . A double pass spike,
although containing 30 percent fewer tubes, requires two manifolds
at its forward end, one for distribution and one for collection, in
addition to a turning manifold at its aft end and the distribution
manifold around the bell module exit. This amounts to an extra man-
ifold over the single up pass configuration pictured. In the analogous
pass-and-one-half inward wall toroidal configuration of Fig. 177 ,
this extra manifold is obviated by a direct two-for-one tube splice,
which is geometrically inconvenient in a multichamber combustor.
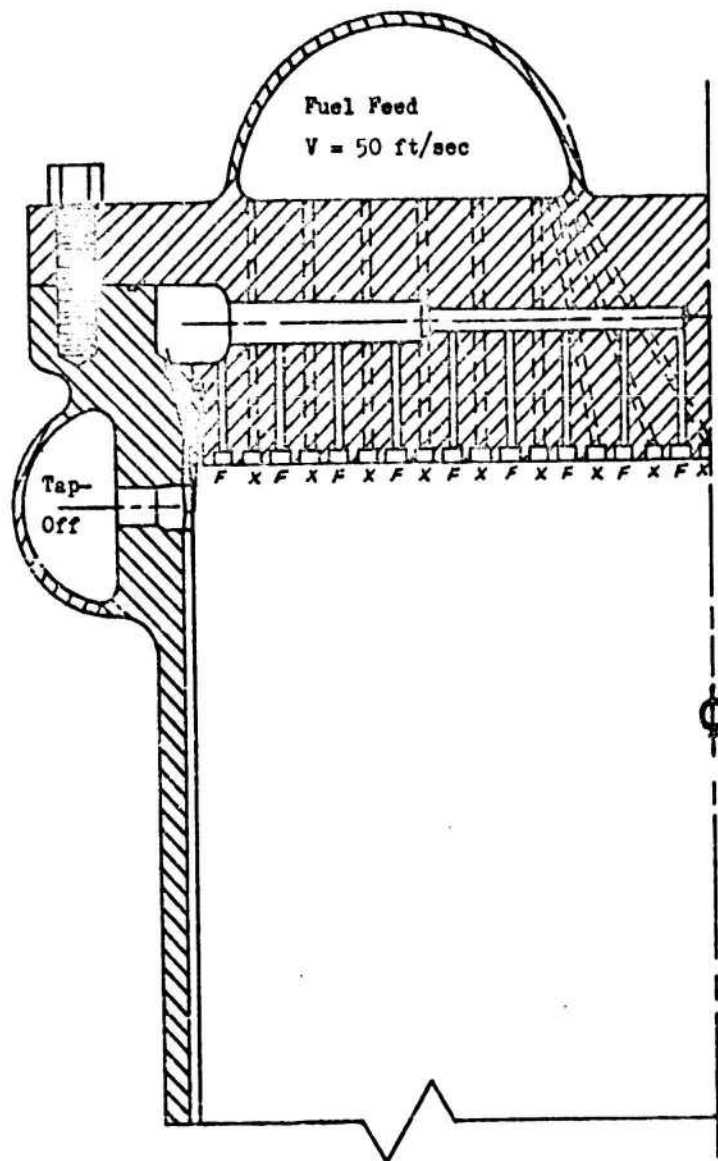
Figure 179. Up Pass Flow Path Injector

Figure 180. Single Down Pass Flow Path Injector

325

(C) Thrust vector control requirements are satisfied by side injection
of liquid N_2O_4 in the 2000K systems shown. Mechanical gimbaling by
conventional and cam ring gimbals was considered for the toroidal
configuration. A high weight was computed for a conventional point
gimbal at this large diameter. The cam ring gimbal was found to be
somewhat lighter, but required two 2870 horsepower gas turbines
(comparable to the output of an extra turbopump) to actuate the rings
tangentially. Combustor and spike nozzle segment rotation requires
hot gas seals and propellant transfer bellows. It was concluded that
mechanical TVC methods were competitive if a 6 degree displacement
were used over a large fraction of the burning time, but if the time
averaged requirement was closer to 1-1½ degrees, as was expected,
side fluid injection would be more feasible.

(C) The hinging or gimbaling of modules was also investigated in connection
with the 2000K multichamber configuration, but side liquid injection
was selected for the engine layout. Major areas where gimbaling of
multichamber bell chambers differs from gimbaling of bell clusters
include increased complexity of intermodular bleed baffling and the
module/common expansion spike coolant transition. In the fixed module
configuration, intermodular bleed gas (if required) can be contained
between a common outboard shroud, the spike/centerbody thrust structure,
forward baffles around each chamber fitting with omega joints to
accept the oxidizer turbine exhaust ducts, and the outside of the
chamber nozzles, as shown. If these chambers were made movable, the
outboard shroud must be segmented, and the gas ducts must either be
placed asymmetrically or gas must be ducted from both turbopumps.
If four chambers were hinged radially (Fig. 181a) to produce a side
force equivalent to a 6-degree gimbal of the entire engine, each
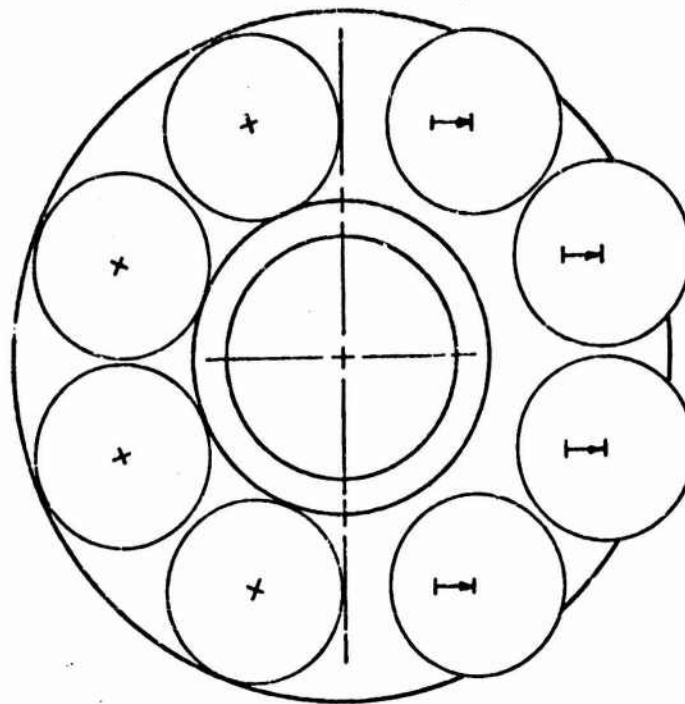
(b) MANEUVER:
Yaw About Vertical
Axis By Module Gimbaling
(2 Plane) $\Delta\beta$ = 13 Degrees
For 6 Degrees Equivalent
Gimbal

Roll Mode
Possible
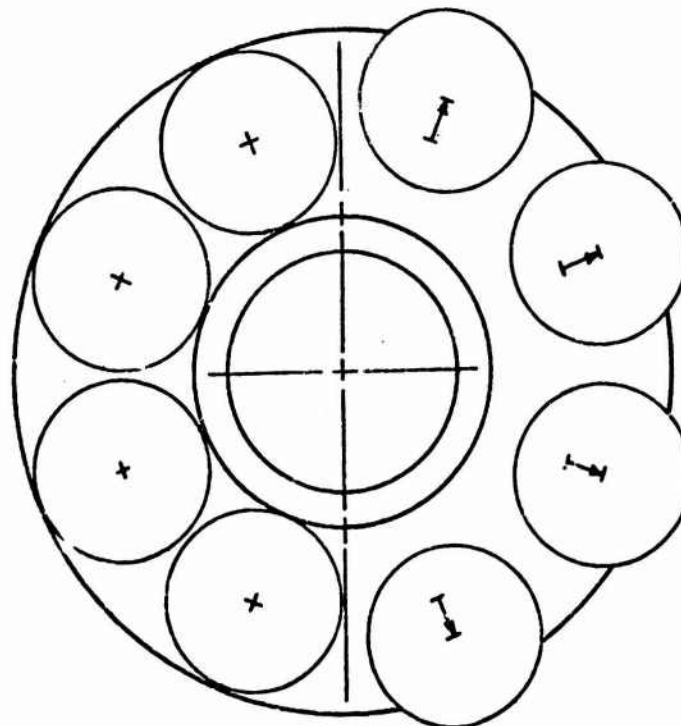
(a) MANEUVER:
Yaw About Vertical
Axis By Module
Hinging (1 Plane)
$\Delta\beta$ = 20 Degrees For
6 Degrees Equivalent
Gimbal

No Roll Mode
Possible

Figure 181. Multichamber Thrust Vector Control By Module Displacement

327

chamber would have to be rotated outward from its nominal position of $\beta = +9$ degrees to $\beta = -11$ degrees, a total travel of 20 degrees. This rotation corresponds to a linear translation of 32 inches at the module exit plane. If four chambers were gimbaled in the direction of desired boattail motion (Fig. 181b) to produce an equivalent 6 degree gimbal side force, each chamber would have to be rotated 15 degrees from the $\beta = +9$ degree position. This corresponds to a translation of 26 inches at the module exit plane. The ducting used to transfer coolant across the moduled spike transition must absorb these translations. Bellows with the necessary elastic deflection would be very long. Another deivce for this span would be an arrangement of three swivel joints (Fig. 182). It would also be possible to employ ablative cooling on the common spike in multichamber combustors with gimbaled modules.

(C) The transmission of thrust components from the 2000K multichamber expansion spike and centerbody was accomplished through a honeycomb shell independent of the module thrust mounts. This shell also serves to exclude intermodular bleed gas from the engine compartment. The shell accepts the line load from the forward end of the spike transition manifold and transmits it to the tank bottom. Here it is assumed that baffling inside the tank transmits the load into the cylindrical vehicle shell. Moment resisting brackets, diffuse the distinct module thrust loads into the same vehicle shell.

(a) Swivel Jointed Coolant Transfer Line Adapted to Module Hinging

Full Position   Actuated Position
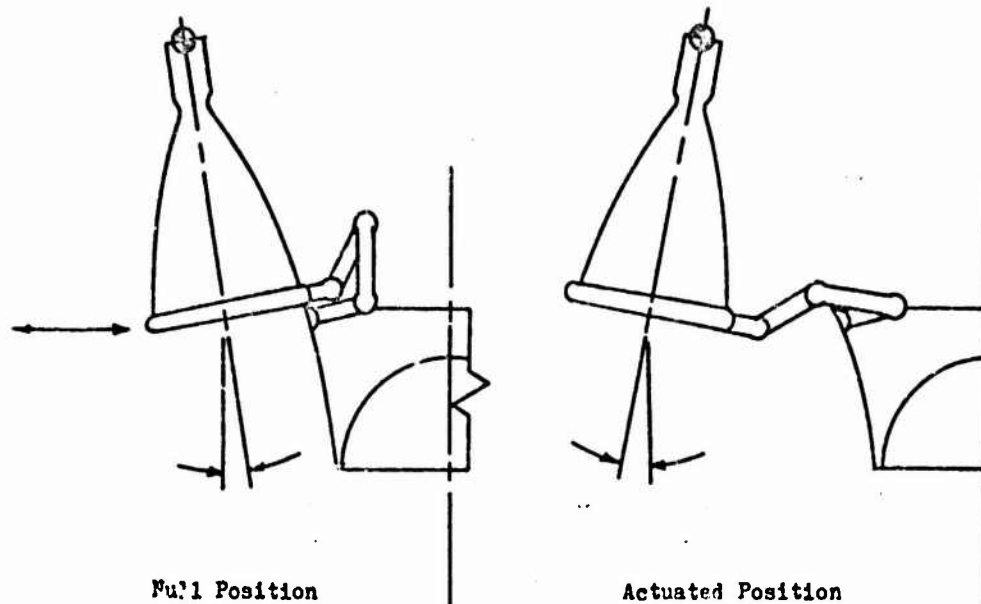
(b) Swivel Jointed Coolant Transfer Line Adapted To Module Gimbaling

Null Position   Actuated Position
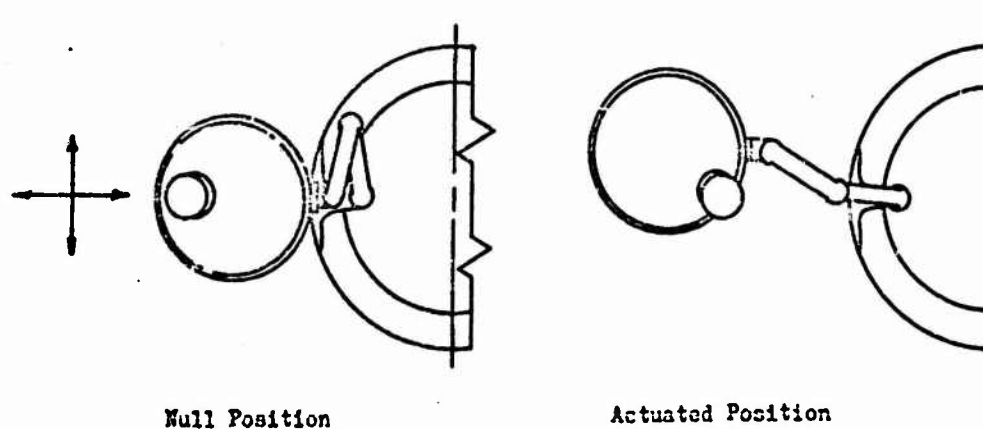
Figure 182. Module/Spike Coolant Transfer For Multichamber
Engine Mechanical Thrust Vector Control Systems

329

ENGINE VERSATILITY

(U) In the future, emphasis will continue to be placed upon rocket engine
     simplification and flexibility in design, versatility in operational
     modes, and utility in a variety of applications that vehicles will
     require (Fig. 183).

(U) The aerospike engine concept is particularly versatile in meeting
     future flexibility and simplicity requirements. Some of the more
     salient features of the aerospike concept contributing to its versatility
     are described in the following paragraphs.

Aerospike Nozzle Performance

(C) An attractive feature of the aerospike engine is altitude compensation,
     which gives high nozzle performance over an entire flight trajectory.
     In operation at vacuum, the outer free-jet boundary of the primary
     flow expands outward, governed by the nozzle exit conditions. At
     low pressure ratios, (sea level operation), high ambient pressure
     influences the outer free-jet boundary of the primary flow field with
     the result that nozzle wall pressures are approximately maintained
     at or above ambient pressure.

(C) The nozzle thrust coefficient (C_F) trend for a high area ratio (constant
     geometry) aerodynamic spike nozzle is shown in Fig. 184. High performance
     at a high pressure ratio results, and the C_F curve follows ideal
     nozzle performance rather than dropping off rapidly at low pressure
     ratios as with the high area ratio bell nozzle. This altitude-
     compensating feature results in highly efficient operation at both
     sea level and high altitude, thereby permitting the same engine (unchanged
     and with high area ratio) to be used for both booster and upper stage
     applications.
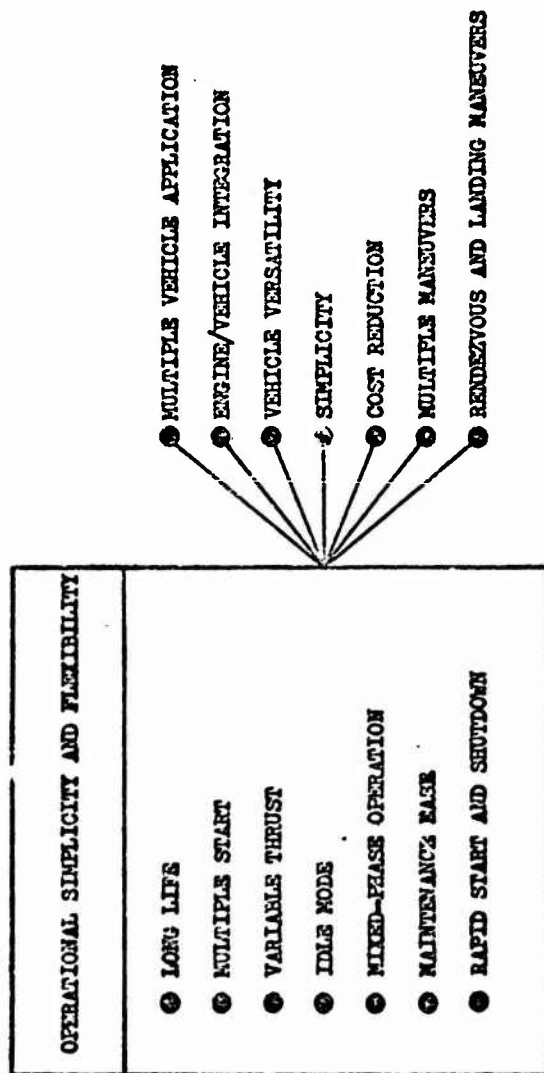
Figure 183. AEROSPIKE ENGINE CAPABILITY

OPERATIONAL SIMPLICITY AND FLEXIBILITY

- LONG LIFE
- MULTIPLE START
- VARIABLE THRUST
- IDLE MODE
- MIXED-PHASE OPERATION
- MAINTENANCE EASE
- RAPID START AND SHUTDOWN

- MULTIPLE VEHICLE APPLICATION
- ENGINE/VEHICLE INTEGRATION
- VEHICLE VERSATILITY
- SIMPLICITY
- COST REDUCTION
- MULTIPLE MANEUVERS
- RENDEZVOUS AND LANDING MANEUVERS

CONFIDENTIAL

331
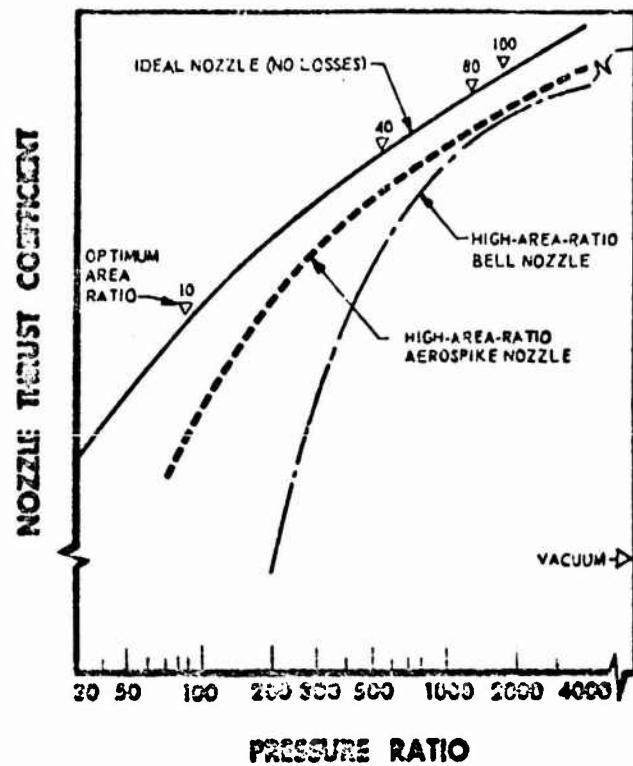
Figure 184. Altitude Compensation, Nozzle Performance

CONFIDENTIAL

332

(C)   Aerospike engines also have, due to the readily changeable outer combustor body, a further capability for efficient multiple application. By using different outer combustor bodies, the area ratio can be changed to improve the performance   for various applications of the same basic engine. By substituting an outer combustor body which produces a different area ratio, the aerospike engine can be optimized for various applications without changing the envelope diameter or the chamber pressure.

Aerospike Engine Geometry

(C)   The combination of the toroidal combustor and the aerodynamic spike nozzle provides an inherently short-length compact engine. The turbopumps, ducts, control, and thrust structure can be packaged neatly and accessibly within the central cavity of the thrust chamber, enclosed by the nozzle. The packaging, plus the shortened structure, make it possible to provide a high performance engine that is 75 percent shorter than an equivalent engine with a conventional bell nozzle.

(C)   The engine gimbal, which provides thrust vector control (TVC), is located in the plane of maximum engine diameter. A gimbal deflection can therefore be accomplished without increasing the engine envelope. This permits the engine to fill the available envelope completely, thereby allowing a higher area ratio nozzle to be used in the design compared to an engine with a nozzle which must be designed to an envelope physically smaller than the available envelope to allow for gimbaling (Fig. 185).
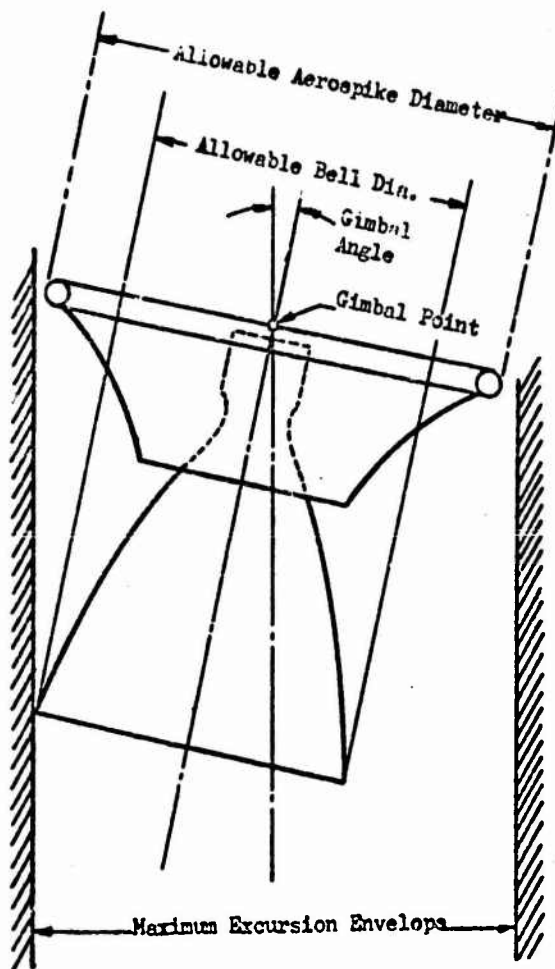
CONFIDENTIAL

Figure 185. Envelope Limits for Bell and Aerospike Engines

(C)   An elongated version of the aerospike engine in which the toroidal combustor and nozzle take an "oval" shape can also be designed. The elongated nozzle can have an elliptical shape or have straight sides. This concept is attractive for vehicles which are aerodynamically optimum with a non-circular aft end. An example would be recoverable transport vehicle designed with aerodynamic lifting surfaces for re-entry and landing (Fig. 186). The elongated aerospike engine will allow an efficient integration of the rocket engine into these vehicle designs. The nozzle flow field and performance for this engine are similar to the circular aerospike engine.

(C)   For increased thrust, clustering of engines for future booster has considerable merit. Clusters of the high-performance altitude compensating aerospike engines would offer an attractive booster propulsion system. An artist's illustration of a future launch vehicle with the same engine used in a cluster for the booster, and singly in the upper stage is shown in Fig. 187. For this application, the booster and upper stage engines could have area ratios optimized for maximum performance by the changeable outer combustor body concept previously described.

(C)   The annular nozzle engines with the nozzle encompassing the entire diameter of the stage are also attractive for high thrust, booster stage engines (Fig. 188). Several design concepts are possible. In general, they all incorporate the concept of a segmented or modular engine. Basically, the module is defined as a complete combustor and nozzle segment with integral pumps and power cycles. Engine modules are identical and independent. The complete flight propulsion system consists of an optimum number of these "building block" modules connected solely by the start and shutdown signal system.

335
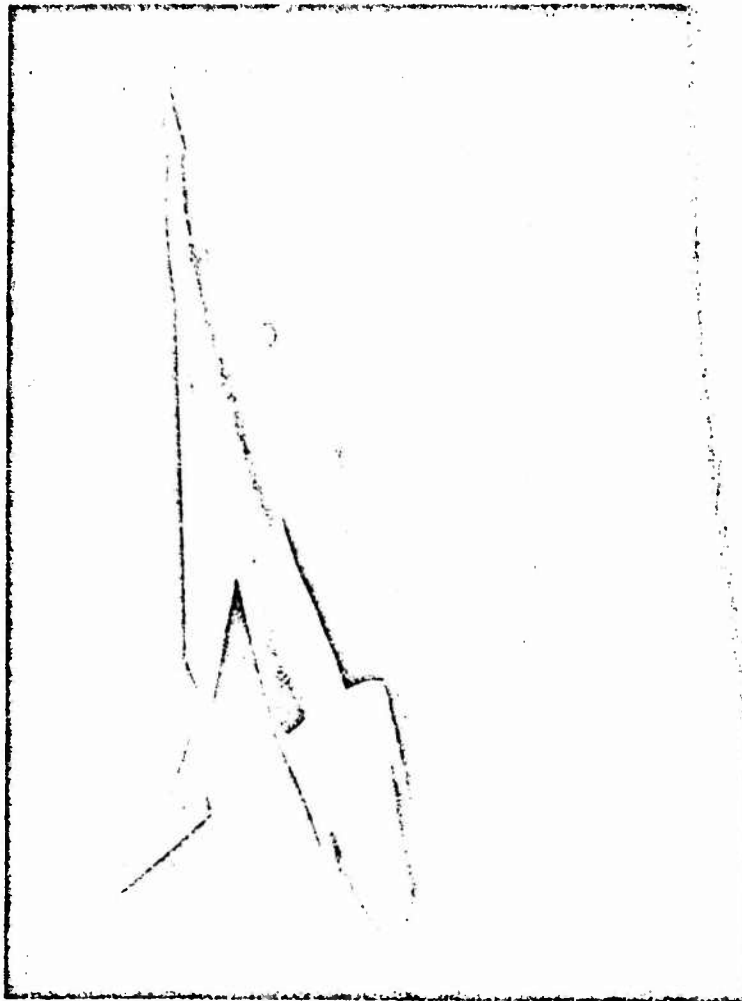
Figure 186. Recoverable Orbital Vehicle with "Oval" Aerospike Nozzle Engine
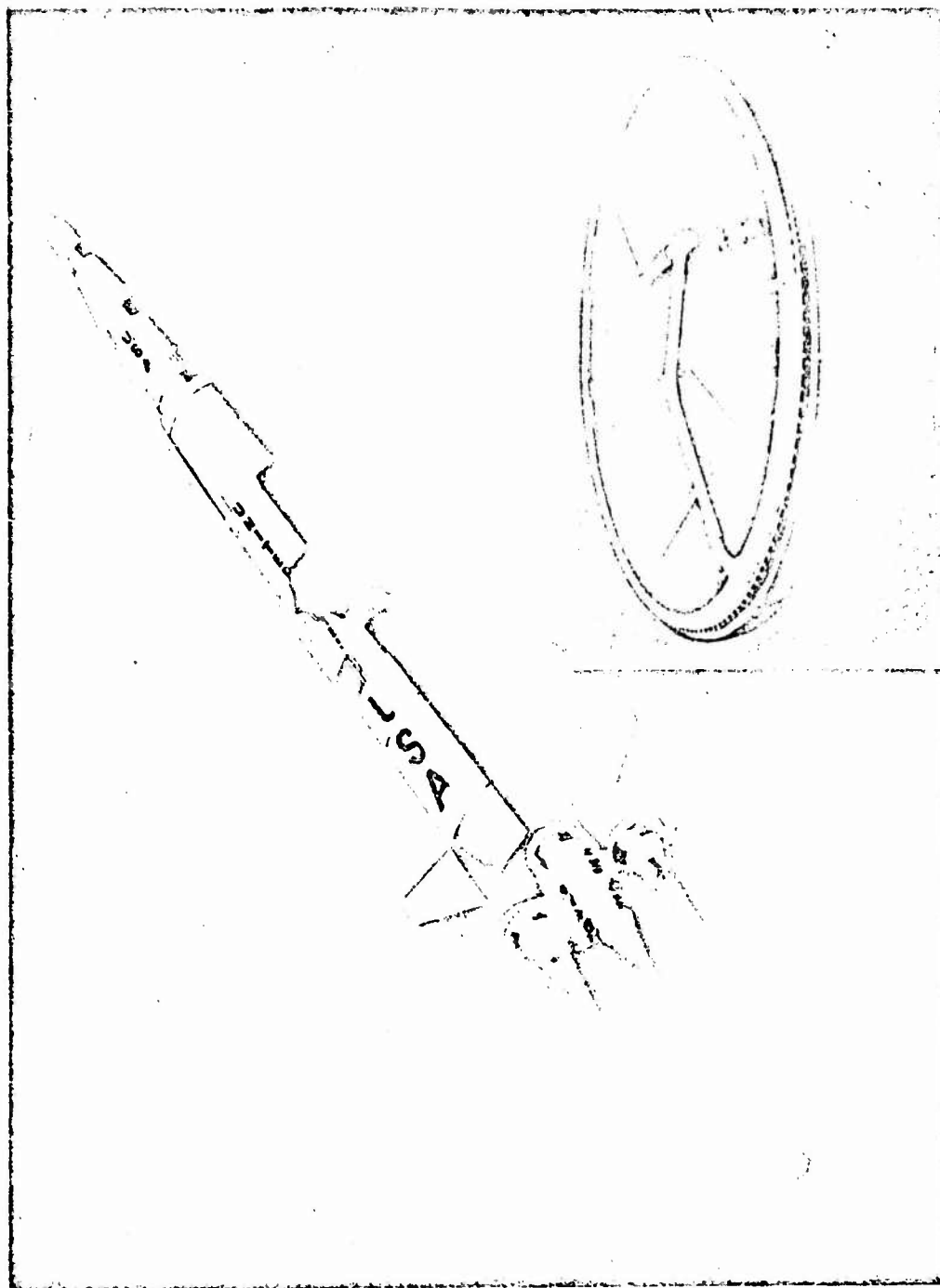
Figure 187. Advanced Launch Vehicle with Clustered Toridal Aerospike Engines

337
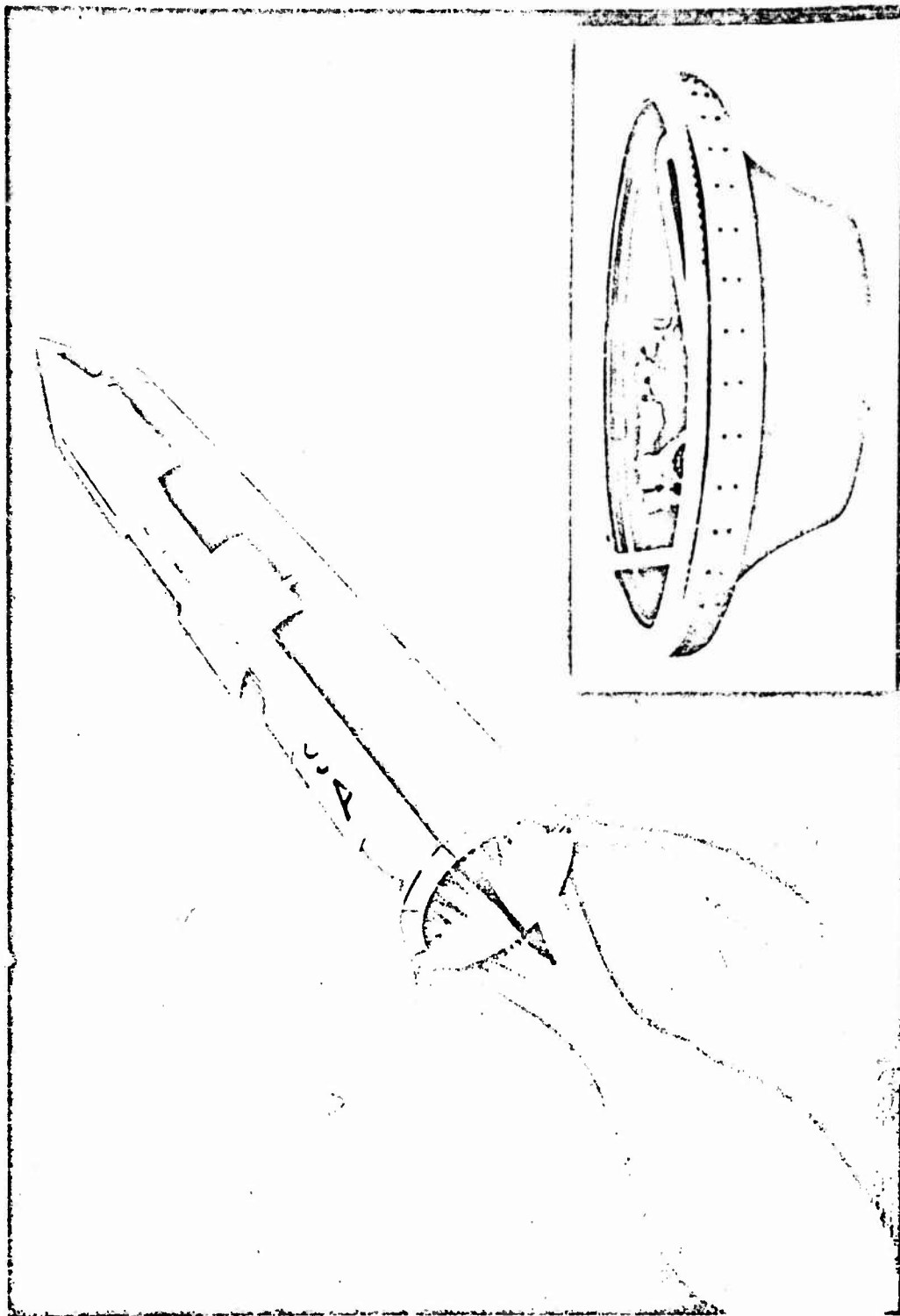
Figure 188. Advanced Launch Vehicle with Single Segmented Toroidal Aerospike Engine

Segmented Testing Development Approach

(c) Inherent in the concept of an annular nozzle combined with a toroidal
combustion chamber is the feature of segmentation. With this feature,
initial engine development can be performed using small, easy to handle
"segments" of the complete annular thrust chamber (see Fig. 189). The
hardware for these segments would be identical to the hardware used
in the complete circular thrust chamber. The segment testing would
be conducted for the development of the high-efficiency injector and
combustor, and in demonstrating long life for the thrust chamber. Thus,
significant reductions in development costs can be achieved by developing
full-scale portions of the engine before assembly into a complete
engine module. A further discussion of the segmented testing feature
of the aerospike concept and the associated potential cost savings is
included in the cost and reliability analysis portion of this report.

340
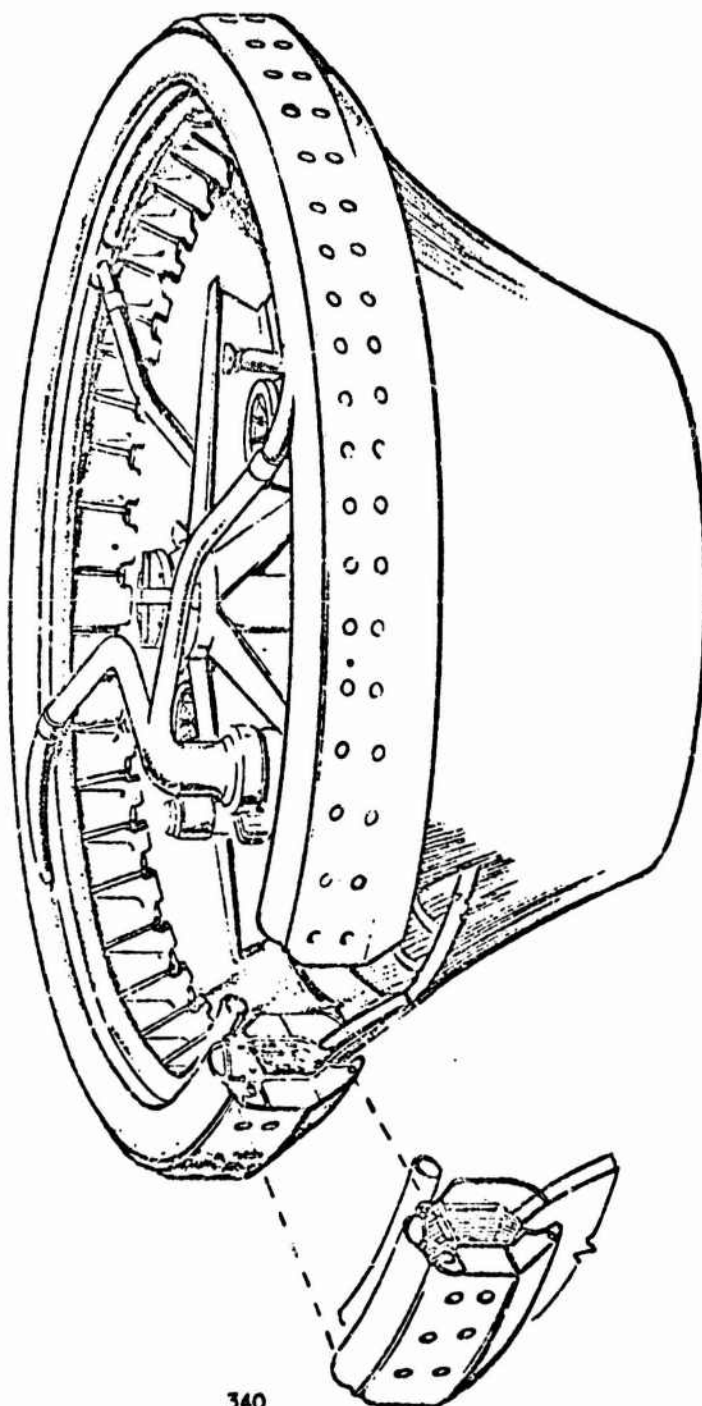
Figure 189. Segment Testing Development Approach

CONFIDENTIAL

RELIABILITY AND DEVELOPMENT PROGRAM COST ANALYSES

(C) Cost and reliability comparisons of the aerospike engine with multichamber
plug cluster systems and conventional bell engines have been accomplished
for both storable and cryogenic propellants. The reliability studies
were used to establish development plans (testing requirements) for each
of the various engine configurations considered by combining both
reliability and cost data in a mathematical model which simulates the
development of a rocket engine. The development plans were then employed
in the cost comparison analyses for the various systems.

(C) The cost studies were conducted parametrically, so that the influence
of design parameters such as thrust, module size, chamber pressure, and
power cycle on R&D cost was determined. In addition, the effect of
changing the reliability goal and development philosophy were analyzed
to establish their influence on the development program requirements.
Previous cost and reliability data from studies of several advanced
systems (Refs. 26 through 29) were also reviewed and employed for the
current studies where applicable.

(U) The analytical techniques used in the cost and reliability studies, and
the results obtained are presented in this section.

Reliability Analysis

(C) One of the primary tools used in the development program analyses to
determine efficient programs for advanced systems is the "conceptual reliability
growth model". This model has been formulated to conceptually describe
the "growth" of reliability of a propulsion system during the development
process. When the results of this model are combined with appropriate
cost information, an efficient development program for any selected engine
configuration can be analytically calculated.

341

(U)   The significant variables utilized in the model are listed in Table 15. The relationship between the model parameters and an actual development program is represented in Fig. 190.

(C)   One of the more important tasks in the reliability studies was to determine the reliability growth parameters (failure modes, failure rates, and probability of fix) for the systems analyzed. An intensive analysis of the advanced system designs, operational data, and of the historical reliability data for current systems was undertaken to accomplish this task.

(C)   The first step in the reliability growth estimation was to analyze the various advanced systems to determine applicable potential failure symptoms, and to identify system operating points which would significantly affect these symptoms. Historical engine development data (F-1 and J-2) were then evaluated using existing mathematical models, to obtain maximum

likelihood estimates of the initial failure rates and probabilities of fix for each failure symptom. Finally, the design configuration and system operating points of the advanced systems were correlated with those of the historical systems to obtain quantitative estimations of the reliability growth model parameters for the future systems.

(C)   Once the reliability parameters were obtained for each system, they were utilized in the reliability growth model and combined with appropriate cost data to establish efficient plans for any given future engine system.

Development Programs

(U)   The method of arriving at the most efficient development plan for the given advanced engine system will be described in this section. In addition, development philosophies of the various systems will be discussed.

TABLE 15

SIGNIFICANT DEVELOPMENT PROGRAM VARIABLES

CONFIDENTIAL

Development Process	Reliability Growth Model Parameters
Engine hardware with unknown weaknesses	Failure symptoms and causes Failure rates
Development testing	Number of components and engine system tests Test durations Stress levels
Failures or symptoms of failures	Expected failures
Corrective action	Probability of fix

The definitions of the basic model parameters are shown below.

Failure Symptom: The observed phenomenon which is the result of a failure; e.g., seal leakage, small line failure.

Failure Cause: The actual cause which initiates the failure phenomenon; e.g., fatigue cracking of seal bellows, excessive system vibration causing small line to fail.

Failure Rate: The rate of occurrence of the failure cause. For "start" conditions the rate is the probability of occurrence during a single start transient.

(TEST-FAIL-FIX CYCLE)

RELIABILITY PREDICTION MODEL
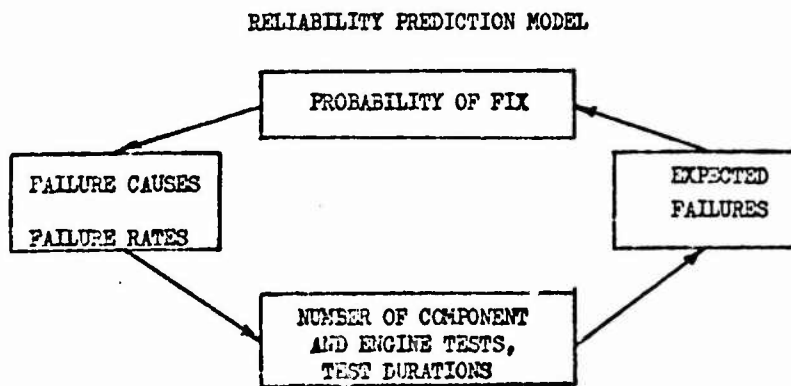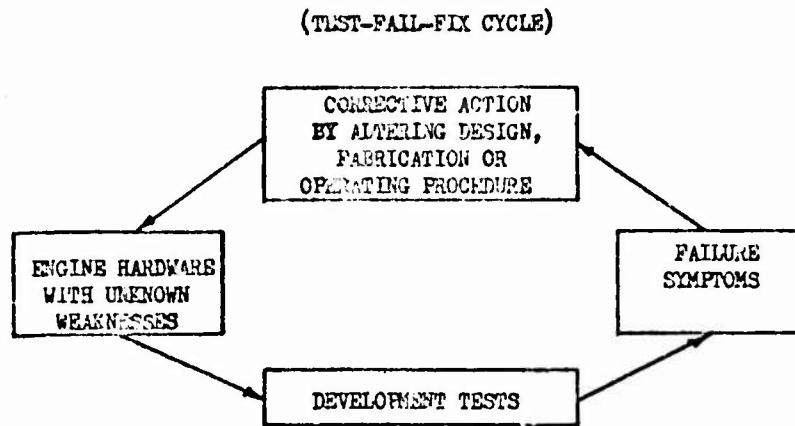
CONFIDENTIAL

Figure 190. Actual Rocket Engine Development Process

(C) <u>Development Program Optimization Procedure.</u> Figure 191 illustrates the procedure which was utilized to determine efficient development programs (testing requirements) for the systems analyzed. The first three steps which provide estimates of the system reliability growth parameters were described in the preceding paragraphs.

(C) The fourth step involves analysis of the advanced system configuration and operating points in order to make initial estimates of effective development test categories. Major components and/or subsystems were selected for testing based upon: (1) the validity of the test environment, (2) the capability to apply "overstress" testing techniques, (3) the economic feasibility of the tests, and/or (4) assumed engineering priorities which require at least a minimum demonstration of a component's design integrity prior to its use on tests of an expensive full size engine module.

(C) An initial system development was determined (Step 5) for each engine system considered. The development program consists of a chronological schedule of blocks of component, subsystem and system test categories, and includes the average intended test durations for each category block.

(C) Parametric cost data were then established (Step 6) on the basis of a cost per test for each of the test categories; both the fixed cost per test (hardware, labor, special test equipment, etc.) and the cost related to expected test duration (propellants) were utilized. These data were then combined and employed with the reliability growth model to determine, through an iterative process, an efficient (optimized) development plan for each system.

DETERMINATION OF SYSTEM CONFIGUR-ATION AND DESIGN OPERATING POINTS

ANALYSIS OF HISTOR-ICAL DATA FROM PREVIOUS SYSTEM DEVELOPMENT PROGRAMS

ESTIMATION OF RELIABILITY GROWTH PARAMETERS FOR "NEW" SYSTEM

1. Expected Failure Modes
2. Probabilities of Fail-ure Symptom Occurence
3. Probabilities of Fix

DETERMINATION OF EFFECTIVE DEVELOPMENT TEST CATEGORIES

1. Component Tests
2. Subsystem Tests
3. Component and Subsystem Failure Mode Stress Levels (Validity of System Environment)

FORMULATION OF SYSTEM DEVELOPMENT PLAN

(Component and Subsystem Test Schedule)

ESTIMATION OF COST PER TEST FOR EACH DEVELOPMENT TEST CATEGORY

GENERATION OF SYSTEM RELIABILITY GROWTH CURVE AND TEST CATEGORY EFFICIENCIES

ADJUSTMENT OF DEVELOPMENT PLAN AND RELATED COSTS

ANALYSIS OF RELATIVE EFFICIENCIES* OF DEVEL-OPMENT TEST CATEGORIES

*$\Delta R / \Delta C$ = Expected Increase in System Reliability per Unit of Development Cost

OPTIMIZED SYSTEM DEVELOPMENT PLAN

1. Required Number of Component and Sub-system Tests
2. Total Expected Operating Duration

Iteration

ESTIMATION OF TOTAL DEVELOPMENT PROGRAM COST

1. Hardware
2. Labor
3. Propellants
4. Facilities
5. Test Equipment

SYSTEM COMPARISONS

1. Perturbations on System Operating Points
2. Alternate Designs
3. Cost-Effectiveness Tradeoffs
4. Perturbations of Basic System/Program Assumptions: Schedule, Labor, Facilities, Propellant Cost.

CONFIDENTIAL

Figure 191. System Development Optimization Procedure

(C)   The iteration loop in Fig. 191 illustrates the basic technique for optimizing the efficiency of the system development program. The iteration proceeds as follows: the initial development plan is utilized in the growth model to generate system reliability growth as a function of the number and type of development tests conducted. At various phases in the program, the relative efficiency of each test category is evaluated. This efficiency is defined as the expected increase in system reliability per unit of development cost invested $(\triangle R/\triangle C)$. Based upon the results of this evaluation, the development program is adjusted in an effort to increase the amount of reliability growth per development dollar. In other words, test categories which are highly efficient are emphasized, and those which are relatively inefficient are either reduced or eliminated through successive iterations.

(C)   Several development plans were generated for each advanced system evaluated. The most efficient (most economical) plans for each were then selected for determining R&D program costs and system comparisons. On the basis of the development plans established for each system, the relative R&D program costs were readily determined by multiplying the cost per test data by the respective test requirements in each category determined from the reliability analysis.

(C)   The R&D cost analyses were conducted parametrically. Variations in engine design parameters such as thrust, chamber pressure, module size and power cycle were examined to determine their influence on R&D program costs.

(C) <u>Conventional Development Approach</u>. The historical development philosophy which evolved during the Thor, Jupiter, Atlas, H-1, and F-1 engine programs has demonstrated its capability to develop a reliable conventional bell engine. This historical philosoph places emphasis on complete engine system testing to arrive at the required reliability goal. Consequently, The test plans based on this approach necessitate a large number of R&D engine tests. However, higher thrust and chamber pressure applications of future systems place severe limitations upon this development approach by prohibitive costs in requiring large numbers of complete system tests.

(C) One of the outstanding features of the aerospike engine is its inherent amenability to the segmented development approach. Although the conventional bell engine can be developed to some extent by use of sub-scale hot-firing models, the approach is not very satisfactory. Actually, it involves development of two separate engines, and in addition, results of the hot-firing sub-scale models are not directly applicable to the full scale prototype hardware.

(C) For the aerospike concept, testing can proceed   through various segment thrust levels (10,000 lbs, 42,000 lbs, 200,000 lbs, etc.) to a full thrust module or engine. The segment tests can be relatively inexpensive long duration pump fed and short duration pressure fed runs which expose more failure modes and the results are directly applicable to the full-size chamber. As a result, the aerospike engine system will require fewer of the expensive complete system tests to attain the same reliability goal as the conventional bell engine.

(C) The same philosophy holds true for the multichamber plug cluster system. In effect, individual bell engine systems, which do not lend themselves to segmentation, must be developed in such a configuration. Again, this requires a larger number of the expensive full engine or module tests than the comparable aerospike configuration to reach a common reliability goal.

(C) An example of the conventional development approach comparison of the aerospike concept with a conventional bell engine is shown in Table 16. This comparison is between an aerospike engine and a conventional bell system of 2000K lbs thrust, 2000 psia chamber pressure, and utilizing NTO/UDMH (50-50) propellants.

(C) Examination of the data in Table 16 show that the largest unit tested in the aerospike configuration for an equivalent 2000K lbs thrust engine system is the 250K lbs thrust module. The conventional bell required over 1000 expensive full-sized 2000K lbs thrust engine tests to achieve the same engine system goal as the aerospike.

(C) The trends are similar when comparing the aerospike system with a multichamber plug cluster configuration. The comparison given in Table 17 is for the test plans to develop an aerospike module and multi-chamber module of 1.5 million pounds thrust, 2000 psia chamber pressure, to a system flight reliability goal of .99. The propellants in this case are LOX/Hydrogen. However, review of past studies and data show the same trends regardless of propellants. The plans shown in this table are for major test categories only. Appropriate factors have been included in the cost analyses to account for all component and sub-scale tests in both programs. All studies to date have shown that for a given system design point, the aerospike engine is less expensive to develop than either a single bell or multichamber plug cluster configuration.

TABLE 16

COMPARISON OF NUMBER OF TESTS AND TEST DURATIONS FOR
CONVENTIONAL VS AEROSPIKE ENGINE

(COMPLETE ENGINE THRUST = 2,000,000 POUNDS)   CONFIDENTIAL

Conventional Engine 72-Month Development Program		
	System Flight Reliability = 0.99	
	No. of Tests	Duration, seconds
Turbopump Tests (2,000,000 Pounds Thrust)	855	79,200
Combustor Tests (uncooled) (2,000,000 Pounds Thrust)	408	600
Combustor Tests (cooled) (2,000,000 Pounds Thrust)	408	1,500
Engine Tests (2,000,000 Pounds Thrust)	1,080	71,000

Aerospike 72-Month Development Program		
	System Flight Reliability = 0.99	
	No. of Tests	Duration, seconds
10,000-Pound-Thrust Uncooled Combustor	182	500
10,000-Pound-Thrust Cooled Combustor	507	157,800
42,000-Pound-Thrust Uncooled Combustor	307	900
42,000-Pound-Thrust Cooled Chamber	557	65,900
250,000-Pound-Thrust Cooled Combustor	57	600
Turbopump (250,000 Pounds Thrust)	1057	131,000
250,000-Pound-Thrust Module	981	84,500

TABLE 17

COMPARISON OF NUMBER OF TESTS FOR

MULTICHAMBER MODULE VS AEROSPIKE MODULE

ENGINE SYSTEM FLIGHT RELIABILITY = 0.99

(COMPLETE ENGINE THRUST = 24,000,000 POUNDS)

CONFIDENTIAL

AEROSPIKE MODULE	
Test Category	Number of Tests
200K lbs segment (pump fed and pressure fed)	1018
Turbopump (LOX and fuel)	1108
Module (1500K lbs thrust)	1696
MULTICHAMBER MODULE	
Test Category	Number of Tests
Full size pressure fed Thrust Chamber	650
Turbopump (LOX and fuel)	1100
Module (1500K lbs thrust)	1813

(C)   The relative advantage and resulting cost savings of the aerospike engine's segmenting capabilities increases with engine system size and chamber pressure. The advantage is also evident at lower thrust levels. For example, a segment approach to development on the current Air Force ADP engine study (AFC4(611)-11399) shows definite advantage for a 250K lbs thrust engine and a 30,000 lbs thrust F_2/H_2 engine study program (AFC4(611)-11617) has shown the segment development approach to be advantageous.

(U)   Pertinent cost and reliability study results are given later in this section.

(C)   <u>Advanced Development Approach</u>. In the development program analyses conducted during previous advanced systems studies (Ref. 26 and 27), unconventional design and testing concepts which would significantly reduce future development costs were evaluated. The most promising concept evolving from the studies was the turbopump module concept. The benefits of this concept are derived from the ability to divide a toroidal engine system into its two major subassemblies: 1) the thrust chamber assembly, and 2) a turbopump module.

(C)   The turbopump module incorporates all components external to the thrust chamber such as valves, high pressure lines, and tapoff turbine gas lines. Techniques have been examined for conducting tests with these two subassemblies in such a way as to simulate engine environment on the component test stands. In this manner, the number of expensive engine system tests required in the development program could be minimized. Ideally, only sufficient engine system tests to assure that system interactions are consistent with the reliability goal need be conducted. Preliminary studies show R&D program cost savings on the order of 26 percent are possible for the aerospike system with this engine simulation technique.

(C) The bell engine and multichamber plug cluster would also realize cost savings by engine simulation techniques. The savings are not as large for these systems as the aerospike, however. This is again due to the capability of the aerospike engine to be divided into small segments which can be pump-fed during R&D test. These tests expose thrust chamber mainstage failure modes early in the program at a relatively low cost. With the bell and multichamber configuration, particularly at higher thrust and chamber pressure levels, many expensive full-scale system tests are still necessary to expose thrust chamber mainstage failure modes.

(C) As an example of the effect of the advanced development philosophy effect on R&D test programs, Table 18 shows the comparison of the 1.5 million pounds thrust aerospike and multichamber modules to achieve a system flight reliability goal of 0.99. Compare these test figures with the conventional development test plan for the same two modules given previously in Table 17.

(C) Note that there are still over 1000 expensive full size system tests required with the multichamber configuration. The same trend would be true for the single bell configuration. As an example of why this high number of full system tests is required for bell or multichamber configurations, the present F-1 engine development program can be cited. During the development of the F-1, an important thrust chamber failure mode, mainstage combustion instability, was not exposed during pressure fed full-size thrust chamber tests. Engine tests to achieve longer durations were required to expose this failure mode.

(C) The success of engine system simulation techniques depends upon the ability to "create" the engine environment for each of the major sub-assemblies being tested. The factors which must be duplicated to ensure exposure to all potential failure modes with this type of testing were

TABLE 18

COMPARISON OF NUMBER OF TESTS FOR

MULTICHAMBER PLUG CLUSTER VS AEROSPIKE MODULE

ADVANCED DEVELOPMENT (SIMULATION) PHILOSOPHY

ENGINE SYSTEM FLIGHT RELIABILITY = 0.99

(COMPLETE ENGINE THRUST = 24,000,000 POUNDS)

CONFIDENTIAL

AEROSPIKE MODULE	
Test Category	Number of Tests
200K lbs segment (pump and pressure fed)	3733
LOX Turbopump Module (1500K lbs thrust)	2392
Fuel Turbopump Module (1500K lbs thrust)	1881
Module (1500K lbs thrust)	280*
MULTICHAMBER MODULE	
Test Category	Number of Tests
Full size pressure fed Thrust Chamber	674
LOX Turbopump Module (1500K lbs thrust)	1236
Fuel Turbopump Module (1500K lbs thrust)	1465
Module (1500K lbs thrust)	1246

* Minimum number of tests required to assure system interactions are consistent with the reliability goal.

UNCLASSIFIED

(C) The bell engine and multichamber plug cluster would also realize cost
savings by engine simulation techniques. The savings are not as large
for these systems as the aerospike, however. This is again due to the
capability of the aerospike engine to be divided into small segments
which can be pump-fed during R&D test. These tests expose thrust chamber
mainstage failure modes early in the program at a relatively low cost.
With the bell and multichamber configuration, particularly at higher
thrust and chamber pressure levels, many expensive full-scale system
tests are still necessary to expose thrust chamber mainstage failure modes.

(C) As an example of the effect of the advanced development philosophy effect
on R&D test programs, Table 18 shows the comparison of the 1.5 million
pounds thrust aerospike and multichamber modules to achieve a system
flight reliability goal of 0.99. Compare these test figures with the
conventional development test plan for the same two modules given previously
in Table 17.

(C) Note that there are still over 1000 expensive full size system tests
required with the multichamber configuration. The same trend would be
true for the single bell configuration. As an example of why this high
number of full system tests is required for bell or multichamber
configurations, the present F-1 engine development program can be cited.
During the development of the F-1, an important thrust chamber failure
mode, mainstage combustion instability, was not exposed during pressure
fed full-size thrust chamber tests. Engine tests to achieve longer durations
were required to expose this failure mode.

(C) The success of engine system simulation techniques depends upon the
ability to "create" the engine environment for each of the major sub-
assemblies being tested. The factors which must be duplicated to ensure
exposure to all potential failure modes with this type of testing were

353

CONFIDENTIAL
UNCLASSIFIED

TABLE 18

COMPARISON OF NUMBER OF TESTS FOR

MULTICHAMBER PLUG CLUSTER VS AEROSPIKE MODULE

ADVANCED DEVELOPMENT (SIMULATION) PHILOSOPHY

ENGINE SYSTEM FLIGHT RELIABILITY = 0.99

(COMPLETE ENGINE THRUST = 24,000,000 POUNDS)

CONFIDENTIAL

AEROSPIKE MODULE	
Test Category	Number of Tests
200K lbs segment (pump and pressure fed)	3733
LOX Turbopump Module (1500K lbs thrust)	2392
Fuel Turbopump Module (1500K lbs thrust)	1881
Module (1500K lbs thrust)	280*
MULTICHAMBER MODULE	
Test Category	Number of Tests
Full size pressure fed Thrust Chamber	674
LOX Turbopump Module (1500K lbs thrust)	1236
Fuel Turbopump Module (1500K lbs thrust)	1465
Module (1500K lbs thrust)	1246

* Minimum number of tests required to assure system interactions
are consistent with the reliability goal.

categorized as 1) configuration, 2) procedure, 3) ambient environment, and 4) dynamic environment. The first three criteria could be achieved with present technology. However, the duplication of the dynamic environment is a major technolgical area which must be demonstrated before the feasibility of this concept can be assured.

(C) A program (NAS8-19, System Dynamics Investigation) is currently in progress at Rocketdyne to study the dynamic interface between the thrust chamber and the turbopumps for an advanced aerospike system. The goal in this study is to simulate engine feed system dynamics on a thrust chamber test stand, which is fed by a pressurized propellant supply. As part of this effort, analyses are being conducted of the necessary facility designs to accomplish the objectives, and mathematical models are being developed to predict system start transients. This program will provide valuable technological data required to understand the thrust chamber and feed system dynamics for advanced engine systems.

Reliability and Cost Analyses Results

(C) The reliability growth model previously described was utilized in predicting the reliability vs. number of development tests for various advanced systems. The number of tests in each category required to reach a selected reliability goal then determine the development program expenditure from cost per test data. This section gives typical comparison results from the cost and reliability analyses.

(C) Aerospike vs. Conventional Bell Engine. A storable propellant aerospike and conventional bell engine of 2,000,000 pounds thrust were compared for future funding requirements. The results illustrate the segmented development approach advantage of the aerospike concept.

(C) Figure 192 illustrates the relative cost per test of the various test categories shown in Table 16. It is evident that the full system tests are the governing factor in a development program. Figure 193 illustrates the tremendous cost savings advantage of the modular aerospike engine over the single bell. Again, this advantage increases the larger the systems and chamber pressures considered. As previously stated, the aerospike shows definite advantages down to and including the 30,000 pounds thrust Air Force F_2/H_2 engine. Further studies and analysis would be required to determine the quantitative cost advantage of the aerospike system at the lower thrust and chamber pressure levels.

(C) Aerospike vs Multichamber Plug Cluster. Figure 194 illustrates a reliability growth comparison of an aerospike and multichamber engine system of 1.7 million pounds thrust utilizing NTO/UDMH- N_2H_4 (50-50) propellants. The engine system consists of 6 modules of 282,000 pounds thrust for both aerospike and multichamber configuration. Figure 194 illustrates that the aerospike system can reach a given reliability goal faster than a multichamber system.

(C) The multichamber system was approximately 12 percent more expensive to develop than the aerospike for the common engine reliability goal chosen. The cost and reliability data for this storable propellant case was for a conventional development philosophy.

(C) Studies conducted with LOX/Hydrogen propellants showed the same cost trends for aerospike and multichamber systems. These analyses also pointed out that the aerospike system cost advantage grew with increasing system thrust and chamber pressure.

Relative Cost/Test, percent   CONFIDENTIAL
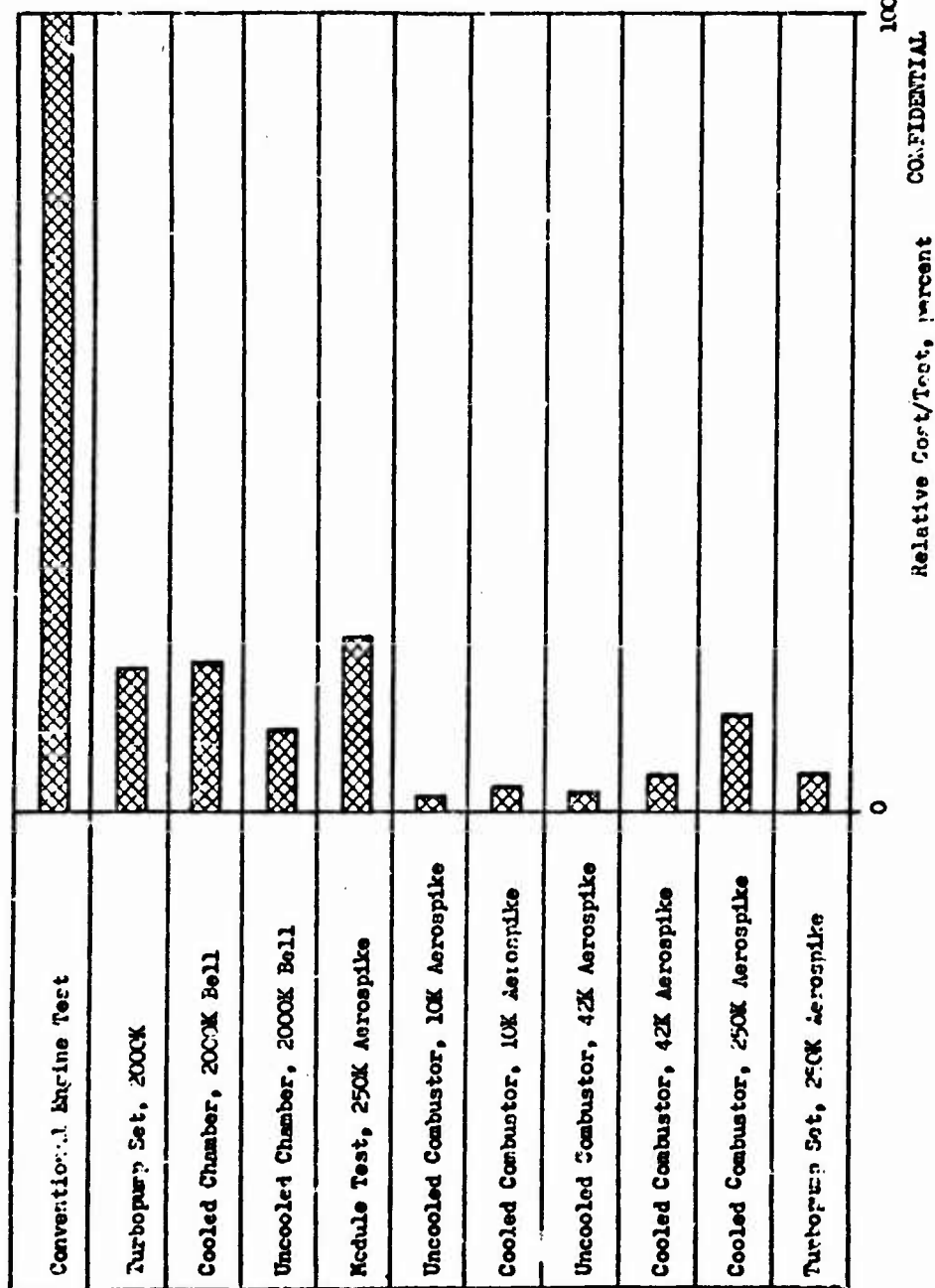
Figure 132. Comparison of Relative Cost/Test of Aerospike and Conventional Engines
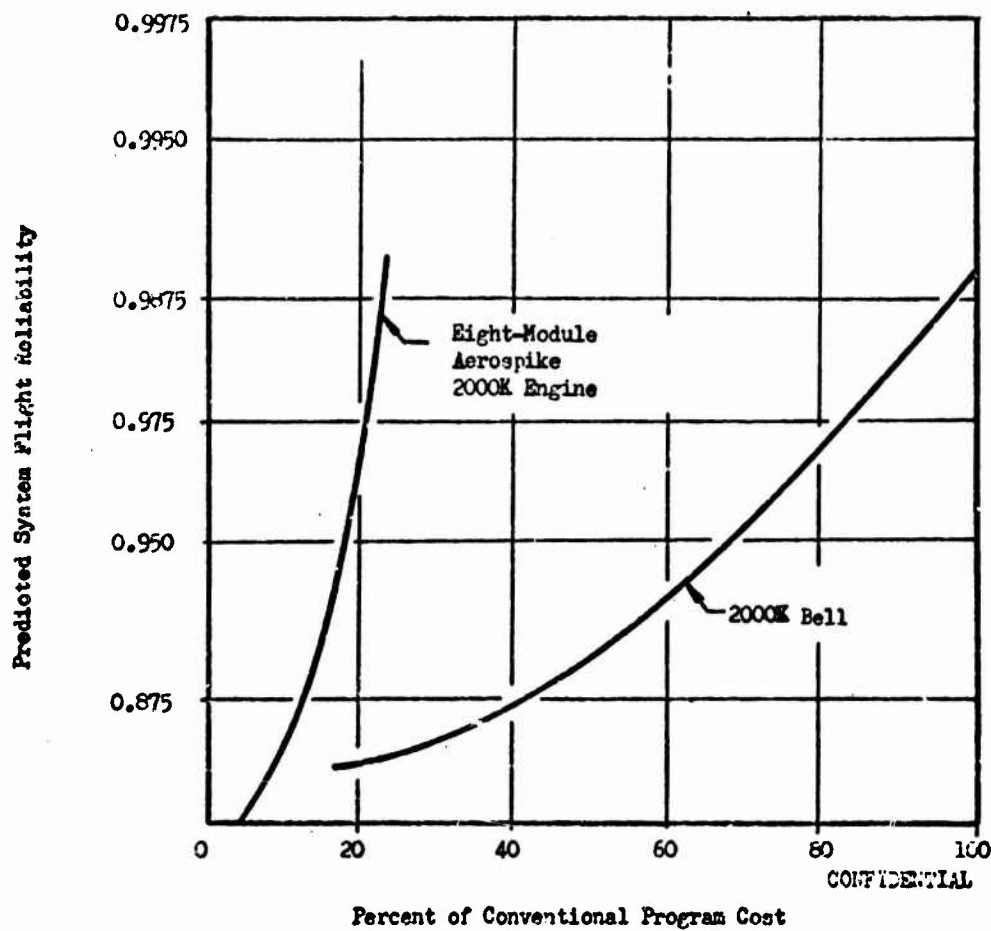
Figure 193. Comparison of Aerospike Flight Reliability Growth to
Conventional Bell Reliability, Each with Respect to
Bell Program Cost (Constant R&D Time).
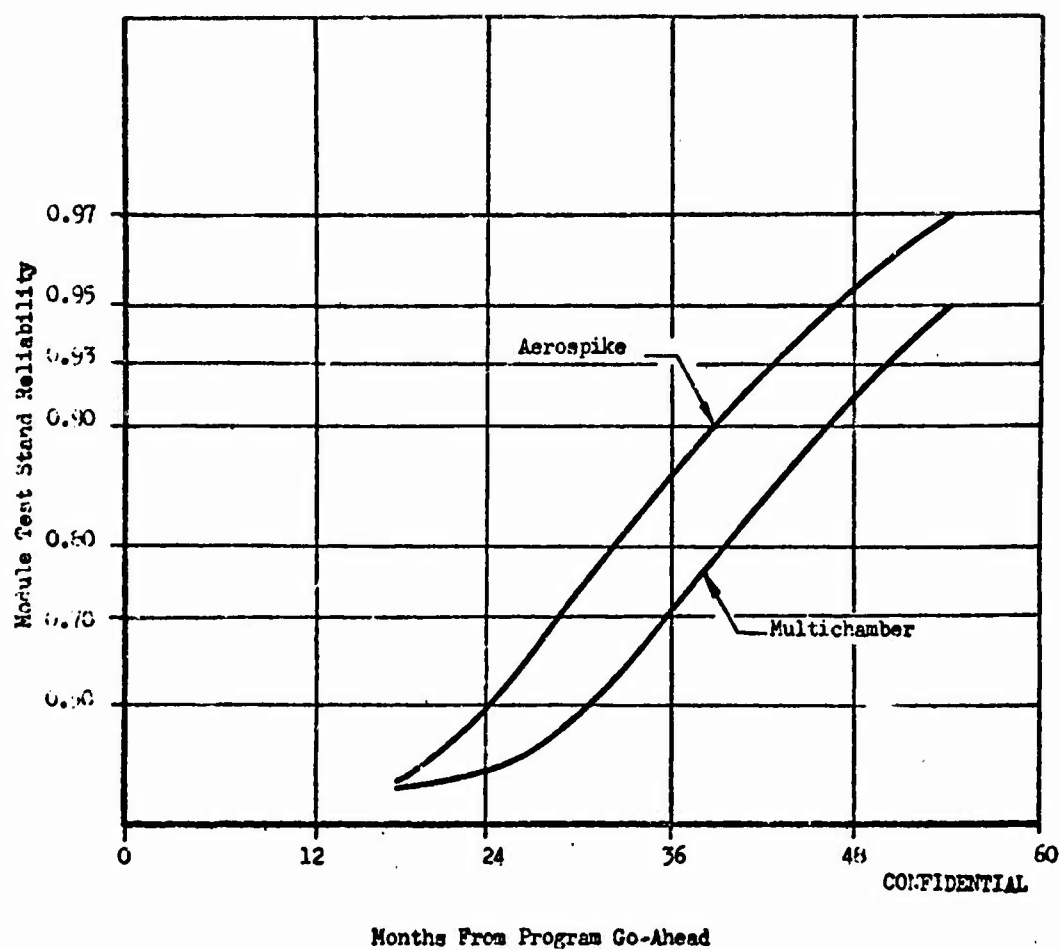
Figure 194. Module Reliability Growth, Constant Cost

(C) For the conventional development plan given previously in Table 17, the R&D program cost savings of the aerospike engine ranged from 9 percent at 1.5 million pounds to nearly 13 percent at 3.0 million pounds thrust.

(C) For the advanced development approach (system simulation during component level tests) as suggested by typical test plans given in Table 18, the 1.5 million pound thrust module multichamber system is 19 percent more expensive to develop to an equivalent reliability goal than the aerospike, and 35 percent more at the 3 million pound thrust module size.

(C) Effect of Design Parameters on R&D Cost. The effect of design point parameters on R&D program costs for the aerospike and multichamber systems were studied for both LOX/Hydrogen and NTO/UDMH (50-50). The trends were found to hold approximately the same relationships for both propellant systems.

(C) Cost analyses conducted during the toroidal system and multichamber plug cluster studies (Ref. 27 and 29) indicated that R&D program costs increase approximately 2 percent per 1000 psi increase in chamber pressure for a given module thrust size. This increase is due primarily to higher hardware costs and more system tests required due to higher failure rates associated with the higher system pressures.

(C) The R&D program costs increased approximately 22 percent per million
pounds increase in thrust for the aerospike module size range of 1.0 to
3.0 million pounds. The increase was due primarily to higher test
hardware costs and higher propellant costs associated with larger systems.
The multichamber plug cluster system was found to increase approximately
28 percent per million pounds in the same thrust range. This difference
was due to the problems associated with testing the full size pressure
fed thrust chamber required in a multichamber plan. Testing of this type
becomes extremely expensive as hardware sizes and pressures increase.

(C) Engine power cycle also had a great affect on R&D program costs. For
example, the staged combustion (topping) power cycle was found to be
approximately 17 percent more expensive at 2000 psia P_c and 22 percent
more expensive at 3000 psia for a given thrust and reliability goal
than an equivalent tapoff system. The additional expense for the topping
cycle was caused by the additional major subsystem (precombustor), the
higher turbopump hardware costs, and the expensive precombustor/turbopump
component tests. Figure 195 is a typical reliability-cost comparison of
the two cycles and illustrates the advantage of a tapoff power cycle.

(C) Selection of engine system reliability goals had a significant effect
on R&D costs. R&D costs were found to increase approximately 6 percent
from .985 to .99 system flight reliability and 25 percent from .99 to
.9975 system reliability. The sharp increase in cost at the higher
reliability goals was due primarily to the high number of expensive
system module tests to attain the higher module reliability goals.
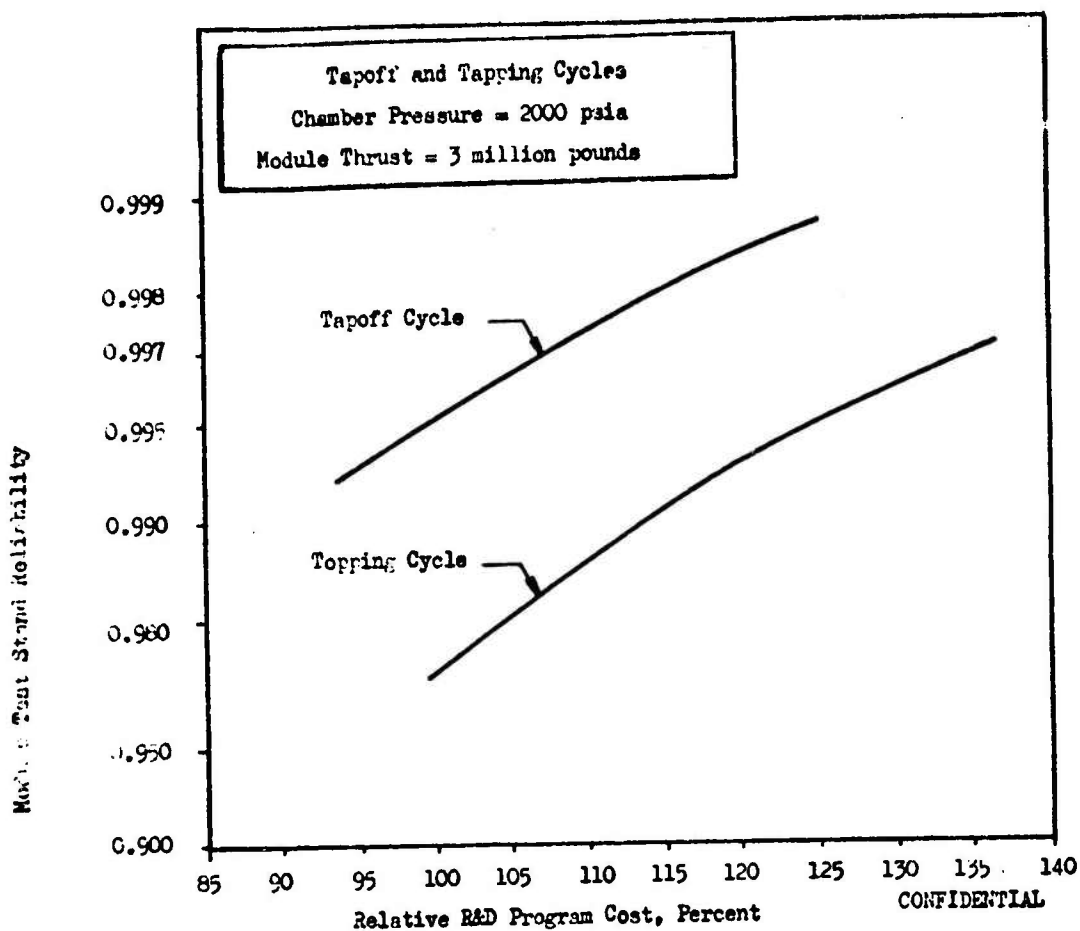
Figure 195. Relative R&D Program Costs vs Module Reliability

(C) Test Facilities. The various R&D program cost analyses performed at
Rocketdyne indicate facility expenditures will not affect the cost
trends reported in this section to any significant degree. The relative
base cost will shift upwards with addition of facility costs and the
relationships of cost vs. size, chamber pressure, configuration, etc.
will remain approximately the same. Facilities were found to comprise
15 to 20 percent of the total R&D expenditures if all new facilities
were built. It should be kept in mind, however, that testing of a full
size pressure-fed thrust chamber becomes exceedingly difficult and
expensive at high thrusts and high chamber pressures. This places
restrictions on the practicability of testing thrust chambers for the
multichamber and single bell engine configurations. The small segment,
long duration pump fed tests of the aerospike configuration become
more attractive and practical in the higher thrust and chamber pressure
ranges.

CONCLUSIONS

(U) The following major conclusions resulting from this study are summarized below. They are listed under headings of performance, weight, heat transfer, design, versatility, reliability and cost, and general conclusions.

(C) <u>Performance</u>

(1) The performance of the continuous annular throat aerospike nozzle is at least comparable to and in many instances better than the 80 percent length bell nozzle at design pressure ratio. Aerospike performance is significantly better than the bell at low pressure ratios.

(2) Performance of the continuous annular throat aerospike is approximately 1.5 percent greater than the best multichamber configuration at all pressure ratios.

(3) Nozzle shrouds, sonic pins in the throat, and chamber baffles in toroidal chambers can be designed to influence nozzle efficiency by less than 1/2 percent.

(4) No altitude performance advantage can be gained by using a large number of multichamber modules. Eight touching chambers will perform as well as any larger number.

(5) Tests with elongated module exit shapes showed no performance advantage over circular exit modules.

(6) Intermodule bleed may provide a promising method of disposing of turbine exhaust gases provided the region between chambers is isolated from ambient pressure.

(C) Weight

(1) The toroidal aerospike configuration was generally lighter in weight than the lightest multichamber configuration and the single bell engine at the 2,000,000 pound thrust level and over a wide range of chamber pressure and area ratio.

(2) The eight touching multichamber configuration was considerably lighter than a sixteen module configuration at the 2,000,000 pound thrust level.

(3) Elongated module exit chambers will be several times heavier than circular exit configurations, the difference in weight becoming greater as the exit shape a/b ratio increases.

(C) Heat Transfer

(1) Regenerative cooling of multichamber configurations becomes more difficult as the number of modules increases. The selection of number of modules for a given application could well be influenced by coolant pressure drop requirements.

(2) Regenerative cooling requirements for continuous throat toroidal configurations are approximately the same as for a sixteen module multichamber configuration.

(3) The use of N_2O_4 as a coolant at supercritical pressure may well be preferable to using UDMH-N_2H_4 (50-50) even when chamber pressure is considerably below the critical pressure of N_2O_4.

(c) **Design**

(1) From the standpoint of design complexity, the multichamber
combustor appears to require more complex thrust structure than
the toroidal configurations.

(2) Use of tangential tapered manifolds in plumbing together multi-
chamber modules, as opposed to point-to-point plumbing, results
in a much cleaner design.

(3) Splayed exit multichamber configurations are difficult to
fabricate. The long length and high tilt angle associated with
this combustor results in a considerably larger engine envelope
compared to other aerospike configurations.

(4) Considerations of development cost savings through sub-scale
testing (segmentation) are important at thrusts as low as
30,000 pounds. Testing would probably proceed from heat transfer
and injector evaluation with truncated multichamber modules or
toroidal test segments directly to full thrust chamber testing
under simulated altitude conditions.

At higher thrust levels, the development cost savings obtainable
from sub-scale testing become increasingly significant. Unless
multichamber engines of very great N are considered (pressure
drop and simplicity goals point to N as low as performance will
permit) toroidal combustors can always be segmented to lower
test thrust levels than multichambers.

(5) Static and dynamic envelope lengths for single bell engines are
significantly greater than those for either toroidal or multi-
chamber aerospikes. Differentiation between overall lengths of

toroidal and multichamber aerospike engines requires knowledge of
module number of the latter and optimum expansion nozzle lengths
of each.

(6) The continuous nature of the toroidal combustion chamber spike
nozzle surface eliminates a class of design problems associated
with the discontinuity of multichamber combustors at the module/
spike nozzle interface. Regenerative coolant transmission across
this interface in the nominal circular exit module-common axi-
symmetric spike configuration requires a collection manifold
around each module exit, a transfer duct, and a distribution manifold
around the spike.

(c) <u>Versatility</u>

(1) The altitude compensation feature allows a high performing, high
area ratio aerospike engine to be utilized unchanged in booster
and vacuum applications. High booster thrust is provided by
clustering four or more independent engine units.

(2) The toroidal aerospike concept is unique in its capability of
being adapted to and fully utilizing unusual afterbody shapes
such as those proposed for recoverable stages.

(3) The segment testing concept, which is unique to the toroidal
combustion chamber, allows such important engine characteristics
as combustion efficiency and stability, engine performance, cooling
capability, and thrust chamber life to be economically developed
and demonstrated with full scale - - but partial thrust segments
of the complete engine.

(C) Reliability and Cost

    (1) The segmented aerospike engine will require fewer complete system tests to attain the same reliability goal as the conventional bell engine or the multichamber engine.

    (2) An advanced development plan in which the thrust chamber and turbopump modules are developed in a simulated engine environment provides a significant reduction in the number of engine segment tests required. The plan provides more substantial reductions for the aerospike engine than the multichamber engine.

    (3) With the engine segment test approach, the aerospike engine can achieve a given reliability goal with less dollar expenditure than for the conventional single bell engine or a multichamber engine.

(C) General

Based on the combination of factors considered the following conclusions are made.

    (1) The toroidal aerospike configuration is superior to the multichamber configuration for an annular aerodynamic spike nozzle based on performance, weight, cooling considerations, and design considerations. A multichamber configuration would perhaps be preferable if an engine system were needed which could utilize existing hardware.

    (2) Consideration of performance, weight, cooling capability, and design complexity leads to the conclusion that multichamber configurations should be of conventional touching exit design. For the range of thrust, chamber pressure, and area ratio investigated an eight module configuration is superior to configurations with a greater number of modules in all criteria considered in this study. A good criterion for selecting the number of modules for a booster engine is to use the fewest number (down to eight) which will provide near touching circular exits and a non-separated module flow.

APPENDIX 1

METHOD OF ANALYSIS OF HIGH-AREA-RATIO-RATIO-COLD-FLOW DATA

APPENDIX 1

METHOD OF ANALYSIS OF HIGH-AREA-RATIO COLD-FLOW DATA

(U) C_T was defined in the first quarterly progress report as follows:

$$C_T = \frac{I_s}{I_{s_{pi}}} = \frac{F_p + F_b}{(1 + \frac{\dot{w}_s}{\dot{w}_p}) F_{pi}}$$

where
I_s = the actual specific impulse
F_b = the base thrust, $\int P_b \, dA_b$
F_p = the net primary thrust
$I_{s_{pi}}$ = ideal specific impulse based on primary fluid properties
F_{pi} = ideal thrust for $\dot{w}_p$ weight flowrate and properties

(U) Substituting the relationships $F_m = F_p + F_b$ and $C_{F_{opt}} = \dfrac{F_{pi}}{P_c A^*_t}$,

where
F_m = total measured net thrust

A^*_t = primary aerodynamic throat area

and rearranging terms results in

$$C_T = \frac{F_m}{(1 + \frac{\dot{w}_s}{\dot{w}_p}) C_{F_{opt}} P_c A^*_t}$$

(U) A flow function (f_p) was calculated using one dimensional, isentropic, compressible flow theory for critical flow (Ref 6). This function,

$f_p = \dfrac{\dot{w}_p \sqrt{T_p}}{P_c A^*_t}$, includes real gas effects for the gas at the nozzle

throat. Thus:

$$c_T = \frac{F_m}{(1 + \frac{\dot{w}_s}{\dot{w}_p}) \, C_{F_{opt}} \, \frac{\dot{w}_p \sqrt{T_p}}{f_p}} = \frac{F_m \, f_p}{C_{F_{opt}} \, \dot{w}_T \sqrt{T_p}}$$

(U) The factors F_m and T_p were measured directly; the factors f_p, $\dot{w}_T$ and $C_{F_{opt}}$ are obtained using measured data and gas properties.

APPENDIX 2

HIGH-AREA-RATIO TEST DATA

APPENDIX 2

HIGH-AREA-RATIO TEST DATA

Test Number	Chamber Pressure, psia	F total, pounds	P cowl, pounds	P base, psia	ẇp, lb/sec	ẇs/ẇp, percent	Pc/Pa	CT total	CT without cowl
				Contoured Model, Open Base ε = 147.5					
5	932.7	140.5	0.25	0.114	0.8418		10327	97.01	97.64
7	936.4	141.1	0.28	0.112	0.8430		12697	97.86	97.67
8	922.2	138.4	0.28	0.100	0.8359		12799	97.46	97.26
9	924.0	138.9	0.27	0.096	0.8281		11737	97.93	97.74
10	928.8	140.0	0.38	0.091	0.8275		69173	98.26	97.99
12	932.7	141.9	0.38	0.114	0.8373		68534	98.67	98.41
13	918.0	139.5	0.38	0.108	0.8203		66217	98.46	98.19
14	930.9	144.5	0.38	0.412	0.8364	1.40	68747	98.68	98.62
15	932.0	144.0	0.33	0.340	0.8381	1.03	71782	98.56	98.30
16	926.2	148.3	0.38	No Data	0.8348	5.10	66305	97.98	97.55
17	928.2	146.4	0.38	0.760	0.8361	3.30	79125	98.29	93.03
18	928.8	147.8	0.38	0.888	0.8406	4.25	72575	98.41	98.16
21	919.6	123.9	-0.15	2.786	0.8273		317	91.08	91.19
22	937.0	126.1	-0.15	2.749	0.8430		312	90.95	91.06
23	930.7	117.2	-0.17	5.559	0.8401		157	85.45	86.58
25	906.9	114.6	-0.17	5.817	0.8224		164	86.76	86.89
27	917.0	138.4	0.24	0.124	0.8297		9552	98.24	98.07
29	920.6	130.6	-0.08	No Data	0.8312		936	94.34	94.40
30	920.3	132.8	-0.12	0.126	0.8311		2024	95.08	95.17
31	920.8	136.2	0.11	0.112	0.8313		4142	96.91	96.83
32	921.3	133.3	0	0.128	0.8325		2169	95.35	95.35
33	936.1	140.8	0.07	0.358	0.8394	1.11	3316	97.37	97.33
34	937.8	142.1	-0.02	0.415	0.8435	3.05	1837	96.65	96.66
35	934.9	146.2	0.11	0.655	0.8401	4.43	4213	97.08	97.81

CONFIDENTIAL

Test Number	Chamber Pressure, psia	F_{total}, pounds	F_{cowl}, pounds	P_{base}, psia	W_p, lb/sec	W_s/W_p, percent	P_c/P_a	C_T total	C_T without cowl
36	944.2	141.9	0.11	1.095	0.8475	4.72	1124	95.11	95.03
37	940.1	144.0	-0.17	0.918	0.8556	4.75	1733	96.06	96.17
38	933.1	143.7	0.06	0.973	0.8395	4.75	3036	96.69	96.65
39	932.4	141.9	-0.03	1.059	0.8411	4.74	1816	95.91	95.93
40	930.4	142.1	0.25	0.319	0.8322	1.06	9935	99.00	98.83
41	926.0	117.0	-0.24	No Data	0.8344	0	178	87.10	87.28
42	922.1	117.5	-0.24	No Data	0.8363	0	177	87.60	87.78
44	749.7	111.4	0.28	0.065	0.6671	0	12,432	97.93	97.68
Contoured Model, Radial-Inward Secondary Flow Injection (Large Gap), ϵ = 147.5									
45	929.7	141.2	0.38	0.106	0.8363	0	69,836	98.42	98.16
46	959.8	145.2	0.38	0.298	0.8455	1.50	58,315	98.75	98.49
Contoured Model, Radial-Inward Secondary Flow Injection (Large Gap), ϵ = 156.8									
47	943.0	135.6	0.38	No Data	0.8036	0	58,000	98.24	97.96
48	956.0	137.8	0.38	No Data	0.8132	0	58,000	98.61	98.34
51	906.4	131.6	0.38	0.281	0.7634	1.72	52,798	98.46	96.18
52	920.1	133.4	0.38	0.276	0.7745	1.39	58,103	98.48	98.20
53	916.5	134.5	0.38	0.339	0.7725	2.73	49,143	98.29	98.02
Contoured Model, Radial-Inward Secondary Flow Injection (Small Gap), ϵ = 156.8									
54	912.0	132.8	0.38	0.211	0.7710	2.04	55,141	98.05	97.77

APPENDIX 2 (CONT.)

Test Number	P_c psia	Ftotal, pounds	Fcowl, pounds	Pbase, psia	$\dot{w}_2$ lb/sec	$\dot{w}_g/\dot{w}_p$ percent	P_c/P_a	C_T total	C_T without cowl
Contoured Model, Open Base Cavity, ϵ = 156.8									
55	911.25	130.3	0.38	0.077	0.7650	0.0	66,400	98.24	97.95
Contoured Model, 1/4 inch Instrumented Sting in Wake, ϵ = 156.8									
56	911.68	130.3	0.38	0.079	0.7660	0.0	52,873	98.23	97.94
58	920.41	137.5	0.38	0.905	0.7762	4.79	61,938	97.95	97.68
59	913.52	146.7	0.38	0.753	0.7698	4.83	60,077	98.27	98.00
Contoured Model, Radial Outward Secondary Flow Injection, ϵ = 156.8									
60	908.22	133.4	0.38	No Data	0.7695	2.05	53,634	98.64	98.36
61	911.87	130.7	0.38	0.097	0.7681	0.0	56,141	98.55	98.26
62	912.99	133.7	0.37	0.324	0.7719	1.66	44,031	98.66	98.39
Conical Model, Open Base Cavity, ϵ = 129.9									
65	898.74	157.9	0.15	0.589	0.9557	0.0	52,769	95.09	95.00
66	890.69	161.6	No Data	1.066	0.9495	2.03	48,273	96.18	95.88
67	Dynamic Test								
68	Dynamic Test								
69	886.24	164.3	0.42	1.216	0.9505	3.08	60,857	96.05	95.80
70	888.25	162.0	0.41	0.992	0.9413	1.61	52,037	96.14	95.90
71	893.83	162.7	0.40	0.975	0.9408	1.46	52,480	95.91	95.67

APPENDIX 2 (CONT.)

Test Number	P_c psia	F_{total} pounds	F_{cowl} pounds	P_{base} psia	$\dot{w}_p$ lb/sec	$\dot{w}_s/\dot{w}_p$ percent	P_o/P_a	C_T total	C_T without cowl
Conical Model, 1/4 Inch Instrumented Sting, $\epsilon = 129.9$									
73	897.72	157.7	0.13	0.636	0.9591	0	55,137	94.95	94.87
74	897.93	157.9	0.14	0.635	0.9616	0	51,773	95.03	94.95
75	891.66	156.8	0.14	0.631	0.9528	0	50,384	95.15	95.06
76	894.19	157.3	0.09	0.640	0.9533	0	52,632	95.29	95.23
77	894.14	166.5	0.51	1.460	0.9569	4.47	47,664	96.45	96.16
Conical Model, 0.049 Inch Plain Sting, $\epsilon = 129.9$									
78	887.67	156.4	0.06	0.607	0.9507	0	50,158	95.31	95.27
Conical Model, Open Base Cavity, $\epsilon = 129.9$									
79	Dynamic Test								
80	Dynamic Test								

APPENDIX 3

COLD-FLOW TEST DATA

APPENDIX 3 COLD-FLOW TEST DATA

Test Number	Chamber Pressure psia	F_{total} pounds	P_{base} psia	$P_{i.s.}$ psia	$\dot{w}_P$ lb/sec	$\dot{w}_s/\dot{w}_P$ percent	$\dot{w}_{i.s.}/\dot{w}_P$ percent	P_c/P_s	C_T total
		Model I-3, Scaled Hot Firing Model, $\epsilon_o^* = 24.54$, Air, Open Base							
22	150.2	144.7	0.885	–	2.102	0	–	527.0	0.9663
23	150.5	145.0	0.897	–	2.105	0	–	537.5	0.9653
24	150.5	145.1	0.890	–	2.104	0	–	524.4	0.9653
25	151.2	136.1	–	–	2.118	0	–	126.0	0.9532
26	150.6	136.0	1.440	–	2.115	0	–	126.1	0.9552
27	150.5	136.9	1.128	–	2.116	0	–	155.9	0.9516
29	150.2	138.1	0.892	–	2.111	0	–	201.6	0.9523
30	149.8	144.2	0.884	–	2.094	0	–	531.2	0.9655
31	149.5	140.8	0.895	–	2.102	0	–	300.3	0.9605
32	150.6	145.3	0.894	–	2.114	0	–	551.6	0.9656
34	150.8	134.4	1.860	–	2.147	0	–	100.6	0.9536
39	150.6	145.0	0.895	–	2.142	0	–	539.8	0.9609
40	150.6	145.2	0.906	–	2.142	0	–	545.7	0.9623
44	150.2	148.0	0.973	–	2.200	0	–	173.0	0.9494
45	150.8	149.9	3.203	–	2.222	0	–	60.4	0.9438
46	151.4	132.2	3.300	–	2.194	0	–	60.8	0.9442
47	151.3	134.8	5.490	–	2.247	0	–	35.5	0.9409
52	149.9	133.6	5.330	–	2.195	0	–	35.2	0.9388
53	150.4	135.9	7.361	–	2.194	0	–	19.8	0.9272
54	150.7	145.4	0.909	–	2.172	0	–	540.9	0.9634

APPENDIX 3 COLD-FLOW TEST DATA (Cont.)

Test Number	Chamber Pressure psia	F_{total} pounds	P_{base} psia	$P_{l.s.}$ psia	$\dot{W}_P$ lb/sec	$\dot{W}_s/\dot{W}_P$ percent	$\dot{W}_{l.s.}/\dot{W}_P$ percent	P_c/P_a	C_T total
			Model I-3, Scaled Hot Firing Model, $\epsilon^*_o = 24.54$, Air, Open Base						
92	100.5	95.0	0.601	-	1.412	0	-	298.8	0.9621
94	100.4	92.8	0.600	-	1.413	0	-	206.8	0.9541
95	50.2	48.3	0.287	-	0.702	0	-	497.0	0.9654
55	150.8	148.2	1.314	-	2.193	0.983	-	509.1	0.9725
63	149.7	124.8	5.515	-	2.145	0.976	-	35.2	0.9414
67	150.4	149.1	1.438	-	2.161	1.512	-	539.8	0.9760
59	151.0	150.3	1.552	-	2.123	2.013	-	535.1	0.9750
60	151.0	143.1	1.778	-	2.140	2.010	-	170.9	0.9642
64	148.8	125.2	5.626	-	2.142	2.027	-	35.2	0.9418
66	150.4	149.8	1.590	-	2.159	2.009	-	557.0	0.9760
56	150.8	151.1	1.724	-	2.192	3.013	-	539.1	0.9723
57	150.9	151.3	1.724	-	2.200	3.022	-	523.2	0.9714
61	151.2	143.9	1.917	-	2.136	2.648	-	169.1	0.9645
65	148.0	125.8	5.749	-	2.141	3.072	-	35.0	0.9390
62	151.2	146.3	2.621	-	2.128	5.021	-	166.8	0.9593

APPENDIX 3 COLD-FLOW TEST DATA (Cont.)

Test Number	Chamber Pressure psia	F_{total} pounds	P_{base} psia	$P_{i.s.}$ psia	$\dot{w}_P$ lb/sec	$\dot{w}_B/\dot{w}_P$ percent	$\dot{w}_{i.s.}/\dot{w}_P$ percent	P_c/P_a	C_T total
			Model I-1, Scaled Hot Firing Model, $\epsilon_o^* = 24.54$, Air, Radial-Inward Base						
71	150.7	149.1	1.398	–	2.165	1.701	–	535.7	0.9708
72	150.4	142.9	1.545	–	2.177	3.098	–	168.9	0.9575
73	150.4	142.9	1.480	–	2.189	3.098	–	168.7	0.9574
74	150.8	126.2	5.873	–	2.180	1.511	–	35.5	0.9408
75	150.7	126.5	5.369	–	2.184	1.507	–	35.4	0.9414
			Model I-2, Scaled Hot Firing Model, $\epsilon_o^* = 24.54$, Air, Radial-Outward Base						
76	150.7	126.6	5.392	–	2.169	1.511	–	35.2	0.9436
77	150.6	126.5	5.684	–	2.179	1.511	–	35.2	0.9434
78	151.0	144.4	2.181	–	2.183	3.050	–	170.6	0.9644
79	150.7	144.3	2.171	–	2.166	3.059	–	169.4	0.9656
80	150.9	149.8	1.519	–	2.193	1.728	–	539.9	0.9741

APPENDIX 3 COLD-FLOW TEST DATA (Cont.)

Test Number	Chamber Pressure psia	F total pounds	P base psia	P i.s. psia	$\dot{W}_P$ lb/sec	$\dot{W}_B/\dot{W}_P$ percent	$\dot{W}_{l.c.}/\dot{W}_P$ percent	P_c/P_a	C_T total
Model I-4, Scaled Hot Firing Model, $\epsilon_o^* = 24.54$, Air, Supersonic Base, $\epsilon = 3.5$									
83	150.2	147.7	0.809	-	2.125	2.296	-	535.5	0.9589
84	151.0	149.2	0.813	-	2.128	2.254	-	527.4	0.9574
85	151.2	142.2	0.848	-	2.131	3.893	-	172.6	0.9407
86	150.6	126.4	5.342	-	2.140	2.015	-	35.5	0.9361
Model I-4, Scaled Hot Firing Model, $\epsilon_o^* = 24.54$, Air, Supersonic Base, $\epsilon = 15$									
87	150.2	126.2	5.410	-	2.132	2.024	-	35.3	0.9371
88	150.3	147.7	0.804	-	2.129	2.283	-	519.2	0.9582
Model I-5, Scaled Hot Firing Model, $\epsilon_o^* = 24.54$, Air, Porous Plate Base									
104	150.2	146.6	-	-	2.167	0.604	-	525.2	0.9687

APPENDIX 3 COLD-FLOW TEST DATA (Cont.)

Test Number	Chamber Pressure psia	F total pounds	P base psia	P l.s. psia	$\dot{W}_P$ lb/sec	$\dot{W}_s/\dot{W}_P$ percent	$\dot{W}_{l.s.}/\dot{W}_P$ percent	P_c/P_a	C_T total
		Model I-3, Scaled Hot Firing Model, $\epsilon^*_c = 24.26$, CF_4, Open Base							
42	150.0	150.9	1.002	-	3.721	0	-	255.4	condensation*
96	49.1	47.5	0.323	-	1.136	0	-	144.4	0.9464
98	99.4	101.1	0.654	-	2.365	0	-	287.2	0.9555
99	99.4	92.5	0.967	-	2.362	0	-	91.5	0.9412
100	99.2	88.9	2.091	-	2.342	0	-	54.3	0.9414
101	99.2	84.4	3.495	-	2.346	0	-	35.0	0.9319
102	49.9	51.9	0.535	-	1.163	1.733	-	275.4	0.9665
103	49.8	51.8	0.539	-	1.159	1.739	-	258.9	0.9676

*Because of the effects of two-phase flow, C_F was not calculated for test 42. P_b/P_c is 0.0067, 0.0066 and 0.0066 for tests 42, 96 and 98 respective, indicating little or no effect on performance due to P_c or condensation.

APPENDIX 3   COLD-FLOW TEST DATA (Cont.)

Test Number	Chamber Pressure psia	F_{total} pounds	P_{base} psia	$P_{i.s.}$ psia	$\dot{W}_P$ lb/sec	$\dot{W}_a/\dot{W}_P$ percent	$\dot{W}_{i.s.}/\dot{W}_P$ percent	P_c/P_e	C_m total
			Model II-6, Point Expansion, $\epsilon_o^* = 43.30$, Air, Open Base						
106	150.4	154.3	0.204	–	2.203	0	–	1525.2	0.9848
107	151.2	154.5	0.199	–	2.197	0	–	1520.7	0.9859
108	149.4	152.8	0.210	–	2.204	0	–	1475.6	0.9667
130	150.8	154.0	0.203	–	2.182	0	–	1436.9	0.9855
110	149.5	152.3	0.209	–	2.200	0	–	1461.4	0.9953
112	148.5	143.4	0.471	–	2.152	0	–	298.4	0.9686
113	149.4	145.9	0.301	–	2.177	0	–	397.2	0.9756
115	150.2	147.6	0.232	–	2.192	0	–	472.4	0.9727
116	150.5	151.2	0.203	–	2.184	0	–	797.2	0.9820
117	150.4	135.0	1.177	–	2.200	0	–	100.4	0.9463
118	151.0	135.3	1.191	–	2.184	0	–	100.7	0.944
119	151.4	138.9	0.974	–	2.169	0	:	150.5	0.9486
120	149.8	137.4	0.881	–	2.163	0	–	147.9	0.9480

APPENDIX 3 COLD-FLOW TEST DATA (Cont.)

Test Number	Chamber Pressure psia	F_{total} pounds	P_{base} psia	$P_{l.s.}$ psia	$\dot{W}_P$ lb/sec	$\dot{W}_s/\dot{W}_P$ percent	$\dot{W}_{l.s.}/\dot{W}_P$ percent	P_c/P_a	C_T total
		Model II-6, Point Expansion, $\epsilon_o^* = 48.30$, Air, Open Base							
121	150.0	139.2	1.102	—	2.156	0.697	—	149.2	0.9533
122	149.8	139.0	1.066	—	2.154	0.705	—	148.0	0.9519
123	149.2	138.5	1.064	—	2.150	0.710	—	147.8	0.9519
129	150.6	149.4	0.441	—	2.175	0.735	—	452.6	0.9783
132	151.4	157.1	0.401	—	2.188	0.952	—	1481.0	0.9877
125	148.4	139.4	1.253	—	2.157	1.490	—	146.8	0.9597
128	150.2	149.9	0.534	—	2.164	1.471	—	453.9	0.9775
133	148.6	154.8	0.464	—	2.147	1.927	—	1410.3	0.9839
134	150.7	156.2	0.499	—	2.183	1.902	—	1403.3	0.9838
126	151.5	144.5	1.443	—	2.184	2.914	—	150.1	0.9575
127	148.6	150.5	0.630	—	2.154	2.956	—	452.5	0.9711

APPENDIX 3 COLD-FLOW TEST DATA (Cont.)

Test Number	Chamber Pressure psia	F total pounds	P base psia	P 1.s. psia	$\dot{W}_P$ lb/sec	$\dot{W}_s/\dot{W}_P$ percent	$\dot{W}_{1.s.}/\dot{W}_P$ percent	P_c/P_a	C_T total
		Model III-7, Shrouted Nozzle, ϵ^*_o = 43.64, Air, Open Base							
136	151.6	144.2	0.098	-	2.064	0	-	1491.1	0.9793
137	148.6	141.0	0.100	-	2.037	0	-	1381.9	0.9789
138	150.2	138.5	0.105	-	2.068	0	-	571.9	0.9712
140	149.4	123.8	1.065	-	2.039	0	-	99.5	0.9333
141	149.8	124.0	1.064	-	2.032	0	-	100.4	0.9330
142	149.5	123.8	1.068	-	2.028	0	-	99.1	0.9339
143	150.8	130.2	0.833	-	2.023	0	-	154.9	0.9515
144	150.6	130.2	0.835	-	2.031	0	-	153.6	0.9525
145	149.2	131.2	0.617	-	2.015	0	-	200.6	0.9593
146	149.4	131.4	0.630	-	2.013	0	-	199.1	0.9592
147	149.2	133.4	0.266	-	2.003	0	-	297.6	0.9613
148	148.8	131.9	0.398	-	2.004	0	-	248.2	0.9589
149	149.8	135.2	0.107	-	2.018	0	-	403.2	0.9608
150	149.9	138.0	0.100	-	2.027	0	-	538.9	0.9698
151	151.7	138.8	0.100	-	2.053	0	-	486.4	0.9684

APPENDIX 3 COLD-FLOW TEST DATA (Cont.)

Model III-7, Shrouded Nozzle, $\epsilon_o^* = 48.64$, Air, Open Base

Test Number	Chamber Pressure psia	F_{total} pounds	P_{base} psia	$P_{i.s.}$ psia	$\dot{W}_P$ lb/sec	$\dot{W}_s/\dot{W}_P$ percent	$\dot{W}_{i.s.}/\dot{W}_P$ percent	P_c/P_a	C_T total
152	151.9	138.8	0.105	–	2.053	0	–	472.3	0.9680
153	151.2	134.2	0.309	–	2.051	0	–	278.2	0.9565
155	80.5	76.4	0.043	–	1.078	0	–	1355.9	0.9806
158	73.2	69.5	0.041	–	0.971	0	–	1415.6	0.9810
160	102.2	97.2	0.044	–	1.353	0	–	1510.0	0.9801
176	100.7	92.2	0.058	–	1.345	0	–	495.1	0.9704
173	100.9	95.9	0.054	–	1.354	0	–	1477.5	0.9793
174	102.6	97.7	0.052	–	1.369	0	–	1581.7	0.9813
175	100.8	93.2	0.053	–	1.348	0	–	607.6	0.9738
161	101.8	97.4	0.107	–	1.350	0.747	–	1473.9	0.9807
163	101.8	94.0	0.127	–	1.365	0.742	–	476.7	0.9713
168	100.6	87.5	0.614	–	1.355	0.752	–	150.5	0.9511
162	101.5	93.0	0.138	–	1.356	1.494	–	1493.5	0.9792
164	101.6	94.4	0.182	–	1.366	1.492	–	447.1	0.9720
167	100.8	88.3	0.672	–	1.356	1.498	–	151.8	0.9546
166	100.6	94.2	0.244	–	1.353	3.007	–	430.1	0.9678

APPENDIX 3 COLD-FLOW TEST DATA (Cont.)

Test Number	Chamber Pressure psia	F_{total} pounds	P_{base} psia	$P_{i.n.}$ psia	$\dot{W}_P$ lb/sec	$\dot{W}_B/\dot{W}_F$ percent	$\dot{W}_{i.s.}/\dot{W}_P$ percent	P_c/P_ε	C_T total
Model III-9, Eight Chamber Touching Multichamber, $\varepsilon^*_{CL} = 49.8$, No Extension									
239	100.2	96.7	0.080	0.072	1.384	0	0	1401.4	0.9684
231	99.8	84.8	0.532	0.604	1.389	0	0	148.40	0.9122
232	99.5	88.0	0.433	0.335	1.375	0	0	197.85	0.9385
233	99.8	90.0	0.378	0.397	1.384	0	0	237.51	0.9497
234	100.0	89.6	0.135	0.326	1.380	0	0	266.03	0.9416
235	100.0	94.1	0.105	0.168	1.331	0	0	554.02	0.9656
236	100.1	95.5	0.089	0.122	1.375	0	0	785.71	0.9671
237	100.3	96.1	0.086	0.101	1.381	0	0	994.05	0.9672
238	100.2	96.6	0.076	0.072	1.383	0	0	1408.29	0.9670
240	100.3	97.4	-	0.078	1.387	0.738	0	1402.80	0.9569
243	100.4	91.4	-	-	1.390	0.732	0	267.02	0.9478
245	100.8	85.9	-	0.587	1.394	0.764	0	153.03	0.9114
246	100.4	85.7	-	0.586	1.393	0.764	0	152.38	0.9111

APPENDIX 3 COLD-FLOW TEST DATA (Cont.)

Test Number	Chamber Pressure psia	F total pounds	P_{base} psia	$P_{l.s.}$ psia	$\dot{w}_P$ lb/sec	$\dot{w}_B/\dot{w}_P$ percent	$\dot{w}_{l.s.}/\dot{w}_P$ percent	P_c/P_a	C_T total
Model III-9, Eight Chamber Touching Multichamber, ϵ^*_{CL} = 49.8 , No Extension									
241	100.5	98.0	—	0.087	1.395	1.494	0	1419.49	0.9614
242	100.4	91.7	—	0.356	1.391	1.500	0	267.83	0.9441
247	100.5	86.0	—	0.593	1.404	1.504	0	153.01	0.9045
Model III-9, Eight Chambers Touching Multichamber, ϵ^*_{CL} = 49.8, No Extension, Engine Out									
257	98.3	82.4	0.073	0.067	1.190	0	0	1410.13	0.9692
258	98.1	82.3	0.066	0.066	1.177	0	0	1451.18	0.9691
263	98.3	73.1	0.632	0.640	1.198	0	0	147.96	0.9195
260	98.1	82.7	—	0.069	1.187	0.589	0	1466.59	0.9655
261	98.2	72.4	—	0.667	1.191	0.588	0	143.17	0.9057
Model III-8, Eight Chambers Touching Multichamber, ϵ^*_{CL} = 49.8 , No Centerbody, No Shroud									
253	99.9	96.3	0.078	0.076	1.385	0	0	1411.81	0.9657
254	100.1	96.5	0.090	0.073	1.384	0	0	1407.48	0.9687
255	99.9	86.2	0.659	—	1.393	0	0	151.99	0.9268
256	100.0	86.1	0.661	0.658	1.395	0	0	151.65	0.9261

APPENDIX 5 COLD-FLOW TEST DATA (Cont.)

CONFIDENTIAL

Test Number	Chamber Pressure psia	F_{total} pounds	P_{base} psia	$P_{i.s.}$ psia	$\dot{w}_p$ lb/sec	$\dot{w}_s/\dot{w}_p$ percent	$\dot{w}_{i.s.}/\dot{w}_p$ percent	P_c/P_a	C_T total
		Model III-10, Eight Chambers Touching Multichamber $\varepsilon_{CL}^* = 49.8$, 30% Length							
180	100.1	97.2	-	-	1.402	0	0	1936.17	0.9698
182	100.0	97.7	0.091	0.066	1.378	0	0	1500.15	0.9700
183	100.4	97.0	0.072	0.059	1.367	0	0	1514.10	0.9698
184	100.4	95.3	0.082	0.147	1.375	0	0	703.08	0.9695
185	100.4	93.5	0.091	0.216	1.389	0	0	435.76	0.9619
186	100.3	91.7	0.087	0.283	1.373	0	0	343.02	0.9529
187	100.4	96.3	0.073	0.105	1.374	0	0	958.93	0.9686
188	100.4	96.6	0.076	0.082	1.370	0	0	1208.62	0.9707
189	99.8	94.3	0.096	0.165	1.364	0	0	614.91	0.9687
190	99.5	88.3	0.472	0.472	1.383	0	0	203.19	0.9457
191	99.7	88.3	0.453	0.453	1.385	0	0	203.76	0.9410
192	99.9	85.1	0.575	0.574	1.388	0	0	150.88	0.9174

APPENDIX 3 COLD-FLOW TEST DATA (cont.)

Model III-10, Eight Chambers Touching Multichamber $\epsilon_{CL}^* = 49.8$, 30% Length

Test Number	Chamber Pressure psia	F_{total} pounds	P_{base} psia	$P_{i.s.}$ psia	$\dot{W}_P$ lb/sec	$\dot{W}_s/\dot{w}_P$ percent	$\dot{W}_{i.s.}/\dot{W}_P$ percent	P_c/P_a	C_T total
193	100.0	89.8	0.102	0.349	1.404	0	0	268.60	0.9444
194	100.0	90.1	0.428	0.405	1.399	0	0	237.08	0.9514
221	101.2	97.6	-	0.067	1.378	0	0	1491.31	0.9675
196	100.9	99.0	0.095	0.031	1.402	0	0	7944.88	0.9585
197	101.0	98.4	0.090	0.040	1.403	0	0	3014.03	0.9669
205	100.9	97.6	-	0.070	1.396	0	0	1469.56	0.9707
198	101.2	98.5	0.094	0.067	1.403	0	0.259	2521.18	0.9592
199	101.2	98.6	0.087	0.189	1.407	0	1.133	1550.48	0.9698
206	101.2	98.2	-	0.139	1.409	0	0.707	1473.93	0.9669
211	100.2	90.1	0.093	0.348	1.399	0	0.712	273.70	0.9368

APPENDIX 3 COLD-FLOW TEST DATA (Cont.)

Test Number	Chamber Pressure psia	F_{total} pounds	P_{base} psia	$P_{i.s.}$ psia	$\dot{w}_p$ lb/sec	$\dot{w}_s/\dot{w}_p$ percent	$\dot{w}_{i.s.}/\dot{w}_p$ percent	P_c/P_a	C_T total
		Model III-10, Eight Chambers Touching Multichamber ϵ^*_{CL} = 49.8 , 30% Length							
207	101.3	99.2	0.062	0.223	1.411	0	1.398	1498.30	0.9670
210	101.2	97.1	0.067	0.226	1.397	0	1.437	1007.14	0.9680
212	103.4	90.4	0.198	0.376	1.417	0	1.424	265.12	0.9345
213	100.2	90.2	0.093	0.361	1.406	0	1.435	273.40	0.9310
216	100.3	85.9	0.580	0.580	1.412	0	1.432	153.55	0.9077
208	101.6	100.5	0.085	0.365	1.414	0	2.877	1442.77	0.9667
209	100.0	98.2	0.084	0.362	1.395	0	2.906	1015.85	0.9651
214	100.4	92.0	0.337	0.415	1.410	0	2.866	273.79	0.9362
215	100.3	86.2	0.590	0.594	1.411	0	2.873	154.09	0.8976
218	100.8	98.2	-	0.680	1.390	0.729	0	1485.41	0.9694
219	101.2	98.5	-	0.663	1.383	0.725	0	1522.72	0.9664
223	100.8	91.8	-	0.358	1.377	0.728	0	1516.70	0.9045

APPENDIX 3 COLD-FLOW TEST DATA (Cont.)

Model III-10, Eight Chambers Touching Multichamber ε^*_{CL} = 49.8, 30% Length

Test Number	Chamber Pressure psia	F_{total} pounds	P_{base} psia	$P_{i.s.}$ psia	$\dot{W}_P$ lb/sec	$\dot{W}_B/\dot{W}_P$ percent	$\dot{W}_{i.s.}/\dot{W}_P$ percent	P_c/P_a	C_T total
226	99.8	85.2	–	0.574	1.392	0.732	0	150.24	0.9092
220	101.5	99.0	–	0.071	1.391	1.415	0	1503.48	0.9637
222	101.2	92.6	–	0.355	1.389	1.450	0	283.35	0.9450
227	101.0	85.6	–	0.581	1.398	1.492	0	151.56	0.9021
224	100.4	92.5	–	–	1.374	2.959	0	266.60	0.9368
225	99.8	92.2	–	0.358	1.384	2.982	0	265.99	0.9405

UNCLASSIFIED

APPENDIX 3 COLD-FLOW TEST DATA (Cont.)

Test Number	Chamber Pressure psia	F_{total} pounds	P_{base} psia	$P_{i.s.}$ psia	$\dot{w}_P$ lb/sec	$\dot{w}_g/\dot{w}_P$ percent	$\dot{w}_{i.s.}/\dot{w}_P$ percent	P_c/P_a	C_T total
		Model III-11, Eight Chambers Spaced Multichamber, ϵ^*_{CL} = 50.4, 30% Length							
266	100.6	83.79	1.046	0.977	1.376	0	0	101.24	0.9200
267	100.8	87.58	0.732	0.644	1.372	0	0	150.85	0.9411
268	100.6	89.53	0.543	0.492	1.375	0	0	202.04	0.9536
269	100.4	89.26	0.133	0.374	1.377	0	0	253.63	0.9416
270	100.6	94.17	0.085	0.136	1.377	0	0	748.62	0.9621
271	100.5	94.93	0.094	0.106	1.379	0	0	958.70	0.9621
272	100.7	95.79	0.096	0.067	1.384	0	0	1514.74	0.9591
273	101.0	95.83	0.100	0.067	1.386	0	0	1519.25	0.9597
274	100.9	95.89	0.098	0.068	1.390	0	0	1517.75	0.9614
275	101.0	96.27	0.097	0.050	1.394	0	0	2022.02	0.9591
276	101.0	93.20	0.087	0.191	1.404	0	0	530.35	0.9576
277	101.2	95.31	0.035	0.150	1.405	0	0.713	916.17	0.9567
278	101.2	95.04	0.072	0.180	1.402	0	1.424	938.95	0.9546
287	100.8	88.11	—	0.654	1.393	0.737	0	152.12	0.9406
280	101.2	96.67	—	0.107	1.402	1.506	0	940.17	0.9623
283	101.2	92.02	—	0.369	1.417	1.490	0	271.05	0.9510
285	101.0	88.59	—	—	1.327	1.511	0	153.33	0.9348
286	101.0	88.50	—	0.654	1.381	1.521	0	152.69	0.9370
281	101.2	97.29	—	0.108	1.402	2.625	0	919.16	0.9586
282	101.1	93.02	—	0.370	1.416	2.929	0	257.23	0.9497

CONFIDENTIAL
UNCLASSIFIED

APPENDIX 3 COLD-FLOW TEST DATA (Cont.)

Model III-12, Sixteen Chamber Touching Multichamber, ϵ^*_{CL} = 51.4, 30% Length

Test Number	Chamber Pressure psia	F total pounds	P base psia	P i.s. psia	$\dot{w}_p$ lb/sec	$\dot{w}_s/\dot{w}_p$ percent	$\dot{w}_{i.s.}/\dot{w}_p$ percent	P_c/P_a	C_T total
292	101.4	80.10	1.116	0.739	1.353	0	0	101.99	0.8944
293	101.2	79.91	1.133	0.783	1.350	0	0	101.02	0.8944
294	101.1	83.63	0.709	0.560	1.350	0	0	150.83	0.9200
295	101.1	83.73	0.707	0.559	1.352	0	0	150.95	0.9210
296	101.1	86.43	0.522	0.443	1.352	0	0	202.49	0.9389
297	101.0	85.34	0.521	0.431	1.353	0	0	201.86	0.9334
299	10..1	89.42	0.095	-	1.357	0	0	410.66	0.9479
300	101.0	88.94	0.325	0.329	1.355	0	0	302.35	0.9522
301	100.8	88.76	0.089	0.261	1.342	0	0	375.91	0.9423
302	101.0	93.60	0.101	0.190	1.347	0	0	1047.83	0.9654
303	101.0	94.29	0.094	0.072	1.346	0	0	1492.98	0.9655
304	100.9	94.25	0.088	0.073	1.345	0	0	1483.82	0.9661
305	100.9	94.64	0.083	0.060	1.344	0	0	2013.17	0.9650
352	149.5	135.40	0.132	0.269	2.023	0	0	545.46	0.9617
353	149.5	131.49	0.118	0.393	2.021	0	0	372.21	0.3449
354	149.5	138.94	0.130	0.128	2.020	0	0	1220.11	0.3672
355	149.5	127.31	0.963	0.848	2.020	0	0	149.82	0.9180
356	149.8	123.35	1.016	0.894	2.020	0	0	150.38	0.9180
306	101.2	94.35	0.069	0.231	1.352	0	0.751	1218.25	0.9615
308	101.2	95.08	0.081	0.360	1.464	0	1.464	1218.25	0.9623

APPENDIX 3 COLD-FLOW TEST DATA (Cont.)

CONFIDENTIAL

Test Number	Chamber Pressure psia	F_{total} pounds	P_{base} psia	$P_{i.s.}$ psia	$\dot{w}_P$ lb/sec	$\dot{w}_B/\dot{w}_P$ percent	$\dot{w}_{i.s.}/\dot{w}_P$ percent	P_c/P_a	C_T total
		Model III-12, Sixteen Chamber Touching Multichamber, ε^*_{CL} = 51.4, 30% Length							
313	101.3	95.03	0.213	0.088	1.368	0.753	0	1229.82	0.9688
320	101.5	84.60	0.771	0.557	1.371	0.755	0	153.55	0.9183
321	101.5	84.60	0.776	0.559	1.367	0.734	0	152.74	0.9184
347	101.6	91.07	0.348	0.281	1.371	0.760	0	372.12	0.9555
309	101.3	95.56	0.309	0.095	1.363	1.531	0	1209.26	0.9669
310	101.3	95.59	0.303	0.089	1.364	1.534	0	1229.82	0.9666
314	101.4	89.87	0.502	0.347	1.369	1.509	0	279.57	0.9472
319	101.5	85.21	0.850	0.556	1.372	1.512	0	153.26	0.9190
322	101.6	85.10	0.855	0.677	1.376	1.524	0	152.62	0.9166
348	101.5	91.47	0.406	0.269	1.363	1.531	0	365.03	0.9531
311	101.3	96.37	0.462	-	1.368	3.041	0	1174.90	0.9614
312	101.3	96.56	0.458	0.089	1.366	3.040	0	1209.26	0.9617
315	101.4	90.61	0.630	-	1.369	3.022	0	278.02	0.9407
316	101.5	90.80	0.629	0.345	1.374	3.021	0	278.03	0.9421
317	101.5	86.23	0.987	0.596	1.369	3.020	0	153.34	0.9159
318	101.5	86.23	0.937	0.554	1.371	3.023	0	153.34	0.9165

APPENDIX 3 COLD-FLOW TEST DATA (Cont.)

Model III-12, Sixteen Chambers Touching Multichamber With Filler Plate, ε^*_{CL} = 51.4, 30% Length

Test Number	Chamber Pressure psia	F_{total} pounds	P_{base} psia	$P_{i.s.}$ psia	$\dot{w}_P$ lb/sec	$\dot{w}_s/\dot{w}_P$ percent	$\dot{w}_{i.s.}/\dot{w}_P$ percent	P_c/P_a	C_T total
324	101.1	82.6	0.699	0.278	1.343	0	0	150.33	0.9081
325	101.1	82.6	0.697	0.275	1.343	0	0	150.23	0.9072
326	101.1	88.3	0.381	0.202	1.341	0	0	274.40	0.9465
327	101.1	89.4	0.177	0.181	1.345	0	0	367.25	0.9483
328	101.2	93.3	0.082	0.159	1.345	0	0	1077.40	0.9659
329	101.1	94.1	0.080	0.162	1.342	0	0	1269.76	0.9661
337	101.5	89.1	0.085	0.184	1.364	0	0	380.31	0.9436
338	101.6	65.2	0.091	0.185	1.367	0	0	377.32	0.9435
330	101.1	95.0	0.086	-	1.345	0	0.762	1253.10	0.9667
331	101.2	95.0	0.087	0.419	1.346	0	0.760	1245.69	0.9679
334	101.4	95.8	0.116	0.596	1.353	0	1.547	1230.13	0.9680
339	101.5	84.2	0.684	0.612	1.378	0	1.450	153.16	0.9087
335	101.5	97.2	0.148	0.950	1.360	0	2.958	1246.14	0.9679
340	101.6	85.2	0.666	0.942	1.376	0	2.948	15?.29	0.9060
336	101.5	97.9	0.150	1.127	1.364	0	3.999	1205.75	0.9668
341	101.6	84.7	0.763	0.615	1.379	0.754	1.444	153.42	0.9018
344	101.6	97.8	0.242	0.855	1.378	0.746	2.656	1222.18	0.9629
345	101.6	97.8	0.231	0.853	1.379	0.748	2.643	1334.73	0.9508
342	101.6	85.3	0.839	0.610	1.380	1.545	1.442	152.99	0.9012
343	101.6	93.2	0.311	0.853	1.377	1.547	2.647	1222.18	0.9603

APPENDIX 4

WEIGHT FLOW AND WEIGHT FLOW DEPENDENT PARAMETER CALCULATIONS
FOR TETRAFLUOROMETHANE (CF$_4$)

APPENDIX 4

WEIGHT FLOW AND WEIGHT FLOW DEPENDENT PARAMETER CALCULATIONS FOR
TETRAFLUOROMETHANE (CF_4)

(U) At Rocketdyne's Rocket Nozzle Test Facility (RNTF) metering the mass-
flow of the test fluids is accomplished through the use of critical
flow nozzles (Sonic Venturi Meters).

(U) For a perfect gas the equation of continuity, the perfect gas equation
and the isentropic relations to go from the reservoir stagnation
conditions to the throat leads to the following equation

$$\dot{W} = f \; \frac{A^* P_0}{\sqrt{T_0}} \qquad (1)$$

where

$$f = \sqrt{\frac{\gamma}{R} \left(\frac{2}{\gamma + 1}\right)^{\frac{\gamma + 1}{\gamma - 1}}}$$

(U) When the geometrical throat area is used Eq. 1 should be multiplied by
a discharge coefficient (C_w) to account for viscous effects and dis-
tortions in the sonic velocity profile.

(U) The term f is called the critical flow constant and historically has
been referred to as Fliegners constant. The above relationship is
however based on the assumption that the gas has a specific heat ratio
(γ) that is independent of pressure and temperature and a compress-
ibility factor of unity. For most gases at high pressures and/or low
temperature significant errors in mass flow calculations are introduced

400

if the above relations are used. For example at the operating temperatures and pressure employed at RNTF with air as a test fluid errors on the order of 1 percent could be introduced into the mass flow calculations if the ideal ratio of specific heats ($\gamma = 1.40$) was employed.

(U) To circumvent this problem critical flow functions that take into account such "real-gas" effects as compressibility and specific heat variations with temperature and pressure are employed.

(U) The method employed to obtain the pressure-temperature dependent critical flow function is based on a procedure where the throat static state is assumed and the upstream stagnation state at the same entropy, but at an enthalpy that is increased by the enthalpy change needed to accelerate the gas to the speed of sound, is determined. Use of this method requires either tabulated values of entropy, enthalpy, specific volume or density and sonic velocity as a function of temperature and pressure or an equation of state which will give suitable first and second derivatives.

(U) The detailed procedure involves the following steps

1. For a given stagnation temperature (T_o) and pressure (P_o) estimate the throat static pressure (P^*) and temperature (T^*) having an entropy (S_o) the same as that at the stagnation conditions.

2. Determine the local sonic velocity for the throat static conditions and solve for the enthalpy, required to obtain the sonic velocity using the following equation

$$\Delta h = a^{*2}/2gJ \qquad (2)$$

401

3. Determine the stagnation enthalpy (h_o) required to obtain the sonic velocity.

$$h_o = h* + \Delta h \tag{3}$$

4. For the given stagnation entropy (S_o) and calculated enthalpy (h_o) determine the corresponding stagnation pressure (P_o') and temperature (T_o'). If P_o' and T_o' are not equal to the initial specified P_o and T_o step 1 through 4 is repeated until agreement is obtained.

5. The pressure-temperature dependent critical flow function for a specific gas is then calculated using the following equation

$$f(T_o, P_o) = \frac{\dot{W}\sqrt{T_o}}{P_o A*} = \frac{\rho* a*\sqrt{T_o}}{P_o} \tag{4}$$

(U) The gas properties of air required for the above calculations can be obtained from Ref. 20 . However as the pressure and temperature dependent critical flow function is available in various published papers (Ref. 21 and 22) additional calculation was not required.

(U) For Tetrafluoromethane the Martin-Hou equation of state (Ref. 23) was used to obtain the pressure-temperature volume relationship. Tabulated values of entropy and enthalpy were obtained from Ref. 24 . The ratio of the specific heats was calculated in the manner outlined in Ref. 10 and the sonic velocity calculations are described in Ref. 25 .

(U) To obtain the one dimensional ideal thrust coefficient the following fundamental thrust equation is used

$$F = \dot{m} V_e + (P_e - P_a) A_e \tag{5}$$

(U) For optimum conditions $(P_e = P_a)$ the above equation reduces to

$$F_{opt} = \dot{m} \, V_e \qquad (6)$$

(U) Dividing through by $P_o A^*$ the relationship for the one dimensional ideal optimum thrust coefficient is

$$C_{F_{opt}} = \frac{F_{opt}}{P_o A^*} = \frac{\dot{m} \, V_e}{P_o A^*}$$

which reduces to

$$C_{F_{opt}} = \frac{\rho^* a^* \, V_e}{P_o} = \frac{f \, (T_o, \, P_o) \, V_e}{\sqrt{T_o}} \qquad (7)$$

(U) If the pressure-temperature dependent critical flow function is available the one dimensional optimum thrust coefficient can be readily obtained by calculation of the exit velocity obtained for an isentropic expansion of the flow from reservoir stagnation (P_o) to ambient pressure (P_e) as given by the following equation

$$V_e = \sqrt{2 g_c J \left(h \, (T_o, \, P_o) - h \, (P_e, \, S_o) \right)}$$

(U) A series of these calculations have indicated that for the operating temperatures and pressures employed at the RNTF a representative ratio of specific heats can be employed to obtain an optimum C_F. For Air the representative γ is 1.4 and for CF_4 the representative γ is 1.2.

APPENDIX 5

ENGINE SEGMENT TEST DATA

APPENDIX 5 ENGINE SEGMENT TEST DATA

Test Number	Segment Angle Degrees	P_o Chamber Pressure psia	P_A Ambient Pressure psia	P_c/P_A	P_B Base Pressure psia	P_B/P_c	$\dot{W}_p$ Primary Flow Rate lb/sec	$\dot{W}_s/\dot{W}_p$ Ratio or Secondary to Primary Flow Rate Percent
001	45	199.75	.1649	1213	.473	.00257	.420	0
002	45	200.0	.1704	1175	.702	.00351	.419	.853
003	45	199.55	.1630	1226	.461	.00231	.416	0
004	45	199.80	1.670	119.7	1.486	.00744	.418	0
005	45	199.90	1.675	119.4	1.587	.00794	.417	.860
006	45	199.92	.1685	1188	.696	.00348	.417	.863
007	45	199.80	1.668	119.9	1.578	.00790	.417	.863
008	45	200.10	1.663	120.4	1.473	.00736	.418	0
038	90	196.65	.1832	1078	.340	.00173	.783	0
039	90	195.90	.1649	1190	.570	.00291	.780	.898
040	90	198.25	1.675	118.8	1.594	.00804	.794	.874
041	90	199.85	1.659	120.6	1.451	.00726	.802	0
042	90	199.15	.1676	1193	.346	.00174	.794	0
043	90	197.30	1.663	119.3	1.586	.00804	.797	.635
026	180*	200.20	1.656	121.4	1.746	.00862	1.632	.850
027	180*	199.90	1.660	120.2	1.443	.00722	1.632	0
029	180*	195.25	.1887	1040	.357	.00183	1.562	0
030	180*	199.40	.1924	1038	.624	.00313	1.599	.863

* One-half of the full (360 degrees) throat annulus blocked-off.

CONFIDENTIAL

APPENDIX 5 ENGINE SEGMENT TEST DATA (CONTINUED)

Test Number	Segment Angle Degrees	P_c Chamber Pressure psia	P_A Ambient Pressure psia	P_c/P_A	P_B Base Pressure psia	P_B/P_c	W_P Primary Flow Rate lb/sec	W_s/W_P Ratio or Secondary to Primary Flow Rate Percent
031	180*	197.75	1.666	118.9	1.554	.00786	1.601	0
032	180*	199.55	1.672	119.9	1.395	.00699	1.621	0
033	180**	196.55	1.670	118.1	1.514	.00770	1.598	.868
034	180***	197.0	1.670	117.8	2.025	.01028	3.0435	.875
035	180****	199.35	1.636	121.7	1.782	.00894	3.098	0
036	180***	197.75	.1905	1038	.435	.00220	3.081	0
037	180***	198.40	.1685	1172	.665	.00335	3.086	.862
020	360**	199.25	1.681	117.2	2.097	.01058	3.141	.908
021	360**	197.30	1.677	116.8	1.849	.00957	3.109	0
022	360**	197.60	.1658	1187	.444	.00225	3.102	0
023	360**	198.30	.1640	1204	.690	.00348	3.101	.887
024	360**	199.35	.1676	1181	.450	.00226	3.115	0
025	360**	198.65	1.679	117.8	2.088	.01051	3.113	.860

* Full throat annulus open

** No splitter plates - reference model

REFERENCES

*1. R-5940, DDC No. AD- 4583: *Advanced Aerodynamic Spike Configurations, First Quarterly Progress Report*, Rocketdyne, a Division of North American Aviation, Inc., Canoga Park, California, October 1964, Confidential.

2. Addy, A. L. : *On the Steady State and Transient Operating Characteristics of Long Cylindrical Shroud Supersonic Ejectors*, University of Illinois, June 1963.

3. PWA PR-1013, "*Final Report, Plug Cluster Nozzle Study*," Pratt and Whitney Aircraft Division of United Aircraft Corporation, Florida Research and Development Center, September 1964, Confidential.

4. Shapiro, A. H. : *The Dynamic and Thermodynamics of Compressible Fluid Flow*, Volumes I and II, Ronald Press, New York.

5. Liepmann, H. W. and A. Roshko: *Elements of Gas Dynamics*, John Wiley and Sons, Inc., New York, 1960.

6. Persh, J. and L. Roland: *A Method for Calculating Turbulent Boundary Layer Development in Supersonic and Hypersonic Nozzles, Including the Effects of Heat Transfer*, NAVORD 2400, Aeroballistic Research Report No. 320.

7. Schlichting, Dr. Herman: *Boundary Layer Theory*, 4th Ed., McGraw-Hill, New York, 1960.

8. Elliot, David, G. Donald, R. Bartz, and Sidney Silver: *Calculations of Turbulent Boundary-Layer Growth and Heat Transfer in Axi-Symmetric Nozzles*, Technical Report No. 32-387, Jet Propulsion Laboratory, California Institute of Technology, Pasadena, California.

9. Eckert, E. R. G. and Robert M. Drake Jr.: *Heat and Mass Transfer* 2nd Ed., McGraw-Hill, New York, 1959

10. Bulletin X-34, Proposed Program for Calculation of C_p, C_v and C_p/C_v for "Freon-14", E.I. DuPont de Nemours and Co., Wilmington, Delaware.

11. R-6273, Aerodynamic Nozzle Study, Interim Report, Rocketdyne, a Division of North American Aviation, Inc., Canoga Park, California, Confidential.

12. PWA FR-1415, Study for Evaluation of Plug Multichamber Configuration, Pratt & Whitney Aircraft, October 1965, Confidential.

13. McCarthy, J. R., W. S. Hines, J. D. Seader, D. M. Tribes: Regenerative Cooling Characteristics of 50-50 Fuel and Nitrogen Tetroxide at Supercritical Pressures, Presented at the Interagency Chemical Rocket Propulsion Group Sixth Interagency Liquid Propulsion Symposium, Rocketdyne, 23 September 1964.

14. R3552-4P, Final Program Progress Report for Product Engineering, Rocketdyne, Division of North American Aviation, Incorporated, 6633 Canoga Avenue, Canoga Park, California, 23 February 1963, Confidential.

15. Elliot, D. G., D. R. Bartz, S. Silver: Calculation of Turbulent Boundary-Layer Growth and Heat Transfer in Axi-Symmetric Nozzles, T.R. 32-387, Jet Propulsion Laboratory, Pasadena, California, 2-15-63.

16. R-6199, Investigation of Cooling Problems at High Chamber Pressures, Final Report for Period 1 July 1963 to 31 March 1965, Rocketdyne, A Division of North American Aviation, Inc., May 1965.

17. R5136-4P, Final Technical Report for Product Engineering, Contract AF04(694)-110, Vol. 4, Rocketdyne, 31 May 1964, Confidential.

18. R-6494, Multichamber, Plug Nozzle Systems Analysis, Rocketdyne, a Division of North American Aviation, Inc., Canoga Park, California, Confidential.

19. R-6582, Aerodynamic Nozzle Study, Rocketdyne, a Division of North American Aviation, Inc., Canoga Park, California, Confidential.

20. Circular 564, Tables of Thermal Properties of Gases, U. S. Department of Commerce, National Bureau of Standards, Washington, D.C., November 1, 1955.

21. Reimer, Robert M., Computation of the Critical Flow Function, Pressure Ratio and Temperature Ratio for Real Air, Journal of Basic Engineering, June 1964.

22. Johnson, Robert C., Real-Gas Effects in Critical-Flow-Through Nozzles and Tabulated Thermodynamic Properties, NASA TN-D-2565, Lewis Research Lab.

23. Glotzer, Herman L., Properties of "Freon-14" Fluorcarbon in the Gaseous State, Technical Bulletin B-36, E. I. duPont Nemours and Co., Wilmington, Delaware.

24. Technical Report T-14, Preliminary Thermodynamic Properties of Freon-14, E. I. duPont Nemours and Co., Wilmington, Delaware.

25. Smith, S. J., Suitability of Martin-Hou Equation of State for Describing Freon-14, IAPR No. 65-19, 1 March 1965, Rocketdyne, a Division of North American Aviation, Inc., Canoga Park, California.

26. R-6226, Interim Report, Toroidal System Analysis Study, Rocketdyne, a Division of North American Aviation, inc., Canoga Park, California, 30 June 1965, Confidential.

*27. R-6516, Final Report, Toroidal System Analysis Study, Rocketdyne, a Division of North American Aviation, Inc., Canoga Park, California, April 1966, Confidential.

411

*28. R-6494, Multichamber, Plug Nozzle Systems Analysis, Rocketdyne, a Division of North American Aviation, Inc., Canoga Park, California, May 1966, Confidential.

*29. R-6953-1, Evaluation of High Thrust, Advanced Booster Propulsion Systems, Final Report, Rocketdyne, a Division of North American Aviation, Inc., Canoga Park, California, June 1967, Confidential.

*Classified material (all Confidential, Group 4) from asterisked reports has been used in this report.

DOCUMENT CONTROL DATA - R&D		
(Security classification of title, body of abstract and indexing annotation must be entered when the overall report is classified)		

1. ORIGINATING ACTIVITY (Corporate author)	2a. REPORT SECURITY CLASSIFICATION
Rocketdyne, a Division of North American Aviation, Inc., 6633 Canoga Avenue, Canoga Park, California	Confidential
	2b. GROUP 4

3. REPORT TITLE

FINAL REPORT, ADVANCED AERODYNAMIC SPIKE CONFIGURATIONS
Volume I - Analytical and Cold Flow Studies

4. DESCRIPTIVE NOTES (Type of report and inclusive dates)

Final Report (1 July 1964 through 30 June 1967)

5. AUTHOR(S) (Last name, first name, initial)

Advanced Projects
Large Engines
Rocketdyne

6. REPORT DATE	7a. TOTAL NO. OF PAGES	7b. NO. OF REFS
September 1967	436	29

8a. CONTRACT OR GRANT NO.	9a. ORIGINATOR'S REPORT NUMBER(S)
AF04(611)-9948	
b. PROJECT NO.	R6959
3058	
c.	9b. OTHER REPORT NO(S) (Any other numbers that may be assigned this report)
d.	AFRPL-TR-67-245-Vol I

10. AVAILABILITY/LIMITATION NOTICES

This document is subject to special export controls and each transmittal to foreign governments or foreign nationals may be made only with prior approval of AFRPL (RPPR/STINFO), Edwards, California 93523

11. SUPPLEMENTARY NOTES	12. SPONSORING MILITARY ACTIVITY
	Air Force Rocket Propulsion Laboratory Research and Technology Division Edwards, California

13. ABSTRACT

Investigations of the aerodynamic spike nozzle concept are discussed in this report. Cold-flow test programs to evaluate high area ratio aerodynamic spike nozzles, engine segment testing techniques, and combustor configurations for aerodynamic spike nozzles were completed. A description of the models tested and the test results are presented. Analytical (performance, weight, heat transfer, reliability and cost) and design studies of the aerodynamic spike nozzle concept were conducted and the results are presented.

DD FORM 1473

14. KEY WORDS	LINK A		LINK B		LINK C	
	ROLE	WT	ROLE	WT	ROLE	WT
1. Aerodynamic nozzles						
2. Multichamber nozzles						
3. Effect of Secondary flow						
4. Base configuration effects						
5. Cold-flow testing						
6. Nozzle performance						
7. Nozzle base pressure						
8. Engine designs						
9. Nozzle heat transfer						
10. Nozzle weight						
11. Reliability						
12. Engine versatility						
13. Development cost						
14. Segmented nozzle testing						

INSTRUCTIONS

1. ORIGINATING ACTIVITY: Enter the name and address of the contractor, subcontractor, grantee, Department of Defense activity or other organization (corporate author) issuing the report.

2a. REPORT SECURITY CLASSIFICATION: Enter the overall security classification of the report. Indicate whether "Restricted Data" is included. Marking is to be in accordance with appropriate security regulations.

2b. GROUP: Automatic downgrading is specified in DoD Directive 5200.10 and Armed Forces Industrial Manual. Enter the group number. Also, when applicable, show that optional markings have been used for Group 3 and Group 4 as authorized.

3. REPORT TITLE: Enter the complete report title in all capital letters. Titles in all cases should be unclassified. If a meaningful title cannot be selected without classification, show title classification in all capitals in parenthesis immediately following the title.

4. DESCRIPTIVE NOTES: If appropriate, enter the type of report, e.g., interim, progress, summary, annual, or final. Give the inclusive dates when a specific reporting period is covered.

5. AUTHOR(S): Enter the name(s) of author(s) as shown on or in the report. Enter last name, first name, middle initial. If military, show rank and branch of service. The name of the principal author is an absolute minimum requirement.

6. REPORT DATE: Enter the date of the report as day, month, year; or month, year. If more than one date appears on the report, use date of publication.

7a. TOTAL NUMBER OF PAGES: The total page count should follow normal pagination procedures, i.e., enter the number of pages containing information.

7b. NUMBER OF REFERENCES: Enter the total number of references cited in the report.

8a. CONTRACT OR GRANT NUMBER: If appropriate, enter the applicable number of the contract or grant under which the report was written.

8b, 8c, & 8d. PROJECT NUMBER: Enter the appropriate military department identification, such as project number, subproject number, system numbers, task number, etc.

9a. ORIGINATOR'S REPORT NUMBER(S): Enter the official report number by which the document will be identified and controlled by the originating activity. This number must be unique to this report.

9b. OTHER REPORT NUMBER(S): If the report has been assigned any other report numbers (either by the originator or by the sponsor), also enter this number(s).

10. AVAILABILITY/LIMITATION NOTICES: Enter any limitations on further dissemination of the report, other than those

imposed by security classification, using standard statements such as:

(1) "Qualified requesters may obtain copies of this report from DDC."

(2) "Foreign announcement and dissemination of this report by DDC is not authorized."

(3) "U. S. Government agencies may obtain copies of this report directly from DDC. Other qualified DDC users shall request through

_____."

(4) "U. S. military agencies may obtain copies of this report directly from DDC. Other qualified users shall request through

_____."

(5) "All distribution of this report is controlled. Qualified DDC users shall request through

_____."

If the report has been furnished to the Office of Technical Services, Department of Commerce, for sale to the public, indicate this fact and enter the price, if known.

11. SUPPLEMENTARY NOTES: Use for additional explanatory notes.

12. SPONSORING MILITARY ACTIVITY: Enter the name of the departmental project office or laboratory sponsoring (paying for) the research and development. Include address.

13. ABSTRACT: Enter an abstract giving a brief and factual summary of the document indicative of the report, even though it may also appear elsewhere in the body of the technical report. If additional space is required, a continuation sheet shall be attached.

It is highly desirable that the abstract of classified reports be unclassified. Each paragraph of the abstract shall end with an indication of the military security classification of the information in the paragraph, represented as (TS), (S), (C), or (U)

There is no limitation on the length of the abstract. However, the suggested length is from 150 to 225 words.

14. KEY WORDS: Key words are technically meaningful terms or short phrases that characterize a report and may be used as index entries for cataloging the report. Key words must be selected so that no security classification is required. Identifiers, such as equipment model designation, trade name, military project code name, geographic location, may be used as key words but will be followed by an indication of technical context. The assignment of links, rules, and weights is optional.